Manipulating 0D, 1D and 2D nanomaterials by vortex fluidic device

By

Ahmed Hussein Mohammed Al-Antaki

Thesis

Submitted to Flinders University

for the degree of

Doctor of Philosophy in Chemistry

College of Science and Engineering

29/09/2021

CONTENTS

LIST OF FIGURES

APPENDICES

LIST OF TABLES

LIST OF ABBREVIATIONS

AFM	Atomic force microscopy
FT-IR	Fourier transform infrared spectroscopy
h-BN	Hexagonal boron nitride
BNNTs	Boron nitride nanotubes
HRTEM	High resolution transmission electron microscopy
ID	Inner diameter
IONP	Iron oxide nanoparticle
MW	Molecular weight
MWCNT	Multi walled carbon nanotube
NMP	N-methyl pyrrolidine
DMF	Dimethylformamide
0D	Zero dimensional
1D	One dimensional
2D	Two dimensional
NIR	Near infrared
OD	Outer diameter
SAED	Selected area electron diffraction
SWCNT	Single walled carbon nanotube
SEM	Scanning electron microscopy
SANS	Small angle neutron scattering
TEM	Transmission electron microscopy
TGA	Thermo-gravimetric analysis
UV-Vis	Ultraviolet visible spectroscopy
VFD	Vortex fluidic device
DWCNT	Double walled carbon nanotube
XRD	X-ray powder diffraction
DLS	Dynamic light scattering

SUMMARY

The focus of the research in this thesis is expanding the application of the vortex fluidic device (VFD), in both the top down and bottom up fabrication of nanomaterials. The VFD is a versatile thin film microfluidic platform which imparts mechanical energy in the liquid, and can operate under so called confined mode or continuous flow where scalability of any process is addressed early in the research. It has been used for exfoliating 2D materials, slicing 1D material, the *in situ* growth of metal oxides, and the fabrication of composites with other nanomaterials. In all studies, the operating parameters of the VFD were systematically varied in arriving at an optimised process. The operating parameters include, rotational speed of the glass tube, flow rate, tilt angle, and the concentration of reagents or feedstocks.

A process for exfoliating along with fragmenting 2D MXene (Ti_2C) has been developed, down to a few sheets of the material and particles ca 68 nm in diameter, respectively. The process operates under an inert atmosphere to avoid oxidation, and avoids the need for auxiliary reagents or harsh chemicals, relying on the shear stress in the dynamic thin film of the VFD. In the presence of oxygen, oxidation to anatase (TiO_2) occurs, facilitated by the high mass transfer of oxygen into the thin film. The oxidation can be controlled by carrying out the processing in 30% hydrogen peroxide, converting MXene (Ti_2C) into a composite of anatase nanoparticles with the 2D material, TiO_2 NPs/MXene, with self-assembled fragments of MXene and anatase organised into spheres approximately 2 μm± 0.5 μm in diameter. The TiO_2 NPs anatase spheres decorate the surface of the exfoliated MXene sheets.

The VFD was effective also in exfoliating hexagonal-BN sheets (*h*-BN) down to a few sheets, or by changing the operating parameters of the device, the formation of *h*-BN scrolls, as a process high in green chemistry metrics, using water as the solvent. However, using the common 45^o tilt angle of the tube in the VFD, which is the optimised tilt angle for a wide range of applications, there was a build-up of material in the rapidly rotating tube. This build up was avoided by operating the device with the tube tilted at -45^o, as a paradigm shift in the operation of the VFD.

A simple and robust process has been developed for purifying as received boron nitride nanotubes (BNNTs). This was necessary to then develop a process in the VFD for disentangling and slicing BNNTs, in the absence of surfactants and harsh chemicals, relying on the mechanical energy in the dynamic thin film along with energy imparted from a NIR pulsed laser operating at 1064 nm. The ensuing optimised process highlights a utility of the VFD in being able to readily incorporate field effects around the rotating tube. The ability to slice BNNTs opens potential applications beyond those for entangled BNNTs, including vehicles for drug and protein delivery, with the payload inside the tubes, and boron neutron capture therapy.

In situ laser ablation was effective in decorating *h*-BN sheets with superparamagnetic magnetite nanoparticles in water, also as a green chemistry initiative. This involved irradiating a pure iron metal target inside the rapidly rotating tube in the VFD. The resulting composite material *h*-BN@magnetite was effective in removing phosphate from waste water. In the same vein, nanoparticles of dicopper oxide (Cu_2O) can be generated in the VFD in water as a one step process under continuous flow, with the particles averaging 14 nm in diameter. These nanoparticles can be converted to slightly smaller nanoparticles of copper oxide (CuO), 11 nm in diameter, by mild heating of an aqueous suspension of the dicopper oxide nanoparticles in water.

The new chemistry and processing capabilities of the VFD reported in this thesis make a significant contribution to unlocking the full potential of the thin film microfluidic platform, filling this gap of research towards many industrial applications. This includes avoiding the use of reagents which can pose a threat to the environment, while making the process attractive to industry. Moreover, the materials prepared in the VFD are themselves high value-added functional nanomaterials.

DECLARATION

I certify that this thesis does not incorporate without acknowledgment any material previously submitted for a degree or diploma in any university; and that to the best of my knowledge and belief it does not contain any material previously published or written by another person except where due reference is made in the text.

Signed: Ahmed Al-Antaki

Date: 29/09/2021

ACKNOWLEDGEMENTS

I acknowledge with many thanks my PhD thesis supervisors, Prof. Colin L. Raston and Prof. Warren D. Lawrance, and Raston group. Furthermore, the financial support and research funding from the Iraq Government, Ministry of Higher Education and Scientific Research, University of Kufa, and the Australian Research Council and Government of South Australia is graciously acknowledged, as is access to microscope facilities at the Australia Microscopy & Microanalysis Research Facility (AMMRF) and the Australian National Fabrication Facility (ANFF) for accessing microscopic facilities, and proof reading by Dr. Xuan Luo.

Also, I would like to thank my family members, especially my parents, my wife Yusur Al-Shammari and my wife's parents for truly believing in me and for providing me with great support.

DETAILS OF PUBLICATIONS

Journal articles

1. Ahmed Hussein Mohammed Al-antaki, Thaar MD Alharbi, Suela Kellici, Nicholas P Power, Warren Lawrance, Colin L Raston, Vortex Fluidic Mediated Synthesis of TiO2 Nanoparticle/MXene Composites, ChemNanoMat 2020, 6(4), 657-662.
2. Ahmed Hussein Mohammed Al-antaki, Suela Kellici, Nicholas P Power, Warren Lawrance, Colin L Raston, Continuous flow vortex fluidic-mediated exfoliation and fragmentation of two-dimensional MXene, Royal Society Open Science, 2020, 7(5), 192255.
3. Ahmed Hussein Mohammed Al-Antaki, Warren Lawrance, and Colin L. Raston, Dynamic thin film mediated slicing of boron nitride nanotubes, Nanoscale Advances 2019, 1(12), 4722-4728.
4. Ahmed Hussein Mohammed Al-Antaki, Xuan Luo, XiaoFei Duan, Robert N. Lamb, Wayne D. Hutchison, Warren Lawrance, and Colin L. Raston, Continuous Flow Copper Laser Ablation Synthesis of Copper (I and 2 II) Oxide Nanoparticles in Water. ACS Omega 2019, 4(8), 13577-13584.
5. Ahmed Hussein Mohammed Al-Antaki, Xuan Luo, Thaar M. D. Alharbi, David P. Harvey, Scott Pye, Jin Zou, Warren Lawrance and Colin L. Raston, Inverted vortex fluidic

exfoliation and scrolling of hexagonal-boron nitride. RSC Advances 2019, 9 (38), 22074-22079.

6. Al-Antaki, A. H. M.; Luo, X.; Duan, A.; Lamb, R. N.; Eroglu, E.; Hutchison, W.; Zou, Y. C.; Zou, J.; Raston, C. L., Continuous flow synthesis of phosphate binding h-BN@magnetite hybrid material. RSC Advances 2018, 8 (71), 40829-40835.
7. High shear vortex fluidic morphologically controlled polysulfone formed under anhydrous conditions, publication date Apr 25, 2021 publication description Aghil Igder, Ahmed Hussein Mohammed Al-Antaki, Scott J. Pye, Alireza Keshavarz, Ata Nosratia and Colin L. Raston.
8. Xuejiao Cao, Nikita Joseph, Matt Jellicoe, Ahmed Hussein Mohammed Al-Antaki, Xuan Luo, Dongxiao Su, Shan He, Colin Raston, Vortex fluidics mediated non-covalent physical entanglement of tannic acid and gelatin for entrapment of nutrients, RSC Food & Function, 2021, 12, 1087–1096.
9. Shan He, Nikita Joseph, Marzieh Mirzamani, Scott J Pye, Ahmed Hussein Mohammed Al-Antaki, Andrew E Whitten, Yaonan Chen, Harshita Kumari, Colin L Raston, Vortex fluidic mediated encapsulation of functional fish oil featuring in situ probed small angle neutron scattering, npj Science of Food, 2020, 4(1), 1-11.
10. Xuan Luo, Ahmed Hussein Mohammed Al-Antaki, Aghil Igder, Keith A Stubbs, Peng Su, Wei Zhang, Gregory A Weiss, Colin L Raston, Vortex fluidic-mediated fabrication of fast gelated silica hydrogels with embedded laccase nanoflowers for real-time biosensing under flow, ACS Applied Materials & Interfaces, 12(46), 2020, 51999-52007.
11. Aghil Igder, Scott Pye, Ahmed Hussein Mohammed Al-Antaki, Alireza Keshavarz, Colin L Raston, Ata Nosrati, Vortex fluidic mediated synthesis of polysulfone, 2020, RSC Advances, 10(25), 14761-14767.
12. Alharbi, Thaar M. D., A. H. M. Al-Antaki, M. Moussa, W. D. Hutchison and C. L. Raston (2019). "Three-step-in-one synthesis of supercapacitor MWCNT superparamagnetic magnetite composite material under flow." Nanoscale Advances 1(9): 3761-3770.
13. Luo X.; Al-Antaki A. H. M.; Alharbi T. M. D.; Hutchison W. D.; Zou Y.; Zou J.; Sheehan A.; Zhang W., Raston C. L., Laser ablated vortex fluidic mediated synthesis of superparamagnetic magnetite nanoparticles in water under flow, ACS Omega 2018, 3 (9), 11172-11178.
14. Luo, X.; Al-Antaki, A. H. M.; Harvey, D. P.; Ruan, Y.; He, S.; Zhang, W.; Raston, C. L., Vortex fluidic mediated synthesis of macroporous bovine serum albumin-based microspheres. ACS Applied Materials & Interfaces 2018, 10 (32), 27224-27232.

15. Luo, X.; Al-Antaki, A. H. M.; Vimalanathan, K.; Moffatt, J.; Zheng, K.; Zou, Y.; Zou, J.; Duan, X.; Lamb, R. N.; Wang, S.; Li, Q.; Zhang, W.; Raston, C. L., Laser irradiated vortex fluidic mediated synthesis of luminescent carbon nanodots under continuous flow. *Reaction Chemistry & Engineering* **2018,** *3* (2), 164-170.
16. Luo, X.; Al-Antaki, A. H. M.; Pye, S.; Meech, R.; Zhang, W.; Raston, C. L., High-shear-imparted tunable fluorescence in polyethylenimines. *ChemPhotoChem* **2018,** *2* (4), 343-348.

Patent contributions

1. Processing for controlling structure and/or properties of carbon and boron nanomaterials, 2017. (Luo, X.; Al-Antaki, A. H. M.; Vimalanathan, K.; Moffatt, J.; Zheng, K.; Zou, Y.; Zou, J.; Duan, X.; Lamb, R. N.; Wang, S.; Li, Q.; Zhang, W.; Raston, C. L., Laser irradiated vortex fluidic mediated synthesis of luminescent carbon nanodots under continuous flow. Reaction Chemistry & Engineering 2018, 3 (2), 164-170). The PCT international application number (PCT/AU2017/000237 filed on Nov. 10,2017)
2. A novel process for fabricating polyethyleneimine (PEI)-based fluorescent nanoparticles from PEI with different molecular weights, 2017. (Luo, X.; Al-Antaki, A. H. M.; Pye, S.; Meech, R.; Zhang, W.; Raston, C. L., High-shear-imparted tunable fluorescence in polyethylenimines. *ChemPhotoChem* **2018,** *2* (4), 343-348).

Conference presentations

1. Ahmed Hussein Mohammed Al-Antaki, Sula Kellici, Warren Lawrence and Colin Raston, **2019 '**Vortex fluidic mediated exfoliation of 2D MXene', College of Science and Engineering HDR 3^{ed} Conference in Flinders University.
2. Ahmed Hussein Mohammed Al-Antaki, Sula Kellici, Warren Lawrence and Colin Raston, **2019 '**Vortex fluidic mediated exfoliation of 2D MXene', Flinders Institute for Nanoscale Science and Technology's 9th Annual Conference.
3. Ahmed Hussein Mohammed Al-Antaki, Warren Lawrence and Colin Raston, **2018 '**Manipulating boron nitride nanotubes (BNNTs) and hexagonal –BN (*h*-BN) in dynamic thin films**'**, HDR conference in College of Scinece and Enginering, Flinders University.
4. Ahmed Hussein Mohammed Al-Antaki, Warren Lawrence and Colin Raston, **2018 '**Manipulating boron nitride nanotubes (BNNTs) and hexagonal –BN (*h*-BN) in dynamic thin films**'**, Flinders Institute for Nanoscale Science and Technology's 8th Annual

Conference.

5. Ahmed Hussein Mohammed Al-Antaki, Warren Lawrence and Colin Raston, **2018 ‘**Manipulating boron nitride nanotubes (BNNTs) and hexagonal –BN (*h*-BN) in dynamic thin films**’,** ICONN international conference, Wollongong, Australia.
6. Ahmed Hussein Mohammed Al-Antaki, Warren Lawrence and Colin Raston, **2017 ‘**Manipulating boron nitride nanotubes (BNNTs) and hexagonal –BN (*h*-BN) in dynamic thin films**’**, HDR confernece in College of Scinece and Enginering, Flinders University.
7. Ahmed Hussein Mohammed Al-Antaki, Warren Lawrence and Prof. Colin Raston, **2017 ‘**Manipulating boron nitride nanotubes (BNNTs) and hexagonal –BN (*h*-BN) in dynamic thin films**’**, RACI Centenary Congress, Melbourne, Australia.
8. Ahmed Hussein Mohammed Al-Antaki, Xuan Luo, Warren Lawrence and Colin Raston, **2017 ‘**Controlling the size and content of Iron oxide incorporated in hexagonal boron nitride using dynamic thin film processing**’**, Flinders Institute for Nanoscale Science and Technology’s 7th Annual Conference.
9. Ahmed Hussein Mohammed Al-Antaki, Colin Raston, **2016 ‘**Manipulating boron nitride nanotubes (BNNTs) and hexagonal –BN in dynamic thin films**’,** Flinders Institute for Nanoscale Science and Technology’s 7th Annual Conference.

1. INTRODUCTION

This chapter serves to introduce the different areas of science relevant to the research program undertaken in thesis. Incorporating different hybridization states of atoms within materials (sp, sp^2 and sp^3), different oxidation states of metals, and different types of structural arrangement of atoms, result in different properties at the nanometre dimensions, and thus different applications in materials science and nanotechnology. Indeed, the ability to fabricate and manipulate nanomaterials using a variety of techniques has opened a myriad of potential applications where there is size and morphology dependent applications. This chapter is divided into different classes of materials featured in the research, namely MXene and composites thereof, hexagonal-BN (*h*-BN) and composites thereof, boron nitride nanotube (BNNTs), and dicopper oxide and copper oxide, along with the background of the development and applications thus far of the vortex fluidic device (VFD).

1.1 MXene ($M_{n+1}X_nT_x$)

MXene is a family of layered compounds (2D materials) consisting of nanosheets of titanium with carbide or carbonitrides, first reported in 2011.[1] The MXene form is $M_{n+1}X_nT_x$, where M is transition metal (Ti, Zr, Nb, V, Ta, or Mo), X is C and/or N, and n is 1, 2, or 3. Also, MXene has functional groups (T) such as (−O, −OH, −F) on both sides of the nano-sheets, as in Figure 1.1.[2] Recently its use as an electrochemical energy storage medium was established, which involved inserting lithium or sodium ions between the 2D layers.[3,4] This composite material has supercapacitor properties, and has been used in batteries as an alternative material to current ones, Figure 1.2(a).[5] An electrochemical reaction is any process either caused or accompanied by the passage of an electric current, involving in most cases the transfer of electrons between two substances - a solid and a liquid.[6] However, the mechanism of electrochemistry associated with this kind of material is not clearly understood.[7] Another application of MXene is in biology,[8-10] featuring in a device for biosensing which is based on field-effect transistors (MXene-FET). The device is able to detect small biological molecules including dopamine which is significant in that the molecule regulates many brain functions, as exemplified in Figure 1.2(b).[11] MXene also features in other electronic devices.[12,13]

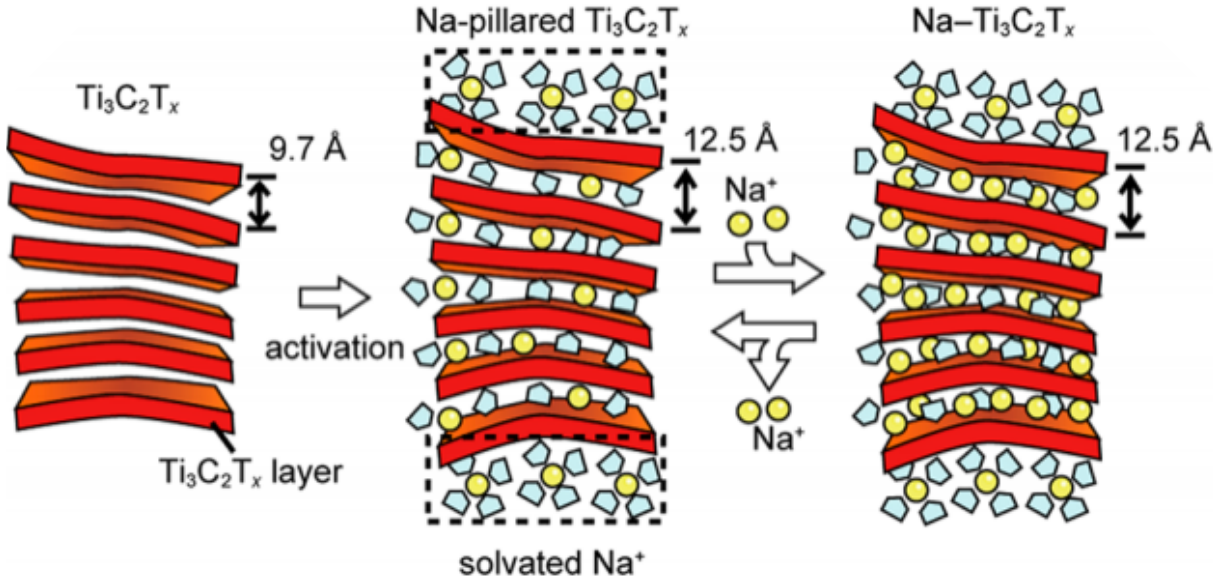

Figure 1.1. Illustration of the steps involved in intercalation of Na^+ between 2D sheets in $Ti_3C_2T_x$, as reported in ref. 7.[7] Copyright © 2016 (Kajiyama) by ACS Nano.

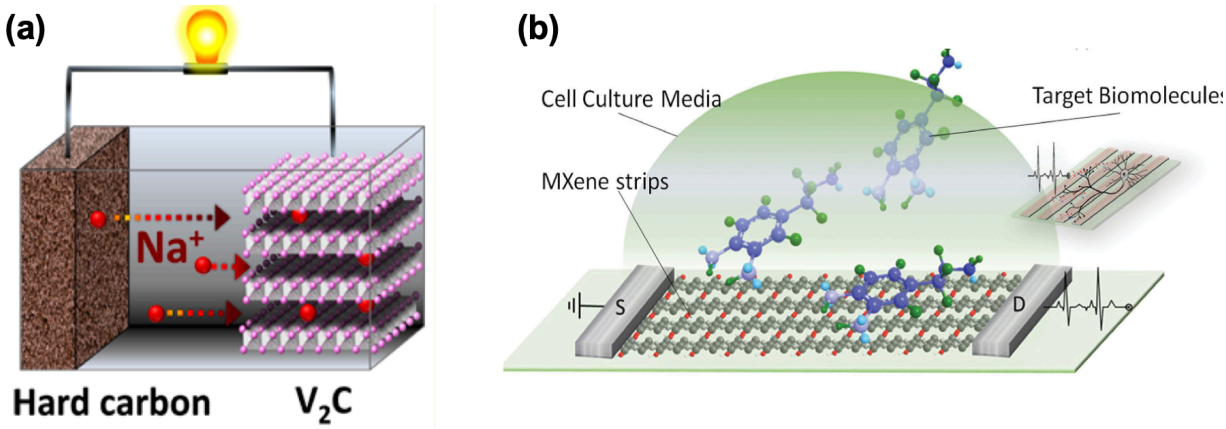

Figure 1.2. (a) Sodium-ion capacitors as a positive electrode 2D MXene (V_2C) material. This figure is copied from ref. 5.[5] Copyright © 2015 (Yohan Dall'Agnese) by the Journal of Physical Chemistry Letters. (b) Schematic of MXene-FET (MXene- field-effect transistors) as part in biosensing device. This figure is copied from ref. 11.[11] copyright © 2016 (Bingzhe Xu) by Advanced Materials.

1.1.1 Exfoliation MXene

The exfoliation (delamination) of MXenes provides unique materials with different functional groups, microstructure and morphology which impacts on the electrochemical response of the material. MXene can be exfoliated using dimethyl sulfoxide (DMSO), urea, dimethylformamide (DMF), acetone, ethyl alcohol, tetrahydrofuran, chloroform, toluene,

thiophene and formaldehyde, or need surfactant such as *p*-phosphonic acid calix[4]arenes.[14] These are in association with different energy sources, notably sonication,[3,14] heating[15,16] or both sonication and heating,[17] Figure 1.3(a-f). The high flexibility and high conductivity properties of exfoliated MXene down to a few layers, led to its utility in electromagnetic interference (EMI) shielding, which can be used in the presence of electric fields, as highlighted in Figure 1.3(g).[18,19]

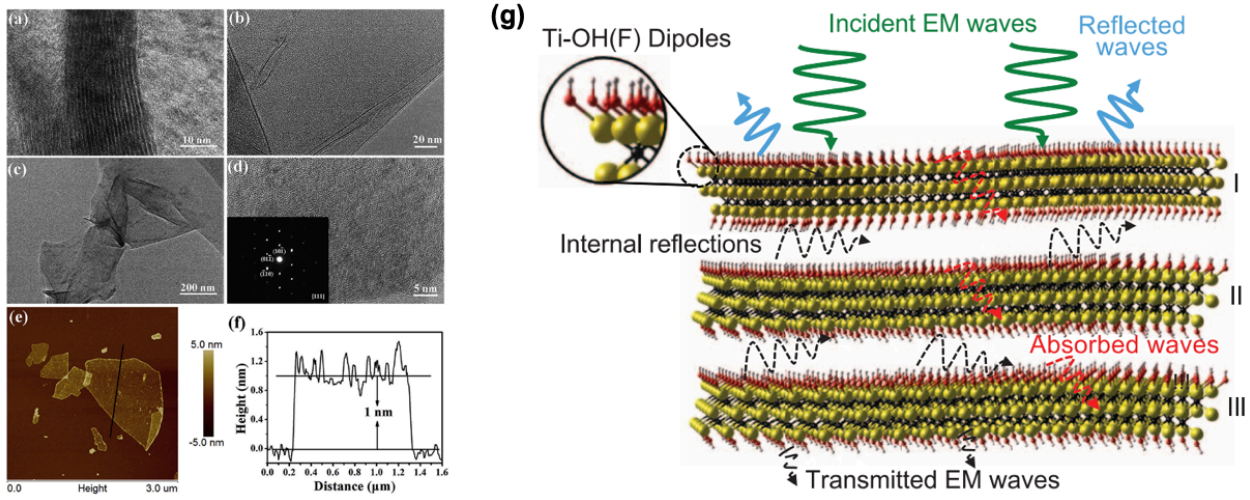

Figure 1.3. (a and b) TEM images of etched $Ti_3C_2T_x$ sheets under 35ºC after exfoliation, (a) before sonication, and (b) after sonication for 1h. (c) Low magnification TEM image of $Ti_3C_2T_x$. (d) Selected area electron diffraction (SAED) pattern with HRTEM image for $Ti_3C_2T_x$ establishing a lack of defects (e, f) AFM image and associated height profile of $T_3C_2T_x$ sheets ca 1 nm. This figure is copied from ref.17.[17] Copyright © 2017 (Tian Zhang) by Journal of Alloys Compounds. (g) Proposed electromagnetic interference shielding mechanism. This figure is copied from ref. 19.[19] Copyright © 2016 (Faisal Shahzad) by science.

1.1.2 Fabrication MXene

Kellici *et al* used sonication in the presence of *p*-phosphonated calix[N]arenes (PCXN), where N represents the number of phenol moieties in the macrocycles, with the different ring sizes resulting in different shapes of exfoliated MXene, Figure 1.4(a-f).[14] Other researchers used spray drying to convert flat nanosheets of 2D MXene ($Ti_3C_2T_x$) to a 3D crumpled structure, without the need to use any templates, Figure 1.4(g-i).[20]

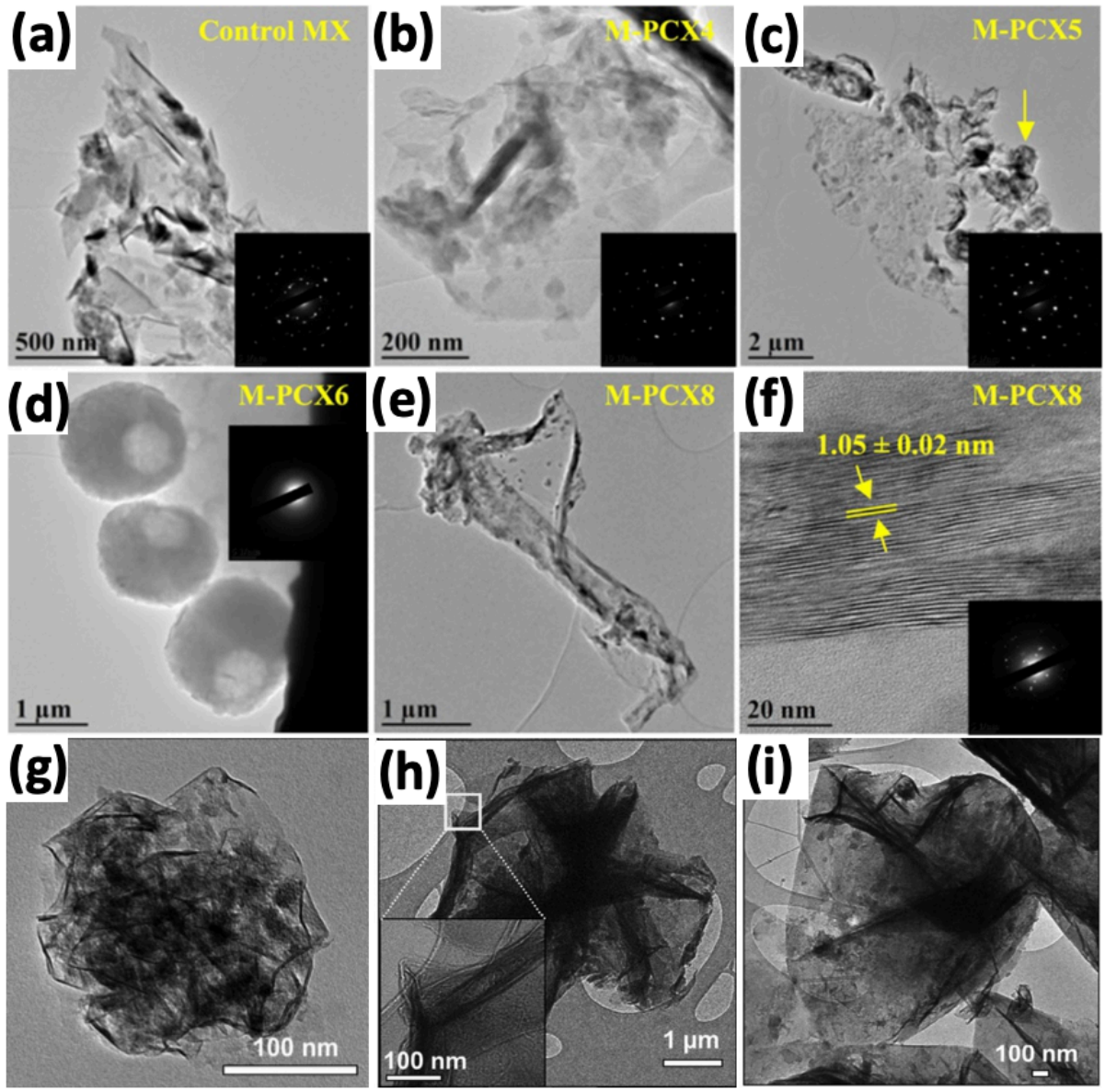

Figure 1.4. Selected area electron diffraction (SAED) pattern inset on TEM image for MXene samples. (a) MXene before processing (Ti_2C). Fabrication of MXene via sonication in the presence PCXN. (b) Exfoliated MXene with PCX4. (c) Crumpled sheets of M-PCX5. (d) Spheres shape of amorphous M-PCX6, from the SAED. (e) M-PCX8 scrolling. (f) M-PCX8 material with the distance between the layers 1.05 ± 0.02 nm, similar the values spacing in the literature review of sodium ion in Ti_2CT_x. This figure is copied from ref.14.[14] Copyright © 2017 (Arni Vaughn) by chemistry A European Journal Communication. Crumpled $Ti_3C_2T_x$ MXene image via TEM from spray dried at a concentration of (g) 0.1 mg/mL, (h) 1 mg/mL [showing few scrolling and layers via low magnification] and (i) Dehydration of 1 mg/mL for crumpled MXene by spray method. This figure is copied from ref. 20.[20] Copyright © 2017 (S. A. Shah) by Chemical Communication.

1.1.3 Fragmentation MXene

Ultrasound has been used to fragment MXene into nanoparticles with lateral dimensions of 2 to 8 nm, as monolayer thick product formed in aqueous TMAOH (tetramethylammonium hydroxide), as summarised in Figure 1.5. The method can also be used for different types of MXene, including Ti_3C_2, Nb_2C and Ti_2C.[21] The dimensions of the lateral fragmented material depend on the chemical stability of the MAX phases, which is prepared via etching the A layers from the laminar material, where M is a transition metal (Ti, Zr, Nb, V, Ta, or Mo), A is a main group element, mostly Al or Si, and X is C and/or N, and n is 1, 2, or 3. The nanoparticles of MXene have potential applications in a number of related fields including optical and display fields.[21]

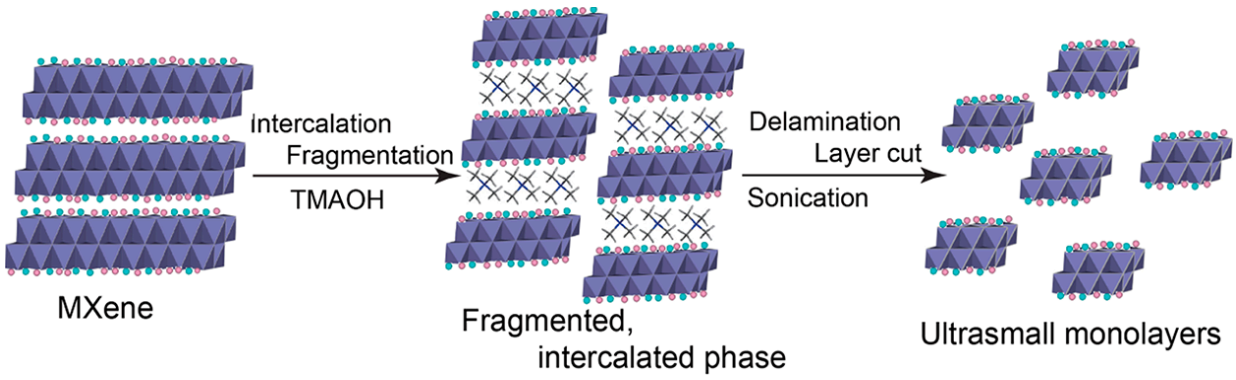

Figure 1.5. Schematic of the synthesis of ultra-small Ti_3C_2 sheets (2−8 nm) involving intercalation of TMAOH followed by delamination and fragmentation while under sonication. This figure is copied from ref.21.[21] Copyright © 2017(Zhiqiang Wang) by ACS Nano.

1.1.4 Decoration MXene

There is a growing interest in nanocomposite materials involving MXenes, for example MXene($Ti_3C_2T_x$)/MnO_2, as a material for use in high performance electrodes for flexible supercapacitors,[22] MXene($Ti_3C_2T_x$)/α-Fe_2O_3 as a material for use as a negative electrode material for supercapacitors,[23] and as a material for enhancing interfacial electronic coupling and functionalities of $Ti_3C_2T_x$/MnO_2.[24] MXenes have been decorated with (i) TiO_2(QDs) for Li-S batteries,[25] (ii) Cu_2O as a catalyst for thermal decomposition of ammonium perchlorate,[26] (iii) enzymes for electrochemical biosensors,[27] (iv) CNTs for improved electrochemical performance,[4] (v) Pt nanoparticles for sensing applications[28] and (vi) with others for determining ion exchange capacity.[29] In addition, TiO_2 nanoparticle/MXene composites feature in rendering MXene biocompatible for enzyme attachement,[27] enhancing the efficiency of MXenes modified GCE (glassy carbon electrode) for H_2O_2

reduction,[30] nitrite detection,[31] low detection limits of glucose[32] and sodium alanate,[33] Li-ion battery anodes[34] and photocatalyst.[35] Also noteworthy is that thermal methods have been used to oxidize MXene to TiO_2 or TiO_2 NPs/MXene.[33,35,36] with H_2O_2 also effective in preparing the same material.[34]

1.1.4.1 MXene decorated by anatase TiO_2 NPs

J. Yu *et al* prepared anatase TiO_2 NPs/MXene composite by a simple calcination method, with the composite material effective for photocatalytic CO_2 reduction as a solar driven process, Figure 1.6.[35]

Other researchers have prepared some composite materials by simple hydrothermal processing with the composite excellent for photocatalytic degradation of carbamazepine (CBZ). The symbol [001-T/MX] is a hetero-structural derivative TiO_2 (001) facet-decorated $Ti_3C_2T_x$ MXene, Figure 1.7.[37] Gao *et al* exfoliate MXene ($Ti_3C_2T_x$) via sonication and decorate ultrathin of 2D MXene with TiO_2 quantum dots (QDs) as one step process using cetyltrimethylammonium (CTAB) and $TiCl_3$ at 200ºC for 6h. This processing results in a larger area of electrode-electrolyte for polysulfide and higher sulfur loading, for incorporating into batteries. The resulting TiO_2 QDs@MXene/S cathode has long term stability with potential in new generation Li–S batteries, Figure 1.8.[25]

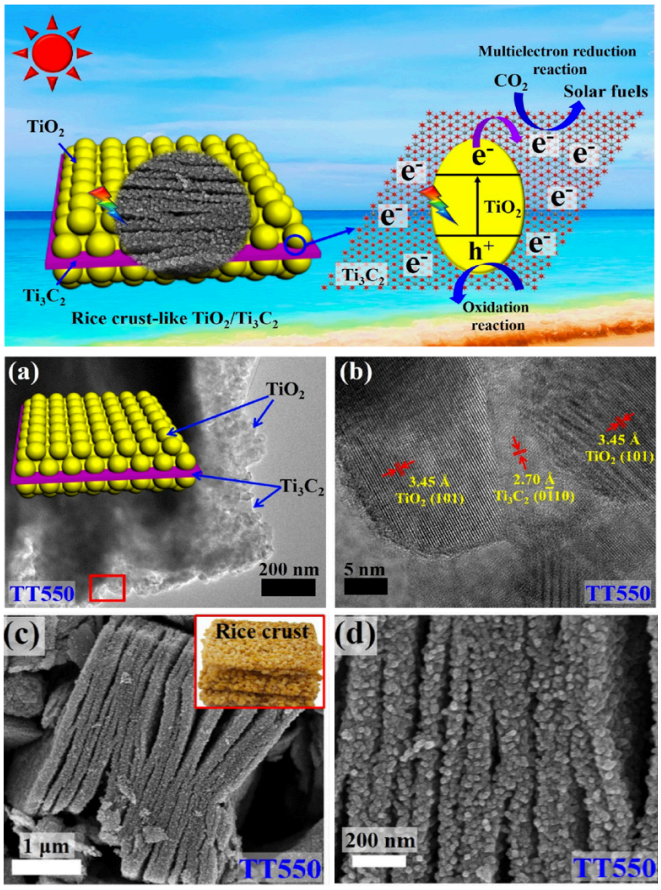

Figure 1.6. Schematic of the mechanism of photocatalytic CO_2 reduction on TiO_2/Ti_3C_2 composite material. (a) TEM image and schematic of the sandwich structure of TiO_2/Ti_3C_2 under 550ºC (TT550) (inset). (b) Corresponding (red rectangle in (a)) high resolution TEM (HRTEM) image of TiO_2/Ti_3C_2 under 550ºC (TT550). (c, d) Field emission scanning electron microscope (FESEM) images of TT550 (TiO_2/Ti_3C_2 under 550ºC). This figure is copied from ref.35. [35] Copyright © 2018 (Jingxiang Low) by Journal of Catalysis.

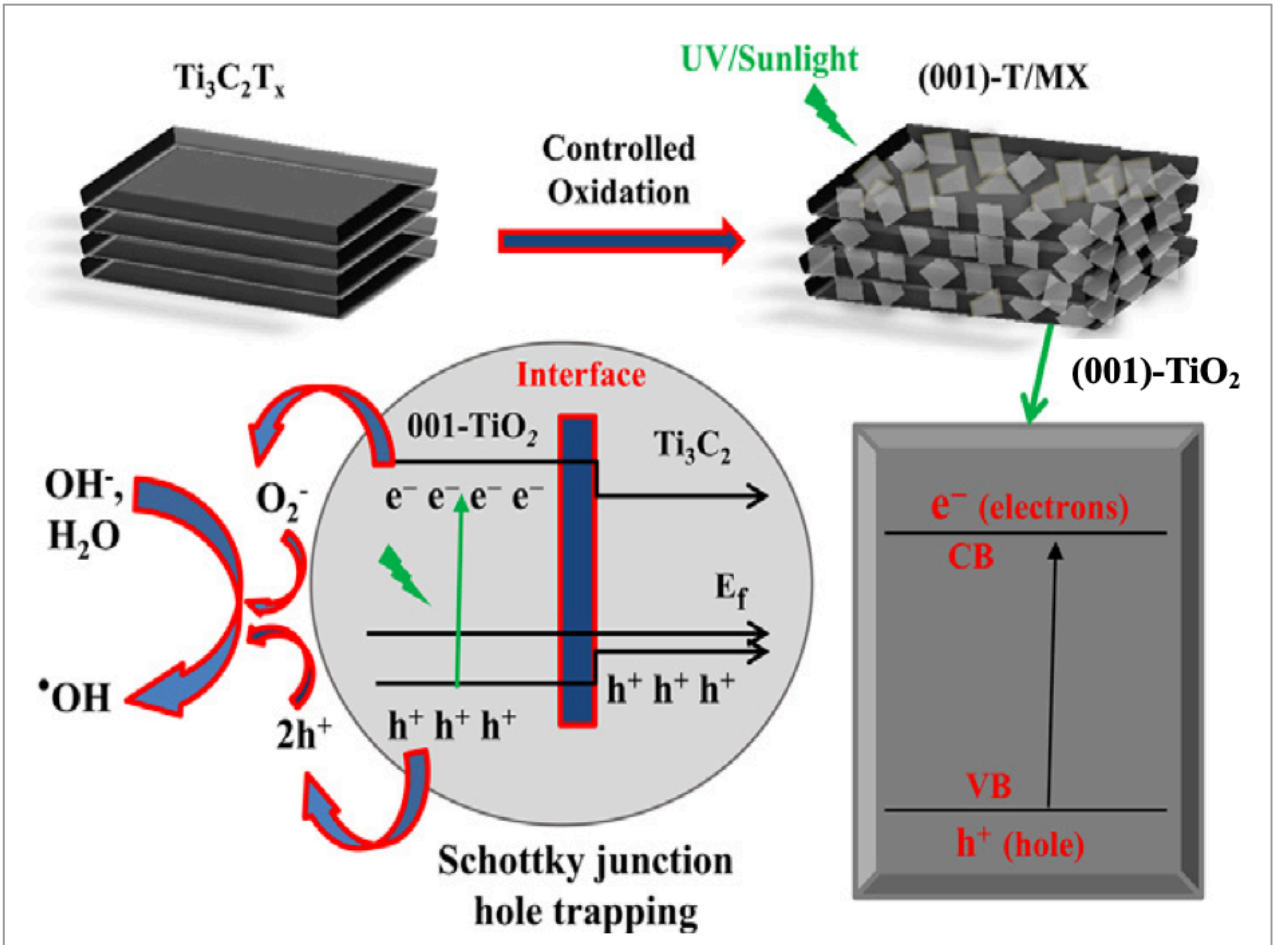

Figure 1.7. Schematic of oxidation of MXene to anatase in forming a composite material TiO_2/MXene ((001)-T/MX), along with the mechanism of the degradation of CBZ by the photocatalyst. The photocatalytic degradation of (001)-T/MX was able to decompose CBZ because of the high concentration of •OH and $•O_2$ radicals from under natural light sources. This figure is copied from ref.37.[37] Copyright © 2018 (Asif Shahzad) Chemical Engineering Journal.

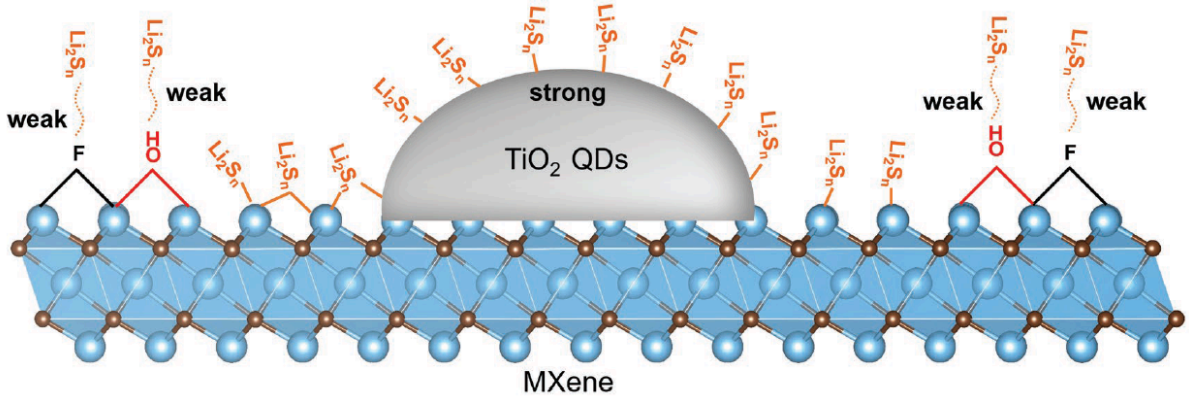

Figure 1.8. Cartoon illustrating the ability of TiO_2 QDs on MXene nano-sheets to form strong bonds with polysulfides, Li_2S_n, rather than weak bonds associated with functional groups on surface of the MXene sheets. This figure is copied from ref.25.[25] Copyright © 2018 (Xiao-Tian Gao) by Small.

1.1.4.2 MXene decorated by other compounds

A recent paper reported on the coating of 2D Nb_2C MXene nano-sheets with cetanecyltrimethylammonium chloride (CTAC), as CTAC@Nb_2C-MSN (MSN is mesopores silica nanoplatforms). These have potential to be used as chemotherapeutic material for cancer therapy. Near-infrared (NIR) (1064 nm) irradiation of 2D Nb_2C MXenes was effective in increasing photothermal hyperthermia (by 28.6%), establishing a bio-window for biomedical applications of the MXene *in vitro* and *in vivo*, Figure 1.9.[38]

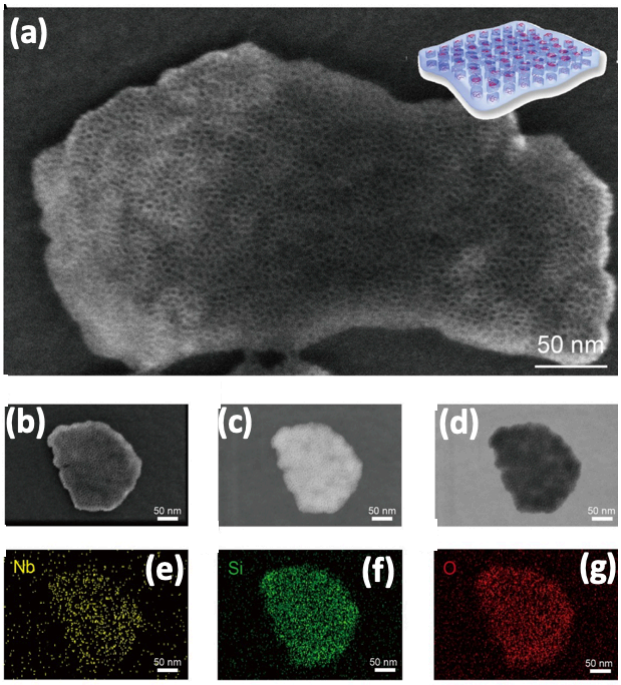

Figure 1.9. (a) HRSEM image of core/shell-structured nano-sheet composite of CTAC@Nb_2C-MSN. (b) SEM image for the same nano-composite, (c and d) dark and bright-field TEM images, respectively. (e-g) EDS mapping for Nb, Si and O elements respectively, for CTAC@Nb_2C-MSN nano-sheets, for a common same scale bar (50 nm). This figure is copied from ref.38.[38] Copyright © 2018 (Xiaoxia Han) by Theranostics.

1.2 Hexagonal boron nitride (*h*-BN)

Polymorphs of boron nitride include the hexagonal arrangement of alternating boron and nitrogen atoms in 2D sheets, with the atoms sp^2 hybridized, as for isostructural graphene, Figure 1.10. However, in contrast to graphite, layered *h*-BN is transparent and is an electrical insulator. This material, known as hexagonal boron nitride (*h*-BN), has attracted considerable interest, due to its similarity in structure with that of graphene. There are other polymorphs of BN with distinctly different properties, but other than boron nitride nanotubes (BNNTs, see below), they do not match strictly with the polymorphs of carbon.[39]

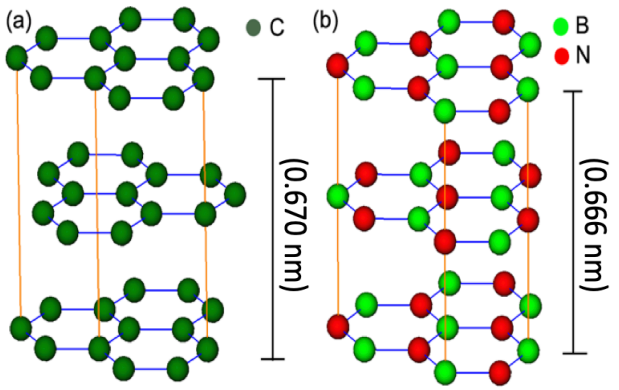

Figure 1.10. Crystal structure of (a) graphite; (b) *h*-BN. This figure is copied from ref.39.[39] Copyright © 2008 (Wei-Qiang Han) by Nanotechnologies for the life Sciences.

In general, the electronic properties of hexagonal carbon (*h*-C) where there are hexagonal six membered rings, can be metallic, semiconducting or semi metallic,

depending on the dimensions and overall structure. On the other hand, because of the large band gap, *h*-BN is typically an insulator or semiconductor. *h*-BN can be prepared in different shapes, including, boron nitride nanotubes (BNNTs), nano-sheets (BNNSs), nano-ribbons (BNNRs) and nano-meshes (BNNMs), Figure 1.11(a, b).[40] Electron energy loss spectroscopy (EELS) is a technique to study the ionization edge between two layers of BN which is effective in limiting the number of layers to one atom thick *h*-BN. Overall *h*-BN can have different numbers of layers - single, double and multiple, similar to what happens for graphite, Figure 1.11(c).[41]

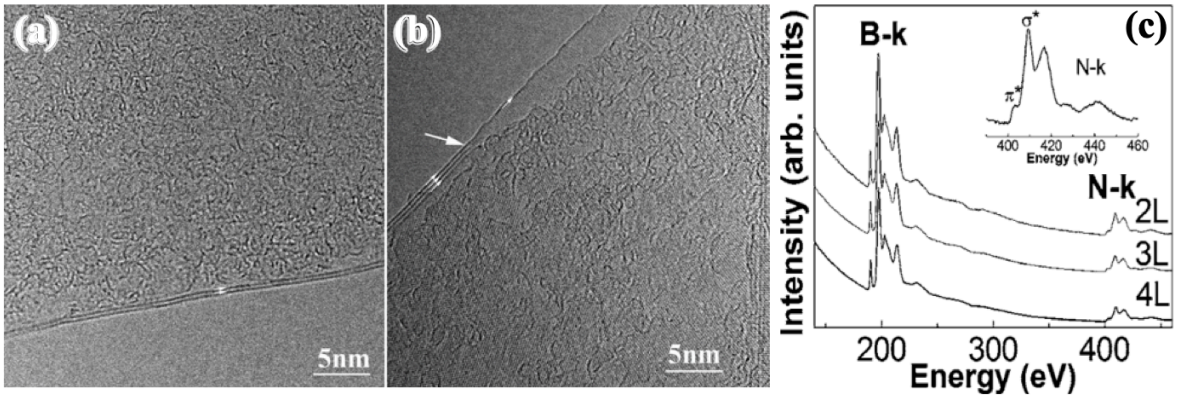

Figure 1.11. (a) Double layers of *h*-BN sheets. (b) Monolayer *h*-BN in the top-right side with three layers in the bottom-left side. This figure is copied from ref.40.[40] Copyright © 2012 (Yi Lin) by Nanoscale. (c) *h*-BN sheets have double, triple and quadruple layers, as established using EELS spectroscopy; the inset is the close-edge spectrum. This figure is copied from ref.41.[41] Copyright © 2008 (Wei-Qiang Han) Applied Physics Letters.

1.2.1 Scrolling of *h*-BN

Chen *et al* developed a method to exfoliate and scroll *h*-BN, using of a spinning disc processor (SDP) with N-methyl-2-pyrollidone (NMP) as the solvent of choice.[42] The shear forces in the dynamic thin film (1-200 μm) in the SDP microfluidic platform is effective in simultaneously exfoliating and scrolling the 2D sheets, Figure 1.12.[42] Others used N-(2-aminoethyl)-3a-hydroxy-5b-cholan-24-amide (LCA) with magnetic stirrer to fabricate *h*-BN scrolls from exfoliation *h*-BN, using 1,2-Dichlorobenzene (ODCB) as the

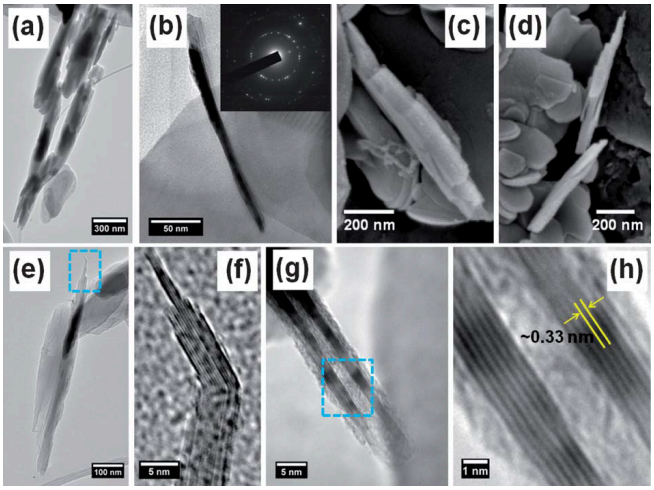

Figure 1.12. Scrolling of *h*-BN using a spinning disc processor: (a, b) TEM images with a selected area electron diffraction (SAED) pattern inset. (c, d) SEM images. (e) TEM image with an HRTEM image of the area indicated in (f). (g, h) the distance between layers (0.33 nm) via HRTEM images. This figure is copied from ref.42.[42] Copyright © 2013 (Chen Xianjue) by Nanoscale.

solvent. Subsequent washing with methanol is effective in removing LCA from the *h*-BN scrolls, Figure 1.13.[43]

Figure 1.14 showcases another method of preparing *h*-BN scrolls but now incorporating nanoparticles.[44] This method also involved the use of N-(2-aminoethyl)-3a-hydroxy-5b-cholan-24-amide (LCA), analogous to the scrolling of pure *h*-BN scrolls and h-BN-magnetic nanoparticles via heating then storing for 24 h at room temperature.

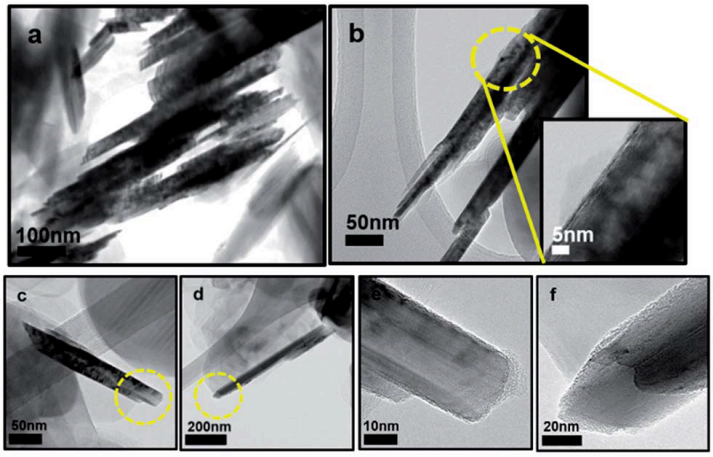

Figure 1.13. Nano-scrolls of *h*-BN produced in the presence of LCAs, along with exfoliated *h*-BN sheets. (a and b) TEM images of *h*-BNS showing the distance between the layers (0.33 nm), as derived using HRTEM. (c and d) HRTEM images of single BNS fully rolled up and (e and f) zoomed TEM images of the end of the scrolls in images (c and d). This figure is copied from ref.43.[43] Copyright © 2014 (Da Young Hwang) by Nanoscale.

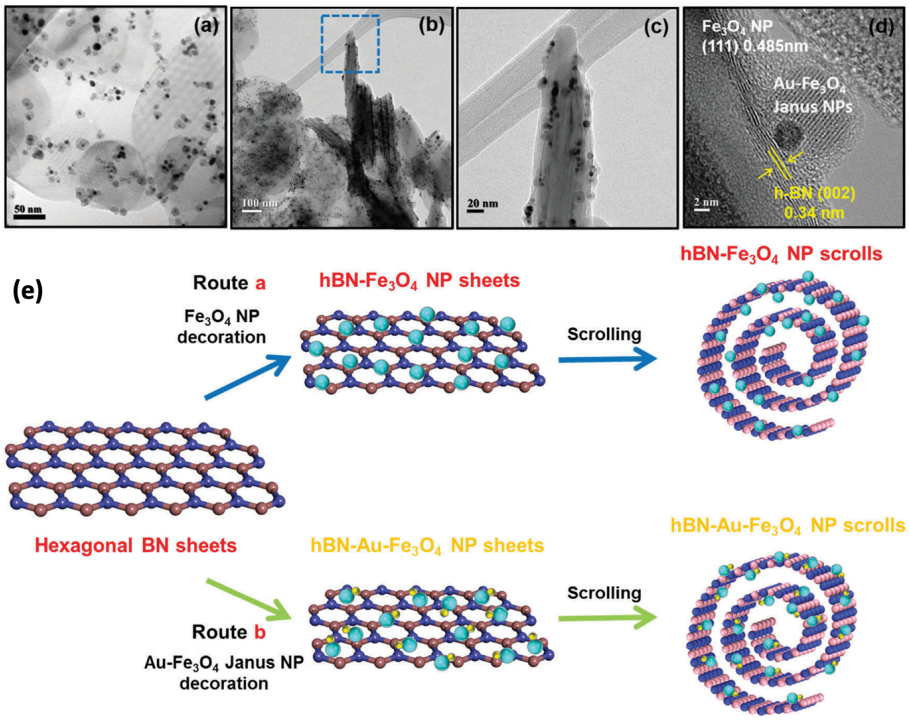

Figure 1.14. *h*-BN–Au@Fe_3O_4 nano-scrolls formed in LCA. (a) TEM image of Au@Fe_3O_4 nanoparticles decorated on *h*-BN sheets. (b) TEM image of *h*-BN nano-scrolls decorated with Au@Fe_3O_4. (c) HRTEM image of Au@Fe_3O_4 decorated *h*-BN nano-scrolls showing that the NPs are located both inside and outside the scrolls, taken from the blue frame of the edge in (b). (d) HRTEM image of Au@Fe_3O_4 NPs showing lattice spacing with the distance between *h*-BN layers within a scroll. (e) Schematic of the two methods used to prepare scrolls of *h*-BN. (Route a) Fe_3O_4 nanoparticles decorated *h*-BN nanoscrolls. (Route b) Au@Fe_3O_4 Janus nanoparticles decorated multilayers h-BN sheets. This figure is copied from ref.44.[44] Copyright © 2017 (Hwang DY) by Physical Chemistry Chemical Physics.

1.2.2 Exfoliation of *h*-BN

The synthesis of exfoliated *h*-BN sheets has been developed using a number of disparate methods. For example, the thermal reaction of B_2O_3, N_2, with different plant biomass directed on-site synthesis for the mass production of highly crystalline and high-quality *h*-BN nano-sheets, Figure 1.15.[45] Zhang *et al* exfoliated *h*-BN sheets to nanosheets using ultrasonic energy in aqueous solution containing 30 wt% of monoethanolamine (MEA), Figure 1.16.[46]

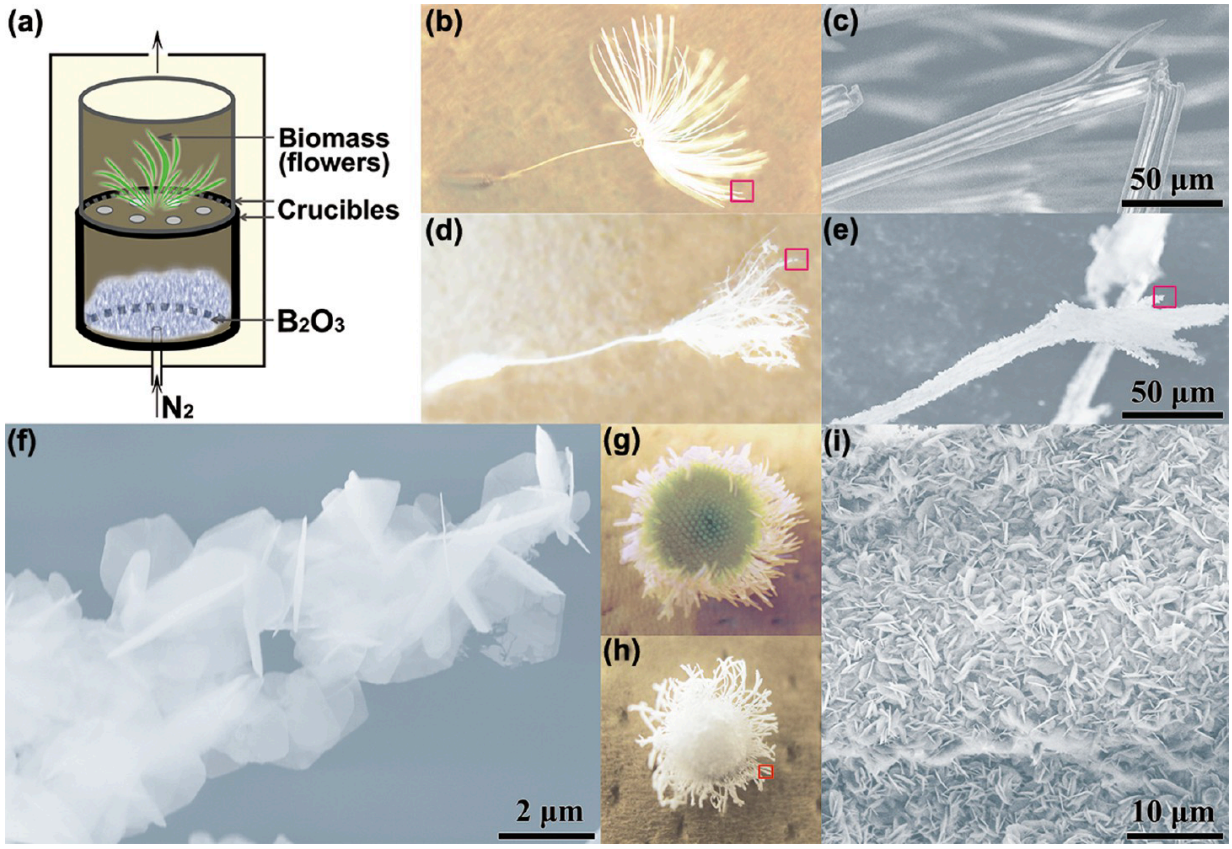

Figure 1.15. Illustration of the synthesis of BNNSs (Boron nitride nanosheets) using biomass and B_2O_3 under N_2. (b and c) images of dandelion parachute before the synthesis of the *h*-BN sheets. (d and e) SEM images of dandelion parachute after the synthesis of the BN sheets. (f) SEM image of a zoomed area of image(e) as an assembly of BN nano-sheets. (g, h) Images of fleabane flower before and after processing, respectively. (i) SEM images of zoom in section in picture (h). This figure is copied from ref.45.[45] Copyright © 2014 (Xue-Bin Wang) by ACS Nano.

Details in Figure 1.17 report the outcome of mixing NaOH and KOH (molten alkali-assisted liquid method) with *h*-BN powder followed by tip probe sonication for 1h, affording *h*-BN nanosheets (BNNSs). These have been used for enhanced thermal conductivity of nanofluids.[47]

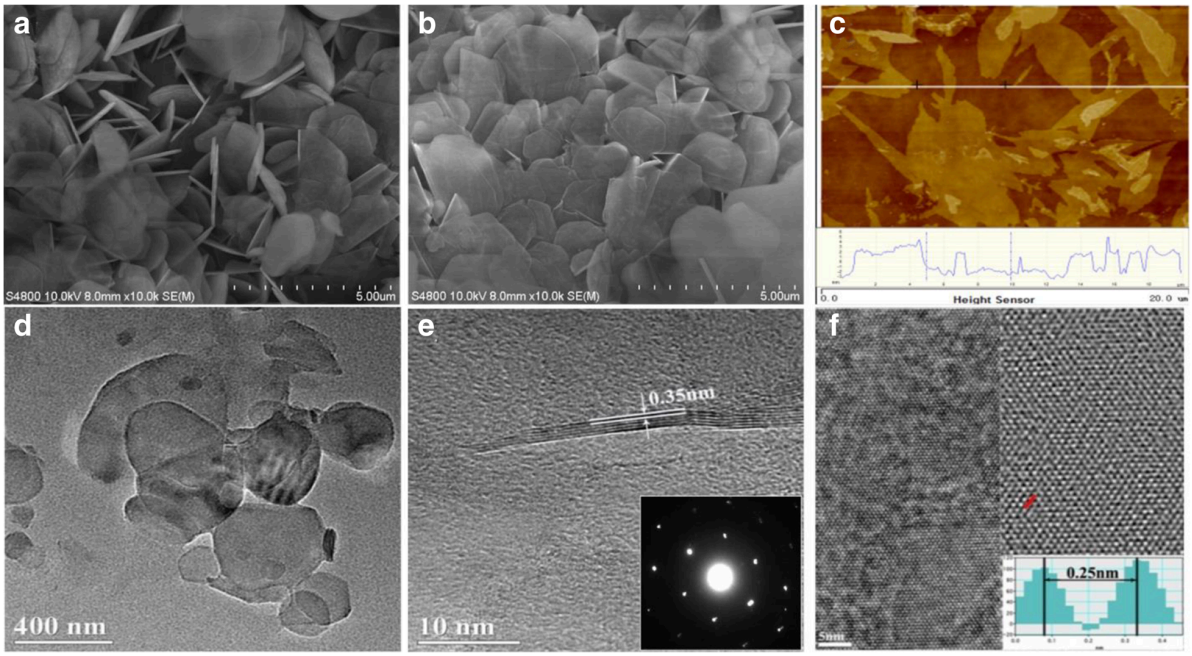

Figure 1.16. (a) SEM images of as received *h*-BN. (b) SEM image of boron nitride nano-sheets (BNNSs). (c) AFM image for exfoliated *h*-BN. (d) TEM images for exfoliated *h*-BN of BNNSs, (e) HRTEM image for exfoliated BNNSs with inset SAED pattern, and (f) BNNS (left) and its IFFT image (right). This figure is copied from ref.46.[46] Copyright © 2017 (Bangwen Zhang) by Nanoscale Research Letters.

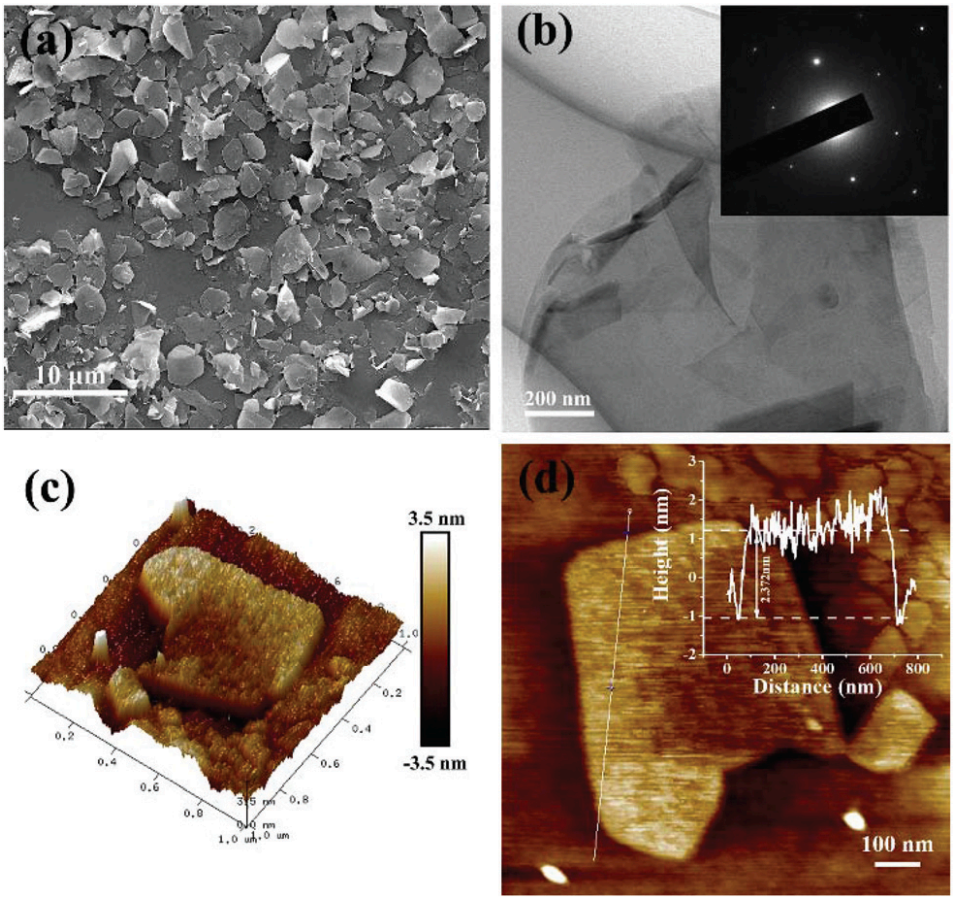

Figure 1.17. (a and B) SEM and TEM images, respectively, of boron nitride nano-sheets (BNNSs), (b) Selected area electron diffraction (SAED) pattern demonstrating the typical structure of exfoliated *h*-BN; (c) AFM generated 3D image of BNNSs. (d) AFM derived height profile of nanosheets of BNNSs. This figure is copied from ref.47.[47] Copyright © 2018 (Xiao Hou) by Nanoscale.

1.2.3 Decoration *h*-BN with metal oxide or metal

Lim *et al* have developed a simple method to control the decoration of *h*-BN with nanoparticles of magnetite (Fe_3O_4) under a relatively low magnetic field, affording hybrid platelets. Poly(sodium 4-styrenesulfonate) is effective in controlling the build-up of Fe_3O_4 on the surface of *h*-BN, Figure 1.18.[48] In another report, the choice of temperature was important factor for oxidation of Ni, Cu and stainless steel in the presence of *h*-BN to prepare oxide copper, nickel and surface of stainless steel coating *h*-BN , Figure 1.19.[49]

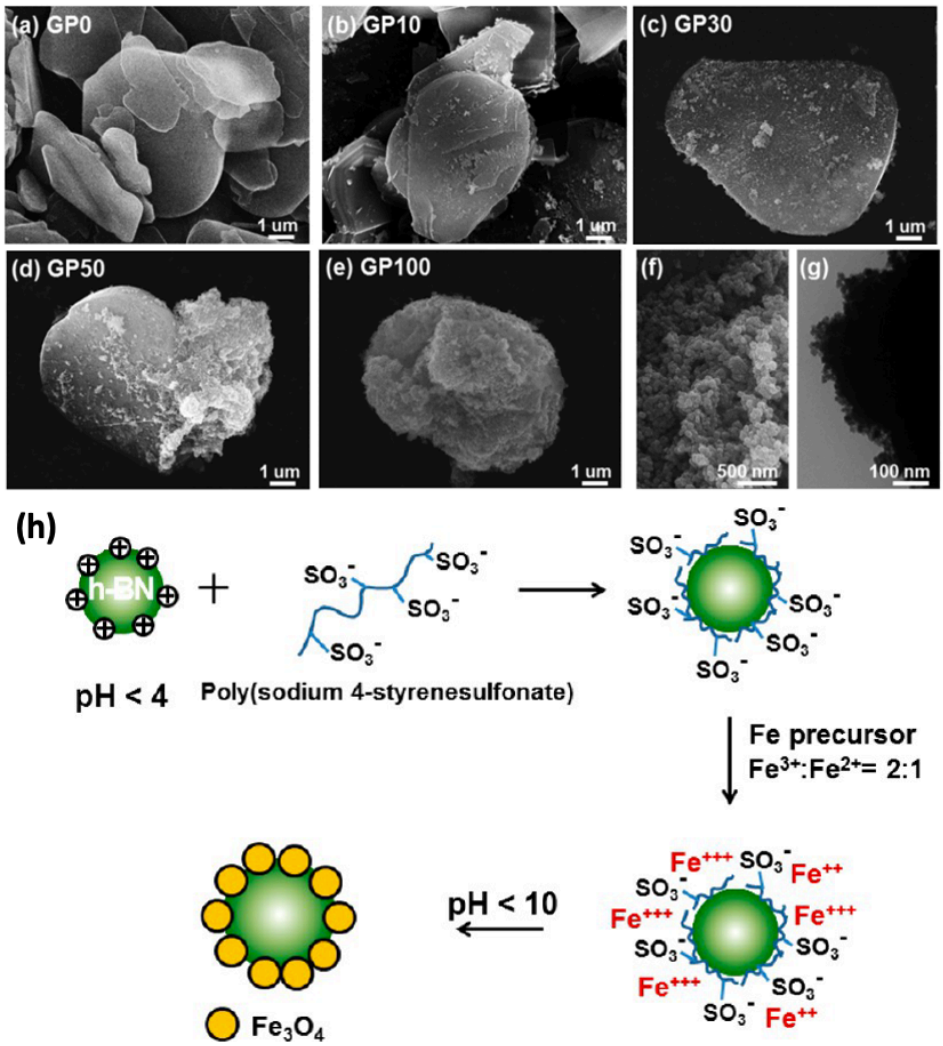

Figure 1.18. (a-e) SEM images of Fe_3O_4@*h*-BN platelets synthesized using different concentrations of iron salt solutions: GP0, GP10, GP30, GP50 and GP100 for 0, 10, 30, 50 and 100 wt % of Fe_3O_4 coated *h*-BN, respectively. (f) Zoomed in SEM and (g) TEM images of the same material. (h) Reaction scheme. This figure is copied from ref.48.[48] Copyright © 2013 (Ho Sun Lim) by Chemistry of Materials.

Electroless deposition of spheroidal Ni particles distributed on *h*-BN has been established, using nickel(II) sulfate dissolved in choline chloride-ethylene glycol (ChCl-EG) as an ionic liquid. The size of the Ni particles on *h*-BN are around 10-1000 nm, Figure 1.20.[50]

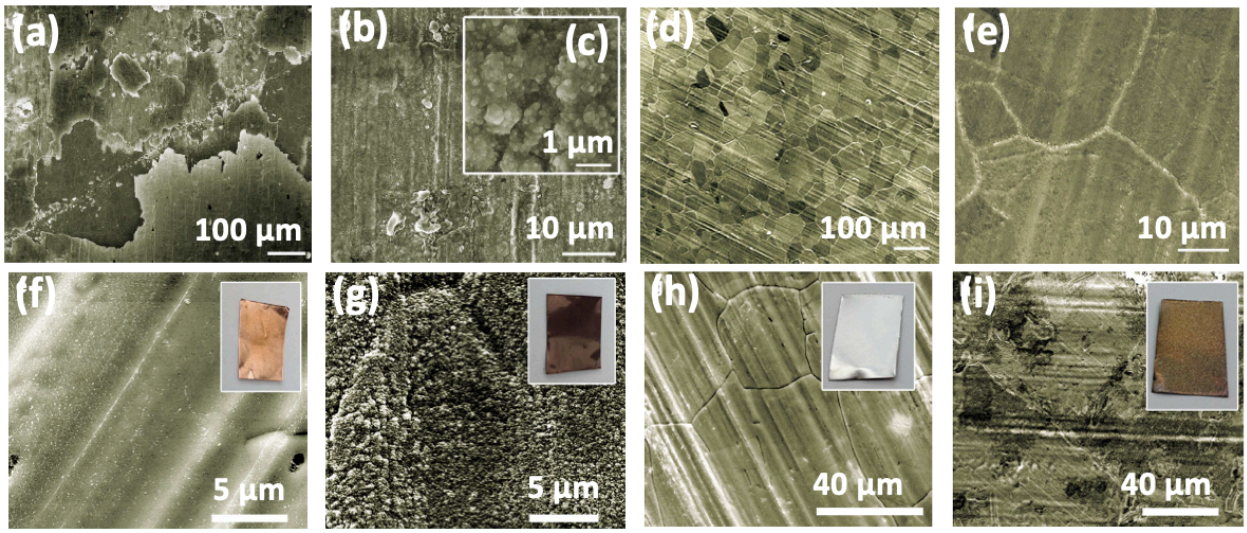

Figure 1.19. Coatings of thin layers of *h*-BN for high-performance oxidation-resistance. (a-c) SEM images for the oxidation of pure nickel foils under 300 mTorr of oxygen at 1,100ºC for 30 min. (d and e) SEM images with the thickness of *h*-BN layers (5 nm) coated on nickel foil after oxidation under 300 mTorr of oxygen at 1,100ºC for 30 min. The image (c) was before coating with *h*-BN. (f and g) SEM images for oxidation of copper foils coated with *h*-BN at 500ºC and 1,100ºC under 300 mTorr of oxygen for 30 min. (h and i) SEM images for the oxidation of the surface of stainless-steel coated with *h*-BN at 500ºC and 1,100ºC for under 300 mTorr of oxygen 30 min. SEM images in (e) and (g) have straight lines which arises from the polishing process. (f, h) Photograph inserts show that for each metal after coating with *h*-BN, the color of the copper and stainless steel has not changed. (g, i) Photograph inserts show copper and stainless steel devoid of a *h*-BN which have changed color after oxidation. This figure is copied from ref.49.[49] Copyright © 2013 (Zheng Liu) by Nature communications.

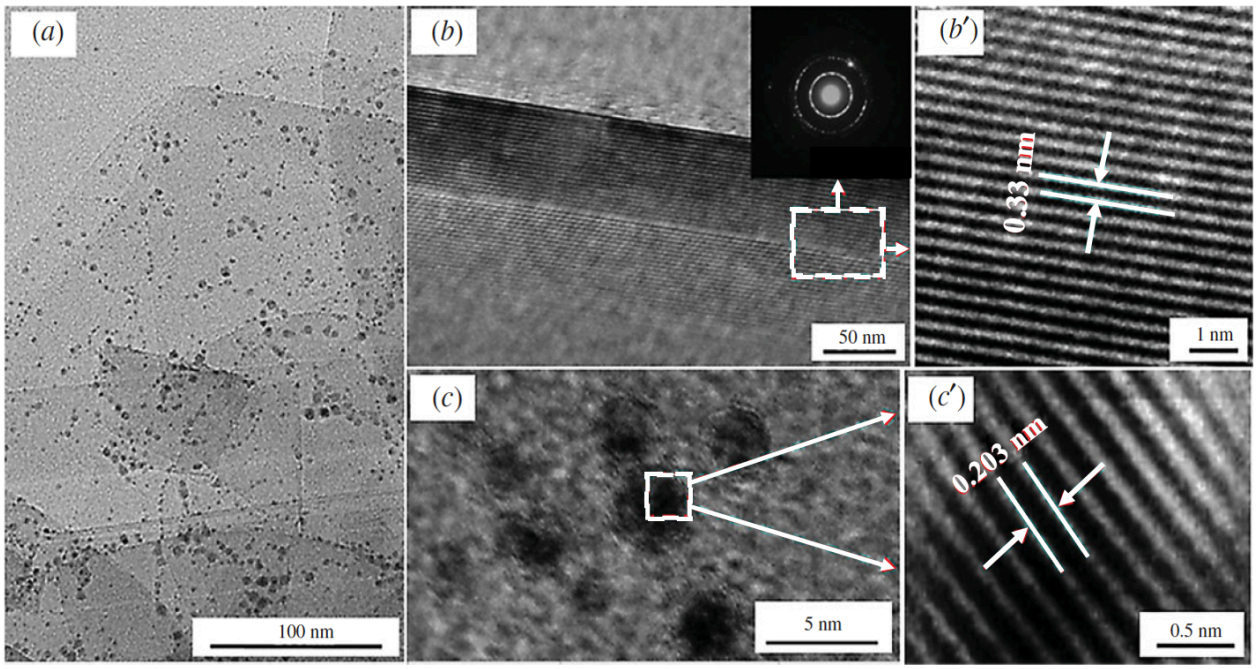

Figure 1.20. (a) TEM images of Ni NPs@*h*-BN powder formed in 30 g/L of choline chloride-ethylene glycol ChCl-EG. (b) HRTEM images of the material (inset selected area electron diffraction SAED patterns image). (b') FFT analysis of *h*-BN powders, (c) HRTEM images of Ni NPs, and (c') FFT analysis of Ni grains on the surface of *h*-BN. This figure is copied from ref 50.[50]

1.3 Boron nitride nanotubes (BNNTs)

The structure of boron nitride nanotubes (BNNTs) is similar to that of carbon nanotubes (CNTs). BNNTs were first synthesized in 1995.[51] They can be imagined as rolled up hexagonal boron nitride (*h*-BN) sheets like CNTs in which alternating B and N atoms completely substitute C atoms. Similar to CNTs, BNNTs have three kinds of chiralities, arm chair, zig-zag and chiral (helical). The electrical properties for CNTs depend on the chiralities and geometrical parameters. However, the chiralities for BNNTs have no effect on the electrical properties. Indeed, all BNNTs are electrical insulators with a bandgap of approximately 5.5-5.8 eV, which is independent of the direction and rolling vector of the BN sheets.[52-54] Other properties of BNNTs are that they are chemically inert, oxidation resistant, structurally stable and have high neutron absorption.[55] Recent publications establish that the oxidation of BNNTs starts at approximately 900ºC,[56] which is much higher than for the oxidation temperature for CNTs, being about 400ºC, as established using TGA studies. The high oxidation resistance of BNNTs allows applications in high temperature environments, Figure 1.21.[57] Interestingly, studies on polymer/BNNT composite materials has only recently started to get attention. Such exciting composites of BNNTs, taking on the properties of the BNNTs with high flexibility modulus and high thermal conductivity, makes them advantageous as novel nano-fillers, in imparting high mechanical reinforcement, high thermal conductivity and low coefficient of thermal expansion. Polymer/BNNT composites that have been studied to date have been prepared as thin films using solution–mixing, evaporation and melt-mixing techniques.[58] Methods for preparing BNNTs feature

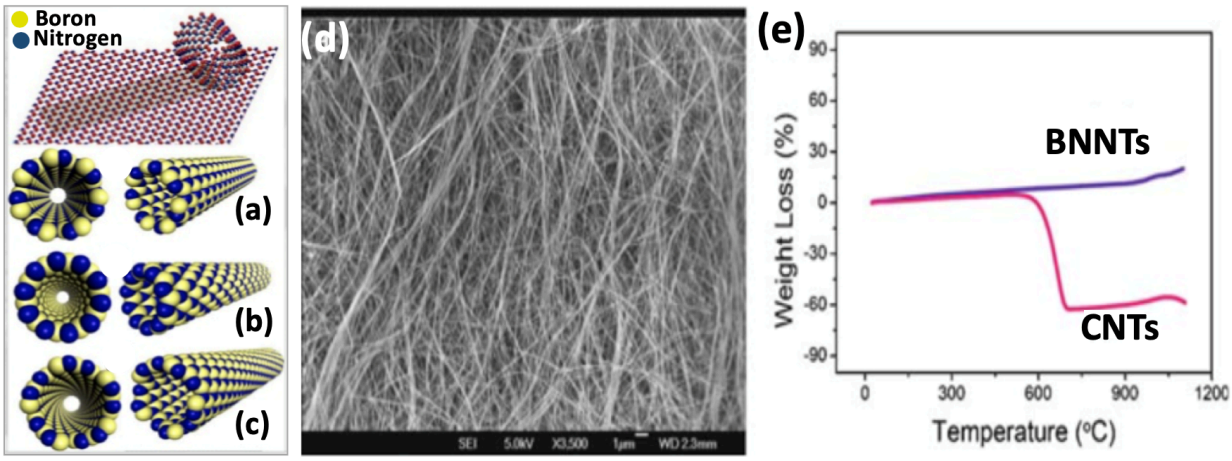

Figure 1.21. The structure of boron nitride nanotubes (BNNTs) including space filling representations, featuring (a) arm-chair BNNT; (b) zig-zag BNNT and (c) chiral BNNTs. This figure is copied from ref.52 and 54.[52,54] Copyright © 2010 (Dmitri Golberg) by ACS Nano, © 2010 (Chunyi Zhi) by Materials Science and Engineering: R: Reports. (d) SEM image of purified BNNTs grown at 1500°C, and (e) thermogravimetric analysis (TGA) of CNTs compared with BNNTs. This figure is adapted from ref. 57.[57] Copyright © 2009 (Jiesheng Wang) by BCN Nanotubes and Related Nanostructures, Springer.

substitution reactions,[59] laser ablation,[60] chemical vapour deposition (CVD),[61,62] arc-discharge[51,63] and ball-milling.[64]

Given the unique properties of BNNTs they have potential for a large number of applications. However, this will require a detailed understanding of their toxicity, to make sure there are no unforeseen environmental and health issues down the track. That said, there is no clear consensus regarding their cytotoxicity and impact on living systems and the environment, Figure 1.22.[65-68] There are three inter-related boron nitride structures, (i) straight-walled BNNT,[69,70,73] (ii) bamboo-type BN[70-73]and (iii) flower-type BN[73], Figure 1.23.[73]

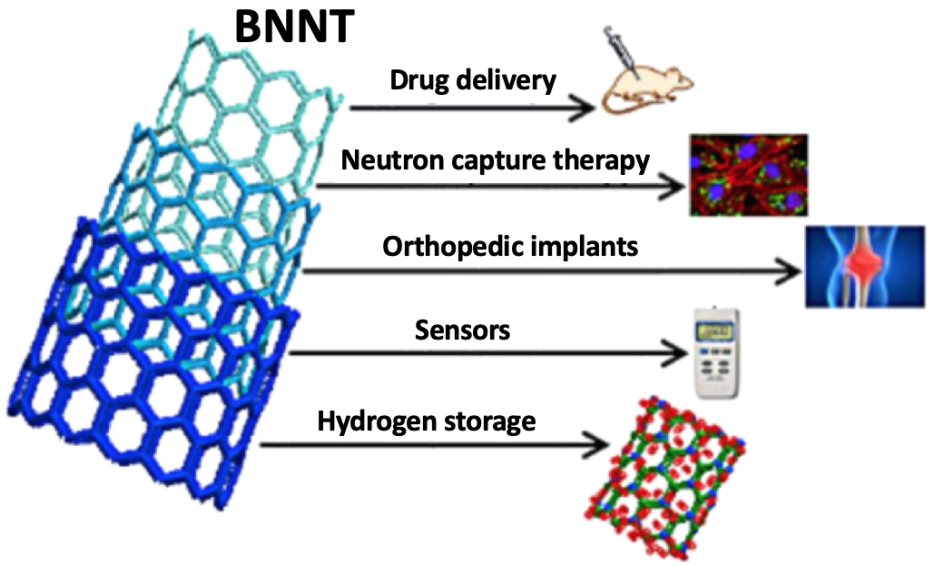

Figure 1.22. Possible applications for boron nitride nanotubes (BNNTs) with a model of the concentric rings in the material. This figure is copied from ref 65.[65] Copyright © 2015 (Saban Kalay) by Beilstein journal of nanotechnology.

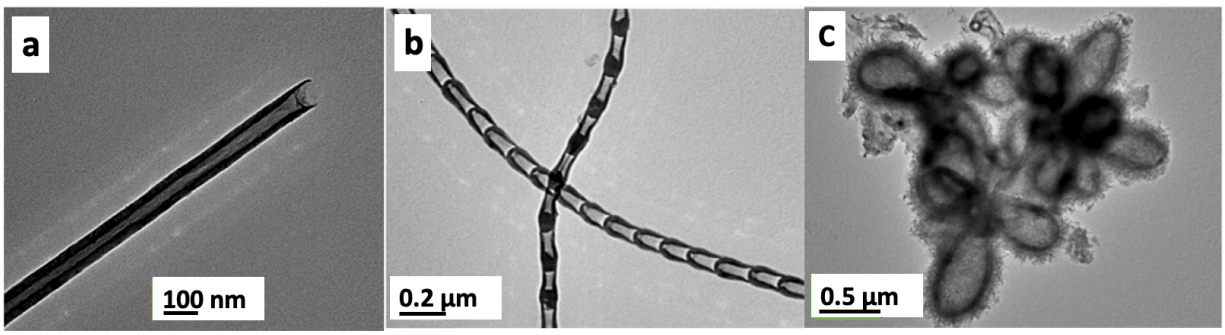

Figure 1.23. TEM image for BNNT structure (a) straight- walled BNNT, (b) bamboo-type BN and (c) flower-type BN.[73] Copyright © 2010 (Arava Leela Mohana Reddy) by International journal of hydrogen energy.

1.3.1 Purification BNNTs

There are reports on purifying BNNTs using heating and washing with HCl, Figure 1.24.[74,75] Other groups have purified BNNTs using polymers (amine-t-PEG (amine-terminated polyethylene glycol)),[76] which essentially acts as a surfactant, in coating the BNNTs, thereby facilitating their separation and purification, Figure 1.25.[76] Also, researchers have used poly(m-phenylenevinylene-co-2,5-dioctoxy-p-phenylenevinylene) (PmPV) to purify BNNTs which involves wrapping of the tubes.[77]

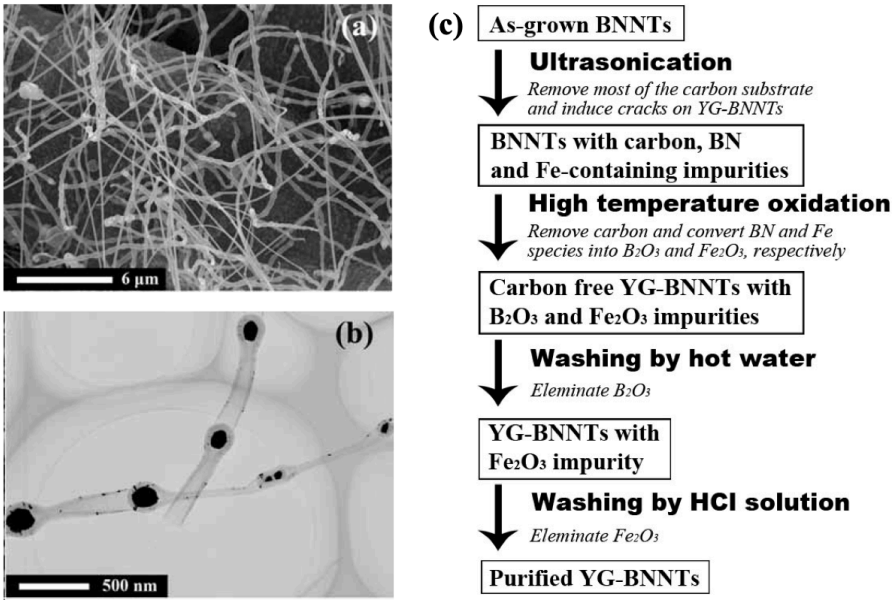

Figure 1.24. (a, b) SEM and TEM images of the as-grown YG-BNNTs (Yard-Glass shaped BNNTs), respectively. (c) Flow diagram highlighting the steps involved the purification process. This figure is adapted from ref 75. [75] Copyright © 2014 (Lin Xue-Song) by Iranian Journal of Chemistry and Chemical Engineering.

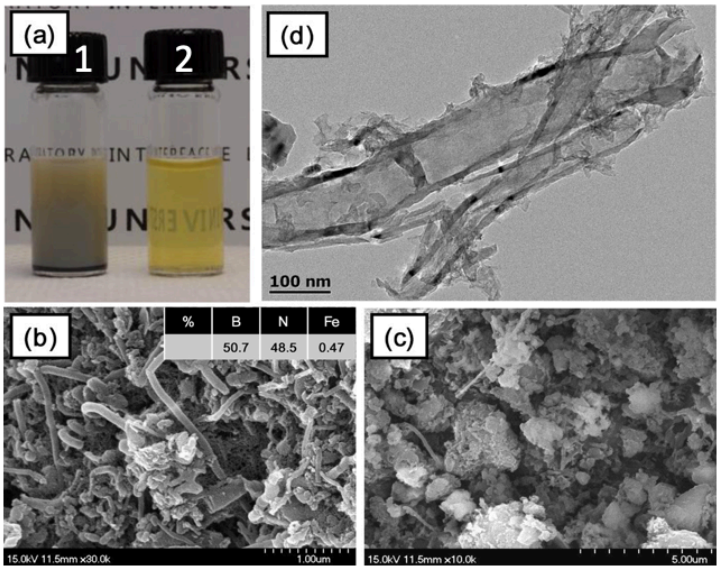

Figure 1.25. (a) Photograph showing BNNTs suspended in water using amine-t-PEG (vial 1), and the supernatant solution (vial 2). (b and c) SEM images of the material in the supernatant and of the precipitate, respectively. (d) TEM image of polymer (amine-t-PEG) wrapped BNNT. This figure is copied from ref. 76.[76] Copyright © 2013 (Jin-Hyuk Choi) by Materials Research Bulletin.

1.3.2 Slicing BNNTs

A number of applications of BNNTs depend on the length of the tube, including in nanodevices,[65] nanomedicine,[77] sensors and composites.[78] There have been studies on dispersing BNNTs using methoxy-poly(ethylene glycol)-1,2-distearoylsn-glycero-3-phosphoethanolamine-N conjugates (mPEG-DSPE) which effectively coat the tubes. This composite material, mPEG-DSPE/BNNTs, is colloidally stable in water for over 24 hours. The length of mPEG-DSPE/BNNTs as such, dispersed in water can be reduced using ultrasonication, from 10 μm down to 500 nm.[79] In another study, the length of the BNNTs can be reduced to ca 200 nm via sonication in an aqueous ammonia solution. However, the associated high energy sonication process results in some unzipping of the BNNTs and damage to the ends of the tube, Figure 1.26.[80]

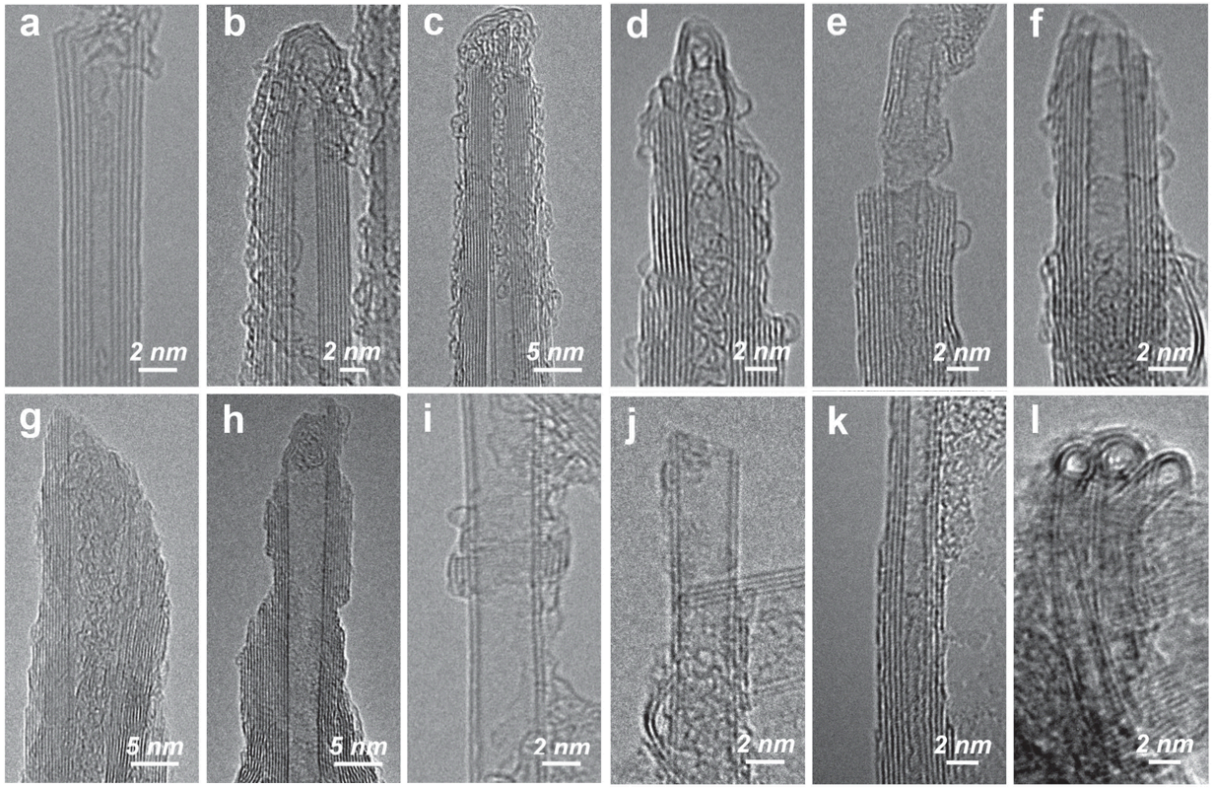

Figure 1.26. HR-TEM images of (a–c) as received of BNNTs. (d–f) HRTEM showing defects at the ends of tube of BNNTs after sonication for two hours in 3% concentrated aqueous ammonia. (g–i) HRTEM images after sonication for eight hours in 3% concentrated aqueous ammonia. (j–l) two hours in 10% of aqueous ammonia. This figure is copied from ref.80.[80] Copyright © 2014 (Yunlong Liao) by Advanced Functional Materials.

Zheng *et al* used a nanomechanical method involving atomic force microscopy (AFM) to slice BNNTs, Figure 1.27.[81,82] However, this approach is not scalable. In contrast, relatively short BNNTs have been prepared with some control of the length using bottom up chemical vapor deposition (CVD).[62,83]

1.4 Nanomaterial oxides

The properties of metal oxide nanoparticles (physical and chemical) are distinctly different to their bulk materials, and they are attracting considerable attention. They find application in diverse fields, including chemical manufacturing, environmental technology, energy conversion and storage and in biological areas.[84-87] A diversity of techniques have been used to prepare metal oxide particles in general, including electrophoretic and electrochemical deposition,[88] vacuum deposition,[89] sonochemical processing,[90] microwave plasma,[91] lithography and diffusion controlled nanoparticle growth,[92] and pulsed laser ablation (PLA), Figure 1.28. [93-100]

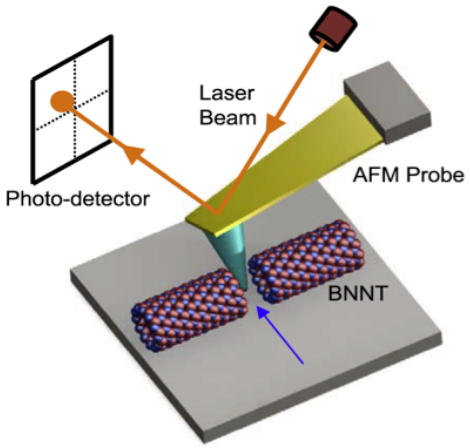

Figure 1.27. Graphical illustration of the cutting of BNNTs as a nanomechanical process using an AFM tip. The blue arrow shows the direction of movement of the AFM tip. Interestingly there is no bending or stretching of sliced BNNTs. This figure is copied from ref.82.[82] Copyright © 2013 (Meng Zheng) by Nanotechnology.

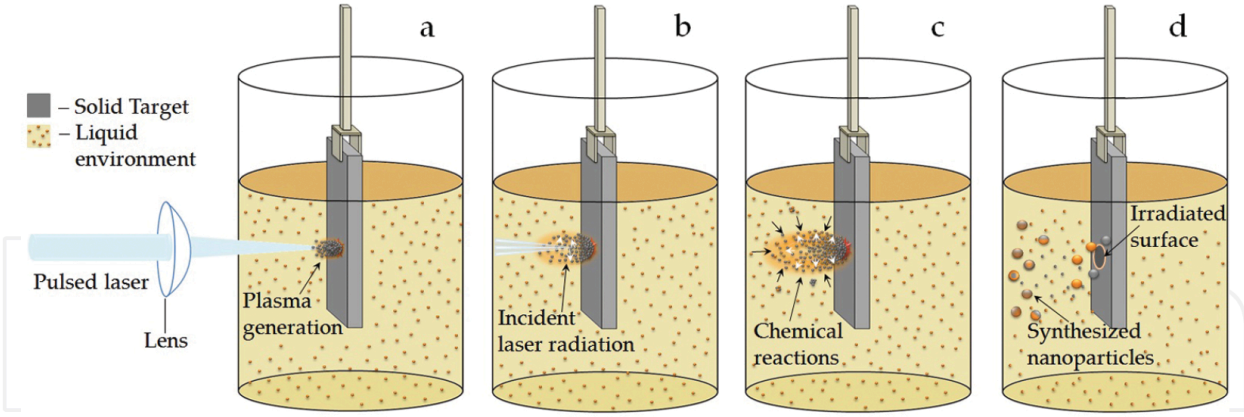

Figure 1.28. Nano-second pulsed laser ablation (PLA) in liquid: (a) Creating a plasma plume over the target metal after laser irradiation. (b) Interactions the plasma plume with the solvent. (c) Development of chemical reaction with the plasma plume around the target. (d) Aggregation of nanoparticles in the solvent and on the target surface after laser processing. This figure is copied from ref.99.[99] Copyright © 2016 (Valery A. Svetlichnyi) by Nanomaterials synthesis and Surface Modification, In Technology Croatia.

Transition metal oxide nanoparticles have a diverse number of applications. In the present study, the focus is on dicopper oxide (Cu_2O) and copper oxide (CuO), and magnetite. Nanoparticles of oxides of copper have been prepared using such techniques, with uniform size and shape of the nanoparticles.[90,92] They find particular use in catalytic organic transformations, electrocatalysis, and photocatalysis.[101-103] Also, iron oxide

nanoparticles (magnetite) find application in a number of applications, including in biomedical and bio-transport arenas.[104,105]

1.4.1 Dicopper oxide

Dicopper oxide (Cu_2O) has potential applications in solar energy conversion,[106,107] gas sensors,[108] electrode materials,[109] photocatalysis[110] and decomposition of water to H_2 and O_2 under visible light.[111] Cu_2O has been prepared using a number of different methods such as microwave irradiation of $CuSO_4$−EDTA precursor in an alkaline solution in the presence of glucose as the reducing agent, affording cubes of the Cu_2O, Figure 1.29.[112] In addition, pulse laser ablation (PLA) of pure copper in a liquid has been used to create small nanoparticles (10 nm) of the compound.[113]

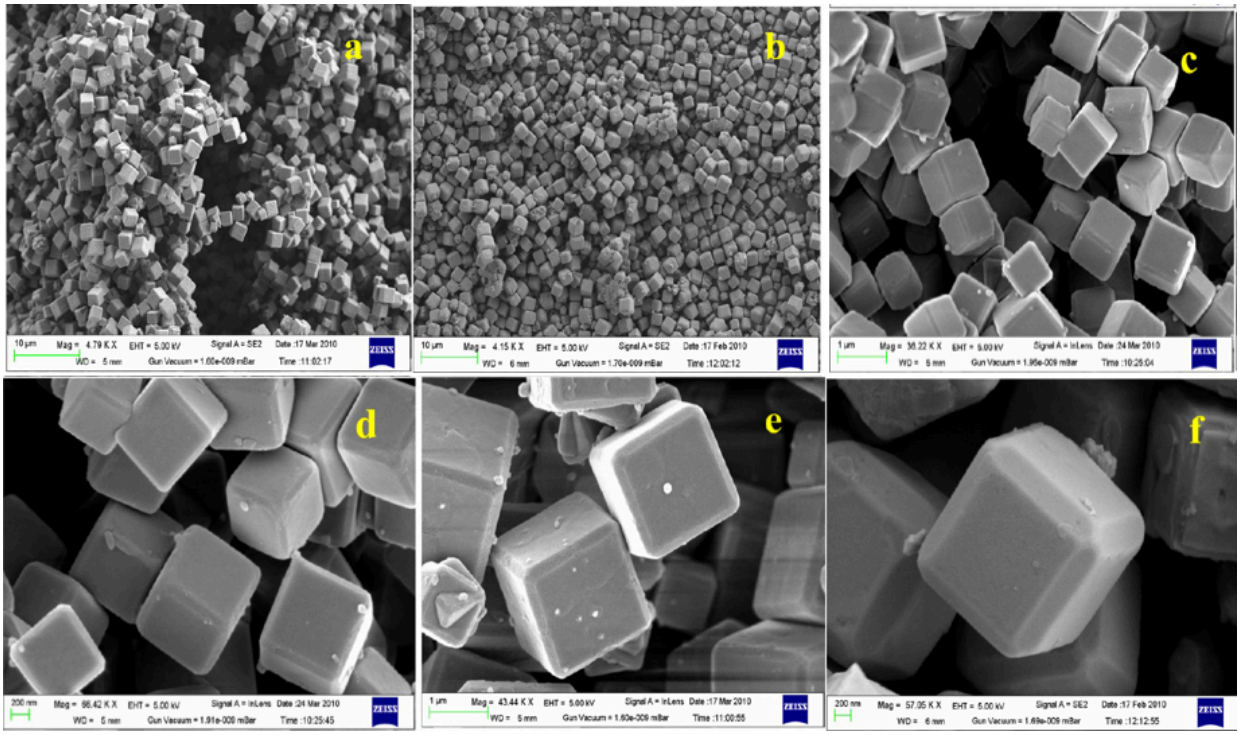

Figure 1.29. Field emission scanning electron microscopy (FESEM) images of Cu_2O cubes with different scale bar (a and b) 10 μm. (c and e) 1 μm. (d and f) 200 nm. This figure is copied from ref.112.[112] Copyright © 2012 (Mrinmoyee Basu) The Journal of Physical Chemistry C.

1.4.2 Copper oxide

YAG pulsed laser ablation of elemental copper using the second harmonic (wavelength 532 nm, 5 ns pulse) in a liquid is a simple process for generating high purity copper oxide (CuO) nanoparticles, as environmentally friendly method in avoiding the use of harsh chemicals, although the power consumption is high. The size of the particles was in the

range 13 nm to 28 nm, with the laser ablation carried out in the presence of 9% aqueous H_2O_2, Figure 1.30.[95] This method used the limit volume of solvent (batch processing) which is of limited utility for scaling up the process.

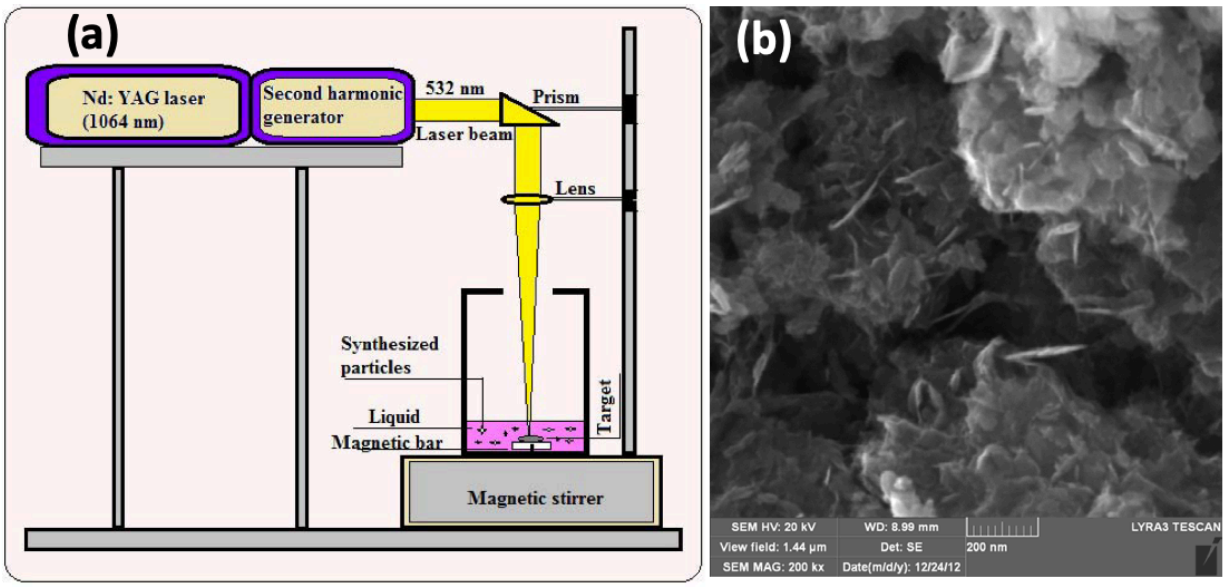

Figure 1.30. (a) Illustration of copper metal target pulse laser irradiation to create copper oxide in solution. (b) Field emission scanning electron microscopy (FESEM) image of the resulting copper oxide nanoparticles. This figure is copied from ref.95.[95] Copyright © 2013 (M. A. Gondal) by 10th International Conference on high Capacity Optical Networks and Enabling Technologies IEEE:2013.

In another publication, laser assisted direct photothermochemical patterning of CuO (copper (II) oxide) nanoparticles was reported, in gaining access to Cu electrodes. Ethylene glycol is effective in dispersing and reducing the size of CuO nanoparticles generated via high flux laser irradiation of pure Cu metal, without the need for additional processing.[114]

1.4.3 Iron Oxide (magnetite)

The synthesis and application of iron oxide nanoparticles (IONPs) is important in either as α-Fe_2O_3 (hematite), Fe_3O_4 (magnetite), α-FeOOH (Goethite) or γ-Fe_2O_3 (maghemite).[115] Magnetite particles less than 20 nm have superparamagnetic properties,[104] and have a number of applications alone, such as in biotransport and biomedicine.[104,105] They have been prepared using a number of methods, including co-precipitation,[104] sol−gel,[116] microemulsion,[117] ultrasonic spray pyrolysis,[118] microwave plasma,[91] and pulse laser ablation (PLA).[100]

1.5 Vortex fluidic device (VFD)

Traditional batch processing can suffer from batch to batch variation, and can pose challenges in scaling up for large scale applications. These can be addressed using continuous flow processing.[119,120] Conventional fluid flow is through channels, as in chip-based microfluidic devices, but these can suffer from clogging. But this is not a problem for continuous flow processing involving dynamic thin films, which was originally associated with spinning disc processor (SDP),[121-125] followed thereafter by the rotating tube processor (RTP),[126-129] which also has a dynamic thin film. The SDP typically operates with a horizontal disc, and for the RTP the rotating tube is fixed in a horizontal position, both having rotational speeds less than 3k rpm, generating a thin film below 200 μm. The shear stress and micro-mixing in both of these thin film microfluidic platforms finds utility a number of applications. However, these devices are inherently expensive to build and require large volumes (ca 100 mL) even for research purposes in optimising any application. This led to the development of the vortex fluidic device, in the Raston research laboratory at Flinders University. It is essentially a RTP but which is closed at one end, but with the angle of the rotating tube variable, as the so-called tilt angle.[119]

The VFD has a borosilicate glass or quartz tube (O.D diameter 20 mm, I.D.17.5 mm and 19.5 cm long) open at one end, which is rotated at high speed (up to 9k rpm) and inclined from -45º to 90º relative to the horizontal position. Due to high rotational speed of the tube, the VFD has high shear stress in the dynamic thin film along with intense micromixing. Solutions can be delivered to the bottom of the tube (hemispherical in shape) with control over the flow rates and rotational speed as some key operational features of the device, Figure 1.31.[130,131] This is the continuous flow mode of operation of the device. In addition, the VFD can be operated in the confined mode where a finite volume of liquid is added to the rapidly rotating tube. Under continuous flow mode, liquid is constantly fed into the tube, so that the system can be scaled up, allowing for the processing of large volumes of liquid simply by extending the operating time. Field effects on or around the rotating tube are also important, for example, the use of a pulsed laser for slicing carbon nanotubes, and this filed effect features in some of the studies in this thesis.[119,130,132,133] The use of a laser for the proposed slicing of BNNTs is in providing vibrational energy to weaken bonds of the material under shear. Both confined mode and continuous modes of the VFD can be used to explore processing with the pulsed laser operating at 1064 nm, as well as in the visible and UV range, 532 nm and 355 nm respectively, along with variation in the laser power.[134,135] In addition, heating can be used in VFD processing to control the temperature of the experiments where the induced mechanical energy in the VFD at room temperature is

limited.[136] Also noteworthy is that in the Raston research laboratory, a plasma can be generated over the surface of the this film of liquid in the device. This has been used to effectively manipulate the morphology and chemical character of colloidal graphene oxide in water.[137] More recently, Alharbi *et al* used UV irradiating (λ= 254 nm, 20 W) around the rotating tube housing the dynamic thin film in the VFD to reduce graphene oxide to graphene in water, as another example of field effects in the VFD, as well as highlighting the green chemistry metrics of the process.[138]

1.5.1 VFD applications

The VFD is a significant advance in microfluidics, but instead of passing liquids through channels under low Reynolds numbers (low shear) where clogging can be an issue, thin film of liquids is generated with controllable high shear, and high Reynolds numbers. Solheim *et al* have developed a mathematical model to account for the shape of the thin film in the VFD tube, at any tilt angle, and for any volume of liquid in the tube, with the results supported experimentally using neutron image. In addition, the residence time of the solution in the tube increases as the rotational speed decreases under continuous flow, as demonstrated for organic reaction in the device.[139] Indeed, VFD has utility in controlling organic reactions, and a number of other applications, in generating high-value products, including the processing of proteins, polymers, small drug molecules, nano-foods and biodiesel, in a more benign way which is not only attractive to industry in addressing issues such as scalability under continuous flow up front, but also in addressing environmental impact issues in minimising the impact of any process on the environment. A detailed literature review on the VFD was published in 2017, which highlights the novelty of the processing outcomes in the device as well as the extended applications at the time.[119,130] The VFD can generate products with more precise control in materials and synthesis outcomes than using conventional batch process which can suffer from batch to batch variation. This relates to the intense micromixing and shear stress, and associated high

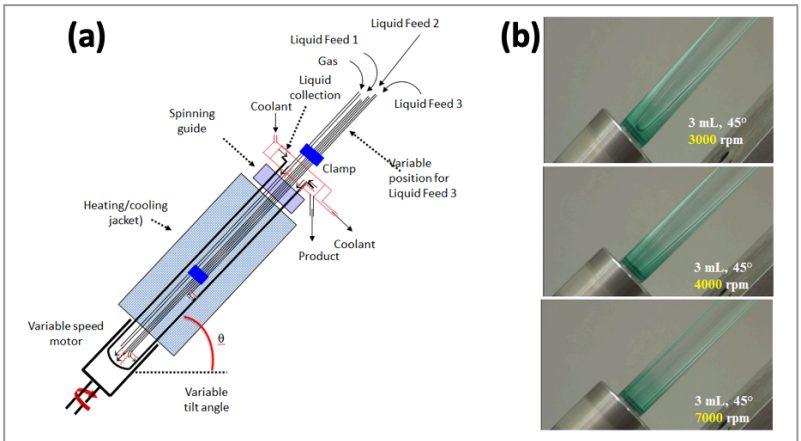

Figure 1.31. (a) The Vortex Fluidic Device (VFD) showing the salient features of the thin film microfluidic platform. (b) Variation in film thickness with change in rotation speed (3k, 4k and 7k rpm) for the tilt angle of 45° relative to the vertical position, which is optimal for most applications. This figure is copied from ref.131.[131] Copyright © 2013 (Lyzu Yasmin) by Scientific reports.

mass transfer, and high heat transfer in the device.[130] In developing any new process in the VFD, the operating parameters need to be systematically explored, and this includes flow rate of the solution and the rotation speed of the tube, along with tilt angle, and concentration of reagents. However, for a raft of applications, a reliable strategy is to first optimise the process using the confined mode of the device, where processing time is an operating parameter, for then using these parameters for optimising continuous flow processing, which is important for scaling up purposes.

1.5.1.1 VFD mediated materials synthesis

The Raston research has established the ability to manipulate materials in the VFD, including carbon nano-onions (CNOs), graphene, calcium carbonate, single-walled carbon nanotube (SWCNT), double-walled carbon nanotube (DWCNT), multi-walled carbon nanotube (MWCNT), C_{60}, graphite, graphene oxide and hexagonal boron nitride, and composites of graphene and C_{60}.[119, 140-143]

1.5.1.1.1 Exfoliation

Chen *et al* exfoliated graphite and *h*-BN in N-methyl-pyrrolidone (NMP) as the solvent of choice, using the confined mode of operation of the VFD (30 min), using the first generation designed VFD which housed a 10 mm O.D. glass tube (8.5 mm I.D., 16 cm long of the tube), with the tilt angle at 45º. The percentage of exfoliated graphite and *h*-BN was ≤1 wt.% (rotational speed of the tube optimised at 7k rpm, for 30 min processing) and ≤5 wt.% (rotational speed of the tube optimised at 8k rpm, for 30 min processing) respectively, Figure 1.32.[142] Subsequently, they used water as solvent in the dynamic thin film in the VFD (confined mode) to exfoliate graphite and then decorate the multi-layered 2D sheets with microalgal cells. The composite was active in removing nitrate from wastewater.[144] Related to this is (i) the preparation of a composite material of graphene oxide (GO) with the same cells in the VFD, which is also effective in removing nitrate from wastewater, also for the

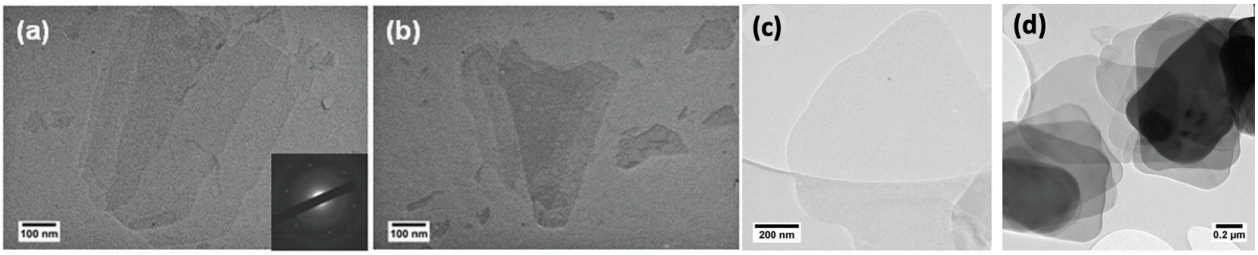

Figure 1.32. (a, b) TEM images of exfoliated graphene sheets (with selected area electron diffraction (SAED) pattern, inset in (a)), and (c, d) exfoliation *h*-BN layers. This figure is copied from ref.142.[142] Copyright © 2012 (Xianjue Chen) by Chemical Communications.

confined mode of operation of the device, Figure 1.33, and (ii) wrapping bacterial cells with graphene oxide sheets under the same mode of operation of the VFD.[145,146]

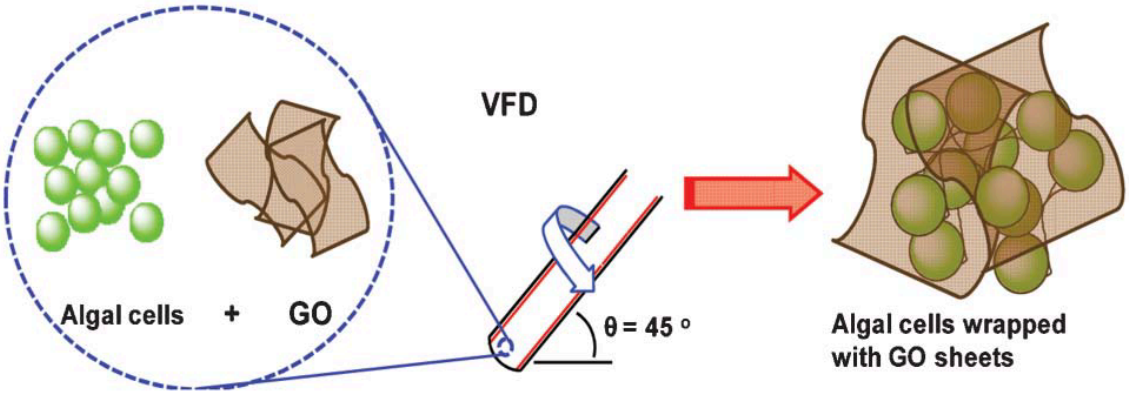

Figure 1.33. Illustration of the ability of VFD for the wrapping single algae cell. This figure is copied from ref.146.[146] Copyright © 2013 (Wahid M. H.) RSC Advances.

1.5.1.1.2 Scrolling

Alharbi *et al* used a colloidal suspension of graphene oxide (GO) sheets in water to fabricate in high yield, under continues flow processing in the VFD, graphene oxide scrolls (GOS). The optimized conditions were for a rotational speed of 4k rpm at a tilt angle of 45°, with the rotating glass tube in the VFD simultaneously irradiated with a pulsed laser operating at 1064 nm and 250 mJ. The overall optimized process is in the absence of any additional reagents, Figure 1.34.[140] Related to this is the work by Vimalananthan *et al* on exfoliating graphite directly into graphene scrolls in the VFD, in a 1:1 mixture of toluene and

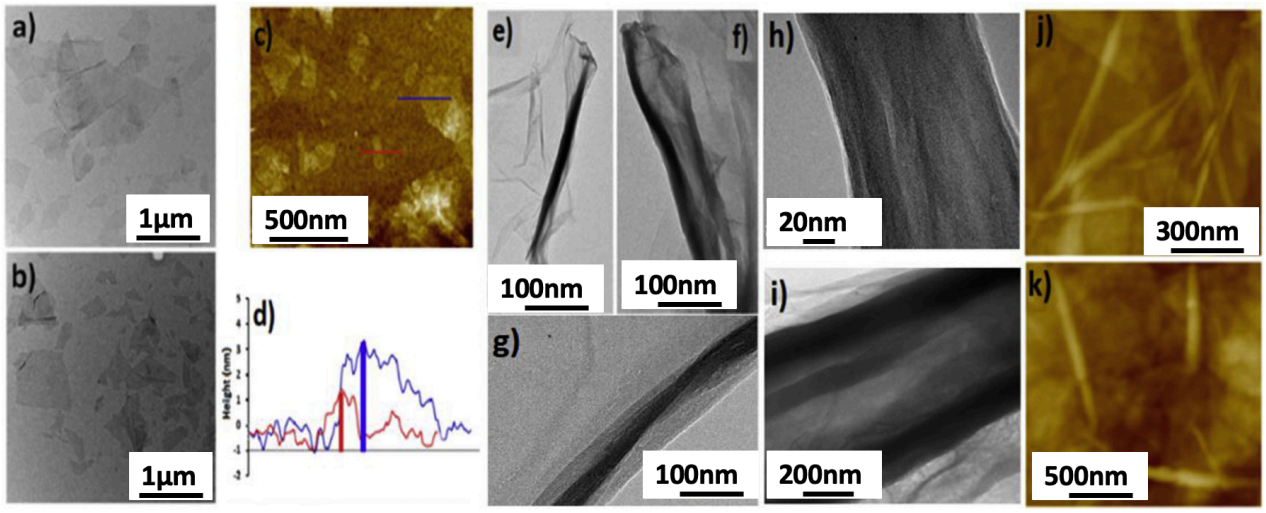

Figure 1.34. (a and b) TEM images of graphene oxide before processing in the VFD to form graphene oxide scrolls, and the corresponding AFM with height profile in (c and d), respectively. (e-i) TEM images for graphene oxide scrolls. (j-k) AFM images of graphene oxide scrolls collected from the VFD after processing a 4k rpm, θ, 45° for a flow rate of 0.45 mL/min while irradiated with a pule laser operating at 1064 nm and 250 mJ. This figure is copied from ref.140.[140] Copyright © 2018 (Thaar M. D. Alharbi) Carbon.

water in the confined mode, as a high yielding process. The semi-conductivity property for graphite changes to high conductivity after scrolling the 2D material.[141]

1.5.1.1.3 Slicing and fragmenting CNTs

The three types of carbon nanotubes (SWCNTs, DWCNTs and MWCNTs) can be sliced in a 1:1 mixture of N-methylpyrollidinone (NMP) and water under continuous flow conditions in the VFD, while the high shear stress liquid is irradiated with a pulsed laser operating at 1064 nm wavelength and 250 mJ of laser energy. Slicing of the CNTs was in the absence of any reagents with the product having reduced side wall defects, Figure 1.35(a, b).[119,132] The mechanism of slicing the SWCNTs in the VFD is understood through bending of the tubes under shear stress in a dynamic thin film with increasing of C-C vibration form NIR laser irradiation, which was enough to break C-C bond in the tube. Thus, the nanotubes are sliced laterally. Subsequent work established the ability to control the length of sliced SWCNTs in the same solvent mixture by varying the laser power. Using the pulsed laser operating at 1064 nm and 250 mJ, 400 mJ and 600 mJ, results in length distributions of

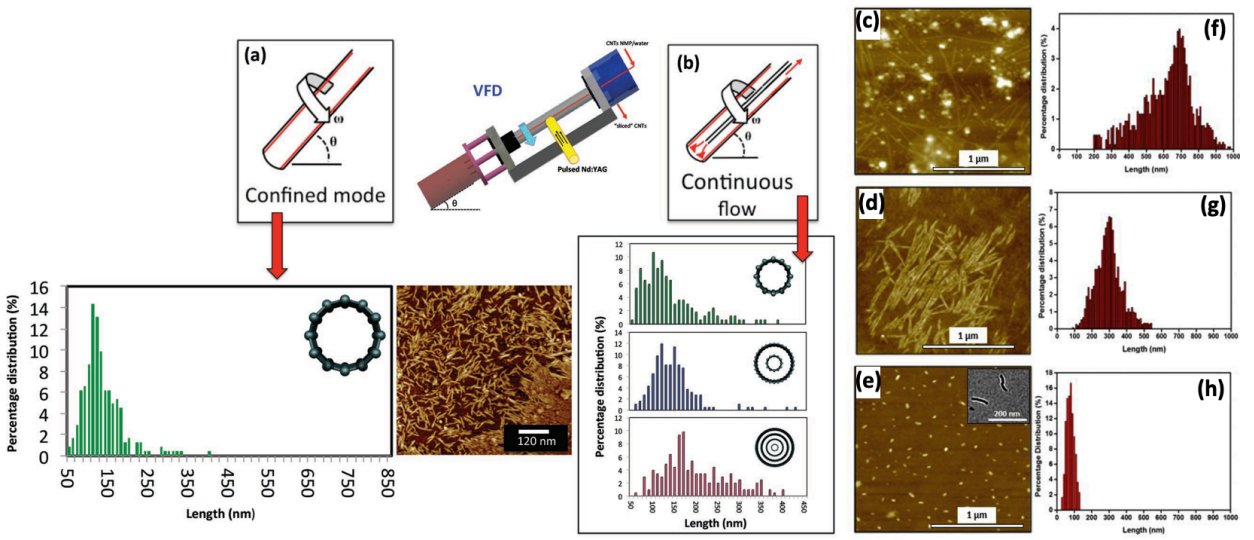

Figure 1.35. (a) Sliced SWCNTs formed in a 20 mm O.D. tube of the VFD (confined mode) at 7.5k rpm and tilt angle 45º with the tube irradiated with a pulsed laser (1064 nm) operating at 260 mJ as energy, affording sliced SWCNTs with an average length ca 100 nm, as shown by the AFM image. (b) Continuous flow VFD-mediated sliced single, double and multi-walled under the same conditions same conditions, with a flow rate of 0.45 mL/min. This figure is adapted from ref. 119 and 132.[119,132] Copyright © 2017 (Kasturi Vimalanathan) by Advanced Materials Technologies, © 2017 (Joshua Britton) by Angewandte Chemie International Edition in English.(c-e) AFM of sliced SWCNTs formed under continuous flow in the VFD, at 8.5k rpm, the concentration of SWCNT 0.08 mg/mL in NMP and water, volume ratio 1:1, tilt angle 45º and flow rate 0.45 mL/min, with the laser operating at 1064 nm, and 250 mJ, 400 mJ and 600 mJ, respectively (insert on image (e)TEM image for short SWCNTs). (f-h) Length distributions for samples prepared under the conditions described for the AFM images in (c-d). This figure is adapted from ref.147.[147] Copyright © 2018 (Thaar M. D. Alharbi) by carbon.

sliced SWCNT around 700 nm, 300 nm and 80 nm, respectively. The optimized conditions for the VFD processing were rotational speed 8.5k rpm, flow rate 0.45 mL/min, concentration of SWCNTs 0.08 mg/mL and tilt angle 45º, Figure 1.35(c-h).[147]

Luo *et al* have developed a process for generating carbon dots (CDs) from MWCNTs suspended in hydrogen peroxide (30%) in the VFD while the liquid is irradiated with a pulsed laser operating at 1064 nm and 450 mJ. Here the laser is effective in generating hydroxyl radicals which then oxidizes the MWCNTs while they are subject to high shear and absorption of the NIR laser light. The average size of CDs was 6 nm with the highest emission intensity of the solution at 450 nm under 345 nm excitation wavelength. Future work here will develop the potential of tuning the intrinsic fluorescence by controlling the size of the CDs, for shifting the excitation to red wavelengths, Figure 1.36.[148]

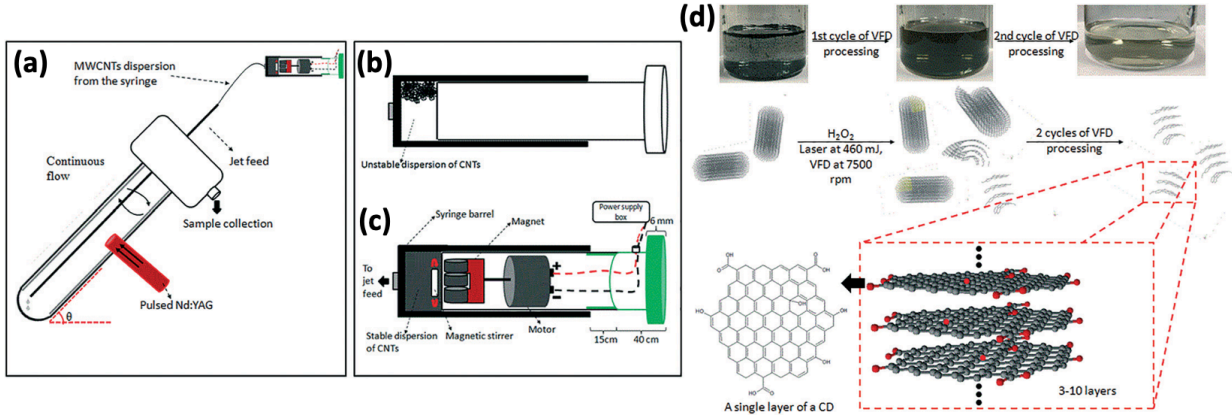

Figure 1.36. (a) Illustration of VFD setting with laser beam for forming carbon dots (CDs). (b) Normal syringe housing an otherwise unstable dispersion of MWCNTs in 30% aqueous. (c) Syringe housing a magnetic stirrer driven by an electric motor inside the plunger which creates the dispersion. (d) Processing steps for fabricating CDs in a 20 mm O.D. VFD tube, rotational 7.5k rpm, tilt angle 45º and flow rate 0.45 mL/min, after recycling twice through the VFD irradiated at 1064 nm (pulsed laser), 460 mJ. This figure is copied from ref.148.[148] Copyright © 2018 (Xuan Luo) by Reaction Chemistry and Engineering.

1.5.1.1.4 VFD mediated synthesis of composite material

One of the earliest papers on the VFD, in 2012, reported on the decoration of carbon nano-onions (CNOs) with palladium nanoparticles 2 to 7 nm in diameter within the aqueous thin film of liquid in the device. This involves pre-treating the CNOs with *p*-phosphonic acid calix[8]arene, then aqueous H_2PdCl_4, followed by VFD processing under an atmosphere of hydrogen, Figure 1.37.[149] The material was readily incorporated into sensors for detecting >10% hydrogen, using a drop casting method.[150] In a similar way, Chen *et al* used a similar procedure for decorating a different type of carbon, namely graphene, with Pd-NP, which is also a material for constructing a functional hydrogen sensing device.

In related work from the Raston group, platinum nanoparticles were decorated on carbon Nano-onions using ascorbic acid as the reducing agent in aqueous solution. The composite nanomaterial Pt-NPs@CNOs was generated under continuous flow in a VFD, Figure 1.38.[151] All the published papers above on decorating different types of carbon with Pd and Pt used a 10 mm diameter VFD tube, which was the original tube size. Now the processing is predominantly in a 20 mm diameter tube.

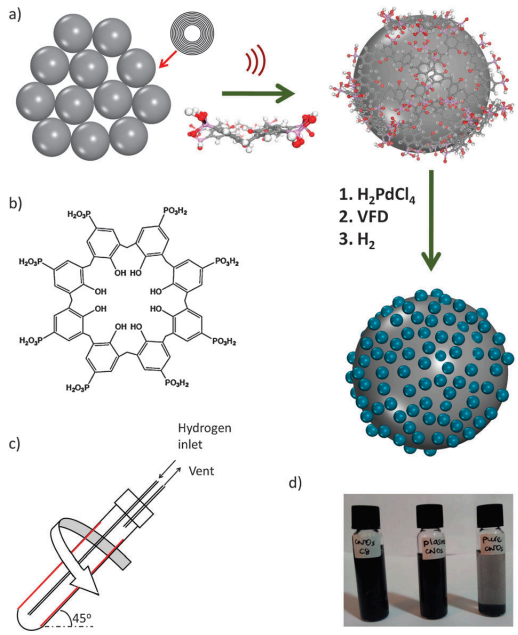

Figure 1.37. (a) Illustration of the synthesis of a composites material containing CNO and Pd NPs, in the presence of $PdCl_4^{2-}$. (b) *p*-Phosphonic acid calix[8]arene used in the synthesis in (a), and the VFD. (d) Photographs of solutions, left to right, of the composite comprising CNOs–calixarene, CNOs after processing with Pd(II) solutions and as received CNOs, respectively. This figure is copied from ref.149.[149] Copyright © 2012 (Faizah Md Yasin) by Chemical communications.

1.5.1.1.5 Self- assembly

The shear stress in the dynamic thin film in the VFD is effective in controlling self-assembly and crystallisation processes, as bottom up processes in forming nanoparticles with a precise control over the size, shape, and phase of the material. This is possibly by systematically exploring the parameter space of the VFD, namely tilt angle, rotation speed, and temperature. Ramiz *et al* used the VFD to control the phase and shape of calcium carbonate crystals formed at room temperature under confined mode of operation of the device.[152] The VFD is also effective in forming nanotubules of fullerene C_{60} under continuous flow, using two jet feeds to separately deliver a toluene solution of the fullerene and water, with the tubules optimised at more than 4μm in length and *ca.* 100 nm to 400 nm inner diameter, Figure 1.39(a-g).[153] In a related study, Ibrahim *et al* used two jet feeds to separately deliver an *o*-xylene solution of C_{60} and N-N-dimethylformamide (DMF) as the anti-solvent in forming symmetrical right cones in high yield

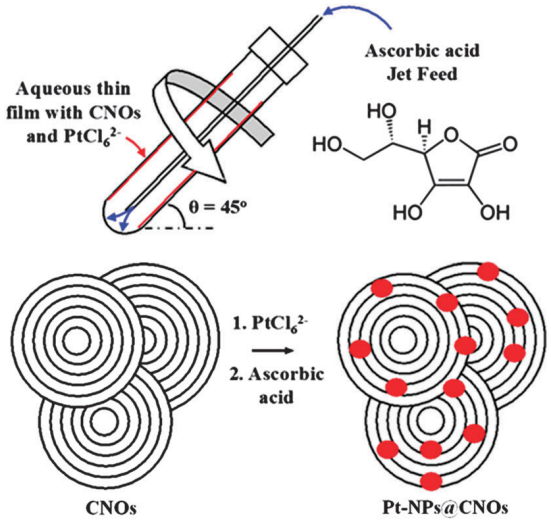

Figure 1.38. Graphical illustration of the Pt NPs/ CNOs composite material prepared in a 10 mm dimeter VFD tube, using ascorbic acid as the reducing agent. This figure is copied from ref.151.[151] Copyright © 2013 (Yuhan A. Goh) by Chemical Communications.

with diameters 0.5 to 2.5 μm, pitch angle 25º to 55º and wall thickness 120 to 310 nm, Figure 1.39(h-m).[154] Their formation is in the absence of surfactants and any other reagents, and is scalable, operating under continuous flow conditions. Interestingly, other solvents containing dissolved C_{60} afforded different shapes.[154] Another example of continuous flow processing in the VFD, is taking advantage of the shear stress in the dynamic thin film, to assemble host-guest vesicles containing carboplatin residing in the cavity of a calixarene lipid mimic. The mean hydrodynamic diameter of the host-guest vesicles is 134± 25 nm with 75% uptake of the carboplatin relative to all the cavities available, with the nano-vehicles having a high anticancer activity.[155]

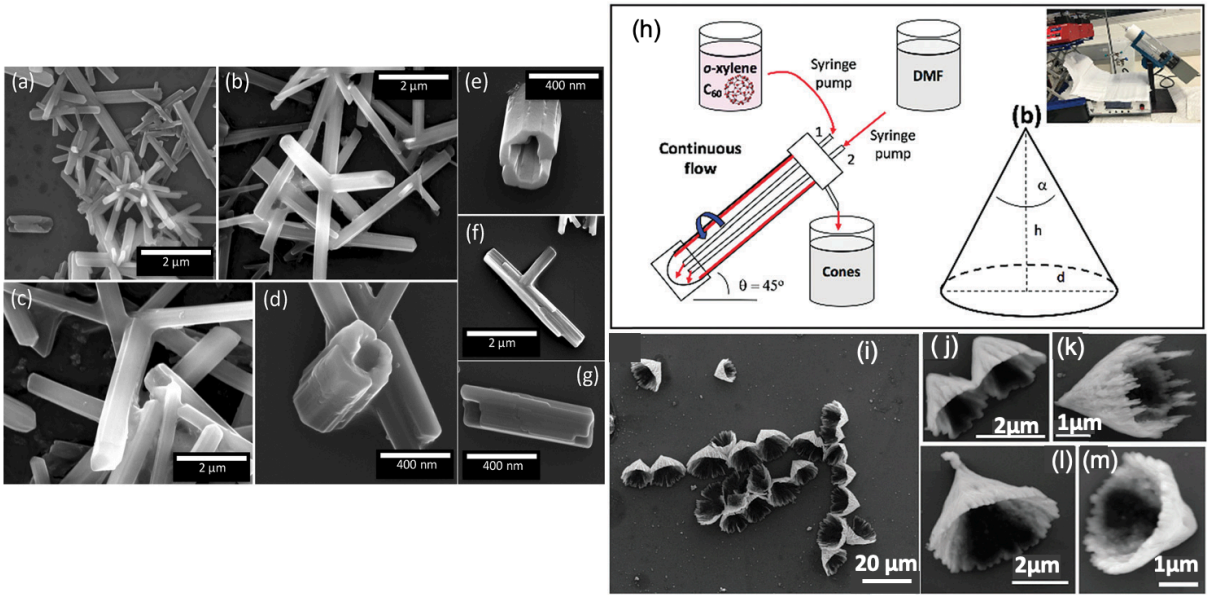

Figure 1.39. (a-g) SEM images of nanotubules of C_{60} revealing lengths 0.4 to 3 μm with inner diameters ca. 0.1 to 0.4 μm. This figure is copied from ref.153.[153] Copyright © 2017 (Kasturi Vimalanathan) by Angewandte Chemie. (h) Illustration of the self-assembly of C_{60} into cones in a VFD (picture inset of the device), using a volume ratio of 1:1 for *o*-xylene and DMF. (i-m) SEM images of the C_{60} cones prepared under continuous flow at 0.5 mL/min for both solvents, rotational speed 4k rpm, tilt angle 45º and concentration of C_{60} in *o*-xylene at 0.5 mg/mL. This figure is copied from ref.154.[154] Copyright © 2018 (Ibrahim K. Alsulami) by Chemical Communications.

1.5.1.1.6 Coiling SWCNTs

The shear stress in a dynamic thin film comprised of a 1:1 mixture of toluene containing dispersed SWCNTs and water in a VFD is effective in disentangling as received single walled carbon nanotubes (SWCNTs) and assembling them into organized Nano rings, as a confined mode process. The diameters of these rings are 100 to 200 nm or 300 to 700 nm for respectively a 10 mm or 20 mm O.D. VFD tube, Figure 1.40(a-e).[156] This is another example of the shear stress in the VFD being effective for controlling self-assembly

processes/probing the structure of self-organized systems. Subsequently this coiling of SWCNTs into nanorings of coil CNTs has been developed into a continuous flow high yielding process, also in the absence of any toxic chemicals and surfactants. Magnetic force microscopy (MFM) established a magnetic interaction with the MFM tip, which is strongly dependent on the thickness of the coiled SWCNT rings, Figure 1.40(f-i).[157]

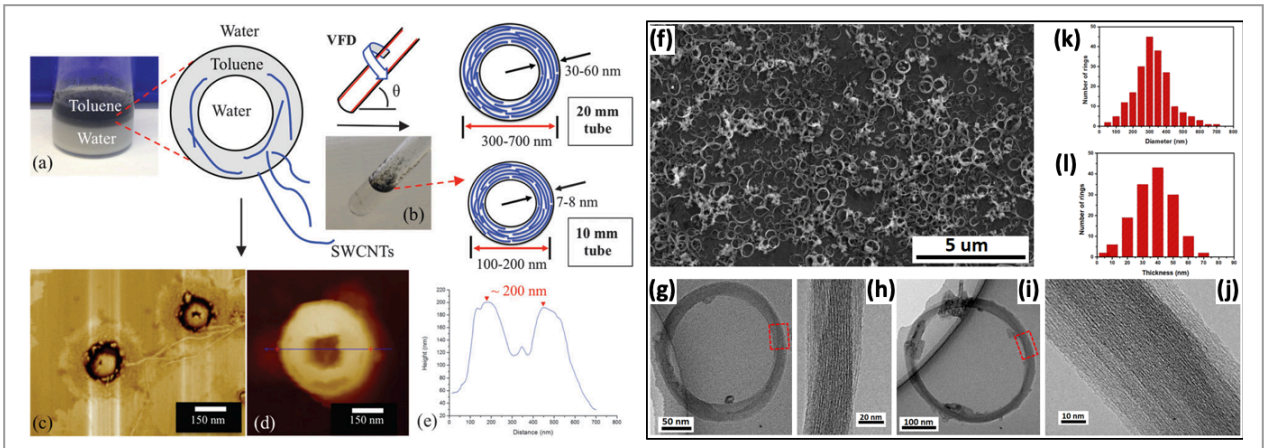

Figure 1.40. (a) SWCNTs in a mixture of toluene and water after sonication, in forming nano-rings. (b) Photograph of a colloidal solution after passing through a VFD with tilt angle set at 45º. (c and d) AFM images of nano-rings of SWCNTs after drop casting a colloidal solution. (e) Height profile of the nano-ring form the image in (d). This figure is copied from ref.156.[156] Copyright © 2014 (kasturi Vimalanathan) by Chemical communications. (f) SEM image of coiled SWCNT nano-rings formed under continuous flow processing in the VFD, at 8k rpm rotational speed, flow rate 0.45 mL/min (SWCNT in a mixture of toluene and water (0.16 mg/mL)) and tilt angle 45º. (g-j) TEM and HRTEM images of the coiled SWCNT nano-rings, respectively. (k and i) Distributions of diameter and thickness of the nano-rings, respectively. This figure is copied from ref.157.[157] Copyright © 2019 (Thaar M.D. Alharbi) by ACS Applied Nano Materials.

1.5.1.1.7 Metal oxide and Metal oxide/composite

The VFD has been used to entrap microalgal cells within a composite of polyvinylpyrrolidone (PVP) polymer and superparamagnetic magnetite nanoparticles under confined mode operation of the device, Figure 1.41.[158] The cells are still functional within the composite which can be retrieved from an aqueous dispersion using an external magnet. [158] The magnetic nanoparticles were prepared in a separate process in the VFD, operating under continuous flow conditions. Continuous flow processing in the VFD in targeting mesoporous silica is possible at room temperature, avoiding the need for 24 hours hydrothermal processing under batch conditions to prepare the same material, with the added ability to control the pore size in the VFD, which has not been established for batch processing. Both types of processing still require calcination to remove the templating polymer.[159] Use of the VFD also lends itself to incorporating palladium nanoparticles in the

material.[160] VFD processing is effective in sol–gel synthesis, in gaining access to a silica xerogel at room temperature, simply by removing the templating polymer used in the synthesis of the above mesoporous material.[161] Laser ablation of an iron rod inside the VFD under the continuous flow of water passing through the device is effective in preparing superparamagnetic magnetite nanoparticles (*ca.* 15 nm). This is a one-step process in air in the absence any chemicals or surfactants.[98]

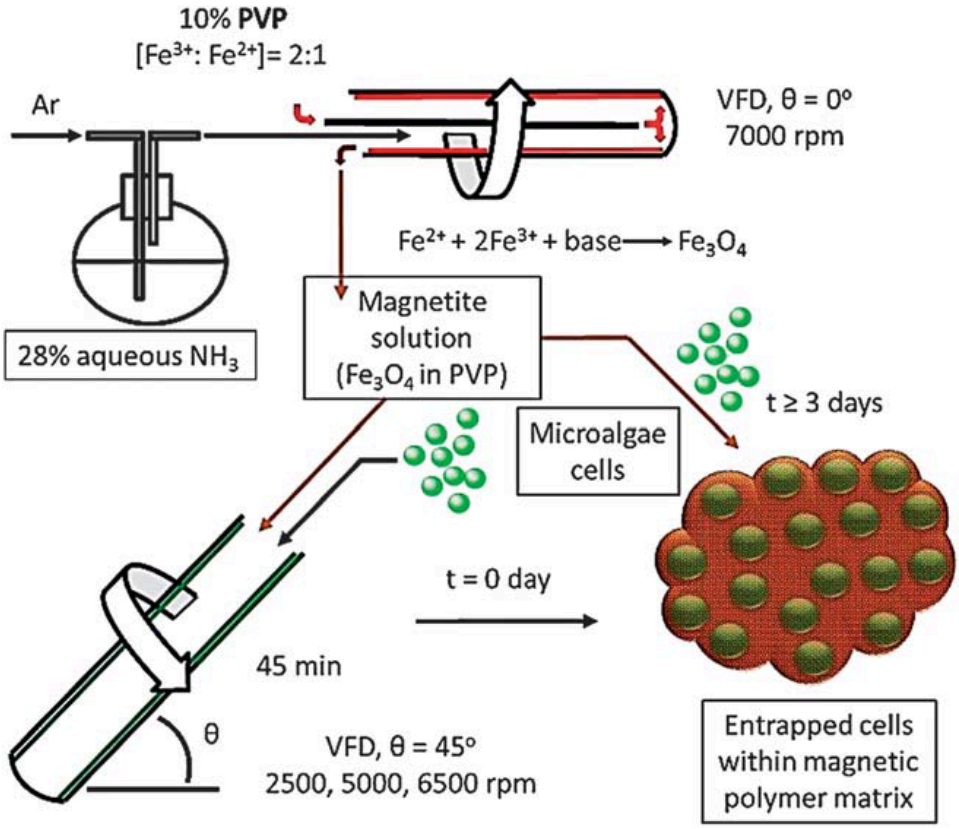

Figure 1.41. Illustration of the synthesis of superparamagnetic nanoparticles of magnetite embedded in PVP, for then incorporating algal cells, with all the processing in the VFD. This figure is copied from ref.158.[158] Copyright © 2013 (Ela Eroglu) by Nanoscale.

1.5.1.2 Proteins

Britton *et al* established the ability to coat the inside of the VFD tubes with protein, for use in continuous flow enzyme-mediated catalysis with a dramatic increase in the rate of the reactions while dispensing with the need to separate enzyme from the product.[162] Other applications of the VFD involving proteins include enhancing enzyme catalyzed reaction (enzymes in solution) under continuous flow with excellent stereo- and regio-specificities,[163] protein folding,[164] protein purification [133] and phase separation (extraction) in the separation of C-Phycocyanin from *Spirulina maxima*.[165]

1.5.1.3 Polymer processing in the VFD

Fluorescent nanoparticles (10 nm) are readily prepared under continuous flow in the VFD, from polyethylenimine (PEI). Here the device effectively degrades the polymer in air in forming the functional nanoparticles which absorb in the UV light and show significantly reduced cytotoxicity compared to as-received polymers, Figure 1.42.[136] Other polymer work in the VFD includes the above discussed polyvinyl pyrrolidine (PVP) encapsulation of superparamagnetic magnetite nanoparticles.[166] Interestingly the same polymer is effective in controlling the growth of dandelion-shaped $LnPO_4$ particles at room temperature.[167]

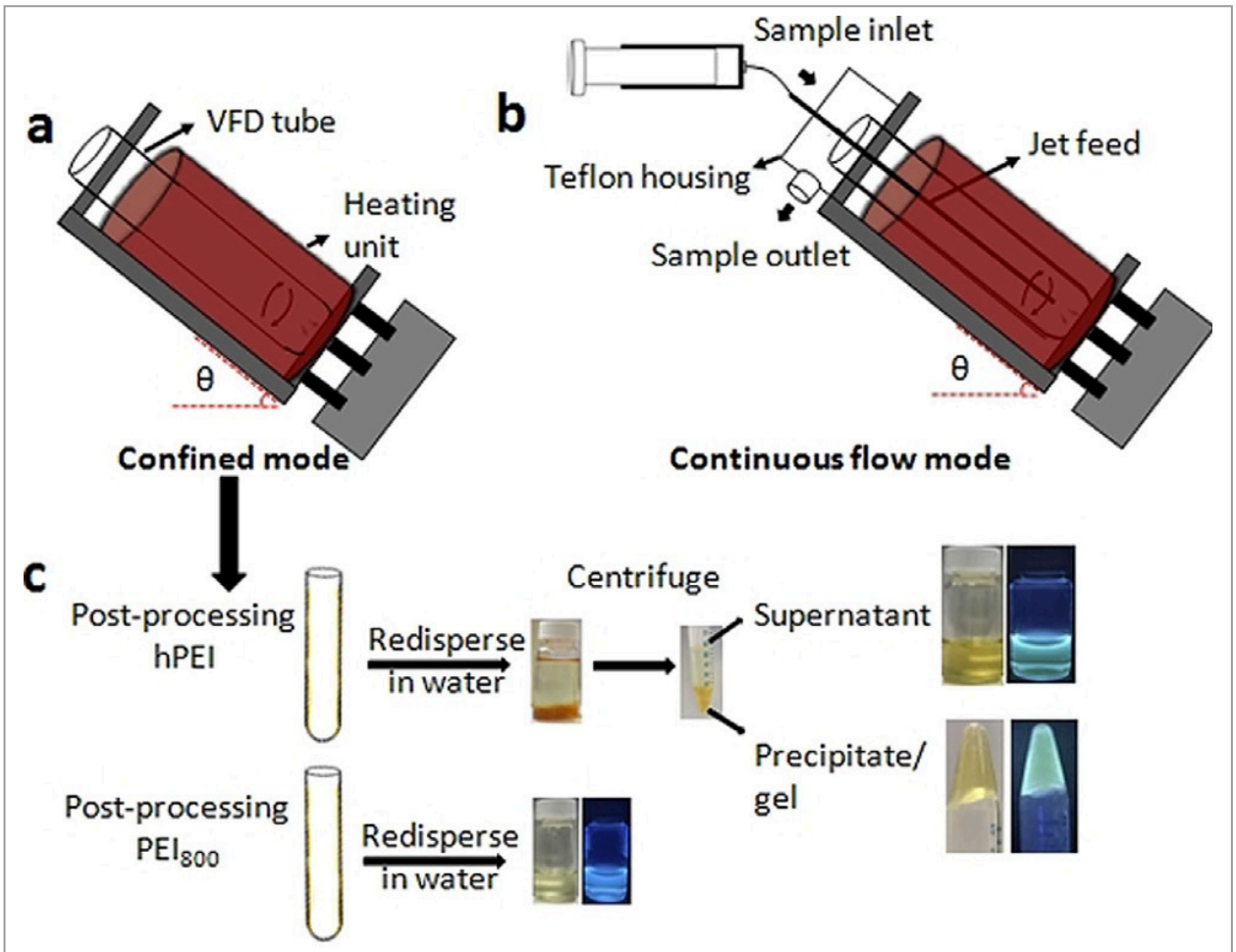

Figure 1.42. Illustration of the set up for heating the VFD tube to fabricate PEI (poly ethylene amine). (a and b) Heating unit on the VFD, tilt angle θ = 45º, using both confined mode and continuous flow mode of operation, respectively. (c) hPEI (high molecular weight of poly ethylene amine) and PEI800 (800 of molecular weight of poly ethylene amine) after passing through the VFD under confined mode. This figure is copied from ref.136.[136] Copyright © 2018 (Xuan Luo) by ChemPhotoChem.

1.5.1.4 Organic synthesis and Inorganic synthesis

Yasmin *et al* used the VFD to prepare resorcin[4]arenes and pyrogallol[4]arenes as predominantly their C_{4v} isomer, from the reaction of resorcinol or pyrogallol with aromatic aldehydes under continuous flow mode of operation. In addition, the confined mode of operation of the VFD was effective in converting any C_{2v} isomer and C_{2h} isomer to the C_{4v} isomer, Figure 1.43.[168] The Diels–Alder reaction is effective in the VFD under confined mode processing,[169] as is C–N bond forming reactions in N-aryl compounds from 2-chloropyrazine and the corresponding imine, in the absence of transition metal catalyst, using the confined mode operation of the device.[170] Related to this is C-N bond forming reactions in accessing pyrimidine and quinoxaline analogues.[171] Polysubstituted and 2,4,6-trisubstituted pyridines

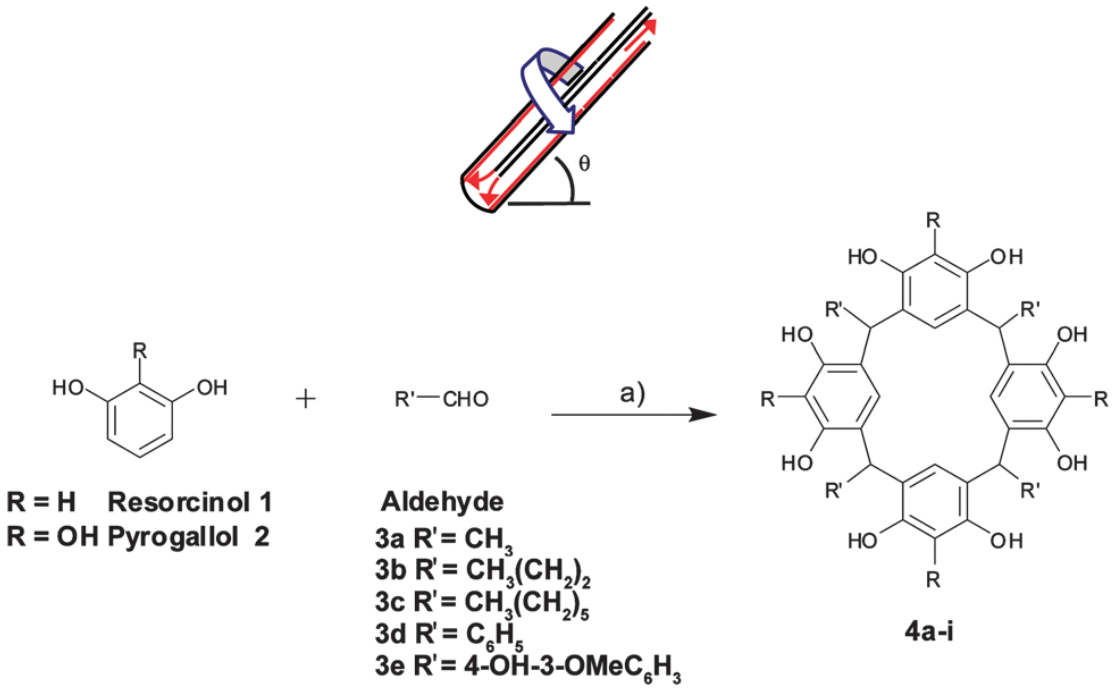

Figure 1.43. Schematic for the synthesis of calix[4]arenas in the VFD under continuous flow conditions, 1 mL/min, 7k rpm, θ, 45º at 80ºC, in a mixture of ethanol and concentrated HCl. This figure is copied from ref.168.[168] Copyright © 2013 (Lyzu Yasmin) by Chemical Communications.

fluorescent compounds have been prepared under confined mode operation of the VFD,[172] with continuous flow processing used for the acylation of amines in taking advantage of the high heat transfer of the exothermic reactions.[173] Other organic reaction studied in the VFD include photo-redox catalysis,[174] the synthesis of alkyl-based esters,[175] the de-coloration of a photochromic dye in the VFD by a plasma generated over the dynamic thin film of liquid, [176] organic oxidations,[177] imine formation[178] and the synthesis of di-carboxylate esters.[179]

The VFD has had success in the synthesis of inorganic materials. This includes the controlled synthesis of different phases of calcium carbonate (calcite, aragonite and vaterite)

with control also on the size and shape of the particles, down to nanometer dimensions.[152] There is also the synthesis of nanoparticles of pro-vaterite, as amorphous material which is stable for 14 days.[180] Jutarat *et al* have prepared perovskite ($CH_3NH_3PbI_{3-x}Cl_x$) in dimethyl sulfoxide (DMSO) from the reactions lead chloride ($PbCl_2$) and methylammonium iodide (CH_3NH_3I), and incorporating this into a solar cell result in increased efficiency 26% higher than material prepared using batch processing.[181]

1.5.1.5 Nano food processing

Initial results report on the potential of VFD processing in the food industry. The shear stress in the VFD is effective in reducing enzymatic hydrolysis times from about 2–3 hours to 20 minutes. A second process is the pasteurization of raw milk, with the processing time reduced from 30 to 10 minutes, with another in reducing the encapsulated particle size from micro sized to hundreds of nanosize dimensions.[182] In addition, the VFD is effective in encapsulation of fish oil under continuous flow conditions, while controlling the size of the particles down to 50 nm to 250 nm, Figure 1.44.[183]

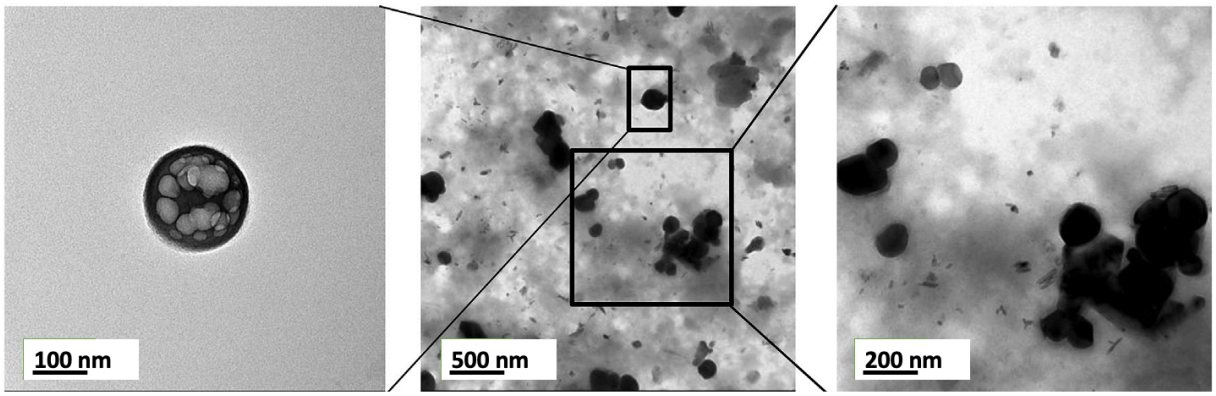

Figure 1.44. TEM images (uranyl acetate stained) of encapsulated particles produced after passing fish oil through the VFD with 8k rpm, 45º, flow rate 0.1 mL/min and concentration of mole ratio (1:1) was 2g/100 mL. This figure is copied from ref.183.[183] Copyright © 2019 (Shan He) by LWT.

1.5.1.5 Biodiesel

The production of biodiesel is an important application of the VFD tube. The first report on this was in 2014, as a room temperature continuous flow process to convert sunflower oil to biodiesel in the absence of a co-solvent or the use of complex catalysts. This has improved clean technology metrics for biodiesel production, with the ability to recycle the catalyst three times and without the need for further complex down-streaming operated, Figure 1.45.[184] In addition, free fatty acid (FFA) had high conversion to biodiesel with

undetectable FFA content, as an effective room temperature continuous flow process,[185] and direct conversion of microalgal biomass biodiesel as a novel one step process.[186]

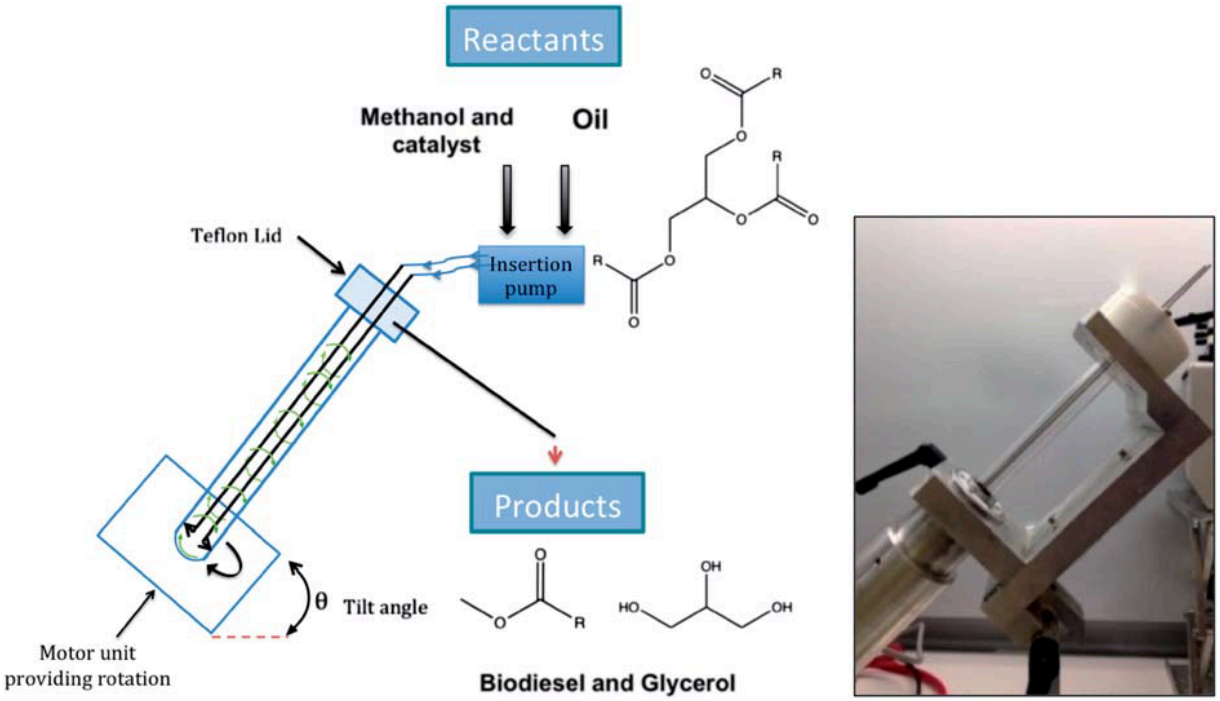

Figure 1.45. Illustration of the VFD processing set up for preparing biodiesel from sunflower oil which is devoid of Fatty Acid Methyl Ester (FAME)) the optimized conditions were 5250 rpm, tilt angle 45º and flow rate 0.5 mL/min for 10 mL of 1 M of (KOH, NaOH or NaOMe in methanol). This figure is copied from ref.184.[184] Copyright © 2014 (Joshua Britton) by RSC Advances.

1.6 Research Program

The main concept of this thesis relates to the ability to manipulate 0D, 1D and 2D materials within nanoscale dimensions to harness their properties for a wide range of potential applications, including the next generation batteries, photocatalysts, medicine, gas storage, removing toxic compound from wastewater, nanodevice technology and catalysis. The properties of materials can be tailored based on their size, shape and morphology. Thus, employing the use of controllable mechanoenergy generated from the shear stress in the dynamic thin film of the VFD, this research probes the development of novel methods to gain access to new forms of 0D, 1D and 2D nanomaterials using green chemistry metrics, which includes incorporating scalability at the inception of science. This approach attempts to ensure the environmental and economic feasibility of the resulting technology.

The overall aims of this thesis are:

1- Develop the use of thin film micro fluidics in exfoliation and fragmentation 2D MXene (MXene is a family of layered compounds consisting of 2D nano-sheets).
2- Decorate and fabricate MXene/anatase Ti_2O NPs composite material.
3- Develop the use of VFD processing for other 2D materials, including the exfoliation and scrolling of *h*-BN.
4- Decorate *h*-BN sheets with superparamagnetic magnetite for application in removing phosphate from wastewater.
5- Develop the use the VFD microfluidic platform to slice BNNTs.
6- Explore the use of the shear stress in the dynamic thin film to create Cu_2O NPs and CuO NPs.
7- Incorporate green chemistry metrics into the processing, under continuous flow conditions, avoiding to use harsh chemical and agents.

The rapidly advancing and diversifying nature of continuous flow processing to generate different dimensions of nanomaterials makes it popular in both academic and industrial research. Translating reactions in the laboratory to the commercial arena is favoured by incorporating scalability at the inception of the science, operating under continuous flow conditions. Although much younger than conventional batch materials processing, thin film flow generated materials have impacted multiple areas of the materials sciences. All the experiments of this thesis used 20 mm O.D, 17.5 mm I.D. and 19.5 cm long VFD tubes.

The challenges of this thesis were as follow:

1- Dispersions of the MXene, *h*-BN sheets and BNNTs are unstable, which necessitated the design of a magnetically stirred syringe (MSS)), housing an electric motor inside the plunger to maintain a uniform suspension of the liquid delivered to the rapidly rotating tube in the VFD.
2- *h*-BN adheres to the wall of the VFD tube at the tilt angle of +45º, and this was overcome by using a tilt angle of -45º, which was reported in one of my first authored papers.
3- The purity of the purchased BNNTs was ≥ 50%, and this necessitated the development of a simple two-step process to increase the purity, prior to VFD mediated slicing experiments.

Initially, the VFD was explored to mediate 2D materials chemistry transformations under shear stress, to exfoliate 2D MXene and fragmentation of MXene to nanoparticles. Due to the sensitivity of the MXene to air, all experiments to optimise conditions of the VFD were carried out under N_2 gas. After exploring a number of different solvents, IPA and water volume ratio (1:1) were found to be optimal for exfoliation, down to 3 nm thick sheets, and fragmentation of MXene down to ca 68 nm dimeter nanoparticles.

Chapter 3, presents the first report on the fabrication of anatase TiO_2 NPs/MXene composite, building on work of others reported as early as 2014. Since then a lot of work has been reported by different methods to prepare such material, including heating or using H_2O_2. Herein, aqueous solutions of 30% H_2O_2 were used to prepare the composite under continuous flow conditions. Exfoliation of MXene with oxidation on the surface is down to 300 nm $\pm$ 200 nm thick sheets decorated with anatase, TiO_2 NPs/MXene spheres are ca 2 μm $\pm$ 0.5 μm in diameter.

Chapter 4, present the first report on the exfoliation and scrolling of *h*-BN in water in the VFD, using a tilt angle -45º, avoiding the use of harsh chemicals or agents. The thickness of the exfoliated *h*-BN was ca. 2 nm and the height of *h*-BN scrolls was between 10 nm to 67 nm.

Chapter 5, presents the first report on the synthesis of *h*-BN@ magnetite composite material, generated *in situ* in the VFD via laser ablation of a pure iron rod (1064 nm, 360 mJ) using water as the solvent. The composite *h*-BN@ magnetite was superparamagnetic magnetite with the diameter of the magnetite nanoparticles between 8.5 to 18.5 nm. This material was effective in removing the phosphate from wastewater, and can be readily recycled.

Chapter 6, presents a new synthetic methodology on the purification of as received BNNTs (the purity ≥ 50%) prior to VFD mediated slicing, facilitated by laser irradiation (1064 nm, 250 mJ). The IPA and water volume ratio (1:1) was the optimal solvent for slicing the BNNTs in the VFD. The length of the sliced BNNTs was 340 nm to 400 nm, dramatically down from ca 200 μm for the as received material. The mechanism of lateral slicing BNNTs involves shear stress bending with breaking of the B-N bonds with induced vibrational energy from the pulsed laser.

Chapter 7, present the first report on fabricating dicopper oxide (Cu_2O) NPs via laser ablation (1064 nm, 600 mJ) in water, which readily convert to copper oxide (CuO) NPs after heating solution in air at 50ºC for 10 h. The average size of both Cu_2O NPs and CuO NPs derived from application of the Scherrer equation for the powder X-ray diffraction data was 14 nm and 11 nm, respectively. Importantly these particles are formed with the need for surfactants.

1.7 References

1. Naguib, M.; Kurtoglu, M.; Presser, V.; Lu, J.; Niu, J.; Heon, M.; Hultman, L.; Gogotsi, Y.; Barsoum, M. W., Two-Dimensional Nanocrystals Produced by Exfoliation of Ti_3AlC_2. *Advanced Materials* **2011,** *23* (37), 4248-4253.
2. Yang, Y.; Umrao, S.; Lai, S.; Lee, S., Large-Area Highly Conductive Transparent Two-Dimensional Ti_2CT_x Film. *The Journal of Physical Chemistry Letters* **2017,** *8* (4), 859-865.
3. Mashtalir, O.; Naguib, M.; Mochalin, V. N.; Dall'Agnese, Y.; Heon, M.; Barsoum, M. W.; Gogotsi, Y., Intercalation and delamination of layered carbides and carbonitrides. *Nature Communications* **2013,** *4*, 1716.
4. Mashtalir, O.; Lukatskaya, M. R.; Zhao, M.-Q.; Barsoum, M. W.; Gogotsi, Y., Amine-Assisted Delamination of Nb_2C MXene for Li-Ion Energy Storage Devices. *Advanced Materials* **2015,** *27* (23), 3501-3506.
5. Dall'Agnese, Y.; Taberna, P.-L.; Gogotsi, Y.; Simon, Patrice, Two-dimensional vanadium carbide (MXene) as positive electrode for sodium-ion capacitors. *The Journal of Physical Chemistry Letters* **2015,** *6* (12), 2305-2309.
6. Shankar, S. S.; Shereema, R. M.; Rakhi, R. B., Electrochemical Determination of Adrenaline Using MXene/Graphite Composite Paste Electrodes. *ACS Applied Materials & Interfaces* **2018,** *10* (50), 43343-43351.
7. Kajiyama, S.; Szabova, L.; Sodeyama, K.; Iinuma, H.; Morita, R.; Gotoh, K.; Tateyama, Y.; Okubo, M.; Yamada, A., Sodium-Ion Intercalation Mechanism in MXene Nanosheets. *ACS nano* **2016,** *10* (3), 3334-3341.
8. Rasool, K.; Helal, M.; Ali, A.; Ren, C. E.; Gogotsi, Y.; Mahmoud, Kajan, Antibacterial Activity of $Ti_3C_2T_x$ MXene. *ACS Nano* **2016,** *10* (3), 3674-3684.
9. Nasrallah, G. K.; Al-Asmakh, M.; Rasool, K.; Mahmoud, Khaled A., Ecotoxicological assessment of $Ti_3C_2T_x$ (MXene) using a zebrafish embryo model. Environmental Sciences:Nano, **2018,** *5* (4), 1002-1011.
10. Yu, X.; Cai, X.; Cui, H.; Lee, S.-W.; Yu, X.-F.; Liu, B. J. N., Fluorine-free preparation of titanium carbide MXene quantum dots with high near-infrared photothermal performances for cancer therapy. *Nanoscale* **2017,** *9* (45), 17859-17864.
11. Xu, B.; Zhu, M.; Zhang, W.; Zhen, X.; Pei, Z.; Xue, Q.; Zhi, C.; Shi, P., Ultrathin MXene-Micropattern-Based Field-Effect Transistor for Probing Neural Activity. *Advenced Materials* **2016,** *28* (17), 3333-3339.
12. Khazaei, M.; Arai, M.; Sasaki, T.; Chung, C.-Y.; Venkataramanan, N. S.; Estili, M.; Sakka, Y.; Kawazoe, Y., Novel Electronic and Magnetic Properties of Two-Dimensional Transition Metal Carbides and Nitrides. *Advanced Materials* **2013,** *23* (17), 2185-2192.

13. Lukatskaya, M. R.; Mashtalir, O.; Ren, C. E.; Dall'Agnese, Y.; Rozier, P.; Taberna, P. L.; Naguib, M.; Simon, P.; Barsoum, M. W.; Gogotsi, Y., Cation Intercalation and High Volumetric Capacitance of Two-Dimensional Titanium Carbide. *Science* **2013,** *341* (6153), 1502-1505.
14. Vaughn, A.; Ball, J.; Heil, T.; Morgan, D. J.; Lampronti, G. I.; Maršalkaitė, G.; Raston, C. L.; Power, N. P.; Kellici, S., Selective Calixarene-Directed Synthesis of MXene Plates, Crumpled Sheets, Spheres, and Scrolls. *Chemistry A European Journal* **2017,** *23* (34), 8128-8133.
15. Tan, T. L.; Jin, H. M.; Sullivan, M. B.; Anasori, B.; Gogotsi, Y., High-Throughput Survey of Ordering Configurations in MXene Alloys Across Compositions and Temperatures. *ACS Nano* **2017,** *11* (5), 4407-4418.
16. Srivastava, P.; Mishra, A.; Mizuseki, H.; Lee, K.-R.; Singh, A. K., Mechanistic Insight into the Chemical Exfoliation and Functionalization of Ti_3C_2 MXene. *ACS Applied Materials & Interfaces* **2016,** *8* (36), 24256-24264.
17. Zhang, T.; Pan, L.; Tang, H.; Du, F.; Guo, Y.; Qiu, T.; Yang, J., Synthesis of two-dimensional $Ti_3C_2T_x$ MXene using HCl+LiF etchant: Enhanced exfoliation and delamination. *Journal of Alloys and Compounds* **2017,** *695*, 818-826.
18. Frey, N. C.; Bandyopadhyay, A.; Kumar, H.; Anasori, B.; Gogotsi, Y.; Shenoy, V. B., Surface-Engineered MXenes: Electric Field Control of Magnetism and Enhanced Magnetic Anisotropy. *ACS Nano* **2019,** *13* (3), 2831–2839.
19. Shahzad, F.; Alhabeb, M.; Hatter, C. B.; Anasori, B.; Man Hong, S.; Koo, C. M.; Gogotsi, Y., Electromagnetic interference shielding with 2D transition metal carbides (MXenes). *Science* **2016,** *353* (6304), 1137-1140.
20. Shah, S. A.; Habib, T.; Gao, H.; Gao, P.; Sun, W.; Green, M. J.; Radovic, M., Template-free 3D titanium carbide ($Ti_3C_2T_x$) MXene particles crumpled by capillary forces. *Chemical Communications* **2017,** *53* (2), 400-403.
21. Wang, Z.; Xuan, J.; Zhao, Z.; Li, Q.; Geng, F., Versatile Cutting Method for Producing Fluorescent Ultrasmall MXene Sheets. *ACS Nano* **2017,** *11* (11), 11559-11565.
22. Jiang, H.; Wang, Z.; Yang, Q.; Hanif, M.; Wang, Z.; Dong, L.; Dong, M., A novel $MnO_2/Ti_3C_2T_x$ MXene nanocomposite as high performance electrode materials for flexible supercapacitors. *Electrochimica Acta* **2018,** *290*, 695-703.
23. Zou, R.; Quan, H.; Pan, M.; Zhou, S.; Chen, D.; Luo, X., Self-assembled MXene($Ti_3C_2T_x$)/α-Fe_2O_3 nanocomposite as negative electrode material for supercapacitors. *Electrochimica Acta* **2018,** *292*, 31-38.
24. Jin, X.; Shin, S.-J.; Kim, N.; Kang, B.; Piao, H.; Choy, J.-H.; Kim, H.; Hwang, S.-J., Superior role of MXene nanosheet as hybridization matrix over graphene in enhancing interfacial electronic coupling and functionalities of metal oxide. *Nano Energy* **2018,** *53*, 841-848.
25. Gao, X.-T.; Xie, Y.; Zhu, X.-D.; Sun, K.-N.; Xie, X.-M.; Liu, Y.-T.; Yu, J.-Y.; Ding, B., Ultrathin MXene Nanosheets Decorated with TiO_2 Quantum Dots as an Efficient Sulfur Host toward Fast and Stable Li–S Batteries. *Small* **2018,** *14* (41), 1802443.
26. Gao, Y.; Wang, L.; Li, Z.; Zhou, A.; Hu, Q.; Cao, X., Preparation of MXene-Cu_2O nanocomposite and effect on thermal decomposition of ammonium perchlorate. *Solid State Sciences* **2014,** *35*, 62-65.
27. Zhu, J.; Ha, E.; Zhao, G.; Zhou, Y.; Huang, D.; Yue, G.; Hu, L.; Sun, N.; Wang, Y.; Lee, L. Y. S.; Xu, C.; Wong, K.-Y.; Astruc, D.; Zhao, P., Recent advance in MXenes:

A promising 2D material for catalysis, sensor and chemical adsorption. *Coordination Chemistry Reviews* **2017,** *352*, 306-327.

28. Lorencova, L.; Bertok, T.; Filip, J.; Jerigova, M.; Velic, D.; Kasak, P.; Mahmoud, K. A.; Tkac, J., Highly stable $Ti_3C_2T_x$ (MXene)/Pt nanoparticles-modified glassy carbon electrode for H_2O_2 and small molecules sensing applications. *Sensors and Actuators B: Chemical* **2018,** *263*, 360-368.
29. Ghidiu, M.; Kota, S.; Halim, J.; Sherwood, A. W.; Nedfors, N.; Rosen, J.; Mochalin, V. N.; Barsoum, M. W., Alkylammonium Cation Intercalation into Ti_3C_2 (MXene): Effects on Properties and Ion-Exchange Capacity Estimation. *Chemistry of Materials* **2017,** *29* (3), 1099-1106.
30. Lorencova, L.; Bertok, T.; Dosekova, E.; Holazova, A.; Paprckova, D.; Vikartovska, A.; Sasinkova, V.; Filip, J.; Kasak, P.; Jerigova, M.; Velic, D.; Mahmoud, K. A.; Tkac, J., Electrochemical performance of $Ti_3C_2T_x$ MXene in aqueous media: towards ultrasensitive H2O2 sensing. *Electrochimica Acta* **2017,** *235*, 471-479.
31. Liu, H.; Duan, C.; Yang, C.; Shen, W.; Wang, F.; Zhu, Zhenfeng, A novel nitrite biosensor based on the direct electrochemistry of hemoglobin immobilized on MXene-Ti_3C_2. *Sencer and Actuators B: Chemistry* **2015,** *218*, 60-66.
32. Rakhi, R. B.; Nayak, P.; Xia, C.; Alshareef, H. N., Novel amperometric glucose biosensor based on MXene nanocomposite. *Scientific Reports* **2016,** *6*, 36422.
33. Fan, Y.; Yuan, Z.; Zou, G.; Zhang, Q.; Liu, B.; Peng, Q., Two-dimensional MXene/A-TiO_2 composite with unprecedented catalytic activation for sodium alanate. *Catalysis Today* **2018,** *318*, 167-174.
34. Ahmed, B.; Anjum, D. H.; Hedhili, M. N.; Gogotsi, Y.; Alshareef, H. N., H_2O_2 assisted room temperature oxidation of Ti_2C MXene for Li-ion battery anodes. *Nanoscale* **2016,** *8* (14), 7580-7587.
35. Low, J.; Zhang, L.; Tong, T.; Shen, B.; Yu, J., TiO_2/MXene Ti_3C_2 composite with excellent photocatalytic CO_2 reduction activity. *Journal of Catalysis* **2018,** *361*, 255-266.
36. Naguib, M.; Mashtalir, O.; Lukatskaya, M. R.; Dyatkin, B.; Zhang, C.; Presser, V.; Gogotsi, Y.; Barsoum, M. W., One-step synthesis of nanocrystalline transition metal oxides on thin sheets of disordered graphitic carbon by oxidation of MXenes. *Chemical Communications* **2014,** *50* (56), 7420-7423.
37. Shahzad, A.; Rasool, K.; Nawaz, M.; Miran, W.; Jang, J.; Moztahida, M.; Mahmoud, K. A.; Lee, D. S., Heterostructural TiO_2/$Ti_3C_2T_x$ (MXene) for photocatalytic degradation of antiepileptic drug carbamazepine. *Chemical Engineering Journal* **2018,** *349*, 748-755.
38. Han, X.; Jing, X.; Yang, D.; Lin, H.; Wang, Z.; Ran, H.; Li, P.; Chen, Y., Therapeutic mesopore construction on 2D Nb(2)C MXenes for targeted and enhanced chemo-photothermal cancer therapy in NIR-II biowindow. *Theranostics* **2018,** *8* (16), 4491-4508.
39. Han, W.-Q., Anisotropic Hexagonal Boron Nitride Nanomaterials: Synthesis and Applications. *Nanotechnologies for the Life Sciences* **2008,** *41*, 1-60.
40. Lin, Y.; Connell, J. W., Advances in 2D boron nitride nanostructures: nanosheets, nanoribbons, nanomeshes, and hybrids with graphene. *Nanoscale* **2012,** *4* (22), 6908-6939.
41. Han, W.-Q.; Wu, L.; Zhu, Y.; Watanabe, K.; Taniguchi, T., Structure of chemically

derived mono-and few-atomic-layer boron nitride sheets. *Applied Physics Letters* **2008,** *93* (22), 223103.
42. Chen, X.; Boulos, R. A.; Dobson, J. F.; Raston, C. L., Shear induced formation of carbon and boron nitride nano-scrolls. *Nanoscale* **2013,** *5* (2), 498-502.
43. Hwang, D. Y.; Suh, D. H., Formation of hexagonal boron nitride nanoscrolls induced by inclusion and exclusion of self-assembling molecules in solution process. *Nanoscale* **2014,** *6* (11), 5686-5690.
44. Hwang, D. Y.; Choi, K. H.; Park, J. E.; Suh, D. H., Evolution of magnetism by rolling up hexagonal boron nitride nanosheets tailored with superparamagnetic nanoparticles. *Physical Chemistry Chemical Physics* **2017,** *19* (5), 4048-4055.
45. Wang, X.-B.; Weng, Q.; Wang, X.; Li, X.; Zhang, J.; Liu, F.; Jiang, X.-F.; Guo, H.; Xu, N.; Golberg, D.; Bando, Y., Biomass-Directed Synthesis of 20 g High-Quality Boron Nitride Nanosheets for Thermoconductive Polymeric Composites. *ACS Nano* **2014,** *8* (9), 9081-9088.
46. Zhang, B.; Wu, Q.; Yu, H.; Bulin, C.; Sun, H.; Li, R.; Ge, X.; Xing, R., High-Efficient Liquid Exfoliation of Boron Nitride Nanosheets Using Aqueous Solution of Alkanolamine. *Nanoscale Research Letters* **2017,** *12* (1), 596.
47. Hou, X.; Wang, M.; Fu, L.; Chen, Y.; Jiang, N.; Lin, C.-T.; Wang, Z.; Yu, J., Boron nitride nanosheet nanofluids for enhanced thermal conductivity. *Nanoscale* **2018,** *10* (27), 13004-13010.
48. Lim, H. S.; Oh, J. W.; Kim, S. Y.; Yoo, M.-J.; Park, S.-D.; Lee, W. S., Anisotropically alignable magnetic boron nitride platelets decorated with iron oxide nanoparticles. *Chemistry of Materials* **2013,** *25* (16), 3315-3319.
49. Liu, Z.; Gong, Y.; Zhou, W.; Ma, L.; Yu, J.; Idrobo, J. C.; Jung, J.; MacDonald, A. H.; Vajtai, R.; Lou, J.; Ajayan, P. M., Ultrathin high-temperature oxidation-resistant coatings of hexagonal boron nitride. *Nature Communications* **2013,** *4*, 2541.
50. Yang, Q.; Ru, J.; Song, P.; Hu, M.; Feng, Jjrsos, Fabrication and characterization of Ni-decorated h-BN powders with ChCl-EG ionic liquid as addition by electroless deposition. *Royal Society open Science* **2018,** *5* (5), 180146.
51. Chopra, N. G.; Luyken, R. J.; Cherrey, K.; Crespi, V. H.; Cohen, M. L.; Louie, S. G.; Zettl, A., Boron Nitride Nanotubes. *Science* **1995,** *269* (5226), 966-967.
52. Golberg, D.; Bando, Y.; Huang, Y.; Terao, T.; Mitome, M.; Tang, C.; Zhi, C., Boron Nitride Nanotubes and Nanosheets. *ACS Nano* **2010,** *4* (6), 2979-2993.
53. Golberg, D.; Bando, Y.; Tang, C.; Zhi, C. In *Functional boron nitride nanotubes*, Nanoelectronics Conference (INEC), 2010 3rd International, 2010; pp 47-48.
54. Zhi, C.; Bando, Y.; Tang, C.; Golberg, D., Boron nitride nanotubes. *Materials Science and Engineering: R: Reports* **2010,** *70* (3), 92-111.
55. Ferreira, T. H.; Miranda, M. C.; Rocha, Z.; Leal, A. S.; Gomes, D. A.; Sousa, E. M. B., An Assessment of the Potential Use of BNNTs for Boron Neutron Capture Therapy. *Nanomaterials* **2017,** *7* (4), 82.
56. Chen, Y.; Zou, J.; Campbell, S. J.; Le Caer, G. J. A. p. l., Boron nitride nanotubes: pronounced resistance to oxidation. *Applied Physics Letters* **2004,** *84* (13), 2430-2432.
57. Wang, J.; Lee, C. H.; Bando, Y.; Golberg, D.; Yap, Y. K., Multiwalled boron nitride nanotubes: growth, properties, and applications. In *BCN Nanotubes and Related Nanostructures*, Springer: 2009; pp 23-44.

58. Meng, W.; Huang, Y.; Fu, Y.; Wang, Z.; Zhi, C., Polymer composites of boron nitride nanotubes and nanosheets. *Journal of Materials Chemistry C* **2014,** *2* (47), 10049-10061.
59. Golberg, D.; Bando, Y., Unique morphologies of boron nitride nanotubes. *Applied Physics Letters* **2001,** *79* (3), 415-417.
60. Laude, T.; Matsui, Y.; Marraud, A.; Jouffrey, B., Long ropes of boron nitride nanotubes grown by a continuous laser heating. *Applied Physics Letters* **2000,** *76* (22), 3239-3241.
61. Li, Y.; Peng, Z.; Larios, E.; Wang, G.; Lin, J.; Yan, Z.; Ruiz-Zepeda, F.; José-Yacamán, M.; Tour, J. M., Rebar Graphene from Functionalized Boron Nitride Nanotubes. *ACS Nano* **2015,** *9* (1), 532-538.
62. Ahmad, P.; Khandaker, M. U.; Khan, Z. R.; Amin, Y. M., Synthesis of boron nitride nanotubes via chemical vapour deposition: a comprehensive review. *RSC Advances* **2015,** *5* (44), 35116-35137.
63. Loiseau, A.; Willaime, F.; Demoncy, N.; Hug, G.; Pascard, H., Boron Nitride Nanotubes with Reduced Numbers of Layers Synthesized by Arc Discharge. *Physical Review Letters* **1996,** *76* (25), 4737-4740.
64. Zhuang, C.; Xu, H.; Li, L.; Liu, Y.; Ban, C.; Liu, X., Systematic investigation of the ball milling–annealing growth and electrical properties of boron nitride nanotubes. *RSC Advances* **2016,** *6* (114), 113415-113423.
65. Kalay, S.; Yilmaz, Z.; Sen, O.; Emanet, M.; Kazanc, E.; Çulha, M., Synthesis of boron nitride nanotubes and their applications. *Beilstein journal of nanotechnology* **2015,** *6* (1), 84-102.
66. Ciofani, G.; Raffa, V.; Menciassi, A.; Cuschieri, A., Folate functionalized boron nitride nanotubes and their selective uptake by glioblastoma multiforme cells: implications for their use as boron carriers in clinical boron neutron capture therapy. *Nanoscale research letters* **2008,** *4* (2), 113.
67. Li, X.; Wang, X.; Jiang, X.; Yamaguchi, M.; Ito, A.; Bando, Y.; Golberg, D., Boron nitride nanotube-enhanced osteogenic differentiation of mesenchymal stem cells. *Journal of Biomedical Materials Research Part B: Applied Biomaterials* **2016,** *104* (2), 323-329.
68. Wu, J.; Yin, L., Platinum nanoparticle modified polyaniline-functionalized boron nitride nanotubes for amperometric glucose enzyme biosensor. *ACS applied materials & interfaces* **2011,** *3* (11), 4354-4362.
69. Chatterjee, S.; Kim, M. J.; Zakharov, D. N.; Kim, S. M.; Stach, E. A.; Maruyama, B.; Sneddon, L. G., Syntheses of Boron Nitride Nanotubes from Borazine and Decaborane Molecular Precursors by Catalytic Chemical Vapor Deposition with a Floating Nickel Catalyst. *Chemistry of Materials* **2012,** *24* (15), 2872-2879.
70. Li, L. H.; Chen, Y.; Glushenkov, A. M., Boron nitride nanotube films grown from boron ink painting. *Journal of Materials Chemistry* **2010,** *20* (43), 9679-9683.
71. Song, Y.; Sun, Y.; Shin, D. H.; Yun, K. N.; Song, Y.-H.; Milne, W. I.; Lee, C. J., Excellent oxidation endurance of boron nitride nanotube field electron emitters. Applied Physics Letters, **2014,** *104* (16), 163102.
72. Zhong, B.; Huang, X.; Wen, G.; Yu, H.; Zhang, X.; Zhang, T.; Bai, H., Large-Scale Fabrication of Boron Nitride Nanotubes via a Facile Chemical Vapor Reaction Route and Their Cathodoluminescence Properties. *Nanoscale Res Lett* **2010,** *6* (1), 36.

73. Leela Mohana Reddy, A.; Tanur, A. E.; Walker, G. C., Synthesis and hydrogen storage properties of different types of boron nitride nanostructures. *International Journal of Hydrogen Energy* **2010,** *35* (9), 4138-4143.
74. Chen, H.; Chen, Y.; Yu, J.; Williams, J. S., Purification of boron nitride nanotubes. *Chemical Physics Letters* **2006,** *425* (4), 315-319.
75. Xue-Song, L.; Dian-Qiang, C.; Bo, Z.; Jian-Lin, Y., Purification of Yard-Glass Shaped Boron Nitride Nanotubes. *Iranian Journal of Chemistry and Chemical Engineering (IJCCE)* **2014,** *33* (1), 29-36.
76. Choi, J.-H.; Kim, J.; Seo, D.; Seo, Y.-S., Purification of boron nitride nanotubes via polymer wrapping. *Materials Research Bulletin* **2013,** *48* (3), 1197-1203.
77. Gao, Z.; Zhi, C.; Bando, Y.; Golberg, D.; Serizawa, T., Noncovalent Functionalization of Boron Nitride Nanotubes in Aqueous Media. *Opens Application Roads in Nanobiomedicine* **2014,** *1*, 7.
78. Tiano, A. L.; Park, C.; Lee, J. W.; Luong, H. H.; Gibbons, L. J.; Chu, S.-H.; Applin, S.; Gnoffo, P.; Lowther, S.; Kim, H. J.; Danehy, P. M.; Inman, J. A.; Jones, S. B.; Kang, J. H.; Sauti, G.; Thibeault, S. A.; Yamakov, V.; Wise, K. E.; Su, J.; Fay, C. C., *Boron nitride nanotube: synthesis and applications*. SPIE: **2014**; Vol. 9060, 1-19.
79. Lee, C. H.; Zhang, D.; Yap, Y. K., Functionalization, dispersion, and cutting of boron nitride nanotubes in water. *The Journal of Physical Chemistry C* **2011,** *116* (2), 1798-1804.
80. Liao, Y.; Chen, Z.; Connell, J. W.; Fay, C. C.; Park, C.; Kim, J. W.; Lin, Y., Chemical sharpening, shortening, and unzipping of boron nitride nanotubes. *Advanced Functional Materials* **2014,** *24* (28), 4497-4506.
81. Hsu, J.-H.; Chang, S.-H., Surface adhesion between hexagonal boron nitride nanotubes and silicon based on lateral force microscopy. *Applied Surface Science* **2010,** *256* (6), 1769-1773.
82. Zheng, M.; Chen, X.; Park, C.; Fay, C. C.; Pugno, N. M.; Ke, C., Nanomechanical cutting of boron nitride nanotubes by atomic force microscopy. *Nanotechnology* **2013,** *24* (50), 505719.
83. Geohegan, D. B.; Puretzky, A. A.; Ivanov, I. N.; Jesse, S.; Eres, G.; Howe, J. Y., In situ growth rate measurements and length control during chemical vapor deposition of vertically aligned multiwall carbon nanotubes. *Applied Physics Letters* **2003,** *83* (9), 1851-1853.
84. Laurent, S.; Forge, D.; Port, M.; Roch, A.; Robic, C.; Vander Elst, L.; Muller, R. N., Magnetic Iron Oxide Nanoparticles: Synthesis, Stabilization, Vectorization, Physicochemical Characterizations, and Biological Applications. *Chemical Reviews* **2008,** *108* (6), 2064-2110.
85. Sowani, H.; Mohite, P.; Damale, S.; Kulkarni, M.; Zinjarde, S., Carotenoid stabilized gold and silver nanoparticles derived from the Actinomycete Gordonia amicalis HS-11 as effective free radical scavengers. *Enzyme and microbial technology* **2016,** *95*, 164-173.
86. Vijayan, S. R.; Santhiyagu, P.; Ramasamy, R.; Arivalagan, P.; Kumar, G.; Ethiraj, K.; Ramaswamy, B. R., Seaweeds: a resource for marine bionanotechnology. *Enzyme and microbial technology* **2016,** *95*, 45-57.
87. Suriani, A.; Dalila, A.; Mohamed, A.; Mamat, M.; Malek, M.; Soga, T.; Tanemura, M., Fabrication of vertically aligned carbon nanotubes–zinc oxide nanocomposites and

their field electron emission enhancement. *Materials & Design* **2016,** *90*, 185-195.
88. Golden, T. D.; Shumsky, M. G.; Zhou, Y.; VanderWerf, R. A.; Van Leeuwen, R. A.; Switzer, J. A., Electrochemical Deposition of Copper(I) Oxide Films. *Chemistry of Materials* **1996,** *8* (10), 2499-2504.
89. Korotcenkov, G., Gas response control through structural and chemical modification of metal oxide films: state of the art and approaches. *Sensors and Actuators B: Chemical* **2005,** *107* (1), 209-232.
90. Kumar, R. V.; Diamant, Y.; Gedanken, A., Sonochemical Synthesis and Characterization of Nanometer-Size Transition Metal Oxides from Metal Acetates. *Chemistry of Materials* **2000,** *12* (8), 2301-2305.
91. Li, S.-Z.; Hong, Y. C.; Uhm, H. S.; Li, Z.-K., Synthesis of Nanocrystalline Iron Oxide Particles by Microwave Plasma Jet at Atmospheric Pressure. *Japanese Journal of Applied Physics* **2004,** *43* (11A), 7714-7717.
92. Guo, Q.; Teng, X.; Rahman, S.; Yang, H., Patterned Langmuir−Blodgett Films of Monodisperse Nanoparticles of Iron Oxide Using Soft Lithography. *Journal of the American Chemical Society* **2003,** *125* (3), 630-631.
93. Tsuji, T.; Iryo, K.; Watanabe, N.; Tsuji, M., Preparation of silver nanoparticles by laser ablation in solution: influence of laser wavelength on particle size. *Applied Surface Science* **2002,** *202* (1), 80-85.
94. Amikura, K.; Kimura, T.; Hamada, M.; Yokoyama, N.; Miyazaki, J.; Yamada, Y., Copper oxide particles produced by laser ablation in water. *Applied Surface Science* **2008,** *254* (21), 6976-6982.
95. Gondal, M.; Qahtan, T. F.; Dastageer, M.; Saleh, T. A.; Maganda, Y. W. In *Synthesis and characterization of copper oxides nanoparticles via pulsed laser ablation in liquid*, *10th International Conference on High Capacity Optical Networks and Enabling Technologies IEEE:* **2013**; pp 146-150.
96. Markert, J.; Messina, T.; Dam, B.; Huijbregste, J.; Rector, J.; Griessen, R., Infinite-layer copper-oxide laser-ablated thin films: substrate, buffer-layer, and processing effects. *IEEE transactions on applied superconductivity* **2003,** *13* (2), 2684-2686.
97. Haram, N.; Ahmad, N., Effect of laser fluence on the size of copper oxide nanoparticles produced by the ablation of Cu target in double distilled water. *Applied Physics A* **2013,** *111* (4), 1131-1137.
98. Luo, X.; Al-Antaki, A. H. M.; Alharbi, T. M. D.; Hutchison, W. D.; Zou, Y.-c.; Zou, J.; Sheehan, A.; Zhang, W.; Raston, C. L., Laser-Ablated Vortex Fluidic-Mediated Synthesis of Superparamagnetic Magnetite Nanoparticles in Water Under Flow. *ACS Omega* **2018,** *3* (9), 11172-11178.
99. Svetlichnyi, V. A.; Shabalina, A. V.; Lapin, I. N.; Goncharova, D. A., Metal oxide nanoparticle preparation by pulsed laser ablation of metallic targets in liquid. In *Applications of Laser Ablation–Thin Film Deposition, Nanomaterial Synthesis and Surface Modification*, InTech Croatia: 2016; pp 245-263.
100. Svetlichnyi, V. A.; Shabalina, A. V.; Lapin, I. N.; Goncharova, D. A.; Kharlamova, T. S.; Stadnichenko, A. I., Comparative study of magnetite nanoparticles obtained by pulsed laser ablation in water and air. *Applied Surface Science* **2019,** *467-468*, 402-410.
101. Allen, S. E.; Walvoord, R. R.; Padilla-Salinas, R.; Kozlowski, M. C., Aerobic copper-catalyzed organic reactions. *Chemical reviews* **2013,** *113* (8), 6234-6458.

102. Yin, G.; Nishikawa, M.; Nosaka, Y.; Srinivasan, N.; Atarashi, D.; Sakai, E.; Miyauchi, M., Photocatalytic Carbon Dioxide Reduction by Copper Oxide Nanocluster-Grafted Niobate Nanosheets. *ACS Nano* **2015,** *9* (2), 2111-2119.
103. Poreddy, R.; Engelbrekt, C.; Riisager, A., Copper oxide as efficient catalyst for oxidative dehydrogenation of alcohols with air. *Catalysis Science & Technology* **2015,** *5* (4), 2467-2477.
104. Demirer, G. S.; Okur, A. C.; Kizilel, S., Synthesis and design of biologically inspired biocompatible iron oxide nanoparticles for biomedical applications. *Journal of Materials Chemistry B* **2015,** *3* (40), 7831-7849.
105. Furlani, E. P., Magnetic Biotransport: Analysis and Applications. *Materials (Basel)* **2010,** *3* (4), 2412-2446.
106. Poizot, P.; Laruelle, S.; Grugeon, S.; Dupont, L.; Tarascon, J. M., Nano-sized transition-metal oxides as negative-electrode materials for lithium-ion batteries. *Nature* **2000,** *407* (6803), 496-499.
107. Wee, S. H.; Huang, Po-Shun.; Lee, Jung-Kun.; Goyal, Amit, Heteroepitaxial Cu_2O thin film solar cell on metallic substrates. Scientific Reporte **2015,** *5*, 16272.
108. Zhang, J.; Liu, J.; Peng, Q.; Wang, X.; Li, Y., Nearly Monodisperse Cu_2O and CuO Nanospheres: Preparation and Applications for Sensitive Gas Sensors. *Chemistry of Materials* **2006,** *18* (4), 867-871.
109. Laskowski, R.; Blaha, P.; Schwarz, K. J. P. R. B., Charge distribution and chemical bonding in Cu_2O. *PHYSICAL REVIEW B* **2003,** *67* (7), 075102.
110. Huang, W.-C.; Lyu, L.-M.; Yang, Y.-C.; Huang, M. H. Jjotacs, Synthesis of Cu_2O nanocrystals from cubic to rhombic dodecahedral structures and their comparative photocatalytic activity. *JACS* **2011,** *134* (2), 1261-1267.
111. Hara, M.; Kondo, T.; Komoda, M.; Ikeda, S.; N. Kondo, J.; Domen, K.; Hara, M.; Shinohara, K.; Tanaka, A., Cu2O as a photocatalyst for overall water splitting under visible light irradiation. *Chemical Communications* **1998,** (3), 357-358.
112. Basu, M.; Sinha, A. K.; Pradhan, M.; Sarkar, S.; Pal, A.; Mondal, C.; Pal, T., Methylene Blue–Cu2O reaction made easy in acidic medium. *The Journal of Physical Chemistry C* **2012,** *116* (49), 25741-25747.
113. Nath, A.; Khare, A., Size induced structural modifications in copper oxide nanoparticles synthesized via laser ablation in liquids. *Journal of Applied Physics* **2011,** *110* (4), 043111.
114. Kang, B.; Han, S.; Kim, J.; Ko, S.; Yang, M., One-Step Fabrication of Copper Electrode by Laser-Induced Direct Local Reduction and Agglomeration of Copper Oxide Nanoparticle. *The Journal of Physical Chemistry C* **2011,** *115* (48), 23664-23670.
115. Legodi, M. A.; de Waal, D., The preparation of magnetite, goethite, hematite and maghemite of pigment quality from mill scale iron waste. *Dyes and Pigments* **2007,** *74* (1), 161-168.
116. Liu, B.; Wang, D.; Huang, W.; Yao, A.; Kamitakahara, M.; Ioku, K., Preparation of Magnetite Nanoparticles Coated with Silica via a Sol-gel Approach. *Journal of the Ceramic Society of Japan* **2007,** *115* (1348), 877-881.
117. Zhuang, L.; Zhang, W.; Zhao, Y.; Shen, H.; Lin, H.; Liang, J., Preparation and Characterization of Fe_3O_4 Particles with Novel Nanosheets Morphology and Magnetochromatic Property by a Modified Solvothermal Method. *Scientific Reports*

2015, *5*, 9320.
118. Thorek, D. L. J.; Chen, A. K.; Czupryna, J.; Tsourkas, A., Superparamagnetic Iron Oxide Nanoparticle Probes for Molecular Imaging. *Annals of Biomedical Engineering* **2006,** *34* (1), 23-38.
119. Vimalanathan, K.; Raston, C. L., Dynamic Thin Films in Controlling the Fabrication of Nanocarbon and Its Composites. *Advanced Materials Technologies* **2017,** *2* (6), 1600298.
120. Luo, X.; Su, P.; Zhang, W.; Raston, C. L., Microfluidic Devices in Fabricating Nano or Micromaterials for Biomedical Applications. *Advanced Materials Technologies*, *4,* 1900488.
121. Hartlieb, K. J.; Raston, C. L.; Saunders, M., Controlled Scalable Synthesis of ZnO Nanoparticles. *Chemistry of Materials* **2007,** *19* (23), 5453-5459.
122. Anantachoke, N.; Makha, M.; Raston, C. L.; Reutrakul, V.; Smith, N. C.; Saunders, M., Fine Tuning the Production of Nanosized β-Carotene Particles Using Spinning Disk Processing. *Journal of the American Chemical Society* **2006,** *128* (42), 13847-13853.
123. Chin, S. F.; Iyer, K. S.; Raston, C. L., Fabrication of carbon nano-tubes decorated with ultra fine superparamagnetic nano-particles under continuous flow conditions. *Lab on a Chip* **2008,** *8* (3), 439-442.
124. Chin, S. F.; Iyer, K. S.; Raston, C. L.; Saunders, M., Size Selective Synthesis of Superparamagnetic Nanoparticles in Thin Fluids under Continuous Flow Conditions. *Advanced Functional Materials* **2008,** *18* (6), 922-927.
125. Iyer, K. S.; Raston, C. L.; Saunders, M., Hierarchical aqueous self-assembly of C_{60} nano-whiskers and C_{60}–silver nano-hybrids under continuous flow. *Lab on a Chip* **2007,** *7* (9), 1121-1124.
126. Lodha, H.; Jachuck, R.; Suppiah Singaram, S., Intensified Biodiesel Production Using a Rotating Tube Reactor. *Energy & Fuels* **2012,** *26* (11), 7037-7040.
127. Dev, S.; Iyer, K. S.; Raston, C. L., Nanosized drug formulations under microfluidic continuous flow. *Lab on a Chip* **2011,** *11* (19), 3214-3217.
128. Dev, S.; Prabhakaran, P.; Filgueira, L.; Iyer, K. S.; Raston, C. L., Microfluidic fabrication of cationic curcumin nanoparticles as an anti-cancer agent. *Nanoscale* **2012,** *4* (8), 2575-2579.
129. Dev, S.; Toster, J.; Vadhan Prasanna, S.; Fitzgerald, M.; Swaminathan Iyer, K.; Raston, C. L., Suppressing regrowth of microfluidic generated drug nanocrystals using polyelectrolyte coatings. *RSC Advances* **2013,** *3* (3), 695-698.
130. Britton, J.; Stubbs, K. A.; Weiss, G. A.; Raston, C. L., Vortex fluidic chemical transformations. *Chemistry–A European Journal* **2017,** *23* (54), 13270-13278.
131. Yasmin, L.; Chen, X.; Stubbs, K. A.; Raston, C. L., Optimising a vortex fluidic device for controlling chemical reactivity and selectivity. *Scientific reports* **2013,** *3*, 2282.
132. Britton, J.; Dyer, R. P.; Majumdar, S.; Raston, C. L.; Weiss, G. A., Ten-Minute Protein Purification and Surface Tethering for Continuous-Flow Biocatalysis. *Angewandte Chemie International Edition in English* **2017**, 56 (9), 2296-2301.
133. Alharbi, T. M. D.; Vimalanathan, K.; Lawrance, W. D.; Raston, C. L., Controlled slicing of single walled carbon nanotubes under continuous flow. Carbon 2018, 140, 428-432.
134. Vimalanathan, K.; Gascooke, J. R.; Suarez-Martinez, I.; Marks, N. A.; Kumari, H.; Garvey, C. J.; Atwood, J. L.; Lawrance, W. D.; Raston, C. L., Fluid dynamic lateral slicing of high tensile strength carbon nanotubes. *Scientific Reports* **2016**, *6,* 22865.

135. Golberg, D.; Bando, Y.; Eremets, M.; Takemura, K.; Kurashima, K.; Yusa, H., Nanotubes in boron nitride laser heated at high pressure. *Applied Physics Letters* **1996,** *69* (14), 2045-2047.
136. Luo, X.; Al-Antaki, A. H. M.; Pye, S.; Meech, R.; Zhang, W.; Raston, C. L., High-Shear-Imparted Tunable Fluorescence in Polyethylenimines. *ChemPhotoChem* **2018,** *2* (4), 343-348.
137. Jones, D.; Chen, X.; Sibley, A.; Quinton, J.; Shearer, C.; Gibson, C.; Raston, C., Plasma enhanced vortex fluidic device manipulation of graphene oxide. *Chemical Communications* **2016,** *52* (71), 10755-10758.
138. Alharbi, T. M. D.; Alghamdi, A. R. M.; Vimalanathan, K.; Raston, C. L., Continuous flow photolytic reduction of graphene oxide. Chemical Communications 2019, 55 (76), 11438-11441.
139. Solheim, T. E.; Salvemini, F.; Dalziel, S. B.; Raston, C. L., Neutron imaging and modelling inclined vortex driven thin films. *Scientific Reports* **2019,** *9* (1), 2817.
140. Alharbi, T. M. D.; Harvey, D.; Alsulami, I. K.; Dehbari, N.; Duan, X.; Lamb, R. N.; Lawrance, W. D.; Raston, C. L., Shear stress mediated scrolling of graphene oxide. *Carbon* **2018,** *137*, 419-424.
141. Vimalanathan, K.; Suarez-Martinez, I.; Peiris, M. C. R.; Antonio, J.; de Tomas, C.; Zou, Y.; Zou, J.; Duan, X.; Lamb, R. N.; Harvey, D. P.; Alharbi, T. M. D.; Gibson, C. T.; Marks, N. A.; Darwish, N.; Raston, C. L., Vortex fluidic mediated transformation of graphite into highly conducting graphene scrolls. *Nanoscale Advances* **2019,** *1* (7), 2495-2501.
142. Chen, X.; Dobson, J. F.; Raston, C. L., Vortex fluidic exfoliation of graphite and boron nitride. *Chemical Communications* **2012,** *48* (31), 3703-3705.
143. Alsulam, I. K.; Alharbi, T. M. D.; Moussa, M.; Raston, C. L., High-Yield Continuous-Flow Synthesis of Spheroidal C_{60}@Graphene Composites as Supercapacitors. *ACS Omega* **2019,** *4* (21), 19279-19286.
144. Wahid, M. H.; Eroglu, E.; Chen, X.; Smith, S. M.; Raston, C. L., Functional multi-layer graphene–algae hybrid material formed using vortex fluidics. *Green Chemistry* **2013,** *15* (3), 650-655.
145. Wahid, M. H.; Eroglu, E.; LaVars, S. M.; Newton, K.; Gibson, C. T.; Stroeher, U. H.; Chen, X.; Boulos, R. A.; Raston, C. L.; Harmer, S.-L., Microencapsulation of bacterial strains in graphene oxide nano-sheets using vortex fluidics. *RSC Advances* **2015,** *5* (47), 37424-37430.
146. Wahid, M. H.; Eroglu, E.; Chen, X.; Smith, S. M.; Raston, C. L., Entrapment of Chlorella vulgaris cells within graphene oxide layers. *RSC Advances* **2013,** *3* (22), 8180-8183.
147. Alharbi, T. M. D.; Vimalanathan, K.; Lawrance, W. D.; Raston, C. L., Controlled slicing of single walled carbon nanotubes under continuous flow. *Carbon* **2018,** *140*, 428-432.
148. Luo, X.; Al-Antaki, A. H. M.; Vimalanathan, K.; Moffatt, J.; Zheng, K.; Zou, Y.; Zou, J.; Duan, X.; Lamb, R. N.; Wang, S.; Li, Q.; Zhang, W.; Raston, C. L., Laser irradiated vortex fluidic mediated synthesis of luminescent carbon nanodots under continuous flow. *Reaction Chemistry & Engineering* **2018,** *3* (2), 164-170.
149. Yasin, F. M.; Boulos, R. A.; Hong, B. Y.; Cornejo, A.; Iyer, K. S.; Gao, L.; Chua, H. T.; Raston, C. L., Microfluidic size selective growth of palladium nano-particles on carbon nano-onions. *Chemical Communications* **2012,** *48* (81), 10102-10104.

150. Md Yasin, F.; Iyer, K. S.; Raston, C. L., Palladium nano-carbon-calixarene based devices for hydrogen sensing. *New Journal of Chemistry* **2013,** *37* (10), 3289-3293.
151. Goh, Y. A.; Chen, X.; Yasin, F. M.; Eggers, P. K.; Boulos, R. A.; Wang, X.; Chua, H. T.; Raston, C. L., Shear flow assisted decoration of carbon nano-onions with platinum nanoparticles. *Chemical Communications* **2013,** *49* (45), 5171-5173.
152. Boulos, R. A.; Zhang, F.; Tjandra, E. S.; Martin, A. D.; Spagnoli, D.; Raston, C. L., Spinning up the polymorphs of calcium carbonate. *Scientific Reports* **2014,** *4*, 3616.
153. Vimalanathan, K.; Shrestha, R. G.; Zhang, Z.; Zou, J.; Nakayama, T.; Raston, C. L., Surfactant-free Fabrication of Fullerene C_{60} Nanotubules Under Shear. *Angewandte Chemie* **2017,** *129* (29), 8518-8521.
154. Alsulami, I. K.; Alharbi, T. M.; Harvey, D. P.; Gibson, C. T.; Raston, C. L., Controlling the growth of fullerene C_{60} cones under continuous flow. *Chemical Communications* **2018,** *54* (57), 7896-7899.
155. Mo, J.; Eggers, P. K.; Chen, X.; Ahamed, M. R. H.; Becker, T.; Yong Lim, L.; Raston, C. L., Shear induced carboplatin binding within the cavity of a phospholipid mimic for increased anticancer efficacy. *Scientific Reports* **2015,** *5*, 10414.
156. Vimalanathan, K.; Chen, X.; Raston, C. L., Shear induced fabrication of intertwined single walled carbon nanotube rings. *Chemical Communications* **2014,** *50* (77), 11295-11298.
157. Alharbi, T. M. D.; Shingaya, Y.; Vimalanathan, K.; Nakayama, T.; Raston, C. L., High Yielding Fabrication of Magnetically Responsive Coiled Single-Walled Carbon Nanotube under Flow. *ACS Applied Nano Materials* **2019**, *2* (8), 5282–5289.
158. Eroglu, E.; D'Alonzo, N. J.; Smith, S. M.; Raston, C. L., Vortex fluidic entrapment of functional microalgal cells in a magnetic polymer matrix. *Nanoscale* **2013,** *5* (7), 2627-2631.
159. Tong, C. L.; Boulos, R. A.; Yu, C.; Iyer, K. S.; Raston, C. L., Continuous flow tuning of ordered mesoporous silica under ambient conditions. *RSC Advances* **2013,** *3* (41), 18767-18770.
160. Tong, C. L.; Eroglu, E.; Duan, X.; Lamb, R. N.; Jarrett, K.; Buckley, C. E.; Raston, C. L., Nitrate uptake using mesoporous silica embedded with zero-valent palladium nanoparticles. *RSC Advances* **2015,** *5* (26), 20557-20561.
161. Tong, C. L.; Stroeher, U. H.; Brown, M. H.; Raston, C. L., Continuous flow vortex fluidic synthesis of silica xerogel as a delivery vehicle for curcumin. *RSC Advances* **2015,** *5* (11), 7953-7958.
162. Britton, J.; Raston, C. L.; Weiss, G. A., Rapid protein immobilization for thin film continuous flow biocatalysis. *Chemical Communications* **2016,** *52* (66), 10159-10162.
163. Britton, J.; Meneghini, L. M.; Raston, C. L.; Weiss, G. A., Accelerating Enzymatic Catalysis Using Vortex Fluidics. *Angewandte Chemie International Edition* **2016,** *55* (38), 11387-11391.
164. Yuan, T. Z.; Ormonde, C. F.; Kudlacek, S. T.; Kunche, S.; Smith, J. N.; Brown, W. A.; Pugliese, K. M.; Olsen, T. J.; Iftikhar, M.; Raston, C. L., Shear-Stress-Mediated Refolding of Proteins from Aggregates and Inclusion Bodies. *ChemBioChem* **2015,** *16* (3), 393-396.
165. Luo, X.; Smith, P.; Raston, C. L.; Zhang, W., Vortex Fluidic Device-Intensified Aqueous Two Phase Extraction of C-Phycocyanin from Spirulina maxima. *ACS Sustainable Chemistry & Engineering* **2016,** *4* (7), 3905-3911.

166. D'Alonzo, N. J.; Eggers, P. K.; Raston, C. L., Vortex fluidics synthesis of polymer coated superparamagnetic magnetite nanoparticles. *New Journal of Chemistry* **2017,** *41* (2), 552-558.
167. D'Alonzo, N. J.; Eggers, P. K.; Eroglu, E.; Raston, C. L., Shear Stress Induced Fabrication of Dandelion-Shaped Lanthanide Phosphate Nanoparticles. *Australian Journal of Chemistry* **2017,** *70* (7), 823-829.
168. Yasmin, L.; Coyle, T.; Stubbs, K. A.; Raston, C. L., Stereospecific synthesis of resorcin[4]arenes and pyrogallol[4]arenes in dynamic thin films. *Chemical Communications* **2013,** *49* (93), 10932-10934.
169. Yasmin, L.; Stubbs, K. A.; Raston, C. L. Vortex fluidic promoted Diels–Alder reactions in an aqueous medium. *Tetrahedron Letters* **2014,** *55* (14), 2246-2248.
170. Gandy, M. N.; Raston, C. L.; Stubbs, K. A., Towards aryl C–N bond formation in dynamic thin films. *Organic & Biomolecular Chemistry* **2014,** *12* (26), 4594-4597.
171. Ho, L. A.; Raston, C. L.; Stubbs, K. A., Transition-Metal-Free Cross-Coupling Reactions in Dynamic Thin Films To Access Pyrimidine and Quinoxaline Analogues. *European Journal of Organic Chemistry* **2016,** *2016* (36), 5957-5963.
172. Yasmin, L.; Eggers, P. K.; Skelton, B. W.; Stubbs, K. A.; Raston, C. L., Thin film microfluidic synthesis of fluorescent highly substituted pyridines. *Green Chemistry* **2014,** *16* (7), 3450-3453.
173. Britton, J.; Chalker, J. M.; Raston, C. L., Rapid Vortex Fluidics: Continuous Flow Synthesis of Amides and Local Anesthetic Lidocaine. *Chemistry–A European Journal* **2015,** *21* (30), 10660-10665.
174. Gandy, M. N.; Raston, C. L.; Stubbs, K. A., Photoredox catalysis under shear using thin film vortex microfluidics. *Chemical Communications* **2015,** *51* (55), 11041-11044.
175. Britton, J.; Dalziel, S. B.; Raston, C. L., Continuous flow Fischer esterifications harnessing vibrational-coupled thin film fluidics. *RSC Advances* **2015,** *5* (3), 1655-1660.
176. Ciampi, S.; Eggers, P. K.; Haworth, N. L.; Darwish, N.; Wagner, P.; Coote, M. L.; Wallace, G. G.; Raston, C. L., Decoloration rates of a photomerocyanine dye as a visual probe into hydrogen bonding interactions. *Chemical Communications* **2015,** *51* (23), 4815-4818.
177. Pye, S. J.; Dalgarno, S. J.; Chalker, J. M.; Raston, C. L., Organic oxidations promoted in vortex driven thin films under continuous flow. *Green Chemistry* **2018,** *20* (1), 118-124.
178. Britton, J.; Castle, J. W.; Weiss, G. A.; Raston, C. L., Harnessing Thin-Film Continuous-Flow Assembly Lines. *Chemistry–A European Journal* **2016,** *22* (31), 10773-10776.
179. Britton, J.; Dalziel, S. B.; Raston, C. L., The synthesis of di-carboxylate esters using continuous flow vortex fluidics. *Green Chemistry* **2016,** *18* (7), 2193-2200.
180. Peng, W.; Chen, X.; Zhu, S.; Guo, C.; Raston, C. L., Room temperature vortex fluidic synthesis of monodispersed amorphous proto-vaterite. *Chemical Communications* **2014,** *50* (79), 11764-11767.
181. Sudchanham, J.; Batmunkh, M.; Reutrakul, V.; Shapter, J. G.; Raston, C. L.; Pakawatpanurut, P., Vortex Fluidics Improved Morphology of $CH_3NH_3PbI_{3-x}Cl_x$ Films for Perovskite Solar Cells. *Chemistry Select* **2017,** *2* (1), 369-374.
182. He, S.; Joseph, N.; Luo, X.; Raston, C. L., Vortex fluidic mediated food processing.

PLOS ONE **2019,** *14* (5).
183. He, S.; Joseph, N.; Luo, X.; Raston, C., Continuous flow thin film microfluidic mediated nano-encapsulation of fish oil. *LWT- Food Science and Technology* **2019,** *103*, 88-93.
184. Britton, J.; Raston, C. L., Continuous flow vortex fluidic production of biodiesel. *RSC Advances* **2014,** *4* (91), 49850-49854.
185. Britton, J.; Raston, C. L., Rapid high conversion of high free fatty acid feedstock into biodiesel using continuous flow vortex fluidics. *RSC Advances* **2015,** *5* (3), 2276-2280.
186. Sitepu, E. K.; Corbin, K.; Luo, X.; Pye, S. J.; Tang, Y.; Leterme, S. C.; Heimann, K.; Raston, C. L.; Zhang, W., Vortex fluidic mediated direct transesterification of wet microalgae biomass to biodiesel. *Bioresource Technology* **2018,** *266*, 488-497

2.Continuous flow vortex fluidic mediated exfoliation and fragmentation of 2D MXene

Ahmed Hussein Mohammed Al-antaki[a,b], Suela Kellici[c] , Nicholas P. Power[d], Warren D. Lawrance[e], Colin L. Raston[a*]

a. *Flinders Institute for Nanoscale Science and Technology, College of Science and Engineering, Flinders University, Adelaide, SA 5042, Australia.*
b. *Department of Chemistry, Faculty of Sciences, Kufa University, Kufa, Najaf, Iraq.*
c. *School of Engineering, London South Bank University, 103 Borough Road London, SE1 0AA (UK).*
d. *School of Life, Health and Chemical Sciences, The open University, Walton Hall, Milton Keynes, MK7 6AA (UK).*
e. *College of Science and Engineering, Flinders University, Adelaide, SA 5042.*

Author contributions: **AA** performed all the VFD and all characterisation experiments; wrote all the primary content. **SK** and **NP** prepared MXene. **WL** and **CR** supervised and coordinated the project and helped on the research directions and plan, and the final revision of the manuscript. All of the co-authors assisted with the revision of the manuscript before and during the publication process.

Graphical Abstract

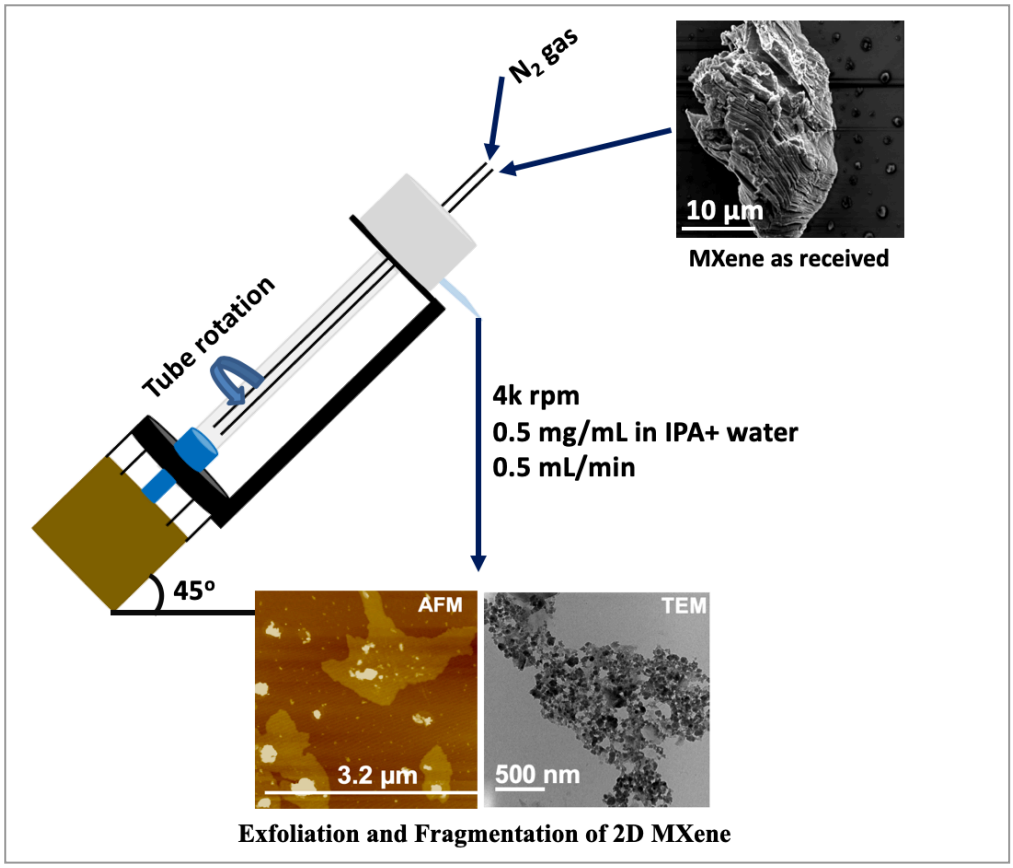

Exfoliation and Fragmentation of 2D MXene

2.1 Abstract

MXene (Ti_2CT_x) is exfoliated in a vortex fluidic device (VFD), as a thin film microfluidic platform, under continuous flow conditions, down to *ca* 3 nm thin multi-layered two dimensional (2D) material, as determined using AFM. The optimised process, under an inert atmosphere of nitrogen to avoid oxidation of the material, was established by systematically exploring the operating parameters of the VFD, along with concentration of the dispersed starting material and the choice of solvent, which was a 1:1 mixture of isopropyl alcohol and water. There is also some fragmentation of the 2D material into nanoparticles *ca* 68 nm in diameter.

2.2 Introduction

MXenes are a unique class of two dimensional (2D) material, first reported in 2011.[1] They are transition metal carbides and carbonitrides and have a number of potential applications, including in biology,[2-5] batteries,[6-8] electronic devices [9,10] and supercapacitors.[10,11] They are prepared from $M_{n+1}AX_n$ phases via etching the A layers from the laminar material, where M is a transition metal (Ti, Zr, Nb, V, Ta, or Mo), A is a main group element, mostly Al or Si, and X is C and/or N, and n is 1, 2, or 3. The substitution Al or Si with functional groups, T (−O, −OH, −F) either side of the sheets ($M_{n+1}X_nT_x$) imparts greater application of the MXene relative to MAX phases.[12] The work function of MXene sheets and those functionalized with F, OH, and O groups have been studied using first-principles calculations.[9] The bandgap of MXene sheets are ultra-low when the sheets are –OH functionalised.[9,13] There is also a work function dependence on the transition metal and associated charge transfer between the functional groups and the substrate, and overall changes in the total surface dipole moments.[10]

The exfoliation (delamination) of MXenes provides unique material with different functional groups, microstructure and morphology which impacts on electrochemical response of the material. The exfoliation of MXene requires harsh chemical or surfactant in a number of different methods, as in sonication,[7,14] heating,[15,16] or both sonication and heating,[17] and the use of electric fields.[18,19] Interestingly, sonication can result in different shaped material[14,20] presumably arising from extreme localised conditions associated with cavitation. In the present study, we explore the utility of the vortex fluidic device (VFD), figure 2.1, for exfoliating Ti_2CT_x type MXene in the absence of harsh chemicals or surfactant. The VFD microfluidic platform delivers mechanoenergy in the dynamic film. We hypothesised that it would be effective in exfoliating the 2D material, based on its success in exfoliating graphene and *h*-BN.[21-23] The resulting exfoliation is at room temperature as a single step

process in a mixture of isopropyl alcohol (IPA) and water (ratio 1:1), under continuous flow conditions (see below), and under an inert atmosphere of nitrogen gas to avoid oxidation of the MXene.[17]

The vortex fluidic device (VFD),[21, 24-26] figure 2.1, has a borosilicate glass tubes (O.D. 20 mm, I.D. 17.5 mm and 19.5 cm in length) open at one end. The operating parameters of the device are then systematically explored for optimising any process. The tube is rotated at high speed (up to 9k rpm) and can be inclined at an angle,θ, of -45º to 90º relative to the horizontal position, with +45º being optimal for a large number of applications, including in the present study. The VFD has two types of processing – confined mode and continuous flow. The confined mode is where a finite volume of liquid is placed in the glass tube which is tilted at 45o and spun at high speed for a designated period, Fig. 2.1(b). This mode of operation of the VFD has proved invaluable in optimising any processing in translating it into continuous flow where liquid is delivered to the inside of the rotating tube at a controlled flow rate, figure 2.1(c).[27] The utility of processing in the VFD beyond the aforementioned exfoliation of graphene from graphite and *h*-BN,[21-23] covers scrolling graphene[23] and graphene oxide,[28] protein folding,[29] enhancing enzymatic reactions,[24] controlling organic synthesis,[25,30] probing the structure of self- organised systems,[31] protein separation,[32] and more.[33-37]

2.3 Experimental procedure

2.3.1 Materials. Ti_2AlC powder precursor was obtained commercially (KANTHAL, Maxthal 211 Ti_2AlC). The etching of the aluminium from Ti_2AlC was conducted in a 20% aqueous hydrofluoric acid (HF), solution (Sigma Aldrich) for 24 h at room temperature. The resulting suspension was filtered and washed with deionised water (DI) to reach a pH > 6.[14] This as prepared MXene was dispersed in distillation IPA (isopropyl alcohol) from sigma-Aldrich and Mili-Q water.

2.3.2 Synthesis of MXene nanoparticles and exfoliation of MXene. MXene was dispersed in distillation IPA and Milli-Q water using sonication (25 mins, 6 kHz). The mixture was then transferred to an in-house developed magnetically stirred syringe, Figure 2.2.[35,38] The rapidly stirred dispersion of MXene in IPA and water (0.5 mg/mL) was then delivered using a jet feed to the base of the rapidly rotating 20 mm O.D. glass tube in the VFD with another jet feed delivery a low flow rate of dry nitrogen gas. The tube was inclined at 45º and spun at a pre-determined speed, which was optimized at 4k rpm, with the optimized flow rate at 0.5 mL/min, resulting in *ca* 7% exfoliated MXene and fragmentation to

nanoparticles, exiting the tube. We refer to the exfoliated MXene and MXene NPs exiting the tube during continuous flow processing as 'collected'. After 1 h of processing (30 mL passed through the VFD), 3.5 mL remained in the tube which was added 3 mL of a 1:1 Mixture IPA and water. The mixture was centrifugated (700 ×g) for 3 mins to separate large MXene particles. The supernatant afforded *ca* 8% exfoliated MXene sheets and MXene nanoparticles. This material which builds up in the VFD during the continuous flow processing is referred to as 'retained' material.

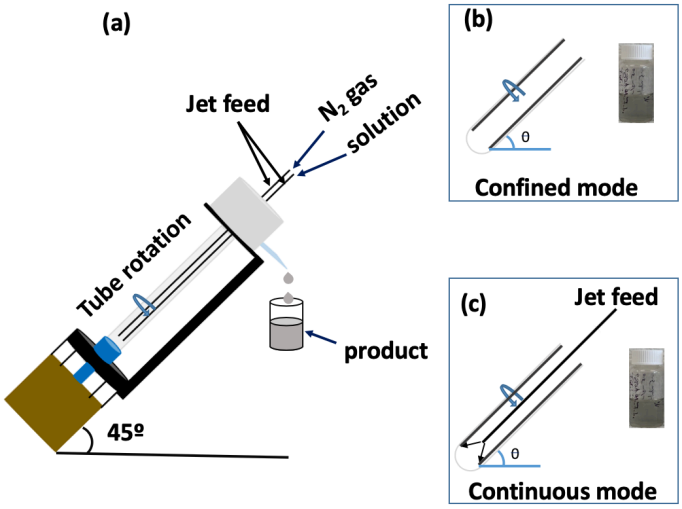

Figure 2.1. (a) Illustration of the VFD which houses a rapidly rotating borosilicate glass tube (20 mm O.D., 17.5 mm I.D.), operating under an inert atmosphere of nitrogen gas. Photograph of the solution obtained (b) under confined mode of operation of the VFD (30 min) and (c) continuous flow, flow rate 0.5 mL/min. Both modes were optimised at 4k rpm, θ 45º, for a concentration of MXene 0.5 mg/mL in a 1:1 ratio of IPA and water.

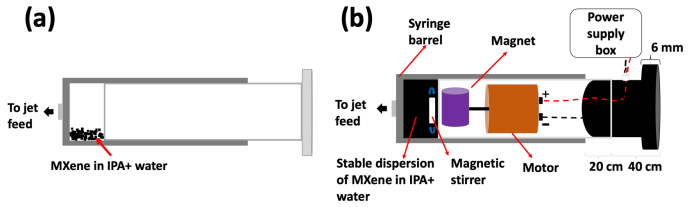

Figure 2.2. (a) Normal syringe housing a dispersion of MXene in IPA and water. (b) Syringe housing a magnetic stirrer driven by a motor inside the plunger.

2.3.3 Characterisation. MXene sheets and MXene nanoparticles were characterized using scanning electron microscopy (SEM) (Inspect FEI F50 SEM), atomic force microscopy (AFM - Nanoscope 8.10 tapping mode), Raman spectroscopy (WiTec Alpha 300R $\lambda_{exc.}$=532 nm), XRD (Bruker D8 ADVANCE ECO, Co- Kα, λ=1.7889 Å), ATR-FTIR Perkin Elmer Frontier, TEM (FEI Tecnai F20 operated at 120 kV), UV-Vis spectrophotometer Cary 50EST70772 and DLS (dynamic light scattering) (model: ZETASIZER Nanoseries nano-zs MALVERN).

2.4 Results and discussion

The VFD is a flexible processing platform, with a number of operating parameters (rotational speed, tilt angle, θ, Figure 2.1, and flow rates) to be systematically explored, along with the choice of solvent. The use of a number of different solvents was investigated, namely water, NMP (N-Methyl-2-pyrrolidone), IPA, DMF (Dimethylformamide), *o*-xylene, *m*-

xylene and toluene. However, their use resulted in little or no exfoliated MXene or resulted in the formation of nanoparticles. The same was also found for combinations of solvents, in a 1:1 ratio, including NMP with water, DMF with *o*-xylene, DMF with toluene, DMF with IPA, toluene with IPA, *m*-xylene with IPA, *o*-xylene with IPA and IPA with water for different speeds and different concentrations, Figure S2.10, S2.11.[39] The use of co-solvents relates

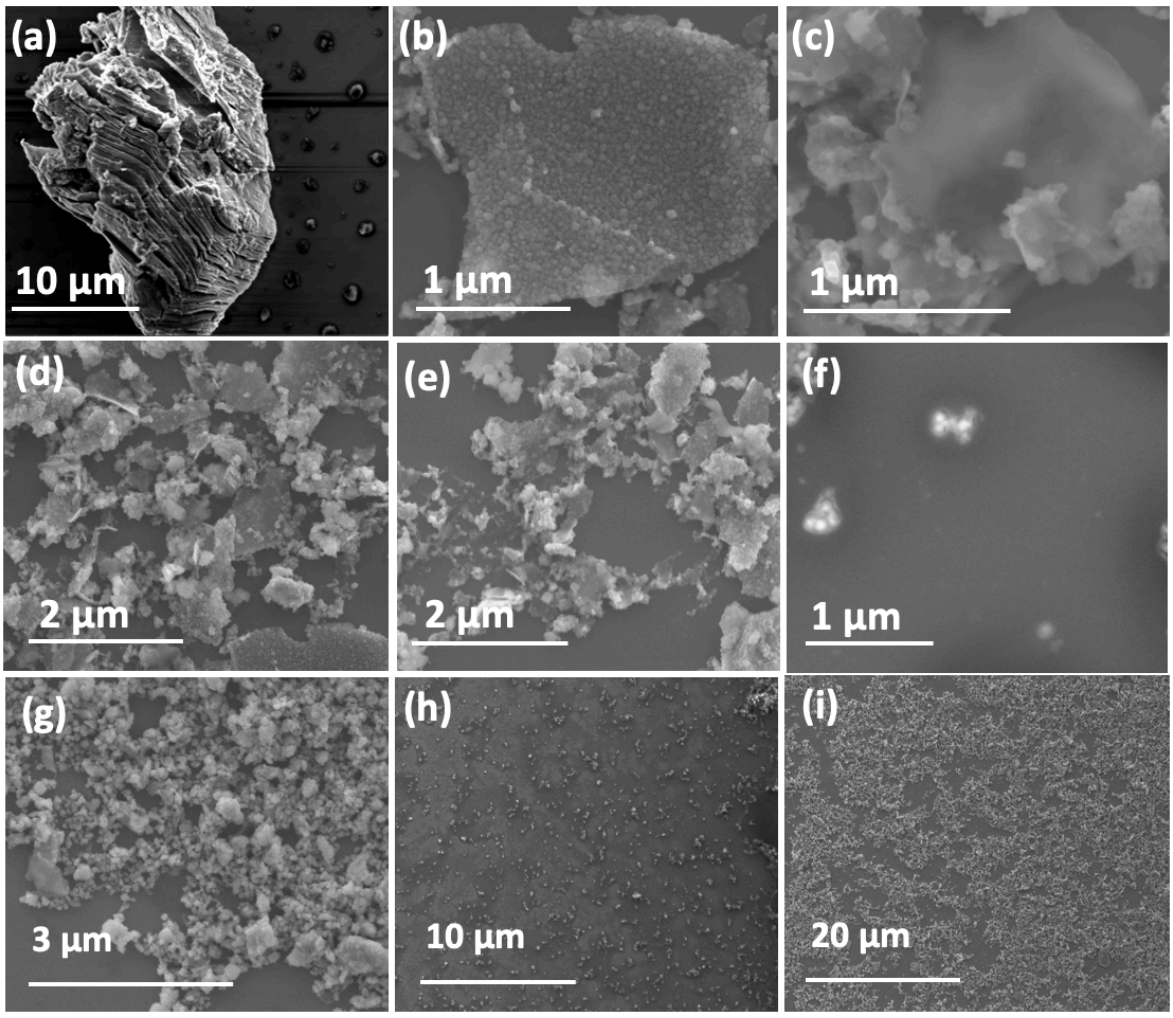

Figure 2.3. SEM images for MXene (collected) drop cast on silicon wafer, post VFD processing under N_2 gas, θ 45º, concentration 0.5 mg/mL in IPA and water (1:1), rotational speed 4k rpm and flow rate 0.5 mL/min. (a) MXene as prepared. (b-e) Exfoliated MXene. (f) Back scattering of MXene nanoparticles. (g-i) MXene nanoparticles.

to their success in a number of process, including forming graphene scrolls directly from graphite.[23] In addition, irradiating the material *in situ* in the VFD was explored using a Nd:YAG pulsed laser operating at 1064 nm at different power settings, as another parameter to enhance the exfoliation, using a mixture of IPA and water with a volume ratio of 1:1, Figure S2.12. Varying the tilt angle θ was also explored, additional to the common tilt angle of +45º, including 20º, -20º and -45º, while varying the rotational speed of the tube, Figure

S2.13. We note that -45° tilt angle was effective in exfoliating h-BN in water.[22] Varying the different operating parameters of the VFD led to determining the optimal conditions for exfoliation of MXene and the highest yield of material exiting (collected) the tube under continuous flow. This was for a tilt angle of 45°, which is consistent with all most optimised processes in the VFD.

A colour change was observed for the suspension of MXene (from dark grey to yellow) after processed in the VFD in air, which is not surprising given that the material is sensitive to air.[14,17] Thus, all experiments were subsequently done under an inert atmosphere of nitrogen to circumvent any oxidation arising from high uptake of molecular oxygen in the thin film in the VFD. Figure S2.4, S2.5 summarises experiments done under N_2 gas using different solvents. These include water, DMF (Dimethylformamide), ethanol and IPA, and

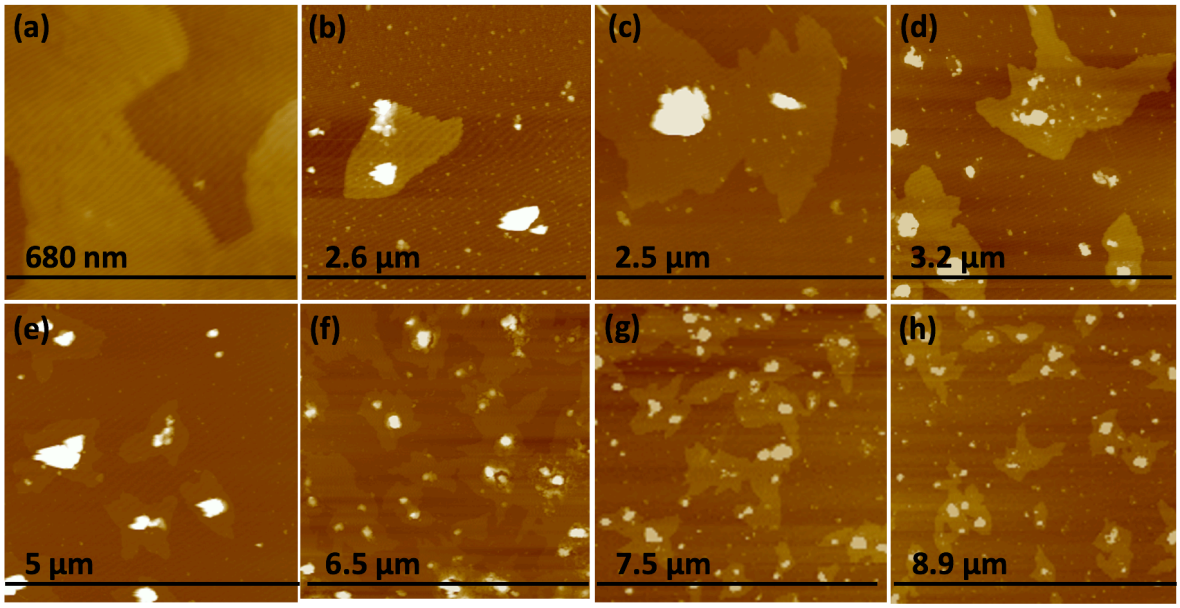

Figure 2.4. AFM images for MXene drop cast on silicon wafers, post VFD processing under N_2 gas, θ 45º, concentration 0.5 mg/mL in IPA and water (1:1), rotational speed 4k rpm and flow rate 0.5 mL/min.

mixtures of solvents, including IPA and water, DMF and water, ethanol and water and DMF and o-xylene. IPA and water, volume ratio 1:1 was deemed to be the optimal solvent and was used for subsequent experiments. The optimised processing is with respect to the highest level of exfoliation in determining the choice of solvents as a 1:1 mixture of IPA and water, and the yield of material exiting the tube, Figure S2.14(a).[39]

We found that the confined mode of operation of the VFD gave little exfoliation of the MXene, unlike continuous flow, and its use was adhered to for all subsequent experiments, Figure S2.8. This included in vary the rotational speed, flow rate, and concentration of MXene in the 1:1 mixture of IPA and water. We found 4k rpm gave the highest level of

exfoliated MXene, with some fragmentation into small nanoparticles of the material, the combined exfoliated MXene and nanoparticles accounted for *ca* 7% of the starting material. The two materials were recalcitrant toward separation by centrifugation.

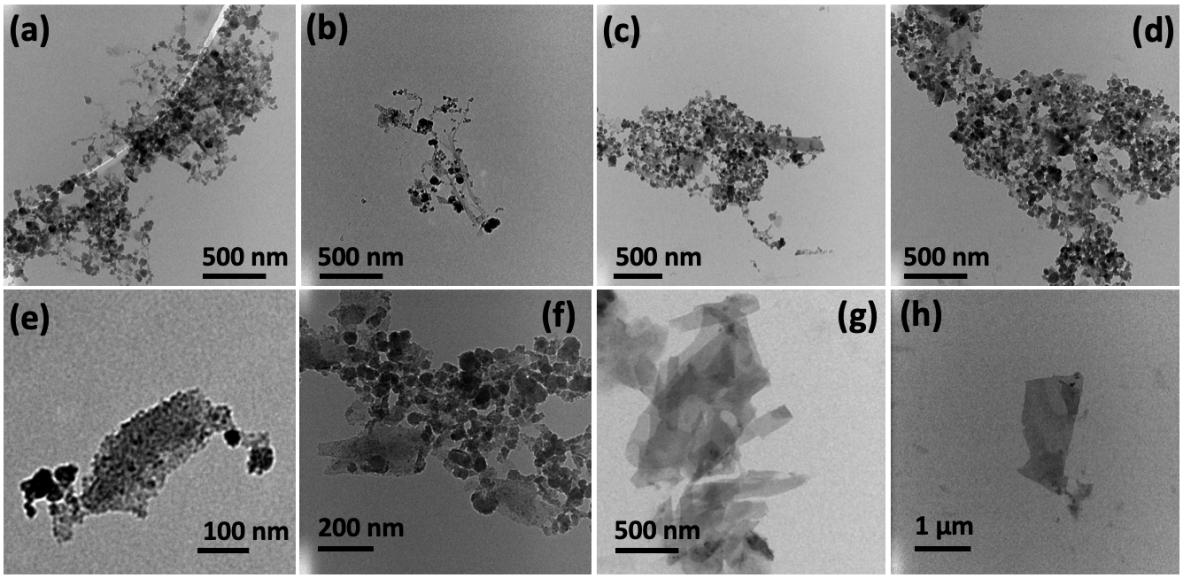

Figure 2.5. TEM images for MXene drop cast on grid, post VFD processing under N_2 gas, θ 45º, concentration 0.5 mg/mL, in IPA and water (1:1), rotational speed 4k rpm and flow rate 0.5 mL/min.

Rotational speeds of 5k, 6k, 7k and 8k rpm gave little exfoliation at the ubiquitous optimal 45º tilt angle, Figure S2.6, S2.7, and S2.14(b). The optimal flow rate of MXene in IPA and water was 0.5 mL/min, with a lower flow rate, 0.25 mL/min, and a higher flow rate, 0.75 mL/min, not as effective. For all these flow rates, the concentrations of MXene in IPA and water (1:1) was varied, at 0.1, 0.25, 0.5, and 1.0 mg/mL. The optimal concentration was found to be 0.5 mg/mL, with other concentrations resulting in lower yields, Figure S2.9 and S2.14(c). Thus, the overall optimum processing parameters for generating exfoliated MXene in a single pass in the VFD are a concentration of the material in a 1:1 ratio of IPA and water, 0.5 mg/mL, flow rate 0.5 mL/min, 4k rpm rotational speed. In addition, after VFD processing under continuous flow for 1 hour, an additional *ca* 8% of both exfoliated MXene and MXene nanoparticles were collected from the tube (retained), Figure S2.15. We initially used SEM images of drop cast material on silicon wafers to ascertain the effect of varying the rotation speed, flow rate, and tilt angle of the VFD, along with the choice of solvent, for the highest degree of exfoliation of MXene. We established the structure of MXene (retained) using ATR-FTIR spectra, Raman spectra, powder X-ray diffraction (PXRD) and UV-Vis spectroscopy, Figure 2.8.

The shear stress in the VFD is effective in both exfoliating and fragmenting MXene. This is consistent with other established top-down nanomaterials syntheses in the device, covering exfoliating,[21,22] and scrolling 2D materials,[22,23,28] slicing carbon nanotubes[26, 40] and more.[33-35,41]

Figure 2.3f shows back scattering SEM to determine the elements present in the product relative to the starting material, for different locations, Figure 2.3(g-i) (collected), S2.1(a-d) (retained). TEM images established the presence of some MXene nanoparticles, Figure 2.5(a-d), S2.3. with Figure 2.6a and Figure 2.6b providing additional TEM, and SEM images respectively, of nanospheres. AFM images provided additional information on the shape of the nanospheres, in measuring their height. The results are in agreement with those from TEM and SEM Figure 2.6(c, e). DLS of solutions of MXene nanoparticles in IPA and water (1:1) generated in the VFD after processing gave average diameter of nanospheres as 68 nm, Figure 2.6d. SEM images established the presence of exfoliated MXene, Figure 2.3(b-e), S2.1(e-l), with AFM images establishing the mean thickness of VFD exfoliated MXene sheets as 3 nm, Figure 2.4, 2.7c and S2.2.

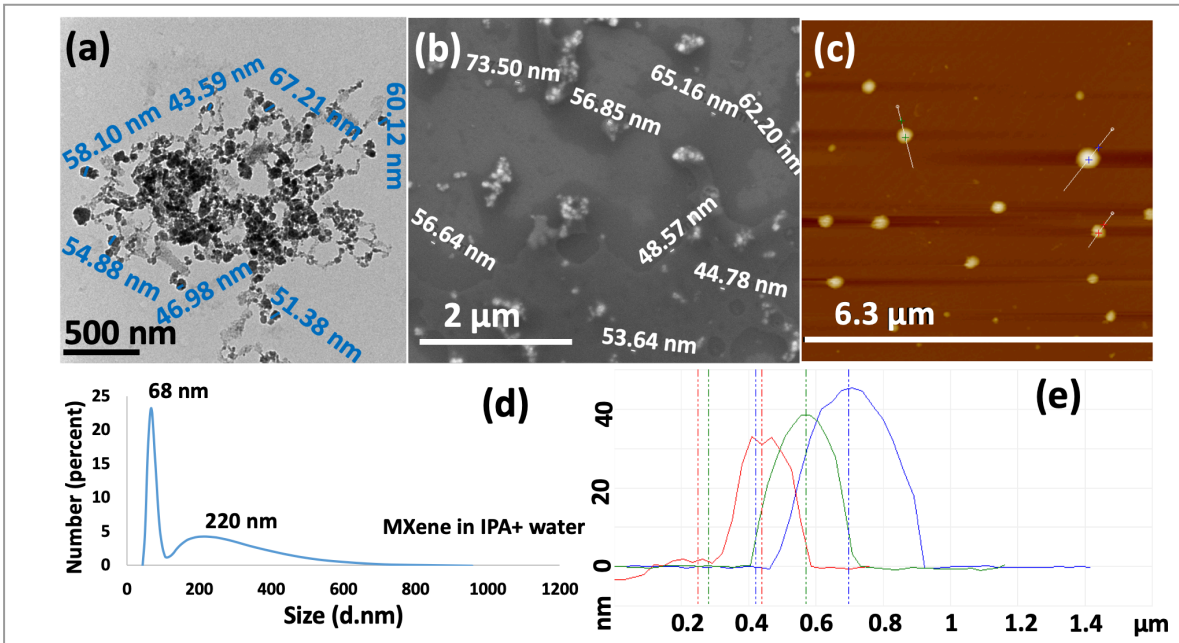

Figure 2.6. MXene nanoparticles formed during VFD processing under N_2 gas, with θ 45º, concentration 0.5 mg/mL in IPA and water (1:1), rotation speed 4k rpm and flow rate 0.5 mL/min. (a) TEM image of MXene nanoparticles drop cast on a grid. (b) SEM image of MXene nanoparticles drop cast on a silicon wafer. (c) AFM image of MXene nanoparticles drop cast on silicon wafer. (d) DLS of exfoliated MXene generated in IPA+ water (1:1). (e) Height of MXene nanoparticles from AFM images.

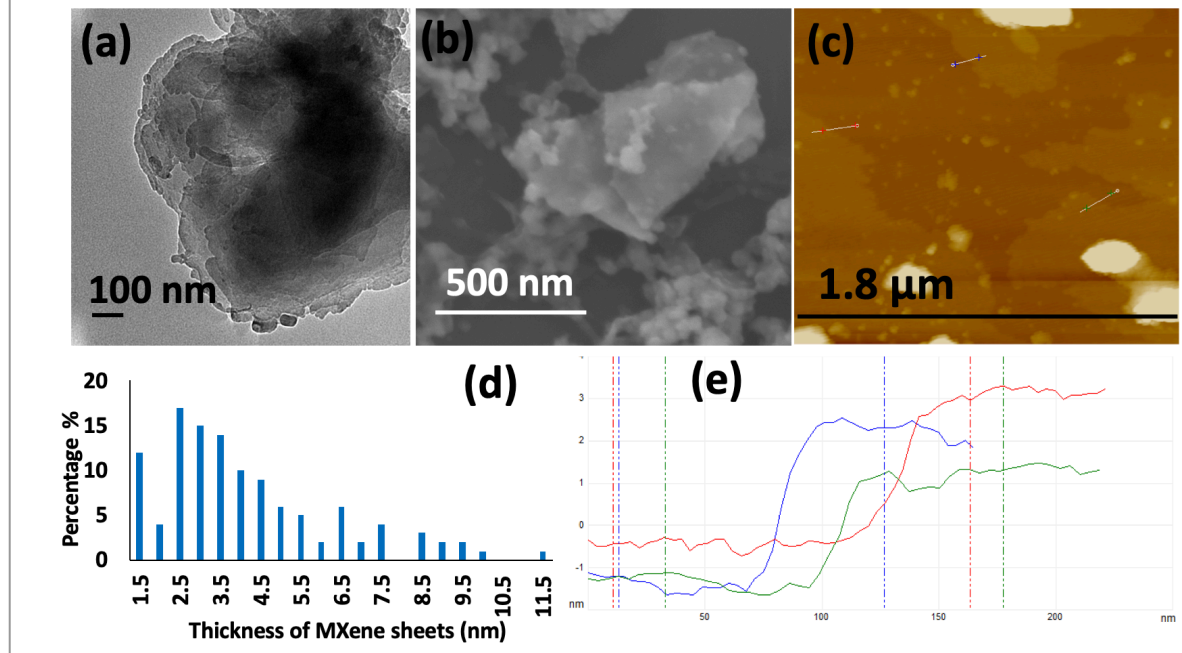

Figure 2.7. Exfoliated MXene generated during VFD processing under N_2 gas, θ 45º, concentration 0.5 mg/mL in IPA and water (1:1), rotation speed 4k rpm and flow rate 0.5 mL/min. (a) TEM image for MXene sheets drop cast on a grid. (b) SEM image of MXene sheets drop cast on a silicon wafer. (c) AFM image of MXene sheets drop cast on a silicon wafer. (d) Count of MXene sheets form AFM images. (e) Height of MXene sheets from AFM image.

The TEM images were used to determine the size and number of MXene sheets generated using the VFD processing, Figure 2.5(e-h), along with the size of the spheres, S2.6(a-e). However, the spheres were found to be unstable, with the drop cast spheres collapsing after 3 days. Interestingly, the spheres have holes in them Figure S2.6(f, g), but the origin of these is unclear. ATR-FTIR for MXene has characteristic peaks, for material exiting the tube during processing in the VFD, and material retained in the tube, and as prepared material, with peaks at 684 cm^{-1} and 991 cm^{-1} for Ti-O and C-F respectively.[42] However, the VFD processed MXene had peaks at 3674 cm^{-1} and 1499 cm^{-1} , corresponding to O-H, respectively, of solvent, Figure 2.8a.[43-45] Raman spectra of MXene as prepared has three peaks at 259 cm^{-1}, 421 cm^{-1} and 607 cm^{-1}. The material exiting the VFD tube at 263 cm^{-1}, 419 cm^{-1} and 613 cm^{-1}, and retained in the tube at 250 cm^{-1}, 405 cm^{-1} and 613 cm^{-1}. The slight shift of Raman peaks for exiting and retained material presumably relates to the presence of nanospheres along with the exfoliated MXene, for material exiting the tube, Figure 2.8b.[14,46] Powder XRD of MXene confirms the presence of Ti_2CT_x MXenes, which has hexagonal $P6_3/mmc$ symmetry with a lattice constant a≈ 0.3 nm.[47,48] The 2θ peaks (Co- Kα, λ=1.7889 Å) of MXene as prepared were 29.4º, 40.6º, 42.4º and 72.4º, with corresponding values for material exiting the tube 29.4º, 40.6º, 42.4º and 72.4º, Figure 2.8c.[49,50] The small shift after VFD processing is associated with a reduction in the thickness of the MXene sheets along with fragmentation. Finally, The UV-Vis spectra of MXene as prepared and the materials produced herein are similar, Figure 2.8d.[51]

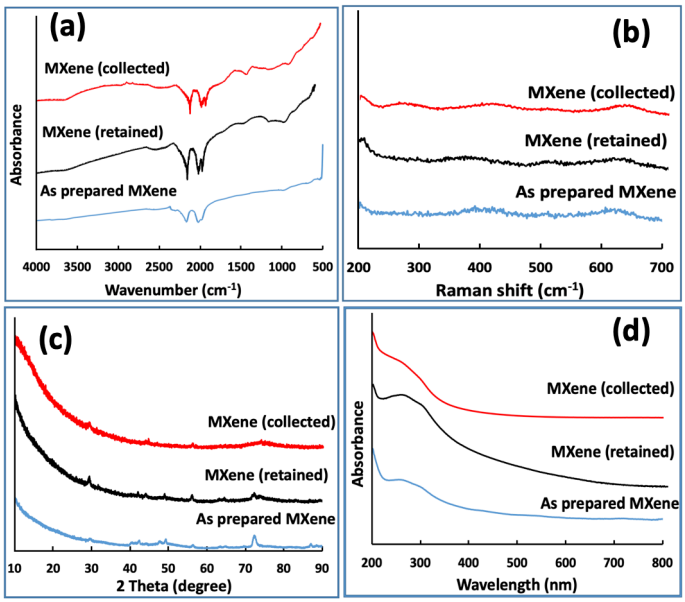

Figure 2.8. Exfoliated MXene prepared using VFD processing under N_2 gas, θ 45º, concentration 0.5 mg/mL in IPA and water (1:1), rotational speed 4k rpm and flow rate 0.5 mL/min. (a) ATR-FTIR spectra. (b) Raman spectra. (c) powder X-ray diffraction (PXRD). (d) UV-Vis spectroscopy.

2.5 Conclusions

We have developed a continuous process for exfoliating 2D-MXene into multilayered sheets *ca* 3 nm thick, driven by the mechanoenergy in the dynamic thin film in the vortex

fluidic device (VFD). During this processing we also established that the VFD can fragment the laminar MXene into nanoparticles (the average diameter 68 d. nm). The optimised parameters for processing the MXene under an inert atmosphere of nitrogen gas were for a concentration of MXene at 0.5 mg/mL in a 1:1 mixture of IPA and water, with a rotational speed of 4k rpm and flow rate 0.5 mL/min. The exfoliated material and nanoparticles of the material have activated sites for utilising in potential applications. Those include environmental remediation[45], biological application[2-5], electronic devices[9,10], supercapacitors.[10,11] and next generation of batteries.[6,7] Understanding the complex fluid dynamics in the thin film in the VFD is a major challenge currently being tackled. The choice of a single solvent or mixed solvent system depends on the application, as does the effect of different operating parameters of the device (tilt angle, rotation speed and flow rate of solvent) which need to be systematically explored.

2.6 Acknowledgements

The authors gratefully acknowledge financial support from the Iraq Government, Ministry of Higher Education and Scientific Research, and the Australian Research Council and the Government of South Australia. Use of facilities in the Australian Microscopy & Microanalysis Research Facility (AMMRF) and the Australian National Fabrication Facility (ANFF) at the South Australian nodes of the AMMRF and ANFF under the National Collaborative Research Infrastructure Strategy are also acknowledged.

2.7 References

1. Naguib, M.; Kurtoglu, M.; Presser, V.; Lu, J.; Niu, J.; Heon, M.; Hultman, L.; Gogotsi, Y.; Barsoum, M. W., Two-Dimensional Nanocrystals Produced by Exfoliation of Ti_3AlC_2. *Advanced Materials* **2011,** *23* (37), 4248-4253.
2. Xu, B.; Zhu, M.; Zhang, W.; Zhen, X.; Pei, Z.; Xue, Q.; Zhi, C.; Shi, P., Ultrathin MXene-Micropattern-Based Field-Effect Transistor for Probing Neural Activity. *Advanced Materials* **2016,** *28* (17), 3333-3339.
3. Rasool, K.; Helal, M.; Ali, A.; Ren, C. E.; Gogotsi, Y.; Mahmoud, K. A., Antibacterial Activity of Ti_3C_2T x MXene. *ACS Nano* **2016,** *10* (3), 3674-3684.
4. Nasrallah, G. K.; Al-Asmakh, M.; Rasool, K.; Mahmoud, K. A., Ecotoxicological assessment of $Ti_3C_2T_x$ (MXene) using a zebrafish embryo model. *Environmental Science Nano* **2018,** *5* (4), 1002-1011.
5. Yu, X.; Cai, X.; Cui, H.; Lee, S.-W.; Yu, X.-F.; Liu, B. J. N., Fluorine-free preparation of titanium carbide MXene quantum dots with high near-infrared photothermal performances for cancer therapy. *Nanoscale* **2017,** *9* (45), 17859-17864.
6. Dall'Agnese, Y.; Taberna, P.-L.; Gogotsi, Y.; Simon, P., Two-dimensional vanadium carbide (MXene) as positive electrode for sodium-ion capacitors. *The Journal of Physical Chemistry Letters* **2015,** *6* (12), 2305-2309.
7. Mashtalir, O.; Naguib, M.; Mochalin, V. N.; Dall'Agnese, Y.; Heon, M.; Barsoum, M. W.; Gogotsi, Y., Intercalation and delamination of layered carbides and carbonitrides.

Nature Communications **2013,** *4*, 1716.
8. Mashtalir, O.; Lukatskaya, M. R.; Zhao, M.-Q.; Barsoum, M. W.; Gogotsi, Y., Amine-Assisted Delamination of Nb2C MXene for Li-Ion Energy Storage Devices. *Advanced Materials* **2015,** *27* (23), 3501-3506.
9. Khazaei, M.; Arai, M.; Sasaki, T.; Chung, C.-Y.; Venkataramanan, N. S.; Estili, M.; Sakka, Y.; Kawazoe, Y., Novel Electronic and Magnetic Properties of Two-Dimensional Transition Metal Carbides and Nitrides. *Advanced Materials* **2013,** *23* (17), 2185-2192.
10. Lukatskaya, M. R.; Mashtalir, O.; Ren, C. E.; Dall'Agnese, Y.; Rozier, P.; Taberna, P. L.; Naguib, M.; Simon, P.; Barsoum, M. W.; Gogotsi, Y., Cation Intercalation and High Volumetric Capacitance of Two-Dimensional Titanium Carbide. *Science* **2013,** *341* (6153), 1502-1505.
11. Wang, X.; Kajiyama, S.; Iinuma, H.; Hosono, E.; Oro, S.; Moriguchi, I.; Okubo, M.; Yamada, A., Pseudocapacitance of MXene nanosheets for high-power sodium-ion hybrid capacitors. *Nature Communications* **2015,** *6*, 6544.
12. Yang, Y.; Umrao, S.; Lai, S.; Lee, S., Large-Area Highly Conductive Transparent Two-Dimensional Ti_2CT_x Film. *The Journal of Physical Chemistry Letters* **2017,** *8* (4), 859-865.
13. Yu, Z.; Tetard, L.; Zhai, L.; Thomas, J., Supercapacitor electrode materials: nanostructures from 0 to 3 dimensions. *Energy & Environmental Science* **2015,** *8* (3), 702-730.
14. Vaughn, A.; Ball, J.; Heil, T.; Morgan, D. J.; Lampronti, G. I.; Maršalkaitė, G.; Raston, C. L.; Power, N. P.; Kellici, S., Selective Calixarene-Directed Synthesis of MXene Plates, Crumpled Sheets, Spheres, and Scrolls. *Chemistry A European Journal* **2017,** *23* (34), 8128-8133.
15. Tan, T. L.; Jin, H. M.; Sullivan, M. B.; Anasori, B.; Gogotsi, Y., High-Throughput Survey of Ordering Configurations in MXene Alloys Across Compositions and Temperatures. *ACS Nano* **2017,** *11* (5), 4407-4418.
16. Srivastava, P.; Mishra, A.; Mizuseki, H.; Lee, K.-R.; Singh, A. K., Mechanistic Insight into the Chemical Exfoliation and Functionalization of Ti_3C_2 MXene. *ACS Applied Materials & Interfaces* **2016,** *8* (36), 24256-24264.
17. Zhang, T.; Pan, L.; Tang, H.; Du, F.; Guo, Y.; Qiu, T.; Yang, J., Synthesis of two-dimensional $Ti_3C_2T_x$ MXene using HCl+LiF etchant: Enhanced exfoliation and delamination. *Journal of Alloys and Compounds* **2017,** *695*, 818-826.
18. Frey, N. C.; Bandyopadhyay, A.; Kumar, H.; Anasori, B.; Gogotsi, Y.; Shenoy, V. B., Surface-Engineered MXenes: Electric Field Control of Magnetism and Enhanced Magnetic Anisotropy. *ACS Nano* **2019**.
19. Shahzad, F.; Alhabeb, M.; Hatter, C. B.; Anasori, B.; Man Hong, S.; Koo, C. M.; Gogotsi, Y., Electromagnetic interference shielding with 2D transition metal carbides (MXenes). *Science* **2016,** *353* (6304), 1137-1140.
20. Shah, S. A.; Habib, T.; Gao, H.; Gao, P.; Sun, W.; Green, M. J.; Radovic, M., Template-free 3D titanium carbide ($Ti_3C_2T_x$) MXene particles crumpled by capillary forces. *Chemical Communications* **2017,** *53* (2), 400-403.
21. Chen, X.; Dobson, J. F.; Raston, C. L., Vortex fluidic exfoliation of graphite and boron nitride. *Chemical Communications* **2012,** *48* (31), 3703-3705.
22. Al-Antaki, A. H. M.; Luo, X.; Alharbi, T. M. D.; Harvey, D. P.; Pye, S.; Zou, J.; Lawrance, W.; Raston, C. L., Inverted vortex fluidic exfoliation and scrolling of

hexagonal-boron nitride. *RSC Advances* **2019,** *9* (38), 22074-22079.
23. Vimalanathan, K.; Suarez-Martinez, I.; Peiris, M. C. R.; Antonio, J.; de Tomas, C.; Zou, Y.; Zou, J.; Duan, X.; Lamb, R. N.; Harvey, D. P.; Alharbi, T. M. D.; Gibson, C. T.; Marks, N. A.; Darwish, N.; Raston, C. L., Vortex fluidic mediated transformation of graphite into highly conducting graphene scrolls. *Nanoscale Advances* **2019,** *1* (7), 2495-2501.
24. Britton, J.; Chalker, J. M.; Raston, C. L., Rapid Vortex Fluidics: Continuous Flow Synthesis of Amides and Local Anesthetic Lidocaine. *Chemistry–A European Journal* **2015,** *21* (30), 10660-10665.
25. Gandy, M. N.; Raston, C. L.; Stubbs, K. A., Towards aryl C-N bond formation in dynamic thin films. *Organic and Biomolecular Chemistry* **2014,** *12* (26), 4594-4597.
26. Alharbi, T. M. D.; Vimalanathan, K.; Lawrance, W. D.; Raston, C. L., Controlled slicing of single walled carbon nanotubes under continuous flow. *Carbon* **2018,** *140*, 428-432.
27. Britton, J.; Stubbs, K. A.; Weiss, G. A.; Raston, C. L., Vortex fluidic chemical transformations. *Chemistry–A European Journal* **2017,** *23* (54), 13270-13278.
28. Alharbi, T. M. D.; Harvey, D.; Alsulami, I. K.; Dehbari, N.; Duan, X.; Lamb, R. N.; Lawrance, W. D.; Raston, C. L., Shear stress mediated scrolling of graphene oxide. *Carbon* **2018,** *137*, 419-424.
29. Yuan, T. Z.; Ormonde, C. F.; Kudlacek, S. T.; Kunche, S.; Smith, J. N.; Brown, W. A.; Pugliese, K. M.; Olsen, T. J.; Iftikhar, M.; Raston, C. L., Shear-Stress-Mediated Refolding of Proteins from Aggregates and Inclusion Bodies. *ChemBioChem* **2015,** *16* (3), 393-396.
30. Pye, S. J.; Dalgarno, S. J.; Chalker, J. M.; Raston, C. L., Organic oxidations promoted in vortex driven thin films under continuous flow. *Green Chemistry* **2018,** *20* (1), 118-124.
31. Alsulami, I.; Alharbi, T.; Harvey, D.; Gibson, C. T.; Raston, C. L., Controlling the growth of fullerene C_{60} cones under continuous flow. *Chemical Communications* **2018**, 54 (57), 7896-7899.
32. Luo, X.; Smith, P.; Raston, C. L.; Zhang, W., Vortex Fluidic Device-Intensified Aqueous Two Phase Extraction of C-Phycocyanin from Spirulina maxima. *ACS Sustainable Chemistry & Engineering* **2016,** *4* (7), 3905-3911.
33. Luo, X.; Al-Antaki, A. H. M.; Alharbi, T. M. D.; Hutchison, W. D.; Zou, Y.-c.; Zou, J.; Sheehan, A.; Zhang, W.; Raston, C. L., Laser-Ablated Vortex Fluidic-Mediated Synthesis of Superparamagnetic Magnetite Nanoparticles in Water Under Flow. *ACS Omega* **2018,** *3* (9), 11172-11178.
34. Luo, X.; Al-Antaki, A. H. M.; Harvey, D. P.; Ruan, Y.; He, S.; Zhang, W.; Raston, C. L., Vortex Fluidic Mediated Synthesis of Macroporous Bovine Serum Albumin-Based Microspheres. *ACS Applied Materials & Interfaces* **2018,** *10* (32), 27224-27232.
35. Luo, X.; Al-Antaki, A. H. M.; Vimalanathan, K.; Moffatt, J.; Zheng, K.; Zou, Y.; Zou, J.; Duan, X.; Lamb, R. N.; Wang, S.; Li, Q.; Zhang, W.; Raston, C. L., Laser irradiated vortex fluidic mediated synthesis of luminescent carbon nanodots under continuous flow. *Reaction Chemistry & Engineering* **2018,** *3* (2), 164-170.
36. Al-Antaki, A. H. M.; Luo, X.; Duan, X.; Lamb, R. N.; Hutchison, W. D.; Lawrance, W.; Raston, C. L., Continuous Flow Copper Laser Ablation Synthesis of Copper(I and II) Oxide Nanoparticles in Water. *ACS Omega* **2019,** *4* (8), 13577-13584.
37. Alharbi, T. M. D.; Shingaya, Y.; Vimalanathan, K.; Nakayama, T.; Raston, C. L., High

Yielding Fabrication of Magnetically Responsive Coiled Single-Walled Carbon Nanotube under Flow. *ACS Applied Nano Materials* **2019**, 2 (8), 5282–5289.

38. Mohammed Al-antaki, A. H.; Luo, X.; Duan, A.; Lamb, R. N.; Eroglu, E.; Hutchison, W.; Zou, Y.-C.; Zou, J.; Raston, C. L., Continuous flow synthesis of phosphate binding h-BN@magnetite hybrid material. *RSC Advances* **2018,** *8* (71), 40829-40835.
39. S. Seyedin, J. Zhang, K. A. S. Usman, S. Qin, A. M. Glushenkov, E. R. S. Yanza, R. T. Jones, J. M. Razal, Facile Solution Processing of Stable MXene Dispersions towards Conductive Composite Fibers, *Advanced Science News*, **2019**, 3, 1900037.
40. Vimalanathan, K.; Gascooke, J. R.; Suarez-Martinez, I.; Marks, N. A.; Kumari, H.; Garvey, C. J.; Atwood, J. L.; Lawrance, W. D.; Raston, C. L., Fluid dynamic lateral slicing of high tensile strength carbon nanotubes. *Scientific Reports* **2016,** *6*, 22865.
41. Wahid, M. H.; Eroglu, E.; Chen, X.; Smith, S. M.; Raston, C. L., Functional multi-layer graphene–algae hybrid material formed using vortex fluidics. *Green Chemistry* **2013,** *15* (3), 650-655.
42. Xue, Q.; Zhang, H.; Zhu, M.; Pei, Z.; Li, H.; Wang, Z.; Huang, Y.; Huang, Y.; Deng, Q.; Zhou, J.; Du, S.; Huang, Q.; Zhi, C., Photoluminescent Ti_3C_2 MXene Quantum Dots for Multicolor Cellular Imaging. *Advanced Materials,* **2017,** *29* (15), 1604847.
43. Satheeshkumar, E.; Makaryan, T.; Melikyan, A.; Minassian, H.; Gogotsi, Y.; Yoshimura, M., One-step Solution Processing of Ag, Au and Pd@MXene Hybrids for SERS. *Scientific Reports* **2016,** *6*, 32049.
44. Li, Y.; Zhou, X.; Wang, J.; Deng, Q.; Li, M.; Du, S.; Han, Y.-H.; Lee, J.; Huang, Q., Facile preparation of in situ coated $Ti_3C_2T_x$/NiO.5ZnO.5Fe_2O_4 composites and their electromagnetic performance. *RSC Advances* **2017,** *7* (40), 24698-24708.
45. Peng, Q.; Guo, J.; Zhang, Q.; Xiang, J.; Liu, B.; Zhou, A.; Liu, R.; Tian, Y., Unique Lead Adsorption Behavior of Activated Hydroxyl Group in Two-Dimensional Titanium Carbide. *Journal of the American Chemical Society* **2014,** *136* (11), 4113-4116.
46. Rakhi, R. B.; Ahmed, B.; Hedhili, M. N.; Anjum, D. H.; Alshareef, H. N., Effect of Postetch Annealing Gas Composition on the Structural and Electrochemical Properties of Ti2CTx MXene Electrodes for Supercapacitor Applications. *Chemistry of Materials* **2015,** *27* (15), 5314-5323.
47. Naguib, M.; Mochalin, V. N.; Barsoum, M. W.; Gogotsi, Y., 25th Anniversary Article: MXenes: A New Family of Two-Dimensional Materials. *Advanced Materials* **2014,** *26* (7), 992-1005.
48. Naguib, M.; Mashtalir, O.; Carle, J.; Presser, V.; Lu, J.; Hultman, L.; Gogotsi, Y.; Barsoum, M. W., Two-Dimensional Transition Metal Carbides. *ACS Nano* **2012,** *6* (2), 1322-1331.
49. Liu, F.; Zhou, A.; Chen, J.; Jia, J.; Zhou, W.; Wang, L.; Hu, Q., Preparation of Ti_3C_2 and Ti_2C MXenes by fluoride salts etching and methane adsorptive properties. *Applied Surface Science* **2017,** *416*, 781-789.
50. Li, Z.; Wang, L.; Sun, D.; Zhang, Y.; Liu, B.; Hu, Q.; Zhou, A., Synthesis and thermal stability of two-dimensional carbide MXene Ti_3C_2. *Materials Science and Engineering: B* **2015,** *191*, 33-40.
51. Sarycheva, A.; Makaryan, T.; Maleski, K.; Satheeshkumar, E.; Melikyan, A.; Minassian, H.; Yoshimura, M.; Gogotsi, Y., Two-Dimensional Titanium Carbide (MXene) as Surface-Enhanced Raman Scattering Substrate. *The Journal of Physical Chemistry C* **2017,** *121* (36), 19983-19988.

ROYAL SOCIETY OPEN SCIENCE

royalsocietypublishing.org/journal/rsos

Research

Cite this article: Mohammed Al-antaki AH, Kellici S, Power NP, Lawrance WD, Raston CL. 2020 Continuous flow vortex fluidic-mediated exfoliation and fragmentation of two-dimensional MXene. *R. Soc. Open Sci.* **7**: 192255.
http://dx.doi.org/10.1098/rsos.192255

Received: 9 January 2020
Accepted: 30 March 2020

Subject Category:
Chemistry

Subject Areas:
nanotechnology/materials science

Keywords:
MXene, exfoliation, fluid flow

Author for correspondence:
Colin L. Raston
e-mail: colin.raston@flinders.edu.au

This article has been edited by the Royal Society of Chemistry, including the commissioning, peer review process and editorial aspects up to the point of acceptance.

Electronic supplementary material is available online at https://doi.org/10.6084/m9.figshare.c.4971134.

ROYAL SOCIETY OF CHEMISTRY

THE ROYAL SOCIETY PUBLISHING

Continuous flow vortex fluidic-mediated exfoliation and fragmentation of two-dimensional MXene

Ahmed Hussein Mohammed Al-antaki[1,3], Suela Kellici[4], Nicholas P. Power[5], Warren D. Lawrance[2] and Colin L. Raston[1]

[1]Flinders Institute for Nanoscale Science and Technology, College of Science and Engineering, and [2]College of Science and Engineering, Flinders University, Adelaide, South Australia 5042, Australia
[3]Department of Chemistry, Faculty of Sciences, University of Kufa, Kufa, Najaf, Iraq
[4]School of Engineering, London South Bank University, 103 Borough Road, London SE1 0AA, UK
[5]School of Life, Health and Chemical Sciences, The Open University, Walton Hall, Milton Keynes MK7 6AA, UK

AHMA, 0000-0001-8576-3805; SK, 0000-0003-1387-2345; NPP, 0000-0002-4630-7580; CLR, 0000-0003-4753-0079

MXene (Ti_2CT_x) is exfoliated in a vortex fluidic device (VFD), as a thin film microfluidic platform, under continuous flow conditions, down to *ca* 3 nm thin multi-layered two-dimensional (2D) material, as determined using AFM. The optimized process, under an inert atmosphere of nitrogen to avoid oxidation of the material, was established by systematically exploring the operating parameters of the VFD, along with the concentration of the dispersed starting material and the choice of solvent, which was a 1 : 1 mixture of isopropyl alcohol and water. There is also some fragmentation of the 2D material into nanoparticles *ca* 68 nm in diameter.

1. Introduction

MXenes are a unique class of two-dimensional (2D) material, first reported in 2011 [1]. They are transition metal carbides and carbonitrides and have a number of potential applications, including in biology [2–5], batteries [6–8], electronic devices [9,10] and supercapacitors [10,11]. They are prepared from $M_{n+1}AX_n$ phases via etching the A layers from the laminar material, where M is a transition metal (Ti, Zr, Nb, V, Ta or Mo), A is a main group element, mostly Al or Si, and X is C and/or N, and n is 1, 2 or 3. Substituting Al or Si with functional groups, T (–O, –OH, –F), either side of the sheets ($M_{n+1}X_nT_x$) imparts greater application of

3. Vortex fluidic mediated synthesis of TiO_2 nanoparticle/MXene composites

Ahmed Hussein Mohammed Al-antaki[a,b], Thaar M. D. Alharbi[a], Suela Kellici[c] , Nicholas P. Power[d], Warren D. Lawrance[e], Colin L. Raston[a*]

a. *Flinders Institute for Nanoscale Science and Technology, College of Science and Engineering, Flinders University, Adelaide, SA 5042, Australia.*
b. *Department of Chemistry, Faculty of Sciences, Kufa University, Kufa, Najaf, Iraq.*
c. *School of Engineering, London South Bank University, 103 Borough Road London, SE1 0AA (UK).*
d. *School of Life, Health and Chemical Sciences, The open University, Walton Hall, Milton Keynes, MK7 6AA (UK).*
e. *College of Science and Engineering, Flinders University, Adelaide, SA 5042.*

Author contributions: **AA** performed all the VFD and all characterisation experiments; wrote all the primary content. **TA** performed all the XPS spectra. **SK** and **NP** prepared MXene. **WL** and **CR** supervised and coordinated the project and helped on the research directions and plan, and the final revision of the manuscript. All of the co-authors assisted with the revision of the manuscript before and during the publication process.

Graphical Abstract

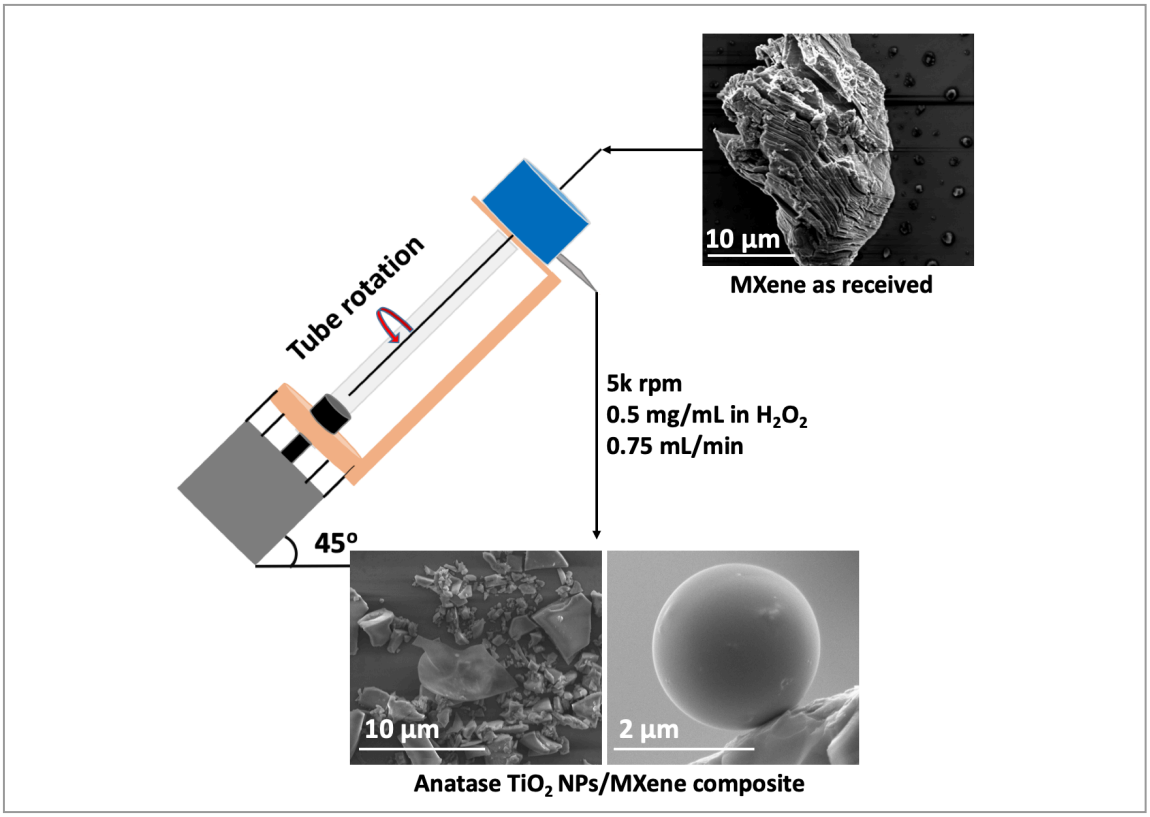

3.1 Abstract

Oxidation of MXene in a vortex fluidic device (VFD) operating under continuous flow results in exfoliation and fragmentation into nanoparticles of surface oxidised 2D material with further oxidation of the nanoparticles into anatase (TiO_2). These MXene and anatase nanoparticles co-assemble into stable micron sized spheres which are topologically smooth,decorating the surface of exfoliated MXene. The formation of this composite material in the dynamic thin film in the VFD was optimised by systematically exploring the operating paprameters of the microfluidic platform, determined at 45º tilt angle for the 20 mm diameter glass tube spinning at 5k rpm, with a flow rate of a colloide dispersion of MXene in aqueous H_2O_2 (30%) at 0.75 mL/min, concentration of MXene 0.5 mg/mL.

3.2 Introduction

The First report describing the new and unique class of 2D MXenes materials was in 2011.[1] They are based on transition metal carbides, carbonitrides and nitrides, and have potential in a number of applications, including in biological,[2-5] batteries,[6-8] electronic devices[9,10] and supercapacitors.[10,11] The unit formula of these materials is $M_{n+1}X_nT_x$ in which M is an early transition metal, including Sc, Ti, Cr, Zr, Nb, Mn, Mo, Hf, V, Ta, or W, X represents either carbon and /or nitrogen, and n is 1, 2, or 3 in defining the number of M layers. Tx represents surface functional groups −O, −OH, −F bound to the transition metals.[12,13] More than twenty types of MXenes have been developed, including Ti_2CT_x, $Ti_3C_2T_x$, V_2CT_x, Nb_2CT_x, Mo_2CT_x and Ti_3CNT_x.[14] Some of them contain two different transition metals, for examples in $Mo_2TiC_2T_x$.[15,16] There is a growing interest in nanocomposite materials involving MXenes, for example MXene($Ti_3C_2T_x$)/α-Fe_2O_3 for use as a negative electrode material for supercapacitors,[17] MXene($Ti_3C_2T_x$)/MnO_2 for high performance electrode materials for flexible supercapacitors,[18] and Ti_3C_2-MnO_2 for enhancing interfacial electronic coupling.[19] In addition, MXenes decorated with TiO_2 quantum dots (QDs) feature in Li-S batteries,[20] MXene-Cu_2O catalyses the thermal decomposition of ammonium perchlorate,[21] MXene-enzymes feature in electrochemical biosensors,[22] MXene-CNTs improve electrochemical performance,[8] and MXene-Pt nanoparticles have sensing application[23] with others for determining ion exchange capacity.[24] More specifically, TiO_2 nanoparticle (NP)/MXene composites feature in rendering MXene biocompatible for enzyme attachment,[22] enhancing the efficiency of MXenes modified glassy carbon electrode for H_2O_2 reduction,[25] nitrite detection,[26] low detection limits of glucose[27] and sodium alanate,[28] Li-ion battery anodes[29] and photocatalyst.[30] Thermal

methods have been used to oxidize MXene to TiO_2 or TiO_2 NPs/MXene.[28,30,31] with H_2O_2 also effective in preparing the same material.[29] Herein we report the oxidation of MXene (Ti_2C) in 30% H_2O_2 in gaining access to TiO_2 NPs/MXene composite materials, which encompasses exfoliation with surface oxidation, fragmentation of the 2D material, and oxidation of the fragmented material, using a vortex fluidic device (VFD). The VFD is a thin film microfluidic platform which has two types of processing, the confined mode where a glass tube inclined at 45º relative to the horizontal position is spun at high speed.[32] This is a proven approach for then translating any reaction into continuous flow process, which is the other mode of operation of the VFD, Figure 3.1.[33] The VFD is a versatile thin film device effective for a growing number of applications, including *in situ* decorating *h*-BN with magnetite nanoparticles,[34] fabricating carbon dots from multi-walled carbon nanotubes,[35] chemo selectivity hydrogenation using cellulose impregnated with Pd NPs lining the VFD tube,[36] organic synthesis,[37,38] probing the structure of self- organised systems,[39,40] exfoliation and scrolling of *h*-BN and graphite,[41-43] slicing CNTs,[44,45] to mention a few.[41,46-54] The VFD typically houses a borosilicate glass tube (O.D. diameter 20 mm, I.D. diameter 17.5 mm, 19.5 cm long) open at one end, which is rotated at high speed (up to 9k rpm) and inclined at an angle of 0º to <90º relative to the horizontal position, Figure 3.1.[37,41,45,47] The behaviour of MXene in the VFD in the presence of 30% H_2O_2 was explored, which involved varying the flow rate of the solution of MXene in H_2O_2 and the rotational speed of the tube, with the tilt angle fixed at 45 degree as the optimal angle for a plethora of applications of the device.

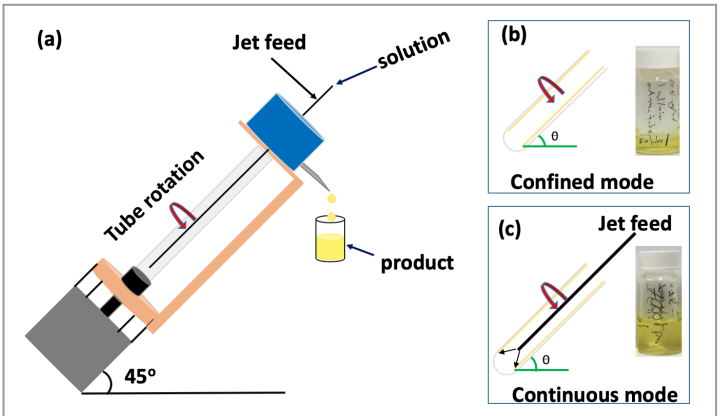

Figure 3.1. (a) Diagrammatic representation of the VFD, for which the optimal processing in a 20 mm O.D. (17.5 mm I.D.) borosilicate glass tube is 5k rpm with a jet feed delivering a solution of MXene in aqueous H_2O_2 (30%), 0.5 mg/mL, flow rate 0.75 mL/min. Also shown are photographs of solutions produced using (b) the confined mode of operation of the VFD, and (c) continuous flow.

3.3 Experimental

3.3.1 Materials. Ti_2AlC powder precursor was obtained commercially (KANTHAL, Maxthal 211 Ti_2AlC). Etching of the aluminium from Ti_2AlC was conducted in a 20% aqueous hydrofluoric acid, HF, solution (Sigma Aldrich) for 24 hr at room temperature. The resulting suspension was filtered and washed with deionised water (DI) to reach a pH > 6.[55] The as prepared MXenes was dispersed in hydrogen peroxide (30%) from Sigma-

Aldrich for all experiments. Control experiments, Figure S3.14, used < 100 nm dimeter TiO_2 purchased from Aldrich.

3.3.2 Decoration and fabrication of TiO_2NPs/MXene spheres and sheets. The procedure throughout involved dispersing 10 mg of MXene in 20 mL of H_2O_2 (30%) which was then placed in a sonic bath for 10 mins at 6 kHz, whereupon the colour of the solution changed from dark grey to green, Figure S3.4(a, b) and Figure S3.5(a-f). The solution was then delivered through a syringe to the base of the rotating 20 mm O.D. glass tube using a stainless-steel jet feed. The optimal conditions for preparing this material was a rotational speed of 5k rpm, tilt angle 45º and flow rate 0.75 mL/min for 0.5 mg/mL of MXene in aqueous H_2O_2. Material exiting the glass tube had spheres and sheets of TiO_2NPs/MXene (*ca* 39%), with other material retained in the tube. The natural material was comprised exclusively of sheets of TiO_2NPs/MXene composite material (*ca* 61%). The spheres were about 2 µm ± 0.5 µm in diameter and the average thickness of the sheets was 300 nm ± 200 nm. We make the distinction between the two composite materials as (i) TiO_2 NPs/MXene spheres where spheres of assembled TiO_2 NPs and MXene nanoparticles. The material retained in the tube under flow is (ii) TiO_2 NPs/MXene sheets where exfoliated MXene is decorated with TiO_2 NPs, with the material exiting the tube under flow.

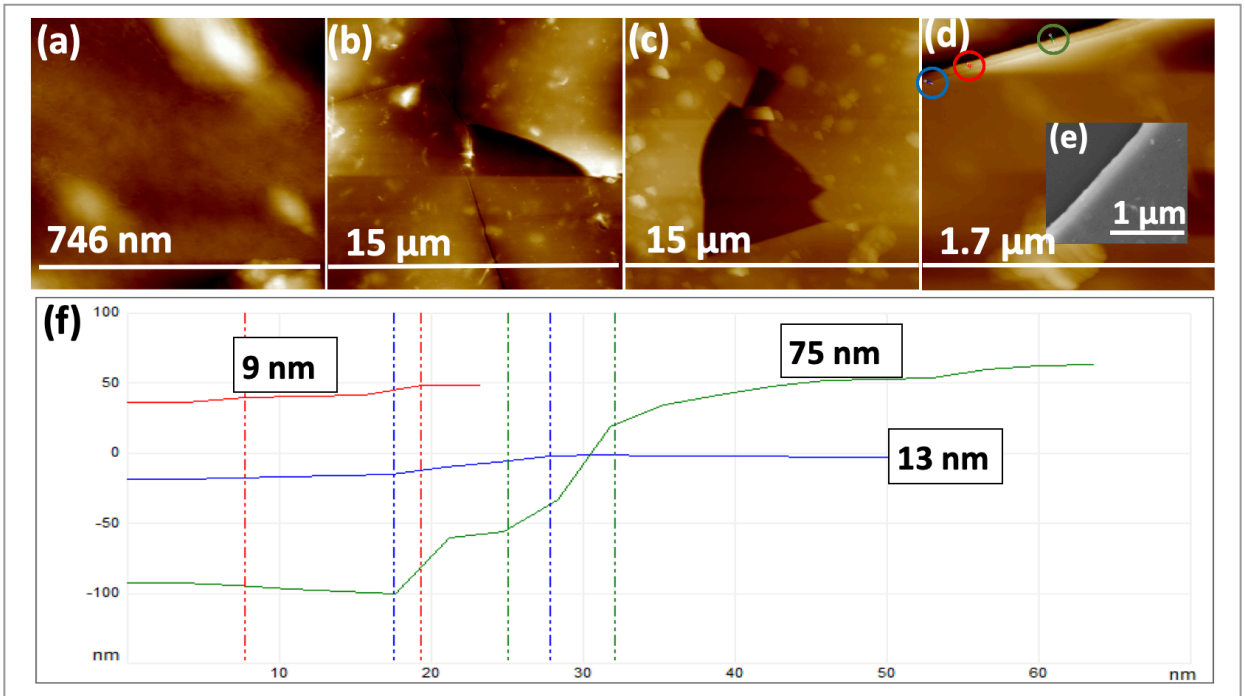

Figure 3.2. AFM images for TiO_2 NPs/MXene composite drop cast on silicon wafer and then oven dried at 60ºC, prepared from MXene in 30% H_2O_2 (0.5 mg/mL) with the optimal VFD of processing parameters as rotational speed 5k rpm, tilt angle 45º, flow rate 0.75 mL/min. (a-d) AFM images for TiO_2 NPs/MXene sheets. (e) SEM image for TiO_2 NPs/MXene sheets. (f) AFM height profile for TiO_2 NPs/MXene sheets.

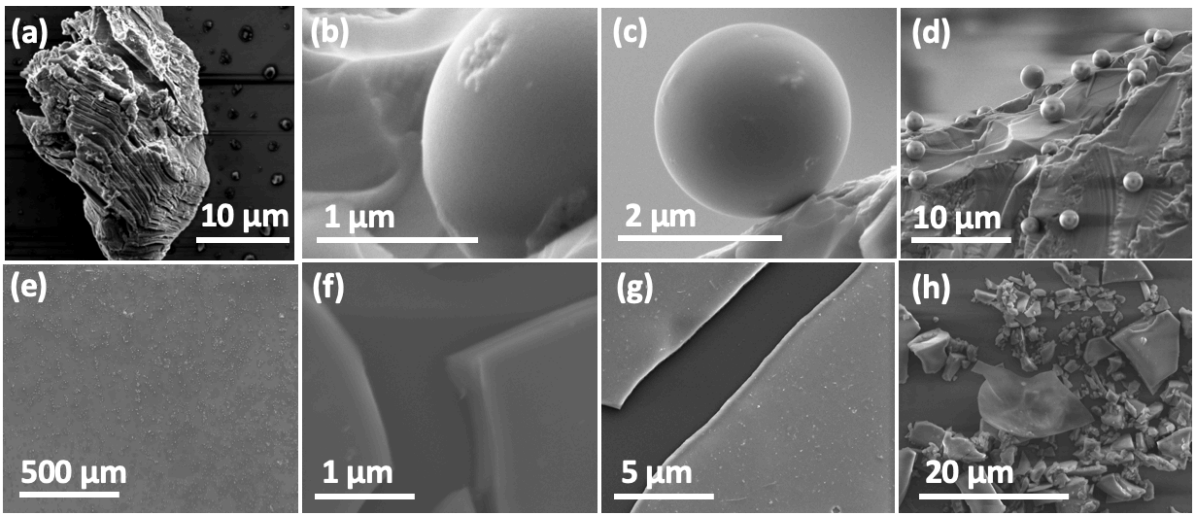

Figure 3.3. SEM images (a) As prepared of MXene. (b-h) TiO_2 NPs/MXene drop cast on silicon wafer, with the material prepared according to the details in Figure 3.2. (b-e) Spheres for TiO_2 NPs /MXene. (f-h) sheets TiO_2 NPs/MXene.

3.3.3 Characterisation TiO_2 NPs/MXene collected (exiting the tube) and retained in the tube were characterized using scanning electron microscopy (SEM) and EDS (Inspect FEI F50 SEM), atomic force microscopy (AFM - Nanoscope 8.10 tapping mode), Raman spectroscopy (WiTec Alpha 300R $\lambda_{exc.}$=532 nm), XRD (Bruker D8 ADVANCE ECO, Co- Kα, λ=1.7889 Å), ATR-FTIR Perkin Elmer Frontier, HRTEM (FEI Tecnai F20 operated at 200 kV), UV-Vis spectrophotometer Cary 50EST70772 and X-ray photoelectron spectroscopy (XPS) using Mg Kα radiation to determine the elemental composition and the chemical states of all components. The XPS equipment was built by SPECS (Berlin, Germany) with a nonmonochromatic X-ray source. High-resolution scans were recorded for carbon (C), titanium (Ti) and oxygen (O) at a pass energy of 10 eV.

3.4 Results and discussion

The concentration of MXene in 30% H_2O_2 was varied while fixing the rotational speed at 4k rpm and the flow rate at 0.5 mL/min with the MXene concentration varied, studying 0.1, 0.3, 0.5, 0.7 and 1.0 mg/mL. Of these, 0.5 mg/mL afforded more regular spheroidal particles. We also studied the effect of time on the sonication of MXene in H_2O_2 prior to VFD processing, for 5 mins, 10 mins and 15 mins. The solution turned green after 10 minutes, signifying some oxidation, and this time was then set for all sample preparation for VFD processing.

The flow rate and rotational speed were then systematically varied with the tilt angle for all experiments fixed at 45º, for reasons discussed above, Figure 3.1.[32,33,56,57] Different flow rates for a concentration of MXene in H_2O_2 at 0.5 mg/mL were used, at 0.25, 0.5, 0.75, 1 and 1.25 mL/min, Figure S3.4(c-g). The optimal flow rate to generate TiO_2NPs/MXene spheres was 0.75 mL/min, with lower yield and less uniform spheres for flow rates of 0.25 and 0.5 mL/min. While spheres also formed at flow rates of 1.0 and 1.25 mL/min they were unstable, disassembling after drop cast on silicon wafer, Figure S3.5. For a flow rate of 0.75 mL/min entering the VFD tube, the effect of using different rotational speeds was explored, studying 4, 5, 6, 7, 8 and 9k rpm, Figure S3.4(h-i). Of these, 5k rpm afforded more uniform spheres, in high yield as a suspension exiting the VFD under flow, Figure S3.5(o-r) and Figure S3.6.

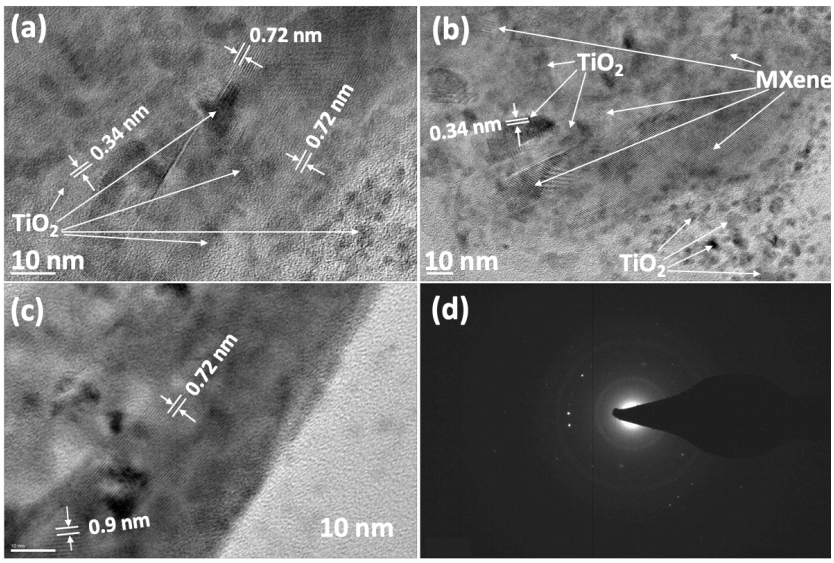

Figure 3.4. HRTEM images for TiO_2 NPs/MXene drop cast on grid, MXene in H_2O_2 (0.5 mg/mL) optimal of VFD processing at 5k rpm rotational speed, tilt angle 45º and flow rate 0.75 mL/min. (a-c) HRTEM. (d) SAED for TiO_2 NPs/MXene composite.

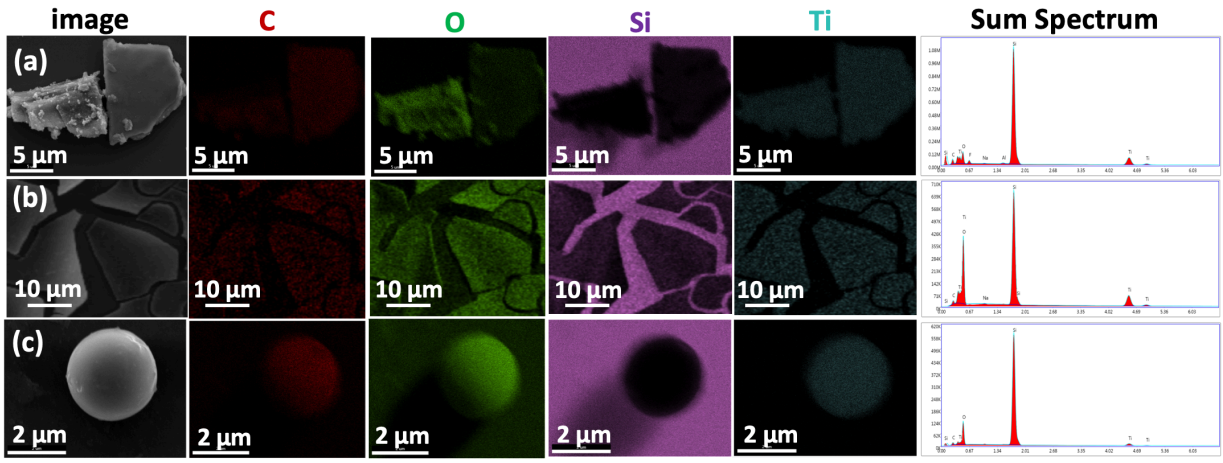

Figure 3.5. EDS mapping for TiO_2 NPs /MXene drop cast on a silicon wafer and air dried at 60ºC, optimal VFD parameters, rotational speed 5k rpm, tilt angle 45º and flow rate 0.75 mL/min. (a) MXene as prepared. (b) Sheets of TiO_2NPs /MXene. (c) Spheres of TiO_2NPs / MXene.

The choice of aqueous H_2O_2 as the solvent for dispersing MXene was for oxidation of the fragmented MXene to anatase TiO_2 NPs, having previously established that in the absence of hydrogen peroxide, and under an atmosphere of nitrogen, the VFD is effective not only in exfoliating MXene, but also in breaking it down into nanoparticles (chapter 2). These nanoparticles decorate the surface of exfoliated MXene. In the present study, the hydrogen peroxide is indeed effective in converting some of the MXene nanoparticles to anatase TiO_2, which can also decorate the surface of exfoliated MXene along with oxidation of the surface of the MXene, and form spheres of self-assembled TiO_2 NPs and MXene nanoparticles, in generating the two TiO_2NPs/MXene composites, (i) and (ii) above, Figure 3.3 and S3.1.

Different outcomes in the processing arising from varying the rotational speed of the VFD and flow rate in particular will be determined by differences in fluid dynamic responses which are inherently complex. Indeed, understanding the fluid behaviour in the thin film in the VFD is a major research effort underway in ultimately being able to predict the outcome of any process. In the present study, the mechanoenergy delivered into the thin film has topological effects for generating spheres of the composite material, which is optimal at a flow rate of 0.75 mL/min and 5k rpm rotational speed, but determining how this occurs is a major research effort in its own right.

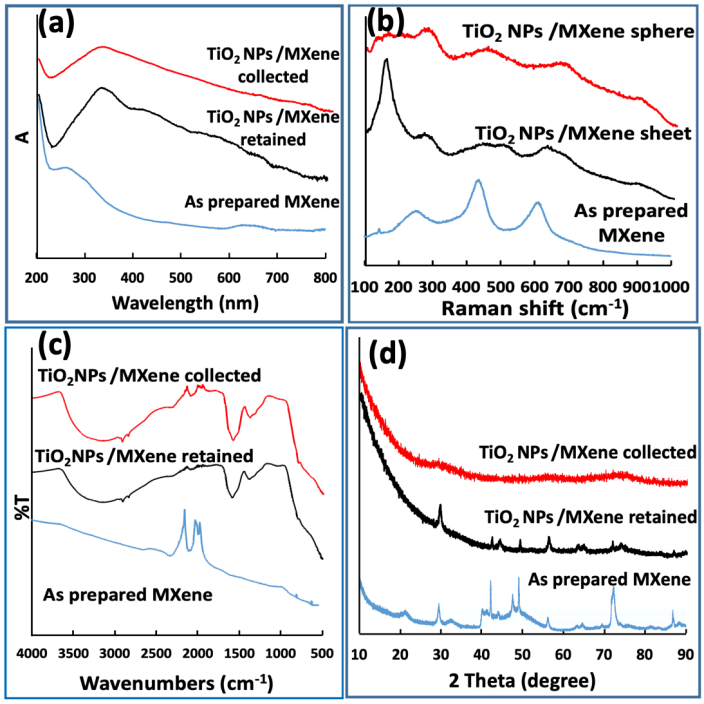

Figure 3.6. TiO_2NPs /MXene collected from solution exiting the VFD tube, for MXene at optimal of VFD processing conditions, rotational speed 5k rpm, tilt angle 45° and flow rate 0.75 mL/min followed by drying in air at 60°C. (a) UV-Vis spectra. (b) Raman spectra for spheres and sheets. (c) ATR-FTIR spectra. (d) Powder X-ray diffraction.

The dynamic thin film in VFD is also effective in exfoliating other 2D materials including graphene and *h*-BN, with and without scrolling.[41-43] In the present study, treating MXene with aqueous H_2O_2 prior to VFD processing (batch processing) reduced the thickness of the MXene starting material from 10 μm to a few hundred nanometres, presumably driven by surface oxidation along dislocations in the material, Figure S3.5(d-f). VFD processing

further reduced the thickness of the material, with AFM images showing the presence of 9, 13, 75 and a few hundred nanometre sheets, Figure 3.2. The SEM images revealed that the

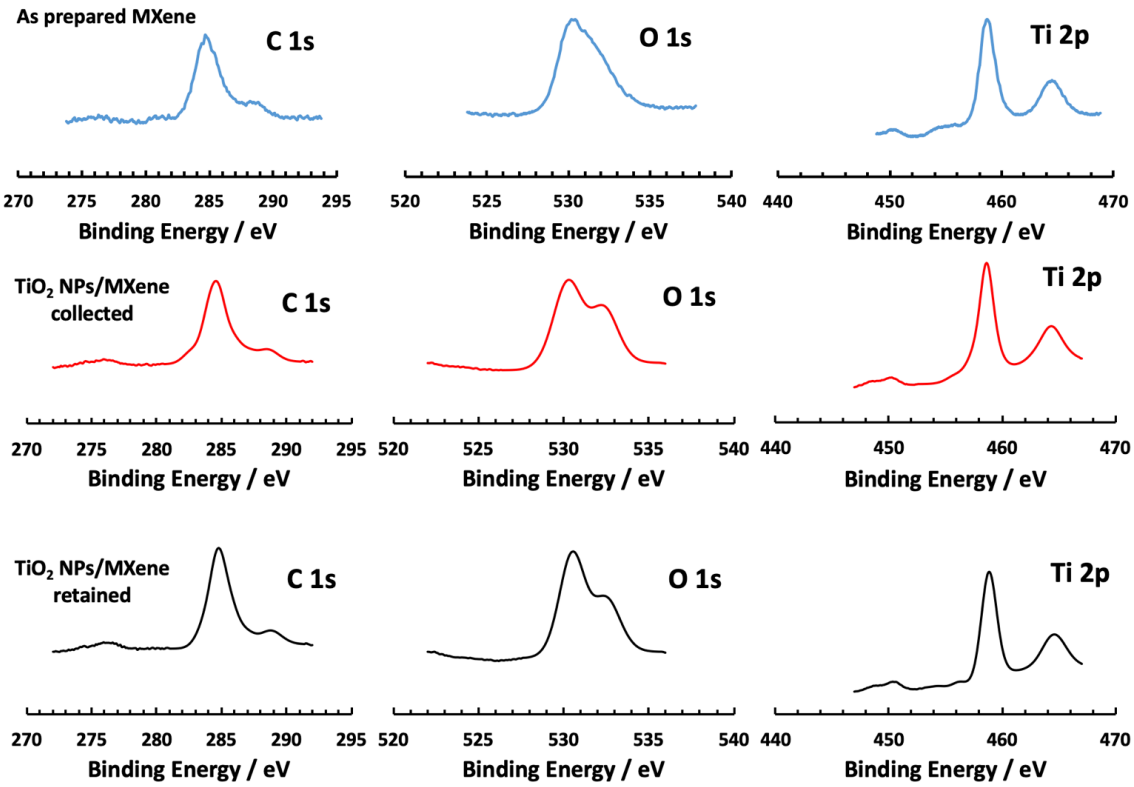

Figure 3.7. XPS of as prepared MXene compare with TiO_2 NPs /MXene collected and retained after drop casting on a silicon wafer and oven dried at 60ºC, for the optimal VFD processing parameters, rotational speed 5k rpm, tilt angle 45º and flow rate of 0.75 mL/min.

sheets (retained) are topologically smooth, Figure 3.3(f-h), S3.1(f). In this context, we note that the reduction of graphene oxide (rGO) in water via VFD while UV irradiated generates topologically smooth rGO sheets from corrugated GO starting material,[58] and the smoothing here and in the present study presumably comes from the unique high shear fluid flow in the VFD. In addition to the MXene sheets, there are spheres of self-assembled TiO_2/MXene nanoparticles, Figure 3.3(b- e), S3.1(a-e). We note that the shear stress in the VFD is effective for controlling self-assembly, for example in forming cones of fullerene C_{60},[39] and the present result in assembling the spheres adds to this unusual property of fluid flow in the device.

HRTEM of TiO_2NPs/MXene sheets revealed lattice planes of MXene[11] and the size of the TiO_2 nanoparticles (NPs),[59] Figure 3.4, S3.2 and S3.3. The selected area electron diffraction (SAED) of the material established the presence of anatase TiO_2 NPs on the

surface of MXene sheets Figure 3.4(d).[29,60] The EDS spectra and EDS mapping (SEM derived) established the presence of C, O and Ti in the spheres and sheets, Figure 3.5, S3.7 and S3.8. In addition, the sum spectra are consistent with oxidation of MXene, given the ratio of C to O peaks in the as prepared MXene relative to TiO_2NPs/MXene spheres and sheets, Figure 3.5. The Raman spectra of MXene as prepared has three peaks at 259, 435 and 609 cm^{-1},[55] which correspond to titanium carbide in MXene.[61] They are slightly shifted in the Raman spectra of TiO_2NPs/MXene spheres and sheets. The reason for this is a reduction in the number of stacked sheets of MXene in the composite material, from micro to nano thickness, Figure 3.2. In addition, the surface functional groups in MXene (−O, −OH and –F) coordinate to titanium in anatase resulting in an increase in vibration energy of Ti-O.[29] A peak in the Raman spectra for anatase at 161 cm^{-1} Figure 3.6(b)[31] corresponds to the $E_{g\,(1)}$ vibrational mode.[31,62] Raman spectroscopy was also used to establish that the spheres and sheets are stable at room temperature, with no change after 60 days, Figure S3.11. SEM images and EDX mapping were also consistent with this finding, Figure S3.9 and S3.10. The ATR-FTIR for MXene as prepared has peaks at 632 and 949 cm^{-1} corresponding to Ti-O and C-F stretching frequencies respectively.[63,64] The VFD processed (collected and retained) material has peaks assignable to MXene, now with additional peaks for H_2O stretching and bending modes at 3380 cm^{-1} and 1608 cm^{-1} respectively.[65] Peaks at 1406 and 813 cm^{-1} are assigned to the lattice vibration of anatase TiO_2 (Ti–O–Ti stretching) and (Ti-O) bending, Figure 3.6(c).[65,66]

UV-Vis spectroscopy of the material exiting the VFD tube, and retained in the tube were recorded and compared with as prepared MXene. The VFD processed materials have different spectra, in accordance with their solutions being yellow, with solutions of as prepared MXene being dark grey. This required collecting suspensions of the two materials (retained in the tube and exiting under flow) followed by immediate removal of the solvent *in vacuo*. This was important rather than recording the spectra immediately due to further reaction (oxidation) and evolution of bubbles which reduced the quality of the UV-Vis spectra.[67] The spectra are consistent with the presence of anatase in the composite material, Fig. 6(a).[30,68,69]

Figure 3.6(d) provides the X-ray diffraction data (XRD) for as prepared MXene showing the expected 2θ peaks at 29.4, 40.6, 42.4 and 72.4°(Co K_α λ= 17889 Å) for the crystal structure of Ti_2CT_x MXene which has hexagonal *P63/mmc* space group and a lattice constant a ≈ 0.3 nm.[70,71] Post VFD processing (after oxidation and fabrication of MXene composites), the XRD of the collected and retained material had peaks corresponding to

MXene,[28] with additional peaks for anatase at 2θ 29.6 (101), 44.3 (004), 63.7 (105), 64.9 (211), 74.1 (204) and 83.8° (215). [20,72,73] The peak at 29.6° overlaps with a peak for MXene, Figure 3.6(d).[30] The Scherrer equation was used to determine the average size of the anatase TiO_2 NPs retained in the VFD tube, at 18.5 nm.[62]

X-ray photoelectron spectroscopy (XPS) was used as a sensitive characterisation technique for ascertaining any oxidation of MXene. The TiO_2NPs/MXene composite material collected and retained in the VFD had the same XPS spectra for C 1s, O 1s and Ti 2p, Figure 3.7. C 1s has peaks at 282.4 eV (C-Ti), 284.8 eV (C-C and C-H) and 288.8 eV (C-O or/and C-F). [69,72,74] O 1s has a peak at 530.6 eV (TiO_2), 531.7 eV (C-T-O_x), 532 eV (C-T-$(OH)_x$) and 533.9 (H_2O_{ads}).[69,74,75] Ti 2p had peaks corresponding to $Ti^{+2}(2p_{3/2})$, Ti^{+3} $(2p_{3/2})$ for Ti-C (sp^3) at 456 eV and 457.2 eV respectively, and $Ti^{+2}(2p_{1/2})$ and Ti^{+3} $(2p_{1/2})$ for Ti-C (sp^1) at 461 eV and 463.2 eV respectively.[14,20,30,55,59] The peaks at 459.1 eV and 465.1 eV for Ti-O (sp^3) and Ti-O (sp^1) for TiO_2.[74]

3.5 Conclusions

The systematic evaluation of the different operating parameters of the VFD, as a proven strategy for a myriad of applications of the device, proved useful in the present work, with optimal conditions for preparing the spheres and exfoliation at 5k rpm rotational speed, 45° tilt angle and flow rate of a solution of 10 mg of MXene in 20 mL of 30% H_2O_2 at 0.75 mL/min. The oxidation of MXene in 30% aqueous H_2O_2 under shear stress in a VFD is a convenient strategy for decorating layers of MXene with anatase TiO_2 NPs in forming a novel shape composite material with a dramatic reduction in the number of stacked sheets. The processing generates NPs of fragmented MXene which co-assemble with anatase NPs in forming novel spheroidal TiO_2NPs/MXenes composite material, which is stable for extended periods. We note that the ready availability of TiO_2NPs/MXene composites using a VFD offers potential for applications requiring biocompatibility for enzymes,[22] use in modified glassy carbon electrodes for H_2O_2 reduction,[25] nitrite detection,[26] glucose and sodium alanate,[28] Li-ion battery anodes[29] and as photocatalyst.[30]

3.6 Acknowledgements

The authors gratefully acknowledge financial support from the Iraq Government, Ministry of Higher Education and Scientific Research, and the Australian Research Council and the Government of South Australia. Use of facilities in the Australian Microscopy & Microanalysis Research Facility (AMMRF) and the Australian National Fabrication Facility

(ANFF) at the South Australian nodes of the AMMRF and ANFF under the National Collaborative Research Infrastructure Strategy are also acknowledged.

3.7 References

1. Naguib, M.; Kurtoglu, M.; Presser, V.; Lu, J.; Niu, J.; Heon, M.; Hultman, L.; Gogotsi, Y.; Barsoum, M. W., Two-Dimensional Nanocrystals Produced by Exfoliation of Ti_3AlC_2. *Advanced Materials* **2011,** *23* (37), 4248-4253.
2. Xu, B.; Zhu, M.; Zhang, W.; Zhen, X.; Pei, Z.; Xue, Q.; Zhi, C.; Shi, P., Ultrathin MXene-Micropattern-Based Field-Effect Transistor for Probing Neural Activity. *Advanced Materials* **2016,** *28* (17), 3333-3339.
3. Rasool, K.; Helal, M.; Ali, A.; Ren, C. E.; Gogotsi, Y.; Mahmoud, Kajan, Antibacterial Activity of Ti_3C_2T x MXene. *ACS Nano* **2016,** *10* (3), 3674-3684.
4. Nasrallah, G. K.; Al-Asmakh, M.; Rasool, K.; Mahmoud, K. A., Ecotoxicological assessment of $Ti_3C_2T_x$ (MXene) using a zebrafish embryo model. *Environmental Science Nano* **2018,** *5* (4), 1002-1011.
5. Yu, X.; Cai, X.; Cui, H.; Lee, Seung-Wuk.; Yu, Xue-Feng.; Liu, B., Fluorine-free preparation of titanium carbide MXene quantum dots with high near-infrared photothermal performances for cancer therapy. *Nanoscale* **2017,** *9* (45), 17859-17864.
6. Dall Agnese, Y.; Taberna, P.-L.; Gogotsi, Y.; Simon, P. Jtjopcl, Two-dimensional vanadium carbide (MXene) as positive electrode for sodium-ion capacitors. *The Journal of Physical Chemistry Letters* **2015,** *6* (12), 2305-2309.
7. Mashtalir, O.; Naguib, M.; Mochalin, V. N.; Dall'Agnese, Y.; Heon, M.; Barsoum, M. W.; Gogotsi, Y., Intercalation and delamination of layered carbides and carbonitrides. *Nature Communications* **2013,** *4*, 1716.
8. Mashtalir, O.; Lukatskaya, M. R.; Zhao, M.-Q.; Barsoum, M. W.; Gogotsi, Y., Amine-Assisted Delamination of Nb2C MXene for Li-Ion Energy Storage Devices. *Advanced Materials* **2015,** *27* (23), 3501-3506.
9. Khazaei, M.; Arai, M.; Sasaki, T.; Chung, C.-Y.; Venkataramanan, N. S.; Estili, M.; Sakka, Y.; Kawazoe, Y., Novel Electronic and Magnetic Properties of Two-Dimensional Transition Metal Carbides and Nitrides. *Advanced Materials* **2013,** *23* (17), 2185-2192.
10. Lukatskaya, M. R.; Mashtalir, O.; Ren, C. E.; Dall'Agnese, Y.; Rozier, P.; Taberna, P. L.; Naguib, M.; Simon, P.; Barsoum, M. W.; Gogotsi, Y., Cation Intercalation and High Volumetric Capacitance of Two-Dimensional Titanium Carbide. *Science* **2013,** *341* (6153), 1502-1505.
11. Wang, X.; Kajiyama, S.; Iinuma, H.; Hosono, E.; Oro, S.; Moriguchi, I.; Okubo, M.; Yamada, A., Pseudocapacitance of MXene nanosheets for high-power sodium-ion hybrid capacitors. *Nature Communications* **2015,** *6*, 6544.
12. Deysher, G.; Sin, S.; Gogotsi, Y.; Anasori, B., Oxidized 2D titanium carbide MXene: Flash oxidized powders. *Materials Today* **2018,** *21* (10), 1064-1065.
13. Yang, Y.; Umrao, S.; Lai, S.; Lee, S., Large-Area Highly Conductive Transparent Two-Dimensional Ti_2CT_x Film. *The Journal of Physical Chemistry Letters* **2017,** *8* (4), 859-865.
14. Du, F.; Tang, H.; Pan, L.; Zhang, T.; Lu, H.; Xiong, J.; Yang, J.; Zhang, C., Environmental Friendly Scalable Production of Colloidal 2D Titanium Carbonitride

MXene with Minimized Nanosheets Restacking for Excellent Cycle Life Lithium-Ion Batteries. *Electrochimica Acta* **2017,** *235*, 690-699.
15. Anasori, B.; Lukatskaya, M. R.; Gogotsi, Y., 2D metal carbides and nitrides (MXenes) for energy storage. *Nature Reviews Materials* **2017,** *2*, 16098.
16. Anasori, B.; Xie, Y.; Beidaghi, M.; Lu, J.; Hosler, B. C.; Hultman, L.; Kent, P. R. C.; Gogotsi, Y.; Barsoum, M. W., Two-Dimensional, Ordered, Double Transition Metals Carbides (MXenes). *ACS Nano* **2015,** *9* (10), 9507-9516.
17. Zou, R.; Quan, H.; Pan, M.; Zhou, S.; Chen, D.; Luo, X., Self-assembled MXene($Ti_3C_2T_x$)/α-Fe_2O_3 nanocomposite as negative electrode material for supercapacitors. *Electrochimica Acta* **2018,** *292*, 31-38.
18. Jiang, H.; Wang, Z.; Yang, Q.; Hanif, M.; Wang, Z.; Dong, L.; Dong, M., A novel MnO_2/$Ti_3C_2T_x$ MXene nanocomposite as high performance electrode materials for flexible supercapacitors. *Electrochimica Acta* **2018,** *290*, 695-703.
19. Jin, X.; Shin, S.-J.; Kim, N.; Kang, B.; Piao, H.; Choy, J.-H.; Kim, H.; Hwang, S.-J., Superior role of MXene nanosheet as hybridization matrix over graphene in enhancing interfacial electronic coupling and functionalities of metal oxide. *Nano Energy* **2018,** *53*, 841-848.
20. Gao, X.-T.; Xie, Y.; Zhu, X.-D.; Sun, K.-N.; Xie, X.-M.; Liu, Y.-T.; Yu, J.-Y.; Ding, B., Ultrathin MXene Nanosheets Decorated with TiO_2 Quantum Dots as an Efficient Sulfur Host toward Fast and Stable Li–S Batteries. *Small* **2018,** *14* (41), 1802443.
21. Gao, Y.; Wang, L.; Li, Z.; Zhou, A.; Hu, Q.; Cao, X., Preparation of MXene-Cu_2O nanocomposite and effect on thermal decomposition of ammonium perchlorate. *Solid State Sciences* **2014,** *35*, 62-65.
22. Zhu, J.; Ha, E.; Zhao, G.; Zhou, Y.; Huang, D.; Yue, G.; Hu, L.; Sun, N.; Wang, Y.; Lee, L. Y. S.; Xu, C.; Wong, K.-Y.; Astruc, D.; Zhao, P., Recent advance in MXenes: A promising 2D material for catalysis, sensor and chemical adsorption. *Coordination Chemistry Reviews* **2017,** *352*, 306-327.
23. Lorencova, L.; Bertok, T.; Filip, J.; Jerigova, M.; Velic, D.; Kasak, P.; Mahmoud, K. A.; Tkac, J., Highly stable $Ti_3C_2T_x$ (MXene)/Pt nanoparticles-modified glassy carbon electrode for H_2O_2 and small molecules sensing applications. *Sensors and Actuators B: Chemical* **2018,** *263*, 360-368.
24. Ghidiu, M.; Kota, S.; Halim, J.; Sherwood, A. W.; Nedfors, N.; Rosen, J.; Mochalin, V. N.; Barsoum, M. W., Alkylammonium Cation Intercalation into Ti_3C_2 (MXene): Effects on Properties and Ion-Exchange Capacity Estimation. *Chemistry of Materials* **2017,** *29* (3), 1099-1106.
25. Lorencova, L.; Bertok, T.; Dosekova, E.; Holazova, A.; Paprckova, D.; Vikartovska, A.; Sasinkova, V.; Filip, J.; Kasak, P.; Jerigova, M.; Velic, D.; Mahmoud, K. A.; Tkac, J., Electrochemical performance of $Ti_3C_2T_x$ MXene in aqueous media: towards ultrasensitive H_2O_2 sensing. *Electrochimica Acta* **2017,** *235*, 471-479.
26. Liu, H.; Duan, C.; Yang, C.; Shen, W.; Wang, F.; Zhu, Zhenfeng, A novel nitrite biosensor based on the direct electrochemistry of hemoglobin immobilized on MXene-Ti_3C_2. *Sencer and Actuators B: Chemistry* **2015,** *218*, 60-66.
27. Rakhi, R. B.; Nayak, P.; Xia, C.; Alshareef, H. N., Novel amperometric glucose biosensor based on MXene nanocomposite. *Scientific Reports* **2016,** *6*, 36422.
28. Fan, Y.; Yuan, Z.; Zou, G.; Zhang, Q.; Liu, B.; Peng, Q., Two-dimensional MXene/A-TiO_2 composite with unprecedented catalytic activation for sodium alanate. *Catalysis*

Today **2018,** *318*, 167-174.
29. Ahmed, B.; Anjum, D. H.; Hedhili, M. N.; Gogotsi, Y.; Alshareef, H. N., H2O2 assisted room temperature oxidation of Ti2C MXene for Li-ion battery anodes. *Nanoscale* **2016,** *8* (14), 7580-7587.
30. Low, J.; Zhang, L.; Tong, T.; Shen, B.; Yu, J., TiO_2/MXene Ti_3C_2 composite with excellent photocatalytic CO_2 reduction activity. *Journal of Catalysis* **2018,** *361*, 255-266.
31. Naguib, M.; Mashtalir, O.; Lukatskaya, M. R.; Dyatkin, B.; Zhang, C.; Presser, V.; Gogotsi, Y.; Barsoum, M. W., One-step synthesis of nanocrystalline transition metal oxides on thin sheets of disordered graphitic carbon by oxidation of MXenes. *Chemical Communications* **2014,** *50* (56), 7420-7423.
32. Yasmin, L.; Chen, X.; Stubbs, K. A.; Raston, C. L., Optimising a vortex fluidic device for controlling chemical reactivity and selectivity. *Scientific reports* **2013,** *3*, 2282.
33. Britton, J.; Stubbs, K. A.; Weiss, G. A.; Raston, C. L., Vortex fluidic chemical transformations. *Chemistry–A European Journal* **2017,** *23* (54), 13270-13278.
34. Mohammed Al-antaki, A. H.; Luo, X.; Duan, A.; Lamb, R. N.; Eroglu, E.; Hutchison, W.; Zou, Y.-C.; Zou, J.; Raston, C. L., Continuous flow synthesis of phosphate binding h-BN@magnetite hybrid material. *RSC Advances* **2018,** *8* (71), 40829-40835.
35. Luo, X.; Al-Antaki, A. H. M.; Vimalanathan, K.; Moffatt, J.; Zheng, K.; Zou, Y.; Zou, J.; Duan, X.; Lamb, R. N.; Wang, S.; Li, Q.; Zhang, W.; Raston, C. L., Laser irradiated vortex fluidic mediated synthesis of luminescent carbon nanodots under continuous flow. *Reaction Chemistry & Engineering* **2018,** *3* (2), 164-170.
36. Phillips, J. M.; Ahamed, M.; Duan, X.; Lamb, R. N.; Qu, X.; Zheng, K.; Zou, J.; Chalker, J. M.; Raston, C. L., Chemoselective and Continuous Flow Hydrogenations in Thin Films Using a Palladium Nanoparticle Catalyst Embedded in Cellulose Paper. *ACS Applied Bio Materials* **2019,** *2* (1), 488-494.
37. Gandy, M. N.; Raston, C. L.; Stubbs, K. A., Towards aryl C-N bond formation in dynamic thin films. *Organic and Biomolecular Chemistry* **2014,** *12* (26), 4594-4597.
38. Pye, S. J.; Dalgarno, S. J.; Chalker, J. M.; Raston, C. L., Organic oxidations promoted in vortex driven thin films under continuous flow. *Green Chemistry* **2018,** *20* (1), 118-124.
39. Alsulami, I.; Alharbi, T.; Harvey, D.; Gibson, C. T.; Raston, C. L., Controlling the growth of fullerene C_{60} cones under continuous flow. *Chemical Communications* **2018**, 54 (57), 7896-7899.
40. Vimalanathan, K.; Gascooke, J. R.; Suarez-Martinez, I.; Marks, N. A.; Kumari, H.; Garvey, C. J.; Atwood, J. L.; Lawrance, W. D.; Raston, C. L., Fluid dynamic lateral slicing of high tensile strength carbon nanotubes. *Scientific reports* **2016,** 6, 22865.
41. Chen, X.; Dobson, J. F.; Raston, C. L., Vortex fluidic exfoliation of graphite and boron nitride. *Chemical Communications* **2012,** *48* (31), 3703-3705.
42. Al-Antaki, A. H. M.; Luo, X.; Alharbi, T. M. D.; Harvey, D. P.; Pye, S.; Zou, J.; Lawrance, W.; Raston, C. L., Inverted vortex fluidic exfoliation and scrolling of hexagonal-boron nitride. *RSC Advances* **2019,** *9* (38), 22074-22079.
43. Vimalanathan, K.; Suarez-Martinez, I.; Peiris, M. C. R.; Antonio, J.; de Tomas, C.; Zou, Y.; Zou, J.; Duan, X.; Lamb, R. N.; Harvey, D. P.; Alharbi, T. M. D.; Gibson, C. T.; Marks, N. A.; Darwish, N.; Raston, C. L., Vortex fluidic mediated transformation of graphite into highly conducting graphene scrolls. *Nanoscale Advances* **2019,** *1* (7),

2495-2501.
44. Alharbi, T. M. D.; Vimalanathan, K.; Alsulami, I. K.; Raston, C. L., Vertically aligned laser sliced MWCNTs. *Nanoscale* **2019**.
45. Alharbi, T. M. D.; Vimalanathan, K.; Lawrance, W. D.; Raston, C. L., Controlled slicing of single walled carbon nanotubes under continuous flow. *Carbon* **2018,** *140*, 428-432.
46. Luo, X.; Smith, P.; Raston, C. L.; Zhang, W., Vortex Fluidic Device-Intensified Aqueous Two Phase Extraction of C-Phycocyanin from Spirulina maxima. *ACS Sustainable Chemistry & Engineering* **2016,** *4* (7), 3905-3911.
47. Britton, J.; Chalker, J. M.; Raston, C. L., Rapid Vortex Fluidics: Continuous Flow Synthesis of Amides and Local Anesthetic Lidocaine. *Chemistry–A European Journal* **2015,** *21* (30), 10660-10665.
48. Yuan, T. Z.; Ormonde, C. F.; Kudlacek, S. T.; Kunche, S.; Smith, J. N.; Brown, W. A.; Pugliese, K. M.; Olsen, T. J.; Iftikhar, M.; Raston, C. L., Shear-Stress-Mediated Refolding of Proteins from Aggregates and Inclusion Bodies. *ChemBioChem* **2015,** *16* (3), 393-396.
49. Alharbi, T. M. D.; Vimalanathan, K.; Lawrance, W. D.; Raston, C. L., Controlled slicing of single walled carbon nanotubes under continuous flow. *Carbon* **2018,** *140*, 428-432.
50. Al-Antaki, A. H. M.; Luo, X.; Duan, X.; Lamb, R. N.; Hutchison, W. D.; Lawrance, W.; Raston, C. L., Continuous Flow Copper Laser Ablation Synthesis of Copper(I and II) Oxide Nanoparticles in Water. *ACS Omega* **2019,** *4* (8), 13577-13584.
51. Alharbi, T. M. D.; Shingaya, Y.; Vimalanathan, K.; Nakayama, T.; Raston, C. L., High Yielding Fabrication of Magnetically Responsive Coiled Single-Walled Carbon Nanotube under Flow. *ACS Applied Nano Materials* **2019,** *2* (8), 5282-5289.
52. Alharbi, Thaar M. D.; Al-Antaki, A. H. M.; Moussa, M.; Hutchison, W. D.; Raston, C. L., Three-step-in-one synthesis of supercapacitor MWCNT superparamagnetic magnetite composite material under flow. *Nanoscale Advances* **2019,** *1* (9), 3761-3770.
53. Luo, X.; Al-Antaki, A. H. M.; Alharbi, T. M. D.; Hutchison, W. D.; Zou, Y.-c.; Zou, J.; Sheehan, A.; Zhang, W.; Raston, C. L., Laser-Ablated Vortex Fluidic-Mediated Synthesis of Superparamagnetic Magnetite Nanoparticles in Water Under Flow. *ACS Omega* **2018,** *3* (9), 11172-11178.
54. Luo, X.; Al-Antaki, A. H. M.; Pye, S.; Meech, R.; Zhang, W.; Raston, C. L., High-Shear-Imparted Tunable Fluorescence in Polyethylenimines. *ChemPhotoChem,* **2018,** *2* (4), 343-348.
55. Vaughn, A.; Ball, J.; Heil, T.; Morgan, D. J.; Lampronti, G. I.; Maršalkaitė, G.; Raston, C. L.; Power, N. P.; Kellici, S., Selective Calixarene-Directed Synthesis of MXene Plates, Crumpled Sheets, Spheres, and Scrolls. *Chemistry A Erupean Journal Communication* **2017,** *23* (34), 8128-8133.
56. Luo, X.; Al-Antaki, A. H. M.; Harvey, D. P.; Ruan, Y.; He, S.; Zhang, W.; Raston, C. L., Vortex Fluidic Mediated Synthesis of Macroporous Bovine Serum Albumin-Based Microspheres. *ACS Applied Materials & Interfaces* **2018,** *10* (32), 27224-27232.
57. Alsulami, I.; Alharbi, T.; Harvey, D.; Gibson, C. T.; Raston, C. L., Controlling the growth of fullerene C_{60} cones under continuous flow. *Chemical Communications* **2018**,*54* **(**57), 7896-7899.
58. Alharbi, T. M. D.; Alghamdi, A. R. M.; Vimalanathan, K.; Raston, C. L., Continuous flow photolytic reduction of graphene oxide. *Chemical Communications* **2019**.

59. Li, X.; Yin, X.; Han, M.; Song, C.; Sun, X.; Xu, H.; Cheng, L.; Zhang, L., A controllable heterogeneous structure and electromagnetic wave absorption properties of Ti_2CT_x MXene. *Journal of Materials Chemistry C* **2017,** *5* (30), 7621-7628.
60. Wang, J.; Dong, S.; Li, H.; Chen, Z.; Jiang, S.; Wu, L.; Zhang, X., Facile synthesis of layered $Li_4Ti_5O_{12}$-$Ti_3C_2T_x$ (MXene) composite for high-performance lithium ion battery. *Journal of Electroanalytical Chemistry* **2018,** *810*, 27-33.
61. Cai, K. J.; Zheng, Y.; Shen, P.; Chen, S. Y., TiCx–Ti2C nanocrystals and epitaxial graphene-based lamellae by pulsed laser ablation of bulk TiC in vacuum. *CrystEngComm* **2014,** *16* (24), 5466-5474.
62. Zhang, J.; Yan, S.; Fu, L.; Wang, F.; Yuan, M.; Luo, G.; Xu, Q.; Wang, X.; Li, C., Photocatalytic Degradation of Rhodamine B on Anatase, Rutile, and Brookite TiO_2. *Chinese Journal of Catalysis* **2011,** *32* (6), 983-991.
63. Xue, Q.; Zhang, H.; Zhu, M.; Pei, Z.; Li, H.; Wang, Z.; Huang, Y.; Huang, Y.; Deng, Q.; Zhou, J.; Du, S.; Huang, Q.; Zhi, C., Photoluminescent Ti_3C_2 MXene Quantum Dots for Multicolor Cellular Imaging. *Advanced Materails* **2017,** *29* (15), 1604847.
64. Shahzad, A.; Rasool, K.; Nawaz, M.; Miran, W.; Jang, J.; Moztahida, M.; Mahmoud, K. A.; Lee, D. S., Heterostructural TiO_2/$Ti_3C_2T_x$ (MXene) for photocatalytic degradation of antiepileptic drug carbamazepine. *Chemical Engineering Journal* **2018,** *349*, 748-755.
65. Liu, Z.; Jian, Z.; Fang, J.; Xu, X.; Zhu, X.; Wu, Sjijop, Low-temperature reverse microemulsion synthesis, characterization, and photocatalytic performance of nanocrystalline titanium dioxide. *Photoenergy* **2012,** *2012*.
66. Alsharaeh, E.; Bora, T.; Soliman, A.; Ahmed, F.; Bharath, G.; Ghoniem, M.; Abu-Salah, K. M.; Dutta, J., Sol-gel-assisted microwave-derived synthesis of anatase Ag/TiO_2/GO nanohybrids toward efficient visible light phenol degradation. *Catalysts* **2017,** *7* (5), 133.
67. Sarycheva, A.; Makaryan, T.; Maleski, K.; Satheeshkumar, E.; Melikyan, A.; Minassian, H.; Yoshimura, M.; Gogotsi, Y., Two-Dimensional Titanium Carbide (MXene) as Surface-Enhanced Raman Scattering Substrate. *The Journal of Physical Chemistry C* **2017,** *121* (36), 19983-19988.
68. Liu, G.; Yang, H. G.; Wang, X.; Cheng, L.; Pan, J.; Lu, G. Q.; Cheng, H.-M., Visible Light Responsive Nitrogen Doped Anatase TiO_2 Sheets with Dominant Facets Derived from TiN. *Journal of the American Chemical Society* **2009,** *131* (36), 12868-12869.
69. Wang, H.; Peng, R.; Hood, Z. D.; Naguib, M.; Adhikari, S. P.; Wu, Z., Titania Composites with 2 D Transition Metal Carbides as Photocatalysts for Hydrogen Production under Visible-Light Irradiation. *ChemSusChem* **2016,** *9* (12), 1490-1497.
70. Naguib, M.; Mochalin, V. N.; Barsoum, M. W.; Gogotsi, Y., 25th Anniversary Article: MXenes: A New Family of Two-Dimensional Materials. *Advanced Materials* **2014,** *26* (7), 992-1005.
71. Naguib, M.; Mashtalir, O.; Carle, J.; Presser, V.; Lu, J.; Hultman, L.; Gogotsi, Y.; Barsoum, M. W., Two-Dimensional Transition Metal Carbides. *ACS Nano* **2012,** *6* (2), 1322-1331.
72. Ignaszak, A.; Song, C.; Zhu, W.; Zhang, J.; Bauer, A.; Baker, R.; Neburchilov, V.; Ye, S.; Campbell, S., Titanium carbide and its core-shelled derivative TiC@TiO_2 as catalyst supports for proton exchange membrane fuel cells. *Electrochimica Acta* **2012,** *69*, 397-405.

73. Wang, J.; Polleux, J.; Lim, J.; Dunn, B., Pseudocapacitive Contributions to Electrochemical Energy Storage in TiO_2 (Anatase) Nanoparticles. *The Journal of Physical Chemistry C* **2007,** *111* (40), 14925-14931.
74. Halim, J.; Cook, K. M.; Naguib, M.; Eklund, P.; Gogotsi, Y.; Rosen, J.; Barsoum, M. W., X-ray photoelectron spectroscopy of select multi-layered transition metal carbides (MXenes). *Applied Surface Science* **2016,** *362*, 406-417.
75. D. Zuo, S. Song, C. An, L. Tang, Z. He, J. Zheng, *Nano Energy* **2019**, *62*, 401-409.

ACES Asian Chemical Editorial Society
DOI: 10.1002/cnma.201900779
CHEMNANOMAT
Full Paper

Vortex Fluidic Mediated Synthesis of TiO_2 Nanoparticle/MXene Composites

Ahmed Hussein Mohammed Al-antaki,[a, b] Thaar M. D. Alharbi,[a] Suela Kellici,[c] Nicholas P. Power,[d] Warren Lawrance,[e] and Colin L. Raston*[a]

Abstract: Oxidation of MXene in a vortex fluidic device (VFD) operating under continuous flow results in exfoliation and fragmentation into nanoparticles of surface oxidised 2D material with further oxidation of the nanoparticles into anatase (TiO_2). These MXene and anatase nanoparticles co-assemble into stable micron sized spheres which are topologically smooth, decorating the surface of exfoliated MXene. The formation of this composite material in the dynamic thin film in the VFD was optimised by systematically exploring the operating parameters of the microfluidic platform, determined at 45° tilt angle for the 20 mm diameter glass tube spinning at 5k rpm, with a flow rate of a colloidal dispersion of MXene in aqueous H_2O_2 (30%) at 0.75 mL/min at a concentration of MXene of 0.5 mg/mL.

Introduction

The first report describing the new and unique class of 2D MXene materials was in 2011.[1] They are based on transition metal carbides, carbonitrides and nitrides, and have potential in a number of applications, including in biological,[2–5] batteries,[6–8] electronic devices[9–10] and supercapacitors.[10–11] The unit formula of these materials is $M_{n+1}X_nT_x$ in which M is an early transition metal, including Sc, Ti, Cr, Zr, Nb, Mn, Mo, Hf, V, Ta, or W, X represents either carbon and/or nitrogen, and n is 1, 2, or 3 in defining the number of M layers. T_x represents surface functional groups - O, - OH, - F bound to the transition metals.[12–13] More than twenty types of MXenes have been developed, including Ti_2CT_x, $Ti_3C_2T_x$, V_2CT_x, Nb_2CT_x, Mo_2CT_x and Ti_3CNT_x.[14] Some of them contain two different transition metals, for example in $Mo_2TiC_2T_x$.[15–16] There is growing interest in nanocomposite materials involving MXenes, for example MXene ($Ti_3C_2T_x$)/α-Fe_2O_3 for use as a negative electrode material for supercapacitors,[17] MXene ($Ti_3C_2T_x$)/MnO_2 for high performance electrode materials for flexible supercapacitors,[18] and Ti_3C_2-MnO_2 for enhancing interfacial electronic coupling.[19] In addition, MXenes decorated with TiO_2 quantum dots (QDs) feature in Li- S batteries,[20] MXene-Cu_2O catalyses the thermal decomposition of ammonium perchlorate,[21] MXene-enzyme feature in electrochemical biosensors,[22] MXenes-CNTs improve electrochemical performance,[8] and MXene-Pt nanoparticles have sensing application[23] with others for determining ion exchange capacity.[24] More specifically, TiO_2 nanoparticle (NP)/MXene composites feature in rendering MXene biocompatible for enzyme attachment,[22] enhancing the efficiency of MXene modified glassy carbon electrodes for H_2O_2 reduction,[25] nitrite detection,[26] low detection limits of glucose[27] and sodium alanate,[28] Li-ion battery anodes[29] and photocatalysis.[30] Thermal methods have been used to oxidize MXene to TiO_2 or TiO_2NPs/MXene.[28,30–31] with H_2O_2 also effective in preparing the same material.[29] Herein we report the oxidation of MXene (Ti_3C) in 30% H_2O_2 in gaining access to TiO_2NPs/MXene composite materials, which encompasses exfoliation with surface oxidation, fragmentation of the 2D material, and oxidation of the fragmented material, using a vortex fluidic device (VFD). The VFD is a thin film microfluidic platform which has two types of processing, the confined mode where a glass tube, usually inclined at 45° relative to the horizontal position, is spun at high speed.[32] This is a proven approach for then translating any reaction into a continuous flow process, which is the other mode of operation of the VFD, Figure 1.[33] The VFD is a versatile thin film device effective for a growing number of applications, including *in situ* decorating *h*-BN with magnetite nanoparticles,[34] fabricating carbon dots from multi-walled carbon nanotubes,[35] chemo selective hydrogenation using

[a] A. H. M. Al-antaki, T. M. D. Alharbi, Prof. C. L. Raston
Flinders Institute for Nanoscale Science and Technology
College of Science and Engineering
Flinders University
Adelaide, SA 5042 (Australia)
E-mail: alan0192@flinders.edu.au
alha0190@flinders.edu.au
Colin.raston@flinders.edu.au
[b] A. H. M. Al-antaki
Department of Chemistry
Faculty of Sciences
Kufa University
Kufa, Najaf (Iraq)
E-mail: Ahmed.alantaki@uokufa.edu.iq
[c] Dr. S. Kellici
School of Engineering
London South Bank University
103 Borough Road, London, SE1 0AA (UK)
E-mail: kellicis@lsbu.ac.uk
[d] Dr. N. P. Power
School of Life, Health & Chemical Sciences
The Open University
Walton Hall, Milton Keynes, MK7 6AA (UK)
E-mail: nicholas.power@open.ac.uk
[e] Prof. W. Lawrance
College of Science and Engineering
Flinders University
Adelaide, SA 5042 (Australia)
E-mail: warren.lawrance@flinders.edu.au
Supporting information for this article is available on the WWW under https://doi-org.ezproxy.flinders.edu.au/10.1002/cnma.201900779

4.Inverted vortex fluidic exfoliation and scrolling of hexagonal-boron nitride

Ahmed Hussein Mohammed Al-antaki [a, b], Xuan Luo [a], Thaar M.D. Alharbi [a], David P. Harvey [a], Scott Pye [a], Jin Zou [c], Warren D. Lawrance [d], Colin L. Raston [a, *]

a. *Flinders Institute for Nanoscale Science and Technology, College of Science and Engineering, Flinders University, Adelaide, SA 5042, Australia.*
b. *Department of Chemistry, Faculty of Sciences, Kufa University, Kufa, Najaf, Iraq.*
c. *Materials Engineering, Centre for Microscopy and Microanalysis, The University of Queensland, Brisbane, QLD 4072, Australia.*
d. *College of Science and Engineering, Flinders University, Adelaide, SA 5042.*

Author contributions: **AA** performed all the VFD and all characterisation experiments; wrote all the primary content. **XL** performed Raman spectra. **TA** performed TEM images. **DH** performed TGA analysis. **SP** performed the design of *h*-BN sheet and scrolls via software. **JZ** preformed TEM images. **WL** and **CR** supervised and coordinated the project and helped on the research directions and plan, and the final revision of the manuscript. All of the co-authors assisted with the revision of the manuscript before and during the publication process.

Graphical Abstract

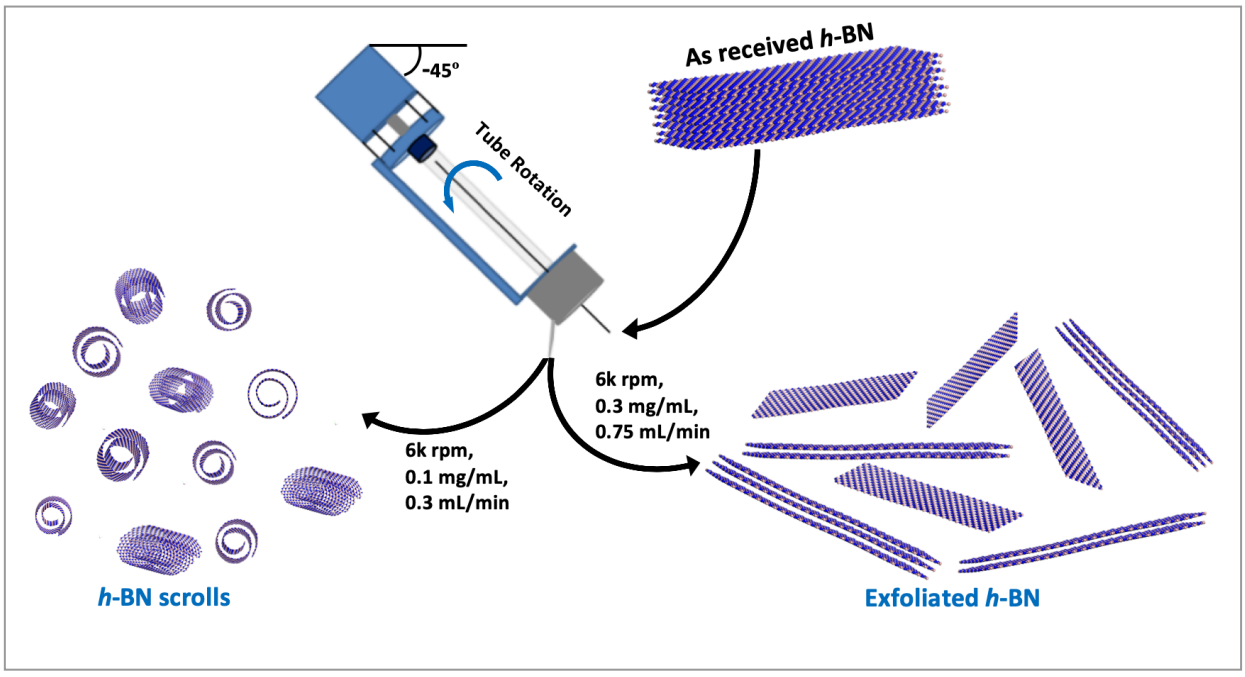

4.1 Abstract

Exfoliation or scrolling of hexagonal boron nitride (*h*-BN) occurs in a vortex fluidic device (VFD) operating under continuous flow, with a tilt angle of -45º relative to the horizontal position. This new VFD processing strategy is effective in avoiding the build-up of material that occurs when the device is operated using the conventional tilt angle of +45º, where the *h*-BN precursor and scrolls are centrifugally held against the wall of the tube. At a tilt angle of -45º the downward flow aided by gravity facilitates material exiting the tube with the exfoliation of *h*-BN and formation of *h*-BN scrolls then optimized by systematically varying the other VFD operating parameters, including flow rate and rotational speed, along with concentration of *h*-BN and the choice of solvent. Water was the most effective solvent, which enhances the green chemistry metrics of the processing.

4.2 Introduction

Polymorphs of boron nitride include the hexagonal arrangement of alternating boron and nitrogen atoms in 2D sheets, with the atoms sp^2 hybridized, comparable to that of graphite. However, in contrast to graphite, layered hexagonal boron nitride (*h*-BN) is transparent and it is an insulator,[1] but nevertheless it has attracted considerable attention. Other polymorphs of *h*-BN do not strictly match polymorphs of carbon, for example, as in the boron nitride analogues of fullerenes, known as fulborenites.[2,3] The main polymorphs of boron nitride are rhombohedral BN (*r*-BN), cubic BN (*c*-BN), wurtzite BN (*w*-BN) and hexagonal BN (*h*-BN), with the latter 2D material featuring in the present study. None of the polymorphs of BN have been found in nature.[4]

In general, hexagonal carbon (*h*-C), possessing hexagonal six membered rings, as in graphite, graphene or carbon nanotubes, can be metallic or semiconducting depending on the dimensions and overall structure. However, *h*-BN is an insulator or indirect semiconductor, having a large band gap around 5.9 eV.[5] Defects in *h*-BN can perturb the band gap[5] with single crystals of *h*-BN flakes used to study band gap properties.[5,6] The availability of high-quality *h*-BN flakes is important for developing applications in far-ultraviolet (FUV) light-emitting diodes (LEDs).[7] In addition, *h*-BN has potential in optoelectronic applications, for use in high-performance electronic devices. Electron energy loss spectroscopy (EELS) on the ionization edge between two-layers of BN is effective in determining the number of layers of one atom thick *h*-BN.[8] *h*-BN can also be coerced into forming scrolls which are essentially individual sheets of *h*-BN rolled up at the van der Waals limit.[9-11] Contemporary studies have

established the ability to make the analogous graphene and graphene oxide scrolls.[11-16] *h*-BN scrolls have a number of potential applications, as platforms for the delivery of composites and nucleobases,[17-20] for example, which rely on coordination interactions between N or O with the empty orbital of boron.[20] In addition, *h*-BN scrolls have potential use in gas storage, including hydrogen and methane.[21-23] *h*-BN scrolls should be easier to produce than graphene scrolls[17,18,24,25] with the interaction between successive turns in the scrolls more favoured by the difference in electronegativity between B and N atoms. We have prepared *h*-BN scrolls from *h*-BN dispersed in N-Methyl-2-pyrrolidone (NMP) using a spinning disc processor (SDP) where liquids are subjected to high shear. The choice of NMP solvent here was based on it having a similar surface tension relative to *h*-BN.[11] However, the yield was only 5%, and this required 20 h of recycling a colloidal suspension of *h*-BN onto a 10 cm diameter rotating disc in the SDP. The SDP was the forerunner to the development of the vortex fluidic device (VFD), which is more practical for research purposes, while also addressing scalability of the processing, and is significantly cheaper.[26]

We have explored using the VFD to form *h*-BN scrolls from *h*-BN in water under continuous flow mode of operation in the device, establishing *ca* 10% yield conversion for a single pass through the microfluidic platform. For this, and also for simple exfoliation (no scroll formation) we used commercially available *h*-BN comprised of multiple layers. Effective processing of *h*-BN required reconfiguring the typical continuous flow mode of operation of the VFD, to overcome any build-up of material on the walls of the rapidly rotating tube during the processing. Typically, the VFD operates at a tilt angle of +45º, with the liquid whirling up and out of the

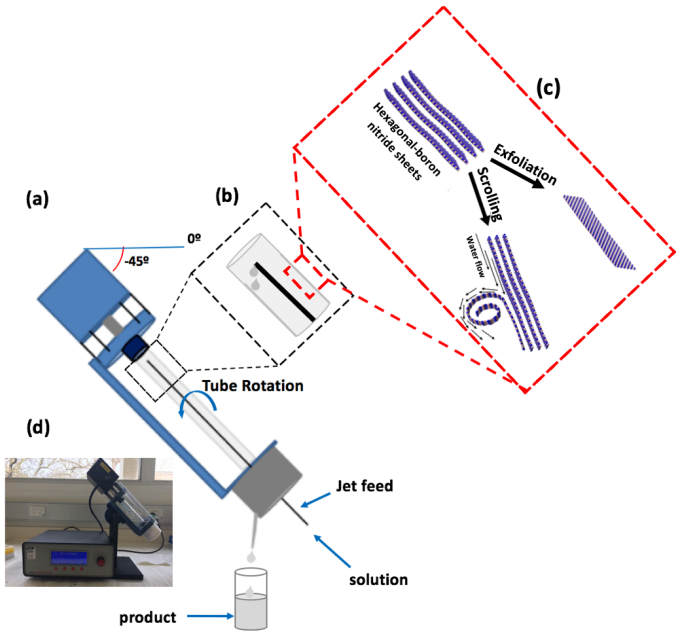

Figure 4.1. (a) Diagram of the vortex fluidic device (VFD), where the glass tube is spun at 6k rpm, at a tilt angle of -45º using a flow rate of 0.3 mL/min, for generating *h*-BN scrolls (0.1 mg/mL of *h*-BN dispersed in water) or at a flow rate of 0.75 mL/min for exfoliating *h*-BN (0.3 mg/mL of *h*-BN dispersed in water). (b) Zoomed in cartoon showing delivery of the liquid inside the rapidly rotating tube. (c) Illustration of the exfoliation of *h*-BN into scrolls or exfoliation of *h*-BN during VFD processing. (d) Photograph of a VFD.

tube, and this is the optimum angle for a plethora of applications of the device.[12,27] When the tube is now spun in an inverted continuous flow mode, at a tilt angle of -45º relative to the horizontal position, the yield of scrolls and exfoliated *h*-BN increases, with dramatically reduced processing times. Moreover, the processing is effective in water, as a benign solvent, in place of NMP which was used in the SDP for exfoliation the 2D material. A suspension of *h*-BN in water was delivered into the VFD using an in house built magnetically stirred syringe, Figure 4.2.[28,29]

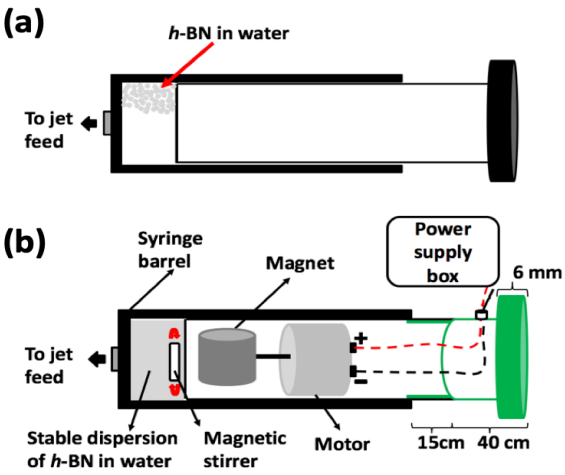

Figure 4.2. (a) Normal syringe. (b) Magnetically stirred syringe driven by a motor inside the plunger.

A detailed understanding of the mechanism of graphene scroll formation from graphite in an SDP has been developed,[11] and it may be applicable to the formation of *h*-BN scrolls in a VFD. The formation of graphene scrolls is driven by the energetically favoured intra-layer stacking once an edge of a graphene sheet is lifted up and curled to strike its own upper surface.[11] Both the SDP and VFD are microfluidic platforms, generating dynamic thin films, the thickness of which depends on the rotational speeds of the disc or tube respectively, along with other factors. The VFD is a more versatile platform and can be operated at different tilt angles, which is usually not the case for the SDP.[26] In addition, the VFD can operate under continuous flow as well as under the confined mode, where a finite volume of liquid is placed in the rapidly rotating tube. The shear stress here is sufficient to exfoliate graphene from graphite, and also single *h*-BN sheets from *h*-BN flakes, albeit in low yield, and without forming scrolls.[30] The research here used a 10 mm O.D. glass tube inclined at +45º, operating under confined mode, using NMP as the solvent.[30] Indeed, this was reported in the first paper on the VFD, and since then there have been a number of applications, including slicing carbon-nanotubes.[31,32] In the present study the exfoliation of *h*-BN has been dramatically increased, now under continuous flow, achieving *ca* 22% yield for a single pass through the microfluidic platform, using only water as the solvent. The VFD of choice housed a borosilicate glass tube (O.D. diameter 20 mm, I.D. diameter 17.5 mm, 19.5 cm long), open at one

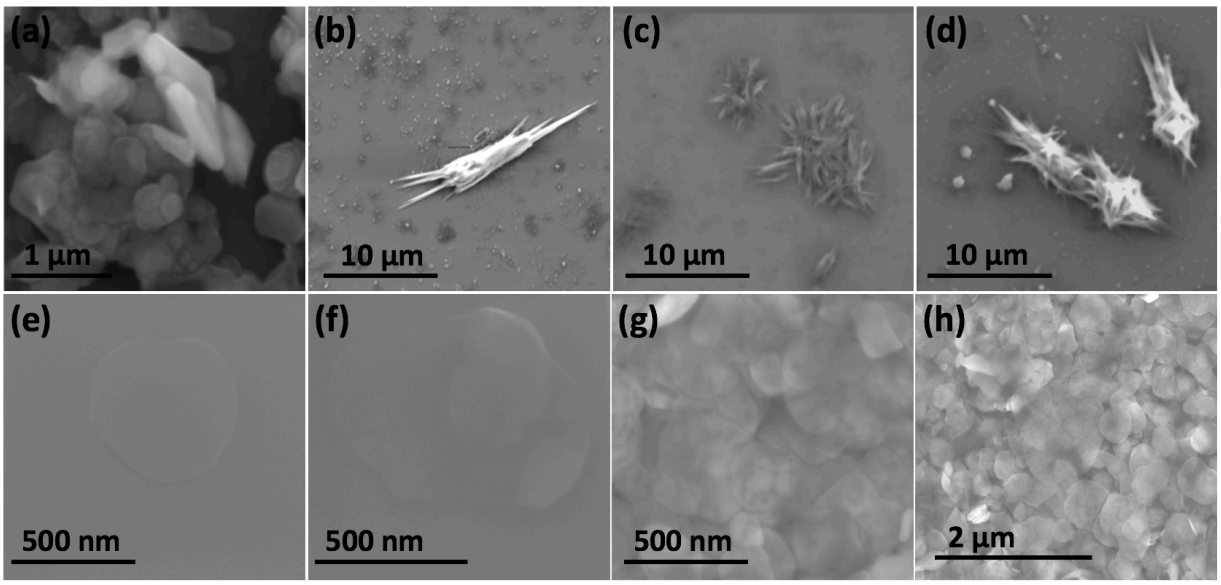

Figure 4.3. SEM images: (a) As received *h*-BN. (b-d) *h*-BN scrolls formed at a flow rate of 0.3 mL/min, concentration of 0.1 mg/mL and (e-h) exfoliated *h*-BN formed at a flow rate of 0.75 mL/min, concentration of 0.3 mg/mL. All samples were centrifuged at 1180 x g post VFD processing (rotational speed 6k rpm, tilt angle -45º) with the supernatant drop cast onto silicon wafers.

end, which was rotated at high speed (between 0 - 9k rpm) and orientated down to -45º tilt angle relative to the horizontal position, Figure 4.1.[30,31,33,34] Herein we report both the use of the VFD to primarily exfoliate *h*-BN with a small amount of *h*-BN scrolls or *vice versa*, depending on the operating parameters of the device which were systematically explored, along with concentration of the material and the choice of solvent.

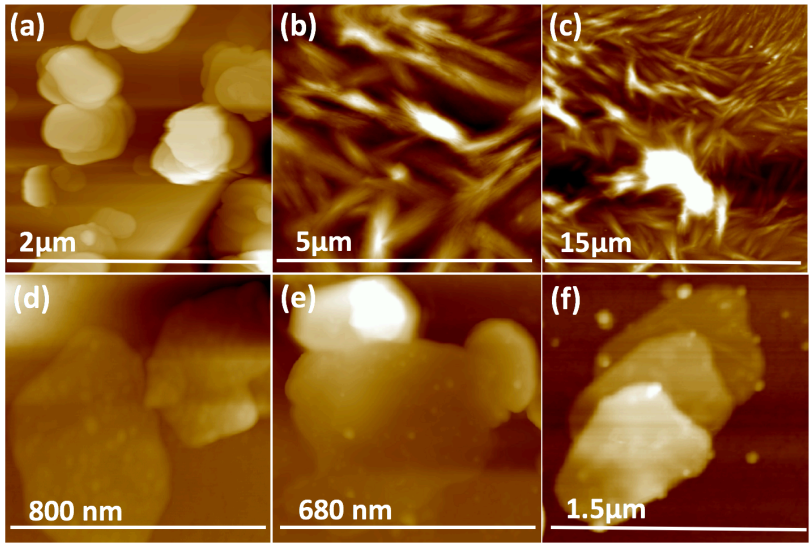

Figure 4.4. AFM images: (a) As received *h*-BN. (b, c) h-BN scrolls prepared at a flow rate of 0.3 mL/min, concentration 0.1 mg/mL, and (d-f) exfoliated *h*-BN prepared at a flow rate of 0.75 mL/min, and concentration 0.3 mg/min. All samples were centrifuged at 1180 x g post VFD processing (rotational speed 6k rpm, tilt angle -45º) with the supernatant drop-cast onto silicon wafers.

4.3 Experiments

4.3.1. Materials. Hexagonal boron nitride (*h*-BN) powder flakes ≈ 1 µm in diameter were obtained from Sigma Aldrich and were dispersed in Milli-Q water for all experiments.

4.3.2 Delivery of a suspension of *h*-BN into the VFD. A suspension of *h*-BN in Milli-Q water was delivered at a controlled flow rate as close as possible to the hemi-spherical base of the rapidly rotating tube. This was achieved using an in house developed syringe with a motor housed in the plunger, for magnetically stirring the solution during delivery into the VFD tube, as illustrated in Figure 4.2.[28,29]

4.3.3 Fabrication of *h*-BN scrolls. Prior to continuous flow processing, the *h*-BN was dispersed in Milli-Q water using sonication (10 mins, 6 kHz). The solution was then transferred to the magnetically stirred syringe and a rapidly stirred dispersion of *h*-BN in water (0.1 mg/mL) was delivered via a jet feed to the base of the rotating glass tube in the VFD. The tube was inclined at -45º and spun at a pre-determined speed, of which 6k rpm was found to be optimal. The flow rate was varied and 0.3 mL/min was found to be optimal.

4.3.4 Exfoliation of *h*-BN. In the same way, *h*-BN dispersed in water (0.3 mg/mL) was delivered via a jet feed to the base of the rotating glass tube in the VFD. The tube was tilted at -45º and spun at a pre-determined speed, of which 6k rpm was found to be optimal. The flow rate was varied and 0.75 mL/min was found to be optimal.

4.3.5 Characterisation. The *h*-BN scrolls and exfoliated *h*-BN were characterized using scanning electron microscopy (SEM-Inspect FEI F50 SEM), atomic force microscopy (AFM - Nanoscope 8.10 tapping mode), Raman spectroscopy (WiTec Alpha 300R λ_{exc}=532 nm), XRD (Bruker D8 ADVANCE ECO, Co- Kα, λ=1.7889 Å), ATR-FTIR Perkin Elmer Frontier,

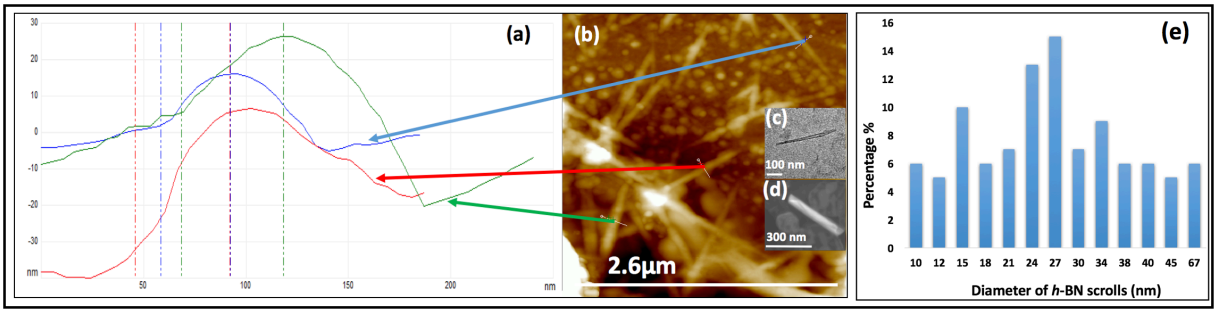

Figure 4.5. (a) AFM height of three representative *h*-BN scrolls. (b) AFM image of drop cast scrolls, for the supernatant and the work up summarized in Figure 4. (c) TEM image for a *h*-BN scroll after drop cast onto a grid. (d) SEM images of a *h*-BN scroll after drop cast on a silicon wafer. (e) Count of *h*-BN scrolls with different diameters (from AFM images).

transmission electron microscopy (TEM) (FEI Tecnai F20 operated at 200 kV) and simultaneous thermal analysis (PerkinElmer STA 8000).

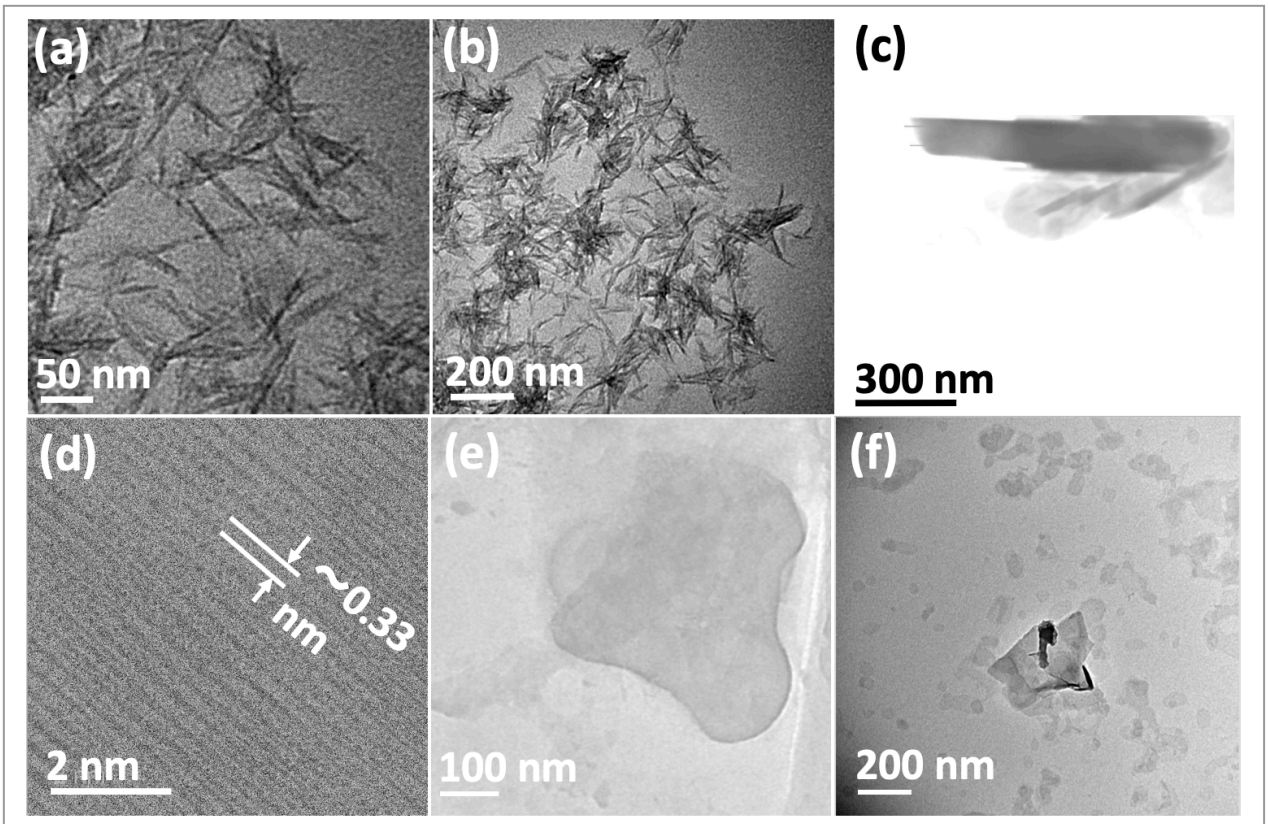

Figure 4.6. TEM images for drop cast material on a grid, prepared in the VFD (rotational speed 6k rpm, tilt angle -45º), (a-c) *h*-BN scrolls prepared at a flow rate of 0.3 mL/min, concentration 0.1 mg/mL. (d) HRTEM image for *h*-BN scrolls. (e-f) Exfoliated *h*-BN prepared at a flow rate of 0.75 mL/min, concentration 0.3 mg/mL.

4.4 Results and Discussion

The VFD is a flexible thin film processing platform, with a number of operating parameters (rotational speed, tilt angle (θ) and flow rate) to be systematically explored, along with the choice of solvent and concentration, as in the present case for exfoliating and scrolling *h*-BN. VFD processing usually explores tilt angles between 0º to 90º, with +45º typically giving the optimal outcome.[35] However, in the present study this angle resulted in material adhering to the wall of the glass tube, with a small amount exiting in the liquid at the top of the tube, as *h*-BN scrolls and exfoliated *h*-BN, *ca*. 1% yield. We hypothesised that centrifugal force was holding the material against the wall of the tube, and that by inverting the tilt angle (< 0º), gravitational pull in the direction of the flow of the liquid would facilitate the material exiting the tube. To this end we explored the effect of 45º, 20º, 0º, -20º and -45º tilt angles, Table S4.1. Interestingly even at the higher speeds where there is greater centrifugal force

in the tube, -45º tilt angle was effective in circumventing the build-up of material in the tube, Figure S4.5. Indeed, at -45º tilt angle there was a dramatic increase in yield of the scrolls and exfoliated material. Interesting the residence time of liquid in the tube at -45º was shorter (>2 mins) than +45º for the same rotation speeds and flow rates, as expected from the gravitational pull down the tube.

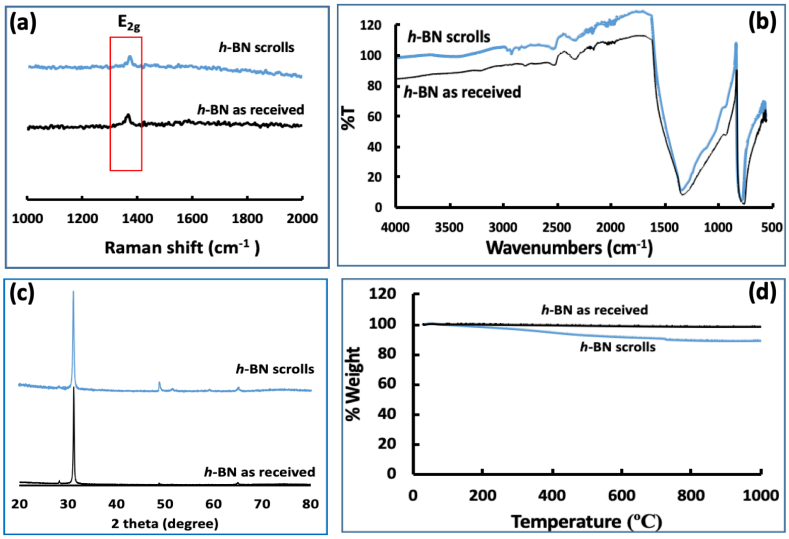

Figure 4.7. (a) Raman spectra, (b) powder XRD, (c) ATR-FTIR spectra, and (d) TGA for *h*-BN as received and *h*-BN scrolls prepared using the optimised VFD protocol (rotation speed 6k rpm, tilt angle -45º, flow rate 0.3 mL/min and concentration 0.1 mg/mL).

The processing was then optimised by systematically varying the other control parameters, at a -45º tilt angle. This involved the use of water as a solvent, with other solvents, namely NMP, IPA, DMF and toluene, affording little or no *h*-BN scrolls and exfoliated *h*-BN. The same was also found for using combinations of solvents, at a 1:1 ratio, including NMP with water, DMF with toluene, water with toluene, and IPA with water. Accordingly, water was deemed to be the optimal solvent for subsequent experiments, for then varying the rotation speed of the glass tube in the VFD, flow rate, and concentration of *h*-BN. We found that 6k rpm gave the highest conversion of *h*-BN into scrolls (ca 10%), and rotational speeds of 4k rpm, 5k rpm, 7k rpm and 8k rpm gave low

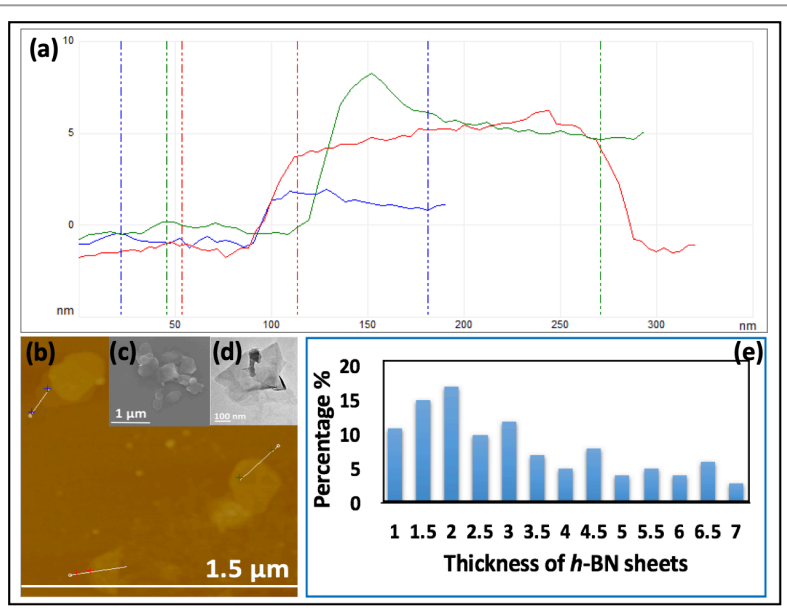

Figure 4.8. (a) AFM height of three exfoliated *h*-BN sheets. (b) AFM image of drop cast exfoliated *h*-BN. (c) SEM images of exfoliated *h*-BN after drop cast on a silicon wafer (c) TEM image of exfoliated *h*-BN after drop cast on a grid. (e) Count of *h*-BN sheets of different thickness from the AFM images, after VFD processing.

yields of the scrolls. A flow rate of 0.3 mL/min was then determined as optimal relative to flow rates of 0.1 mL/min, 0.5 mL/min, 0.7 mL/min and 1 mL/min. These parameters were then set, for then varying the remaining two parameters. Other concentrations of *h*-BN in water were also investigated for all of the flow rates, at 0.1 mg/mL, 0.2 mg/mL, 0.3 mg/mL, 0.5 mg/mL, 0.7 mg/mL and 1.0 mg/mL. Of these, 0.1 mg/mL gave the optimal yield of *h*-BN scrolls as 10% with some exfoliation (flow rate of 0.3 mL/min), with other concentrations resulting in lower yields across all the flow rates. Thus, the overall optimum operating parameters for generating scrolls in a single pass in the VFD are a concentration of 0.1 mg/mL, 0.3 mL/min flow rate and 6k rpm rotational speed, using water as the solvent.

Using the same strategy, we optimised the conditions for exfoliating *h*-BN, systematically exploring tilt angle, rotational speed, flow rate and concentration in different solvents. The highest yield of exfoliated *h*-BN was in water, 6k rpm rotational speed, tilt angle -45º, 0.3 mg/mL concentration and 0.75 mL/min flow rate. Thus, a higher concentration of *h*-BN and a higher flow rate, at the same tilt angle and rotational speed, favours exfoliation over scroll formation. Changing the flow rate and concentration will alter the complex fluid dynamics in the VFD, the very nature of which is currently being explored.

The origin of this presumably relates to subtle changes in the expected complex fluid dynamics in changing these parameters.[35,36]

Figure 4.3(a) is an SEM image of the as received *h*-BN flakes for comparison with VFD processed material. Figure 4.3(b-d) and S4.1 are SEM images showing *h*-BN scrolls formed during the VFD processing (single pass) at the optimised conditions (10% conversion of *h*-BN to scrolls), with the sample prepared by drop casting the supernatant solution onto a silicon wafer, after centrifugation to remove unprocessed flakes (RCF = 1180 x g). They are representative images from different samples. The scrolls range in length, up to *ca* 20 μm, which is greater than the cross-section dimensions of the flakes from which they were generated. This suggests that the scrolling process for the long scrolls is not simply single *h*-BN sheets exfoliated, one at a time, but that there is intertwining of sheets with onset of the formation of the scrolls.

Figure 4.3(e-h) and S4.2 are SEM images of exfoliated *h*-BN drop cast on silicon wafers for the supernatant after centrifugation to remove unprocessed flakes (RCF = 1180 x g). They are representative images from different samples. AFM was also used to investigate the nature of the materials after VFD processing, using the same workup of the solution and drop casting. The AFM image in Figure 4.4(a) is for as received material with the dimensions of the particles consistent with the dimensions

of the *h*-BN flakes determined using SEM. The AFM images in Figure 4.4(b, c) and S4.3(a-d) show the scrolls, with the length of the scrolls longer than the cross section of the starting material, as determined using SEM. Importantly the AFM images establish that the height of the *h*-BN scrolls vary from 10 nm to 67 nm, from counting ~100 *h*-BN scrolls, Figure 4.5. AFM images of exfoliated *h*-BN established the thickness of the *h*-BN sheets after VFD processing as *ca* 2 nm, Figure 4.4(d-f) and S4.3(e, f), determined from counting >100 sheets, Figure 4.8. TEM was also used to further understand the nature of the processed material. Such images in Figure 4.6(a-c) and S4.4 confirmed the shape of the *h*-BN scrolls formed in the VFD. Figure 4.6(d) is a high resolution TEM image which established the inter-planer spacing between successive turns in the *h*-BN scrolls as 0.33 nm, which is at the van der Waals limit, as in *h*-BN itself.[11] Figure 4.6(e, f) are TEM images of exfoliated *h*-BN, which are also in agreement with SEM and AFM images. Raman spectra of *h*-BN has one peak for the B-N E_{2g} symmetry mode at 1368 cm^{-1}. After VFD processing at the optimum conditions, this shifts slightly to higher frequency at 1371 cm^{-1}, Figure 4.7(a), which is in accord with stress imparted in the *h*-BN layer on rolling up BN sheets.[37-39] The Raman spectrum of exfoliated *h*-BN also has a peak for the B-N E_{2g} symmetry mode at 1367 cm^{-1}, Figure 4.9(a).[40-42] The XRD patterns for both the as received *h*-BN and *h*-BN scrolls have the same 2θ peaks at 31.2 (002), 48.6 (100), 51.2 (101), 59.5 (102) and 64.8 (004), which corresponds to the crystallographic planes of *h*-BN.[43] However, the XRD for the *h*-BN scrolls has higher intensity for the (100, 101, 102) peaks, compared to main peaks (002), Figure 4.7(c).[44] In addition, XRD of exfoliated *h*-BN has the same peaks as bulk material, with a change in ratio of the intensity of the (100), (101) and (102) peaks relative to the (002) peak which is

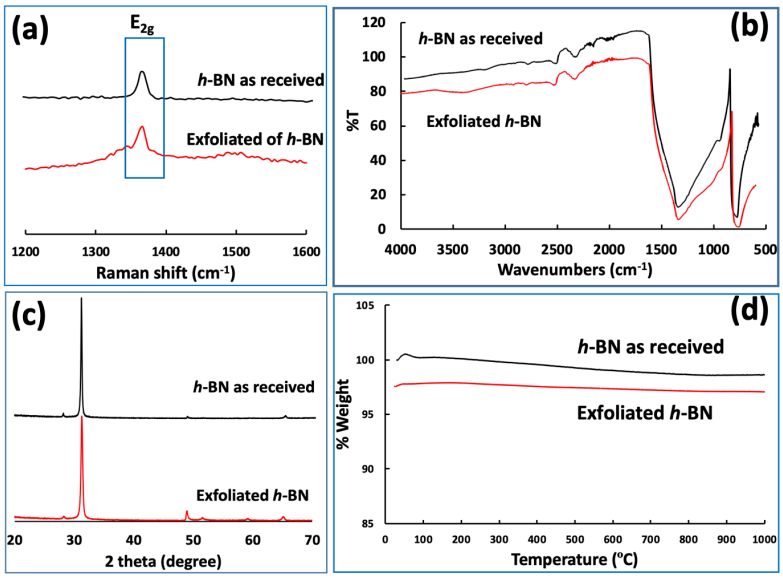

Figure 4.9. (a) Raman spectra, (b) ATR-FTIR spectra, (c) powder XRD diffracted and (d) TGA for h-BN as received and exfoliated h-BN prepared using the optimised VFD protocol (rotational speed 6k rpm, tilt angle -45º, flow rate 0.75 mL/min, and concentration 0.3 mg/mL).

informative for determining the presence of mono- and few-layered of *h*-BN, Figure 4.9(c).[30,45] The reason for this is a reduction in the number of successive *h*-BN layers after processing, in forming *h*-BN scrolls at the van der Waals limit, or exfoliating to a limited number of *h*-BN sheets, with the main peak at 2θ 31.2 (002), corresponds to a *d* spacing of 0.33 nm. ATR-FTIR spectra for as received *h*-BN, *h*-BN scrolls and exfoliated *h*-BN have the expected broad peaks for B–N stretching and B–N–B bending vibrations, at 1348 cm^{-1} and 768 cm^{-1} respectively.[43] However, the ATR-FTIR spectra for *h*-BN scrolls and exfoliated *h*-BN have a broad peak at 3400 cm^{-1} which is assignable to water, presumably confined in the *h*-BN scrolls and intercalated respectively, Figure 4.7(b) and Figure 4.9(b).[41,46] Consistent with this are the results of thermo- gravimetric analysis (TGA) for *h*-BN scrolls, Figure 4.7(d), which shows a weight loss starting at *ca* 205ºC. This continues as the temperature further increases, with the overall weight loss for the *h*-BN scrolls *ca* 10 % which is likely to arise from loss of residual water inside the scrolls prior to heating.[47] The confinement of water in the scrolls is noteworthy in considering the potential use of the material for gas storage.[21,48] TGA for exfoliated *h*-BN shows no weight loss for increasing temperature, Figure 4.9(d).[47]

4.5 Conclusions

h-BN scrolls and exfoliated *h*-BN have been selectively prepared in water in the VFD, in the absence of harsh chemicals. The yield of each material was dramatically improved by operating at a tilt angle of -45º. This is in contrast to a myriad of other applications of the VFD where the tilt angle is optimal at +45º. The residence time of the liquid entering the VFD tube and exiting at the open top is > 2 mins. This is in contrast to the *ca.* 6 minutes residence time for the conventional +45º tilt angle of the tube for identical rotation speeds and flow rates. The ability to fabricate *h*-BN scrolls and exfoliated *h*-BN in water in a VFD under continuous flow conditions is without precedent. They are formed in the absence of surfactants and harsh chemicals and the overall processing is high in green chemistry metrics. To scalable processing, we prepare 5 mg and 72 mg in one run over 24 hours of *h*-BN scrolls and exfoliated *h*-BN respectively. The low amount for the scrolls is because the optimal concentration and flow rate are much less than for fabricating exfoliated sheets, under the same tilt angle and rotational speed. This difference in selectivity reflects the expected changes in the complex fluid dynamics as flow rate and concentration changes. The exfoliation process established is without reduction of the lateral dimensions of the *h*-

BN sheets, *i.e.* without fragmentation, and presumably this also holds for the formation of the scrolls.

4.6 Acknowledgements

The authors gratefully acknowledge financial support from the Iraq Government, Ministry of Higher Education and Scientific research, and the Australian Research Council and the Government of South Australia. The Australian Microscopy & Microanalysis Research Facility (AMMRF) and the Australian National Fabrication Facility (ANFF) at the South Australian nodes of the AMMRF and ANFF under the National Collaborative Research Infrastructure Strategy are acknowledged, as is Dr Jason Gascooke for assistance with SEM imaging.

4.7 References

1. Shi, Y.; Hamsen, C.; Jia, X.; Kim, K. K.; Reina, A.; Hofmann, M.; Hsu, A. L.; Zhang, K.; Li, H.; Juang, Z.-Y.; Dresselhaus, M. S.; Li, L.-J.; Kong, J., Synthesis of Few-Layer Hexagonal Boron Nitride Thin Film by Chemical Vapor Deposition. *Nano Letters* **2010**, *10* (10), 4134-4139.
2. V. Pokropivny, V.; V. Skorokhod, V.; Oleynik, G.; V. Kurdyumov, A.; S. Bartnitskaya, T.; Pokropivny, A.; G. Sisonyuk, A.; M. Sheichenko, D., *Boron Nitride Analogs of Fullerenes (the Fulborenes), Nanotubes, and Fullerites (the Fulborenites).* **2000**; Vol. 154, p 214-222.
3. Wu, H.; Fan, X.; Kuo, J.-L., Metal free hydrogenation reaction on carbon doped boron nitride fullerene: A DFT study on the kinetic issue. *International Journal of Hydrogen Energy* **2012**, *37* (19), 14336-14342.
4. Han, W.-Q., Anisotropic Hexagonal Boron Nitride Nanomaterials: Synthesis and Applications. *Nanotechnologies for the Life Sciences* **2008**, *41,* 1-60.
5. Watanabe, K.; Taniguchi, T.; Kanda, H., Direct-bandgap properties and evidence for ultraviolet lasing of hexagonal boron nitride single crystal. *Nature materials* **2004**, *3* (6), 404.
6. Watanabe, K.; Taniguchi, T.; Niiyama, T.; Miya, K.; Taniguchi, M., Far-ultraviolet plane-emission handheld device based on hexagonal boron nitride. *Nature Photonics* **2009**, *3*, 591.
7. Kubota, Y.; Watanabe, K.; Tsuda, O.; Taniguchi, T., Deep ultraviolet light-emitting hexagonal boron nitride synthesized at atmospheric pressure. *Science* **2007**, *317* (5840), 932-934.
8. Han, W.-Q.; Wu, L.; Zhu, Y.; Watanabe, K.; Taniguchi, T., Structure of chemically derived mono-and few-atomic-layer boron nitride sheets. *Applied Physics Letters* **2008**, *93* (22), 223103.
9. Perim, E.; Galvao, D. S., The structure and dynamics of boron nitride nanoscrolls. *Nanotechnology* **2009**, *20* (33), 335702.

10. Woellner, C. F.; Machado, L. D.; Autreto, P. A. S.; de Sousa, J. M.; Galvao, D. S., Structural transformations of carbon and boron nitride nanoscrolls at high impact collisions. *Physical Chemistry Chemical Physics* **2018**, *20* (7), 4911-4916.
11. Chen, X.; Boulos, R. A.; Dobson, J. F.; Raston, C. L., Shear induced formation of carbon and boron nitride nano-scrolls. *Nanoscale* **2013**, *5* (2), 498-502.
12. Alharbi, T. M. D.; Harvey, D.; Alsulami, I. K.; Dehbari, N.; Duan, X.; Lamb, R. N.; Lawrance, W. D.; Raston, C. L., Shear stress mediated scrolling of graphene oxide. *Carbon* **2018**, *137*, 419-424.
13. Amadei, C. A.; Stein, I. Y.; Silverberg, G. J.; Wardle, B. L.; Vecitis, C. D., Fabrication and morphology tuning of graphene oxide nanoscrolls. *Nanoscale* **2016**, 8 (12), 6783-6791.
14. Hwang, D. Y.; Suh, D. H., Formation of hexagonal boron nitride nanoscrolls induced by inclusion and exclusion of selfassembling molecules in solution process. *Nanoscale* **2014**, *6* (11), 5686-5690.
15. Perim, E.; Machado, L. D.; Galvao, D. S., A brief review on syntheses, structures, and applications of nanoscrolls. *Frontiers in Materials* **2014**, *1*, 31.
16. Chu, L.; Xue, Q.; Zhang, T.; Ling, C., Fabrication of carbon nanoscrolls from monolayer graphene controlled by p-doped silicon nanowires: a md simulation study. *The Journal of Physical Chemistry C* **2011**, *115* (31), 15217-15224.
17. Ding, N.; Chen, X.; Wu, C.-M. L.; Li, H., Adsorption of nucleobase pairs on hexagonal boron nitride sheet: hydrogen bonding versus stacking. *Physical Chemistry Chemical Physics* **2013**, *15* (26), 10767-10776.
18. Lin, Q.; Zou, X.; Zhou, G.; Liu, R.; Wu, J.; Li, J.; Duan, W., Adsorption of DNA/RNA nucleobases on hexagonal boron nitride sheet: an ab initio study. *Physical Chemistry Chemical Physics* **2011**, *13* (26), 12225-12230.
19. Kisku, S. K.; Swain, S. K., Synthesis and characterisation of chitosan/boron nitride composites. *Journal of the American Ceramic Society* **2012**, *95* (9), 2753-2757.
20. Weng, Q.; Wang, X.; Wang, X.; Bando, Y.; Golberg, D., Functionalized hexagonal boron nitride nanomaterials: emerging properties and applications. *Chemical Society Reviews* **2016**, *45* (14), 3989-4012.
21. Weng, Q.; Wang, X.; Zhi, C.; Bando, Y.; Golberg, D., Boron nitride porous microbelts for hydrogen storage. *ACS nano* **2013**, *7* (2), 1558-1565.
22. Reddy, A. L. M.; Tanur, A. E.; Walker, G. C., Synthesis and hydrogen storage properties of different types of boron nitride nanostructures. *international journal of hydrogen energy* **2010**, *35* (9), 4138-4143.
23. Hassani, A.; Mosavian, M. T. H.; Ahmadpour, A.; Farhadian, N., Improvement of methane storage in nitrogen, boron and lithium doped pillared graphene: A hybrid molecular simulation. *Journal of Natural Gas Science and Engineering* **2017**, *46*, 265-274.
24. Lin, Y.; Connell, J. W., Advances in 2D boron nitride nanostructures: nanosheets, nanoribbons, nanomeshes, and hybrids with graphene. *Nanoscale* **2012**, *4* (22), 6908-6939.
25. Fujigaya, T.; Nakashima, N., Methodology for homogeneous dispersion of single-walled carbon nanotubes by physical modification. *Polymer journal* **2008**, *40* (7), 577-589.

26. Vimalanathan, K.; Raston, C. L., Dynamic Thin Films in Controlling the Fabrication of Nanocarbon and Its Composites. *Advanced Materials Technologies* **2017**, *2* (6), 1600298.
27. Alsulami, I.; Alharbi, T.; Harvey, D.; Gibson, C. T.; Raston, C. L., Controlling the growth of fullerene C_{60} cones under continuous flow. *Chemical Communications* **2018**,*54* **(**57), 7896-7899.
28. Mohammed Al-antaki, A. H.; Luo, X.; Duan, A.; Lamb, R. N.; Eroglu, E.; Hutchison, W.; Zou, Y.-C.; Zou, J.; Raston, C. L., Continuous flow synthesis of phosphate binding h-BN@magnetite hybrid material. *RSC Advances* **2018**, *8* (71), 40829-40835.
29. Luo, X.; Al-Antaki, A. H. M.; Vimalanathan, K.; Moffatt, J.; Zheng, K.; Zou, Y.; Zou, J.; Duan, X.; Lamb, R. N.; Wang, S.; Li, Q.; Zhang, W.; Raston, C. L., Laser irradiated vortex fluidic mediated synthesis of luminescent carbon nanodots under continuous flow. *Reaction Chemistry & Engineering* **2018**, *3* (2), 164-170.
30. Chen, X.; Dobson, J. F.; Raston, C. L., Vortex fluidic exfoliation of graphite and boron nitride. *Chemical Communications* **2012**, *48* (31), 3703-3705.
31. Alharbi, T. M. D.; Vimalanathan, K.; Lawrance, W. D.; Raston, C. L., Controlled slicing of single walled carbon nanotubes under continuous flow. *Carbon* **2018**, *140*, 428-432.
32. Vimalanathan, K.; Gascooke, J. R.; Suarez-Martinez, I.; Marks, N. A.; Kumari, H.; Garvey, C. J.; Atwood, J. L.; Lawrance, W. D.; Raston, C. L., Fluid dynamic lateral slicing of high tensile strength carbon nanotubes. *Scientific reports* **2016**, *6*, 22865.
33. Britton, J.; Chalker, J. M.; Raston, C. L., Rapid Vortex Fluidics: Continuous Flow Synthesis of Amides and Local Anesthetic Lidocaine. *Chemistry–A European Journal* **2015**, *21* (30), 10660-10665.
34. Gandy, M. N.; Raston, C. L.; Stubbs, K. A., Towards aryl CN bond formation in dynamic thin films. *Organic and Biomolecular Chemistry* **2014**, *12* (26), 4594-4597.
35. Britton, J.; Stubbs, K. A.; Weiss, G. A.; Raston, C. L., Vortex fluidic chemical transformations. *Chemistry–A European Journal* **2017**, *23* (54), 13270-13278.
36. Britton, J.; Dalziel, S. B.; Raston, C. L., The synthesis of di-carboxylate esters using continuous flow vortex fluidics. *Green Chemistry* **2016**, 18 (7), 2193-2200.
37. Suh, D. H., Formation of hexagonal boron nitride nanoscrolls induced by inclusion and exclusion of self-assembling molecules in solution process. *Nanoscale* **2014**, *6* (11), 5686-5690.
38. Reich, S.; Ferrari, A.; Arenal, R.; Loiseau, A.; Bello, I.; Robertson, J., Resonant Raman scattering in cubic and hexagonal boron nitride. *Physical Review B* **2005**, *71* (20), 205201.
39. Song, L.; Ci, L.; Lu, H.; Sorokin, P. B.; Jin, C.; Ni, J.; Kvashnin, A. G.; Kvashnin, D. G.; Lou, J.; Yakobson, B. I., Large scale growth and characterization of atomic hexagonal boron nitride layers. *Nano letters* **2010**, *10* (8), 3209-3215.
40. Lin, Y.; Bunker, C. E.; Fernando, K. A. S.; Connell, J. W., Aqueously Dispersed Silver Nanoparticle-Decorated Boron Nitride Nanosheets for Reusable, Thermal Oxidation-Resistant Surface Enhanced Raman Spectroscopy (SERS) Devices. *ACS Applied Materials & Interfaces* **2012**, *4* (2), 1110-1117.
41. Nag, A.; Raidongia, K.; Hembram, K. P. S. S.; Datta, R.; Waghmare, U. V.; Rao, C. N. R., Graphene Analogues of BN: Novel Synthesis and Properties. *ACS Nano* **2010**, *4* (3), 1539-1544.

42. Wang, X.; Pakdel, A.; Zhang, J.; Weng, Q.; Zhai, T.; Zhi, C.; Golberg, D.; Bando, Y., Large-surface-area BN nanosheets and their utilization in polymeric composites with improved thermal and dielectric properties. *Nanoscale Research Letters* **2012**, *7* (1), 662.
43. Hou, X.; Wang, M.; Fu, L.; Chen, Y.; Jiang, N.; Lin, C.-T.; Wang, Z.; Yu, J., Boron nitride nanosheet nanofluids for enhanced thermal conductivity. *Nanoscale* **2018**, *10* **(**27), 13004-13010.
44. Yuan, S.; Toury, B.; Journet, C.; Brioude, A., Synthesis of hexagonal boron nitride graphene-like few layers. *Nanoscale* **2014**, *6* (14), 7838-7841.
45. Fan, D.; Feng, J.; Liu, J.; Gao, T.; Ye, Z.; Chen, M.; Lv, X., Hexagonal boron nitride nanosheets exfoliated by sodium hypochlorite ball mill and their potential application in catalysis. *Ceramics International* **2016**, *42* (6), 7155-7163.
46. Gautam, C.; Tiwary, C. S.; Jose, S.; Brunetto, G.; Ozden, S.; Vinod, S.; Raghavan, P.; Biradar, S.; Galvao, D. S.; Ajayan, P. M., Synthesis of Low-Density, Carbon-Doped, Porous Hexagonal Boron Nitride Solids. *ACS nano* **2015**, *9* (12), 12088-12095.
47. Hou, J.; Li, G.; Yang, N.; Qin, L.; Grami, M. E.; Zhang, Q.; Wang, N.; Qu, X., Preparation and characterization of surface modified boron nitride epoxy composites with enhanced thermal conductivity. *RSC Advances* **2014**, *4* (83), 44282-44290.
48. Oku, T., Hydrogen storage in boron nitride and carbon nanomaterials. *Energies* **2014**, *8* (1), 319-337.

RSC Advances

PAPER

View Article Online
View Journal | View Issue

Check for updates

Cite this: *RSC Adv.*, 2019, **9**, 22074

Inverted vortex fluidic exfoliation and scrolling of hexagonal-boron nitride†

Ahmed Hussein Mohammed Al-Antaki,[ab] Xuan Luo,[a] Thaar M. D. Alharbi,[a] David P. Harvey,[a] Scott Pye,[a] Jin Zou,[c] Warren Lawrance[d] and Colin L. Raston*[a]

Received 26th May 2019
Accepted 5th July 2019

DOI: 10.1039/c9ra03970h

rsc.li/rsc-advances

Exfoliation or scrolling of hexagonal boron nitride (h-BN) occurs in a vortex fluidic device (VFD) operating under continuous flow, with a tilt angle of −45° relative to the horizontal position. This new VFD processing strategy is effective in avoiding the build-up of material that occurs when the device is operated using the conventional tilt angle of +45°, where the h-BN precursor and scrolls are centrifugally held against the wall of the tube. At a tilt angle of −45° the downward flow aided by gravity facilitates material exiting the tube with the exfoliation of h-BN and formation of h-BN scrolls then optimized by systematically varying the other VFD operating parameters, including flow rate and rotational speed, along with concentration of h-BN and the choice of solvent. Water was the most effective solvent, which enhances the green chemistry metrics of the processing.

Introduction

Polymorphs of boron nitride include the hexagonal arrangement of alternating boron and nitrogen atoms in 2D sheets, with the atoms sp^2 hybridized, comparable to that of graphite. However, in contrast to graphite, layered hexagonal boron nitride (h-BN) is transparent and it is an insulator,[1] but nevertheless it has attracted considerable attention. Other polymorphs of h-BN do not strictly match polymorphs of carbon, for example, as in the boron nitride analogues of fullerenes, known as fulborenites.[2,3] The main polymorphs of boron nitride are rhombohedral BN (r-BN), cubic BN (c-BN), wurtzite BN (w-BN) and hexagonal BN (h-BN), with the latter 2D material featuring in the present study. None of the polymorphs of BN have been found in nature.[4]

In general, hexagonal carbon (h-C), possessing hexagonal six membered rings, as in graphite, graphene or carbon nanotubes, can be metallic or semiconducting depending on the dimensions and overall structure. However, h-BN is an insulator or indirect semiconductor, having a large band gap around 5.9 eV.[5] Defects in h-BN can perturb the band gap[5] with single crystals of h-BN flakes used to study band gap properties.[5,6] The availability of high-quality h-BN flakes is important for developing applications in far-ultraviolet (FUV) light-emitting diodes (LEDs).[7] In addition, h-BN has potential in optoelectronic applications, for use in high-performance electronic devices. Electron energy loss spectroscopy (EELS) on the ionization edge between two-layers of BN is effective in determining the number of layers of one atom thick h-BN.[8] h-BN can also be coerced into forming scrolls which are essentially individual sheets of h-BN rolled up at the van der Waals limit.[9–11] Contemporary studies have established the ability to make the analogous graphene and graphene oxide scrolls.[11–16] h-BN scrolls have a number of potential applications, as platforms for the delivery of composites and nucleobases,[17–20] for example, which rely on coordination interactions between N or O with the empty orbital of boron.[20] In addition, h-BN scrolls have potential use in gas storage, including hydrogen and methane.[21–23] h-BN scrolls should be easier to produce than graphene scrolls[17,18,24,25] with the interaction between successive turns in the scrolls more favoured by the difference in electronegativity between B and N atoms. We have prepared h-BN scrolls from h-BN dispersed in *N*-methyl-2-pyrrolidone (NMP) using a spinning disc processor (SDP) where liquids are subjected to high shear. The choice of NMP solvent here was based on it having a similar surface tension relative to h-BN.[11] However, the yield was only 5%, and this required 20 h of recycling a colloidal suspension of h-BN onto a 10 cm diameter rotating disc in the SDP. The SDP was the forerunner to the development of the vortex fluidic device (VFD), which is more practical for research purposes, while also addressing scalability of the processing, and is significantly cheaper.[26]

We have explored using the VFD to form h-BN scrolls from h-BN in water under continuous flow mode of operation in the device, establishing *ca.* 10% yield conversion for a single pass through the microfluidic platform. For this, and also for simple

[a]Flinders Institute for Nanoscale Science and Technology, College of Science and Engineering, Flinders University, Adelaide, SA 5042, Australia. E-mail: colin.raston@flinders.edu.au
[b]Department of Chemistry, Faculty of Sciences, Kufa University, Kufa, Najaf, Iraq
[c]Materials Engineering, Centre for Microscopy and Microanalysis, The University of Queensland, Brisbane, QLD 4072, Australia
[d]College of Science and Engineering, Flinders University, Adelaide, SA 5042, Australia
† Electronic supplementary information (ESI) available: Experimental details and characterisation results (Fig. S1–S6). See DOI: 10.1039/c9ra03970h

5. Continuous flow synthesis of phosphate binding *h*-BN@magnetite hybrid material

Ahmed Hussein Mohammed Al-antaki [a], Xuan Luo [a, b], Alex Duan [c], Robert N. Lamb [c], Ela Eroglu [d], Wayne Hutchison [e], Yi-Chao Zou [f], Jin Zou [f], Colin L. Raston [a*]

a. *Flinders Institute for Nanoscale Science and Technology, College of Science and Engineering, Flinders University, Adelaide, SA 5042, Australia.*
b. *Centre for Marine Bioproducts Development, College of Medicine and Public Health, Flinders University, Adelaide, SA 5042, Australia.*
c. *Trace Analysis for Chemical, Earth and Environmental Sciences (TrACEES), The university of Melbourne, Victoria 3010, Australia.*
d. *Department of Chemical Engineering, Curtin University, Perth, Australia.*
e. *School of PEMS, University of New South Wales, ADFA Campus, Canberra BC, ACT 2610, Australia.*
f. *Materials Engineering, Centre for Microscopy and Microanalysis, The University of Queensland, Brisbane, QLD 4072, Australia.*

Author contributions: **AA** performed all the VFD and all characterisation experiments; wrote all the primary content. **XL** performed Raman spectra and zeta potential experiments. **AD** and **RL** performed XPS spectra. **EE** application of composite with phosphate. **WH** performed magnetization saturation. **YZ** and **JZ** performed TEM images. **CR** supervised and coordinated the project and helped on the research directions and plan, and the final revision of the manuscript. All of the co-authors assisted with the revision of the manuscript before and during the publication process.

Graphical Abstract

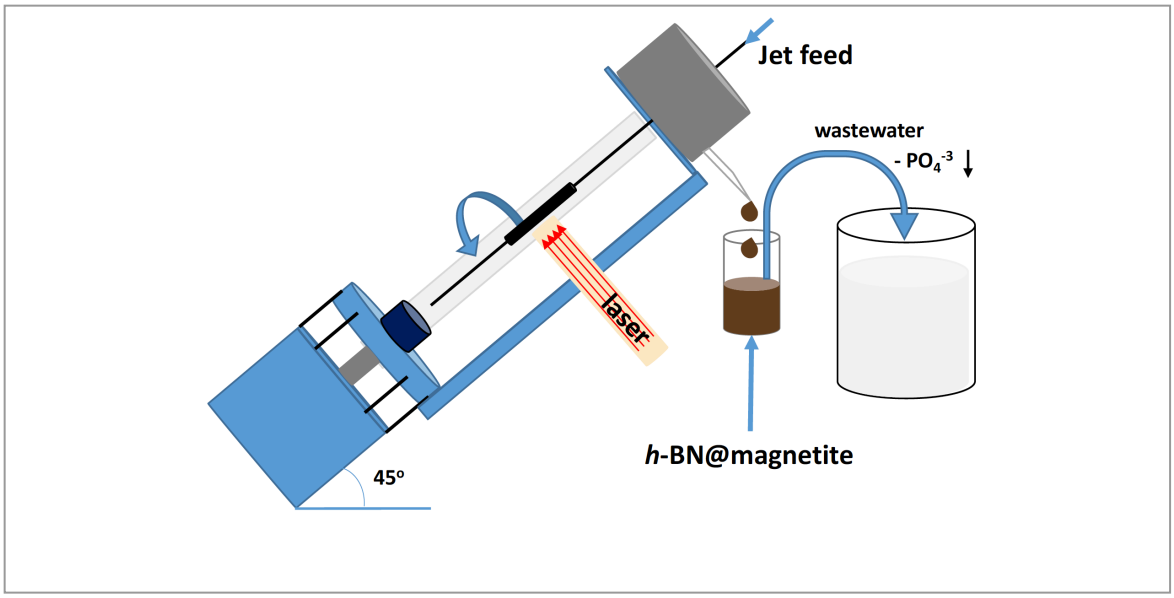

5.1 Abstract

Hexagonal boron nitride (*h*-BN) is rendered magnetically responsive in aqueous media by binding superparamagnetic magnetite nanoparticles 8.5-18.5 nm in diameter on the surface. The composite material was generated under continuous flow in water in a dynamic thin film in a vortex fluidic device (VFD) with the source of iron generated by laser ablation of a pure iron metal target in the air above the liquid using a Nd:YAG pulsed laser operating at 1064 nm and 360 mJ. Optimum operating parameters of the VFD were for a rotational speed of 7.5k rpm for the 20 mm O.D. (17.5 mm I.D.) borosilicate glass tube inclined at 45 degrees, with a *h*-BN concentration at 0.1 mg/mL, delivered at 1.0 mL/min using a magnetically stirred syringe to keep the *h*-BN uniformly dispersed in water prior to injection into the base of the rapidly rotating tube. The resulting composite material, containing 5.75% weight of iron, exhibited high phosphate ion adsorption capacity, up to 171.2 mg PO_4^{3-} per gram Fe, which was preserved on recycling the material five times.

5.2 Introduction

Polymorphs of boron nitride include the hexagonal arrangement of alternating sp^2 hybridized boron and nitrogen atoms in 2D sheets, which is isostructural to graphene sheets in graphite, and this similarity in structure is attracting attention. However, in contrast to graphite, layered hexagonal boron nitride (*h*-BN) is transparent and is an insulator,[1] and its dielectric and thermal properties makes it useful for different electronic applications such as thermal interface materials for semiconductor packaging.[2,3] In general, hexagonal carbon (*h*-C), where there are hexagonal six membered rings, can be metallic or semiconducting, depending on the dimensions and overall structure, whereas *h*-BN has a large band gap around 5.9 eV and the material is typically an insulator or indirect semiconductor.[4-6] Electron energy loss spectroscopy (EELS) provides information on the number of layers in *h*-BN in a similar way to that of graphite.[7] In contrast to graphene, *h*-BN has potential use as a vehicle for the delivery of protein and nucleobases.[8,9] This arises from coordination of N or O donor groups in these macromolecules with electron deficient boron atoms in the *h*-BN. Such interactions are stronger than π-π interactions which prevail between graphene sheets or between carbon nanotube (CNTs) and the like.[10,11] Multilayers of *h*-BN bind nanomaterials in imparting new properties, for example, magnetic response.[12,13] The vortex fluidic device (VFD) is a thin film microfluidic platform which has a number of applications, including enhancing enzymatic reactions and organic synthesis, probing the structure of self-organised systems, protein folding, protein separation, exfoliation of 2D graphite and boron nitride, the fabrication of carbon dots, and more.[14-22] The VFD has a borosilicate glass tubes

(typically 20 mm in O.D. diameter, 17.5 mm I.D. diameter) open at one end, and is rotated at high speed (up to 9k rpm) while inclined at an angle, from 0° to 90° relative to the horizontal position. The VFD can be used in two different modes of operations, (i) the confined mode for processing a finite volume of liquid in the rapidly rotating tube, and (ii) continuous flow mode where liquid is constantly fed into the tube, so that the processing can be scaled up, allowing the processing of large volumes by extending the operating time.[23] The confined mode of operation of the VFD is often used as a proven starting point for optimizing a process, for fast tracking into continuous flow processing, Figure 5.1.[24] In further exploring the expanding applications of the VFD,[23,25] we have investigated for the first time its use in preparing a composite material, containing both *h*-BN and superparamagnetic magnetite nanoparticles. The *h*-BN is decorated with magnetite nanoparticles in situ in the dynamic thin film in the VFD under continuous flow, under an atmosphere of air with the magnetite nanoparticles generated in a plume of iron formed by irradiating a pure iron metal block with a Nd:YAG pulsed laser, as previous reported for making exclusively aqueous solutions of superparamagnetic magnetite nanoparticles.[26] The laser effectively creates a plasma plume over the surface of a pure iron target plate.[27-29] We hypothesised that oxygen functionality on the surface of the magnetite nanoparticles would be effective in providing coordination interactions to B-atoms in *h*-BN, as well as providing a platform for binding phosphate (PO_4^{3-}) ions for waste water treatment.[30]

The dynamic thin film in the VFD imparts high mass transfer of particles into the liquid, and the high shear in the liquid is effective in generating small particles of magnetite, as well as some exfoliation of *h*-BN with then binding of the magnetite nanoparticles.[31] The composite material, *h*-BN@magnetite, can be readily manipulated and confined in solution by a magnetic field, and we have established that it is effective as a novel absorbent in removing excess levels of phosphate from water resources, targeting its potential for avoiding environmental complications on ecosystems, such as eutrophication.[32] Various techniques have already been applied for the removal of phosphorous in general from water bodies, as in biological processes and/or chemical adsorption by various adsorbing materials including activated alumina, ferric-oxides, various polymers, red-mud, sand, and zeolites.[33-37] Iron oxides in general are effective for the removal of both phosphate and arsenate (AsO_4^{3-}) ions from the liquid effluents.[34]

5.3 Experiments

5.3.1 Materials. Hexagonal boron nitride (*h*-BN) powder flakes ~1 μm in diameter with 99% purity were purchased from Sigma-Aldrich. High purity Fe (>99.998%) 8361h iron rod, 5 mm thick (Koch-Light Laboratories) was used in the VFD as the laser target and Milli Q water was used for all the experiments. A suspension of *h*-BN in water was delivered at a controlled flow rate to the hemi-spherical base of the rapidly rotating tube. This was achieved using an in-house developed syringe pump featuring a motor housed in the plunger, for magnetically stirring the solution during delivery into the VFD tube, Figure 5.2.

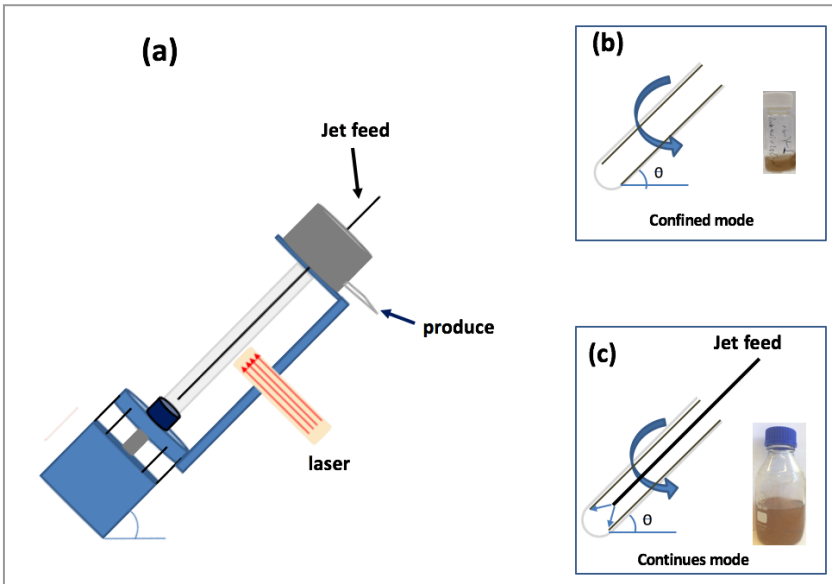

Figure 5.1. (a) Diagrammatic representation of the VFD used in association with a 5 nanosecond pulsed Nd:YAG laser operating at 1064 nm and 360 mJ, with a 8 mm diameter beam; the glass tube is rotated at 7.5k rpm and tilted at 45°. (b) Confined mode of operation of the VFD where a finite volume is placed in the rotating glass tube, for 15 mins. (c) Continuous flow operation of the VFD with the flow rate of the liquid entering the rotating glass tube set at 1 mL/min.

5.3.2 Synthesis of *h*-BN@magnetite. Magnetite nanoparticles were generated in the thin film in the VFD by irradiating an iron rod with a Nd:YAG pulsed laser (Quanta-Ray) operating at 1064 nm wavelength and 360 mJ, while a suspension of *h*-BN in water (at 0.1 mg/mL) was delivered via a jet feed to the base of the tube. This was achieved using the above magnetically stirred solution of *h*-BN and water (from1 L of a suspension of *h*-BN in water which was sonicated in a bath (6KHz) for 25 minutes), at a flow rate of 1 mL/min which was controlled using a syringe pump, with the rotational speed of

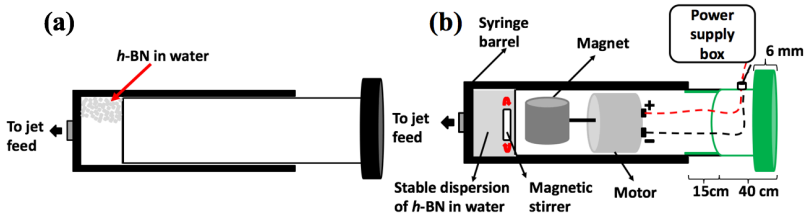

Figure 5.2. (a) Normal syringe. (b) magnetic syringe has a magnet link with motor and sitting together inside the plunger which will affect onto magnetic bar sitting inside the syringe.

the tube in the VFD was set at 7.5k rpm and the tube angled at 45^{o} relative to the horizontal position, Figure 5.3.

5.3.3 Characterisation. Hexagonal boron nitride (*h*-BN) decorated with magnetite nanoparticles was characterized using scanning electron microscopy (SEM) (Inspect FEI F50 SEM), atomic force microscopy (AFM) (Nanoscope 8.10 tapping mode), Raman spectroscopy (WiTec Alpha 300R λexc=532 nm), X-ray photoelectron spectroscopy (XPS – Kratos Axis Ultra, with Monochromatic Al *Ka* X-ray source), X-ray diffraction (XRD) (Bruker D8 ADVANCE ECO, Co- Kα, λ=1.79 Å), FTIR microscope (Nicolet iN10MX IR Microscope, Thermo Scientific), ATR-FTIR Perkin Elmer Frontier, TEM and HRTEM (FEI Tecnai F20 operated at 200 kV). Zeta potential (model: ZETASIZER Nanoseries nano-zs MALVERN) was also measured, along with iron analysis content using an atomic absorption spectrometer (GBC 933 plus) and Brunauer–Emmett–Teller (BET) surface area and porosity (micromeritics TriStar II). Magnetisation measurements were carried out using a Quantum design MPMS at 295 K in the field range ±1.50 T.

5.3.4 Phosphate removal. Three different loadings of the magnetic *h*-BN adsorbent (10 mg; 25 mg; 50 mg) were separately mixed with phosphate containing artificial aquatic-media.[38] (1.25 mL, which mainly includes phosphates, nitrates, carbonate buffer, micronutrients and vitamins at a buffered pH of 7.5. Each mixture was then hand-vortexed (this not the VFD) for about 1 minute for initiating the experiments. The amount of phosphate ions remaining in the solution were monitored at the beginning and by the 30th minute according to our previous findings.[39,40] The mixtures were centrifuged at 13148 ×g for 5 minutes and particle-free supernatants were collected for their spectrophotometric phosphate analysis by the colorimetric ascorbic acid method, or the so called orthophosphate method, which is a standard water-analysing procedure recognized by the United States Environmental Protection Agency.[41] Phosphate analysing kits (HACH®, PhosVer® 3 phosphate reagent powder pillows) were employed before reading the phosphate concentration of the supernatant by a colorimeter (HACH® DR/870).

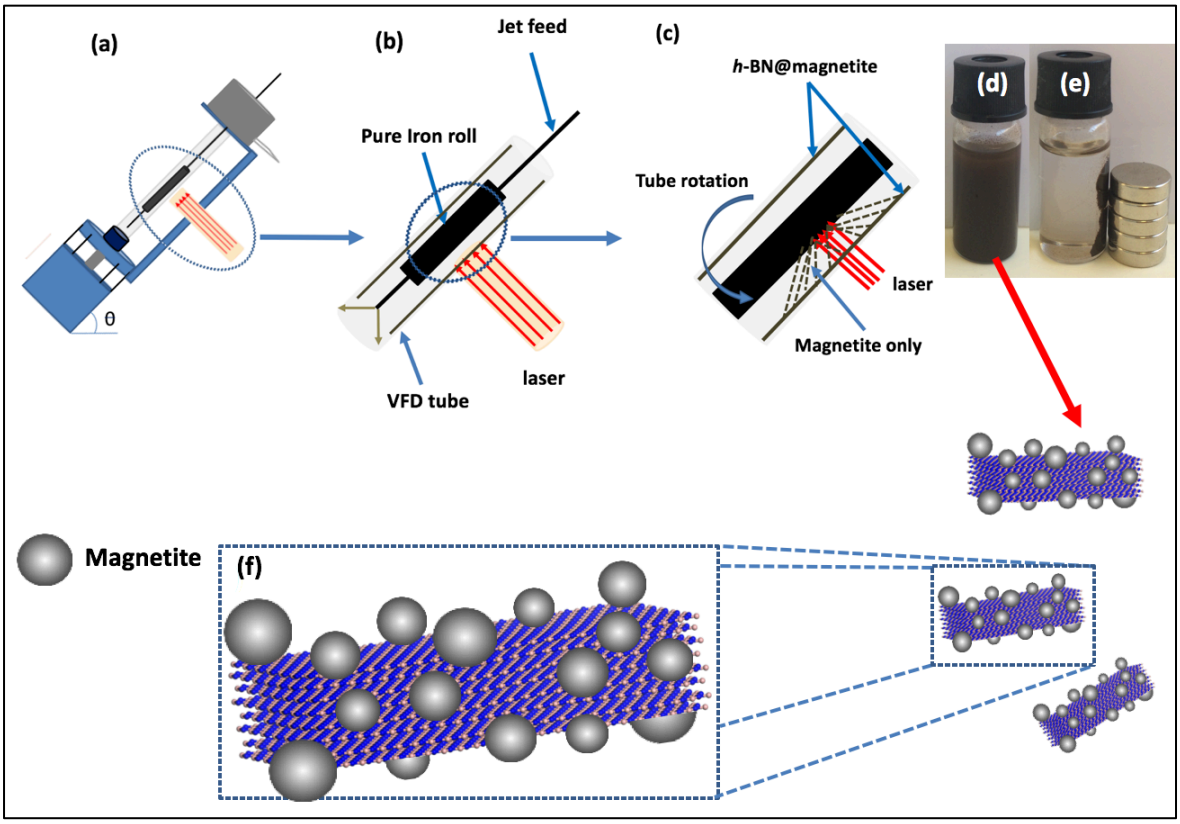

Figure 5.3. (a) VFD showing the position of the pure iron rod as a laser target being irradiated with a Nd:YAG pulsed laser operating at 1064 nm and 360 mJ, with the tube rotating at 7.5k rpm, tilt angle 45º and flow rate 1 mL/min for *h*-BN dispersed in water (0.1 mg/mL). (b) Close up of the arrangement of the glass tube and position of laser irradiation. (c) Synthesis of the iron oxide nanoparticles (magnetite) attached to *h*-BN inside the glass tube. (d) Photograph of the solution exiting the VFD. (e) Photograph showing the effect of a magnet on *h*-BN@magnetite dispersed in water. (f) Cartoon of the *h*-BN@magnetite composite.

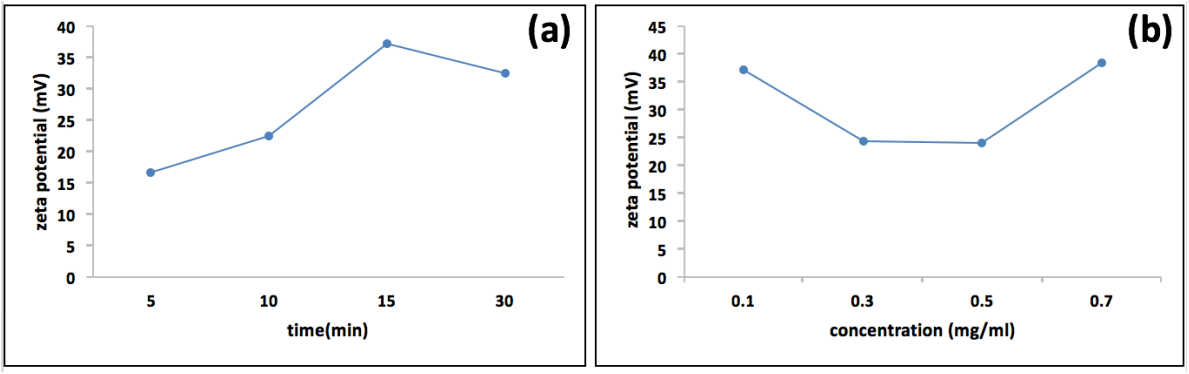

Figure 5.4. Zeta potential measurements for *h*-BN@magnetite prepared using the confined mode of operation of the VFD with the tube rotating at 7.5k rpm and tilted at 45º, with a pure iron rod irradiated using a pulsed laser operating at 1064 nm and 360 mJ, as a function of time, (a) with the concentration of *h*-BN at 0.1 mg/mL, and as a function of concentration of *h*-BN where the processing time was set at 15 min.

5.4 Results and Discussion

We used a one-step VFD mediated process to prepare a new type of *h*-BN hybrid materials directly from the 2D material and elemental iron, in the absence of any agents or harsh chemicals. This is a new use of the VFD, in generating metal oxide (magnetite) particles tethered to *h*-BN, with the stability of the material poised for use in different applications. Figure 5.3 summarises the method of preparation of the *h*-BN@magnetite composite material within the dynamic thin film in a VFD with a pulsed laser operating at 1064 nm 360 mJ irradiating a fixed pure iron target above the liquid.[42] Initially we used the confined mode of operation of the VFD to prepare the composite material, using zeta potential measurements to optimise the conditions for generating dispersions of high colloidal stability, along with SEM (see below). This indicates any build-up of magnetite nanoparticles on the surface of *h*-BN flakes.[43,44] All processing was at a rotational speed of the tube in the VFD at 7.5k rpm, with the tube inclined at 45^{o}, as the optimal parameters for a number of applications of the VFD.[24] The pulsed laser was operated at 1064 nm and 360 mJ, as the optimal conditions for preparing magnetite nanoparticles in the absence of *h*-BN.[26] Variation of processing time in the confined mode of operation of the VFD was first explored, with the volume of the liquid in the tube set at 1 mL, which was adhered to for all experiments using this mode, with the initial concentration of *h*-BN in water set at 0.1 mg/mL. After 5 or 10 minutes post VFD processing the zeta potential was relatively low, below +25 mV, Figure 5.4(a), which is consistent with limited deposition of magnetite nanoparticles on the surface of *h*-BN. The zeta potential increased to +37.2 mV after 15 minutes of reaction which is consistent with colloidal stability of the particles in solution. After 30 minutes the zeta potential dropped, and thus 15 minutes processing time was deemed optimal in the confined mode. With the processing time set, the concentration of *h*-BN in water was then varied, Figure 5.4(b), with 0.3 and 0.5 mg/mL resulting in lower zeta potential than for 0.1 and 0.7 mg/mL. Suspensions of the composite material at 0.3 and 0.5 mg/mL were unstable (precipitate after few mins) and thus zeta potential measurements were not possible. Consequently, 0.1 mg/mL of *h*-BN was deemed the optimised concentration under confined mode, and the processing was then translated into continuous flow mode of operation of the VFD. Zeta potential for as prepared solutions at 0.25, 0.5, 0.75 and 1.25 mL/min flow rates were lower than 1 mL/min, albeit not in the regime for colloidally stable material. Solutions prepared at flow rates of 0.25, 0.5 and 0.75 mL/min were indeed unstable, with *h*-BN@magnetite rapidly precipitating from solution. *h*-BN@magnetite prepared from a flow rate of 1.25 mL/min had a lower zeta potential, presumably reflecting a lower surface coverage of magnetite nanoparticles on the surface of the *h*-BN arising from a shorter

resident time, Figure 5.5. Thus there is a trade-off between optimising the flow rate for higher throughput versus the uptake of the magnetite nanoparticles onto the *h*-BN. To establish the size of the magnetite nanoparticles and how they reside on the surface of *h*-BN, AFM images were obtained. The topography of the surface of the *h*-BN before processing (as received) was smooth, Figure 5.6a-c. For the composite material, patches of aggregated clusters, presumably magnetite nanoparticles, were evident on the outer surface of *h*-BN, Figure 5.6d-f, S5.2. SEM was also used to characterise the material, showing smooth surfaces before VFD processing and deposition of magnetite nanoparticles, Figure 5.7a and b, with then randomly arranged clusters of particles on the surface post VFD processing, Figure 5.7d-f, S5.3. The presence of aggregated materials with its expected high surface area was in agreement with the result from Brunauer-Emmett-Teller (BET) experiments with the specific BET surface area increasing from 11.2 m^2/g for the as received *h*-BN to 91.0 m^2/g for the composite material, Figure S5.4. EDX of the composite material was consistent with the presence of *h*-BN and magnetite, Figure S5.5.

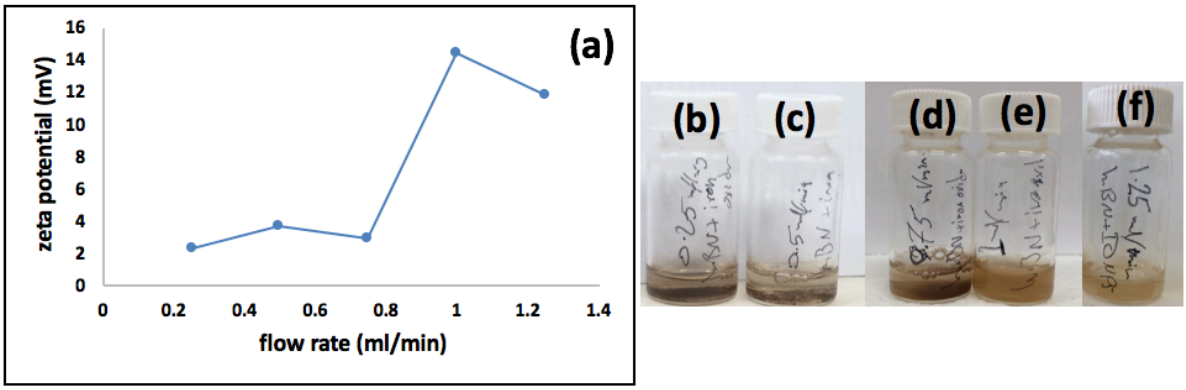

Figure 5.5. (a) Zeta potential for dispersions prepared under continuous flow, at flow rates of 0.25, 0.5, 0.75, 1, 1.25 mL/min, with *h*-BN concentration at 0.1 mg/mL, 7.5k rpm rotational speed, tilt angle 45º and laser operating at 1064 nm and 360 mJ. (b-f) Photographs of the dispersions prepared using flow rates of 0.25, 0.5, 0.75, 1 and 1.25 mL/min respectively.

TEM-HRTEM images were used to determine the size and number of sheets of *h*-BN, Figure 5.8c, S 5.6a-c, as well the size of the magnetite nanoparticles. The latter were determined to be from 8.5 nm to 18.5 nm, Figure 5.8d-f, S5.6e, which is consistent with the size of the particles generated in the absence of *h*-BN.[26] Clearly the conditions studied using the VFD did not result in the formation of scrolls of *h*-BN which is possible under shear, at least for using the related spinning disc processing.[25] In addition, there was little evidence of exfoliation of the *h*-BN, despite the VFD being effective for this, albeit in low percent conversion.[21] The size of the *h*-BN sheets was from 150 nm to 3 µm which is similar to the as received material, with the inter planar spacing for the material 0.33 nm, Figure S5.6f, as expected. The size of the magnetite particles in *h*-BN@magnetite is consistent with the results from AFM and SEM. The presence of magnetite (IONPs) on *h*-BN sheets was confirmed using SAED, with SAED for as received *h*-BN in Figure 5.8a, and that for *h*-BN@magnetite in Figure 5.8b. The X-Ray diffraction (XRD) pattern has 2θ peaks at 31.2 (002), 48.6 (100), 51.2

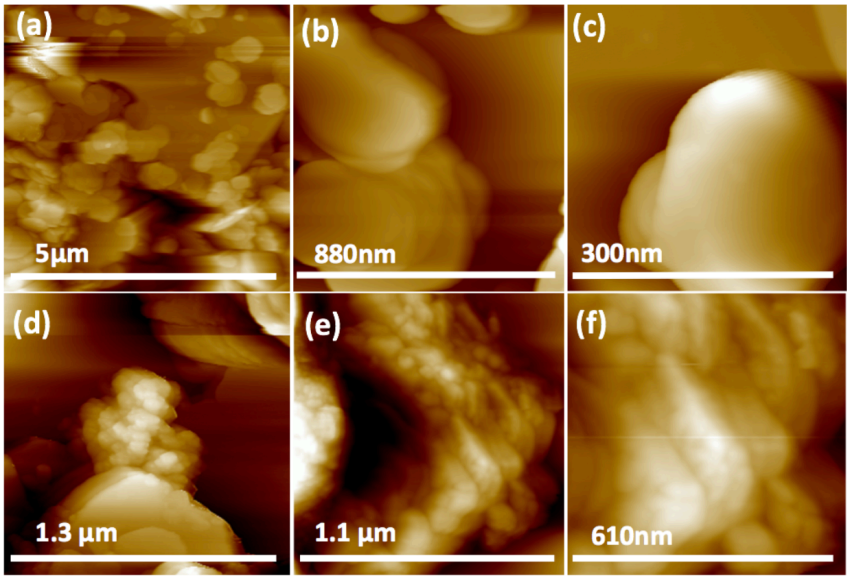

Figure 5.6. AFM images: (a-c) *h*-BN sheet as received. (d-f) *h*-BN@magnetite prepared at 7.5k rpm, tilt angle 45°, laser energy 360 mJ, the flow rate of *h*-BN dispersed in water (0.1 mg/mL) 1 mL/min.

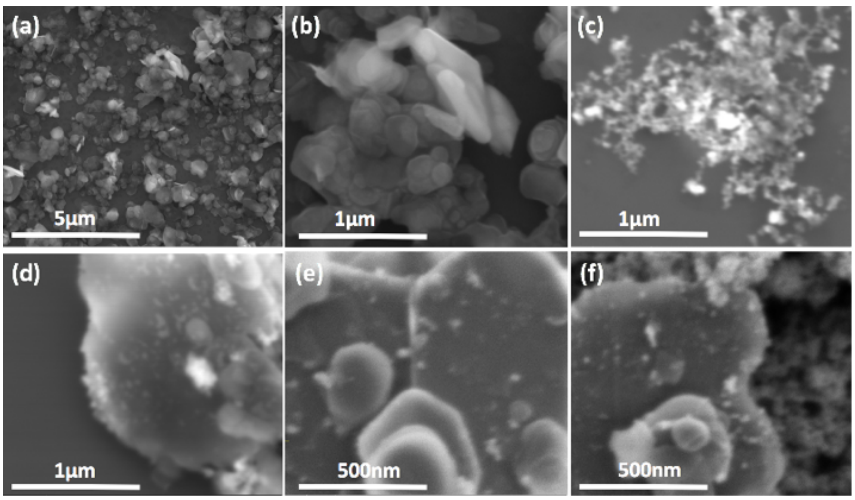

Figure 5.7. SEM images: (a, b) *h*-BN as received. (c) Magnetite formed in the absence of *h*-BN.[26] (d-f) *h*-BN@magnetite; laser operation at 1064 nm and 360 mJ, rotational speed 7.5k rpm, and flow rate of *h*-BN disperse in water (0.1 mg/mL) at 1 mL/min.

(101), 59.5 (102) and 64.8 (004) corresponding to *h*-BN sheets, and peaks at 21.2 (111), 35.5 (220), 41.8 (311), 50.8 (400), 63.4 (422), 67.7 (511) and 74.6 (440) corresponding to magnetite, Figure 5.9a.[45-47] The Raman spectrum has a peak at 1366 cm^{-1} which is consistent with the presence of *h*-BN, as the E_{2g} symmetry band,[48,49] with a peak at 678 cm^{-1} corresponding to that expected for the presence of magnetite nanoparticles, Figure 5.9b.[50] According to the literature, magnetite nanoparticles <20 nm should be superparamagnetic, and this was indeed the case in determining the saturation magnetization (M) which is essentially constant at 34 Am^2/kg Figure 5.9c.[51,52] In contrast, the saturation magnetization (M) of magnetite nanoparticles formed in the VFD in the absence of *h*-BN was 41 Am^2/kg, where the size of the magnetite particles is similar.[26] The reduction in saturation magnetization (M) of about 7 Am^2/kg in the composite material is consistent with attachment of the particles to the *h*-BN. In addition, the low-field interval of the magnetization curves shows very little coercivity and remanence consistent with the presence of predominately superparamagnetic particles, Figure 5.9d. ATR-FTIR and FTIR microscopy established a shift in both B–N stretching and B–N–B bending vibrations, respectively from 1348 cm^{-1} in *h*-BN to 1372cm^{-1} in the composite material, and 768 cm^{-1} to 800 cm^{-1}, Figure S5.7.[53,54] In addition, the spectrum of *h*-BN@magnetite has a peak at 624 cm^{-1} corresponding to Fe–O–Fe vibrations in magnetite, Figure S5.7.[55]

Comparing XPS data for as received *h*-BN and *h*-BN@magnetite Figure 5.10a and b clearly establishes the presence of magnetite in the latter, with binding energies peaks for Fe $2p_{1/2}$ and Fe $2p_{3/2}$ at 724.4 eV and 710.7 eV respectively (Figure 5.10d).[56-58] The main XPS peak corresponding to oxygen atoms in magnetite are at 530.1 eV, Figure 5.10c.[46]

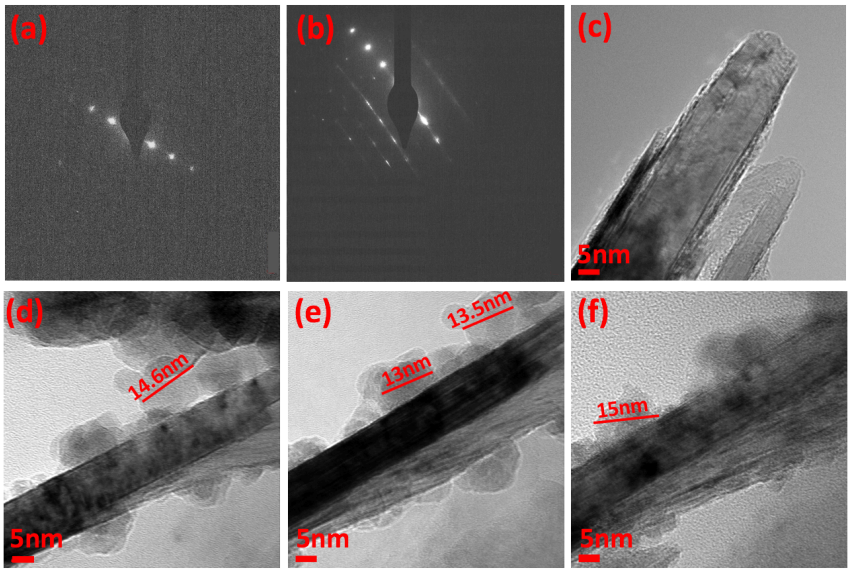

Figure 5.8. (a and b) SAED and HRTEM image of *h*-BN as received. (b, d-f) SAED and HRTEM images for *h*-BN@magnetite with the laser operating at 1064 nm and 360 mJ, rotational speed 7.5k rpm, and flow rate of *h*-BN dispersed in water (0.1 mg/mL) at 1 mL/min.

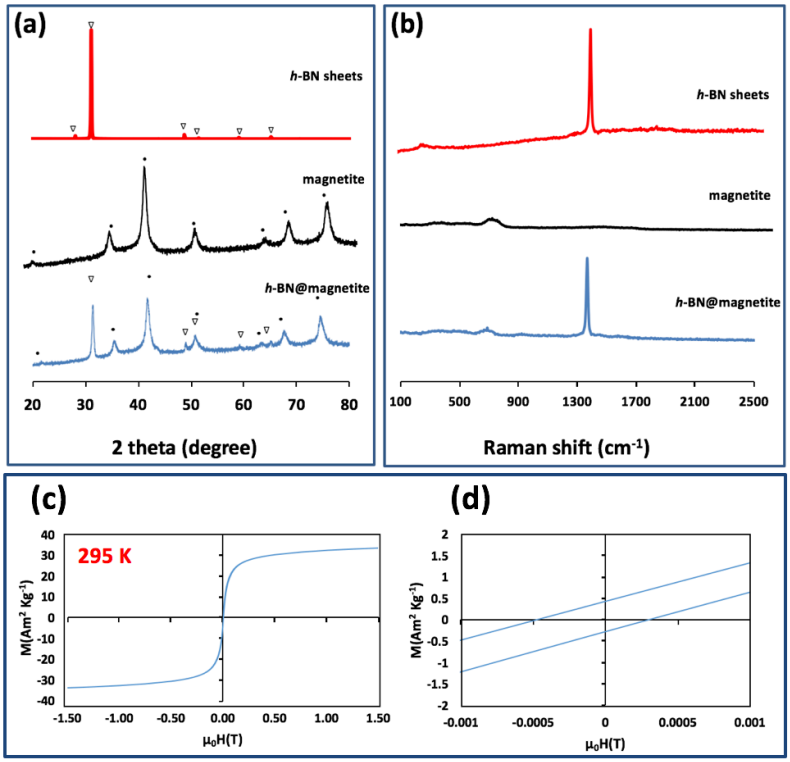

Figure 5.9. (a and b) X- ray diffraction and Raman spectra respectively of *h*-BN sheets as received, magnetite (in the absence of *h*-BN),[26] and *h*-BN@magnetite. (c) Magnetization saturation for *h*-BN@magnetite. (d) Low-field interval of the magnetization curves of h-BN@magnetite; laser operating at 1064 nm and 360 mJ, rotational speed 7.5k rpm, and flow rate of h-BN disperse in water (0.1 mg/mL) at 1 mL/min.

Phosphate removal efficiency of the material were tested by applying three different loading concentrations of the identical *h*-BN@magnetite sample as the adsorbent (10 mg; 25 mg; 50 mg), which were separately mixed with phosphate containing artificial aquatic-media having an initial phosphate concentration of 23.2 ± 0.15 mg/L, which is in the range of a typical sewage and urban wastewaters with 10-30 mg/L phosphate levels.[59] According to our previous findings with superparamagnetic imposed diatom frustules[39] and mesocellular siliceous foams impregnated with iron oxide,[40] the 30th minute was chosen as the optimal time-interval for measuring the phosphate removal capacity of the adsorbent. After 30 minutes, the initial phosphate concentration (23.2 ± 0.15 mg/L) dropped to around 0.9 mg/L (96.1% removal efficiency) with 10 mg adsorbent; 0.2 mg/L (99.1% removal efficiency) with 25 mg adsorbent; and 0.15 mg/L (99.4% removal efficiency) with 50 mg adsorbent. Used samples were then washed with deionized water through hand-vortexing for 1 minute, followed by the removal of supernatant after its centrifugation at 13148 ×g for 5 minutes. Remaining samples were then mixed again with phosphate-containing fresh media (1.25 mL), and the phosphate content of the consecutive cycle was analysed after 30 minutes. As shown in Figure 5.11, the increase in adsorbent loading from 10 mg to 25 mg had a positive effect on the total amount of PO_4^{3-} adsorbed during consecutive cycles. It was also observed that higher loadings of adsorbent (25 and 50 mg) had similar phosphate

adsorption efficiencies, revealing the sufficiency of 25 mg adsorbent for this process. By the end of the 5th consecutive cycle, 50 and 25 mg of adsorbents yielded an overall phosphate adsorption value of around 113.5 mg/L, which was followed by 78.8 mg/L by a 10 mg sample. Recycling the material for sequential mechanical-mixing and washing steps has been proven to be highly effective for the reutilization of the magnetic *h*-BN material as an adsorbent, especially for the highest adsorbent loadings (25, and 50 mg) that particularly sustained their adsorption capacities. On the other hand, 10 mg adsorbent showed lower recovery compared to the higher loadings after each recycling step (Figure 5.11 and S5.11), revealing that the active sites of magnetic nanoparticles on the surface started to get saturated with phosphate ions. Due to the fact that the iron oxide component is mainly responsible for the phosphate removal,[32,39,40] converting the phosphate removal values into their adsorption capacities revealed a reverse correlation between the overall phosphate adsorption capacity and the adsorbent loading

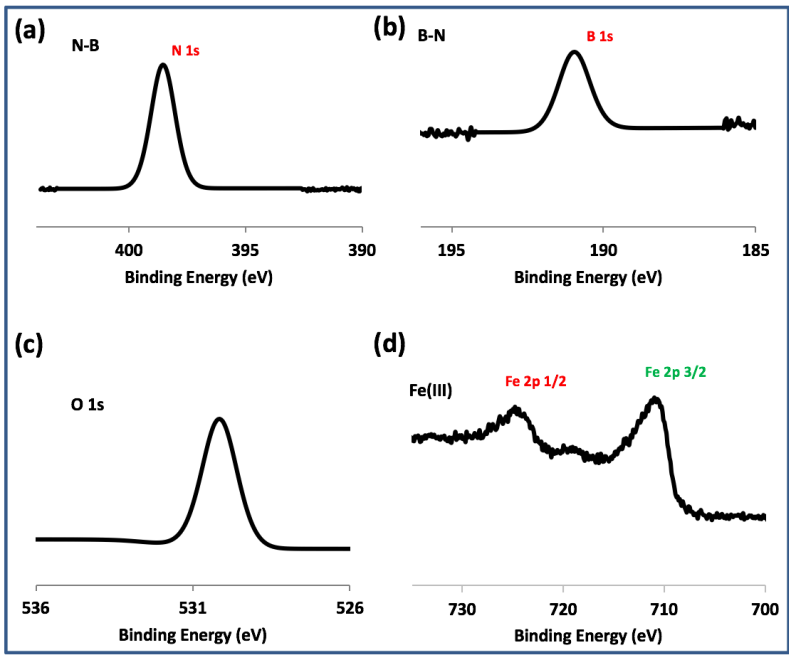

Figure 5.10. XPS spectra of *h*-BN@magnetite; laser operating at 1064 nm and 360mJ, rotational speed 7.5k rpm, and flow rate of *h*-BN disperse in water (0.1 mg/mL) at 1 mL/min.

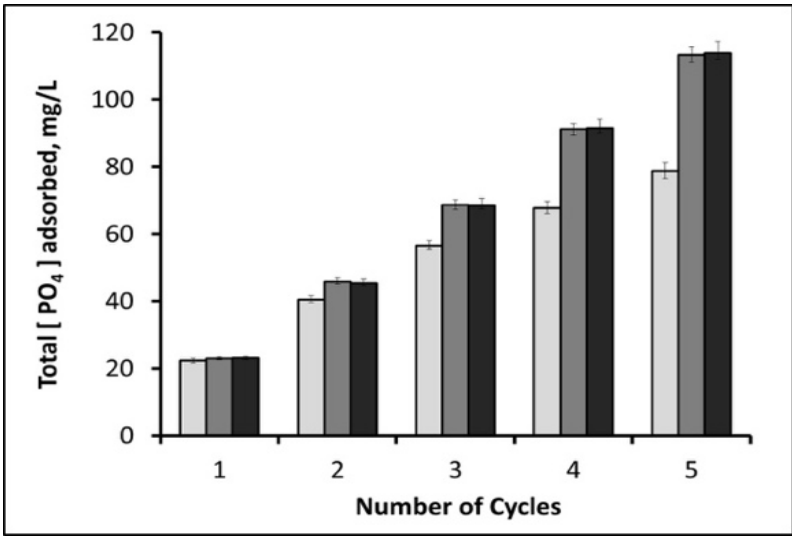

Figure 5.11. Cumulative amount of PO_4^{3-} adsorbed in mg/L after each sequential cycle, for three different loadings of magnetic *h*-BN samples: (1) 10 mg adsorbent (light-grey columns); (2) 25 mg adsorbent (dark-grey columns); and (3) 50 mg adsorbent (black columns).

concentration. Since the material has an iron content of 5.75% (w/w) (atomic absorption spectroscopy), 10 mg sample yielded an overall adsorption capacity of 171.2 mg PO_4^{3-} per gram Fe, followed by 98.5 mg PO_4^{3-} per gram Fe for 25 mg sample, and 49.5 mg PO_4^{3-} per gram Fe for 50 mg sample. These values are within the higher range of the other literature data reported for the various types of adsorbents containing iron oxide nanoparticles.[39,40,59] In our previous studies, superparamagnetic imposed diatom frustules achieved an overall adsorption capacity of around 45 mg PO_4^{3-} per gram Fe,[39] and mesocellular siliceous foams impregnated with iron oxide showed an overall adsorption capacity of around 79.2 mg PO_4^{3-} per gram Fe.[40] High adsorption capacities of the current study reveal the suitability of *h*-BN structure as an ideal frame for the active sites of magnetic nanoparticles.

5.5 Conclusion

The as-synthesis new composite *h*-BN@magnetite is directly available as a one-step synthesis, using a VFD, without the need for adding any other materials or potentially toxic solvent. The superparamagnetic magnetite nanoparticles in *h*-BN@magnetite are dispersed randomly on the *h*-BN surface, with the composite material having high porosity, with a surface area of 91.03 m^2/g. The surface lends itself for binding functional materials, including catalysts,[55] and for application in waste water treatment. This has been established in binding of phosphate in waste water, with the *h*-BN@magnetite being readily collected using a magnetic field. Also significant is that the phosphate adsorption capacity is up to 171.2 mg PO_4^{3-} per gram of Fe, and the materials can be readily recycled.

5.6 Acknowledgements

The authors gratefully acknowledge financial support from the Australian Research Council and the Government of South Australia, and the Iraq Government, Ministry of Higher Education and Scientific research. The Australian Microscopy & Microanalysis Research Facility and the Australian National Fabrication Facility are acknowledged, as is Dr Jason Gascooke for assistance with SEM.

5.7 References

1. Shi, Y.; Hamsen, C.; Jia, X.; Kim, K. K.; Reina, A.; Hofmann, M.; Hsu, A. L.; Zhang, K.; Li, H.; Juang, Z.-Y.; Dresselhaus, M. S.; Li, L.-J.; Kong, J., Synthesis of Few-Layer Hexagonal Boron Nitride Thin Film by Chemical Vapor Deposition. *Nano Letters*

2010, *10* (10), 4134-4139.
2. Han, W.-Q. *Anisotropic Hexagonal Boron Nitride Nanomaterials-Synthesis and Applications*; Brookhaven National Laboratory: 2008, Vol. 41, pp. 1–60.

3. Huang, C., liu Q., Fan W. & Qiu X. .Boron nitride encapsulated copper nanoparticles: a facile one-step synthesis and their effect on thermal decomposition of ammonium perchlorate. *Scientific reports* **2015,** *5*, 16736.
4. Watanabe, K.; Taniguchi, T.; Kanda, H., Direct-bandgap properties and evidence for ultraviolet lasing of hexagonal boron nitride single crystal. *Nature materials* **2004,** *3* (6), 404.
5. Kubota, Y.; Watanabe, K.; Tsuda, O.; Taniguchi, T., Deep ultraviolet light-emitting hexagonal boron nitride synthesized at atmospheric pressure. *Science* **2007,** *317* (5840), 932-934.
6. Watanabe, K.; Taniguchi, T.; Niiyama, T.; Miya, K.; Taniguchi, M., Far-ultraviolet plane-emission handheld device based on hexagonal boron nitride. *Nature Photonics* **2009,** *3*, 591.
7. Han, W.-Q.; Wu, L.; Zhu, Y.; Watanabe, K.; Taniguchi, T., Structure of chemically derived mono-and few-atomic-layer boron nitride sheets. *Applied Physics Letters* **2008,** *93* (22), 223103.
8. Lin, Q.; Zou, X.; Zhou, G.; Liu, R.; Wu, J.; Li, J.; Duan, W., Adsorption of DNA/RNA nucleobases on hexagonal boron nitride sheet: an ab initio study. *Physical Chemistry Chemical Physics* **2011,** *13* (26), 12225-12230.
9. Ding, N.; Chen, X.; Wu, C.-M. L.; Li, H., Adsorption of nucleobase pairs on hexagonal boron nitride sheet: hydrogen bonding versus stacking. *Physical Chemistry Chemical Physics* **2013,** *15* (26), 10767-10776.
10. Lin, Y.; Connell, J. W., Advances in 2D boron nitride nanostructures: nanosheets, nanoribbons, nanomeshes, and hybrids with graphene. *Nanoscale* **2012,** *4* (22), 6908-6939.
11. Fujigaya, T.; Nakashima, N., Methodology for homogeneous dispersion of single-walled carbon nanotubes by physical modification. *Polymer journal* **2008,** *40* (7), 577-589.
12. Hwang, D. Y.; Choi, K. H.; Park, J. E.; Suh, D. H., Evolution of magnetism by rolling up hexagonal boron nitride nanosheets tailored with superparamagnetic nanoparticles. *Physical Chemistry Chemical Physics* **2017,** *19* (5), 4048-4055.
13. Huang, C.; Chen, C.; Ye, X.; Ye, W.; Hu, J.; Xu, C.; Qiu, X., Stable colloidal boron nitride nanosheet dispersion and its potential application in catalysis. *Journal of Materials Chemistry A* **2013,** *1* (39), 12192-12197.
14. Britton, J.; Chalker, J. M.; Raston, C. L., Rapid Vortex Fluidics: Continuous Flow Synthesis of Amides and Local Anesthetic Lidocaine. *Chemistry–A European Journal* **2015,** *21* (30), 10660-10665.
15. Gandy, M. N.; Raston, C. L.; Stubbs, K. A., Towards aryl C-N bond formation in dynamic thin films. *Organic and Biomolecular Chemistry* **2014,** *12* (26), 4594-4597.
16. Pye, S. J.; Dalgarno, S. J.; Chalker, J. M.; Raston, C. L., Organic oxidations promoted in vortex driven thin films under continuous flow. *Green Chemistry* **2018,** *20* (1), 118-124.
17. Alsulami, I.; Alharbi, T.; Harvey, D.; Gibson, C. T.; Raston, C. L., Controlling the growth of fullerene C_{60} cones under continuous flow. *Chemical Communications* **2018**, 54 (57),

7896-7899.
18. Vimalanathan, K.; Shrestha, R. G.; Zhang, Z.; Zou, J.; Nakayama, T.; Raston, C. L., Surfactant-free Fabrication of Fullerene C_{60} Nanotubules Under Shear. *Angewandte Chemie* **2017,** *129* (29), 8518-8521.
19. Yuan, T. Z.; Ormonde, C. F.; Kudlacek, S. T.; Kunche, S.; Smith, J. N.; Brown, W. A.; Pugliese, K. M.; Olsen, T. J.; Iftikhar, M.; Raston, C. L., Shear-Stress-Mediated Refolding of Proteins from Aggregates and Inclusion Bodies. *ChemBioChem* **2015,** *16* (3), 393-396.
20. Luo, X.; Smith, P.; Raston, C.; Zhang, W., Vortex fluidic device-intensified aqueous two phase extraction of C-phycocyanin from Spirulina maxima. *ACS Sustainable Chemistry & Engineering* **2016,** *4* (7), 3905-3911.
21. Chen, X.; Dobson, J. F.; Raston, C. L., Vortex fluidic exfoliation of graphite and boron nitride. *Chemical Communications* **2012,** *48* (31), 3703-3705.
22. Luo, X.; Al-Antaki, A. H. M.; Vimalanathan, K.; Moffatt, J.; Zheng, K.; Zou, Y.; Zou, J.; Duan, X.; Lamb, R. N.; Wang, S.; Li, Q.; Zhang, W.; Raston, C. L., Laser irradiated vortex fluidic mediated synthesis of luminescent carbon nanodots under continuous flow. *Reaction Chemistry & Engineering* **2018,** *3* (2), 164-170.
23. Yasmin, L.; Chen, X.; Stubbs, K. A.; Raston, C. L., Optimising a vortex fluidic device for controlling chemical reactivity and selectivity. *Scientific reports* **2013,** *3*, 2282.
24. Britton, J.; Stubbs, K. A.; Weiss, G. A.; Raston, C. L., Vortex fluidic chemical transformations. *Chemistry–A European Journal* **2017,** *23* (54), 13270-13278.
25. Chen, X.; Boulos, R. A.; Dobson, J. F.; Raston, C. L., Shear induced formation of carbon and boron nitride nano-scrolls. *Nanoscale* **2013,** *5* (2), 498-502.
26. Luo, X.; Al-Antaki, A. H. M.; Alharbi, T. M. D.; Hutchison, W. D.; Zou, Y.-c.; Zou, J.; Sheehan, A.;Zhang, W.; Raston, C. L., Laser-Ablated Vortex Fluidic-Mediated Synthesis of Superparamagnetic Magnetite Nanoparticles in Water Under Flow. *ACS Omega* **2018,** *3* (9), 11172-11178.
27. Teja, A. S.; Koh, P.-Y., Synthesis, properties, and applications of magnetic iron oxide nanoparticles. *Progress in crystal growth and characterization of materials* **2009,** *55* (1), 22-45.
28. Vahabzadeh, E.; Torkamany, M., Iron Oxide Nanocrystals Synthesis by Laser Ablation in Water: Effect of Laser Wavelength. *Journal of Cluster Science* **2014,** *25* (4), 959-968.
29. Salik, M.; Hanif, M.; Wang, J.; Zhang, X., Plasma properties of nano-second laser ablated iron target in air. *International Journal of Physical Sciences* **2013,** *8* (35), 1738-1745.
30. Mahmoudi, M.; Sant, S.; Wang, B.; Laurent, S.; Sen, T., Superparamagnetic iron oxide nanoparticles (SPIONs): development, surface modification and applications in chemotherapy. *Advanced drug delivery reviews* **2011,** *63* (1), 24-46.
31. Pizzolato, E.; Scaramuzza, S.; Carraro, F.; Sartori, A.; Agnoli, S.; Amendola, V.; Bonchio, M.; Sartorel, A., Water oxidation electrocatalysis with iron oxide nanoparticles prepared via laser ablation. *Journal of Energy Chemistry* **2016,** *25* (2), 246-250.
32. Smith, V. H.; Tilman, G. D.; Nekola, J. C., Eutrophication: impacts of excess nutrient inputs on freshwater, marine, and terrestrial ecosystems. *Environmental pollution* **1999,** *100* (1-3), 179-196.
33. Zeng, L.; Li, X.; Liu, J., Adsorptive removal of phosphate from aqueous solutions using

iron oxide tailings. *Water research* **2004,** *38* (5), 1318-1326.
34. Morse, G. K.; Brett, S. W.; Guy, J. A.; Lester, J. N., Review: Phosphorus removal and recovery technologies. *Science of The Total Environment* **1998,** *212* (1), 69-81.
35. Huang, W.; Wang, S.; Zhu, Z.; Li, L.; Yao, X.; Rudolph, V.; Haghseresht, F., Phosphate removal from wastewater using red mud. *Journal of Hazardous Materials* **2008,** *158* (1), 35-42.
36. Tanada, S.; Kabayama, M.; Kawasaki, N.; Sakiyama, T.; Nakamura, T.; Araki, M.; Tamura, T., Removal of phosphate by aluminum oxide hydroxide. *Journal of Colloid and Interface Science* **2003,** *257* (1), 135-140.
37. Xiong, W.; Peng, J., Development and characterization of ferrihydrite-modified diatomite as a phosphorus adsorbent. *Water Research* **2008,** *42* (19), 4869-4877.
38. Bolch, C. J.; Blackburn, S. I., Isolation and purification of Australian isolates of the toxic cyanobacteriumMicrocystis aeruginosa Kütz. *Journal of Applied Phycology* **1996,** *8* (1), 5-13.
39. Toster, J.; Kusumawardani, I.; Eroglu, E.; Iyer, K. S.; Rosei, F.; Raston, C. L., Superparamagnetic imposed diatom frustules for the effective removal of phosphates. *Green Chemistry* **2014,** *16* (1), 82-85.
40. Tong, C. L.; Eroglu, E.; Raston, C. L., In situ synthesis of phosphate binding mesocellular siliceous foams impregnated with iron oxide nanoparticles. *RSC Advances* **2014,** *4* (87), 46718-46722.
41. M. C. Rand, Arnold E. Greenberg, Michael J. Taras, Standard methods for the examination of water and wastewater. *American Public Health Association (APHA): Washington, DC, USA* **2005**.
42. Vimalanathan, K.; Gascooke, J. R.; Suarez-Martinez, I.; Marks, N. A.; Kumari, H.; Garvey, C. J.; Atwood, J. L.; Lawrance, W. D.; Raston, C. L., Fluid dynamic lateral slicing of high tensile strength carbon nanotubes. *Scientific reports* **2016,** *6*, 22865.
43. Pan, B.-f.; Gao, F.; Gu, H.-c., Dendrimer modified magnetite nanoparticles for protein immobilization. *Journal of colloid and interface science* **2005,** *284* (1), 1-6.
44. Pan, B.; Gao, F.; Gu, H., Synthesis and characterization of surface-hyperbranched magnetite nanoparticle for bovine serum albumin immobilization. *China Particuology* **2004,** *2* (6), 261-265.
45. Hou, X.; Wang, M.; Fu, L.; Chen, Y.; Jiang, N.; Lin, C.-T.; Wang, Z.; Yu, J., Boron nitride nanosheet nanofluids for enhanced thermal conductivity. *Nanoscale* **2018**.
46. Lim, H. S.; Oh, J. W.; Kim, S. Y.; Yoo, M.-J.; Park, S.-D.; Lee, W. S., Anisotropically alignable magnetic boron nitride platelets decorated with iron oxide nanoparticles. *Chemistry of Materials* **2013,** *25* (16), 3315-3319.
47. Andrade, A.; Souza, D.; Pereira, M.; Fabris, J.; Domingues, R., Synthesis and characterization of magnetic nanoparticles coated with silica through a sol-gel approach. *Cerâmica* **2009,** *55* (336), 420-424.
48. Suh, D. H., Formation of hexagonal boron nitride nanoscrolls induced by inclusion and exclusion of self-assembling molecules in solution process. *Nanoscale* **2014,** *6* (11), 5686-5690.
49. Reich, S.; Ferrari, A.; Arenal, R.; Loiseau, A.; Bello, I.; Robertson, J., Resonant Raman scattering in cubic and hexagonal boron nitride. *Physical Review B* **2005,** *71* (20), 205201.
50. Chourpa, I.; Douziech-Eyrolles, L.; Ngaboni-Okassa, L.; Fouquenet, J.-F.; Cohen-

Jonathan, S.; Soucé, M.; Marchais, H.; Dubois, P., Molecular composition of iron oxide nanoparticles, precursors for magnetic drug targeting, as characterized by confocal Raman microspectroscopy. *Analyst* **2005,** *130* (10), 1395-1403.

51. Aghaie, A. B.; Hadjmohammadi, M. R., Fe_3O_4@ p-Naphtholbenzein as a novel nano-sorbent for highly effective removal and recovery of Berberine: Response surface methodology for optimization of ultrasound assisted dispersive magnetic solid phase extraction. *Talanta* **2016,** *156*, 18-28.
52. Jafari, A.; Salouti, M.; Shayesteh, S. F.; Heidari, Z.; Rajabi, A. B.; Boustani, K.; Nahardani, A., Synthesis and characterization of Bombesin-superparamagnetic iron oxide nanoparticles as a targeted contrast agent for imaging of breast cancer using MRI. *Nanotechnology* **2015,** *26* (7), 075101.
53. Gautam, C.; Tiwary, C. S.; Jose, S.; Brunetto, G.; Ozden, S.; Vinod, S.; Raghavan, P.; Biradar, S.; Galvao, D. S.; Ajayan, P. M., Synthesis of Low-Density, Carbon-Doped, Porous Hexagonal Boron Nitride Solids. *ACS nano* **2015,** *9* (12), 12088-12095.
54. Tang, C.; Bando, Y.; Huang, Y.; Zhi, C.; Golberg, D., Synthetic routes and formation mechanisms of spherical boron nitride nanoparticles. *Advanced Functional Materials* **2008,** *18* (22), 3653-3661.
55. Molla, A.; Hussain, S., Base free synthesis of iron oxide supported on boron nitride for the construction of highly functionalized pyrans and spirooxindoles. *RSC Advances* **2016,** *6* (7), 5491-5502.
56. Yamashita, T.; Hayes, P., Analysis of XPS spectra of Fe 2+ and Fe 3+ ions in oxide materials. *Applied Surface Science* **2008,** *254* (8), 2441-2449.
57. Aronniemi, M.; Lahtinen, J.; Hautojärvi, P., Characterization of iron oxide thin films. *Surface and interface analysis* **2004,** *36* (8), 1004-1006.
58. Graat, P. C. J.; Somers, M. A. J., Simultaneous determination of composition and thickness of thin iron-oxide films from XPS Fe 2p spectra. *Applied Surface Science* **1996,** *100*, 36-40.
59. Zach-Maor, A.; Semiat, R.; Shemer, H., Fixed bed phosphate adsorption by immobilized nano-magnetite matrix: experimental and a new modeling approach. *Adsorption* **2011,** *17* (6), 929-936.

RSC Advances

PAPER

View Article Online
View Journal | View Issue

Cite this: *RSC Adv.*, 2018, **8**, 40829

Continuous flow synthesis of phosphate binding h-BN@magnetite hybrid material†

Ahmed Hussein Mohammed Al-antaki,[a] Xuan Luo,[ab] Alex Duan,[c] Robert N. Lamb,[c] Ela Eroglu,[d] Wayne Hutchison,[e] Yi-Chao Zou,[f] Jin Zou[f] and Colin L. Raston*[a]

Hexagonal boron nitride (h-BN) is rendered magnetically responsive in aqueous media by binding superparamagnetic magnetite nanoparticles 8.5–18.5 nm in diameter on the surface. The composite material was generated under continuous flow in water in a dynamic thin film in a vortex fluidic device (VFD) with the source of iron generated by laser ablation of a pure iron metal target in the air above the liquid using a Nd:YAG pulsed laser operating at 1064 nm and 360 mJ. Optimum operating parameters of the VFD were a rotational speed of 7.5k rpm for the 20 mm OD (17.5 mm ID) borosilicate glass tube inclined at 45 degrees, with a h-BN concentration at 0.1 mg mL^{-1}, delivered at 1.0 mL min^{-1} using a magnetically stirred syringe to keep the h-BN uniformly dispersed in water prior to injection into the base of the rapidly rotating tube. The resulting composite material, containing 5.75% weight of iron, exhibited high phosphate ion adsorption capacity, up to 171.2 mg PO_4^{3-} per gram Fe, which was preserved on recycling the material five times.

Received 9th October 2018
Accepted 22nd November 2018

DOI: 10.1039/c8ra08336c

rsc.li/rsc-advances

Introduction

Polymorphs of boron nitride include the hexagonal arrangement of alternating sp^2 hybridized boron and nitrogen atoms in 2D sheets, which is isostructural to graphene sheets in graphite, and this similarity in structure is attracting attention. However, in contrast to graphite, layered hexagonal boron nitride (h-BN) is transparent and is an insulator,[1] and its dielectric and thermal properties make it useful for different electronic applications such as thermal interface materials for semiconductor packaging.[2,3] In general, hexagonal carbon (h-C), where there are hexagonal six membered rings, can be metallic or semiconducting, depending on the dimensions and overall structure, whereas h-BN has a large band gap around 5.9 eV and the material is typically an insulator or indirect semiconductor.[4–6] Electron energy loss spectroscopy (EELS) provides information on the number of layers in h-BN in a similar way to that of graphite.[7] In contrast to graphene, h-BN has potential use as a vehicle for the delivery of protein and nucleobases.[8,9] This arises from coordination of N or O donor groups in these macromolecules with electron deficient boron atoms in the h-BN. Such interactions are stronger than π–π interactions which prevail between graphene sheets or between carbon nanotube (CNTs) and the like.[10,11] Multilayers of h-BN bind nanomaterials in imparting new properties, for example, magnetic response.[12,13] The vortex fluidic device (VFD) is a thin film microfluidic platform which has a number of applications, including enhancing enzymatic reactions and organic synthesis, probing the structure of self-organised systems, protein folding, protein separation, exfoliation of 2D graphite and boron nitride, the fabrication of carbon dots, and more.[14–22] The VFD has a borosilicate glass tubes (typically 20 mm in OD diameter, 17.5 mm ID diameter) open at one end, and is rotated at high speed (up to 9000 rpm) while inclined at an angle, from 0° to 90° relative to the horizontal position. The VFD can be used in two different modes of operations, (i) the confined mode for processing a finite volume of liquid in the rapidly rotating tube, and (ii) continuous flow mode where liquid is constantly fed into the tube, so that the processing can be scaled up, allowing the processing of large volumes by extending the operating time.[23] The confined mode of operation of the VFD is often used as a proven starting point for optimizing a process, for fast tracking into continuous flow processing, Fig. 1.[24] In further exploring the expanding applications of the VFD,[23,25] we have investigated for the first time its use in preparing a composite material, containing both h-BN and superparamagnetic magnetite nanoparticles. The h-NB is

[a]*Institute for Nanoscale Science and Technology, College of Science and Engineering, Flinders University, Adelaide, SA 5042, Australia. E-mail: colin.raston@flinders.edu.au*
[b]*Centre for Marine Bioproducts Development, College of Medicine and Public Health, Flinders University, Adelaide, SA 5042, Australia*
[c]*Trace Analysis for Chemical, Earth and Environmental Sciences (TrACEES), The University of Melbourne, Victoria 3010, Australia*
[d]*Department of Chemical Engineering, Curtin University, Perth, Australia*
[e]*School of PEMS, University of New South Wales, ADFA Campus, Canberra BC, ACT 2610, Australia*
[f]*Materials Engineering and Centre for Microscopy and Microanalysis, The University of Queensland, Brisbane, QLD 4072, Australia*

† Electronic supplementary information (ESI) available: Experimental details and characterisation results (Fig. S1–S10). See DOI: 10.1039/c8ra08336c

6. Dynamic thin film mediated slicing of boron nitride nanotubes

Ahmed Hussein Mohammed Al-antaki[a,b], Warren D. Lawrance[c] and Colin L. Raston*[a]

a. *Flinders Institute for Nanoscale Science and Technology, College of Science and Engineering, Flinders University, Adelaide, SA 5042, Australia.*
b. *Department of Chemistry, Faculty of Sciences, Kufa University, Kufa, Najaf, Iraq.*
c. *College of Science and Engineering, Flinders University, Adelaide, SA 5042.*

Author contributions: **AA** performed all the VFD and all characterisation experiments; wrote all the primary content. **WL** and **CR** supervised and coordinated the project and helped on the research directions and plan, and the final revision of the manuscript. All of the co-authors assisted with the revision of the manuscript before and during the publication process.

Graphical Abstract

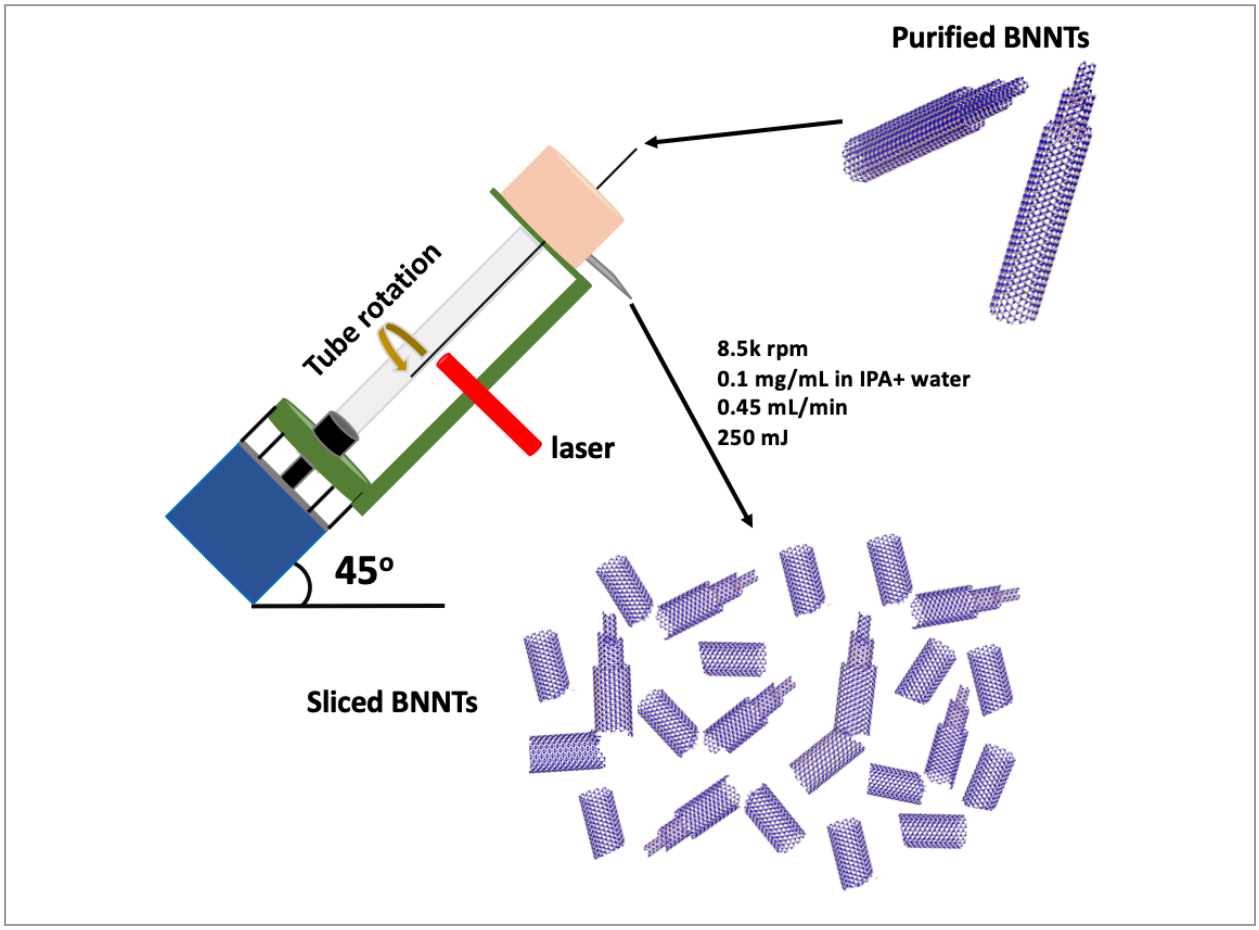

6.1 Abstract

A method has been developed to slice boron nitride nanotubes BNNTs under continuous flow in a vortex fluidic device (VFD), along with a method to partially purify the as received BNNT containing material. The latter involves heating the BNNTs to 600^{o}C followed by dispersing in a 1:3 isopropyl alcohol (IPA) and water mixture at 100^{o}C. The VFD mediated slicing of the BNNTs comprises irradiating the rapidly rotating glass tube (20 mm O.D.) with a pulsed Nd:YAG laser. Systematically exploring the operating parameter space of the VFD established slicing of ca 200 μm long purified BNNTs down to 340 nm to 400 nm, in ca 53 % yield, in a 1:1 mixture of IPA and water, in the absence of reagents/harsh chemicals, at a flow rate of 0.45 mL/min, concentration of BNNTs 0.1 mg/mL and rotational speed 8.5k rpm, with the pulsed laser operating at 1064 nm and 250 mJ/pulse.

6.2 Introduction

The first report of boron nitride nanotubes (BNNTs) was in 1995.[1] The one dimensional (1D) tubular nanostructures (nanotubes) are related to the structure of the ubiquitous carbon nanotubes (CNTs). However, BNNTs possess different physical properties, including having a wide band gap (5.5 eV) dielectric,[1,2] with photogalvanic,[3] thermal conductivity and stability at high temperature (up 900^{o}C),[4] and high neutron absorption.[5] Methods for preparing BNNTs encompass substitution reactions,[6] laser ablation,[7] chemical vapour deposition (CVD),[8,9] arc-discharge[1,10] and ball-milling.[11] There are three inter-related boron nitride structures, (i) straight-walled BNNT,[12,13] (ii) bamboo-type BN[13-15] and (iii) flower-type BN.[16] The straight BNNTs have potential in a number of applications, including in boron neutron capture therapy (BNCT),[5,17] hydrogen storge,[16] orthopaedic implants,[18] biosensing[19] and biomedical areas in general,[2] and more.[20-22] The length of BNNTs is important in a number of applications, in nanodevices,[20] nanomedicines,[22] sensors and composites.[21] Controlling the length of BNNTs has been investigated using sonication,[23,24] atomic force microscopy (AFM)[25,26] and directly during chemical vaper deposition (CVD).[9,27] However, these have limitations associated with damaging the BNNTs, scalability of the processing and the choice of catalyst and temperature, for the aforementioned items (i) – (iii) respectively.

Single walled carbon nanotubes (SWCNTs) and multi-walled carbon nanotubes, can be sliced under high shear in a colloidal suspension in a vortex fluidic device (VFD), Figure 6. 1.[28,29] The length of the sliced CNTs depends on the rotational speed of a borosilicate glass or quartz tube inclined at 45^{o} relative to the horizontal position, the flow rate of liquid, concentration of the starting material and the power of the pulsed laser operating at 1064

nm.[28,29] This motivated us to explore the utility of this approach to slice BNNTs in an analogous way, in the absence of additional reagents and harsh chemicals. The results are reported herein, along with a method for purifying the as received BNNTs prior to VFD processing, which we deemed necessary for simplifying the processing and any ensuing applications of the material.

The vortex fluidic device (VFD)[28,30-32] has a glass or quartz tube (O.D. 20 mm, I.D. 17.5 mm and 19.5 cm in length) open at one end, and is rotated at high speed (typically up to 9k rpm) and inclined at an angle of 0 to 90° relative to the horizontal position, Figure 6.1. It has two types of processing, the confined mode where a finite volume of liquid is added to the rapidly rotating tube, and the continuous flow mode.[33] The former was initially used in the present study to optimise the processing before translating it into continuous flow, Figure 6.1, as an often successful approach for any new application of the device.[33] Overall the VFD is a versatile microfluidic platform. Beyond the above mentioned slicing of CNTs,[28,29] it has been used to decorate *h*-BN with magnetite nanoparticles involving an *in situ* laser ablation of an iron rod above the dynamic thin film,[34] probe the structure of self-organised systems,[35] and control organic synthesis,[31,36] catalysis,[37] the formation of carbon dots,[38] and more.[30,32,39-41]

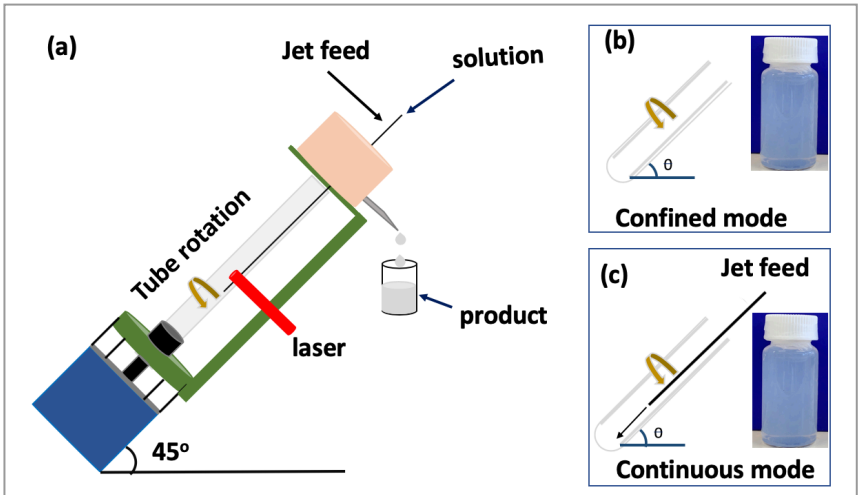

Figure 6.1. (a) Diagram of a VFD housing a rapidly rotating tube (20 mm O.D., 17.5 mm I.D. and length 19.5 cm) tilted at θ, for operating under (b) the confined mode and (c) continuous flow, where liquid is delivered through a jet feed with the photographs in (b) and (c) of colloidal suspensions of sliced BNNTs. Optimized conditions for continuous flow processing; flow rate of BNNTs in a 1:1 mixture of IPA and water, 0.45 mL/min, concentration 0.1 mg/mL, rotational speed 8.5k rpm and θ 45°, with the liquid irradiated by a pulsed Nd:YAG laser (pulse duration ~5 ns) operating with 250 mJ/pulse at 1064 nm.

6.3 Experimental

6.3.1 Materials. BNNTs were purchased from NanoIntegris with a purity ≥ 50% and average tube length and diameter *ca* 200 um and 5 nm, respectively, as specified the

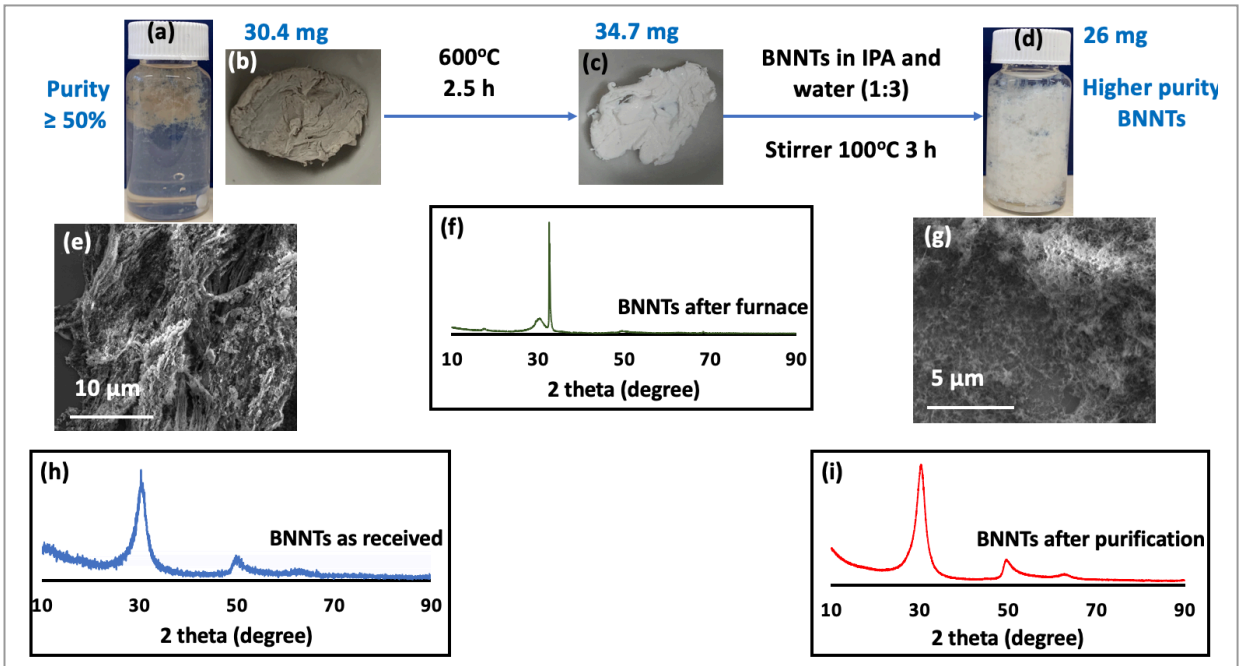

Figure 6.2. (a, b) As received BNNTs in water. (c) Material after heating for 2.5 h at 600°C. (d) BNNTs dispersed in IPA and water (1:3) to remove impurities. (e) SEM image for as received BNNTs. (f) XRD for BNNTs after heating at 600°C. (g) SEM image of the material after removing some impurities. (h) XRD for as received BNNTs. (i) XRD for purified BNNTs.

company. Distilled IPA (isopropanol), purchased from Sigma-Aldrich, and Milli-Q water were used for all experiments.

6.3.2 Purification of BNNTs. To improve the purity of BNNTs ≥ 50%, they were initially heated (30.4 mg of BNNTs as received ,materials) in air at 600°C for 2.5 hours. The resulting partially oxidised material (34.7 mg) containing boric oxide,[42,43] was dispersed in IPA and water (1:3) with dissolution of the boric oxide. The material housed in a sealed vial was stirred for 3 hours at 100°C. Centrifugation (4800 × g) for 5 mins was effective in collecting the BNNTs, which were then oven dried at 70°C. This method gave 26 mg of the material, effectively removing 14.5% by weight as impurities, Figure 6.2, 6.3. Other impurities possibly include material incarcerated inside the BNNTs, which become exposed once the BNNTs are sliced, Figure 6.4(a-f) and S6.1. The 8.7 mg of material present in the IPA and water washing contained 3.85 mg of boron, as determined using inductively coupled plasma mass spectrometry (ICPMS) (see below). However, the calculated amount of boron in the 8.7 mg, assuming it is boron oxide, is 2.7 mg. The higher percent of boron in the washings is likely to arise from removal of non-oxidised or partially oxidise boron particles.

6.3.3 Analyses. ICPMS (Perkin Elmer Nex10w 350D, run in KED mode, He/ low 4.7L/min, internal std Indium) was used to determine the boron content after removing any solvent mixture (IPA and water (1:3)) from the second step of the purification process, and collected via filtration (0.22 μm plastic filter).

6.3.4 Slicing boron nitride nanotube (BNNTs). BNNTs (ca 75% purity) were dispersed in IPA and water, and any slicing was investigated in the VFD by systematically varying the operating parameters of the VFD, starting with the confined mode, then continuous flow, along with the flow rate, concentration and the laser operating parameters. Optimized conditions are: 8.5k rpm rotation speed,θ 45^{o}, flow rate 0.45 mL/min, concentration of the BNNTs in IPA and water (1:1) 0.1 mg/mL (previously sonicated prior to processing for 30 minutes at 6kHz to afford a dispersed solution), the pules Nd:YAG laser operating at 250 mJ/pulse at 1064 nm (pulse duration ~5 ns). The dispersed solution prior to VFD processing is colloidally unstable, and to overcome this, the BNNTs were maintained as a suspension in solution using an in house developed magnetically stirred syringe, Figure 6.5.[34,38,44]

6.3.5 Characterisation. Slicing and the structure of the BNNTs were investigated using scanning electron microscopy (SEM) (SEM-Inspect FEI F50 SEM), atomic force microscopy (AFM - Nanoscope 8.10 tapping mode), XRD (Bruker D8 ADVANCE ECO, Co- Kα, λ = 1.7889 Å), ATR-FTIR Perkin Elmer Frontier, EDS for HRTEM (FEI Tecnai F20 operated at 200 kV), and Raman spectroscopy (Horiba Raman with Wavelength 532 nm).

6.4 Results and discussion

6.4.1 Purification of the BNNTs. The high level of impurity in the as received BNNTs (as specified by the supplier), was addressed prior to the slicing studies. There are reports on purifying BNNTs using heating and washing with HCl [45,46] and using polymers to coat the BNNTs to facilitate separation and purification.[47,48] We explored a number of approaches to remove impurities from the as received material, Figure S6.2-S6.5. This led to the development of a simple two step method for increasing the purity of the BNNTs.

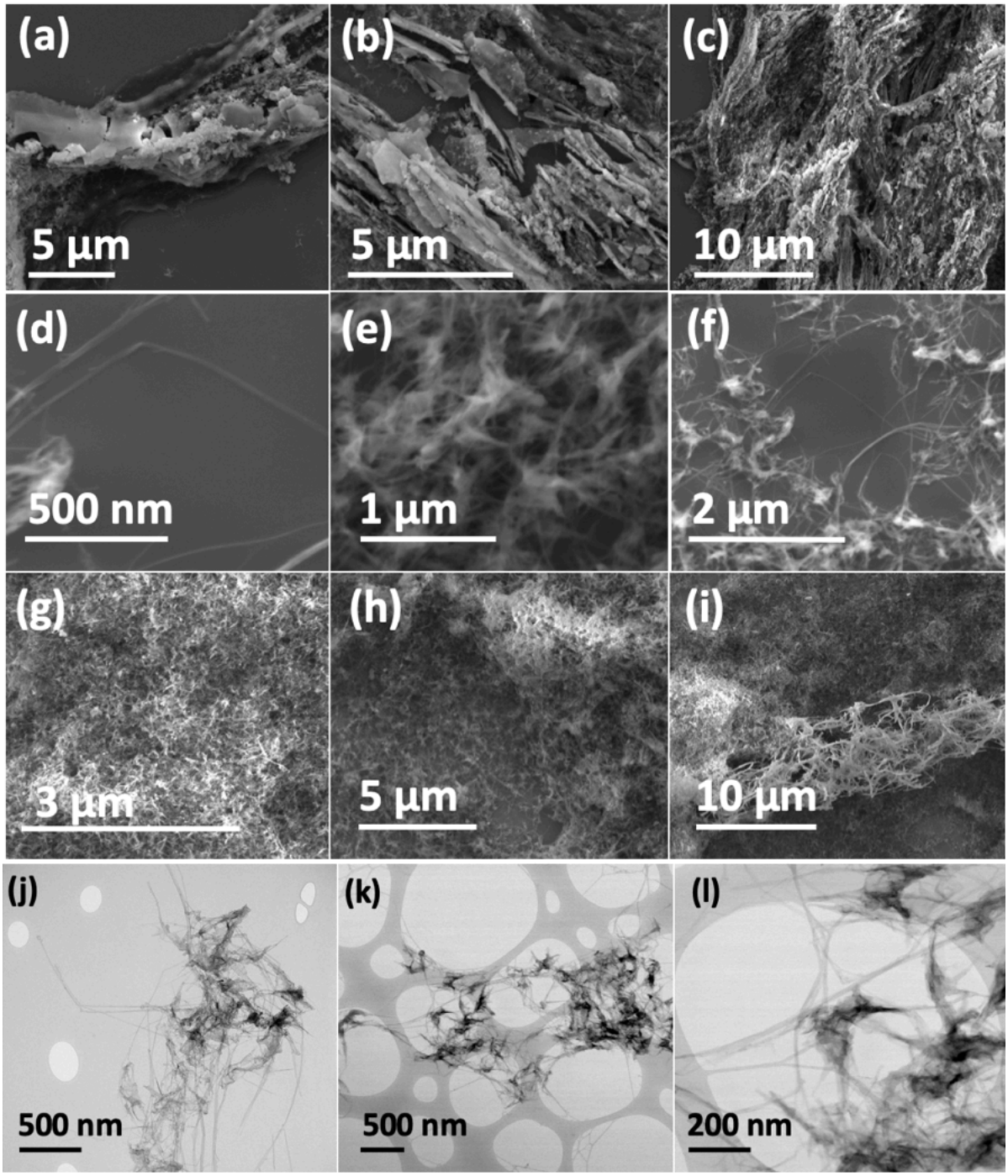

Figure 6.3. (a - i) SEM images of BNNTs drop cast onto silicon wafers. (a-c) As received BNNTs. (d-i) BNNTs after purifying (heating at 600 Cº then dispersed in IPA and water (1:3) for 3h at 100ºC). (j - l) TEM images of drop cast purified BNNTs.

The method involved heating the as received BNNTs in air at 600ºC for 2.5 hours, which effectively oxidised nitrogen and boron impurities, generating NO_2 and boric oxide,[42,43] with an increase in weight of the material, Figure 6.2. The resulting material was white, distinctly different to the grey as received material. Thereafter the high temperature processed material was dispersed in IPA and water (volume ratio 1:3) with the mixture stirred in a

sealed vial at 100°C for 3hours. This effectively dissolved the boric acid with the suspended BNNTs collected by centrifugation (4800× g) and oven dried at 70°C, increasing the purity of the BNNTs 14.5%. Further attempts to increase the purity were to no avail, possibly because the impurities are incarcerated inside the BNNTs with the ends of the tubes capped, Figure 6.2, 6.3, S6.1. XRD of the material after heating for 2.5 hours (step 1 of the processing) had two peaks at 2θ 18.4 and 32.6, which corresponds to boric oxide,[42,43] and three peaks for BNNTs at 2θ 30.4, 50.6 and 64.1, Figure 6.2(h, f).[15,49-51] XRD for the material after the second step was devoid of peaks corresponding to boron oxide, only peaks for BNNTs, Figure 6.2(i). SEM images of BNNTs before and after purification are shown in Figure 6.2(e, g), 4. EDS mapping and EDS spectra for different locations of purified BNNTs using HRTEM showed only two peaks for B and N, Figure S6.6. In addition, HRTEM for BNNTs after purification revealed the number of concentric ring layers in the tubes, Figure S6.1. ATR-FTIR for the material before and after purification established that the BNNTs are stable under the forcing conditions used in the purification process, with two peaks at 1348 cm^{-1} and 790 cm^{-1} for the B-N stretching and B-

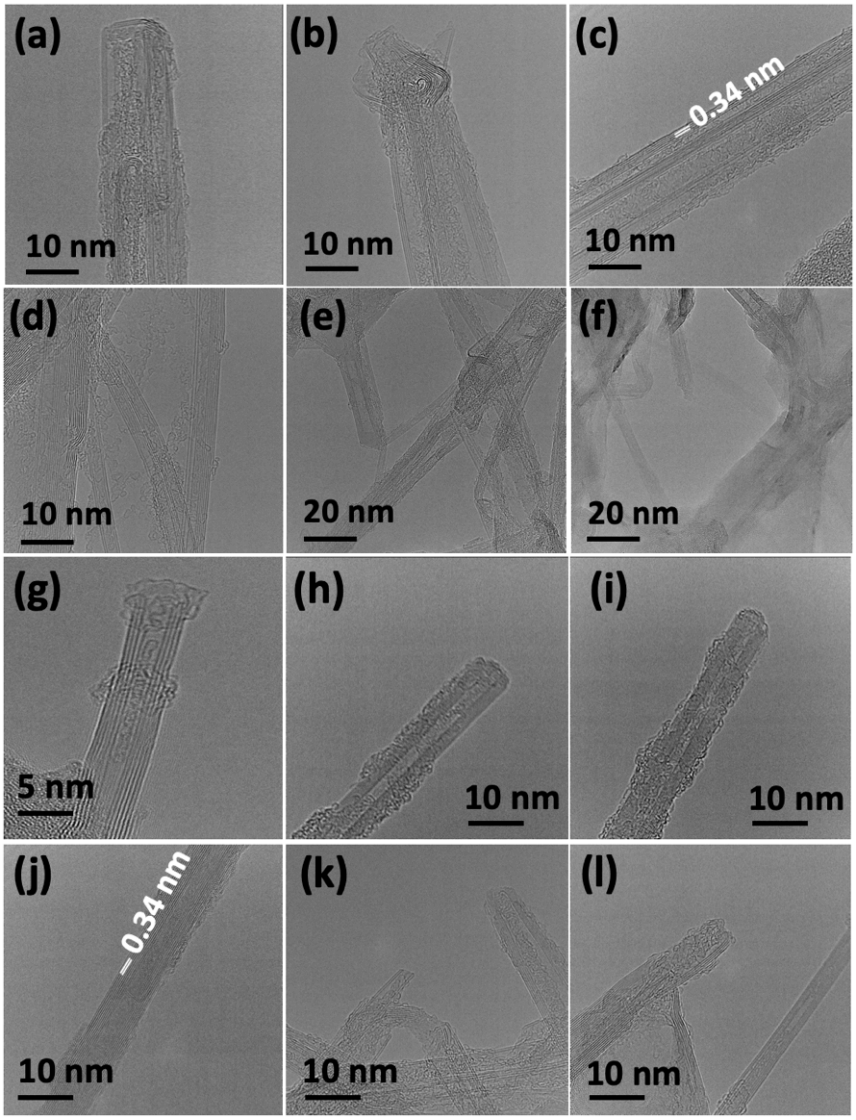

Figure 6.4. HRTEM images of drop cast (a-f) BNNTs after purification (600°C then washing with IPA and water (1:3) for 3h under 100°C. (g-l) Sliced BNNTs using a pulsed laser operating at 1064 nm and 250 mJ, rotational speed 8.5k rpm, concentration of BNNTs 0.1 mg/mL in IPA: water (1:1), flow rate 0.45 mL/min and 45o tilt angle.

N-B bending vibrational modes respectivly,[51] which are vibrational modes parallel and perpendicular to the c-axis of the nanotube, Figure 6.6(b).[52-54]

6.4.2 Slicing of BNNTs. A large number of experiments were undertaken to systematically explore the parameter space for the VFD in arriving at the optimal conditions. The choice of solvent considered water at different pH values, DMF (Dimethylformamide), toluene, NMP (N-Methyl-2-pyrrolidone) and IPA, and also mixtures of solvents, including IPA and water, DMF and water, toluene, THF and water, and toluene and water as an immiscible solvent system. This yielded sliced BNNTs but the yield of the material exiting the tube under continuous flow, except for a 1:1 mixture of IPA and water was low. Thus, a 1:1 mixture of IPA and water was deemed the optimal solvent for subsequent experiments. These experiments were carried out with the glass VFD irradiated with the 8 mm diameter beam from a pulse Nd:YAG laser operation at 1064 nm at 250 mJ/pulse (pulse width ~5 ns). The confined mode failed to produce any sliced BNNTs for the above solvents and solvent systems while irradiated in the same way.

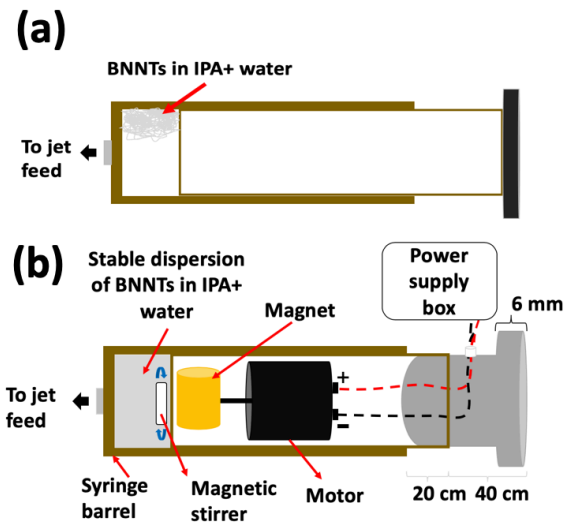

Figure 6.5. (a) Normal syringe where the BNNTs separate out. (b) Magnetically stirred syringe housing an electric motor inside the plunger to maintain a uniform suspension of the liquid delivered to the rapidly rotating tube in the VFD.

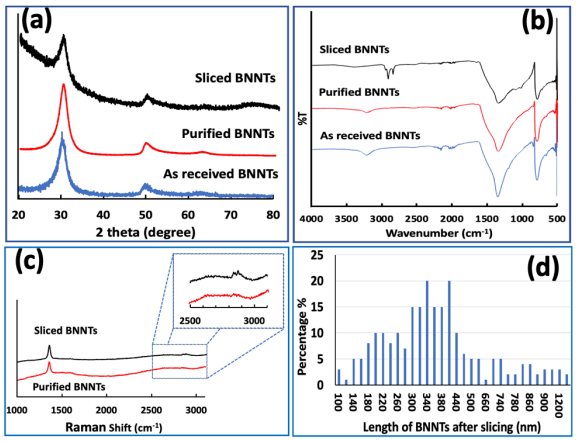

Figure 6.6. (a) XRD for as received BNNTs, purified BNNTs and sliced BNNTs via the VFD with pulsed laser, 1064 nm, 250 mJ, rotational speed 8.5k rpm, concentration of BNNTs 0.1 mg/mL in IPA and water (1:1 volume ratio), flow rate 0.45 mL/min, and tilt angle 45°. (b) ATR-FTIR. (c) Raman. (d) Counting data for 229 BNNTs tubes from AFM images.

The optimal rotation speed, flow rate, and concentration of BNNTs in IPA and water was then explored with different wavelength and power of the laser. All of the experiments were carried out at a tilt angle θ of 45°, as the optimal angle for many applications of the VFD.[28,35,55] We found that 8.5k rpm gave the highest amount of slicing of the BNNTs (*ca* 53%), with 4k rpm, 6k rpm, 7.5k rpm and 8k rpm resulting in lower

conversions. The power and wavelength of the pulsed laser were also varied in tracking towards optimal slicing conditions. This included 260 mJ/pulse for the Nd:YAG second harmonic (532 nm) (a green laser) and different power for a NIR laser (1064 nm), notably 250 mJ, 400 mJ and 600 mJ, Figure S6.7, S6.8 and S6.9. Of these 250 mJ NIR laser processing in IPA and water was optimal for slicing BNNTs. The effectiveness of the NIR laser over the green laser for slicing BNNTs relates to the higher photon desorption efficiency at 1064 nm versus 532 nm.[56]

A flow rate of 0.45 mL/min was then determined as optimal, with other flow rates considered, 0.1 mL/min, 0.3 mL/min and 0.7 mL/min. Concentrations of BNNTs in IPA and water were also investigated for all of the flow rates, at 0.1 mg/mL, 0.2 mg/mL, and 0.3 mg/mL, with 0.1 mg/mL being optimal. Thus, the optimum operating parameters for generating sliced BNNTs in a single pass through the VFD are a concentration of BNNTs of 0.1 mg/mL, flow rate 0.45 mL/min, rotational speed 8.5k rpm, and 250 mJ NIR laser processing, with IPA and water in a 1:1 ratio as the processing medium.

Scanning electron microscopy (SEM) was used to determine the nature of the BNNTs after processing. The images in Figure 6.7(a, b) are for BNNTs after the two steps purification method and before VFD processing. Images in Figure 6.7(c-f), S6.10 reveal the length of BNNTs after slicing in the VFD using the optimal conditions. AFM images were complementary in establishing the length of the sliced BNNTs, Figure 6.8, S6.11 with Figure 6.6(d) presenting the length of the sliced BNNTs derived from measuring 229 tubes. In addition, AFM images were used to study the height (diameter) of six tubes, Figure 6.9. HRTEM was

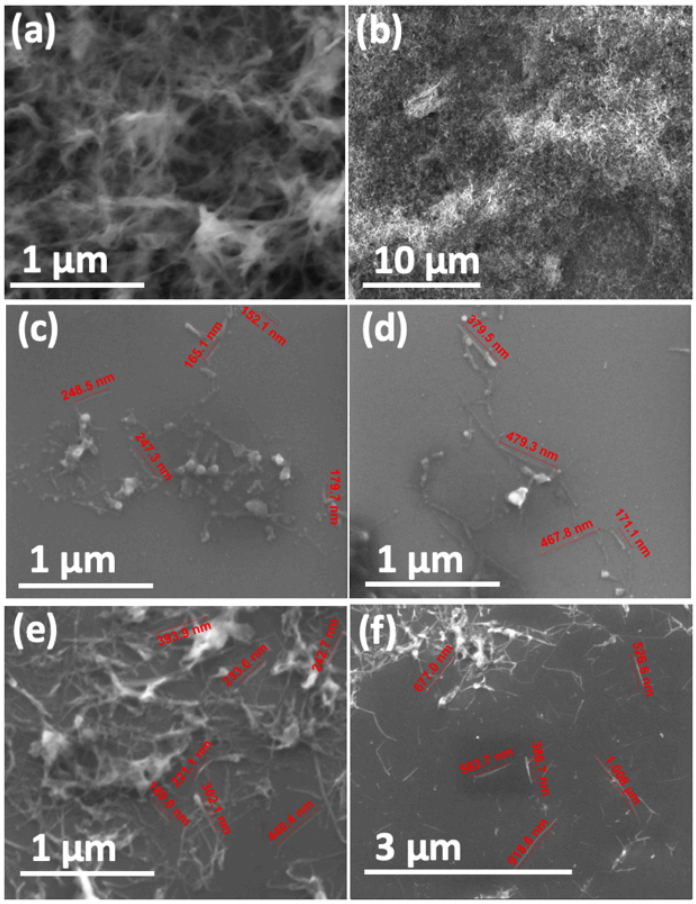

Figure 6.7. SEM images of drop cast BNNTs. (a, b) BNNTs after purifying (no VFD). (c-f) Sliced BNNTs generated in the VFD using a pulsed laser operating at 1064 nm and 250 mJ, rotational speed 8.5k rpm, concentration of BNNTs 0.1 mg/mL in IPA and water (1:1), flow rate 0.45 mL/min, and tilt angle 45°.

used to explore the topology of the BNNTs before and after slicing, Figure 6.4(a-f) and S6.1. This shows the concentric rings and that the ends of the BNNTs after purification have their ends sealed (pre-VFD processing). However, after slicing, HRTEM shows that the ends of the BNNTs are now open, Figure 6.4(g-l) and S6.12. Moreover, slicing of the BNNTs in the VFD while NIR laser irradiated appears to leave the outer layer (tube) undamaged. BNNTs absorb in the NIR[56] and with the bending under shear in the VFD, bond rupture is likely across the concentric rings. This is analogous to the mechanism of slicing SWCNTs, and also MWCNTs.[28,29]

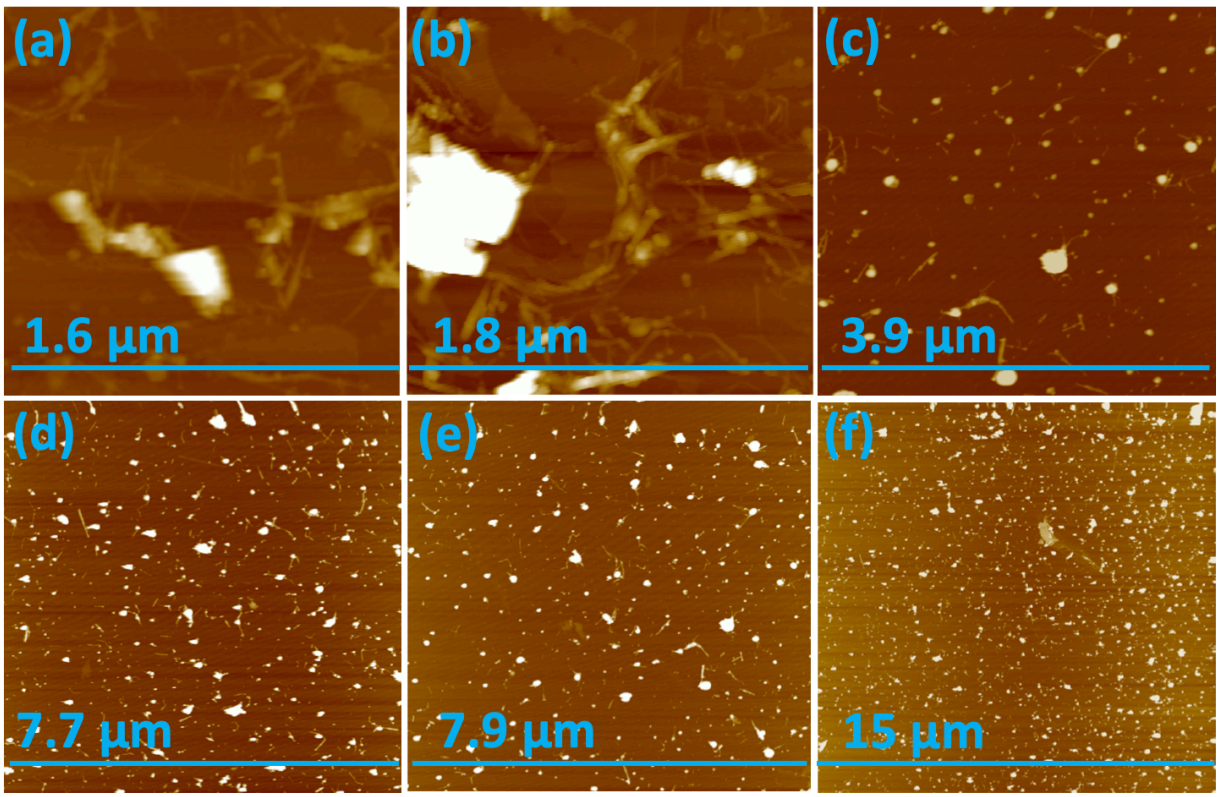

Figure 6.8. AFM images of drop cast sliced BNNTs generated in the VFD using a pulsed laser operating at 1064 nm and 250 mJ, rotation speed 8.5k rpm, concentration of BNNT 0.1 mg/mL in IPA and water (1:1), flow rate 0.45 mL/min and 45° tile angle.

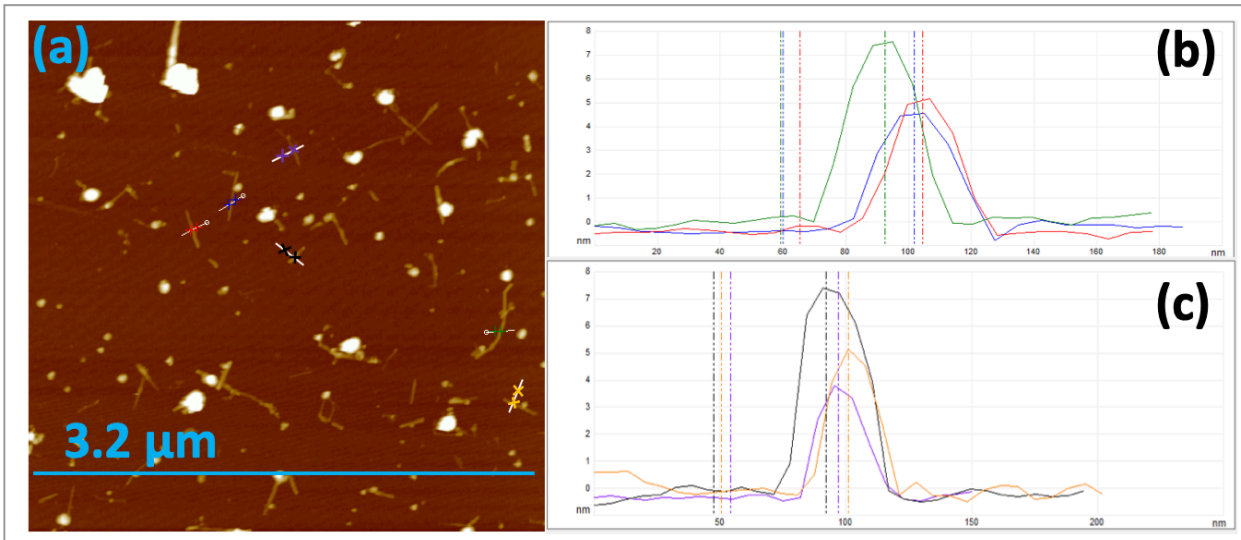

Figure 6.9. (a) AFM image of drop cast sliced BNNTs generated in the VFD using a pulsed laser operating at 1064 nm and 250 mJ, rotational speed 8.5k rpm, concentration of BNNTs 0.1 mg/mL in IPA and water ratio (1:1), flow rate 0.45 mL/min and tilt angle 45º. (b, c) Height of six BNNTs determined using the AFM image.

The XRD of BNNTs, before and after slicing confirm the presence of multi walled BNNTs with the main peak at 2θ 30.4º for pre-VFD processing corresponding to the van der Waals contact distance between concentric rings of 0.34 nm.[50] The same peak is present post-VFD processing (slicing) but is decreased relative to two peaks at 50.6º and 64.1º. The reason was setting the tubes of BNNTs together such as agglomerated which have Van der Waals distance (0.34 nm) between the tubes before slicing.[57] However, that is not after processing, Figure 6.6(a). The ATR-FTIR for BNNTs after purification and after slicing has two peaks at 1348 cm^{-1} and 790 cm^{-1} for the B-N stretching and B-N-B bending vibrational modes respectivly,[51,58] being parallel and perpendicular to the c-axis of the nanotube, Figure 6.6(b).[52-54] However, the ATR-FTIR for BNNTs after slicing has other peaks at 3400 cm^{-1}, 2920 -2850 cm^{-1}, 1100 cm^{-1} and 1020 cm^{-1} corresponding to O-H and C-H stretching, C-O stretching (secondary alcohol) and C-H bending modes respectively for IPA[59,60] The Raman spectrum of BNNTs has one peak for the B-N E_{2g} symmetry mode at 1359.5 cm^{-1}.[49,50,53,61] After processing in the VFD at the optimum conditions, the frequency for the B-N E_{2g} mode is unperturbed, Figure 6.6(c),[23] but now with an additional peak for included IPA at 2872.5 cm^{-1}.[62-64] This is consistent with solvent been taken up in the internal confines of the BNNTs after slicing, which are otherwise protected by endcaps. The sliced BNNTs have OH, CH, and CO peaks, arising from included IPA and water following slicing of the BNNTs which are not removed above 150ºC.

In addition, there is no evidence of dethreading the BNNTs after slicing into shorted lengths, which would be more favoured with the shorted lengths less likely to have defects which would inhibit the dethreading.

6.5 Conclusions

We have developed a simple, two steps method for improving the purity of BNNTs relative to the as received material, which should in general should prove useful for research based on BNNTs. It dramatically improves the ability to study their properties, in the present study their mechanical durability under high shear while being irradiated with a pulse laser. Mechanistically, the BNNTs absorb NIR radiation,[56] effectively heating the material, and under shear, which is likely to result in bending and thus straining B-N bonds, leads to bond rupture and slicing of the tubes. The present study avoids the use of harsh chemical and auxiliary substances, and is without precedent. The achieved length range of the sliced tubes is 340 nm to 400 nm, which has potential in length dependent applications of BNNTs. The scalability of the processing herein was established with 30 mg of sliced BNNTs prepared in a 1:1 mixture of IPA water using the optimum conditions, for continuous flow single pass processing in the VFD over 21 h. The fluid dynamics in the VFD is inherently complex and the choice of solvent or solvent mixture depends on the application being explored and the effect of different operating parameters of the device, all of which need to be systematically explored, as in the present study, except for the tilt angle. This was fixed at 45^{o} given that it is the optimised tilt angle for most processing in the microfluidic platform. A full understanding of the fluid flow in the VFD will facilitate the optimisation of any process, and this is a major international collaborative research project underway.

6.6 Acknowledgements

The authors gratefully acknowledge financial support from the Iraq Government, Ministry of Higher Education and Scientific Research, and the Australian Research Council and the Government of South Australia. Use of facilities in the Australian Microscopy & Microanalysis Research Facility (AMMRF) and the Australian National Fabrication Facility (ANFF) at the South Australian nodes of the AMMRF and ANFF under the National Collaborative Research Infrastructure Strategy are also acknowledged.

6.7. References

1. Chopra, N. G.; Luyken, R. J.; Cherrey, K.; Crespi, V. H.; Cohen, M. L.; Louie, S. G.; Zettl, A., Boron Nitride Nanotubes. *Science* **1995,** *269* (5226), 966-967.
2. Golberg, D.; Bando, Y.; Huang, Y.; Terao, T.; Mitome, M.; Tang, C.; Zhi, C., Boron

Nitride Nanotubes and Nanosheets. *ACS Nano* **2010,** *4* (6), 2979-2993.

3. Král, P.; Mele, E. J.; Tománek, D., Photogalvanic Effects in Heteropolar Nanotubes. *Physical Review Letters* **2000,** *85* (7), 1512-1515.
4. Chen, Y.; Zou, J.; Campbell, S. J.; Le Caer, G., Boron nitride nanotubes: pronounced resistance to oxidation. *Applied Physics Letters* **2004,** *84* (13), 2430-2432.
5. Ferreira, T. H.; Miranda, M. C.; Rocha, Z.; Leal, A. S.; Gomes, D. A.; Sousa, E. M. B., An Assessment of the Potential Use of BNNTs for Boron Neutron Capture Therapy. **2017,** *7* (4), 82.
6. Golberg, D.; Bando, Y., Unique morphologies of boron nitride nanotubes. *Applied Physics Letters* **2001,** *79* (3), 415-417.
7. Laude, T.; Matsui, Y.; Marraud, A.; Jouffrey, B., Long ropes of boron nitride nanotubes grown by a continuous laser heating. *Applied Physics Letters* **2000,** *76* (22), 3239-3241.
8. Li, Y.; Peng, Z.; Larios, E.; Wang, G.; Lin, J.; Yan, Z.; Ruiz-Zepeda, F.; José-Yacamán, M.; Tour, J. M., Rebar Graphene from Functionalized Boron Nitride Nanotubes. *ACS Nano* **2015,** *9* (1), 532-538.
9. Ahmad, P.; Khandaker, M. U.; Khan, Z. R.; Amin, Y. M., Synthesis of boron nitride nanotubes via chemical vapour deposition: a comprehensive review. *RSC Advances* **2015,** *5* (44), 35116-35137.
10. Loiseau, A.; Willaime, F.; Demoncy, N.; Hug, G.; Pascard, H., Boron Nitride Nanotubes with Reduced Numbers of Layers Synthesized by Arc Discharge. *Physical Review Letters* **1996,** *76* (25), 4737-4740.
11. Zhuang, C.; Xu, H.; Li, L.; Liu, Y.; Ban, C.; Liu, X., Systematic investigation of the ball milling–annealing growth and electrical properties of boron nitride nanotubes. *RSC Advances* **2016,** *6* (114), 113415-113423.
12. Chatterjee, S.; Kim, M. J.; Zakharov, D. N.; Kim, S. M.; Stach, E. A.; Maruyama, B.; Sneddon, L. G., Syntheses of Boron Nitride Nanotubes from Borazine and Decaborane Molecular Precursors by Catalytic Chemical Vapor Deposition with a Floating Nickel Catalyst. *Chemistry of Materials* **2012,** *24* (15), 2872-2879.
13. Li, L. H.; Chen, Y.; Glushenkov, A. M., Boron nitride nanotube films grown from boron ink painting. *Journal of Materials Chemistry* **2010,** *20* (43), 9679-9683.
14. Song, Y.; Sun, Y.; Shin, D. H.; Yun, K. N.; Song, Y.-H.; Milne, W. I.; Lee, C. J., Excellent oxidation endurance of boron nitride nanotube field electron emitters. **2014,** *104* (16), 163102.
15. Zhong, B.; Huang, X.; Wen, G.; Yu, H.; Zhang, X.; Zhang, T.; Bai, H., Large-Scale

Fabrication of Boron Nitride Nanotubes via a Facile Chemical Vapor Reaction Route and Their Cathodoluminescence Properties. *Nanoscale Res Lett* **2010,** *6* (1), 36.

16. Leela Mohana Reddy, A.; Tanur, A. E.; Walker, G. C., Synthesis and hydrogen storage properties of different types of boron nitride nanostructures. *International Journal of Hydrogen Energy* **2010,** *35* (9), 4138-4143.
17. Ciofani, G.; Raffa, V.; Menciassi, A.; Cuschieri, A., Folate functionalized boron nitride nanotubes and their selective uptake by glioblastoma multiforme cells: implications for their use as boron carriers in clinical boron neutron capture therapy. *Nanoscale research letters* **2008,** *4* (2), 113.
18. Li, X.; Wang, X.; Jiang, X.; Yamaguchi, M.; Ito, A.; Bando, Y.; Golberg, D., Boron nitride nanotube-enhanced osteogenic differentiation of mesenchymal stem cells. *Journal of Biomedical Materials Research Part B: Applied Biomaterials* **2016,** *104* (2), 323-329.
19. Wu, J.; Yin, L., Platinum nanoparticle modified polyaniline-functionalized boron nitride nanotubes for amperometric glucose enzyme biosensor. *ACS applied materials & interfaces* **2011,** *3* (11), 4354-4362.
20. Kalay, S.; Yilmaz, Z.; Sen, O.; Emanet, M.; Kazanc, E.; Çulha, M., Synthesis of boron nitride nanotubes and their applications. *Beilstein journal of nanotechnology* **2015,** *6* (1), 84-102.
21. Tiano, A. L.; Park, C.; Lee, J. W.; Luong, H. H.; Gibbons, L. J.; Chu, S.-H.; Applin, S.; Gnoffo, P.; Lowther, S.; Kim, H. J.; Danehy, P. M.; Inman, J. A.; Jones, S. B.; Kang, J. H.; Sauti, G.; Thibeault, S. A.; Yamakov, V.; Wise, K. E.; Su, J.; Fay, C. C., *Boron nitride nanotube: synthesis and applications*. SPIE: 2014; Vol. 9060, pp1-19.
22. Gao, Z.; Zhi, C.; Bando, Y.; Golberg, D.; Serizawa, T., Noncovalent Functionalization of Boron Nitride Nanotubes in Aqueous Media. *Opens Application Roads in Nanobiomedicine* **2014,** *1*, 7.
23. Liao, Y.; Chen, Z.; Connell, J. W.; Fay, C. C.; Park, C.; Kim, J. W.; Lin, Y., Chemical sharpening, shortening, and unzipping of boron nitride nanotubes. *Advanced Functional Materials* **2014,** *24* (28), 4497-4506.
24. Lee, C. H.; Zhang, D.; Yap, Y. K., Functionalization, Dispersion, and Cutting of Boron Nitride Nanotubes in Water. *The Journal of Physical Chemistry C* **2012,** *116* (2), 1798-1804.
25. Hsu, J.-H.; Chang, S.-H., Surface adhesion between hexagonal boron nitride nanotubes and silicon based on lateral force microscopy. *Applied Surface Science* **2010,** *256* (6), 1769-1773.

26. Zheng, M.; Chen, X.; Park, C.; Fay, C. C.; Pugno, N. M.; Ke, C., Nanomechanical cutting of boron nitride nanotubes by atomic force microscopy. *Nanotechnology* **2013,** *24* (50), 505719.
27. Geohegan, D. B.; Puretzky, A. A.; Ivanov, I. N.; Jesse, S.; Eres, G.; Howe, J. Y., In situ growth rate measurements and length control during chemical vapor deposition of vertically aligned multiwall carbon nanotubes. *Applied Physics Letters* **2003,** *83* (9), 1851-1853.
28. Alharbi, T. M. D.; Vimalanathan, K.; Lawrance, W. D.; Raston, C. L., Controlled slicing of single walled carbon nanotubes under continuous flow. *Carbon* **2018,** *140*, 428-432.
29. Vimalanathan, K.; Gascooke, J. R.; Suarez-Martinez, I.; Marks, N. A.; Kumari, H.; Garvey, C. J.; Atwood, J. L.; Lawrance, W. D.; Raston, C. L., Fluid dynamic lateral slicing of high tensile strength carbon nanotubes. *Scientific reports* **2016,** *6*, 22865.
30. Britton, J.; Chalker, J. M.; Raston, C. L., Rapid Vortex Fluidics: Continuous Flow Synthesis of Amides and Local Anesthetic Lidocaine. *Chemistry–A European Journal* **2015,** *21* (30), 10660-10665.
31. Gandy, M. N.; Raston, C. L.; Stubbs, K. A., Towards aryl C-N bond formation in dynamic thin films. *Organic and Biomolecular Chemistry* **2014,** *12* (26), 4594-4597.
32. Chen, X.; Dobson, J. F.; Raston, C. L., Vortex fluidic exfoliation of graphite and boron nitride. *Chemical Communications* **2012,** *48* (31), 3703-3705.
33. Britton, J.; Stubbs, K. A.; Weiss, G. A.; Raston, C. L., Vortex fluidic chemical transformations. *Chemistry–A European Journal* **2017,** *23* (54), 13270-13278.
34. Mohammed Al-antaki, A. H.; Luo, X.; Duan, A.; Lamb, R. N.; Eroglu, E.; Hutchison, W.; Zou, Y.-C.; Zou, J.; Raston, C. L., Continuous flow synthesis of phosphate binding h-BN@magnetite hybrid material. *RSC Advances* **2018,** *8* (71), 40829-40835.
35. Alsulami, I.; Alharbi, T.; Harvey, D.; Gibson, C. T.; Raston, C. L., Controlling the growth of fullerene C_{60} cones under continuous flow. *Chemical Communications* **2018**,*54* **(**57), 7896-7899.
36. Pye, S. J.; Dalgarno, S. J.; Chalker, J. M.; Raston, C. L., Organic oxidations promoted in vortex driven thin films under continuous flow. *Green Chemistry* **2018,** *20* (1), 118-124.
37. Phillips, J. M.; Ahamed, M.; Duan, X.; Lamb, R. N.; Qu, X.; Zheng, K.; Zou, J.; Chalker, J. M.; Raston, C. L., Chemoselective and Continuous Flow Hydrogenations in Thin Films Using a Palladium Nanoparticle Catalyst Embedded in Cellulose Paper. *ACS Applied Bio Materials* **2019,** *2* (1), 488-494.
38. Luo, X.; Al-Antaki, A. H. M.; Vimalanathan, K.; Moffatt, J.; Zheng, K.; Zou, Y.; Zou,

J.; Duan, X.; Lamb, R. N.; Wang, S.; Li, Q.; Zhang, W.; Raston, C. L., Laser irradiated vortex fluidic mediated synthesis of luminescent carbon nanodots under continuous flow. *Reaction Chemistry & Engineering* **2018,** *3* (2), 164-170.

39. Luo, X.; Smith, P.; Raston, C. L.; Zhang, W., Vortex Fluidic Device-Intensified Aqueous Two Phase Extraction of C-Phycocyanin from Spirulina maxima. *ACS Sustainable Chemistry & Engineering* **2016,** *4* (7), 3905-3911.
40. Yuan, T. Z.; Ormonde, C. F.; Kudlacek, S. T.; Kunche, S.; Smith, J. N.; Brown, W. A.; Pugliese, K. M.; Olsen, T. J.; Iftikhar, M.; Raston, C. L., Shear-Stress-Mediated Refolding of Proteins from Aggregates and Inclusion Bodies. *ChemBioChem* **2015,** *16* (3), 393-396.
41. Alharbi, T. M. D.; Harvey, D.; Alsulami, I. K.; Dehbari, N.; Duan, X.; Lamb, R. N.; Lawrance, W. D.; Raston, C. L., Shear stress mediated scrolling of graphene oxide. *Carbon* **2018,** *137*, 419-424.
42. Tran, B. H.; Tieu, K.; Wan, S.; Zhu, H.; Cui, S.; Wang, L., Understanding the tribological impacts of alkali element on lubrication of binary borate melt. *RSC Advances* **2018,** *8* (51), 28847-28860.
43. Yang, Q.; Sha, J.; Wang, L.; Zou, Y.; Niu, J.; Cui, C.; Yang, D., Crystalline boron oxide nanowires on silicon substrate. *Physica E: Low-dimensional Systems and Nanostructures* **2005,** *27* (3), 319-324.
44. Al-Antaki, A. H. M.; Luo, X.; Alharbi, T. M. D.; Harvey, D. P.; Pye, S.; Zou, J.; Lawrance, W.; Raston, C. L., Inverted vortex fluidic exfoliation and scrolling of hexagonal-boron nitride. *RSC Advances* **2019,** *9* (38), 22074-22079.
45. Chen, H.; Chen, Y.; Yu, J.; Williams, J. S., Purification of boron nitride nanotubes. *Chemical Physics Letters* **2006,** *425* (4), 315-319.
46. Xue-Song, L.; Dian-Qiang, C.; Bo, Z.; Jian-Lin, Y., Purification of Yard-Glass Shaped Boron Nitride Nanotubes. *Iranian Journal of Chemistry and Chemical Engineering (IJCCE)*. **2014,** *33* (1), 29-36.
47. Choi, J.-H.; Kim, J.; Seo, D.; Seo, Y.-S., Purification of boron nitride nanotubes via polymer wrapping. *Materials Research Bulletin* **2013,** *48* (3), 1197-1203.
48. Zhi, C.; Bando, Y.; Tang, C.; Honda, S.; Sato, K.; Kuwahara, H.; Golberg, D., Purification of Boron Nitride Nanotubes through Polymer Wrapping. *The Journal of Physical Chemistry B* **2006,** *110* (4), 1525-1528.
49. Thakur, V. K.; Yan, J.; Lin, M.-F.; Zhi, C.; Golberg, D.; Bando, Y.; Sim, R.; Lee, P. S., Novel polymer nanocomposites from bioinspired green aqueous functionalization of BNNTs. *Polymer Chemistry* **2012,** *3* (4), 962-969.

50. Wang, L.; Han, D.; Luo, J.; Li, T.; Lin, Z.; Yao, Y., Highly Efficient Growth of Boron Nitride Nanotubes and the Thermal Conductivity of Their Polymer Composites. *The Journal of Physical Chemistry C* **2018,** *122* (3), 1867-1873.
51. E, Songfeng; Li, C.; Li, T.; Geng, R.; Li, Q.; Lu, W.; Yao, Y., Ammonium-tungstate-promoted growth of boron nitride nanotubes. *Nanotechnology* **2018,** *29* (19), 195604.
52. Borowiak-Palen, E.; Pichler, T.; Fuentes, G. G.; Bendjemil, B.; Liu, X.; Graff, A.; Behr, G.; Kalenczuk, R. J.; Knupfer, M.; Fink, J., Infrared response of multiwalled boron nitride nanotubes. *Chemical Communications* **2003,** (1), 82-83.
53. Xu, S.; Fan, Y.; Luo, J.; Zhang, L.; Wang, W.; Yao, B.; An, L., Phonon characteristics and photoluminescence of bamboo structured silicon-doped boron nitride multiwall nanotubes. *Applied Physics Letters* **2007,** *90* (1), 013115.
54. Chen, Z.-G.; Zou, J.; Liu, G.; Li, F.; Wang, Y.; Wang, L.; Yuan, X.-L.; Sekiguchi, T.; Cheng, H.-M.; Lu, G. Q., Novel Boron Nitride Hollow Nanoribbons. *ACS Nano* **2008,** *2* (10), 2183-2191.
55. Luo, X.; Al-Antaki, A. H. M.; Alharbi, T. M. D.; Hutchison, W. D.; Zou, Y.-c.; Zou, J.; Sheehan, A.; Zhang, W.; Raston, C. L., Laser-Ablated Vortex Fluidic-Mediated Synthesis of Superparamagnetic Magnetite Nanoparticles in Water Under Flow. *ACS Omega* **2018,** *3* (9), 11172-11178.
56. Lu, Q.; Hu, Y.; Chen, J.; Li, Y.; Song, W.; Jin, S.; Liu, F.; Sheng, L., Boron nitride nanotubes matrix for signal enhancement in infrared laser desorption postionization mass spectrometry. *Talanta* **2018,** *187*, 106-112.
57. Matveev, A. T.; Firestein, K. L.; Steinman, A. E.; Kovalskii, A. M.; Lebedev, O. I.; Shtansky, D. V.; Golberg, D., Boron nitride nanotube growth via boron oxide assisted chemical vapor transport-deposition process using LiNO3 as a promoter. *Nano Research* **2015,** *8* (6), 2063-2072.
58. Xie, S.-Y.; Wang, W.; Fernando, K. A. S.; Wang, X.; Lin, Y.; Sun, Y.-P., Solubilization of boron nitride nanotubes. *Chemical Communications* **2005,** (29), 3670-3672.
59. Shahravan, A.; Desai, T.; Matsoukas, T., Controlled manipulation of wetting characteristics of nanoparticles with dry-based plasma polymerization method. *Applied Physics Letters* **2012,** *101* (25), 251603.
60. Kim, D.; Nakajima, S.; Sawada, T.; Iwasaki, M.; Kawauchi, S.; Zhi, C.; Bando, Y.; Golberg, D.; Serizawa, T., Sonication-assisted alcoholysis of boron nitride nanotubes for their sidewalls chemical peeling. *Chemical Communications* **2015,** *51* (33), 7104-7107.
61. Tay, R. Y.; Li, H.; Tsang, S. H.; Jing, L.; Tan, D.; Wei, M.; Teo, E. H. T., Facile

Synthesis of Millimeter-Scale Vertically Aligned Boron Nitride Nanotube Forests by Template-Assisted Chemical Vapor Deposition. *Chemistry of Materials* **2015,** *27* (20), 7156-7163.

62. Jin, Z.; Chu, Q.; Xu, W.; Cai, H.; Ji, W.; Wang, G.; Lin, B.; Zhang, X., All-fiber Raman biosensor by combining reflection and transmission mode. *IEEE PHOTONICS TECHNOLOGY LETTER*, **2018,** *30* (4), 387-390.
63. Ocola, L. E.; Costales, M.; Gosztola, Djjn, Development characteristics of polymethyl methacrylate in alcohol/water mixtures: a lithography and Raman spectroscopy study. *Nanotechnology* **2015,** *27* (3), 035302.
64. Mizutani, Y.; Kamogawa, K.; Kitagawa, T.; Shimizu, A.; Taniguchi, Y.; Nakanishi, K. , Solution structures and phase separation in fluoro alcohol/water mixtures: a study with Raman difference and carbon-13 NMR spectroscopy. *The Journal of Physical Chemistry* **1991,** *95* (4), 1790-1794.

Nanoscale Advances

PAPER

View Article Online
View Journal

Cite this: DOI: 10.1039/c9na00481e

Dynamic thin film mediated slicing of boron nitride nanotubes†

Ahmed Hussein Mohammed Al-antaki,[ab] Warren D. Lawrance[c] and Colin L. Raston[*a]

A method has been developed to slice boron nitride nanotubes BNNTs under continuous flow in a vortex fluidic device (VFD), along with a method to partially purify the as received BNNT containing material. The latter involves heating the BNNTs to 600 °C followed by dispersing in a 1 : 3 isopropyl alcohol (IPA) and water mixture at 100 °C. The VFD mediated slicing of the BNNTs comprises irradiating the rapidly rotating glass tube (20 mm OD) with a pulsed Nd:YAG laser. Systematically exploring the operating parameter space of the VFD established slicing of *ca.* 200 μm long purified BNNTs down to 340 nm to 400 nm, in *ca.* 53% yield, in a 1 : 1 mixture of IPA and water, in the absence of reagents/harsh chemicals, at a flow rate of 0.45 mL min^{-1}, a concentration of 0.1 mg mL^{-1} BNNTs and an 8.5k rpm rotational speed, with the pulsed laser operating at 1064 nm and 250 mJ per pulse.

Received 6th August 2019
Accepted 14th October 2019

DOI: 10.1039/c9na00481e

rsc.li/nanoscale-advances

Introduction

The first report of boron nitride nanotubes (BNNTs) was in 1995.[1] The one dimensional (1D) tubular nanostructures (nanotubes) are related to the structure of the ubiquitous carbon nanotubes (CNTs). However, BNNTs possess different physical properties, including having a wide band gap (5.5 eV) dielectric,[1,2] with photogalvanic,[3] thermal conductivity and stability at high temperature (up 900 °C),[4] and high neutron absorption.[5] Methods for preparing BNNTs encompass substitution reactions,[6] laser ablation,[7] chemical vapor deposition (CVD),[8,9] arc-discharge[1,10] and ball-milling.[11] There are three inter-related boron nitride structures, (i) straight-walled BNNT,[12,13] (ii) bamboo-type BN[13–15] and (iii) flower-type BN.[16] The straight BNNTs have potential in a number of applications, including in boron neutron capture therapy (BNCT),[5,17] hydrogen storage,[16] orthopedic implants,[18] biosensing[19] and biomedical areas in general,[2] and more.[20–22] The length of BNNTs is important in a number of applications, in nanodevices,[20] nanomedicines,[22] sensors and composites.[21] Controlling the length of BNNTs has been investigated using sonication,[23,24] atomic force microscopy (AFM)[25,26] and directly during chemical vapor deposition (CVD).[9,27] However, these have limitations associated with damaging the BNNTs, scalability of the processing and the choice of catalyst and temperature, for the aforementioned items (i)–(iii) respectively.

Single walled carbon nanotubes (SWCNTs) and multi-walled carbon nanotubes, can be sliced under high shear in a colloidal suspension in a vortex fluidic device (VFD), Fig. 1.[28,29] The length of the sliced CNTs depends on the rotational speed of a borosilicate glass or quartz tube inclined at 45° relative to the horizontal position, the flow rate of liquid, concentration of the starting material and the power of the pulsed laser operating at 1064 nm.[28,29] This motivated us to explore the utility of this approach to slice BNNTs in an analogous way, in the absence of

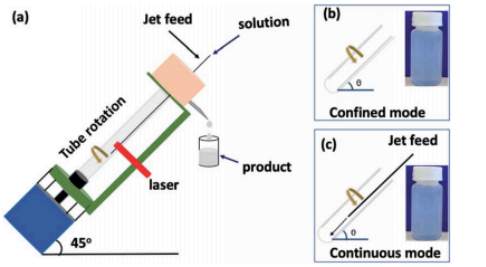

Fig. 1 (a) Diagram of a VFD housing a rapidly rotating tube (20 mm O.D., 17.5 mm I.D. and length 19.5 cm) tilted at θ, for operating under (b) the confined mode and (c) continuous flow, where liquid is delivered through a jet feed with the photographs in (b) and (c) of colloidal suspensions of sliced BNNTs. Optimized conditions for continuous flow processing; flow rate of BNNTs in a 1 : 1 mixture of IPA and water, 0.45 mL min^{-1}, concentration 0.1 mg mL^{-1}, rotational speed 8.5k rpm and θ 45°, with the liquid irradiated by a pulsed Nd:YAG laser (pulse duration ~ 5 ns) operating with 250 mJ per pulse at 1064 nm.

[a]Flinders Institute for Nanoscale Science and Technology, College of Science and Engineering, Flinders University, Adelaide, SA 5042, Australia. E-mail: colin.raston@flinders.edu.au
[b]Department of Chemistry, Faculty of Sciences, Kufa University, Kufa, Najaf, Iraq
[c]College of Science and Engineering, Flinders University, Adelaide, SA 5042, Australia

† Electronic supplementary information (ESI) available: Experimental details and characterisation results (Fig. S1–S17). See DOI: 10.1039/c9na00481e

7. Continuous flow copper laser ablation synthesis of copper (I and II) oxide nanoparticles in water

Ahmed Hussein Mohammed Al-antaki[a,b], Xuan Luo[a,c], XiaoFei Duan[d], Robert N. Lamb[d], Wayne D. Hutchison[e], Warren Lawrance[f], Colin L. Raston[a*]

a. Flinders Institute for Nanoscale Science and Technology, College of Science and Engineering, Flinders University, Adelaide, SA 5042, Australia.

b. Department of Chemistry, Faculty of Sciences, Kufa University, Kufa, Najaf, Iraq.

c. Centre for Marine Bioproducts Development, College of Medicine and Public Health, Flinders University, Adelaide, SA 5042, Australia.

d. Trace Analysis for Chemical, Earth and Environmental Sciences (TrACEES), University of Melbourne, Victoria 3010, Australia.

e. School of Science, University of New South Wales, ADFA campus, Canberra BC, ACT 2610, Australia.

f. College of Science and Engineering, Flinders University, Adelaide, SA 5042, Australia.

Author contributions: **AA** performed all the VFD and all characterisation experiments; wrote all the primary content. **XL** performed some experments. **XD** and **RL** performed XPS spectra. **WH** performed magnetization saturation. **WL** and **CR** supervised and coordinated the project and helped on the research directions and plan, and the final revision of the manuscript. All of the co-authors assisted with the revision of the manuscript before and during the publication process.

Graphical Abstract

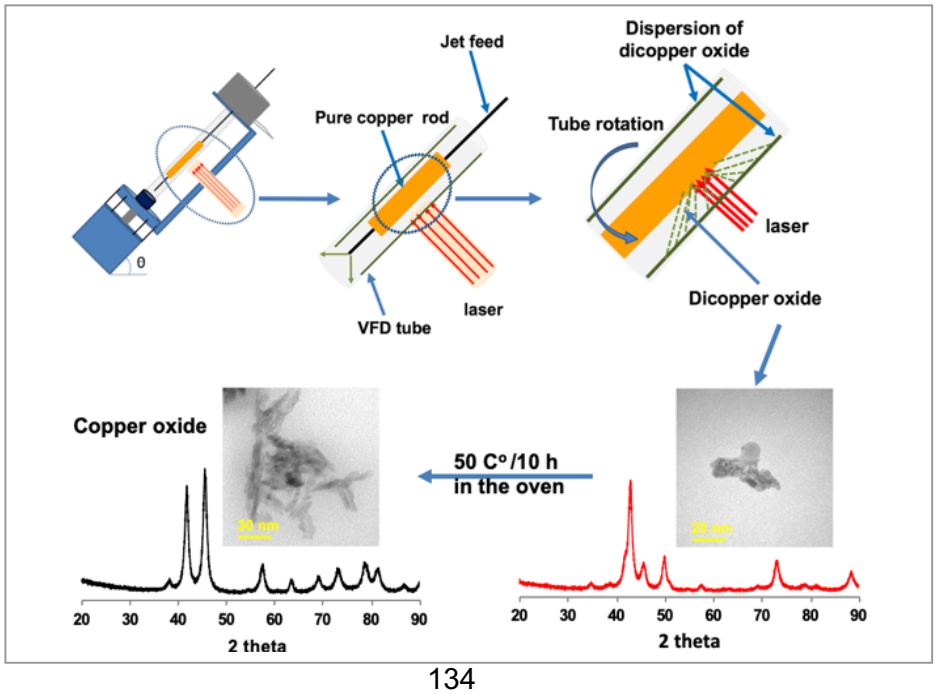

7.1 Abstract

Copper(I) oxide (Cu_2O) nanoparticles (NPs) are selectively prepared in high yield under continuous flow in a vortex fluidic device (VFD), involving irradiation of a copper rod using a pulsed laser operating at 1064 nm and 600 mJ. The plasma plume generated inside the glass tube (20 mm O.D.) which is rapidly rotating (7.5k rpm) reacts with the enclosed air in the microfluidic platform, with then high mass transfer of material into the dynamic thin film of water passing up the tube. The average size of the generated Cu_2ONPs is 14 nm, and they convert to copper (II) oxide (CuO) nanoparticles with an average diameter of 11 nm on heating the as prepared solution of Cu_2ONPs in air at 50ºC for 10 hours.

7.2 Introduction

The physical and chemical properties of nanoparticles of metal oxides are distinctly different to bulk materials and they are attracting considerable attention. They find application in diverse fields, including chemical manufacturing, environmental technology, energy conversion and storage as well as in biological areas.[1-4] A diversity of techniques have been used to prepare metal oxide particles in general, including electrophoretic and electrochemical deposition,[5] vacuum deposition,[6] sonochemical processing,[7] lithography and diffusion controlled nanoparticle growth.[8] Focusing on dicopper oxide (Cu_2O) and copper oxide (CuO), they have been prepared using such techniques, with uniform size and shape of the particles.[7,8] They find particular use in catalytic organic transformations, electrocatalysis, and photocatalysis.[9-11] Developing synthetic methodologies and supports that increase the stability of copper nanoparticles have been explored, especially in regard to their sensitivity to oxygen, water and different reagents. This has led to the development of more complex structured nanoparticles, as in core shell particles, and different ways to oxidise the copper.[12]

Batch processing is typically used in the fabrication of copper oxide nanoparticles, but such processing can result in variation of product from batch to batch, and refined reagents are required. An alternative approach to preparing different metal oxides in general involves the use of lasers, and this includes in the synthesis of copper oxide nanoparticles.[13-17] Pulsed laser ablation (PLA) involves ablating a solid target in a liquid phase or in air which has a number of advantages. These include (a) not requiring the process to be operating under a high vacuum, (b) the processing is simple and is high yielding, and (c) it avoids the use of chemicals. In addition, optimizing the experimental parameters can result in controlling the shape and size of the nanoparticles.[17] PLA involves absorption of the laser radiation at the metal surface as the so called interaction zone, which causes the

transformation of kinetic energy into thermal energy. Also, if the laser power is sufficiently high, a local plasma plume with high temperatures and pressures is formed,[18] and this can lead to the formation of metal oxide particles in the presence of oxygen.

We report the synthesis of copper(I) oxide nanoparticles using PLA under continuous flow conditions, which can minimise batch variation in the process, as discussed above. Continuous flow processing is important in being able to scale up from the research laboratory processing to large scale production, thereby avoiding batch-to-batch variation which can occur for traditional processing while minimising capital outlay, with built in just in time production.[19] The synthesis featured the use of the vortex fluidic device (VFD) as a dynamic thin film microfluidic processing platform, Figure 7.1. The relatively inexpensive VFD houses a borosilicate glass tube (20 mm O.D., 17.5 mm I.D.), open at one end, which is rotated at high speed (up to 9k rpm) and can be inclined from 0º to 90º relative to the horizontal position.[19-21] It has two common modes of operation as follows: (i) the confined mode where a finite volume of liquid is added to the rapidly rotating tube, and (ii) the continuous flow mode where liquid is constantly fed into the tube usually as droplets. Under the centrifugal force, the liquid whirls up and exits at the top of the tube, and this continuous flow mode of operation of the VFD offers scalability to the processing by simply extending the operating time.[22-24] Applications of the VFD also include enhancing enzymatic reactions,[19] controlling organic synthesis,[20,25] probing the structure of self-organised systems,[26] protein separation,[27] exfoliation of 2D graphite and boron nitride,[21] protein folding[28] and more,[23,29-31] Figure 7.1. Herein, we have established that the VFD is selective in forming copper(I) oxide (Cu_2O) NPs with an average particle size of 14 nm in diameter, as a one-step continuous flow process at ambient pressure, with the oval operation avoiding a purification step. The process also minimizes the generation of waste, in avoiding the need for adding any reagents, although specific surfactants can be added at the end of the processing if required. Using an aqueous solution and avoiding harsh chemicals imparts high green chemistry metrics into the processing in developing more sustainable processing for the future.[27] Figure 7.2 is a zoomed in representation of the operation of the VFD in generating Cu_2O NPs when the laser strikes the copper metal rod inside the rapidly rotating glass tube. The confined mode was initially used to establish optimal conditions for generating the Cu_2ONPs, before applying these conditions to continuous flow. This approach has been used for a number of applications of the VFD in translating the processing into continuous flow. Heating solutions of the generated copper(I) oxide particles, Cu_2O NPs, in water results in conversion to nanoparticles of copper(II) oxide, CuO NPs. We note that the VFD is effective in being able to control the size and shape of nanoparticles,

for example, superparamagnetic magnetite nanoparticales.[23] In the context of copper oxide nanoparticles, this is important for downstream applications, for example in gas sensors, magnetic phase transition, superconductors and catalysts.[32,33]

7.3 Experiments

7.3.1 Materials. High purity (>99.998%) 8361h copper metal rod of 8 mm in diameter (KOCH-LIGHT LABORATORIES LTD Colnbrook-Bucks- England) was used for all the processing. Milli-Q water was used.

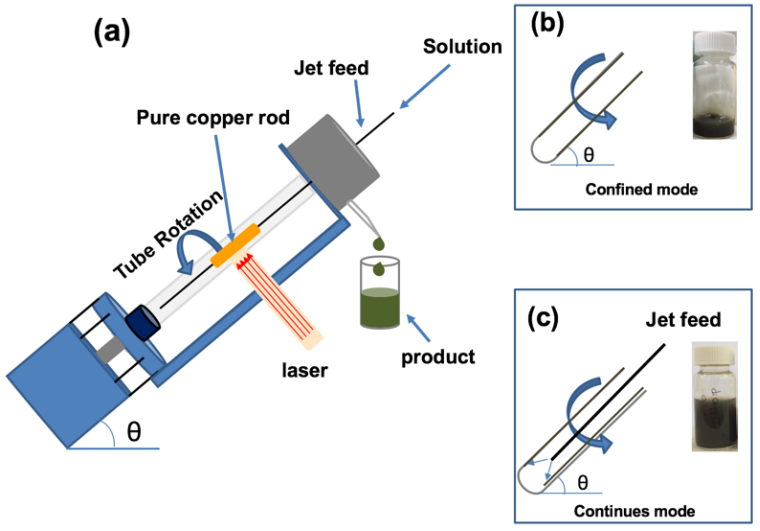

Figure 7.1. (a) Diagrammatic representation of the VFD with a pure copper rod inside the glass tube (20 mm O.D., 17.5 mm I.D.) spun at 7.5k rpm and irradiated with a 5 nanosecond pulsed Nd:YAG laser operating at 1064 nm, and 600 mJ, having a 8 mm diameter beam, (b) confined mode of operation of the VFD, for 15 mins, and (c) continuous flow mode of operation at a flow rate of water at 0.25 mL/min.

7.3.2 Synthesis of Cu_2O and CuO. Nanoparticles of Cu_2O were generated in the dynamic thin film in the VFD tube (borosilicate glass tube of 20 mm O.D., 17.5 mm I.D., and 19.5 cm in length) on irradiating a stationary pure copper rod (>99.998%) located in the middle of the tube. The laser used was generated from a Nd:YAG source, as a pulsed source operating at 1064 nm and 600 mJ/pulse. The laser was operated unfocussed, with a beam diameter of 8 mm, giving a fluence of 1.2 J cm^{-2}. Under continuous flow, water was delivered via a jet feed to the base of the tube, with the flow rate set at 0.25 mL/min, and for confined mode 1 mL of liquid was added to the tube with the experiment run for 15 min. The rotational speed for the glass tube in the VFD was 7.5k rpm, with the tube titled at 45º relative to the horizontal position. The product from confined mode and continuous flow was Cu_2ONPs dispersed in water. The method used to collect the product after 90 minutes was as follows: approximately 20 mL of solution, Figure (S7.5a), was centrifuged at RCF=9980 ×g for 20 min whereupon the supernatant was removed, and the pellet re-dispersed in 5 mL of acetone, followed by centrifugation at RCF=4000 ×g for 10 min. The supernatant was then removed and the pellet left to air dry for 5 min. This method was effective in rapidly removing the water and collecting the Cu_2ONPs as a powder. This powder was then stored in a sealed vial, taking care to exclude oxygen in avoiding oxidising the material to CuONPs, which was shown to occur

after one week. For each 1 mL of the original solution from the continuous flow process, approximately 0.8 mg of product was collected. The method used to deliberately prepare CuONPs was to heat a dispersion of the Cu_2ONPs from the continuous flow process in an oven at 50ºC for 10 h as shown in Figure S7.5b. The water was then removed under reduced pressure (rotary evaporator), affording a brown powder which was stable in air. The same steps were used to isolate the product remaining in the tube after continuous flow processing. On completing the experiment, the material remaining in the VFD tube was shown to be Cu_2ONPs. This was collected from inside the VFD tube after 2 h of processing using the same above method, Figure S7.4e. Approximately 15 mg of Cu_2ONPs was collected inside the VFD, post processing. Cu_2ONPs collected from inside the VFD tube after 2 h using 15 mL of water, afforded approximately 15 mg of the material.

7.3.3 Characterisation. The nanoparticles were characterized using scanning electron microscopy (SEM - Inspect FEI F50), atomic force microscopy (AFM - Nanoscope 8.10 tapping mode), X-ray photoelectron spectroscopy (XPS – Kratos Axis Ultra, with monochromatic Al Ka X-ray source), XRD (Bruker D8 ADVANCE ECO, Co- Kα, λ=1.7889 Aº), ATR- FTIR (Perkin Elmer Frontier), UV-Vis spectroscopy (Agilent technologies Cary 60 Uv-Vis) and TEM (Tecnai_G2_Spirit). Particles were collected using a centrifuge (Dynamica VELOCITY 14R). Magnetisation measurements were carried out using a Quantum design MPMS at 295 K in the field range ±1.50 T.

7.4 Results and Discussion

Copper(I) oxide (Cu_2O) nanoparticles were selectively formed in the VFD under different operating conditions of the device, with this material readily converted to copper(II) oxide (CuO) nanoparticles post VFD processing by gentle heating in air. The optimization experiments were initially carried out in the confined mode of operation of the VFD, for a 15 mins processing time, with 1 mL of Milli-Q water inside the rapidly rotating tube. The tilt angle of all the experiments was set at 45º, which has been established as optimal for many applications of the device.[23,24,34] The effect of choice of laser power was then explored, using 450 mJ, 550 mJ, 600 mJ and 650 mJ. For the lowest power, no product could be isolated, with a low yield obtained at 550 mJ. In contrast, high yields were obtained for 600 mJ and 650 mJ, and accordingly 600 mJ was chosen as optimal in being cognisant of minimising energy usage in developing processing high in green chemistry metrics. The next operating parameter to be optimised was the rotational speed of the tube, and to this end we carried out laser ablation experiments at 4.5k rpm, 5.5k rpm, 6.5k rpm, 7.5k rpm and 8.5k rpm. XRD

was used as the primarily characterisation technique for the resulting Cu_2ONPs. The rotational speeds of 4.5k rpm, 5.5k rpm and 6.5k rpm gave diameters of 19 nm ± 2 nm whereas 8.5k rpm gave 17 nm ± 1 nm particles and 7.5k rpm gave 14 nm ± 1 nm diameter particles, Figure S7.2b. Moreover, the XRD for material generated at 4.5k rpm, 5.5k rpm, 6.5k rpm and 8.5k rpm showed increasing amount of CuONPs relative to 7.5k rpm, and this was chosen as the optimum speed. Overall, the confined mode experiments established the optimal power setting of the laser and optimal rotation speed while minimising the amount of conversion of Cu_2ONPs to CuONPs.

The flow rate of Milli-Q water into the VFD was then optimised, for 1 mL/min, 0.75 mL/min, 0.5 mL/min, 0.25 mL/min and 0.1 mL/min flow rates. The 1 mL/min, 0.75 mL/min, 0.5 mL/min and 0.1 mL/min flow rates resulted in a higher percentage of CuONPs relative to 0.25 mL/min Figure S7.2c, and this flow rate was then considered as optimal for preparing Cu_2ONPs. Thus, the overall optimised conditions were at a laser power of 600 mJ, rotational speed of 7.5k rpm, with a flow rate of 0.25 mL/min. Water was used to dilute the solution, necessitating the drying of the product, Figure S7.2c, 7.3, 7.4). The copper rod showed visible etching and blackening post laser ablation experiments.

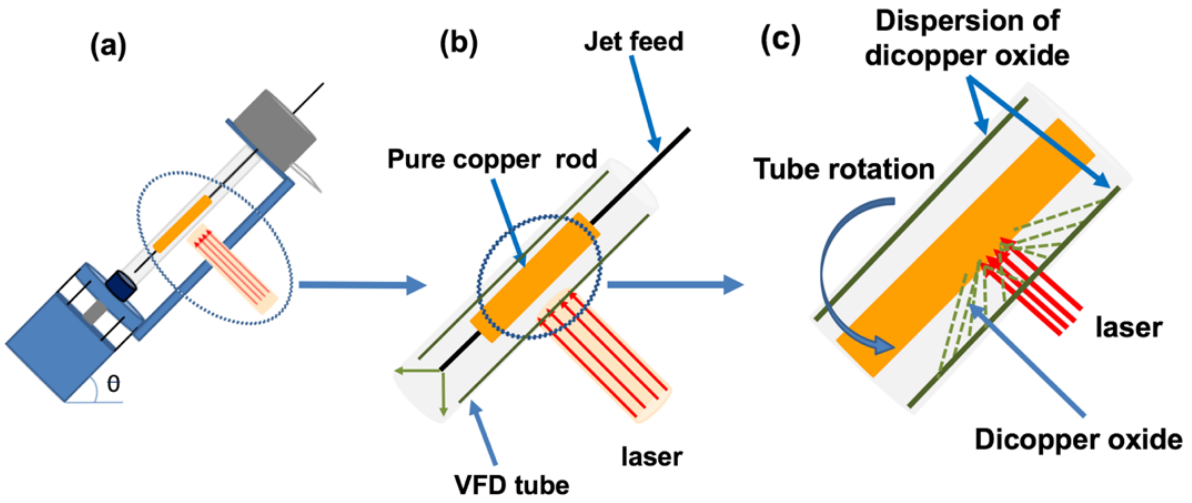

Figure 7.2. (a) VFD showing the position of the pure copper rod as the laser target. (b) and (c) Zoomed in arrangement of the tube and the irradiation of copper rod.

The pH of water used for the experiment was 6.90, but immediately after the VFD processing it was slightly lower at 6.75, with the solution containing a dispersion of Cu_2ONPs. After heating the solution at 50ºC for 10 h in an oven, the pH decreased slightly to 6.69, with the NPs converted to CuO. ATR-FTIR spectra established the presence of Cu_2ONPs and CuONPs, with a broad peak at 3400 cm^{-1} corresponding to O-H stretching vibrations band and 1628 cm^{-1} bending vibration of water and surface bound hydroxyl

moieties.[35,36] Two peaks in the fingerprint region, at 1025 cm^{-1} and 857 cm^{-1} correspond to bending vibrations for surface bound hydroxyl moieties.[36] Any CuO present was identified by peaks at 979 cm^{-1} and 931 cm^{-1}, and at 597 cm^{-1} which corresponds to Cu-O vibrations, Figure 7.3b.[35,37-40] UV-Vis spectra could be used to differentiate between Cu_2ONPs and CuONPs, with solutions of the pure components taking on clear light green and light brown solutions, respectively.[41-43] A clear brown solution of CuONPs[44] was prepared after heating a Cu_2ONPs solution in air at 50ºC for 10 h. Figure 7.3a shows a colour change from green to brown in accordance with the change of band gap energy between Cu_2ONPs and CuONPs. The presence of the different copper oxide structures was established using XRD, at the same time providing the average particle size of the isolated materials using the Scherrer equation. The XRD pattern (Co- Kα, λ=1.7889 Å) was devoid of peaks for elemental copper, ruling out the formation of a core shell structure such as Cu@Cu_2O,[45,46] but with peaks corresponding to Cu_2O, at 34.8º, 42.7º, 49.6º, 62.2º, 72.9º and 88.1º, Figure 7.3c.[46-50] The Cu_2O diffraction pattern had peaks at 2θ of 34.8, 42.7, 49.6, 62.2, 72.9 and 88.1, corresponding to (110), (111), (200), (211), (220) and (311) for cubic cuprite, respectively.[46-50] In addition, there were small peaks assigned to the presence of some CuO, presumably arising from some oxidation during the work up immediately post VFD processing. The peaks for CuONPs are at 2θ of 38.2, 41.6, 45.4, 54.3, 57.4, 63.5, 68.9, 73, 78.6, 81.3 and 86.7º, correspond to (110), (111), (111), (112), (202), (020), (202), (113), (002), (311) and (220), respectively. Heating the Cu_2ONPs at 50ºC for 10 h gave sharp peaks corresponding to the diffraction pattern for exclusively CuO, Figure 7.3c.[51,52] The size of the Cu_2ONPs particles was estimated from the Scherrer equation to be 14±1 nm, and the size of the CuO NPs at 11±1 nm.

The mechanism of forming the nanoparticles by laser irradiation of copper metal in the VFD involves creating Cu_2ONPs in the air in the VFD tube, Figure S7.6. The metal rod contains no copper oxide and thus the oxygen is from the air. Moreover, the thermal energy delivered to the surface of the copper target creates a plume of copper which reacts with oxygen in the air, resulting in the formation of Cu_2ONPs, and this is reflected in a change of colour of the liquid, from colourless to green[48,49] during the processing. When a pure nitrogen gas atmosphere was used in the VFD, as a control experiment, no oxidation was evident and there was no change in colour of the water, Figure S7.6. Thus, oxygen in the air is the reactive species in forming Cu_2ONPs. The time and temperature with oxygen from air were key to converting Cu_2ONPs to CuONPs, Figure S7.5.[53,54] It is also noteworthy that there was no evidence for the formation of core shell Cu@CuO_2NPs or indeed any particles based on elemental copper (XPS and XRD). The need for a partial pressure of oxygen gas is also

evident by the formation of Cu_2ONPs in toluene or isopropyl alcohol (IPA), Figure S7.4, but these reactions were not pursued further given that the focus of the research is on developing processes that are high in green chemistry metrics, in avoiding the generation of an organic solvent waste stream, and avoid the formation of metal carbide nanoparticles.

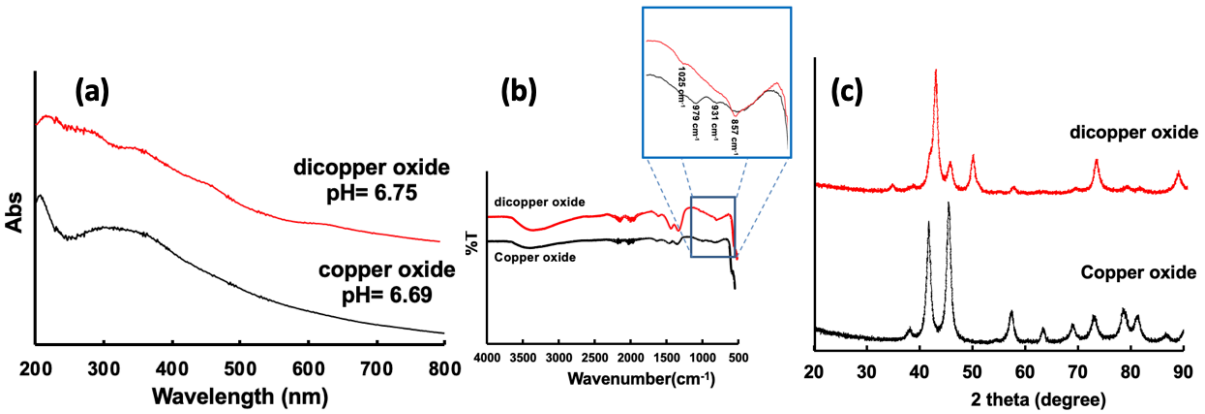

Figure 7.3. (a) UV-Vis spectra, (b) ATR-FTIR and (c) X-ray diffraction patterns for Cu_2ONP prepared in a VFD under continuous flow of water at a flow rate of 0.25 mL/min with the tube inclined at 45º, rotating at 7.5k rpm and irradiated with a 1064 nm pulsed laser operating at 600 mJ. Analogous data were obtained for CuONPs prepared from a dispersion of Cu_2ONPs heated to 50ºC for 10 h.

According to the literature, the binding energy of Cu(I) by XPS is at about 936.5 eV and 956.5 eV for Cu 2p3/2 and Cu 2p1/2 respectively. On the other hand, XPS for Cu (II) is shifted to about 934 eV and 954 eV for Cu 2p3/2 and Cu 2p1/2 respectively. Furthermore, the CuONPs spectrum had two extra peaks at 941.2 eV and 943.7 eV. These correspond to the relative intensities of the shake–up satellites on the surface of the material, Figure 7.4a, c. Moreover, the XPS for O 1s in Cu_2O and CuO were distinctly different with the O 1s in CuO shifting from 534.5 eV and 532.4 eV to 531.3 eV and 529.7 eV respectively, Figure 7.4b, d.[55-58] The XPS results are also consistent with the sample being devoid of elemental copper, as for example in Cu@Cu_2O, being devoid of the Cu(0) peak at 932 eV and associated shake-up satelites,[59] Figure 7.4a. XPS for Cu_2O NPs has peaks at about 936.5 eV and 956.5 eV, representing Cu 2p3/2 and Cu 2p1/2, respectively. The shake–up satellites are at around 944.1 eV with the shake–up satellites for the CuO NPs are at 941.2 eV and 943.7 eV.[55-58]

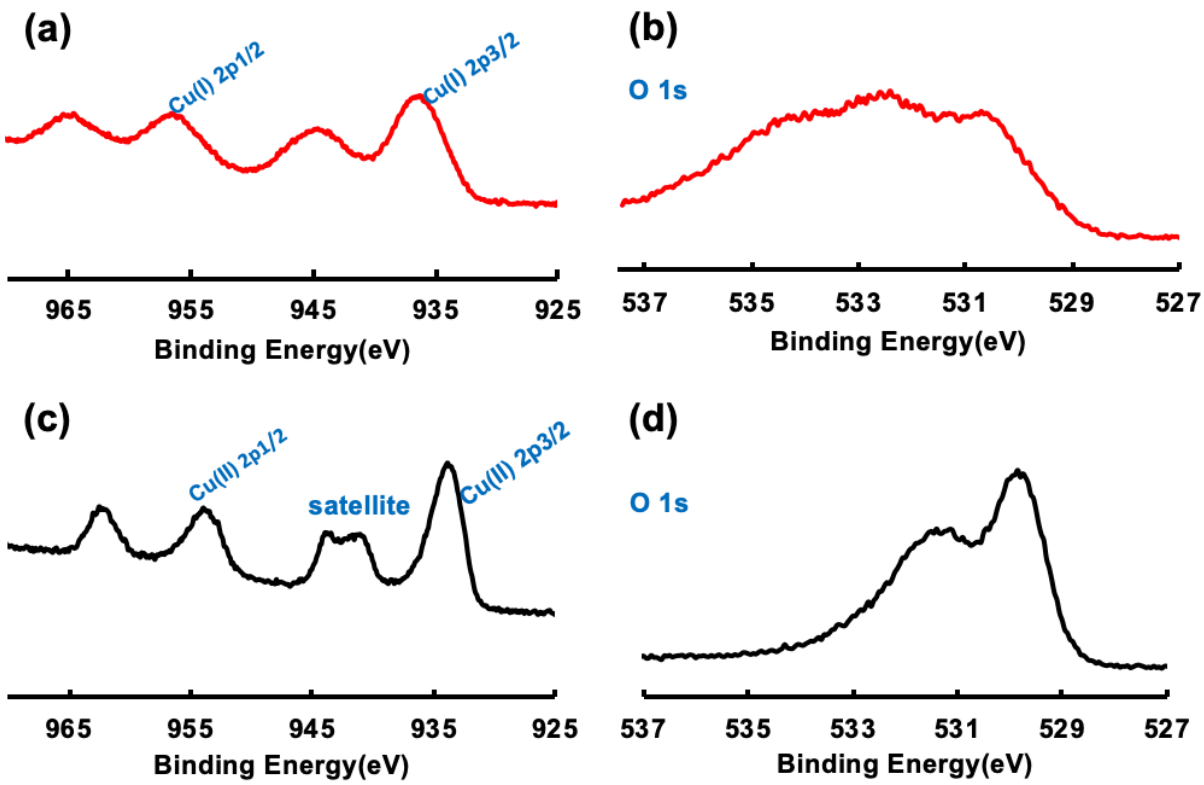

Figure 7.4. (a, b) XPS for copper and oxygen in Cu_2ONPs prepared in a VFD under continuous flow of water (0.25 mL/min) with the glass tube inclined at 45º and rotating at 7.5k rpm, with the 1064 nm wavelength pulsed laser operating at 600 mJ. (c, d) XPS for copper and oxygen in CuONPs prepared from Cu_2ONPs dispersion after heating in air inside the oven at 50ºC for 10 h.

The morphology, size and shape of Cu_2ONPs and CuONPs were investigated by SEM, AFM and TEM. Both nanoparticles were shown to have a similar topography, and were aggregated. The size of the nanoparticles was established using XRD and SEM Figure 7.5, S7.7, S7.8. AFM images gave information on the size of the nanoparticles, Figure 7.7. In addition, TEM images for both Cu_2ONPs and CuONPs provided more detail about the size and the shape of the nanoparticles, showing a different shape for each structure Figure 7.6, S7.9. Dynamic Light Scattering (DLS) on both Cu_2ONPs and CuONPs in solution established the presence of agglomerates, 164 nm and 91 nm diameter respectively, for Cu_2ONPs and CuONPs, Figure 7.8. The size of Cu_2ONPs and CuONPs were measured for about 200 particles from TEM images. These showed size estimations similar to those from the Scherrer equation for bulk material, Figure 7.9. Magnetization data was collected for CuONPs, showing an essentially linear (paramagnetic) response versus applied field to 1.5 T, with a hint of ferromagnetism at very low fields. The results are consistent with the previous measurements by Punoose *et al*.[60] both in terms of the form and magnitude of the magnetization. From Figure 7.10, it can be seen that M is 0.0473 (Am^2kg^{-1}) at room

temperature and 1.5 T for CuONPs collected from outside the VFD tube and 0.0482 M (AM^2 kg^{-1}) for particles from inside the VFD tube. These values of M for the ≈ 11 nm NPs of this work are slightly smaller than those recorded at room temperature and 1.5 T for 6.6 nm NPs by Punoose *et al*.[60] in line with the M versus particle size trends of their work.

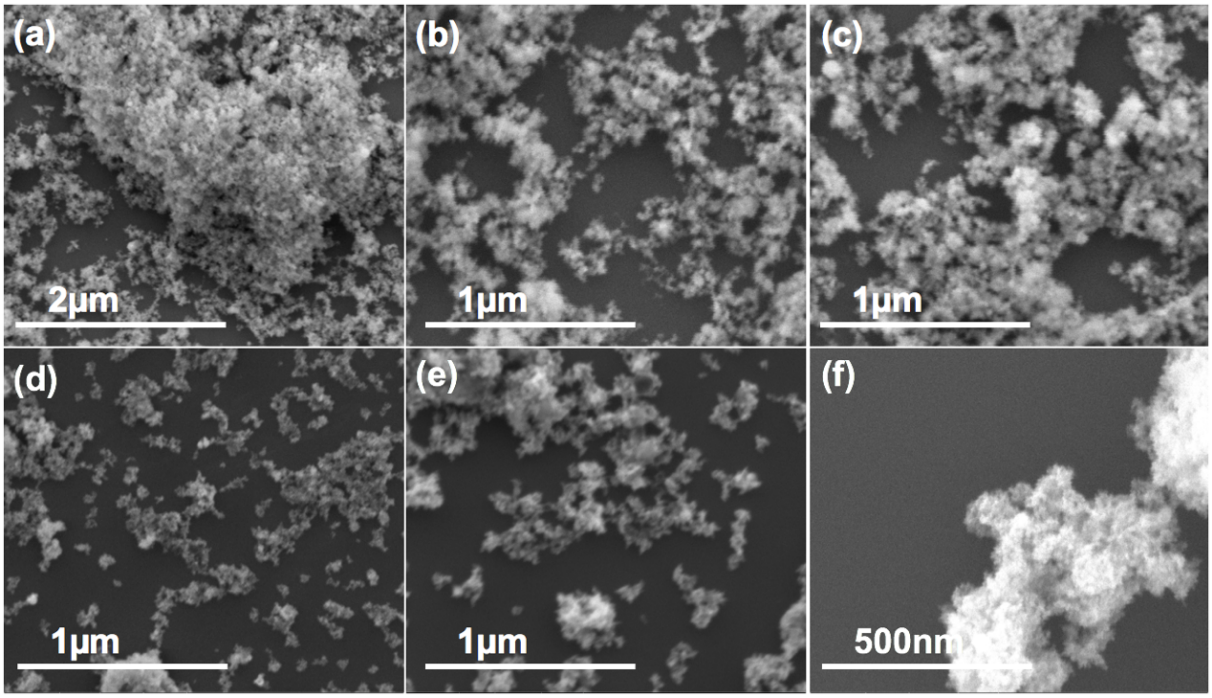

Figure 7.5. SEM images (a-c) of Cu_2ONPs formed using a VFD operating under continuous flow of water at 0.25 mL/min, with the glass tube at 45º tilt angle and rotating at 7.5k rpm, using a 1064 nm pulsed laser operating at 600 mJ, irradiating a pure copper target, (d-f) CuONPs after heating in the as prepared solutions at 50ºC for 10 h. Samples were prepared using drop casting on a silicon wafer.

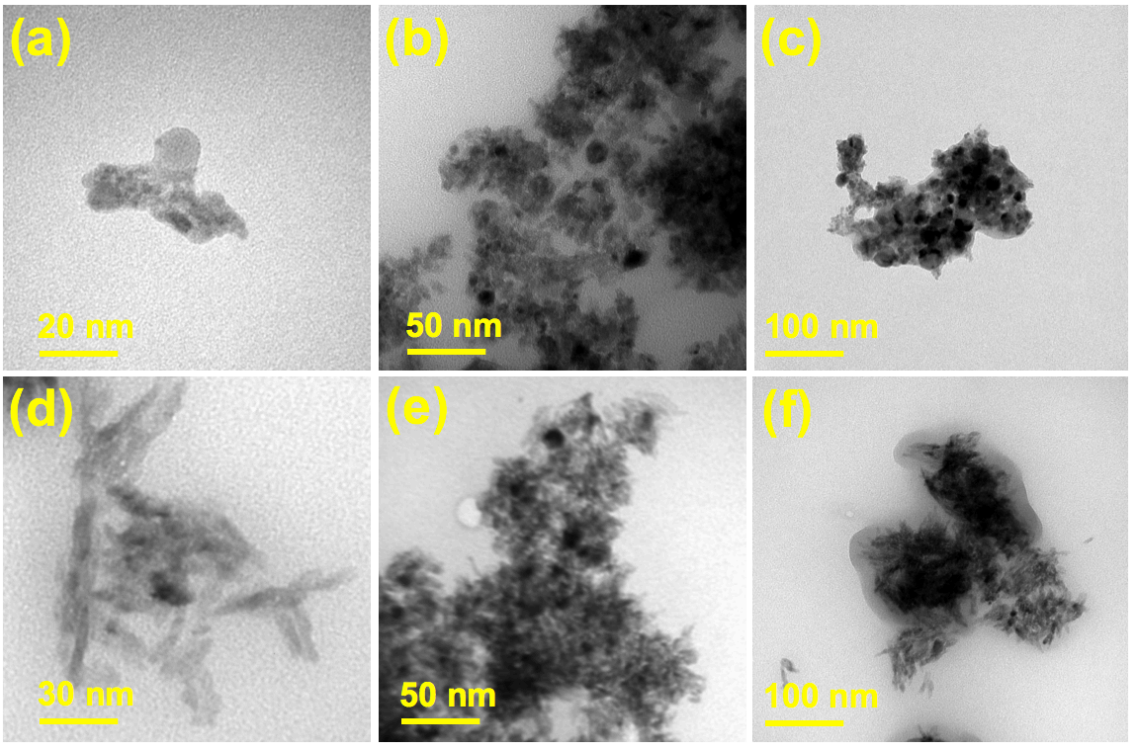

Figure 7.6. TEM images (a-c) of Cu_2ONPs formed using a VFD operating under continuous flow of water at 0.25 mL/min, with the glass tube at 45º tilt angle and rotating at 7.5k rpm, using a 1064 nm pulsed laser operating at 600 mJ, irradiating a pure copper target, (d-f) CuONPs after heating the as prepared solutions at 50ºC for 10 h. Samples were prepared using drop casting on a grid.

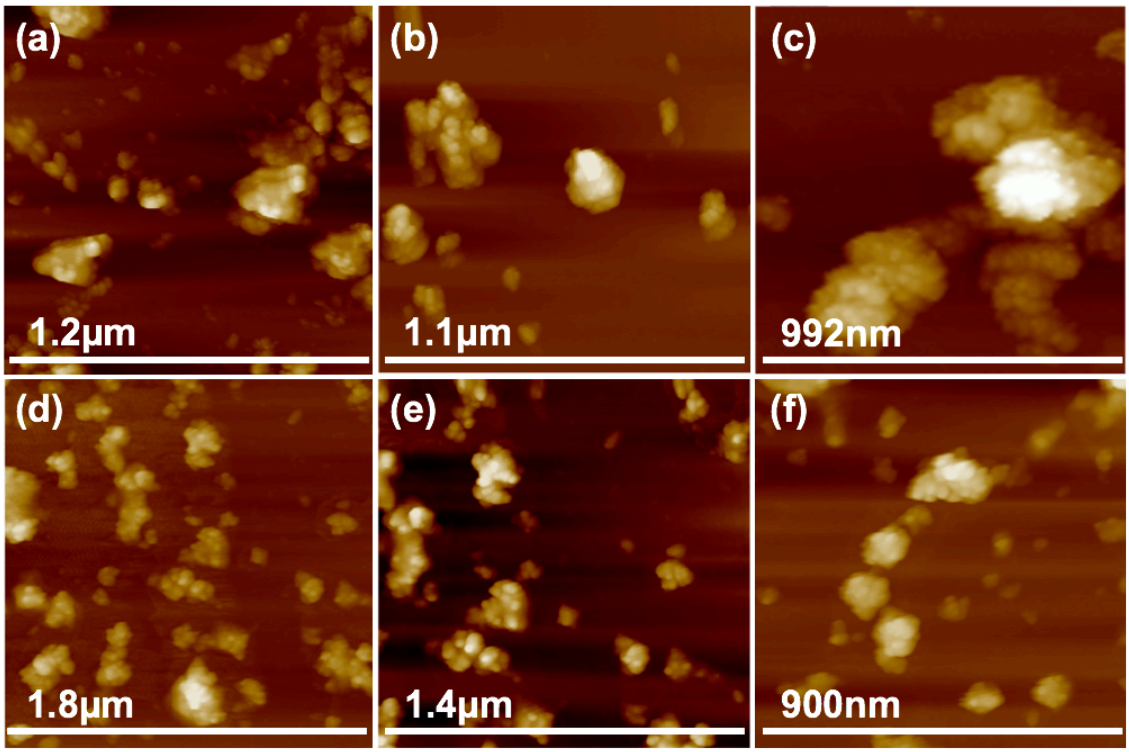

Figure 7.7. AFM images (a-c) of Cu_2ONPs formed using a VFD operating under continuous flow of water at 0.25 mL/min, with the glass tube at 45º tilt angle and rotating at 7.5k rpm, using a 1064 nm pulsed laser operating at 600 mJ, irradiating a pure copper target, (d-f) CuONPs after heating the as prepared solutions at 50ºC for 10 h. Samples were prepared using drop casting on silicon wafer.

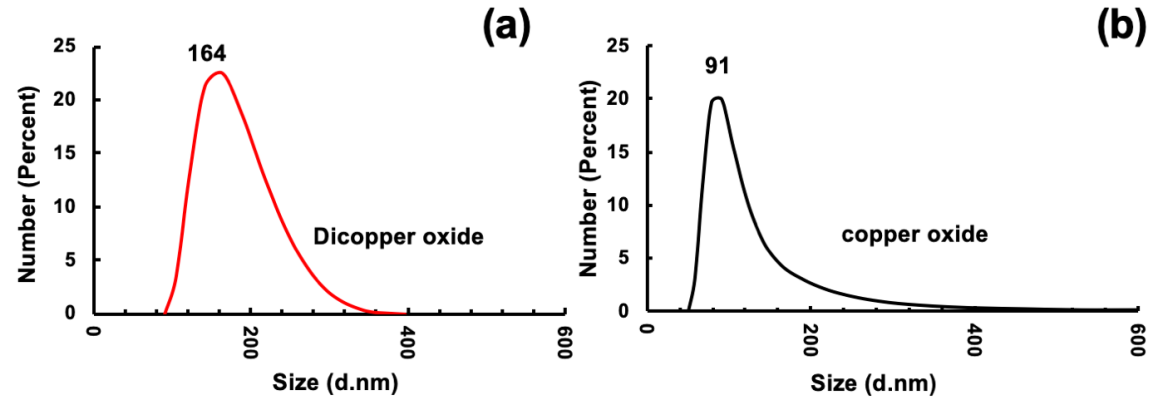

Figure 7.8. DLS of material re-dispersed in water, (a) Cu_2ONPs formed in the VFD with the glass tube at 45º tilt and rotating at 7.5k rpm, flow rate of water 0.25 mL/min, and the 1064 nm pulsed laser operating at 600 mJ irradiating a copper target. (b) CuONPs formed after heating the Cu_2ONPs suspension in air at 50ºC for 10 h.

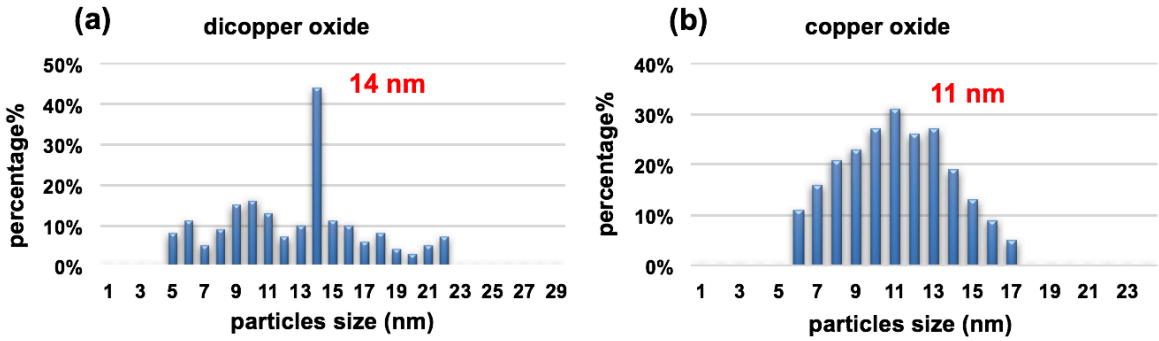

Figure 7.9. Size estimation of nanoparticles using TEM images, for (a) material generated in a VFD with the glass tube at 45º tilt and rotating at 7.5k rpm, flow rate of water 0.25 mL/min, and the 1064 nm pulsed laser operating at 600 mJ irradiating a copper target, and (b) CuONPs prepared from a Cu_2ONPs dispersion in water after heating at 50ºC for 10 h in an oven.

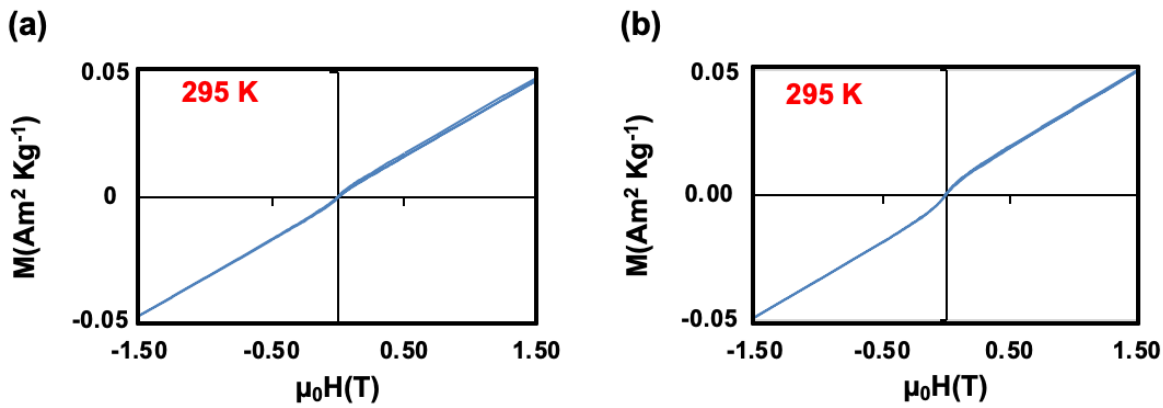

Figure 7.10. Magnetization data for CuONPs formed under continuous flow in the VFD flow of water at 0.25 mL/min, 45º tilt angle, using a 1064 nm pulsed laser operating at 600 mJ irradiating a copper target followed by heating the material as solution at 50ºC for 10 h in an oven. (a) Material from the solution exiting the tube. (b) Material collected from inside the tube after 2 h of processing.

7.5 Conclusions

Cu_2ONPs were prepared by pulsed laser irradiation of a pure copper rod positioned inside a VFD tube, with the material readily converted to copper (II) oxide on mild heating in solution. The NPs are created *in situ,* in a continuous flow process, using water as the choice of solvent. TEM images and XRD data incorporating the use of the Scherrer equation established the presence of nanometre sized particle, with the mechanism of formation of Cu_2ONPs involving oxidation of copper in air above the thin film of liquid in the VFD. The new method of synthesis of these NPs is simple and in high yield, using metal as the source of copper, at the same time avoiding the use of harsh chemicals or agents using water as the choice of solvent,[23,24] and the scene is set for using this method for generating oxides of other metals.

The overall novelty of this work is the ability to selectively prepare relatively small Cu_2O NPs from elemental copper, using a process that minimizes the generation of waste, and this is possible using the VFD thin film microfluidic platform. Also, it is noteworthy to not that the Cu_2O NPs are readily converted to small CuO NPs by mild heating, and that selectively forming Cu_2O NPs in water using laser processing is challenging,[17,23] being difficult to scale and control the homogeneity, with long ablation times resulting mainly in the formation of larger particles.

In exploring the applicability of the process for scaling up, we prepared 200 mg of Cu_2O NPs, as a powder, over 12 h for a single pass through the VFD. In addition, we prepared 200 mg of CuO NPs as a powder, from heating a suspension of 200 mg of Cu_2O NPs in water at 50ºC. This augurs well for the potential application of the copper(I) and (II) oxide NPs.[1-4]

7.6 Acknowledgements

The authors gratefully acknowledge financial support from the Iraq Government, Ministry of Higher Education and Scientific Research, and the Australian Research Council and the Government of South Australia. Use of facilities in the Australian Microscopy & Microanalysis Research Facility (AMMRF) and the Australian National Fabrication Facility (ANFF) at the South Australian nodes of the AMMRF and ANFF under the National Collaborative Research Infrastructure Strategy are also acknowledged, along with assistance from Dr Jason Gascooke in collecting SEM images and Mr Scott Pye for discussions and proof reading.

7.7 References

1. Laurent, S.; Forge, D.; Port, M.; Roch, A.; Robic, C.; Vander Elst, L.; Muller, R. N., Magnetic Iron Oxide Nanoparticles: Synthesis, Stabilization, Vectorization, Physicochemical Characterizations, and Biological Applications. *Chem. Rev.* **2008,** *108* (6), 2064-2110.
2. Sowani, H.; Mohite, P.; Damale, S.; Kulkarni, M.; Zinjarde, S., Carotenoid stabilized gold and silver nanoparticles derived from the Actinomycete Gordonia amicalis HS-11 as effective free radical scavengers. *Enzyme and microbial technology* **2016,** *95*, 164-173.
3. Vijayan, S. R.; Santhiyagu, P.; Ramasamy, R.; Arivalagan, P.; Kumar, G.; Ethiraj, K.; Ramaswamy, B. R., Seaweeds: a resource for marine bionanotechnology. *Enzyme and microbial technology* **2016,** *95*, 45-57.
4. Suriani, A.; Dalila, A.; Mohamed, A.; Mamat, M.; Malek, M.; Soga, T.; Tanemura, M., Fabrication of vertically aligned carbon nanotubes–zinc oxide nanocomposites and their field electron emission enhancement. *Mater. Design* **2016,** *90*, 185-195.
5. Golden, T. D.; Shumsky, M. G.; Zhou, Y.; VanderWerf, R. A.; Van Leeuwen, R. A.; Switzer, J. A., Electrochemical Deposition of Copper(I) Oxide Films. *Chem. Mater.* **1996,** *8* (10), 2499-2504.
6. Korotcenkov, G., Gas response control through structural and chemical modification of metal oxide films: state of the art and approaches. *Sensors and Actuators B: Chem.* **2005,** *107* (1), 209-232.
7. Kumar, R. V.; Diamant, Y.; Gedanken, A., Sonochemical Synthesis and Characterization of Nanometer-Size Transition Metal Oxides from Metal Acetates. *Chem. Mater.* **2000,** *12* (8), 2301-2305.
8. Guo, Q.; Teng, X.; Rahman, S.; Yang, H., Patterned Langmuir−Blodgett Films of Monodisperse Nanoparticles of Iron Oxide Using Soft Lithography. *J. Am. Chem. Soc.* **2003,** *125* (3), 630-631.
9. Allen, S. E.; Walvoord, R. R.; Padilla-Salinas, R.; Kozlowski, M. C., Aerobic copper-catalyzed organic reactions. *Chem. Rev.* **2013,** *113* (8), 6234-6458.
10. Yin, G.; Nishikawa, M.; Nosaka, Y.; Srinivasan, N.; Atarashi, D.; Sakai, E.; Miyauchi, M., Photocatalytic Carbon Dioxide Reduction by Copper Oxide Nanocluster-Grafted Niobate Nanosheets. *ACS Nano* **2015,** *9* (2), 2111-2119.
11. Poreddy, R.; Engelbrekt, C.; Riisager, A., Copper oxide as efficient catalyst for oxidative dehydrogenation of alcohols with air. *Catal. Sci. Technol.* **2015,** *5* (4), 2467-2477.
12. Gawande, M. B.; Goswami, A.; Felpin, F.-X.; Asefa, T.; Huang, X.; Silva, R.; Zou, X.; Zboril, R.; Varma, R. S., Cu and Cu-based nanoparticles: synthesis and applications in catalysis. *Chem. Rev.* **2016,** *116* (6), 3722-3811.
13. Tsuji, T.; Iryo, K.; Watanabe, N.; Tsuji, M., Preparation of silver nanoparticles by laser ablation in solution: influence of laser wavelength on particle size. *Appl. Surf. Sci.* **2002,** *202* (1), 80-85.
14. Amikura, K.; Kimura, T.; Hamada, M.; Yokoyama, N.; Miyazaki, J.; Yamada, Y., Copper oxide particles produced by laser ablation in water. *Appl. Surf. Sci.* **2008,** *254* (21), 6976-6982.
15. Gondal, M.; Qahtan, T. F.; Dastageer, M.; Saleh, T. A.; Maganda, Y. W. In Synthesis and characterization of copper oxides nanoparticles via pulsed laser ablation in liquid,

10th International Conference on High Capacity Optical Networks and Enabling Technologies IEEE: **2013**; pp 146-150.
16. Markert, J.; Messina, T.; Dam, B.; Huijbregste, J.; Rector, J.; Griessen, R., Infinite-layer copper-oxide laser-ablated thin films: substrate, buffer-layer, and processing effects. *IEEE transactions on applied superconductivity* **2003,** *13* (2), 2684-2686.
17. Haram, N.; Ahmad, N., Effect of laser fluence on the size of copper oxide nanoparticles produced by the ablation of Cu target in double distilled water. *Appl. Phys. A* **2013,** *111* (4), 1131-1137.
18. Vitta, Y.; Piscitelli, V.; Fernandez, A.; Gonzalez-Jimenez, F.; Castillo, J., α-Fe nanoparticles produced by laser ablation: Optical and magnetic properties. *Chem. Phys. Lett.* **2011,** *512* (1), 96-98.
19. Britton, J.; Chalker, J. M.; Raston, C. L., Rapid Vortex Fluidics: Continuous Flow Synthesis of Amides and Local Anesthetic Lidocaine. *Chem.–A Eur. J.* **2015,** *21* (30), 10660-10665.
20. Gandy, M. N.; Raston, C. L.; Stubbs, K. A., Towards aryl C-N bond formation in dynamic thin films. *Org. Biomol. Chem.* **2014,** *12* (26), 4594-4597.
21. Chen, X.; Dobson, J. F.; Raston, C. L., Vortex fluidic exfoliation of graphite and boron nitride. *Chem. Commun.* **2012,** *48* (31), 3703-3705.
22. Alharbi, T. M. D.; Vimalanathan, K.; Lawrance, W. D.; Raston, C. L., Controlled slicing of single walled carbon nanotubes under continuous flow. *Carbon* **2018,** *140*, 428-432.
23. Luo, X.; Al-Antaki, A. H. M.; Alharbi, T. M. D.; Hutchison, W. D.; Zou, Y.-c.; Zou, J.; Sheehan, A.; Zhang, W.; Raston, C. L., Laser-Ablated Vortex Fluidic-Mediated Synthesis of Superparamagnetic Magnetite Nanoparticles in Water Under Flow. *ACS Omega* **2018,** *3* (9), 11172-11178.
24. Mohammed Al-antaki, A. H.; Luo, X.; Duan, A.; Lamb, R. N.; Eroglu, E.; Hutchison, W.; Zou, Y.-C.; Zou, J.; Raston, C. L., Continuous flow synthesis of phosphate binding h-BN@magnetite hybrid material. *RSC Adv.* **2018,** *8* (71), 40829-40835.
25. Pye, S. J.; Dalgarno, S. J.; Chalker, J. M.; Raston, C. L., Organic oxidations promoted in vortex driven thin films under continuous flow. *Green Chem.* **2018,** *20* (1), 118-124.
26. Alsulami, I.; Alharbi, T.; Harvey, D.; Gibson, C. T.; Raston, C. L., Controlling the growth of fullerene C_{60} cones under continuous flow. *Chemical Communications* **2018**,*54* **(**57), 7896-7899.
27. Luo, X.; Smith, P.; Raston, C. L.; Zhang, W., Vortex Fluidic Device-Intensified Aqueous Two Phase Extraction of C-Phycocyanin from Spirulina maxima. *ACS Sustainable Chem. Eng.* **2016,** *4* (7), 3905-3911.
28. Smith, J. N. Using Directed Evolution to Increase Solubility of Recombinant Membrane Proteins and Shear Stress-Mediated Investigation of Protein Folding. UC Irvine, 2017.(Theses)
29. Luo, X.; Al-Antaki, A. H. M.; Harvey, D. P.; Ruan, Y.; He, S.; Zhang, W.; Raston, C. L., Vortex Fluidic Mediated Synthesis of Macroporous Bovine Serum Albumin-Based Microspheres. *ACS Appl. Mater. Interf.* **2018,** *10* (32), 27224-27232.
30. Luo, X.; Al-Antaki, A. H. M.; Vimalanathan, K.; Moffatt, J.; Zheng, K.; Zou, Y.; Zou, J.; Duan, X.; Lamb, R. N.; Wang, S.; Li, Q.; Zhang, W.; Raston, C. L., Laser irradiated vortex fluidic mediated synthesis of luminescent carbon nanodots under continuous flow. *React. Chem. Eng.* **2018,** *3* (2), 164-170.
31. Alharbi, T. M. D.; Harvey, D.; Alsulami, I. K.; Dehbari, N.; Duan, X.; Lamb, R. N.;

Lawrance, W. D.; Raston, C. L., Shear stress mediated scrolling of graphene oxide. *Carbon* **2018,** *137*, 419-424.
32. Karthik, P.; Singh, S. P., Copper conductive inks: synthesis and utilization in flexible electronics. *RSC Adv.* **2015,** *5* (79), 63985-64030.
33. Ranu, B. C.; Dey, R.; Chatterjee, T.; Ahammed, S., Copper Nanoparticle-Catalyzed Carbon-Carbon and Carbon- Heteroatom Bond Formation with a Greener Perspective. *ChemSusChem* **2012,** *5* (1), 22-44.
34. Yasmin, L.; Chen, X.; Stubbs, K. A.; Raston, C. L., Optimising a vortex fluidic device for controlling chemical reactivity and selectivity. *Sci. Rep.* **2013,** *3*, 2282.
35. Tadjarodi, A.; Roshani, R., A green synthesis of copper oxide nanoparticles by mechanochemical method. *Current Chem. Lett.* **2014,** *3* (4), 215-220.
36. Zhang, Y. X.; Huang, M.; Li, F.; Wen, Z. Q., Controlled synthesis of hierarchical CuO nanostructures for electrochemical capacitor electrodes. *Int. J. Electrochem. Sci.* **2013,** *8*, 8645-8661.
37. Basu, M.; Sinha, A. K.; Pradhan, M.; Sarkar, S.; Pal, A.; Mondal, C.; Pal, T., Methylene Blue–Cu_2O reaction made easy in acidic medium. *J. Phys. Chem. C* **2012,** *116* (49), 25741-25747.
38. Nagajyothi, P.; Muthuraman, P.; Sreekanth, T.; Kim, D. H.; Shim, J., Green synthesis: in-vitro anticancer activity of copper oxide nanoparticles against human cervical carcinoma cells. *Arabian J. Chem.* **2017,** *10* (2), 215-225.
39. Zhang, Y. C.; Tang, J. Y.; Wang, G. L.; Zhang, M.; Hu, X. Y., Facile synthesis of submicron Cu_2O and CuO crystallites from a solid metallorganic molecular precursor. *J. Cryst. Growth* **2006,** *294* (2), 278-282.
40. Guo, D.; Wang, L.; Du, Y.; Ma, Z.; Shen, L., Preparation of octahedral Cu_2O nanoparticles by a green route. *Mater. Lett.* **2015,** *160*, 541-543.
41. Yang, Y.-C.; Wang, H.-J.; Whang, J.; Huang, J.-S.; Lyu, L.-M.; Lin, P.-H.; Gwo, S.; Huang, M. H., Facet-dependent optical properties of polyhedral Au–Cu_2O core–shell nanocrystals. *Nanoscale* **2014,** *6* (8), 4316-4324.
42. Chen, L.; Zhang, Y.; Zhu, P.; Zhou, F.; Zeng, W.; Lu, D. D.; Sun, R.; Wong, C., Copper Salts Mediated Morphological Transformation of Cu_2O from Cubes to Hierarchical Flower-like or Microspheres and Their Supercapacitors Performances. *Sci. Rep.* **2015,** *5*, 9672.
43. Sabbaghan, M.; Beheshtian, J.; Liarjdame, R. N., Preparation of Cu_2O nanostructures by changing reducing agent and their optical properties. *Mater. Lett.* **2015,** *153*, 1-4.
44. Sankar, R.; Maheswari, R.; Karthik, S.; Shivashangari, K. S.; Ravikumar, V., Anticancer activity of Ficus religiosa engineered copper oxide nanoparticles. *Mater. Sci. Eng.: C* **2014,** *44*, 234-239.
45. Yeh, M.-S.; Yang, Y.-S.; Lee, Y.-P.; Lee, H.-F.; Yeh, Y.-H.; Yeh, C.-S., Formation and Characteristics of Cu Colloids from CuO Powder by Laser Irradiation in 2-Propanol. *J. Phys. Chem. B* **1999,** *103* (33), 6851-6857.
46. Gondal, M.; Qahtan, T. F.; Dastageer, M. A.; Maganda, Y.; Anjum, D. H.; nanotechnology, Synthesis of Cu/Cu_2O nanoparticles by laser ablation in deionized water and their annealing transformation into CuO nanoparticles. *J. Nanosci. Nanotnol.* **2013,** *13* (8), 5759-5766.
47. Bergum, K.; Riise, H. N.; Gorantla, S.; Lindberg, P. F.; Jensen, I. J. T.; Gunnæs, A. E.; Galeckas, A.; Diplas, S.; Svensson, B. G.; Monakhov, E., Improving carrier

transport in Cu_2O thin films by rapid thermal annealing. *Journal of Physics: Condensed Matter,* **2018,** *30* (7), 075702.
48. Yin, M.; Wu, C.-K.; Lou, Y.; Burda, C.; Koberstein, J. T.; Zhu, Y.; O'Brien, S., Copper oxide nanocrystals. *J. Am. Chem. Soc.* **2005,** *127* (26), 9506-9511.
49. Salavati-Niasari, M.; Davar, F., Synthesis of copper and copper (I) oxide nanoparticles by thermal decomposition of a new precursor. *Mater. Lett.* **2009,** *63* (3-4), 441-443.
50. Zhao, Y.-F.; Yang, Z.-Y.; Zhang, Y.-X.; Jing, L.; Guo, X.; Ke, Z.; Hu, P.; Wang, G.; Yan, Y.-M.; Sun, K.-N., Cu_2O Decorated with Cocatalyst MoS_2 for Solar Hydrogen Production with Enhanced Efficiency under Visible Light. *J. Phys. Chem. C* **2014,** *118* (26), 14238-14245.
51. Jiang, X.; Herricks, T.; Xia, Y., CuO Nanowires Can Be Synthesized by Heating Copper Substrates in Air. *Nano Lett.* **2002,** *2* (12), 1333-1338.
52. Yao, W.-T.; Yu, S.-H.; Zhou, Y.; Jiang, J.; Wu, Q.-S.; Zhang, L.; Jiang, J., Formation of Uniform CuO Nanorods by Spontaneous Aggregation: Selective Synthesis of CuO, Cu_2O, and Cu Nanoparticles by a Solid−Liquid Phase Arc Discharge Process. *J. Phys. Chem. B* **2005,** *109* (29), 14011-14016.
53. Soon, A.; Todorova, M.; Delley, B.; Stampfl, C., Thermodynamic stability and structure of copper oxide surfaces: A first-principles investigation. *Phys. Rev. B* **2007,** *75* (12), 125420.
54. Reichel, F.; Jeurgens, L.; Mittemeijer, E., Thermodynamic modeling of the initial microstructural evolution of oxide films grown on bare copper. *Thin Solid Films* **2008,** *516* (7), 1457-1460.
55. Du, F.; Chen, Q.-Y.; Wang, Y.-H., Effect of annealing process on the heterostructure CuO/Cu_2O as a highly efficient photocathode for photoelectrochemical water reduction. *J. Phys. Chem. of Solids* **2017,** *104*, 139-144.
56. Poulston, S.; Parlett, P.; Stone, P.; Bowker, M., Surface oxidation and reduction of CuO and Cu_2O studied using XPS and XAES. *Surf. Interf. Anal.* **1996,** *24* (12), 811-820.
57. Espinós, J.; Morales, J.; Barranco, A.; Caballero, A.; Holgado, J.; González-Elipe, A., Interface effects for Cu, CuO, and Cu_2O deposited on SiO_2 and ZrO_2. XPS determination of the valence state of copper in Cu/SiO_2 and Cu/ZrO_2 catalysts. *J. Phys. Chem. B* **2002,** *106* (27), 6921-6929.
58. Park, B. K.; Jeong, S.; Kim, D.; Moon, J.; Lim, S.; Kim, J. S., Synthesis and size control of monodisperse copper nanoparticles by polyol method. *J. colloid and interf. Sci.* **2007,** *311* (2), 417-424.
59. Fredj, N.; Burleigh, T. D., Transpassive dissolution of copper and rapid formation of brilliant colored copper oxide films. *J. Electrochem. Soc.* **2011,** *158* (4), C104-C110.
60. Punnoose, A.; Magnone, H.; Seehra, M.; Bonevich, J., Bulk to nanoscale magnetism and exchange bias in CuO nanoparticles. *Phys. Rev. B* **2001,** *64* (17), 174420.

ACS OMEGA

Article

Cite This: ACS Omega 2019, 4, 13577−13584

http://pubs.acs.org/journal/acsodf

Continuous Flow Copper Laser Ablation Synthesis of Copper(I and II) Oxide Nanoparticles in Water

Ahmed Hussein Mohammed Al-Antaki,[†,∥] Xuan Luo,[†,‡] XiaoFei Duan,[⊥] Robert N. Lamb,[⊥] Wayne D. Hutchison,[#] Warren Lawrance,[§] and Colin L. Raston*[,†]

[†]Flinders Institute for Nanoscale Science and Technology, College of Science and Engineering, [‡]Centre for Marine Bioproducts Development, College of Medicine and Public Health and [§]College of Science and Engineering, Flinders University, Adelaide, SA 5042, Australia

[∥]Department of Chemistry, Faculty of Sciences, Kufa University, Kufa, 54001 Najaf, Iraq

[⊥]Trace Analysis for Chemical, Earth and Environmental Sciences (TrACEES), University of Melbourne, Melbourne, VIC 3010, Australia

[#]School of Science, University of New South Wales, ADFA campus, Canberra BC, ACT 2610, Australia

Supporting Information

ABSTRACT: Copper(I) oxide (Cu_2O) nanoparticles (NPs) are selectively prepared in high yields under continuous flow in a vortex fluidic device (VFD), involving irradiation of a copper rod using a pulsed laser operating at 1064 nm and 600 mJ. The plasma plume generated inside a glass tube (20 mm O.D.), which is rapidly rotating (7.5 k rpm), reacts with the enclosed air in the microfluidic platform, with then high mass transfer of material into the dynamic thin film of water passing up the tube. The average size of the generated Cu_2ONPs is 14 nm, and they are converted to copper(II) oxide (CuO) nanoparticles with an average diameter of 11 nm by heating the as-prepared solution of Cu_2ONPs in air at 50 °C for 10 h.

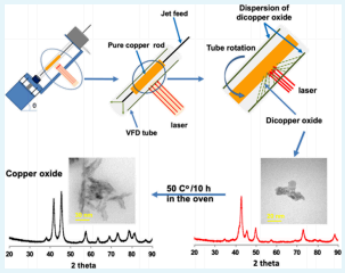

INTRODUCTION

The physical and chemical properties of nanoparticles of metal oxides are distinctly different to bulk materials, and they are attracting considerable attention. They find applications in diverse fields, including chemical manufacturing, environmental technology, energy conversion, and storage as well as in biological areas.[1−4] A diversity of techniques have been used to prepare metal oxide particles in general, including electrophoretic and electrochemical deposition,[5] vacuum deposition,[6] sonochemical processing,[7] lithography, and diffusion-controlled nanoparticle growth.[8] Focusing on dicopper oxide (Cu_2O) and copper oxide (CuO), they have been prepared using such techniques, with the uniform size and shape of the particles.[7,8] They find particular use in catalytic organic transformations, electrocatalysis, and photocatalysis.[9−11] Developing synthetic methodologies and supports that increase the stability of copper nanoparticles have been explored, especially in regard to their sensitivity to oxygen, water, and different reagents. This has led to the development of more complex-structured nanoparticles, as in core−shell particles, and different ways to oxidize the copper.[12]

Batch processing is typically used in the fabrication of copper oxide nanoparticles, but such processing can result in variation of product from batch to batch, and refined reagents are required. An alternative approach to prepare different metal oxides in general involves the use of lasers, and this includes in the synthesis of copper oxide nanoparticles.[13−17] Pulsed laser ablation (PLA) involves ablating a solid target in a liquid phase or in air, which has a number of advantages. These include (a) not requiring the process to be operating under a high vacuum, (b) the processing is simple and high yielding, and (c) it avoids the use of chemicals. In addition, optimizing the experimental parameters can result in controlling the shape and size of the nanoparticles.[17] PLA involves absorption of the laser radiation at the metal surface as the so-called interaction zone, which causes the transformation of kinetic energy into thermal energy. Also, if the laser power is sufficiently high, a local plasma plume with high temperatures and pressures is formed,[18] and this can lead to the formation of metal oxide particles in the presence of oxygen.

We report the synthesis of copper(I) oxide nanoparticles using PLA under continuous flow conditions, which can minimize batch variation in the process, as discussed above. Continuous flow processing is important in being able to scale up from the research laboratory processing to large-scale production, thereby avoiding batch-to-batch variation, which

Received: July 1, 2019
Accepted: July 18, 2019
Published: August 7, 2019

DOI: 10.1021/acsomega.9b01983
ACS Omega 2019, 4, 13577−13584

8. Conclusion and Future work

8.1 Conclusion

The Vortex fluidic device (VFD) has been developed for applications in several areas, including materials fabrication, for example exfoliation,[1-4] scrolling graphene and graphene oxide,[5,6] slicing CNTs,[7-9] unzipping CNTs,[10] decorating graphene,[11,12] fabricating composites,[13,14] coiling SWCNTs[15,16] and self-assembly[17-19], fabricating metal oxides[20,21] and metal oxide/composites,[22,23] folding proteins,[24-28] and fabricating polymers,[29-31] and in organic[32-43] and inorganic synthesis,[44,45] preparing nano-food[46,47] and biodiesel production.[48-50] The VFD is designed to impart high shear into a thin film, with the outcome of the processing critically dependent on the nature of the liquid, rotational speed and tilt angle, for either the confined mode for small volumes of the liquid, [1,4,6,15,18,32,33,36,44,51-55] or continuous flow for larger volumes. [2,3,5,7-14,16,17,19,20,22-26,28-31,34,35,37-43,46-50,56] Research undertaken in this thesis establishes that the dynamic thin film in the VFD can mediate processing, benefiting the fabrication of 0D, 1D and 2D nanomaterials, and importantly this can be under continuous flow conditions.

A continuous flow process for exfoliating 2D-MXene into multilayered sheets of thickness *ca* 3 nm has been developed. The mechanoenergy in the thin film inside the rapidly rotating VFD tube can also fragment the laminar MXene into nanoparticles with an average size 68 nm in diameter, which assemble into spheres. These outcomes followed a systematic approach in varying all the processing parameters of the VFD, as well as the need to carry out all the processing under nitrogen to avoid any oxidation of the MXene into anatase. The optimised conditions were using 0.5 mg/mL of the starting material in a 1:1 mixture of IPA and water, with the tube inclined at +45^{o} and rotating at 4k rpm, with the flow rate at 0.5 mL/min. The potential applications of the exfoliated layered material and the nanoparticles of MXene are in environmental remediation[57], biology[58-61], electronic devices[62,63], supercapacitors.[63,64] and the next generation of batteries.[65,66]

Changing the operating parameters of the VFD can dramatically change the outcome of any process. The oxidation of MXene can be controlled for processing as received material in a 30% aqueous solution of hydrogen peroxide, with the rotational speed at 5k rpm, +45^{o} tilt angle of the tube, and a flow rate of a solution at 0.75 mL/min with a concentration of 10 mg of MXene in 20 mL H_2O_2. This processing was effective in decorating a few layers of exfoliated MXene with anatase TiO_2 NPs, in forming a novel shaped composite. The

processing also generates NPs of fragmented MXene which assemble with anatase TiO_2 NPs into novel spheroidal TiO_2NPs/MXenes composite material. Both the exfoliated sheets of the 2D material and the spheres composite are stable for extended periods, beyond a few weeks. A recent literature review highlighted the ability to use such composites in a number of applications, noting that it is biocompatible with enzymes.[67] These include modified glassy carbon electrodes for H_2O_2 reduction,[68] nitrite detection,[69] glucose and sodium alanate,[70] Li-ion battery anodes[71] and as photocatalyst.[72]

h-BN scrolls and exfoliated *h*-BN were prepared under continuous flow processing in the VFD, using water as the solvent, in the absence of other reagents with the overall system highlighting the green chemistry metrics. The tilt angle (-45º) of the device was the optimised condition for both exfoliation and scrolling *h*-BN. At a tilt angle of +45º, the yield of each material was low with much of it retained in the tube. This was overcome by tilting the tube to -45º. How the fluid dynamics in the liquid change at this angle is yet to be explored, and it will be a major research project in its own right. Nevertheless, the residence time changes dramatically, from ca 2 minutes for -45º to ca 6 minutes for +45º. The low residence time for -45º relates to a net gravitational pull down the tube, and presumably this facilitates movement of the exfoliated/scrolled material along and out of the tube. The processing of exfoliated *h*-BN and scrolled *h*-BN did not alter the lateral dimensions of the material, and there is no fragmentation of the *h*-BN. The scalability of the processing was demonstrated by preparing 5 mg and 72 mg in one run over 24 hours of *h*-BN scrolls and exfoliated *h*-BN, respectively. The optimal concentration and flow rate for fabricating exfoliated sheets were higher than scroll processing under the same tilt angle and same rotational speed, and thus there is less of *h*-BN scrolls. This difference in selectivity reflects the expected changes in the complex fluid dynamics as the flow rate and concentration of *h*-BN are changed.

A one-step synthesis of a new *h*-BN@magnetite composite in water was also prepared in the VFD, also in the absence of any other materials or potentially toxic solvents. Irradiating a pure iron rod inside the VFD tube with a pulsed laser, resulting in ablation of the metal, forming superparamagnetic magnetite nanoparticles which decorated the surface of *h*-BN. Delivering *h*-BN in water to the tube used the in-house developed magnetic stirred syringe (MSS) with the suspension delivered to the hemisphere base of the tube. The resulting composite, *h*-BN@magnetite has a

surface area of 91.0 m^2/g associated with high porosity arising from the superparamagnetic magnetite nanoparticles randomly dispersed on the surface of the outer sheets of *h*-BN. This material lends itself for binding functional materials, for example in applications in catalysts.[73] For the work presented herein, the material was appraised for waste water treatment, taking advantage of the ability to collect *h*-BN@magnetite loaded with phosphate using a magnetic field. In addition, the phosphate adsorption capacity was high, up to 171.2 mg PO_4^{3-} per gram of Fe, and the material can be readily recycled for multiple use.

The high level of impurities in the as received BNNTs (up to 50%) impacted on the ability to slice them in the VFD with an understanding of the level of control of the process, and then for determining their properties and potential applications. This required developing a purification protocol, as a simple two-step process which is without precedent. Following this, controlled slicing was possible, which arises from the high shear (induced mechanical energy) in the VFD coupled with induced vibrational energy while irradiated by a NIR pulse lase, noting that BNNTs absorb NIR radiation.[74] The controlled slicing was optimised by systematically exploring all the operating parameters of the VFD, along with the laser power, affording BNNT tubes ca 340 nm to 400 nm in length. The sliced BNNTs were prepared in a 1:1 mixture of IPA and water under continuous flow processing, with scalability demonstrated in processing 30 mg of the material over 21 hours. This length scale offers scope for appraisal of the material in different applications of BNNTs.

Finally, the pulsed laser ablation method (PLA) was effective in generating dicopper oxide (Cu_2O) nanoparticles in the VFD. This involved irradiating a pure copper rod positioned inside a VFD tube with a NIR pulsed laser. Mild heating of a colloidal suspension of Cu_2O NPs readily converted it to copper oxide (CuO) NPs. The formation of Cu_2O was under continuous flow processing in the VFD, using water as a benign solvent, without the need for any harsh chemicals. The Scherrer equation was applied to the X-ray diffraction data to determine the mean particle sizes, which were consistent with the size determined from TEM images. The mechanism of the formation of Cu_2ONPs involves oxidation of copper in air above the thin film of liquid in the VFD, as a simple method with the material formed in high yield.[21,75] Overall the processing does not produce a waste stream, with water as the solvent of choice, and thus it takes on board minimising the impact of the technology on the environment. In exploring the applicability of the process for scaling up, 200 mg of Cu_2O

NPs was prepared as a powder over 12 h, for a single pass through the VFD. In addition, 200 mg of CuO NPs was prepared via heating a suspension of 200 mg of Cu_2O NPs in water at 50ºC. This augurs well for the potential application of the copper(I) and (II) oxide NPs. [76-79]

Figure 8.1 provides a summary of all the outcomes of the processing in the VFD in this thesis, where there was a drive for developing continuous flow processing in the device using environmentally friendly reaction media, notably water, aqueous hydrogen peroxide and a 1:1 mixture of IPA and water. Thus, the results demonstrate a significant contribution in developing a relatively new processing platform for a sustainable future, and given their green chemistry credentials this will facilitate any uptake of the processing by industries.

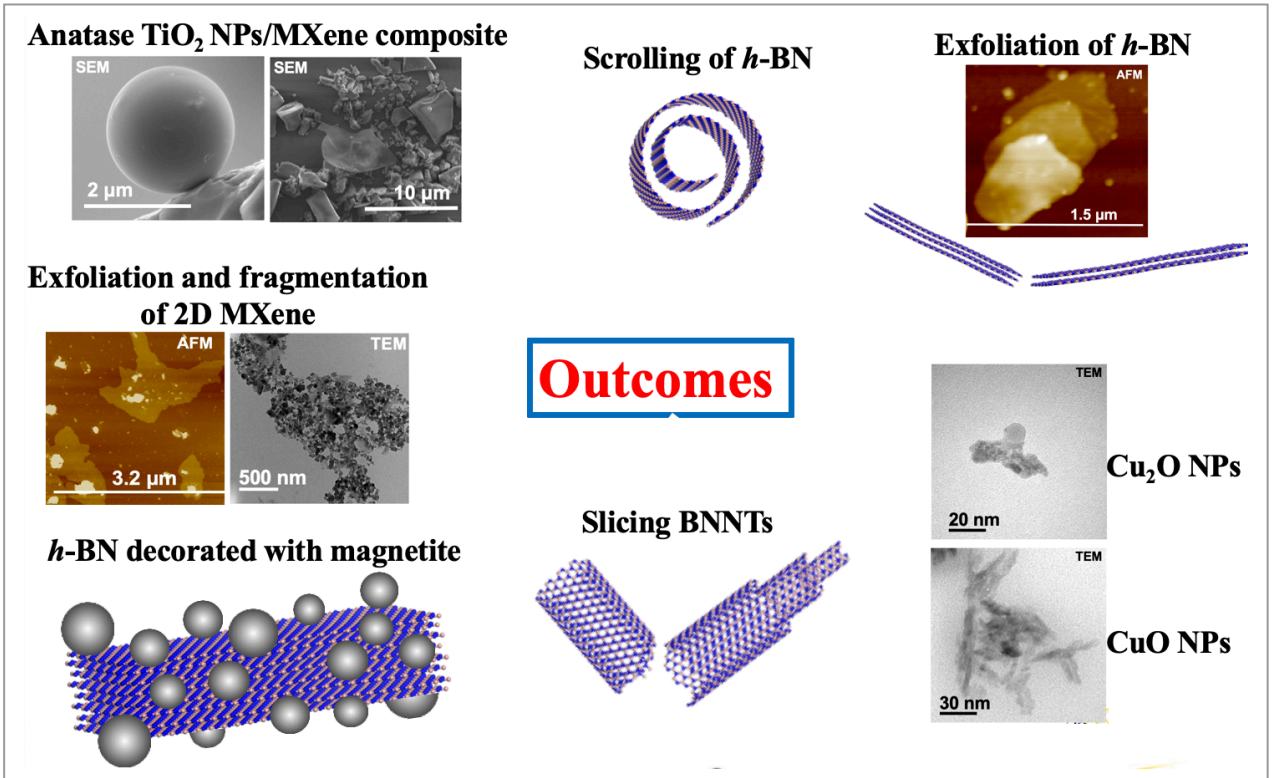

Figure 8.1. Summary of the outcomes of the material processing in this thesis, which is based of four publications and another two manuscripts submitted for publication.[75, 80-82]

8.2 Future work

The outcomes of each project undertaken in this thesis are reported as separate chapters, collectively providing a platform for applications of the corresponding materials. In addition, the findings provide insight for further applications and also for taking the findings to processing of related materials. The VFD is a relatively new microfluidic platform, with few research groups around the world having access to such technology. The findings in this thesis further highlight the remarkable utility of the VFD in being able to prepare/transform

different nanomaterials. It is the unique fluid flow in the VFD that sets the device aside as a paradigm shift in microfluidic devices and materials synthesis in general. Once the fluid flow is established in the VFD, which is a major international research effort underway, there will then be a level of predictability of the outcomes of processing in the device, and this will open up other possibilities in using the VFD to further manipulate the materials targeted in this thesis. This will include decorating 0D, 1D, 2D materials in general with other nanomaterials, as summarized in Fig. 8.2.

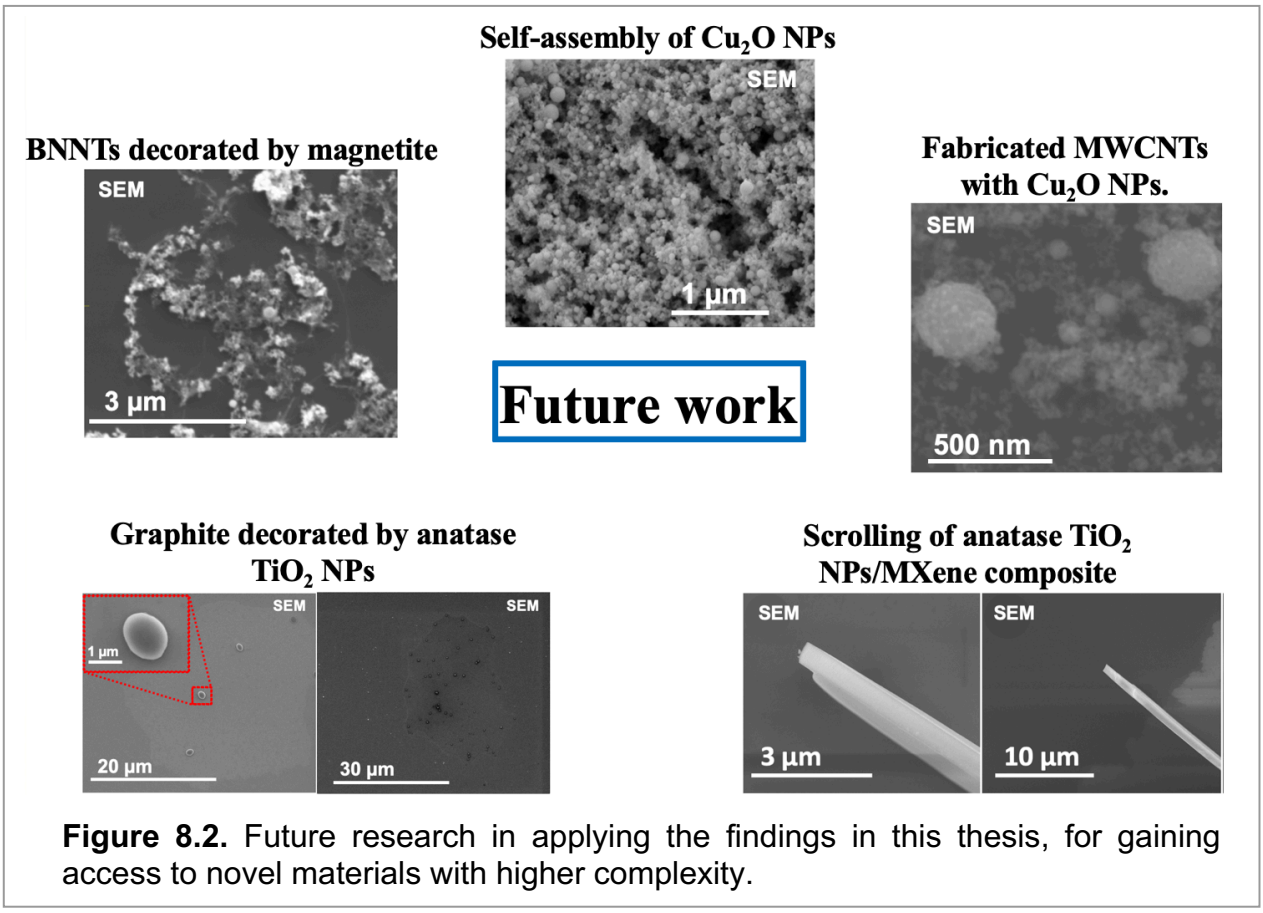

Figure 8.2. Future research in applying the findings in this thesis, for gaining access to novel materials with higher complexity.

8.2.1 Manipulating anatase TiO_2 NPs 2D materials.

Zhang *et al* demonstrated the ability to synthesize TiO_2/GO composites (GO = graphene oxide), but this involved multiple steps, including hydrothermal and freeze-drying. The structure of nanocomposite shows good application such as photocatalytic activity in reducing the pollution of heavy metal in ROC wastewater. Also, it solved the problem of low sensitivity of conventional ways towards the detection of heavy metal ions. [83]

The shear stress in the dynamic thin film in the VFD has potential for developing an effective process to prepare anatase TiO_2 NPs/ graphite or anatase TiO_2 NPs/graphene oxide composites, in a single high yielding process, without the need for other agents or

harsh chemicals. The initial approach will be to incorporate graphite and MXene in the same solvent (hydrogen peroxide) in the VFD, which might lead to oxidation of the MXene in a controlled manner, in affording anatase TiO_2 NPs. There is also a possibility of using the VFD, under similar conditions, to form scrolls of graphite/graphene with the resulting anatase embedded in between successive turns of the scrolls of graphene, at the same time resulting in oxidation with MXene in a controlled way.

8.2.2 BNNTs decorated by magnetite.

BNNT/Fe_3O_4 composite material is potentially accessible in the VFD, by mixing Fe^{2+}: Fe^{3+} (86 mg of $FeCl_2$.$4H_2O$ (99,0%) and 236 mg of $FeCl_3$.$6H_2O$, respectively) in Milli-Q water under nitrogen gas. Due to the magnetic response of such a composite material, there is prospect of directing the material into cells. The magneto hyperthermia assay has potential for up-take of BNNT-Fe_3O_4, to trigger the cell death process in a tumorigenic lineage of HeLa cells.[84] An alternative strategy is pulsed laser ablation of a pure iron rod positioned inside a VFD tube, for preparing magnetite@BNNTs composite with superparamagnetic properties in a single step process. [21,75]

8.2.3 Self-assembly and Fabrication.

One-step processing in decorating MWCNTs with Cu_2O nanoparticles is possible using Fehling's reaction. Such Cu_2O-decorated MWCNT composites are expected to find applications in nano-electronics devices, catalysis, sensors and electrochemical energy storage.[84] Developing such material involves systematically exploring the processing parameter space in the VFD, including tilt angle, rotational speed, and concentrations. There is a likelihood of fabricating dicopper oxide decorated with MWCNTs using water as the solvent, while avoiding the use of other reagents.[85]

The presence of intense micromixing in the VFD can result in the formation of different phases of material at the nanometer dimensions, using a mixture of two or multiple immiscible solvents (antisolvent). This will have implications in a number of applications, including in biology, self-assembly, material science, extraction, drug delivery, nano-foods and biodiesel, and many more. The flexibility of using the VFD in association with other fields, beyond lasers, have been used to slice nanotubes, 2D material exfoliation, fragmentation and scrolling. In addition, heating along the VFD tube has exciting possibilities, as is the use of LED light sources with different wavelength, electric and magnetic fields and plasmas.

Products are generated in high yield under continuous flow mode in the VFD with scalability and size uniformity addressed. Nevertheless, it is critical to systematically explore the effects of tubes with different diameters and length. Also noteworthy is that batch processing is limited by diffusion-control, whereas the liquid in the VFD is beyond such control because of the induced mechanical energy. Importantly, use of the VFD has scalability addressed upfront at the research stage, and for small niche applications of nanomaterials, a single confined mode reaction of VFD would suffice. For large scale processing, a number of VFDs operating in parallel are envisaged. Different from conventional channel-based microfluidic processing, clogging is not an issue in the VFD, but build-up of material in the tube can occur, as in the case of exfoliating and scrolling *h*-BN. This can be overcome by aligning the tube at -45^{o} tilt angle.

The progress of VFD mediated material processing so far is just the 'tip of the iceberg'. This thesis demonstrates considerable potential not only to manipulate 0D, 1D, and 2D material but also in applying these materials and the technology into various applications, for example, solar cell, supercapacitors, batteries, gas storage, sensors, neutron capture therapy, orthopedic implants, advanced drug delivery, tissue engineering, cell manipulation, diagnostics, and more.

8.3 References

1. Chen, X.; Dobson, J. F.; Raston, C. L., Vortex fluidic exfoliation of graphite and boron nitride. *Chemical Communications* **2012,** *48* (31), 3703-3705.
2. Wahid, M. H.; Eroglu, E.; Chen, X.; Smith, S. M.; Raston, C. L., Functional multi-layer graphene–algae hybrid material formed using vortex fluidics. *Green Chemistry* **2013,** *15* (3), 650-655.
3. Wahid, M. H.; Eroglu, E.; Chen, X.; Smith, S. M.; Raston, C. L., Entrapment of Chlorella vulgaris cells within graphene oxide layers. *RSC Advances* **2013,** *3* (22), 8180-8183.
4. Wahid, M. H.; Eroglu, E.; LaVars, S. M.; Newton, K.; Gibson, C. T.; Stroeher, U. H.; Chen, X.; Boulos, R. A.; Raston, C. L.; Harmer, S.-L., Microencapsulation of bacterial strains in graphene oxide nano-sheets using vortex fluidics. *RSC Advances* **2015,** *5* (47), 37424-37430.
5. Alharbi, T. M. D.; Harvey, D.; Alsulami, I. K.; Dehbari, N.; Duan, X.; Lamb, R. N.; Lawrance, W. D.; Raston, C. L., Shear stress mediated scrolling of graphene oxide. *Carbon* **2018,** *137*, 419-424.
6. Vimalanathan, K.; Suarez-Martinez, I.; Peiris, M. C. R.; Antonio, J.; de Tomas, C.; Zou, Y.; Zou, J.; Duan, X.; Lamb, R. N.; Harvey, D. P.; Alharbi, T. M. D.; Gibson, C. T.; Marks, N. A.; Darwish, N.; Raston, C. L., Vortex fluidic mediated transformation of

graphite into highly conducting graphene scrolls. *Nanoscale Advances* **2019,** *1* (7), 2495-2501.
7. Vimalanathan, K.; Gascooke, J. R.; Suarez-Martinez, I.; Marks, N. A.; Kumari, H.; Garvey, C. J.; Atwood, J. L.; Lawrance, W. D.; Raston, C. L., Fluid dynamic lateral slicing of high tensile strength carbon nanotubes. *Scientific reports* **2016,** *6*, 22865.
8. Vimalanathan, K.; Raston, C. L., Dynamic Thin Films in Controlling the Fabrication of Nanocarbon and Its Composites. *Advanced Materials Technologies* **2017,** *2* (6), 1600298.
9. Alharbi, T. M. D.; Vimalanathan, K.; Lawrance, W. D.; Raston, C. L., Controlled slicing of single walled carbon nanotubes under continuous flow. *Carbon* **2018,** *140*, 428-432.
10. Luo, X.; Al-Antaki, A. H. M.; Vimalanathan, K.; Moffatt, J.; Zheng, K.; Zou, Y.; Zou, J.; Duan, X.; Lamb, R. N.; Wang, S.; Li, Q.; Zhang, W.; Raston, C. L., Laser irradiated vortex fluidic mediated synthesis of luminescent carbon nanodots under continuous flow. *Reaction Chemistry & Engineering* **2018,** *3* (2), 164-170.
11. Yasin, F. M.; Boulos, R. A.; Hong, B. Y.; Cornejo, A.; Iyer, K. S.; Gao, L.; Chua, H. T.; Raston, C. L., Microfluidic size selective growth of palladium nano-particles on carbon nano-onions. *Chemical Communications* **2012,** *48* (81), 10102-10104.
12. Md Yasin, F.; Iyer, K. S.; Raston, C. L., Palladium nano-carbon-calixarene based devices for hydrogen sensing. *New Journal of Chemistry* **2013,** *37* (10), 3289-3293.
13. Chen, X.; Yasin, F. M.; Eggers, P. K.; Boulos, R. A.; Duan, X.; Lamb, R. N.; Iyer, K. S.; Raston, C. L., Non-covalently modified graphene supported ultrafine nanoparticles of palladium for hydrogen gas sensing. *RSC Advances* **2013,** *3* (10), 3213-3217.
14. Goh, Y. A.; Chen, X.; Yasin, F. M.; Eggers, P. K.; Boulos, R. A.; Wang, X.; Chua, H. T.; Raston, C. L., Shear flow assisted decoration of carbon nano-onions with platinum nanoparticles. *Chemical Communications* **2013,** *49* (45), 5171-5173.
15. Vimalanathan, K.; Chen, X.; Raston, C. L., Shear induced fabrication of intertwined single walled carbon nanotube rings. *Chemical Communications* **2014,** *50* (77), 11295-11298.
16. Alharbi, T. M. D.; Shingaya, Y.; Vimalanathan, K.; Nakayama, T.; Raston, C. L., High Yielding Fabrication of Magnetically Responsive Coiled Single-Walled Carbon Nanotube under Flow. *ACS Applied Nano Materials* **2019**.
17. Vimalanathan, K.; Shrestha, R. G.; Zhang, Z.; Zou, J.; Nakayama, T.; Raston, C. L., Surfactant-free Fabrication of Fullerene C_{60} Nanotubules Under Shear. *Angewandte Chemie* **2017,** *129* (29), 8518-8521.
18. Boulos, R. A.; Zhang, F.; Tjandra, E. S.; Martin, A. D.; Spagnoli, D.; Raston, C. L., Spinning up the polymorphs of calcium carbonate. *Scientific Reports* **2014,** *4*, 3616.
19. Alsulami, I. K.; Alharbi, T. M.; Harvey, D. P.; Gibson, C. T.; Raston, C. L., Controlling the growth of fullerene C_{60} cones under continuous flow. *Chemical Communications* **2018,** *54* (57), 7896-7899.
20. Tong, C. L.; Boulos, R. A.; Yu, C.; Iyer, K. S.; Raston, C. L., Continuous flow tuning of ordered mesoporous silica under ambient conditions. *RSC Advances* **2013,** *3* (41), 18767-18770.
21. Luo, X.; Al-Antaki, A. H. M.; Alharbi, T. M. D.; Hutchison, W. D.; Zou, Y.-c.; Zou, J.; Sheehan, A.; Zhang, W.; Raston, C. L., Laser-Ablated Vortex Fluidic-Mediated Synthesis of Superparamagnetic Magnetite Nanoparticles in Water Under Flow. *ACS Omega* **2018,** *3* (9), 11172-11178.

22. Eroglu, E.; D'Alonzo, N. J.; Smith, S. M.; Raston, C. L., Vortex fluidic entrapment of functional microalgal cells in a magnetic polymer matrix. *Nanoscale* **2013,** *5* (7), 2627-2631.
23. Tong, C. L.; Eroglu, E.; Duan, X.; Lamb, R. N.; Jarrett, K.; Buckley, C. E.; Raston, C. L., Nitrate uptake using mesoporous silica embedded with zero-valent palladium nanoparticles. *RSC Advances* **2015,** *5* (26), 20557-20561.
24. Britton, J.; Raston, C. L.; Weiss, G. A., Rapid protein immobilization for thin film continuous flow biocatalysis. *Chemical Communications* **2016,** *52* (66), 10159-10162.
25. Britton, J.; Meneghini, L. M.; Raston, C. L.; Weiss, G. A., Accelerating Enzymatic Catalysis Using Vortex Fluidics. *Angewandte Chemie International Edition* **2016,** *55* (38), 11387-11391.
26. Yuan, T. Z.; Ormonde, C. F.; Kudlacek, S. T.; Kunche, S.; Smith, J. N.; Brown, W. A.; Pugliese, K. M.; Olsen, T. J.; Iftikhar, M.; Raston, C. L., Shear-Stress-Mediated Refolding of Proteins from Aggregates and Inclusion Bodies. *ChemBioChem* **2015,** *16* (3), 393-396.
27. Britton, J.; Dyer, R. P.; Majumdar, S.; Raston, C. L.; Weiss, G. A., Ten-Minute Protein Purification and Surface Tethering for Continuous-Flow Biocatalysis. *Angewandte Chemie International Edition in English* **2017,** *56* (9), 2296-2301.
28. Luo, X.; Smith, P.; Raston, C. L.; Zhang, W., Vortex Fluidic Device-Intensified Aqueous Two Phase Extraction of C-Phycocyanin from Spirulina maxima. *ACS Sustainable Chemistry & Engineering* **2016,** *4* (7), 3905-3911.
29. Luo, X.; Al-Antaki, A. H. M.; Pye, S.; Meech, R.; Zhang, W.; Raston, C. L., High-Shear-Imparted Tunable Fluorescence in Polyethylenimines. *ChemPhotoChem* **2018,** *2* (4), 343-348.
30. D'Alonzo, N. J.; Eggers, P. K.; Eroglu, E.; Raston, C. L., Shear Stress Induced Fabrication of Dandelion-Shaped Lanthanide Phosphate Nanoparticles. *Australian Journal of Chemistry.* **2017,** *70* (7), 823-829.
31. D'Alonzo, N. J.; Eggers, P. K.; Raston, C. L., Vortex fluidics synthesis of polymer coated superparamagnetic magnetite nanoparticles. *New Journal of Chemistry* **2017,** *41* (2), 552-558.
32. Yasmin, L.; Coyle, T.; Stubbs, K. A.; Raston, C. L., Stereospecific synthesis of resorcin[4]arenes and pyrogallol[4]arenes in dynamic thin films. *Chemical Communications* **2013,** *49* (93), 10932-10934.
33. Yasmin, L.; Stubbs, K. A.; Raston, C. L., Vortex fluidic promoted Diels–Alder reactions in an aqueous medium. *Tetrahedron Letters* **2014,** *55* (14), 2246-2248.
34. Gandy, M. N.; Raston, C. L.; Stubbs, K. A., Towards aryl C–N bond formation in dynamic thin films. *Organic & Biomolecular Chemistry* **2014,** *12* (26), 4594-4597.
35. Ho, L. A.; Raston, C. L.; Stubbs, K. A., Transition-Metal-Free Cross-Coupling Reactions in Dynamic Thin Films To Access Pyrimidine and Quinoxaline Analogues. *European Journal of Organic Chemistry* **2016,** (36), 5957-5963.
36. Yasmin, L.; Eggers, P. K.; Skelton, B. W.; Stubbs, K. A.; Raston, C. L., Thin film microfluidic synthesis of fluorescent highly substituted pyridines. *Green Chemistry* **2014,** *16* (7), 3450-3453.
37. Britton, J.; Chalker, J. M.; Raston, C. L., Rapid Vortex Fluidics: Continuous Flow Synthesis of Amides and Local Anesthetic Lidocaine. *Chemistry–A European Journal* **2015,** *21* (30), 10660-10665.

38. Gandy, M. N.; Raston, C. L.; Stubbs, K. A., Photoredox catalysis under shear using thin film vortex microfluidics. *Chemical Communications* **2015,** *51* (55), 11041-11044.
39. Britton, J.; Dalziel, S. B.; Raston, C. L., Continuous flow Fischer esterifications harnessing vibrational-coupled thin film fluidics. *RSC Advances* **2015,** *5* (3), 1655-1660.
40. Ciampi, S.; Eggers, P. K.; Haworth, N. L.; Darwish, N.; Wagner, P.; Coote, M. L.; Wallace, G. G.; Raston, C. L., Decoloration rates of a photomerocyanine dye as a visual probe into hydrogen bonding interactions. *Chemical Communications* **2015,** *51* (23), 4815-4818.
41. Pye, S. J.; Dalgarno, S. J.; Chalker, J. M.; Raston, C. L., Organic oxidations promoted in vortex driven thin films under continuous flow. *Green Chemistry* **2018,** *20* (1), 118-124.
42. Britton, J.; Castle, J. W.; Weiss, G. A.; Raston, C. L., Harnessing Thin-Film Continuous-Flow Assembly Lines. *Chemistry–A European Journal* **2016,** *22* (31), 10773-10776.
43. Britton, J.; Dalziel, S. B.; Raston, C. L., The synthesis of di-carboxylate esters using continuous flow vortex fluidics. *Green Chemistry* **2016,** *18* (7), 2193-2200.
44. Peng, W.; Chen, X.; Zhu, S.; Guo, C.; Raston, C. L., Room temperature vortex fluidic synthesis of monodispersed amorphous proto-vaterite. *Chemical Communications* **2014,** *50* (79), 11764-11767.
45. Sudchanham, J.; Batmunkh, M.; Reutrakul, V.; Shapter, J. G.; Raston, C. L.; Pakawatpanurut, P., Vortex Fluidics Improved Morphology of $CH_3NH_3PbI_{3-x}Cl_x$ Films for Perovskite Solar Cells. *Chemistry Select* **2017,** *2* (1), 369-374.
46. He, S.; Joseph, N.; Luo, X.; Raston, C. L., Vortex fluidic mediated food processing. *PLOS ONE* **2019,** *14* (5), e0216816.
47. He, S.; Joseph, N.; Luo, X.; Raston, C., Continuous flow thin film microfluidic mediated nano-encapsulation of fish oil. *LWT- Food Science and Technology* **2019,** *103*, 88-93.
48. Britton, J.; Raston, C. L., Continuous flow vortex fluidic production of biodiesel. *RSC Advances* **2014,** *4* (91), 49850-49854.
49. Britton, J.; Raston, C. L., Rapid high conversion of high free fatty acid feedstock into biodiesel using continuous flow vortex fluidics. *RSC Advances* **2015,** *5* (3), 2276-2280.
50. Sitepu, E. K.; Corbin, K.; Luo, X.; Pye, S. J.; Tang, Y.; Leterme, S. C.; Heimann, K.; Raston, C. L.; Zhang, W., Vortex fluidic mediated direct transesterification of wet microalgae biomass to biodiesel. *Bioresource Technology* **2018,** *266*, 488-497.
51. Yasmin, L.; Chen, X.; Stubbs, K. A.; Raston, C. L., Optimising a vortex fluidic device for controlling chemical reactivity and selectivity. *Scientific reports* **2013,** *3*, 2282.
52. Gandy, M. N.; Raston, C. L.; Stubbs, K. A., Towards aryl C-N bond formation in dynamic thin films. *Organic and Biomolecular Chemistry* **2014,** *12* (26), 4594-4597.
53. Mo, J.; Eggers, P. K.; Chen, X.; Ahamed, M. R. H.; Becker, T.; Yong Lim, L.; Raston, C. L., Shear induced carboplatin binding within the cavity of a phospholipid mimic for increased anticancer efficacy. *Scientific Reports* **2015,** *5*, 10414.
54. Luo, X.; Al-Antaki, A. H. M.; Harvey, D. P.; Ruan, Y.; He, S.; Zhang, W.; Raston, C. L., Vortex Fluidic Mediated Synthesis of Macroporous Bovine Serum Albumin-Based Microspheres. *ACS Applied Materials & Interfaces* **2018,** *10* (32), 27224-27232.
55. Batmunkh, M.; Vimalanathan, K.; Wu, C.; Bati, A. S. R.; Yu, L.; Tawfik, S. A.; Ford, M. J.; Macdonald, T. J.; Raston, C. L.; Priya, S.; Gibson, C. T.; Shapter, J. G., Efficient

Production of Phosphorene Nanosheets via Shear Stress Mediated Exfoliation for Low-Temperature Perovskite Solar Cells. *Small Methods* **2019,** *3* (5), 1800521.

56. Alharbi, T. M. D.; Alghamdi, A. R. M.; Vimalanathan, K.; Raston, C. L., Continuous flow photolytic reduction of graphene oxide. *Chemical Communications* **2019,** *55* (76), 11438-11441.
57. Peng, Q.; Guo, J.; Zhang, Q.; Xiang, J.; Liu, B.; Zhou, A.; Liu, R.; Tian, Y., Unique Lead Adsorption Behavior of Activated Hydroxyl Group in Two-Dimensional Titanium Carbide. *Journal of the American Chemical Society* **2014,** *136* (11), 4113-4116.
58. Nasrallah, G. K.; Al-Asmakh, M.; Rasool, K.; Mahmoud, Kajesn, Ecotoxicological assessment of $Ti_3C_2T_x$ (MXene) using a zebrafish embryo model. *Environmental Sciences: Nano,* **2018,** *5* (4), 1002-1011.
59. Xu, B.; Zhu, M.; Zhang, W.; Zhen, X.; Pei, Z.; Xue, Q.; Zhi, C.; Shi, P., Ultrathin MXene-Micropattern-Based Field-Effect Transistor for Probing Neural Activity. *Advanced Materials* **2016,** *28* (17), 3333-3339.
60. Rasool, K.; Helal, M.; Ali, A.; Ren, C. E.; Gogotsi, Y.; Mahmoud, Kajan, Antibacterial Activity of $Ti_3C_2T_x$ MXene. *ACS Nano* **2016,** *10* (3), 3674-3684.
61. Yu, X.; Cai, X.; Cui, H.; Lee, Seung-Wuk.; Yu, Xue-Feng.; Liu, B., Fluorine-free preparation of titanium carbide MXene quantum dots with high near-infrared photothermal performances for cancer therapy. *Nanoscale* **2017,** *9* (45), 17859-17864.
62. Khazaei, M.; Arai, M.; Sasaki, T.; Chung, C.-Y.; Venkataramanan, N. S.; Estili, M.; Sakka, Y.; Kawazoe, Y., Novel Electronic and Magnetic Properties of Two-Dimensional Transition Metal Carbides and Nitrides. *Advanced Materials* **2013,** *23* (17), 2185-2192.
63. Lukatskaya, M. R.; Mashtalir, O.; Ren, C. E.; Dall'Agnese, Y.; Rozier, P.; Taberna, P. L.; Naguib, M.; Simon, P.; Barsoum, M. W.; Gogotsi, Y., Cation Intercalation and High Volumetric Capacitance of Two-Dimensional Titanium Carbide. *Science* **2013,** *341* (6153), 1502-1505.
64. Wang, X.; Kajiyama, S.; Iinuma, H.; Hosono, E.; Oro, S.; Moriguchi, I.; Okubo, M.; Yamada, A., Pseudocapacitance of MXene nanosheets for high-power sodium-ion hybrid capacitors. *Nature Communications* **2015,** *6*, 6544.
65. Dall'Agnese, Y.; Taberna, P.-L.; Gogotsi, Y.; Simon, Pjtjopcl, Two-dimensional vanadium carbide (MXene) as positive electrode for sodium-ion capacitors. *The Journal of Physical Chemistry Letters* **2015,** *6* (12), 2305-2309.
66. Mashtalir, O.; Naguib, M.; Mochalin, V. N.; Dall'Agnese, Y.; Heon, M.; Barsoum, M. W.; Gogotsi, Y., Intercalation and delamination of layered carbides and carbonitrides. *Nature Communications* **2013,** *4*, 1716.
67. Zhu, J.; Ha, E.; Zhao, G.; Zhou, Y.; Huang, D.; Yue, G.; Hu, L.; Sun, N.; Wang, Y.; Lee, L. Y. S.; Xu, C.; Wong, K.-Y.; Astruc, D.; Zhao, P., Recent advance in MXenes: A promising 2D material for catalysis, sensor and chemical adsorption. *Coordination Chemistry Reviews* **2017,** *352*, 306-327.
68. Lorencova, L.; Bertok, T.; Dosekova, E.; Holazova, A.; Paprckova, D.; Vikartovska, A.; Sasinkova, V.; Filip, J.; Kasak, P.; Jerigova, M.; Velic, D.; Mahmoud, K. A.; Tkac, J., Electrochemical performance of $Ti_3C_2T_x$ MXene in aqueous media: towards ultrasensitive H_2O_2 sensing. *Electrochimica Acta* **2017,** *235*, 471-479.
69. Liu, H.; Duan, C.; Yang, C.; Shen, W.; Wang, F.; Zhu, Z., A novel nitrite biosensor based on the direct electrochemistry of hemoglobin immobilized on MXene-Ti_3C_2. *Sencer and Actuators B: Chemistry* **2015,** *218*, 60-66.

70. Fan, Y.; Yuan, Z.; Zou, G.; Zhang, Q.; Liu, B.; Peng, Q., Two-dimensional MXene/A-TiO_2 composite with unprecedented catalytic activation for sodium alanate. *Catalysis Today* **2018,** *318*, 167-174.
71. Ahmed, B.; Anjum, D. H.; Hedhili, M. N.; Gogotsi, Y.; Alshareef, H. N., H_2O_2 assisted room temperature oxidation of Ti_2C MXene for Li-ion battery anodes. *Nanoscale* **2016,** *8* (14), 7580-7587.
72. Low, J.; Zhang, L.; Tong, T.; Shen, B.; Yu, J., TiO_2/MXene Ti_3C_2 composite with excellent photocatalytic CO_2 reduction activity. *Journal of Catalysis* **2018,** *361*, 255-266.
73. Molla, A.; Hussain, S., Base free synthesis of iron oxide supported on boron nitride for the construction of highly functionalized pyrans and spirooxindoles. *RSC Advances* **2016,** *6* (7), 5491-5502.
74. Lu, Q.; Hu, Y.; Chen, J.; Li, Y.; Song, W.; Jin, S.; Liu, F.; Sheng, L., Boron nitride nanotubes matrix for signal enhancement in infrared laser desorption postionization mass spectrometry. *Talanta* **2018,** *187*, 106-112.
75. Mohammed Al-antaki, A. H.; Luo, X.; Duan, A.; Lamb, R. N.; Eroglu, E.; Hutchison, W.; Zou, Y.-C.; Zou, J.; Raston, C. L., Continuous flow synthesis of phosphate binding h-BN@magnetite hybrid material. *RSC Advances* **2018,** *8* (71), 40829-40835.
76. Laurent, S.; Forge, D.; Port, M.; Roch, A.; Robic, C.; Vander Elst, L.; Muller, R. N., Magnetic Iron Oxide Nanoparticles: Synthesis, Stabilization, Vectorization, Physicochemical Characterizations, and Biological Applications. *Chemical Reviews* **2008,** *108* (6), 2064-2110.
77. Sowani, H.; Mohite, P.; Damale, S.; Kulkarni, M.; Zinjarde, S., Carotenoid stabilized gold and silver nanoparticles derived from the Actinomycete Gordonia amicalis HS-11 as effective free radical scavengers. *Enzyme and microbial technology* **2016,** *95*, 164-173.
78. Vijayan, S. R.; Santhiyagu, P.; Ramasamy, R.; Arivalagan, P.; Kumar, G.; Ethiraj, K.; Ramaswamy, B. R., Seaweeds: a resource for marine bionanotechnology. *Enzyme and microbial technology* **2016,** *95*, 45-57.
79. Suriani, A.; Dalila, A.; Mohamed, A.; Mamat, M.; Malek, M.; Soga, T.; Tanemura, M., Fabrication of vertically aligned carbon nanotubes–zinc oxide nanocomposites and their field electron emission enhancement. *Materials & Design* **2016,** *90*, 185-195.
80. Al-antaki, A. H. M.; Lawrance, W. D.; Raston, C. L., Dynamic thin film mediated slicing of boron nitride nanotubes. *Nanoscale Advances* **2019**, 1(12), 4722-4728.
81. Al-Antaki, A. H. M.; Luo, X.; Duan, X.; Lamb, R. N.; Hutchison, W. D.; Lawrance, W.; Raston, C. L., Continuous Flow Copper Laser Ablation Synthesis of Copper(I and II) Oxide Nanoparticles in Water. *ACS omega* **2019,** *4* (8), 13577-13584.
82. Al-Antaki, A. H. M.; Luo, X.; Alharbi, T. M. D.; Harvey, D. P.; Pye, S.; Zou, J.; Lawrance, W.; Raston, C. L., Inverted vortex fluidic exfoliation and scrolling of hexagonal-boron nitride. *RSC Advances* **2019,** *9* (38), 22074-22079.
83. Zhang, H.; Wang, X.; Li, N.; Xia, J.; Meng, Q.; Ding, J.; Lu, J., Synthesis and characterization of TiO_2/graphene oxide nanocomposites for photoreduction of heavy metal ions in reverse osmosis concentrate. *RSC Advances* **2018,** *8* (60), 34241-34251.
84. Ferreira, T.; Faria, J.; Gonzalez, I.; Outon, L.; Macedo, W.; Gomes, D.; Sousa, E., BNNT/Fe_3O_4 System as an Efficient Tool for Magnetohyperthermia Therapy. *Journal of Nanoscience and Nanotechnology* **2018,** *18* (10), 6746-6755.
85. Reddy, K. R.; Sin, B. C.; Yoo, C. H.; Park, W.; Ryu, K. S.; Lee, J.-S.; Sohn, D.; Lee, Y., A new one-step synthesis method for coating multi-walled carbon nanotubes with cuprous oxide nanoparticles. *Scripta Materialia* **2008,** *58* (11), 1010-1013.

APPENDICES

Chapter 2. Continuous flow vortex fluidic mediated exfoliation and fragmentation of 2D MXene

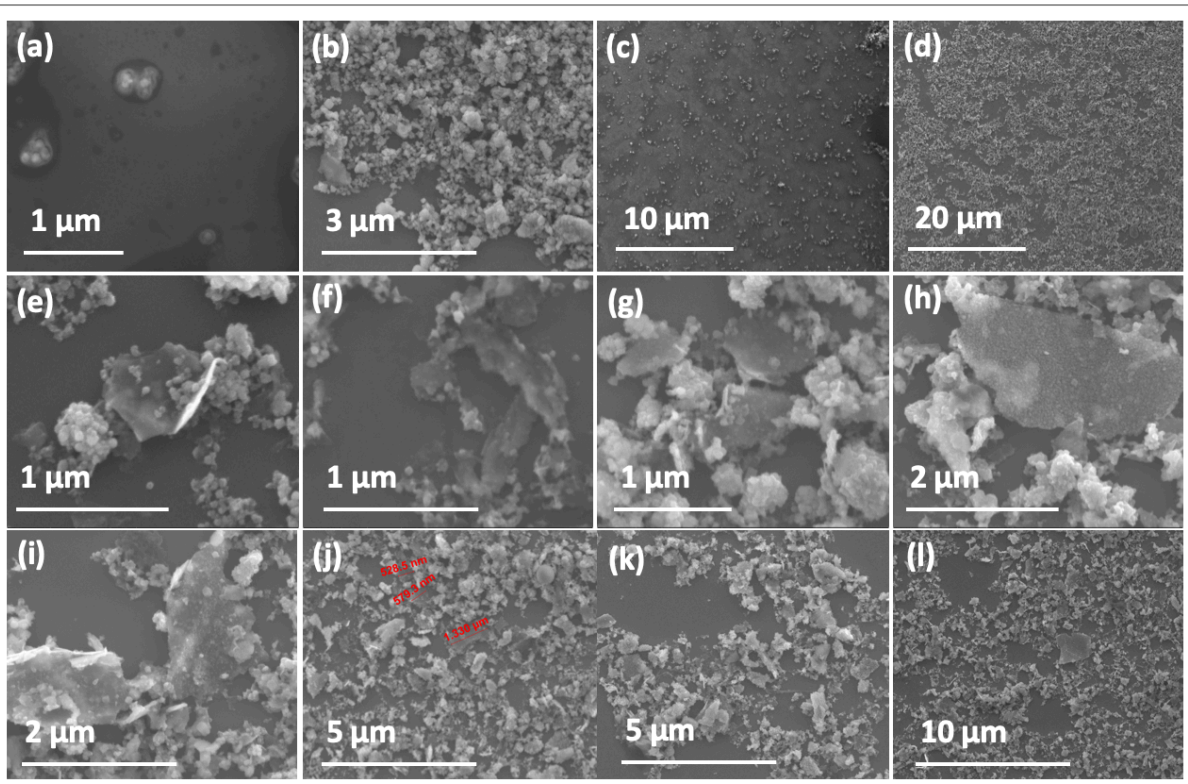

Figure S2.1. SEM images for MXene drop cast on a silicon wafers, post VFD processing under N_2 gas, θ 45º, concentration 0.5 mg/mL in IPA and water (1:1), rotation speed 4K rpm and flow rate 0.5 mL/min. (a-d) MXene nanoparticles (retained). (e-l) Exfoliated MXene sheets (retained).

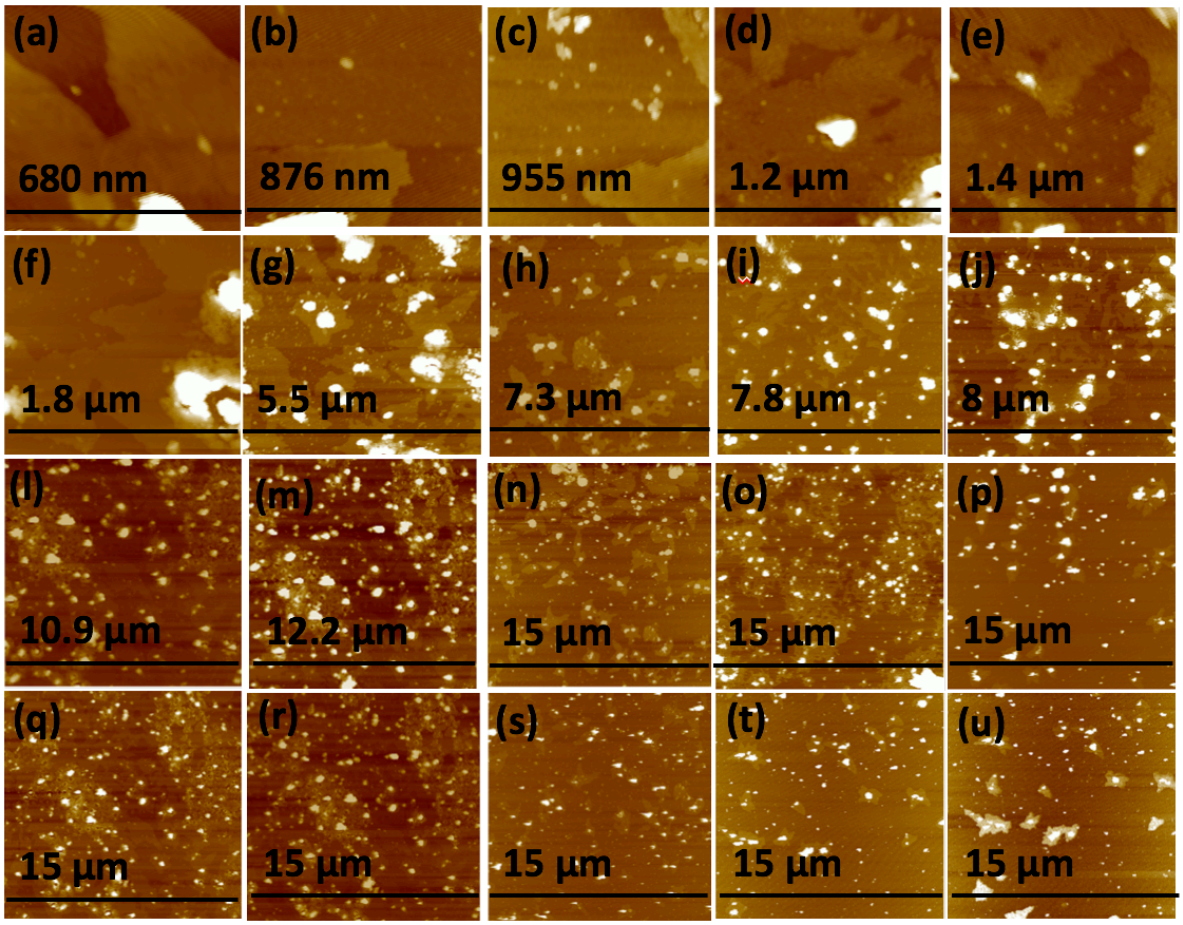

Figure S2.2. AFM images for MXene drop cast on a silicon wafers, post VFD processing under N_2 gas, θ 45º, concentration 0.5 mg/mL in IPA and water (1:1), rotation speed 4k rpm and flow rate 0.5 mL/min (collected and retained).

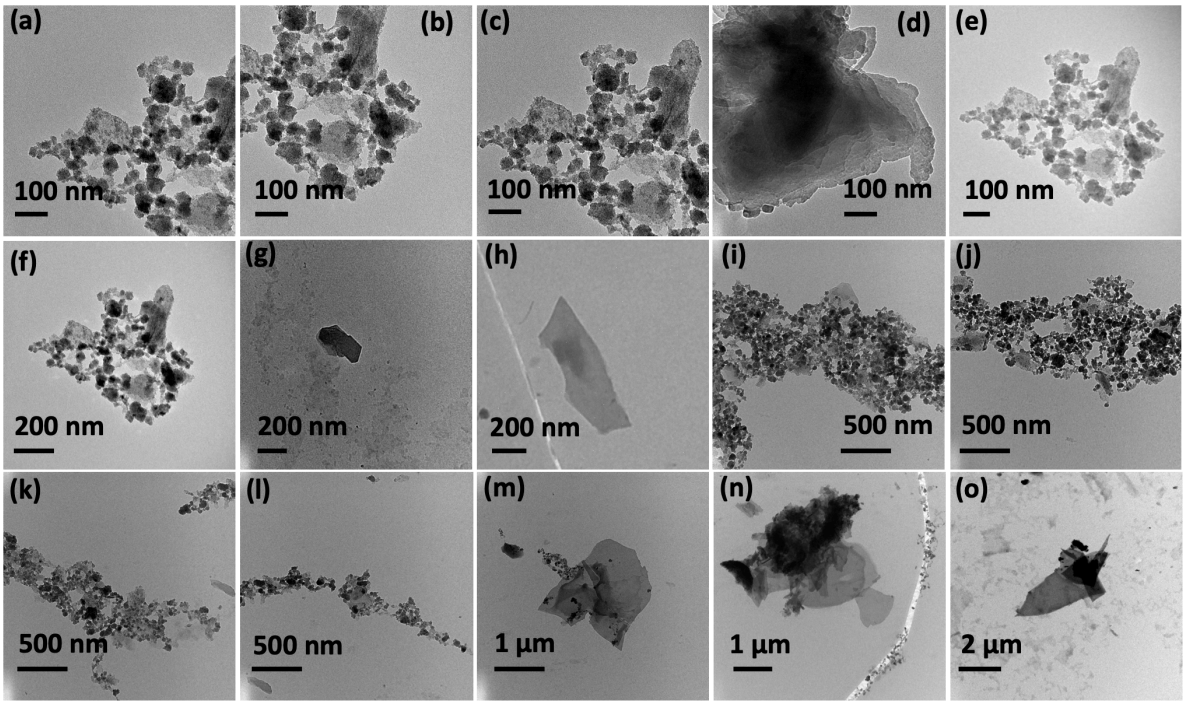

Figure S2.3. TEM images for MXene drop cast on a grid, post VFD processing under N_2 gas, θ 45º, concentration 0.5 mg/mL in IPA and water (1:1), rotation speed 4k rpm and flow rate 0.5 mL/min.

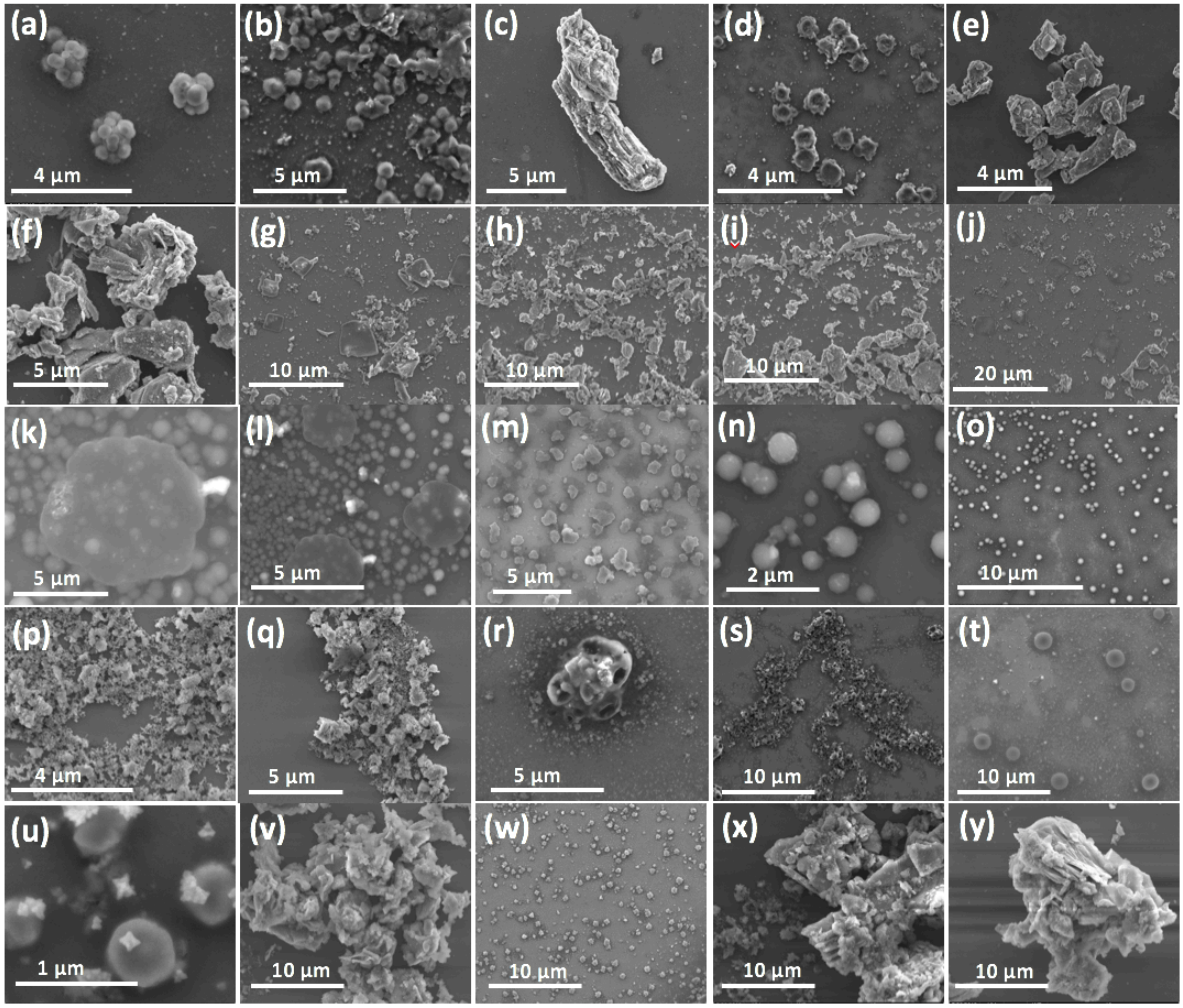

Figure S2.4. SEM images for MXene drop cast on silicon wafers, post VFD processing in water under N_2 gas, θ 45º and flow rate 0.5 mL/min. (a-e) Rotational speed 4k rpm, concentration 0.25 mg/mL. (f-j) Rotational speed 4k rpm, concentration 0.25 mg/mL recycled three times in the VFD. (k-o) Rotational speed was 4k rpm, concentration was 0.5 mg/mL. (p-t) Rotational speed 6k rpm, concentration 0.5 mg/mL. (u-y) Rotation speed 8k rpm, concentration 0.5 mg/mL.

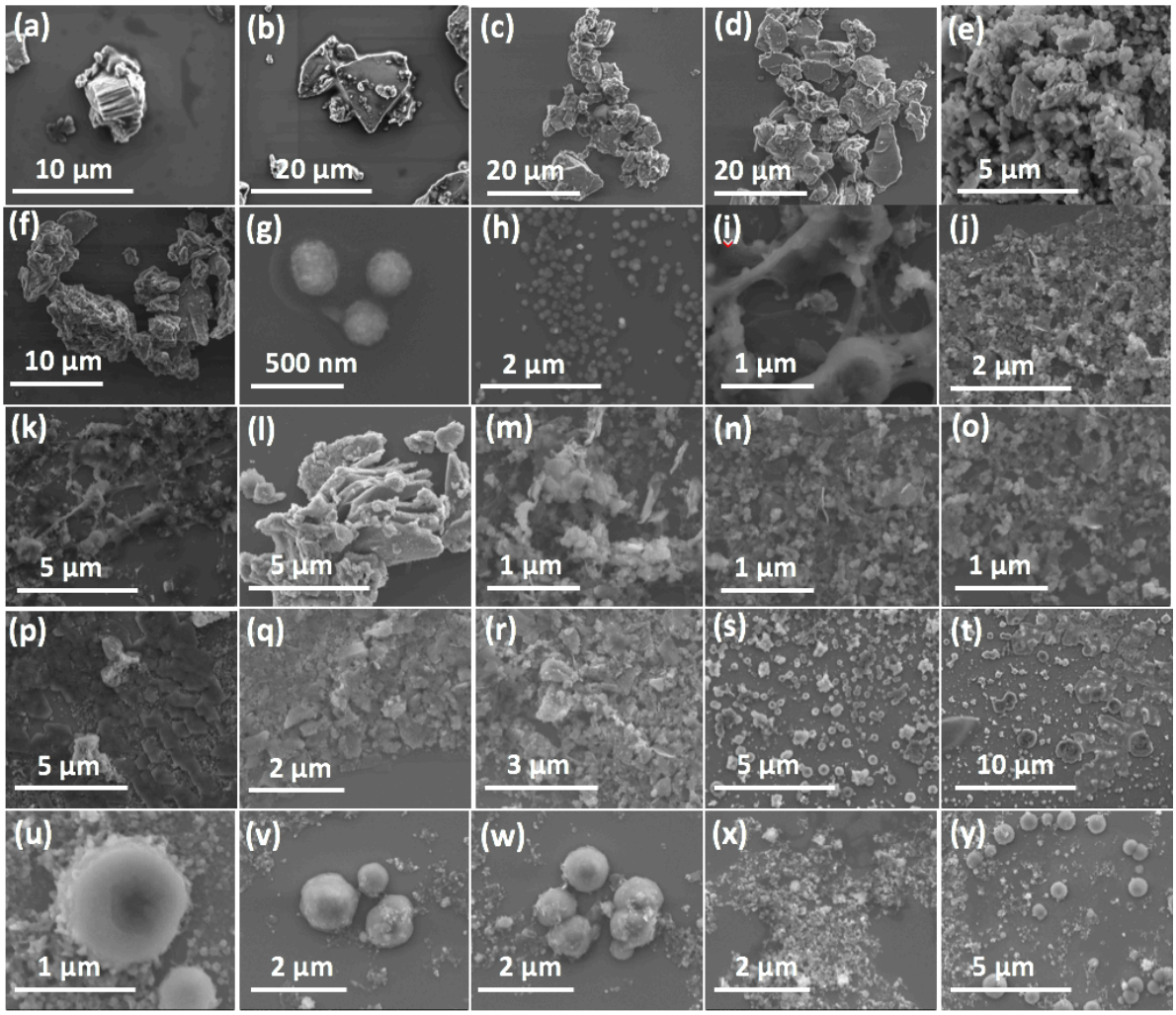

Figure S2.5. SEM images for MXene drop cast on silicon wafers, post VFD processing under N_2 gas, θ 45º, (a, b) Concentration 0.25 mg/mL in DMF and o-xylene (1:1), flow rate 0.5 mL/min and rotation speed 4k rpm. (c, d) Concentration 0.25 mg/mL in DMF and o-xylene (ratio 1:1), flow rate 0.5 mL/min and rotation speed 4k rpm, recycled five times. (e, f) Concentration 0.25 mg/mL in ethanol, flow rate 0.5 mL/min and rotation speed 4k rpm. (g, h) Concentration 0.25 mg/mL in DMF and water (1:1), flow rate 0.5 mL/min and rotation speed 4k rpm. (i-l) Concentration 0.5 mg/mL in ethanol and water (1:1), flow rate 0.5 mL/min and rotation speed 4k rpm. (m-p) Concentration 0.5 mg/mL in ethanol and water (1:1), flow rate 0.75 mL/min and rotation speed 4k rpm. (q-t) Concentration 0.5 mg/mL in ethanol and water (1:1), flow rate 0.5 mL/min and rotation speed 5k rpm. (u-y) Concentration 0.5 mg/mL in DMF and water (1:1), flow rate 0.5 mL/min and rotation speed 4k rpm.

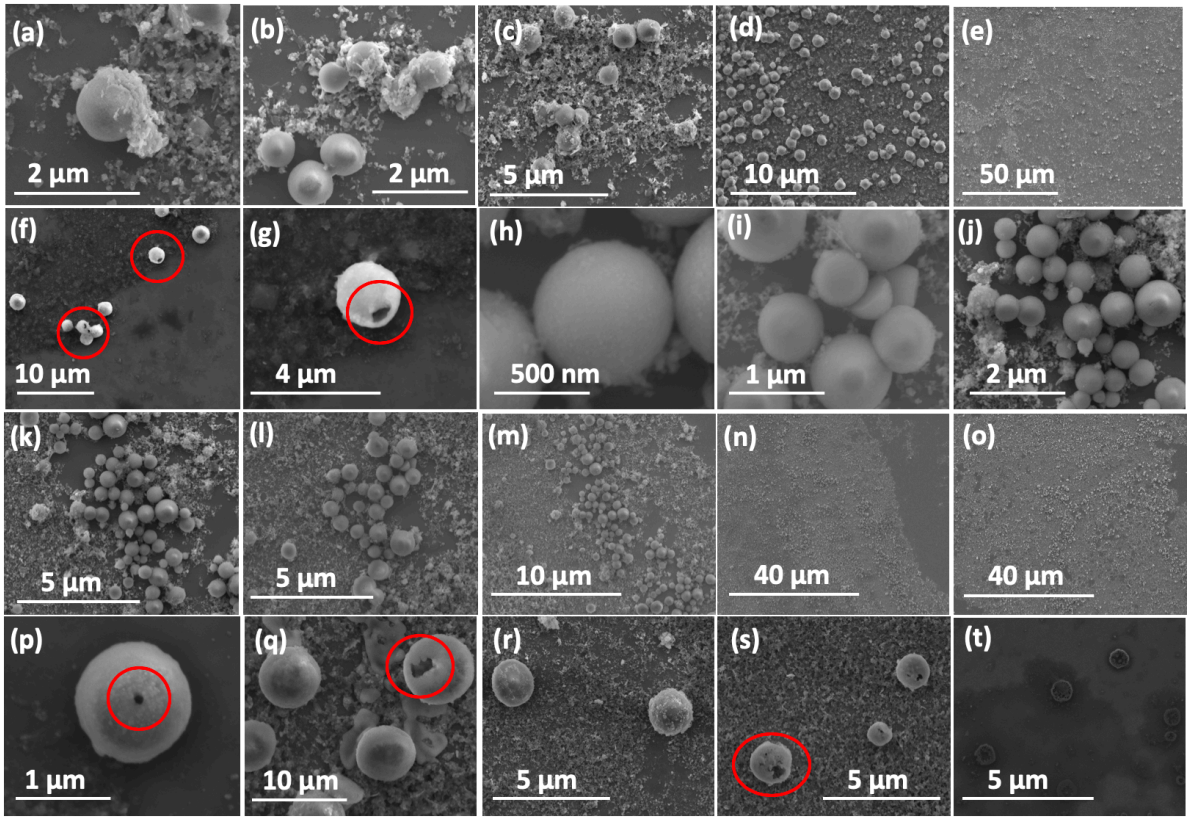

Figure S2.6. SEM images for MXene drop cast on silicon wafers, post VFD processing under N_2 gas, θ 45º, concentration 0.5 mg/mL in IPA and water (1:1) and flow rate 0.5 mL/min. (a-e) Rotational speed 4k rpm. (f, g) After three days for the same sample. (h-o) Rotational speed 5k rpm. (p-t) After one day for the same sample.

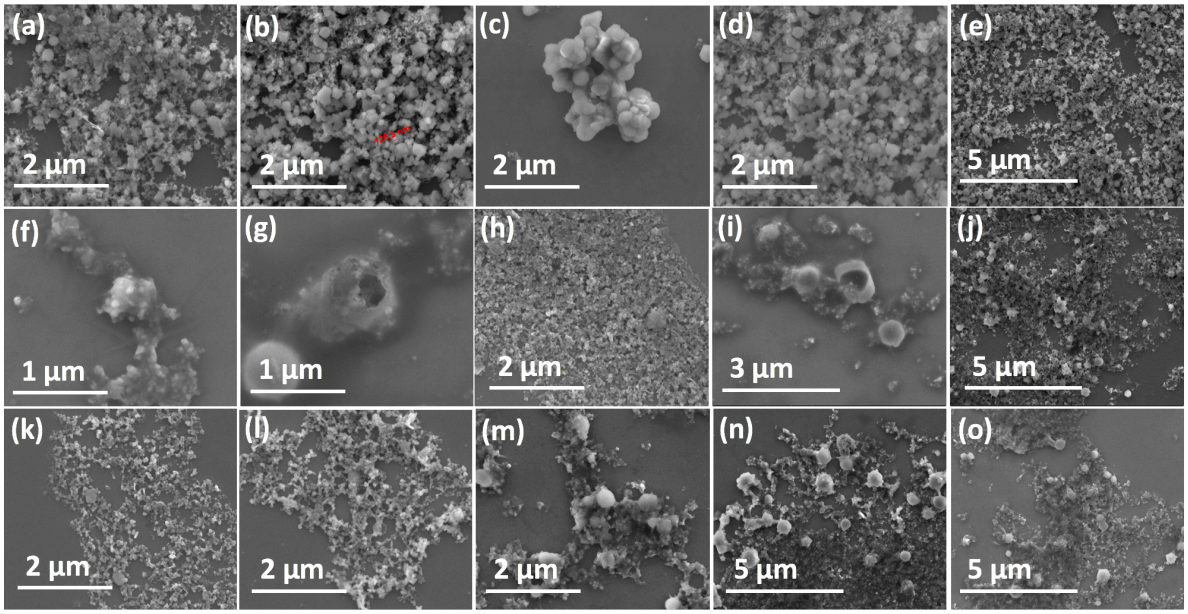

Figure S2.7. SEM images for MXene drop cast on silicon wafers, post VFD processing under N_2 gas, θ 45º, concentration 0.5 mg/mL in IPA and water (1:1) and flow rate 0.5 mL/min. (a-e) Rotational speed as 6k rpm. (f-j) Rotational speed 7k rpm. (k-o) Rotational speed 8k rpm.

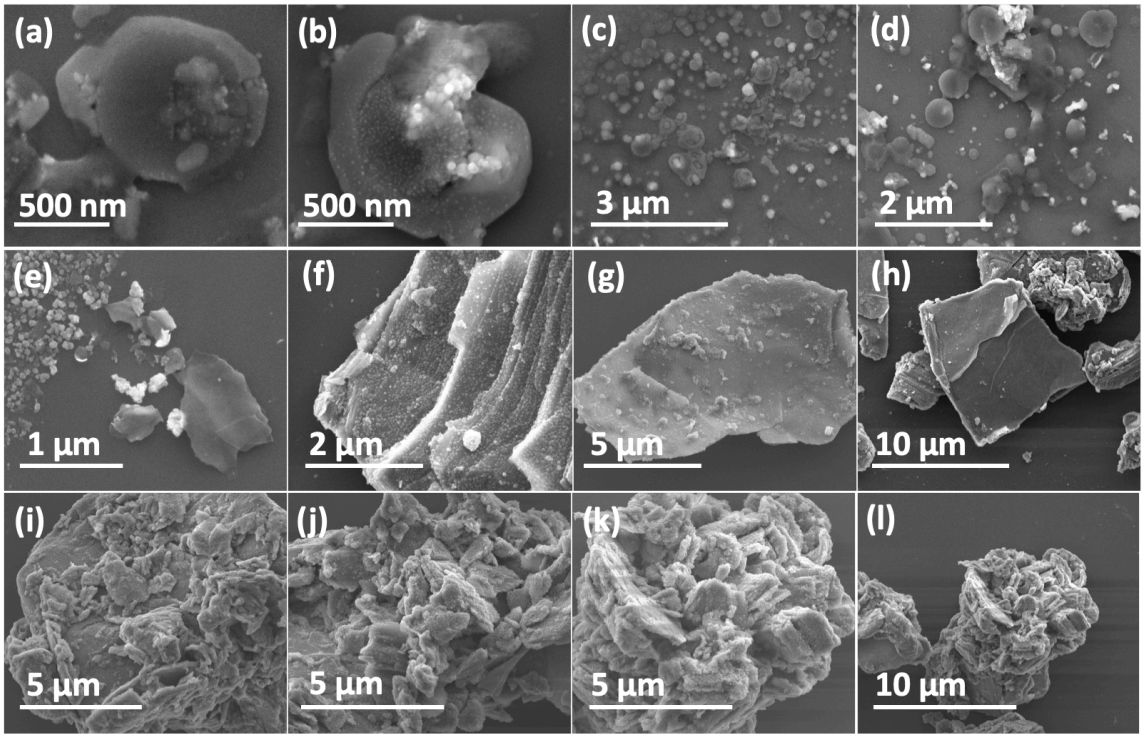

Figure S2.8. SEM images for MXene drop cast on silicon wafers, post VFD processing under N_2 gas, θ 45º, concentration 0.5 mg/mL in IPA and water (1:1) for 30 mins, the rotational speed 4k rpm to compare the result with a continuous flow.

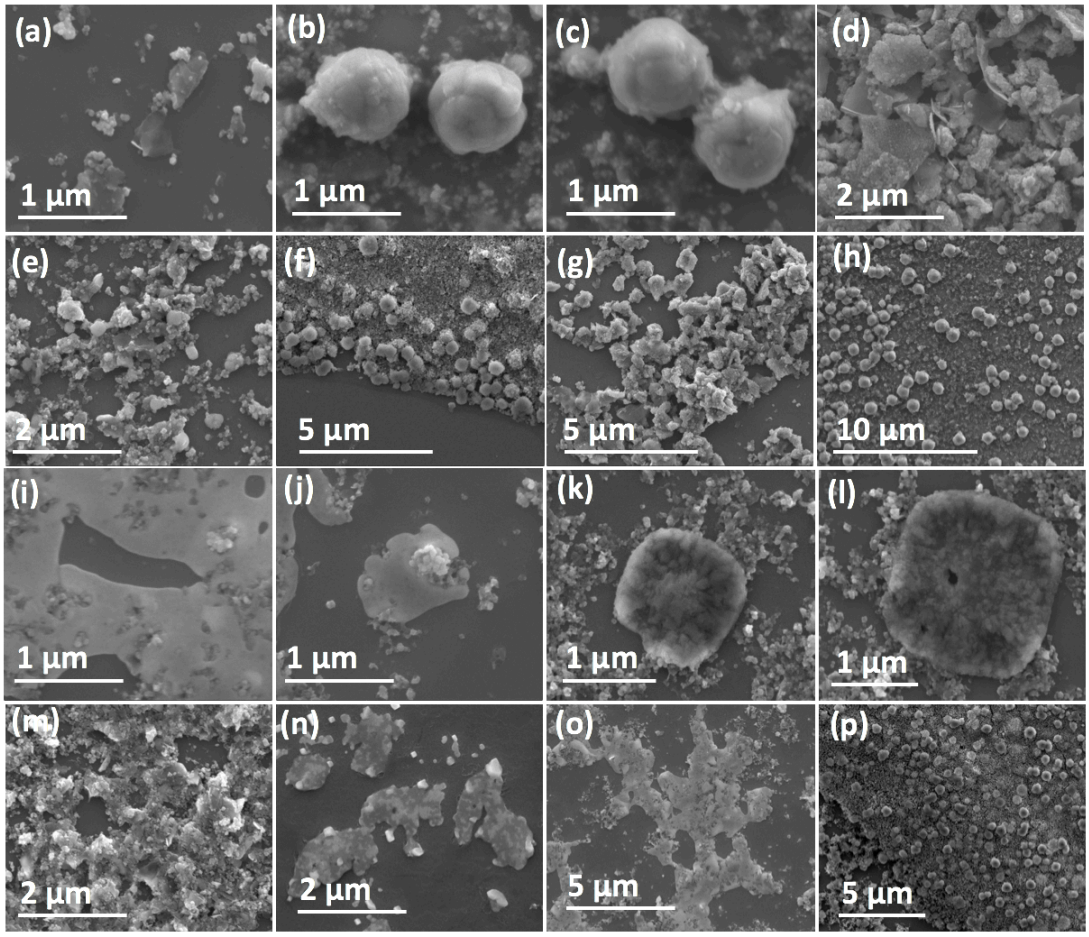

Figure S2.9. SEM images for MXene drop cast on silicon wafers, post VFD processing under N_2 gas, θ 45º, concentration was 1 mg/mL in IPA and water (1:1) and flow rate 0.5 mL/min. (a-h) Rotational speed 4k rpm. (i-p) Rotational speed 5k rpm.

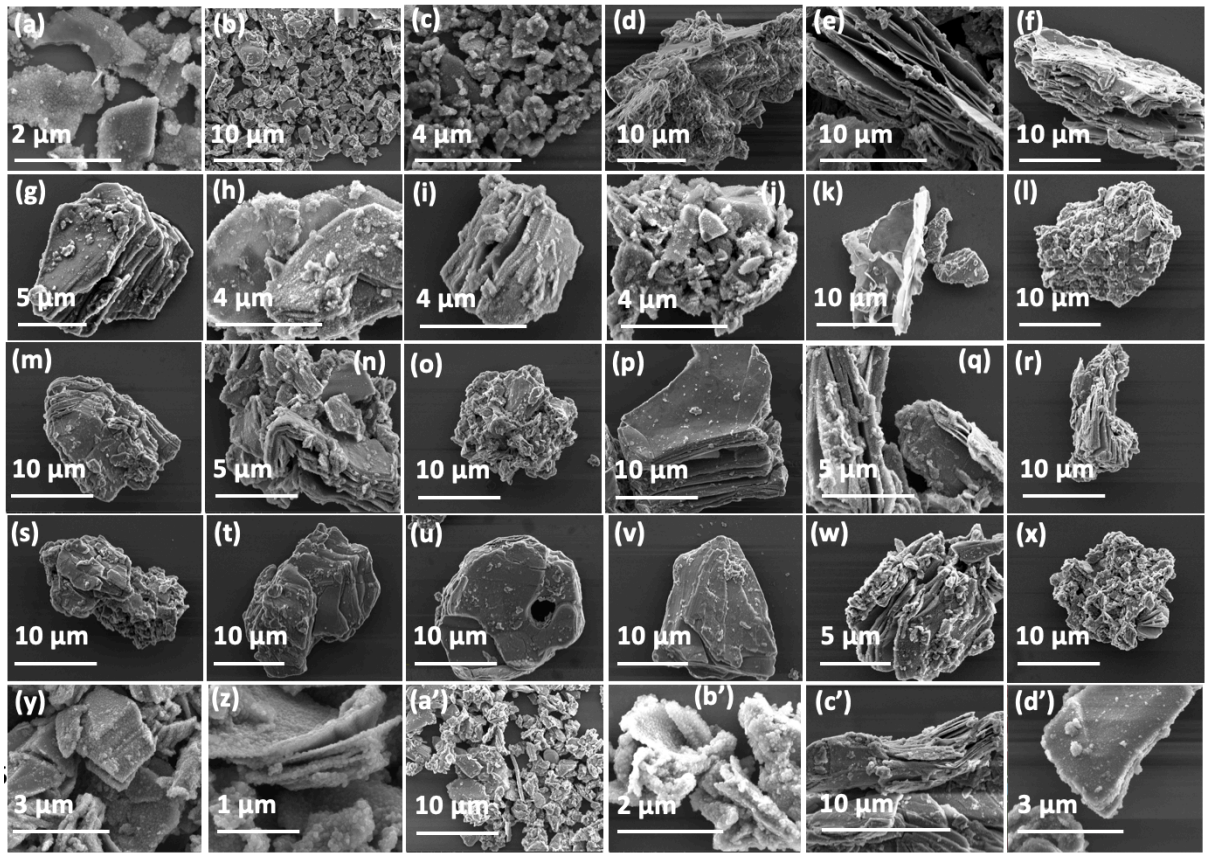

Figure S2.10. SEM images for MXene drop cast on silicon wafer, post VFD processing under air, θ 45º for 15 mins, concentration 1 mg/mL in. (a, b) DMF, rotational speed 4k rpm. (c, d) DMF, rotational speed 6k rpm. (e, f) DMF, rotational speed 7.5k rpm. (g, h) Toluene, rotational speed 4k rpm. (I, j) Toluene, rotational speed 6k rpm. (k, l) Toluene, rotational speed 7.5k rpm. (m, n) m-Xylene, rotational speed 4k rpm. (o, p) m-Xylene, rotational speed 6k rpm. (q, r) m-Xylene, rotational speed 7.5k rpm. (s, t) o-Xylene, rotational speed 4k rpm. (u, v) o-Xylene, rotational speed 6k rpm. (w, x) o-Xylene, rotation speed 7.5k rpm. (y, z) DMF and o-Xylene (1:1), rotational speed 4k rpm. (a', b') DMF and o-xylene as solvent (1:1), rotational speed 6k rpm. (c', d') DMF and o-xylene (1:1), rotational speed 7.5k rpm.

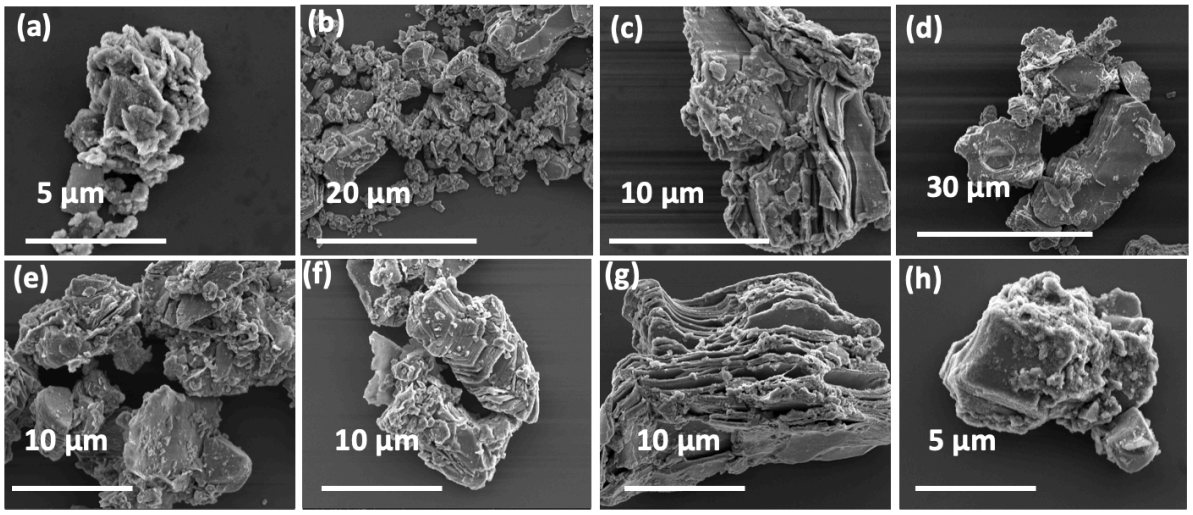

Figure S2.11. SEM images for MXene drop cast on silicon wafers, post VFD processing under air, θ 45º for 30 mins, rotational speed 4k rpm, concentration 0.5 mg/mL in. (a, b) DMF and IPA (1:1). (c, d) m-Xylene and IPA (1:1). (e, f) Toluene and IPA. (g, h) o-Xylene and IPA (1:1).

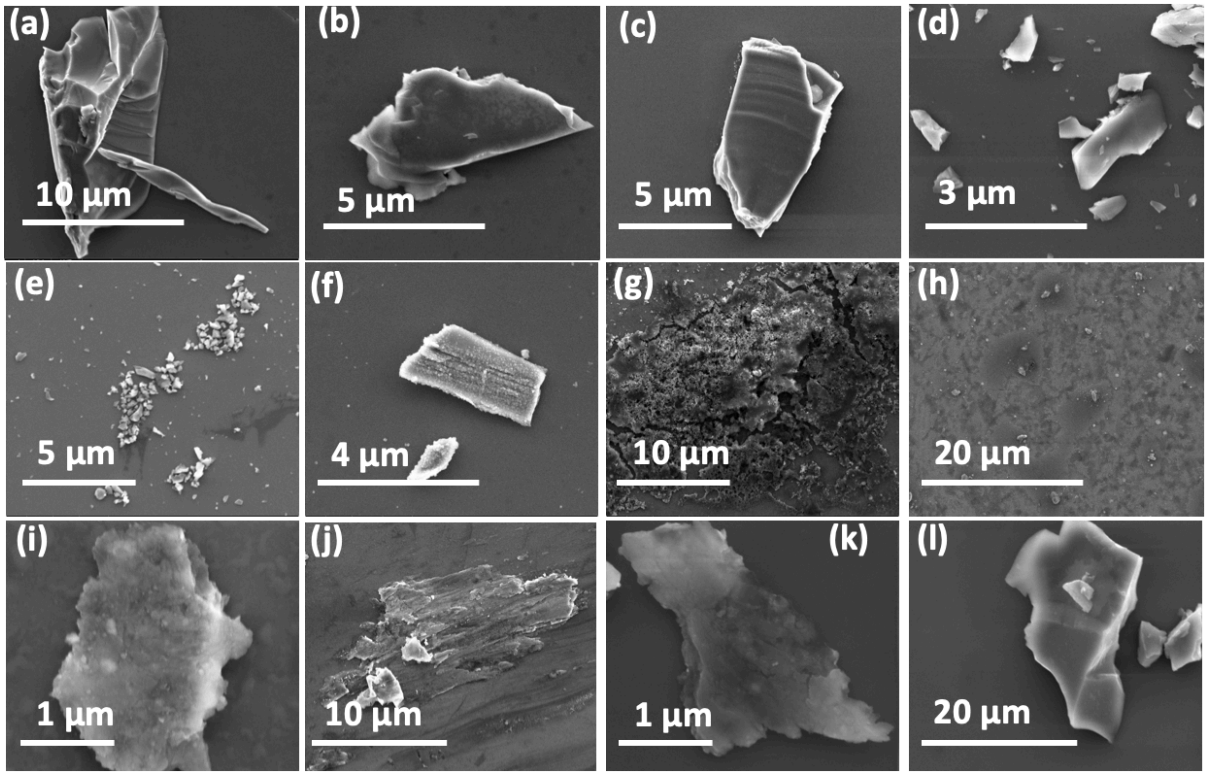

Figure S2.12. SEM images for MXene drop cast on silicon wafers, post VFD processing under air, θ 45º, irradiated quartz tube with a pulsed laser operating at 1064 nm, and concentration 0.5 mg/mL in IPA and water (1:1). (a, b) Rotational speed 4k rpm for10 min, laser at 260 mJ. (c, d) Rotational speed 4k rpm for 30 min, laser at 260 mJ. (e, f) Rotational speed 7.5k rpm for 30 min, laser at 260 mJ. (g, h) Rotational speed 7.5k rpm for 30 min, laser at 660 mJ. (I, j) Rotational speed 7.5k rpm for 30 min, laser at 460 mJ. (k, l) Rotational speed 7.5k rpm, flow rate 0.2 mL/min, and laser at 260 mJ.

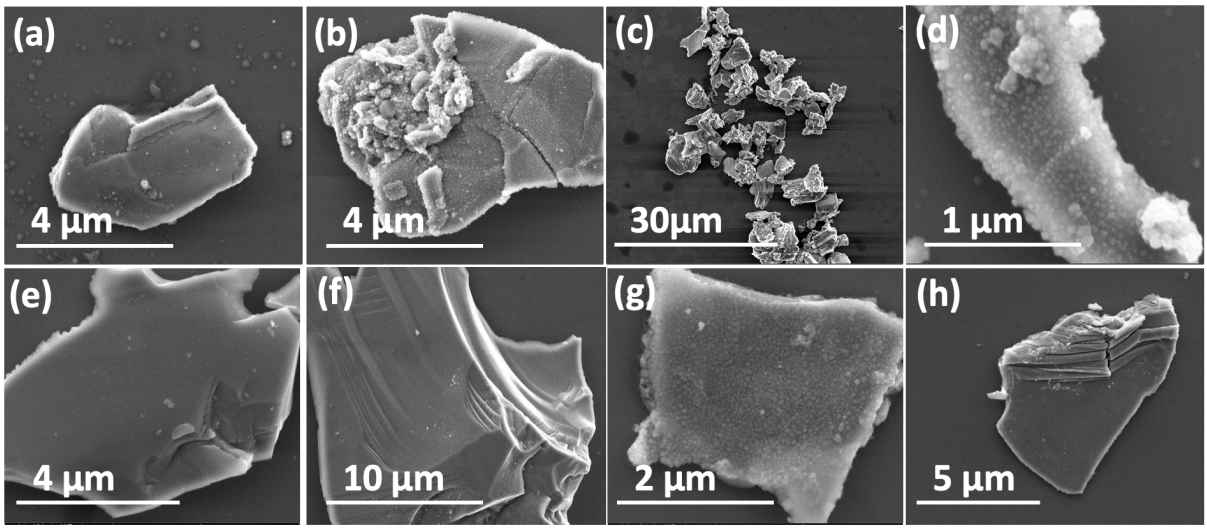

Figure S2.13. SEM images for MXene drop cast on a silicon wafer, post VFD processing under air,θ -45º, concentration 0.1 mg/mL in IPA and water (1:1), and flow rate 0.3 mL/min. (a, b) Rotational speed 2.5k rpm. (c, d) Rotational speed 4k rpm. (e, f) Rotational speed 6k rpm. (g, h) Rotational speed 8k rpm.

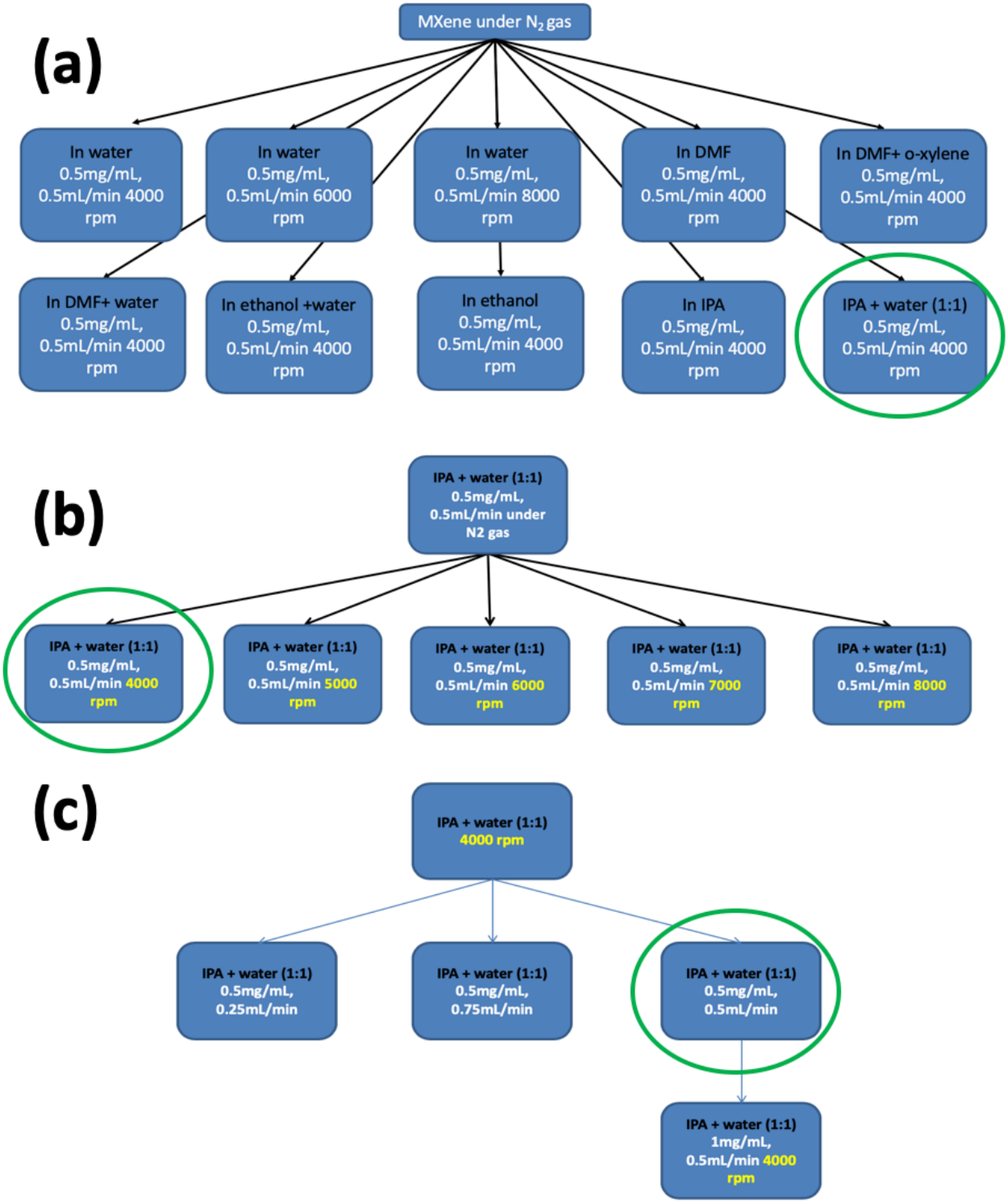

Figure S2.14. Schematic of the experiments used for processing MXene under N_2 gas. (a) Post VFD processing, θ 45°, concentration 0.5 mg/mL in different solvents for 0.5 mL/min flow rate, rotational speeds 4k rpm, and 6k rpm and 8k rpm for water. (b) Post VFD processing, θ 45 °, concentration 0.5 mg/mL in IPA and water (1:1) for different rotation speeds and 0.5 mL/min flow rate. (c) Post VFD processing, θ 45 °, concentration 0.5 mg/mL in IPA and water (1:1) for different flow rates of solution for 4k rpm rotational speed, as well as 1 mg/mL of MXene in IPA and water (1:1), θ 45 °, and 0.5 mL/min flow rate using 4k rpm rotational speed.

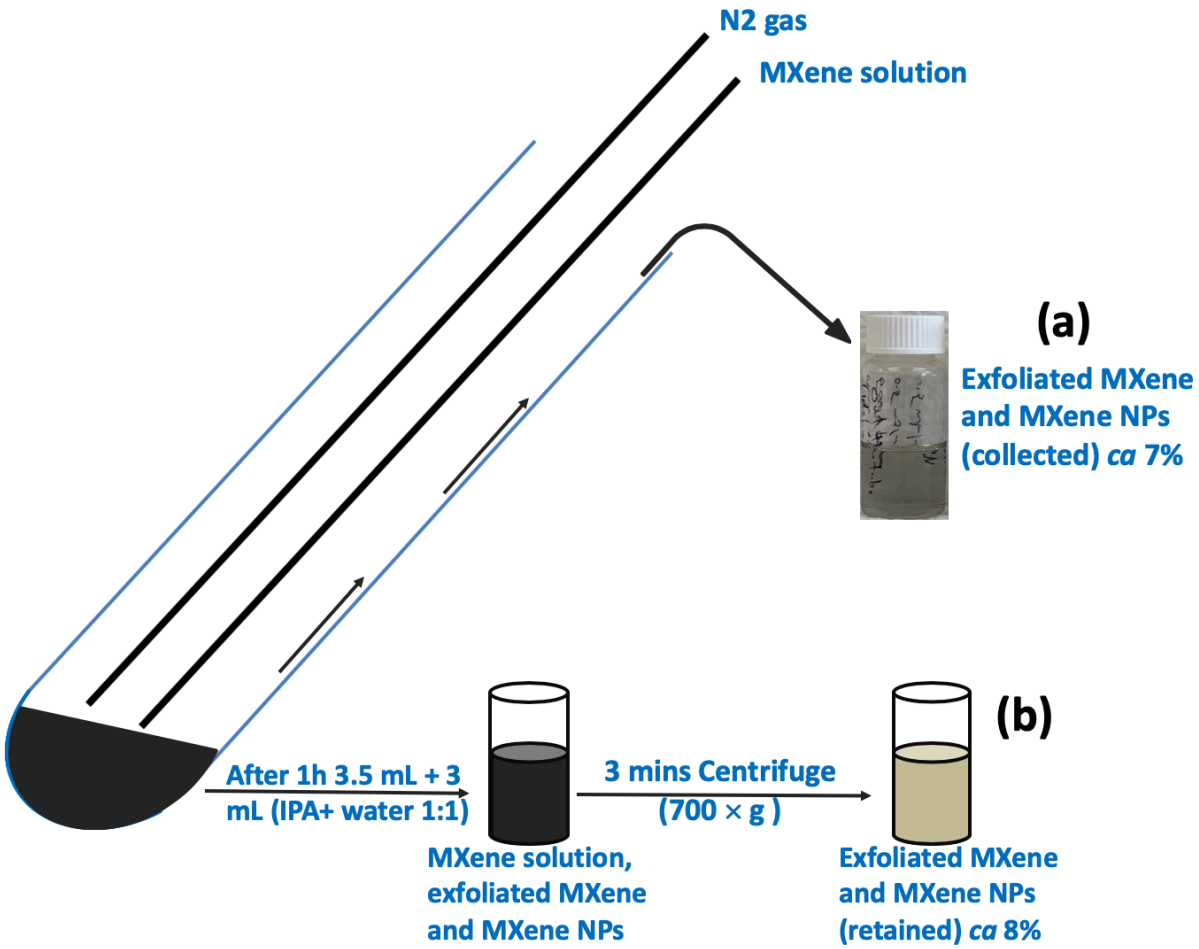

Figure S2.15. Schematic for processing MXene under N_2 gas, θ 45°, concentration 0.5 mg/mL in IPA and water (1:1), rotational speed 4K rpm and 0.5 mL/min flow rate. (a) Exfoliated MXene and MXene nanoparticles (collected). (b) Exfoliated MXene and MXene nanoparticles (retained).

Chapter 3: Vortex fluidic mediated synthesis of TiO_2 nanoparticle/MXene composites

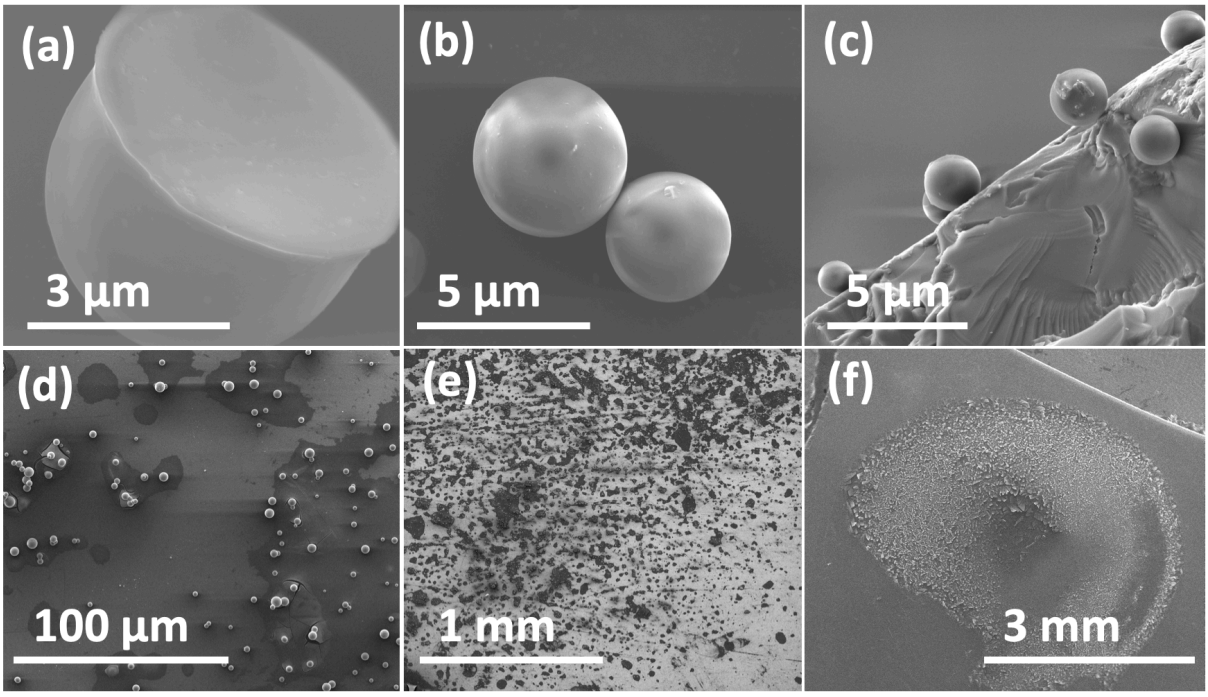

Figure S3.1. SEM images of TiO_2NPs/MXene drop cast on silicon wafer and oven dried at 60°C, MXene VFD processing, rotational speed 5k rpm, tilt angle 45° and flow rate 0.75 mL/min. (a-e) TiO_2 NPs/MXene spheres. (f) TiO_2 NPs/MXene sheets.

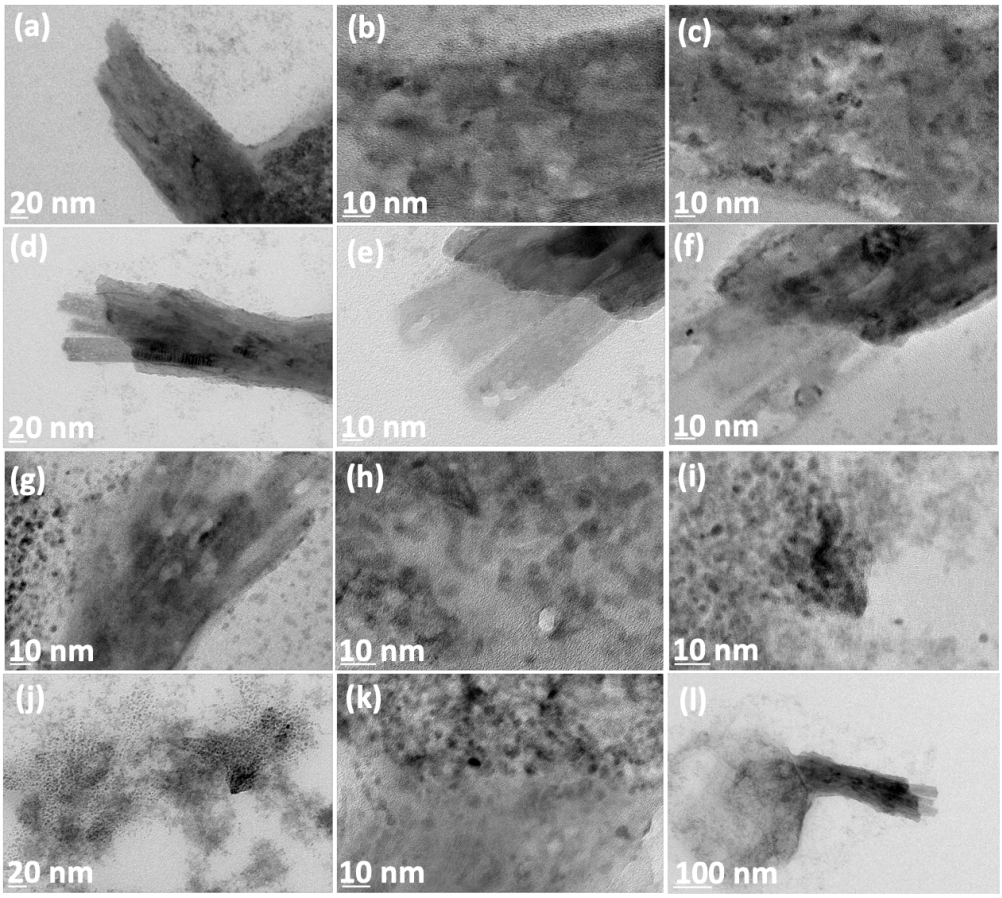

Figure S3.2. TEM and HRTEM images for TiO_2 NPs/MXene drop cast on a grid, MXene after 10 mins in a sonic bath (6 kHz) before VFD processing at rotational speed 5k rpm, tilt angle 45º and flow rate 0.75 mL/min.

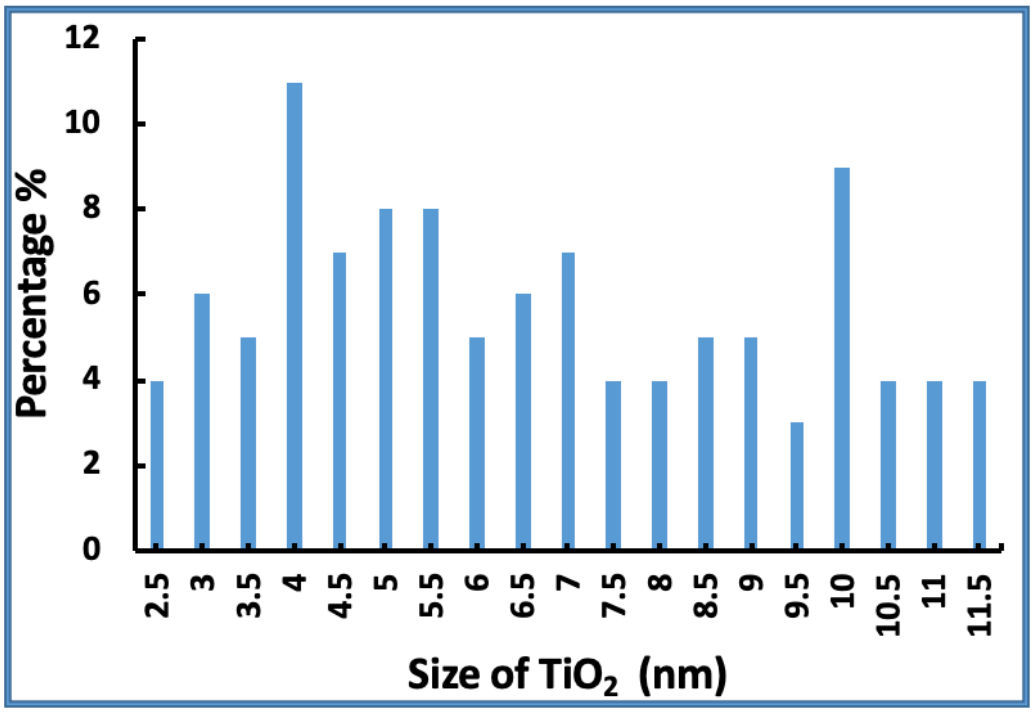

Figure S 3.3. Account for TiO_2 particle size (109 nanoparticles) in TiO_2 NPs/MXene collected, as derived by HRTEM for MXene VFD processing, rotational speed 5k rpm, tilt angle 45º and flow rate 0.75 mL/min.

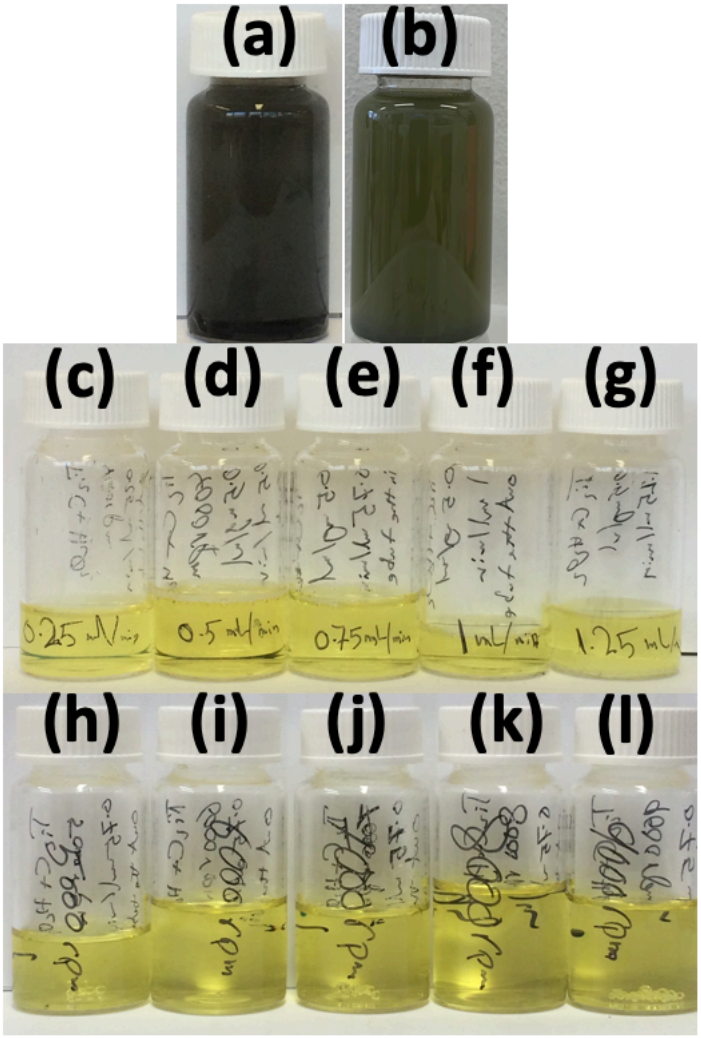

Figure S 3.4. Photos for (a) MXene in 30% H_2O_2 (0.5 mg/mL). (b) MXene in 30% H_2O_2 (0.5 mg/mL) after 10 mins in a sonic bath (6 kHz). (c-g) TiO_2NPs/MXene product outflow, derived from MXene VFD processing at flow rates 0.25 mL/min, 0.5 mL/min, 0.75 mL/min, 1 mL/min and 1.25 mL/min respectively, rotational speed 4k rpm and tilt angle 45°. (h-l) TiO_2NPs/MXene product outflow from MXene VFD processing, flow rate 0.75 mL/min, rotational speeds 5, 6, 7, 8 and 9k rpm respectively and tilt angle 45°.

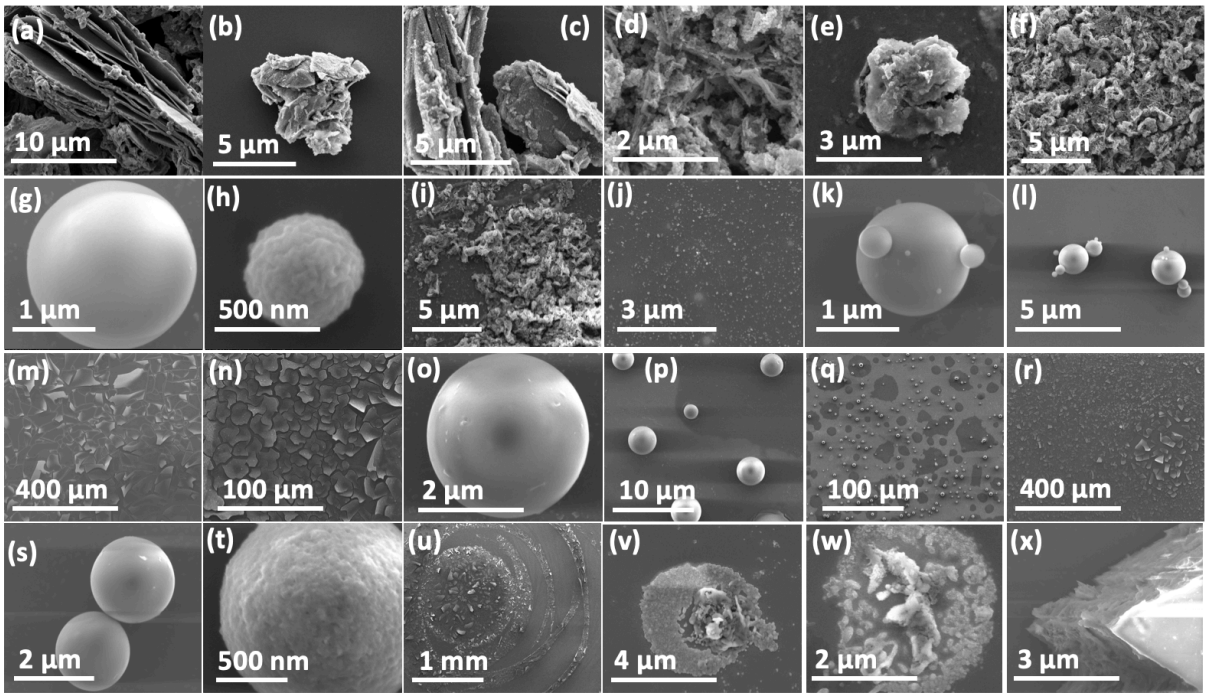

Figure S3.5. SEM images of material drop cast on silicon wafers and oven dried at 60°C. (a-c) MXene as prepared. (d-f) MXene in 30% H_2O_2 (0.5 mg/mL) after 10 mins in a sonic bath (6 kHz). MXene post VFD processing at rotational speed 4k rpm, tilt angle 45°, flow rates (g-j) 0.25 mL/min, (k-n) 0.5 mL/min, (o-r) 0.75 mL/min, (s-u) 1 mL/min, and (v-x) 1.25 mL/min.

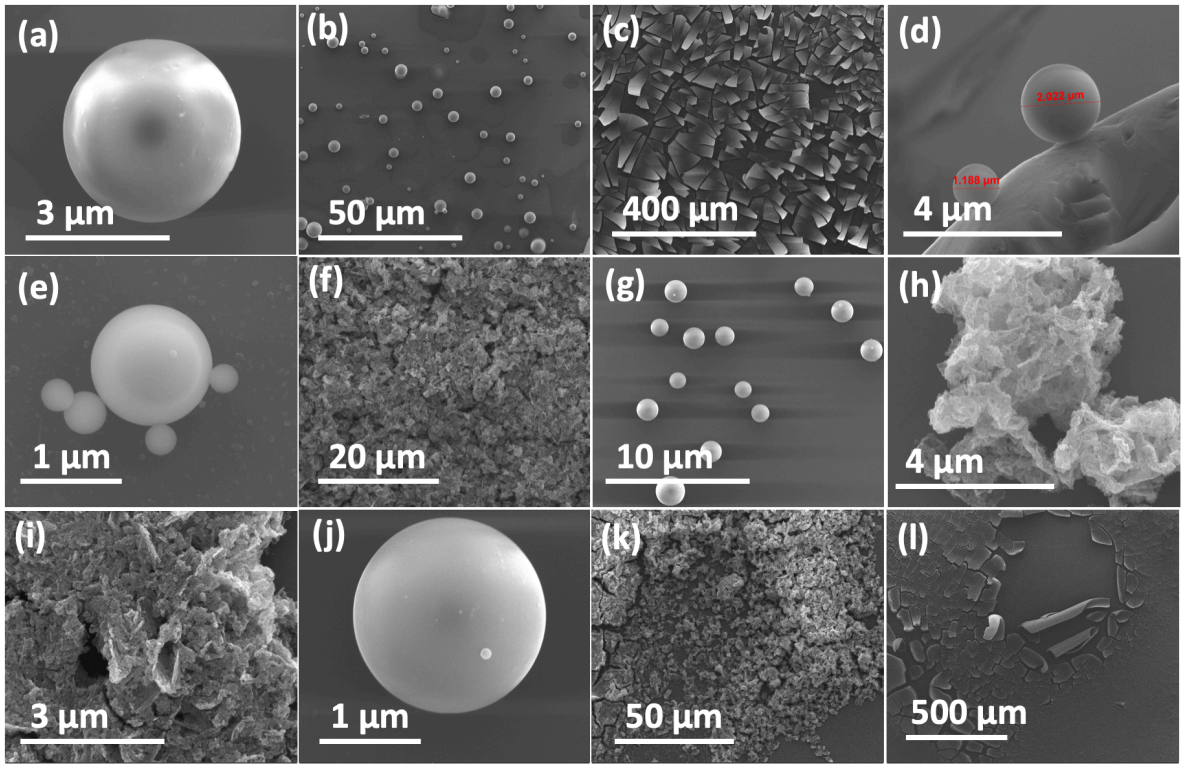

Figure S 3.6. SEM images for TiO_2NPs/MXene drop cast on silicon wafers and oven dried at 60ºC. VFD processing at tilt angle 45°, flow rate 0.75 mL/min with different rotational speeds, (a-c) 6k rpm, (d-f) 7k rpm, (g-i) 8k rpm, and (j-l) 9k rpm.

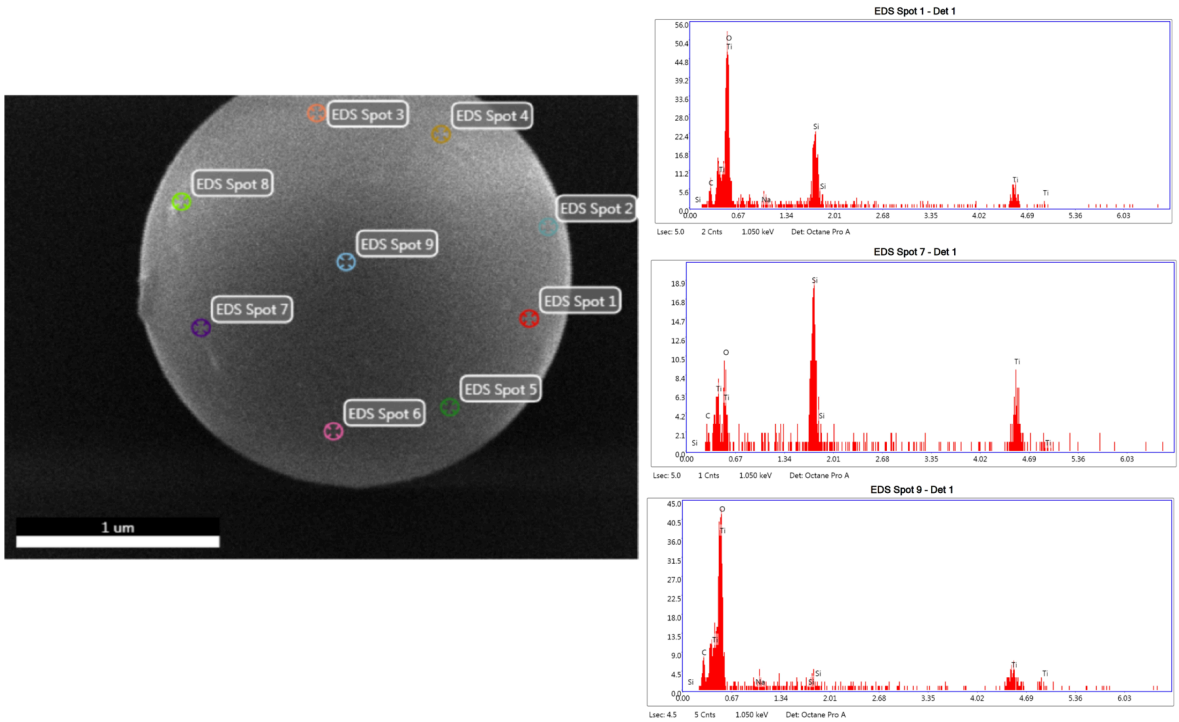

Figure S3.7. EDS for TiO_2 NPs/MXene sphere drop cast on a silicon wafer and oven dried at 60°C, optimal VFD processing, tilt angle 45°, flow rate 0.75 mL/min, and rotational speed 5k rpm.

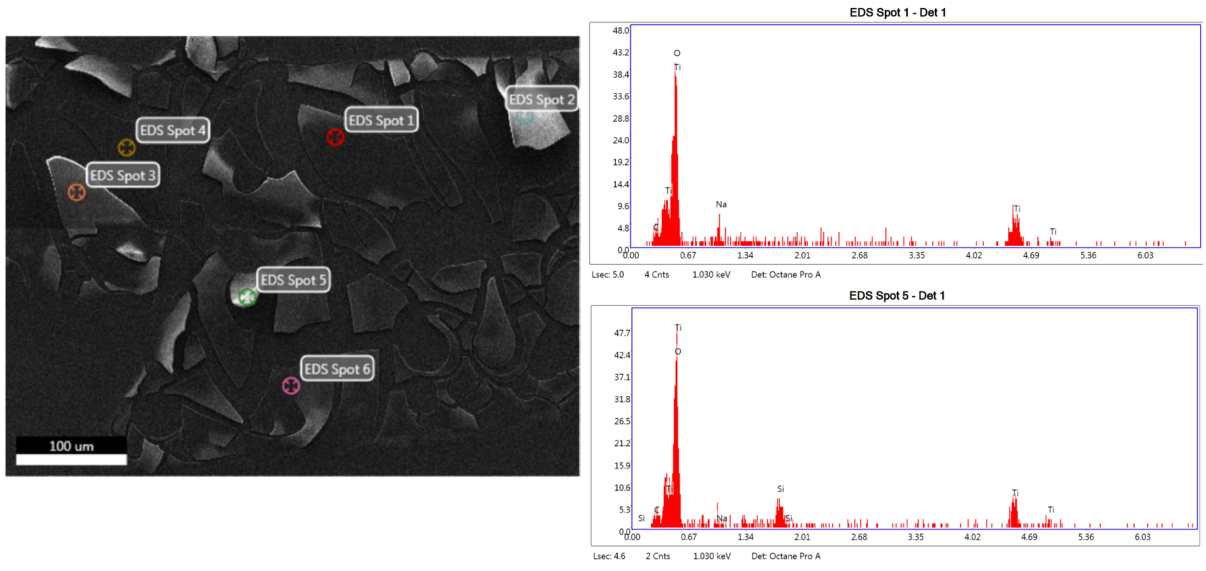

Figure S3.8. EDS for TiO_2 NPs/MXene sheets drop cast onto a silicon wafer and oven dried at 60°C, MXene in 30% H_2O_2 (0.5 mg/mL) after 10 mins in a sonic bath (6 kHz) before optimal, tilt angle 45°, flow rate 0.75 mL/min, and rotational speed 5k rpm.

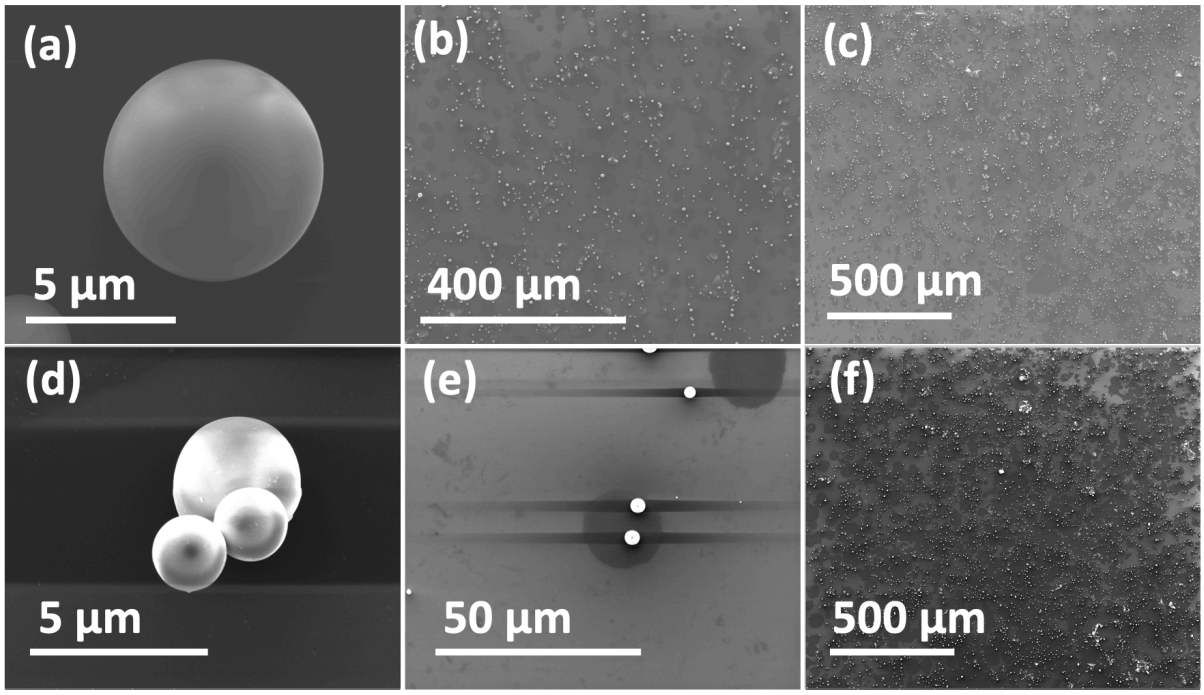

Figure S3.9. SEM images for TiO_2 NPs/MXene drop cast onto silicon wafer and oven dried at 60°C, MXene in 30% H_2O_2 (0.5 mg/mL) after 10 mins in a sonic bath (6 kHz) before VFD processing, tilt angle 45°, flow rate 0.75 mL/min, rotational speed 5k rpm. (a-c) Spheres after 25 days for the same sample. (d-f) Spheres after 60 days for the same sample.

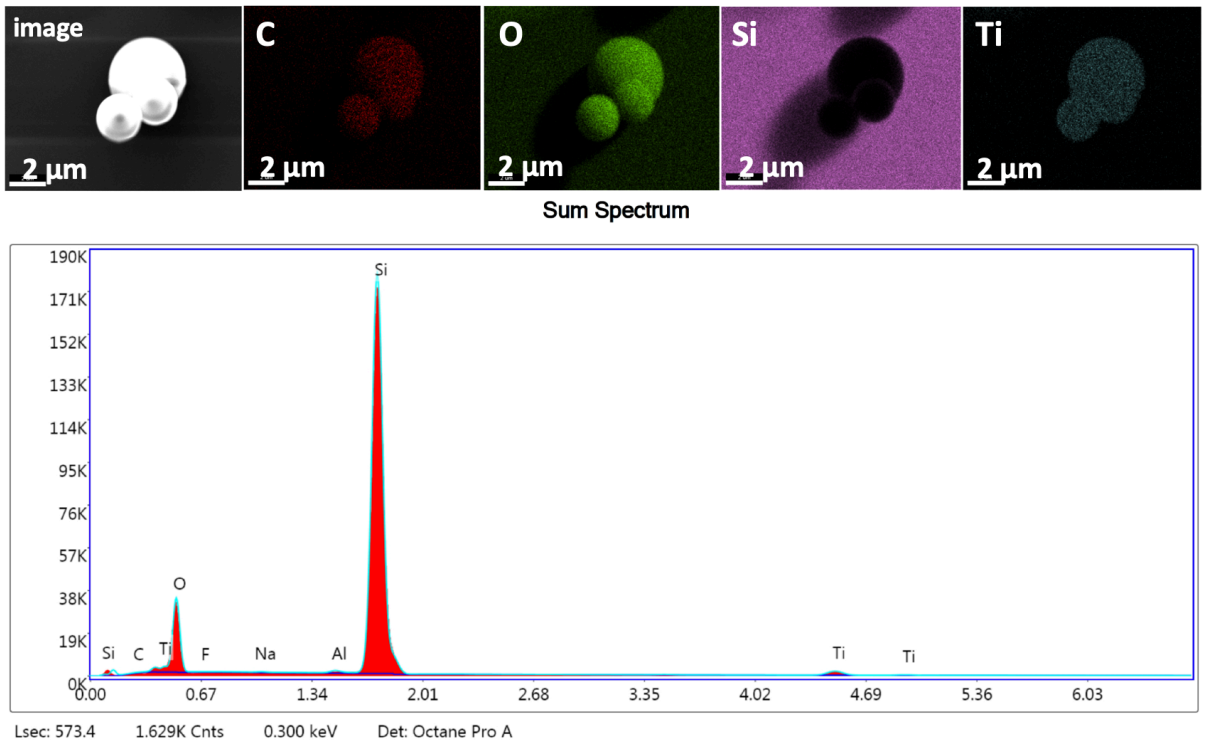

Figure S3.10. EDS mapping of stable TiO_2 NPs/MXene spheres drop cast on a silicon wafer and oven dried at 60°C, optimal VFD processing, tilt angle 45°, flow rate 0.75 mL/min, and rotational speed 5k rpm. The spheres are after 60 days of same preparation.

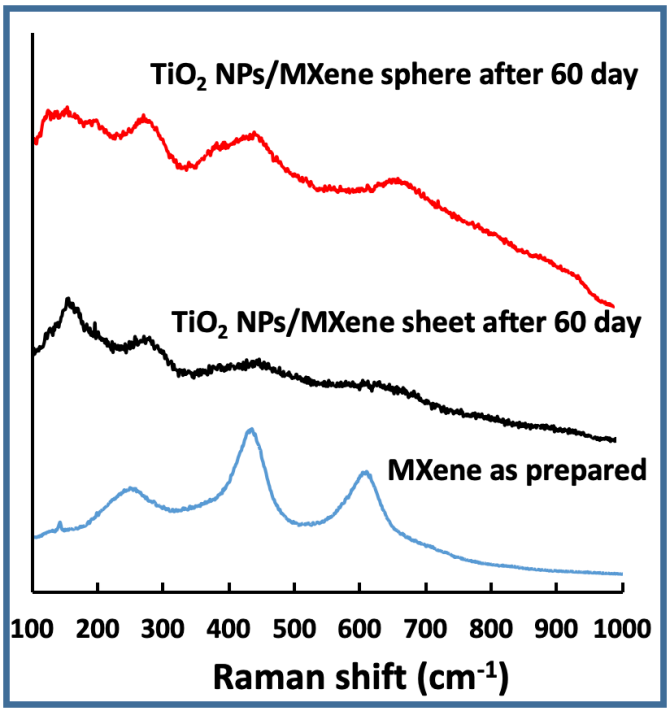

Figure S3.11. Raman spectra for TiO_2 NPs/MXene spheres and sheets prepared from MXene optimal VFD processing, rotational speed 5k rpm, tilt angle 45° and flow rate 0.75 mL/min, after 60 days.

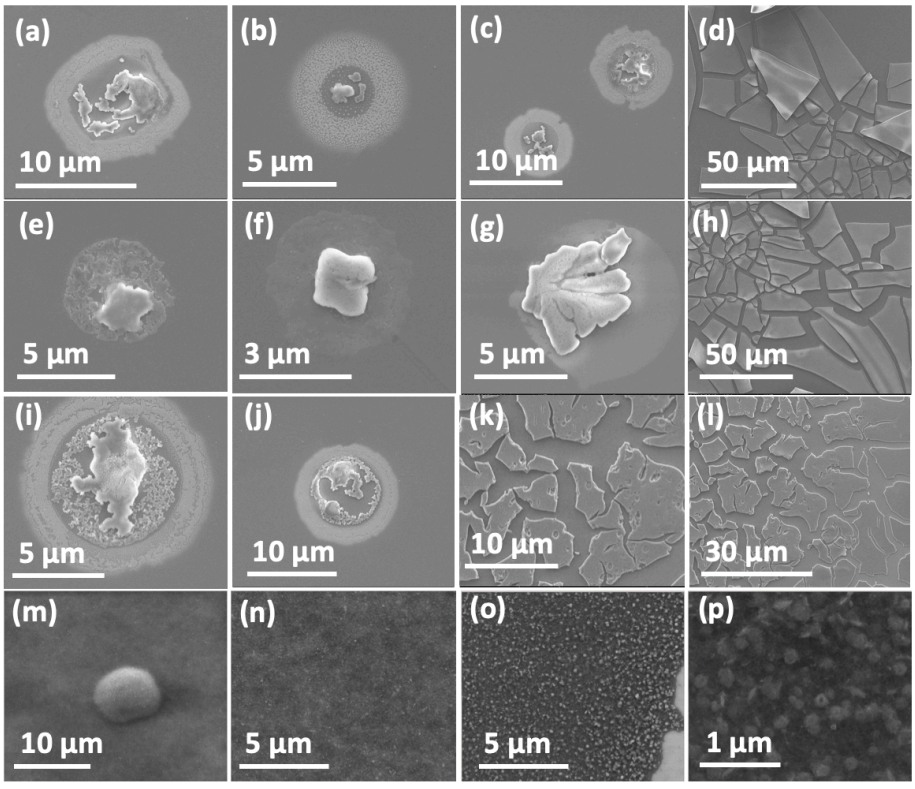

Figure S3.12. SEM images in studying the stability of TiO_2NPs/MXene, MXene optimal VFD processing, tilt angle 45°, flow rate 0.75 mL/min, and rotational speed 5k rpm. (a-d) Drop cast material on a silicon wafer after 1 day, (e-h) after 3 days, (i-l) after 6 days, and (m-p) after 60 days.

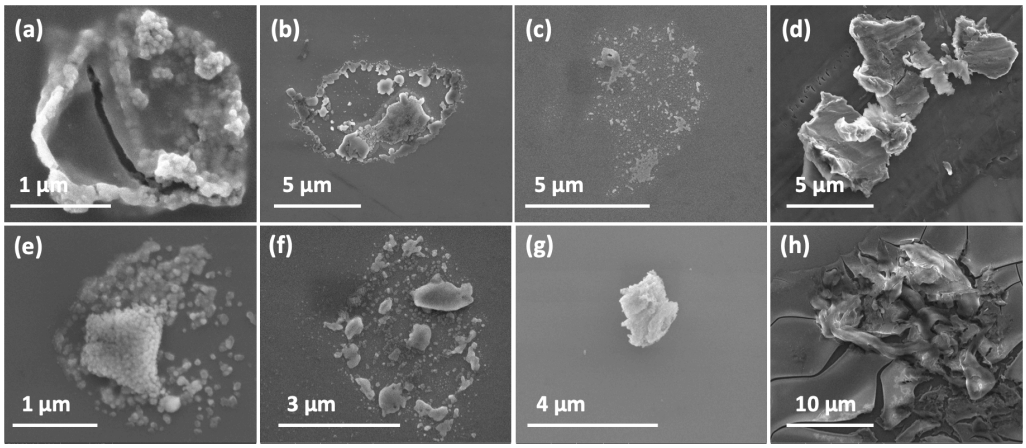

Figure S3.13. SEM image for material from control experiments. (a-d) MXene in water (0.5 mg/mL) after 10 min batch sonication (6 kHz) before delivering to the VFD at a flow rate of 0.39 mL/min with 30% H_2O_2 added at the same time through a second jet feed at a flow rate of 0.39 mL/min, rotational speed 5k rpm, and tilt angle 45°. (e-h) MXene in water and 30% H_2O_2 volume ratio 5:1, concentration of MXene 0.5 mg/mL with the solution previously bath sonicated for 10 min (6 kHz), flow rate of solution was 0.75 mL/min, rotation speed 5k rpm, and tilt angle 45°.

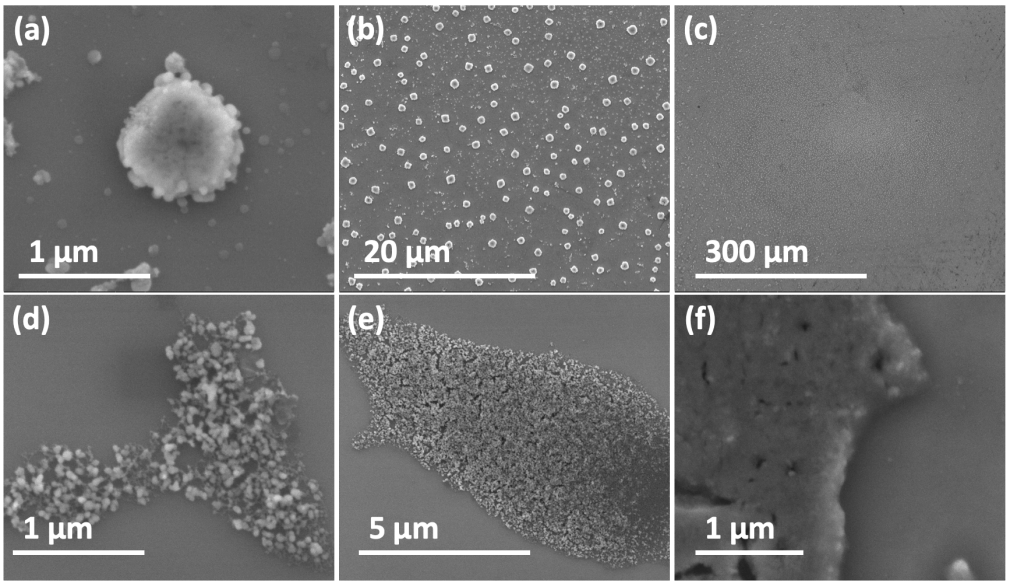

Figure S3.14. SEM images for TiO_2 NPs < 100 nm in diameter in 30% H_2O_2 (0.5 mg/mL) after optimal VFD processing, tilt angle 45°, flow rate 0.75 mL/min, and rotational speed 5k rpm.

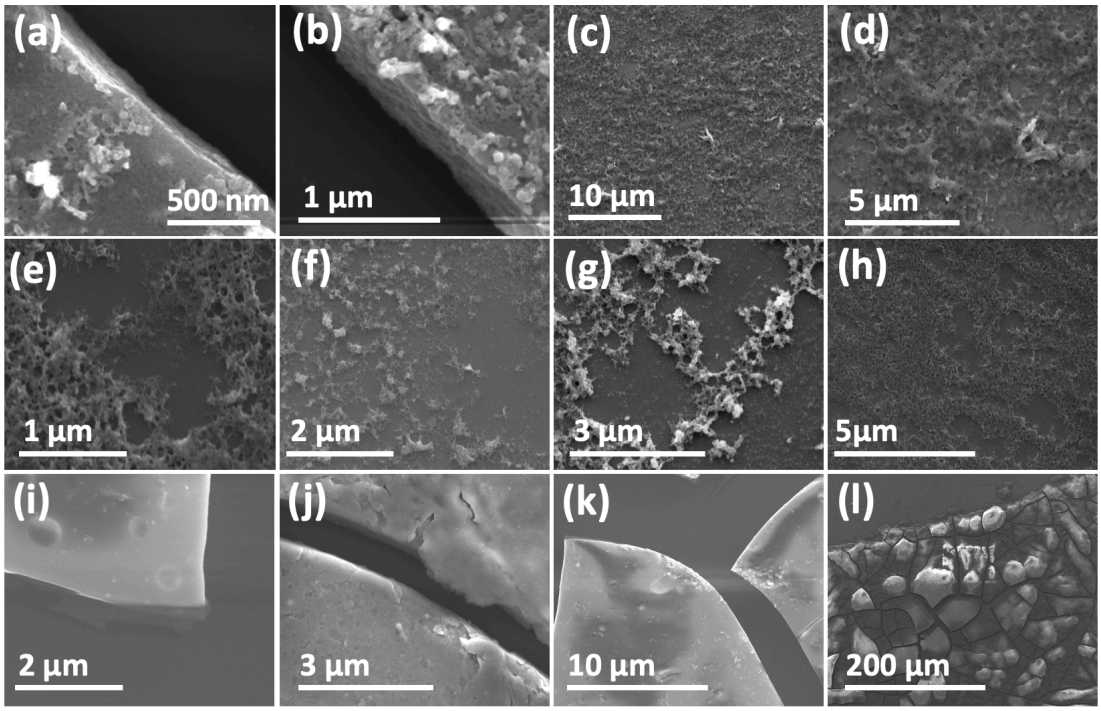

Figure S3.15. SEM images for (a-d) MXene in 30% H_2O_2 + DMF ratio 1-1, then 10 mins of bath sonication (6 kHz) before VFD processing, rotational speed 5k rpm, concentration 0.5 mg/mL, the flow rate 0.75 mL/min and tilt angle 45°. (e-h) Collected TiO_2NPs/MXene from the tube after rotating at 5k rpm, 0.75 mL/min, 0.5 mg/mL with a tilt angle of 45°, re-dispersed in 15 mL of DMF previously passed through the VFD, rotational speed 8k rpm, flow rate 0.75mL/min, tilt angle 45°. (i-l) MXene in 30% H_2O_2 (0.5 mg/mL) after 10 mins bath sonication (6 kHz) before passing through the VFD with another jet feed delivering DMF, tilt angle 45°, rotational speed 5k rpm and flow rate for both MXene in 30% H_2O_2 and DMF 0.38 mL/min.

Chapter 4: Inverted vortex fluidic exfoliation and scrolling of hexagonal-boron nitride

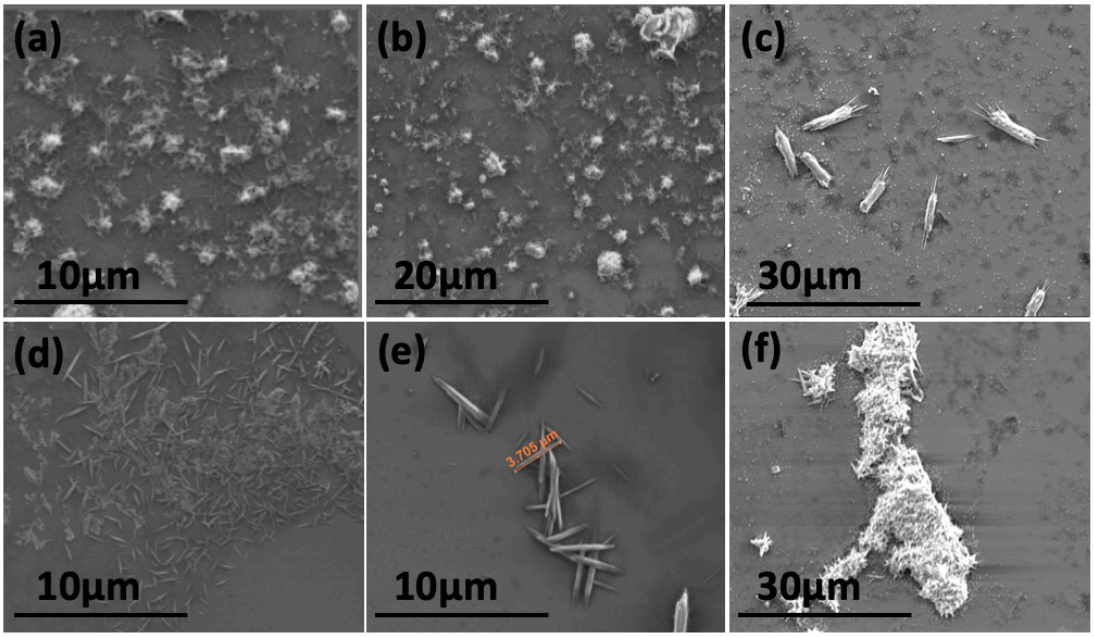

Figure S4.1. SEM images: (a) As received h-BN. (b-f) Drop-cast h-BN scrolls on silicon wafer of the supernatant after centrifuging at RCF = 1180 g, post VFD processing at 6k rpm rotational speed, tilt angle -45º, flow rate 0.3 mL/min, and concentration 0.1 mg/mL.

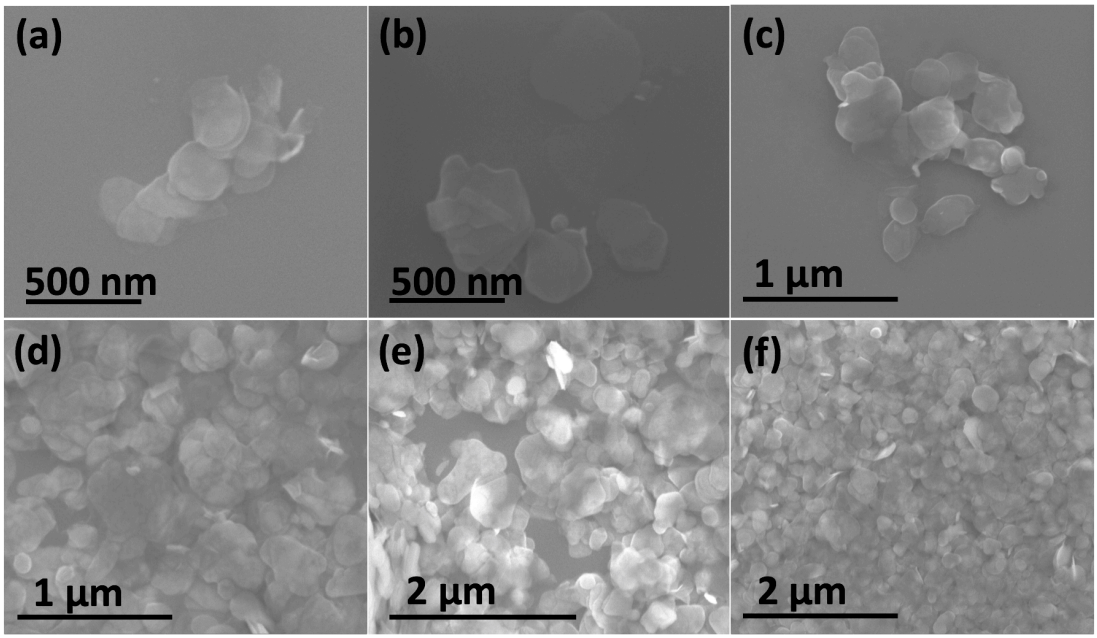

Figure S4.2. (a-f) SEM images of exfoliated h-BN drop cast on silicon wafer using the supernatant after centrifuging at RCF = 1180 g for 3 min, post VFD processing, rotational speed 6k rpm, tilt angle -45º, flow rate 0.75 mL/min, concentration 0.3 mg/mL.

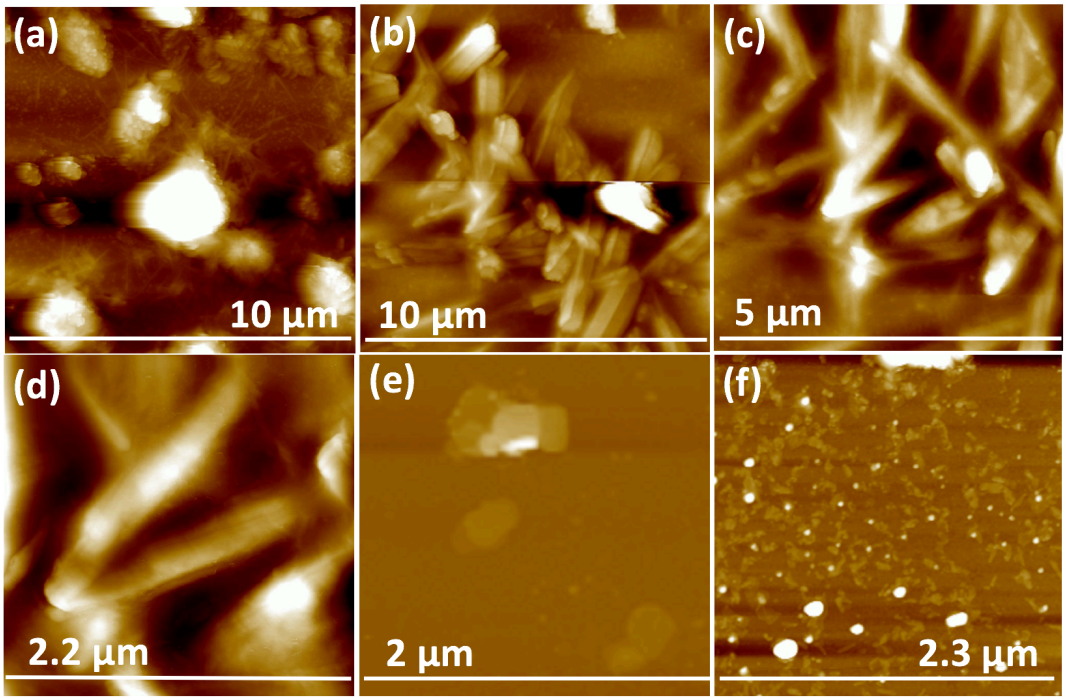

Figure S4.3. AFM images of drop cast h-BN scrolls on silicon wafer using the supernatant after centrifuging at RCF = 1180 g, post VFD processing (rotational speed 6k rpm, tilt angle -45º), (a-d) h-BN scrolls prepared using a flow rate of 0.3 mL/min and concentration 0.1 mg/mL. (e-f) Exfoliated h-BN prepared using a flow rate of 0.75 mL/min, concentration 0.3 mg/mL.

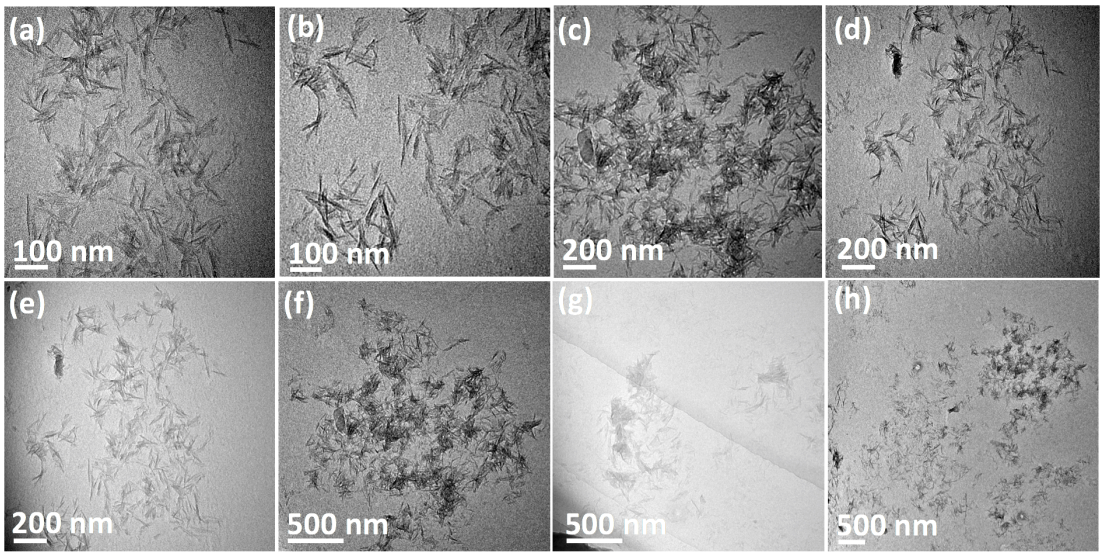

Figure S4.4. TEM images of drop cast h-BN scrolls on a grid, post VFD processing at 6k rpm rotational speed, tilt angle -45º, flow rate 0.3 mL/min and concentration 0.1 mg/mL.

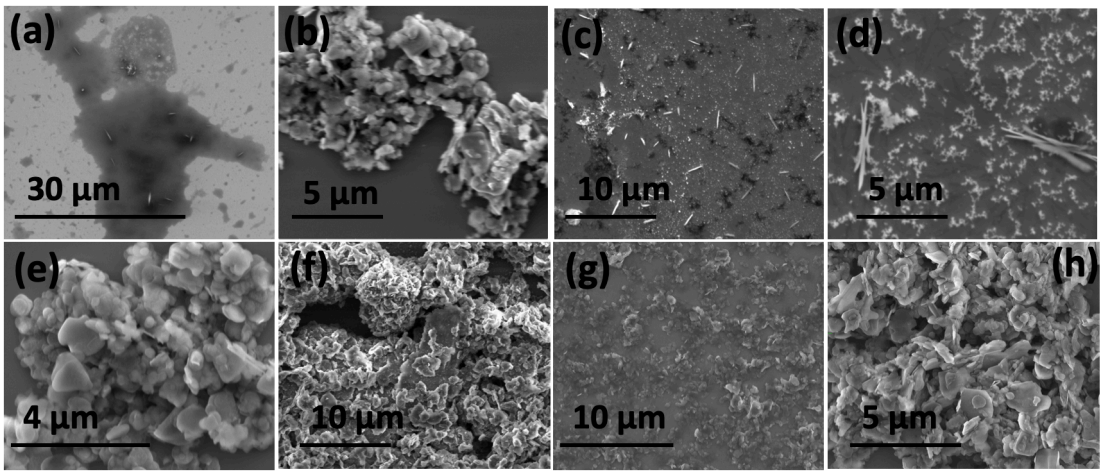

Figure S4.5. SEM images for h-BN in water, post VFD processing at a concentration of 0.1 mg/ mL, rotational speed 6k rpm and flow rate of the h-BN in water at 0.3 mL/min, for different tilt angles. (a, b) +45º. (c, d) +20º. (e, f) 0º. (g, h) -20º.

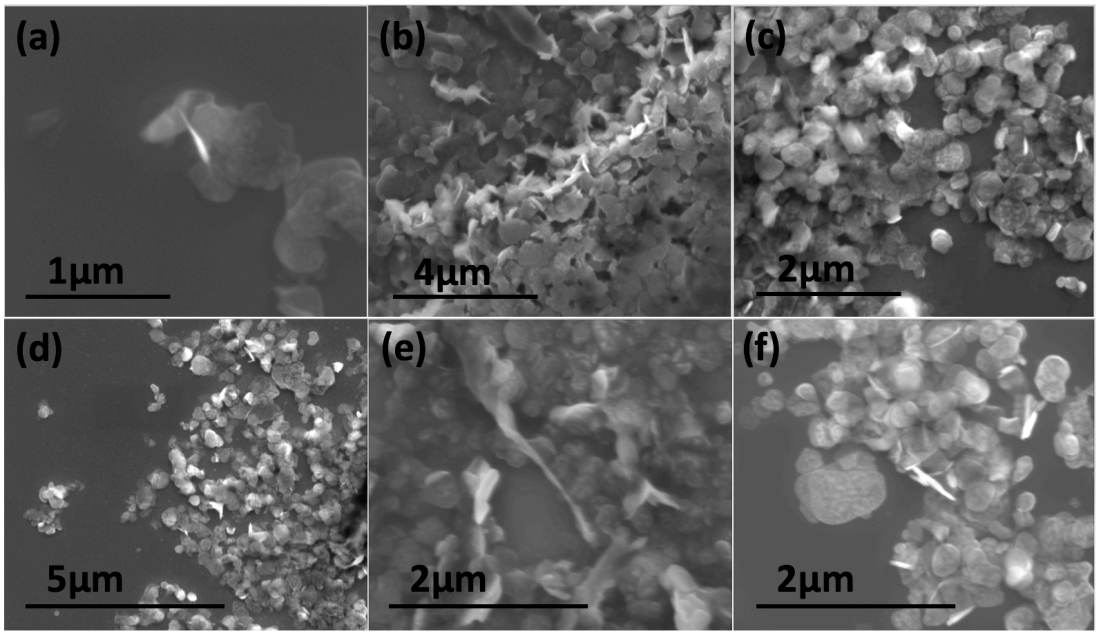

Figure S4.6. The exfoliation product of h-BN after VFD processing to form scrolls, with the initial concentration 0.1 mg/mL, tilt angle +45º using the confined mode for different rotational speeds. (a-b) 2k rpm for 30 min. (c-d) 3.5k rpm for 10 min. (e-f) 5.5 rpm for 10 min.

Table S4.1. The optimisation experiments with VFD. Experimental parameters of the VFD were varied based on the mode of reaction, rotational speed of the tube, tilt angle, flow rate of the reactants, single solvent systems and mix solvent systems.

	solvent	mode	speed	Con.	angel	Flow rate	other	Formation of scrolls or exfoliation
1.	NMP only	confined	4k, 5k, 6k, 7k and 8k rpm	0.1 mg/mL	+45˚	N/A	5, 10, 30 min and 1 h	No
2.	NMP+ water (1:1)	confined	4k, 5k, 6k, 7k and 8k rpm	0.1 mg/mL	+45˚	N/A	10 and 30 min	No
3.	NMP+ water (1:1)	continuous	4k, 5k, 6k, 7k and 8k rpm	0.1 mg/mL	+45˚	0.1, 0.3, 0.5, 0.75 and 1 mL/min		No
4.	NMP+ water (1:1)	continuous	7500rpm	0.1 mg/mL	+20˚	0.1, 0.3, 0.5, 0.75 and 1 mL/min		No
5.	Isopropanol	confined	4k, 5k, 6k, 7k and 8k rpm	0.1 mg/mL	+45˚	N/A	5, 10, 30 min and 1 h	No
6.	Isopropanol + water (1:1)	confined	4k, 5k, 6k, 7k and 8k rpm	0.1 mg/mL	+45˚	N/A	5, 10, 30 min and 1 h	No
7.	Isopropanol + water (1:1)	continuous	4k, 5k, 6k, 7k and 8k rpm	0.1mg/mL	+45˚	0.1, 0.3, 0.5, 0.75 and 1 mL/min		No
8.	Isopropanol + water (1:1)	continuous	4k, 5k, 6k, 7k and 8k rpm	0.1mg/mL	-20˚	0.1, 0.3, 0.5, 0.75 and 1 mL/min		No
9.	Isopropanol + water (1:1)	continuous	4k, 5k, 6k, 7k and 8k rpm	0.1mg/mL	-45˚	0.1, 0.3, 0.5, 0.75 and 1 mL/min	Laser 260 mJ and 600 mJ	No
10.	Toluene	confined	4k, 5k, 6k, 7k and 8k rpm	0.1mg/mL	+45˚	N/A	5, 10, 30 min and 1 h	No
11.	Toluene	continuous	4k, 5k, 6k, 7k and 8k rpm	0.1mg/mL	+45˚	0.1, 0.3, 0.5, 0.75 and 1 mL/min		No
12.	Toluene +water (1:1)	confined	4k, 5k, 6k, 7k and 8k rpm	0.1mg/mL	+45˚	N/A	5, 10, 30 min and 1 h	No
13.	Toluene + water (1:1)	continuous	4k, 5k, 6k, 7k and 8k rpm	0.1mg/mL	+45˚	0.1, 0.3, 0.5, 0.75 and 1 mL/min		No
14.	Toluene + water (1:1)	continuous	4k, 5k, 6k, 7k and 8k rpm	0.1mg/mL	+20˚	0.1, 0.3, 0.5, 0.75 and 1 mL/min		No

15.	Toluene + water (1:1)	continuous	4k, 5k, 6k, 7k and 8k rpm	0.1mg/mL	0 ˚	0.1, 0.3, 0.5, 0.75 and 1 mL/min		No
16.	Water	confined	4k, 5k, 6k, 7k and 8k rpm	0.1mg/mL	+45˚	N/A	5, 10, 30 min and 1 h	No
17.	Water	confined	4k, 5k, 6k, 7k and 8k rpm	0.1mg/mL	+45˚	N/A	Laser 260 mJ and 600 mJ	No
18.	Water with $FeCl_3$	confined	4k, 5k, 6k, 7k and 8k rpm	0.1mg/mL	+45˚	N/A	30 min	No
19.	Water	continuous	4k, 5k, 6k, 7k and 8k rpm	0.1mg/mL	+45˚	0.1, 0.5, 0.75 and 1 mL/min		No
20.	Water	continuous	6000rpm	0.1mg/mL	+45˚	0.3mL/min	Heating unite 70C	No
21.	Water	continuous	7500rpm	0.1mg/mL	+20˚	0.3mL/min	Heating unite 70C	No
22.	Water	continuous	7500rpm	0.1mg/mL	+45˚	0.3mL/min	Laser 260mJ and 600 mJ	No
23.	Water	confined	4k, 5k, 6k, 7k and 8k rpm	0.1mg/mL	+20˚	N/A	5, 10, 30 min and 1 h	No
24.	Water	continuous	4k, 5k, 6k, 7k and 8k rpm	0.1mg/mL	0º	0.1, 0.3, 0.5, 0.75 and 1 mL/min		No
25.	Water	continuous	4k, 5k, 6k, 7k and 8k rpm	0.2mg/mL	0º	0.1, 0.3, 0.5, 0.75 and 1 mL/min		No
26.	Water	continuous	4k, 5k, 6k, 7k and 8k rpm	0.1mg/mL	-20˚	0.1, 0.3, 0.5, 0.75 and 1 mL/min		No
27.	Water	continuous	4k, 5k, 7k and 8k rpm	0.1mg/mL	-45˚	0.1, 0.5, 0.75 and 1 mL/min		No
28.	**Water**	**continuous**	**6000rpm**	**0.1 mg/mL**	**-45˚**	**0.3mL/min**		**Yes Scrolls**
29.	Water	continuous	6000rpm	0.1mg/mL	-45˚	0.3mL/min	Recycle twice	No
30.	Water	continuous	6000rpm	1mg/mL	-45˚	0.3mL/min	Recycle twice	No
31.	Water	continuous	6000rpm	1mg/mL	-45˚	0.3mL/min	Recycle three times	No
32.	Water	continuous	7500rpm	0.1mg/mL	+45˚	0.1, 0.3, 0.5, 0.75 and 1 mL/min	10 mm of VFD tube	No

33.	Water	continuous	7500rpm	0.1mg/mL	+20˚	0.1, 0.3, 0.5, 0.75 and 1 mL/min	10 mm of VFD tube	No
34.	Water	continuous	7500rpm	0.1mg/mL	0˚	0.1, 0.3, 0.5, 0.75 and 1 mL/min	10 mm of VFD tube	No
35.	Water 1M of HCl	continuous	6000rpm	0.1mg/mL	-45˚	0.3mL/min		No
36.	Water 1 M of NaOH	continuous	6000rpm	0.1mg/mL	-45˚	0.3mL/min		No
37.	Water	continuous	4k, 5k, 7k and 8k rpm	0.3 mg/mL	-45˚	0.3, 0.5 and 1mL/min		No
38.	**Water**	**continuous**	**6000rpm**	**0.3mg/mL**	**-45˚**	**0.75mL/min**		**Yes Exfoliation**
39.	Water	continuous	4k, 5k, 6k, 7k and 8k rpm	0.5mg/mL	-45˚	0.3, 0.5, 0.75 and 1mL/min		No
40.	Water	continuous	4k, 5k, 6k, 7k and 8k rpm	0.7mg/mL	-45˚	0.3, 0.5, 0.75 and 1mL/min		No
41.	Water	continuous	4k, 5k, 6k, 7k and 8k rpm	1mg/mL	-45˚	0.3, 0.5, 0.75 and 1mL/min		No

Chapter 5. Continuous flow synthesis of phosphate binding *h*-BN@magnetite hybrid material

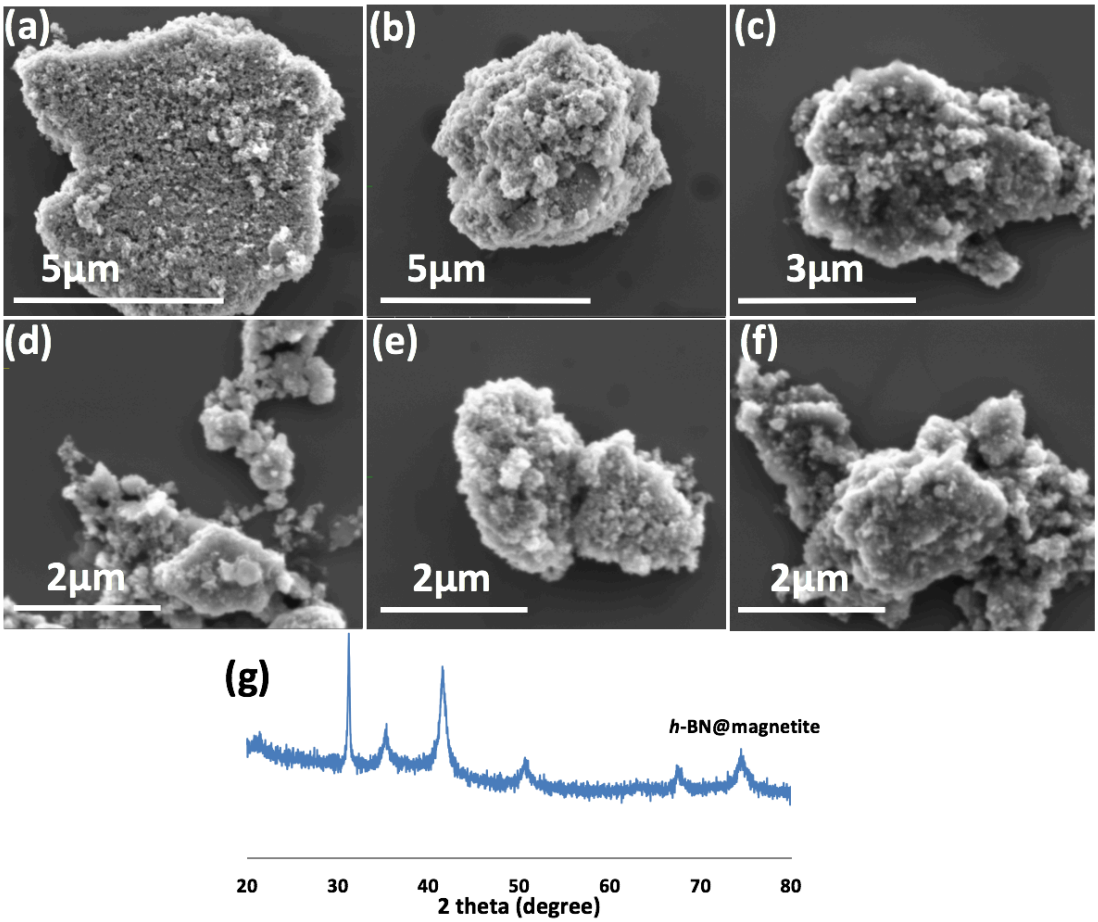

Figure S5.1. *h*-BN@magnetite composite prepared using the confined mode of operation of the VFD for 15 min, with pulsed laser operating at 1064 nm and 360 mJ, irradiating a pure iron target. Rotational speed at 7.5k rpm for a 20 mm OD glass tube, tilt angle 45º and h-BN dispersed in water (0.1 mg/mL). (a-f) SEM images and (g) XRD pattern.

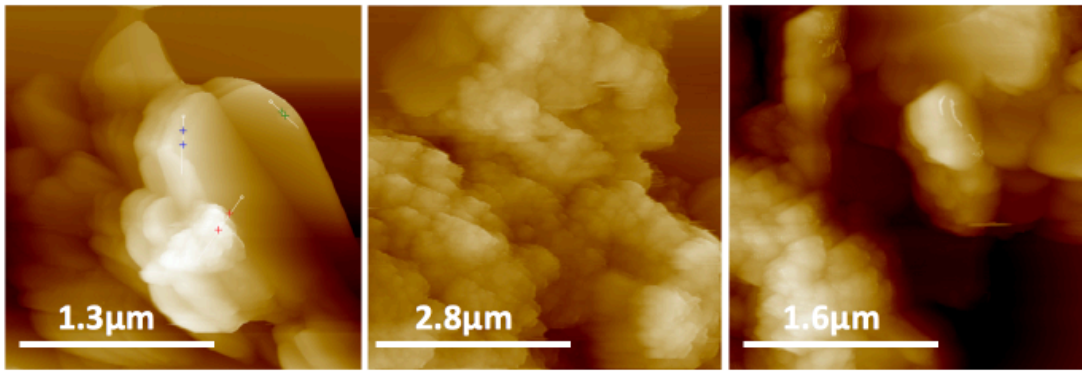

Figure S5.2. AFM images for h-BN@magnetite composite prepared in a VFD under continuous flow mode with a pulsed laser operating at 1064 nm and 360 mJ, irradiating a pure iron target. Rotational speed at 7.5k rpm, tilt angle 45º and flow rate 1 mL/min.

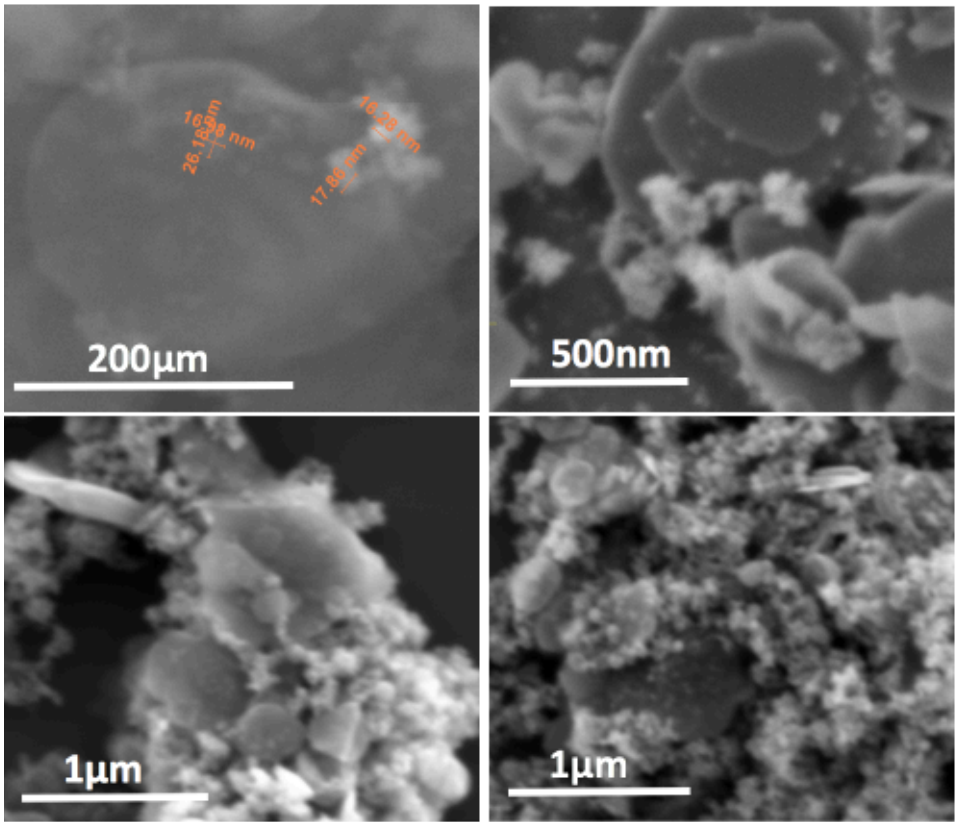

Figure S5.3. SEM images of h-BN@magnetite composite prepared under continuous flow mode with a pulsed laser irradiating a pure iron target, operating at 1064 nm and 360 mJ, with the 20 mm OD glass tube rotating at 7.5k rpm, tilt angle 45º and flow rate at 1 mL/min.

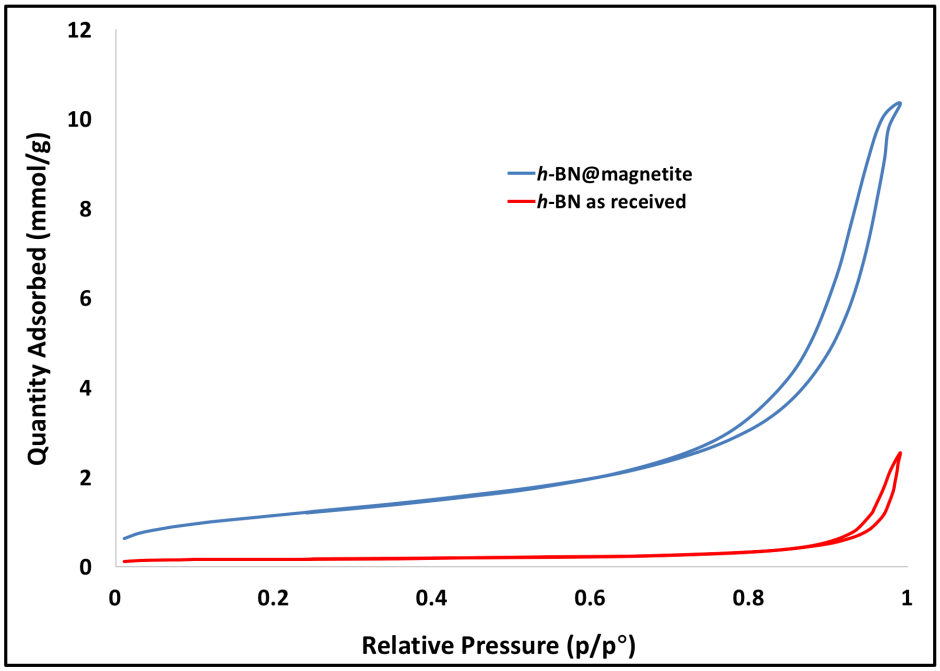

Figure S5.4. BET chart (blue) of h-BN@magnetite prepared under continuous flow with a pulsed laser irradiating a pure iron target, operating at 1064 nm and 360 mJ, with the VFD tube 20 mm in diameter rotating at 7.5k rpm, tilt angle 45º and flow rate at 1 mL/min; (red) as received h-BN.

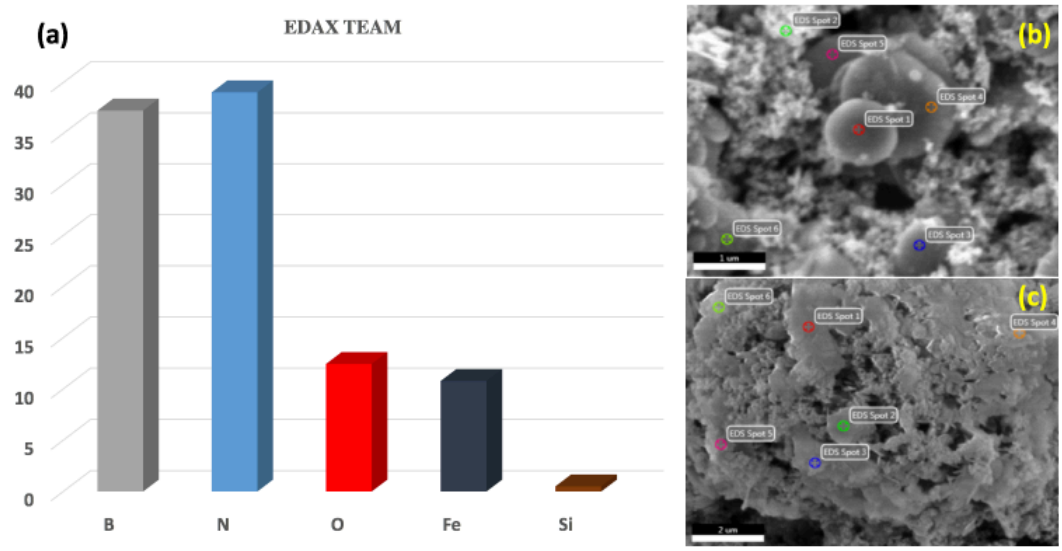

Figure S5.5. (a) EDX data for elemental analysis in b and c. (b and c) SEM images at various locations of (a) EDX data for elemental analysis in b and c. (b and c) SEM images at various locations of h-BN@magnetite composite prepared under continuous flow with a pulsed laser irradiating a pure iron target operating at 1064 nm and 360 mJ, with a glass tube 20 mm in diameter rotating at 7.5k rpm, tilt angle 45º and flow rate at 1 mL/min.h-BN@magnetite composite prepared under continuous flow with a pulsed laser irradiating a pure iron target operating at 1064 nm and 360 mJ, with a glass tube 20 mm in diameter rotating at 7.5k rpm, tilt angle 45º and flow rate at 1 mL/min.

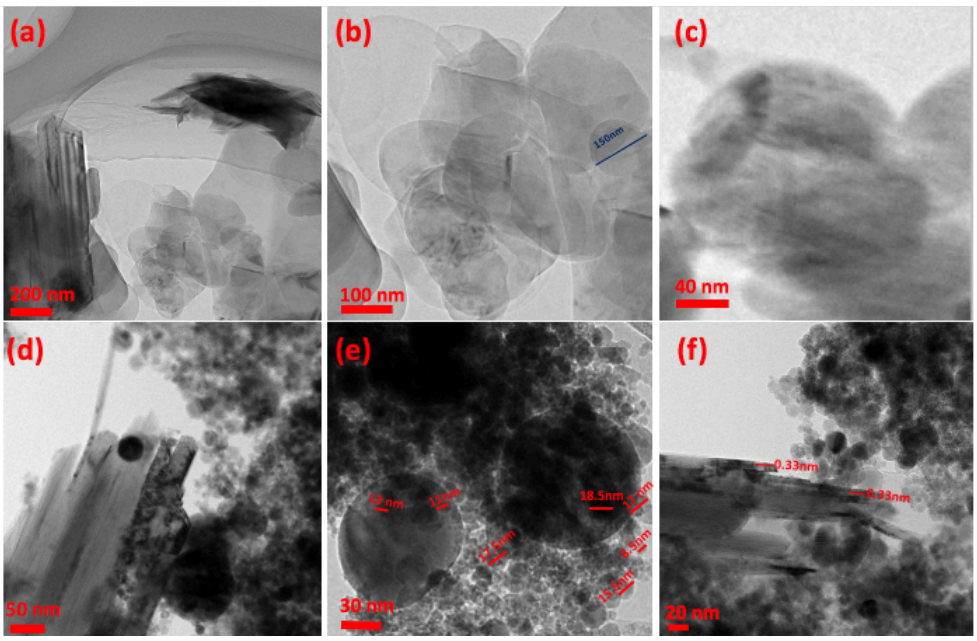

Figure S5.6. HRTEM images (a-c) as received h-BN, (d-f) h-BN@magnetite composite prepared using a pulsed laser irradiating a pure iron target operating at 1064 nm and 360 mJ, with a 20 mm glass tube rotating at 7.5k rpm, tilt angle 45º and flow rate at 1 mL/min.

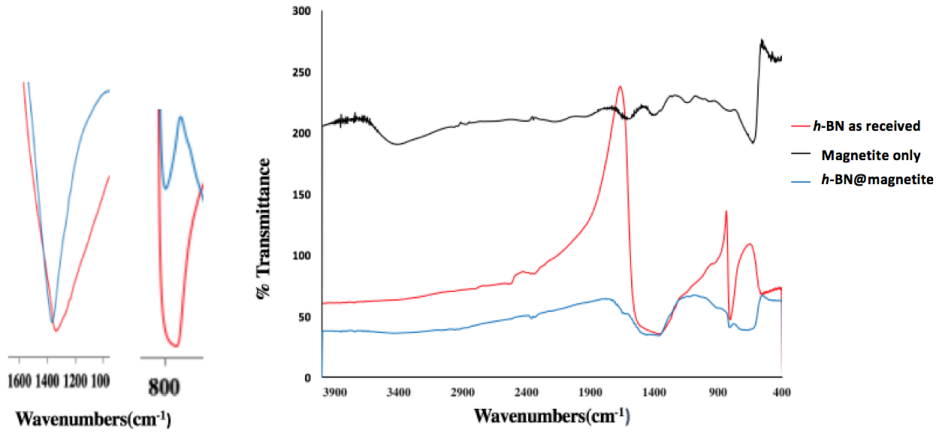

Figure S5.7. ATR FTIR spectra for as received h-BN and h-BN@magnetite composite compared with magnetite prepared with a pulsed laser irradiating a pure iron target, operating at 1064 nm and 360 mJ with a 20 mm OD tube rotating at 7.5k rpm, tilt angle 45º and a flow rate of water at 0.1 mL/min.[1] The h-BN@magnetite was prepared as for the magnetite but with h-BN dispersed in water (0.1 mg/mL) at a flow rate of 1 mL/min.

Control experiments: Three control experiments were undertaken to decouple any effect of the laser on the *h*-BN and shear stress in the dynamic thin film in the VFD, with the characterization of the material using SEM and XRD, and zeta potential.

1- **Processing *h*-BN in the VFD in the absence of a pulsed laser.** *h*-BN dispersed in water (0.1 mg/mL) was delivered via a jet feed to the base of a glass tube 20 mm in diameter using a jet feed, with the flow rate at 1 mL/min, rotational speed 7.5k rpm and tilt angle 45º. The color of the processed liquid was similar to the pre-processed sample, with the zeta potential similar at -19.7mV.

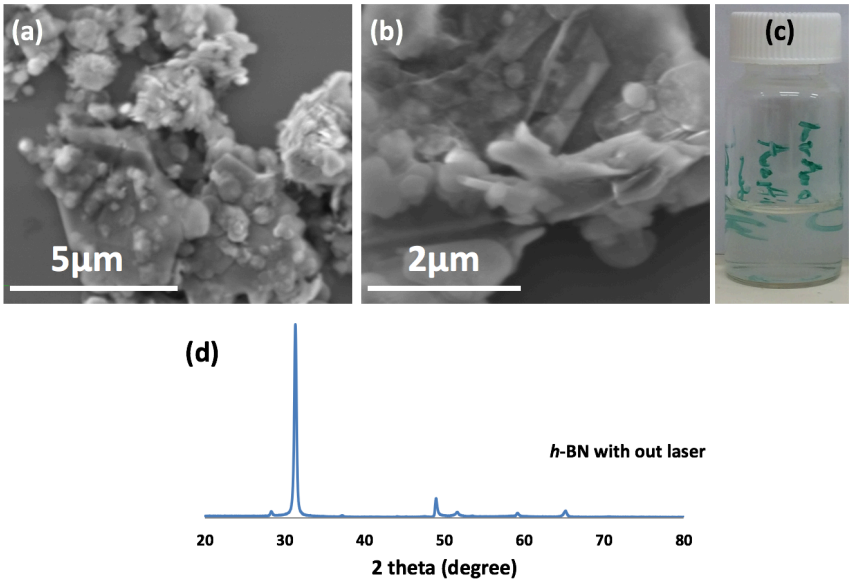

Figure S5.8. (a, b) SEM images for h-BN processed in the VFD under continuous flow with a flow rate of a dispersion of h-BN in water (0.1 mg/mL) at 1 mL/min, rotation speed 7.5k rpm, tilt angle 45º in the absence of a laser. (c) Photograph of the dispersion of h-BN solution after processing. (d) XRD of the h-BN after processing.

2- **Processing with the pulsed laser irradiating the solution without irradiating the iron target**. A dispersion of as received *h*-BN in water (0.1mg/mL) was delivered to the base of a 20 mm OD glass tube at 1 mL/min, with the tube rotating at 7.5k rpm and at a tilt angle of 45°; the pulsed laser was operated at 1064 nm and 360 mJ. The color of the processed liquid was similar to the pre-processed sample, with a similar zeta potential value at -18.4mV.

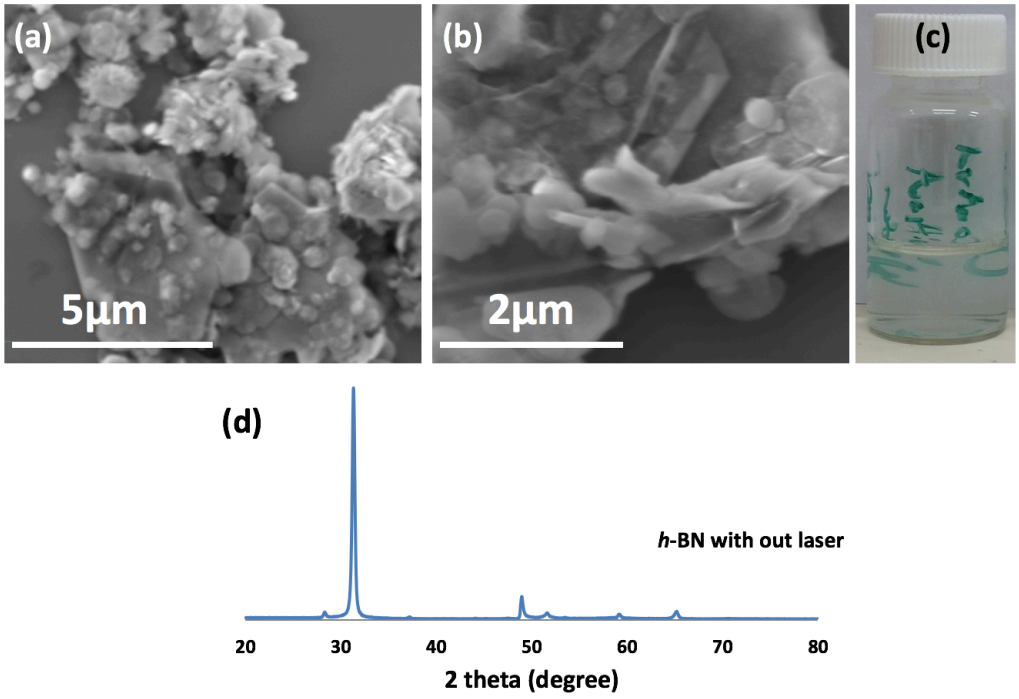

Figure S5.9. (a, b) SEM images for h-BN processed in a VFD, with a dispersion of the as received material delivered to the base of a 20 mm OD glass tube rotating at 7.5k rpm, at a flow rate of a dispersion of h-BN in water (0.1 mg/mL) at 1 mL/min for a tilt angle of 45º and the pulsed laser operating at 1064 nm and 360 mJ, without the laser irradiating the iron rod. (c) Photograph of the processed dispersion of h-BN. (d) XRD of h-BN after processing.

3- **Confined mode processing of a mixture of *h*-BN with IONPs (magnetite nanoparticles).** A mixture of *h*-BN dispersed in water (0.1 mg/mL) and preformed magnetite particles (0.5 mg/mL) previously prepared in the VFD using our recently reported procedure for the exclusive formation of this material.[1] The total volume of liquid in the tube was 1 mL, with the rotational speed set at 7.5k rpm, the tilt angle at 45°, and the processing time at 15 mins, in the absence of a laser. The color of the resulting solution was brown, as expected, and the SEM images similar to *h*-BN@magnetite composite prepared *in situ*. However, the zeta potential had two peaks, -8.03 mV and -17.3mV, presumably the former corresponding with some of the *h*-BN particles devoid of surface bound magnetite particles, noting that the latter is close to zeta potential for as received *h*-BN (-19.7mV). In contrast the zeta potential for *h*-BN@magnetite prepared directly in the presence of a laser is + or -37.2 mV.

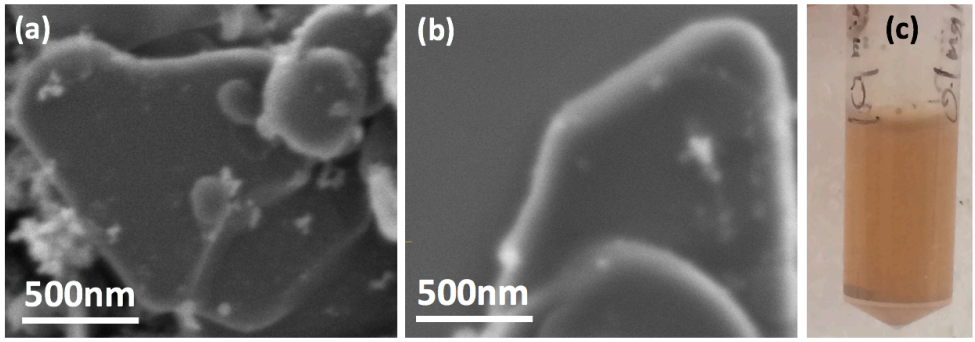

Figure S5.10. (a, b) SEM images for the material formed on processing 1 mL of a mixture of h-BN dispersed in water (0.1 mg/mL) and magnetite nanoparticles (0.5 mg/mL), using the confined mode of operation of the VFD (15 mins, 45° tilt angle, 7.5k rpm rotational speed, 20 mm OD glass tube), in the absence of laser irradiation. The magnetite nanoparticles (12 nm in diameter) where prepared using our published procedure in the VFD.[1] (c) Photograph of the h-BN@magnetite solution after processing under these conditions.

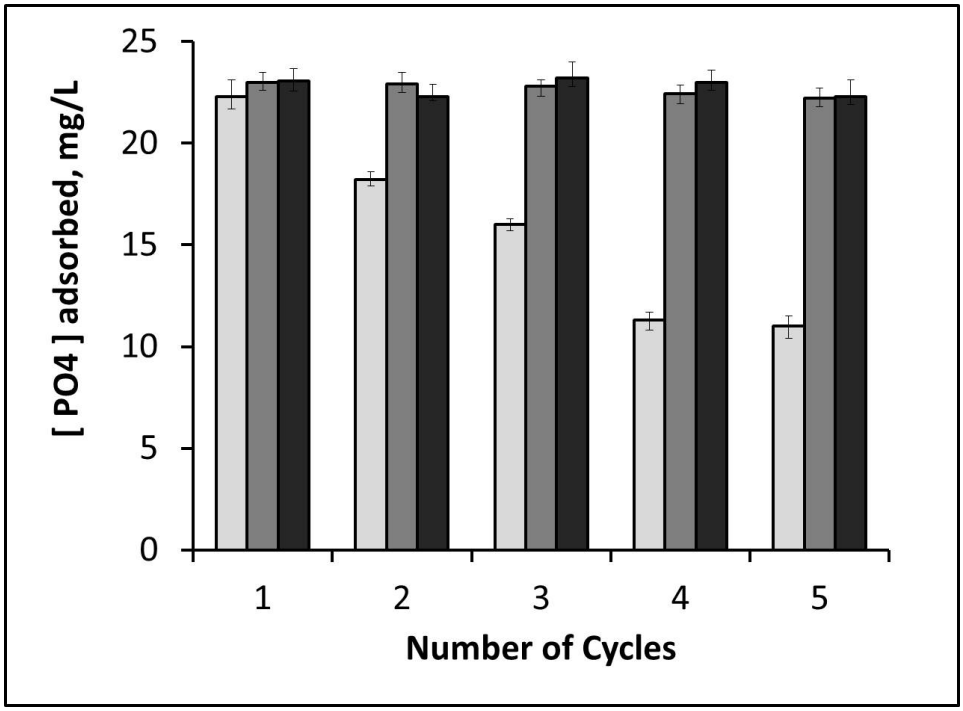

Figure S5.11. Individual amount of PO43- adsorbed in mg L^{-1} by each sequential cycle, for three different loadings of magnetic h-BN samples: (1) 10 mg adsorbent (light-grey columns); (2) 25 mg adsorbent (dark-grey columns); and (3) 50 mg adsorbent (black columns).

1- X. Luo, A. H. M. Al-Antaki, T. M. D. Alharbi, W. D. Hutchison, Y.-c. Zou, J. Zou, A. Sheehan, W. Zhang and C. L. Raston, *ACS Omega*, 2018, **3**, 11172-11178.

Chapter 6: Dynamic thin film mediated slicing of boron nitride nanotubes.

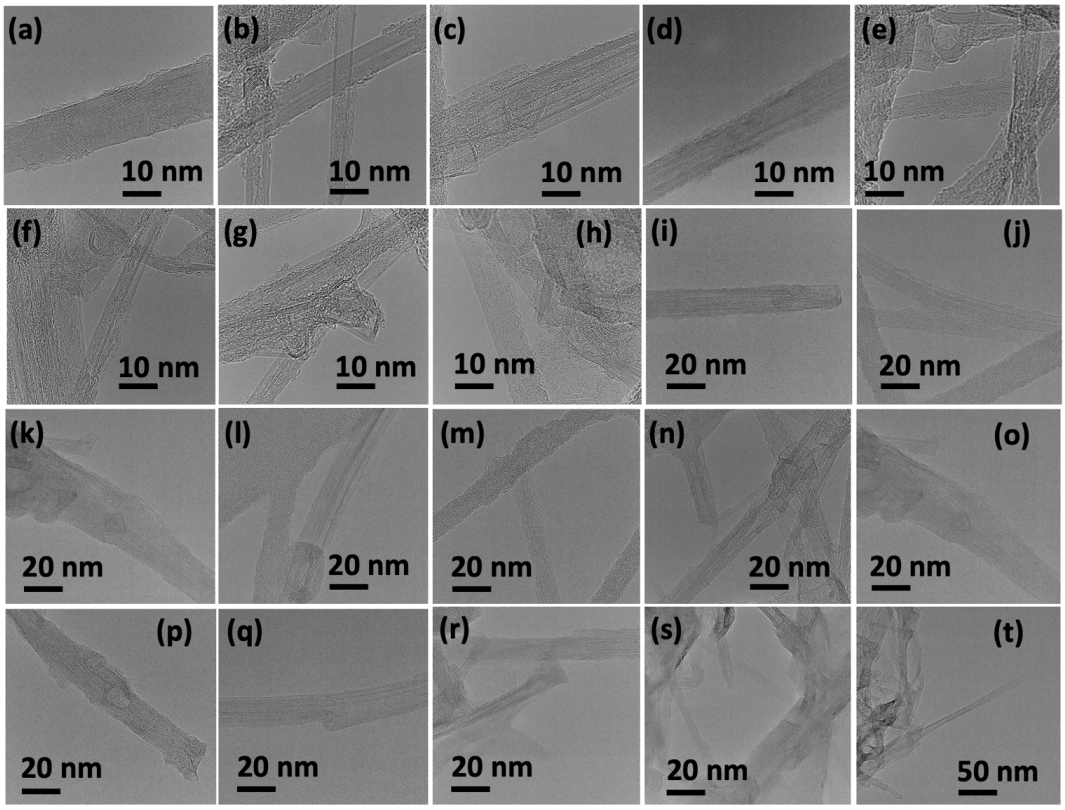

Figure S6.1. HRTEM images of drop cast BNNTs after purification the as received material, after 2.5 h at 60^{o}C followed by 3 h stirring in IPA and water (1:3) at 100^{o}C.

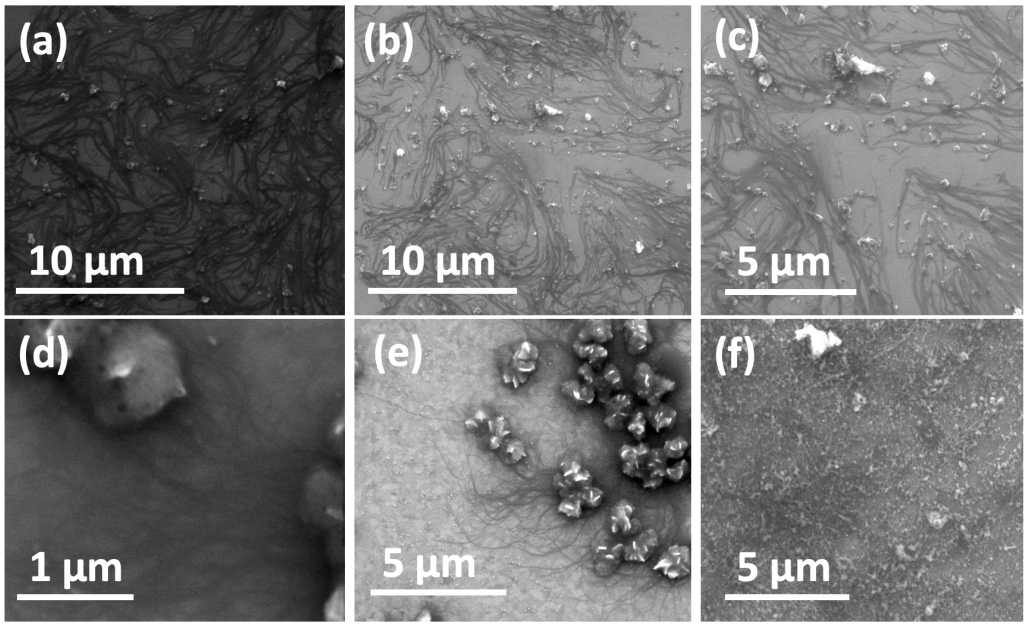

Figure S6.2. SEM images for drop cast of BNNTs (0.1 mg/mL) in toluene and water (1:1) rotational speed 7.5k rpm, confined mode for 1 h while irradiated with a 280 mJ NIR pulse laser. (a-c) pH of water 9. (d, e) pH of water 10. (f) pH of water 5.

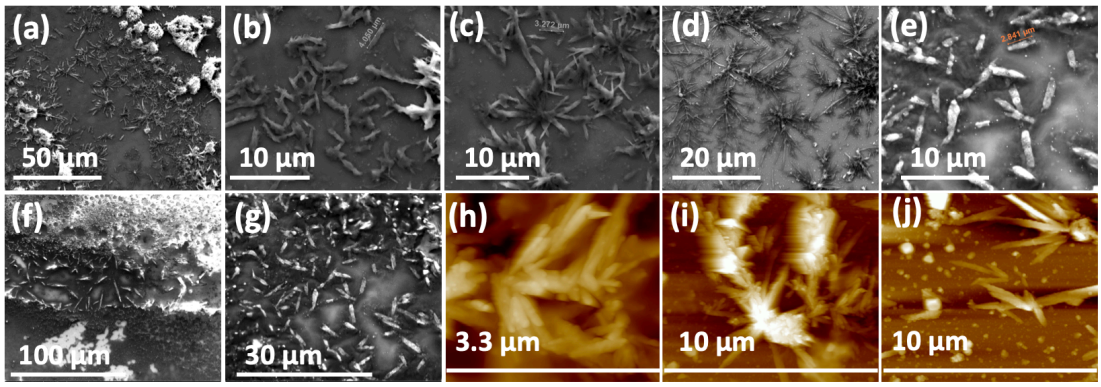

Figure S6.3. Drop cast BNNTs (0.1 mg/mL) in toluene and THF (1:1), flow rate 0.1 mL/min, flow rate of water at pH= 9, 0.15 mL/min, rotational speed 7.5k rpm, 280 mJ NIR, 45° tilt angle. (a-d) SEM images for aqueous phase. (e-g) SEM images for evaporated organic phase. (h-j) AFM images of the evaporated aqueous phase.

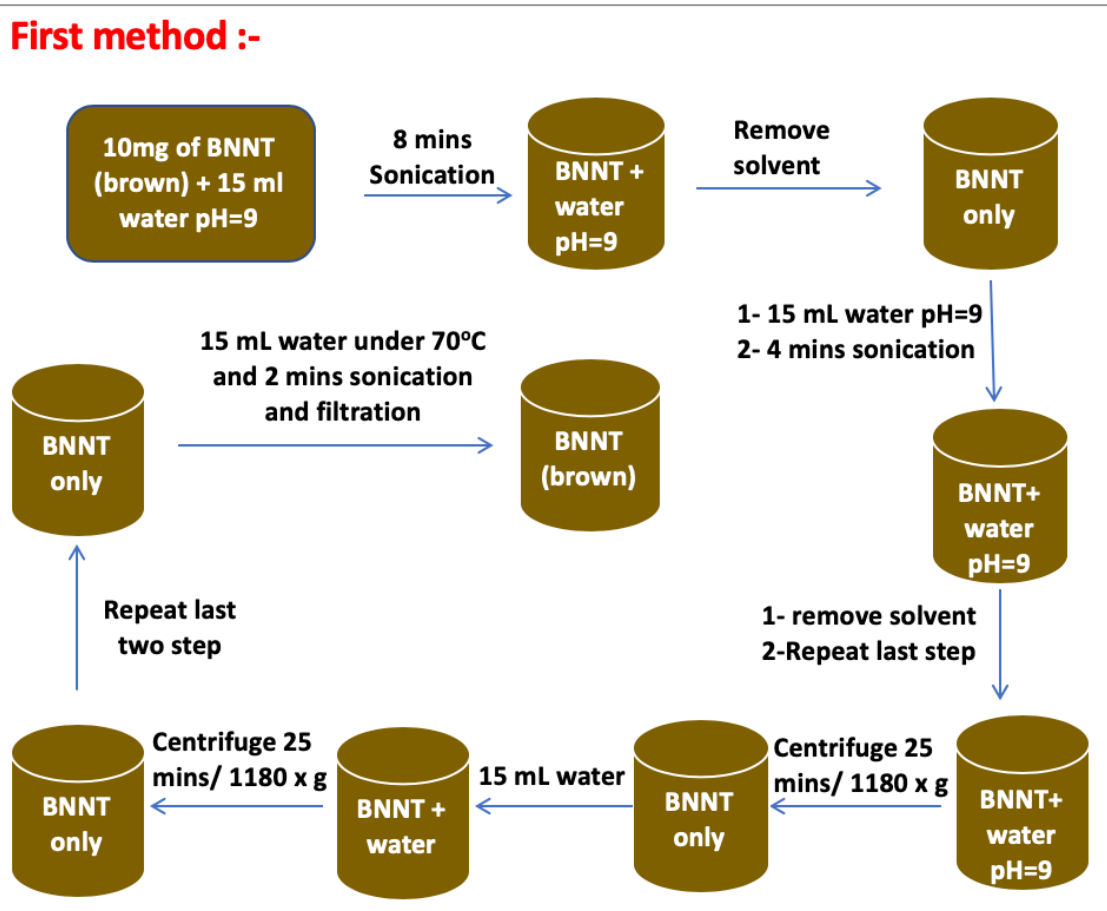

Figure S6.4. First step used to remove the impurities in as received BNNTs.

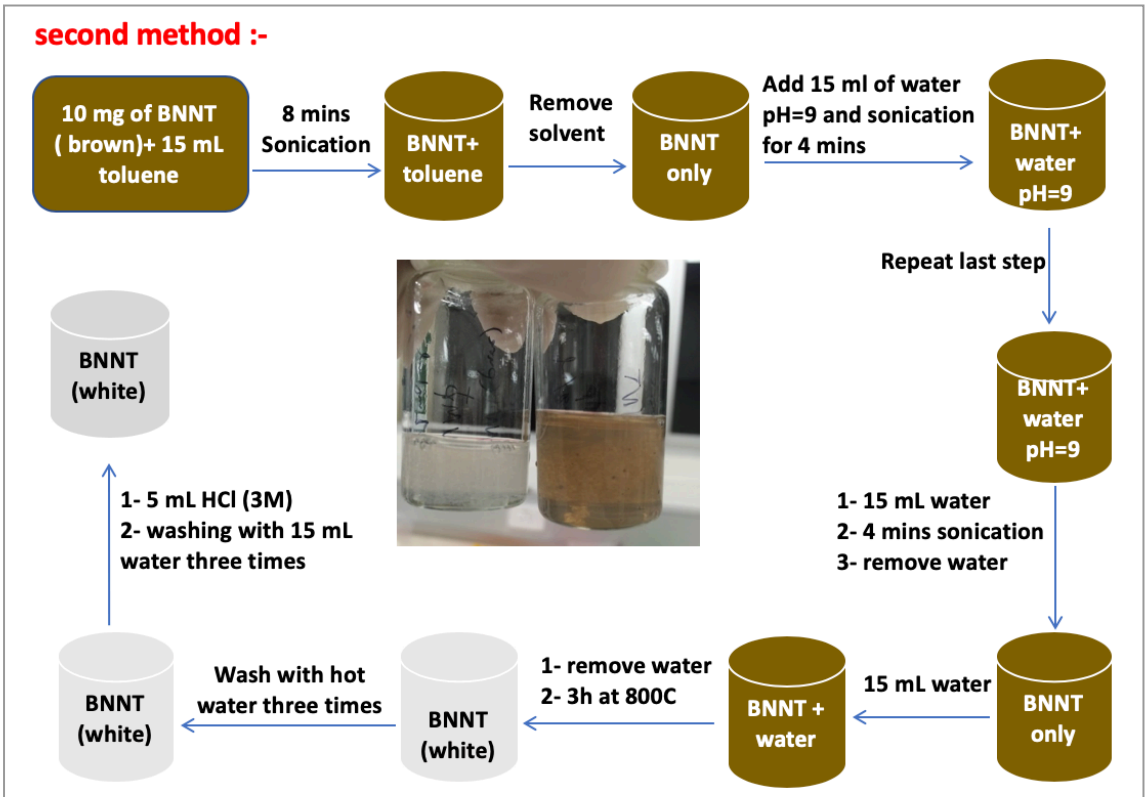

Figure S6.5. Second processing step 2 to purify as received BNNTs.

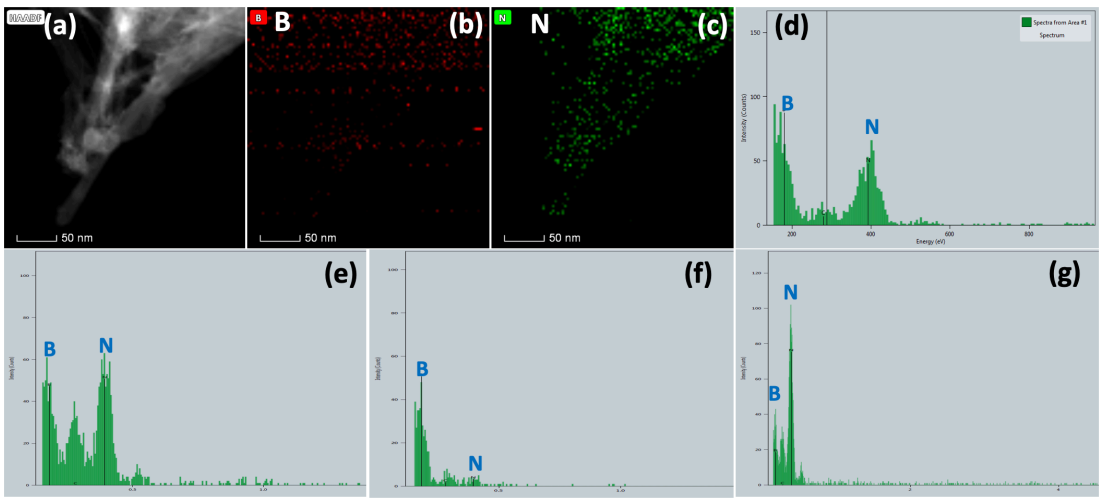

Figure S6.6. Purified BNNTs after 2.5 h at 60°C followed by 3 h stirring in IPA and water (1:3) at 100°C. (a-c) EDS mapping of purified BNNTs associated with HRTEM. (d) EDS spectrum. (e-g) EDS using HRTEM at different locations.

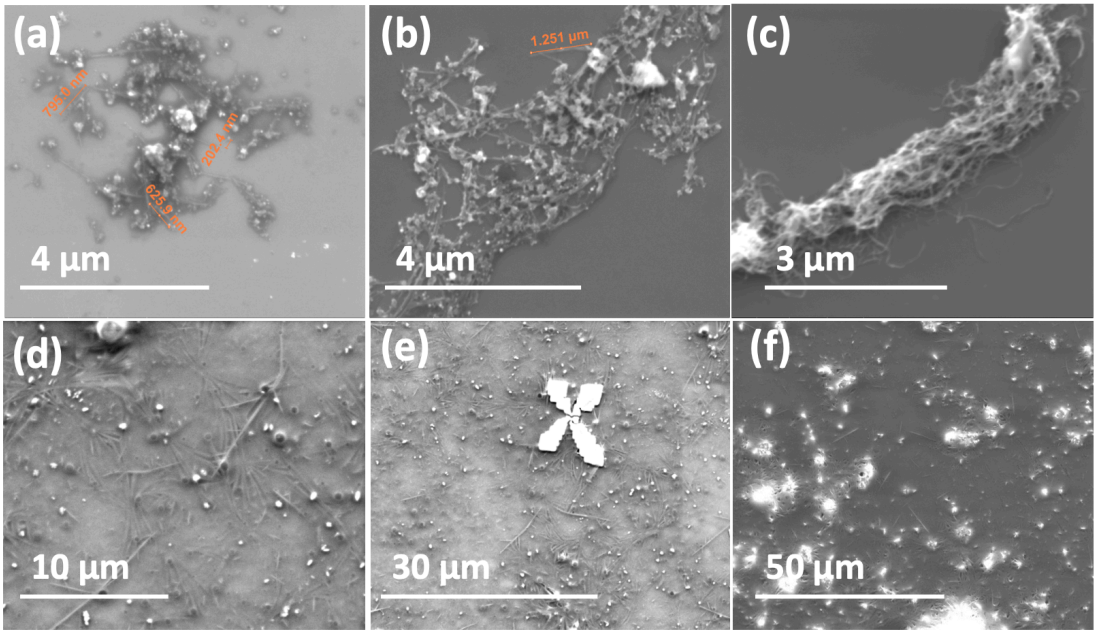

Figure S6.7. SEM images of drop cast BNNTs (0.1 mg/mL) in IPA and water (1:1), rotational speed 7.5k rpm, flow rate 0.1 mL/min, 45^{o} tilt angle. (a-c) Green laser processing (532 nm), 260 mJ. (d-f) NIR laser (1062 nm), 600 mJ.

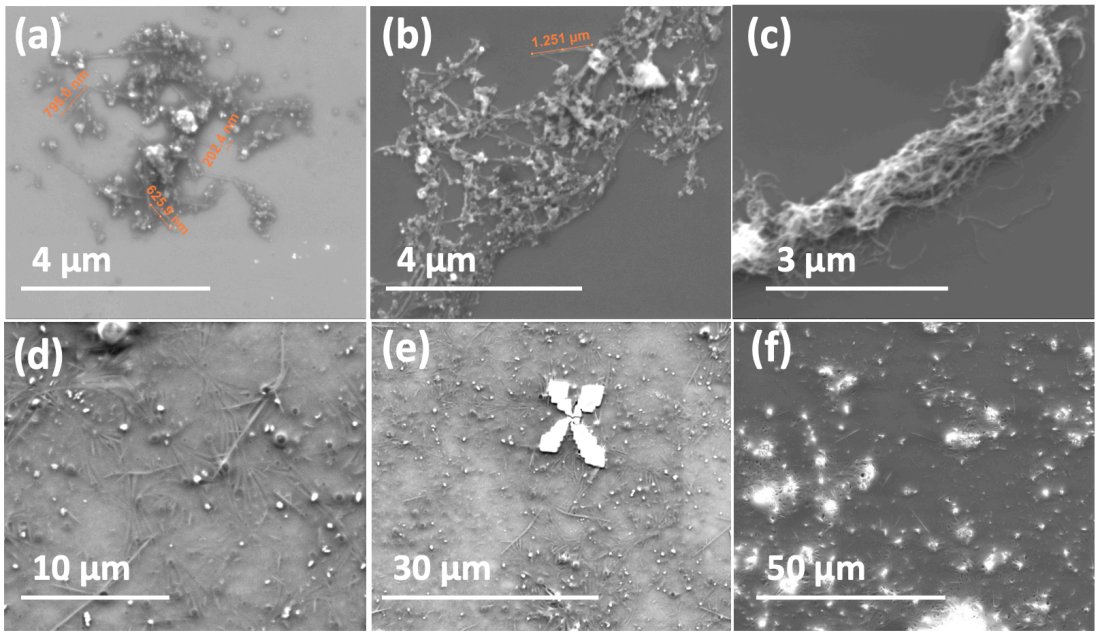

Figure S6.8. SEM images of drop cast BNNTs in IPA and water (1:1) after processing in a VFD with 400 mJ NIR laser irradiation, concentration 0.1 mg/mL, flow rate 0.45 mL/min, rotational speed 8.5k rpm and 45^{o} tilt angle.

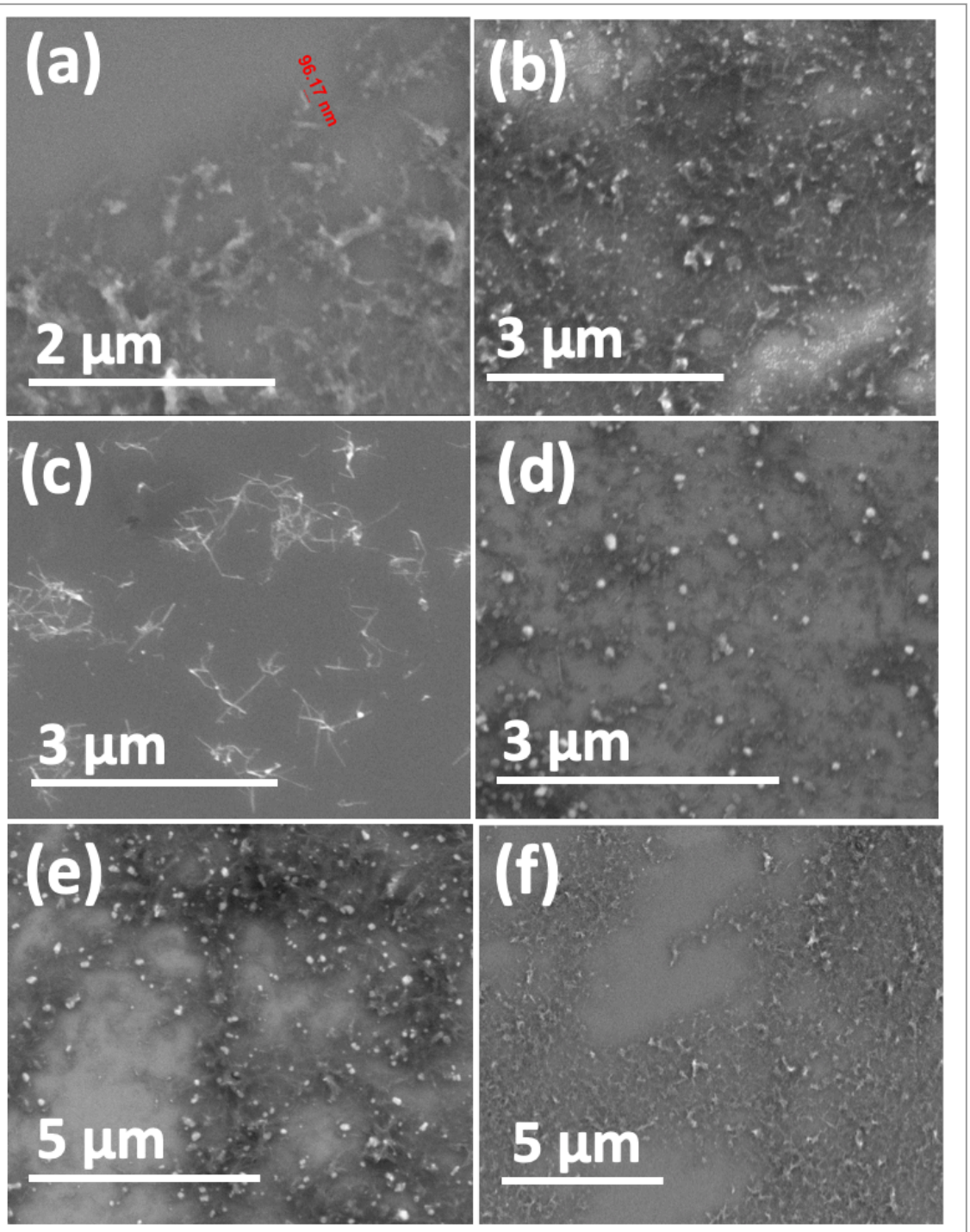

Figure S6.9. SEM images for drop cast BNNTs prepared in IPA and water (1:1) after processing in a VFD while irradiated with 600 mJ NIR laser, concentration 0.1 mg/mL, flow rate 0.45 mL/min, rotational speed 8.5k rpm and 45^{o} tilt angle.

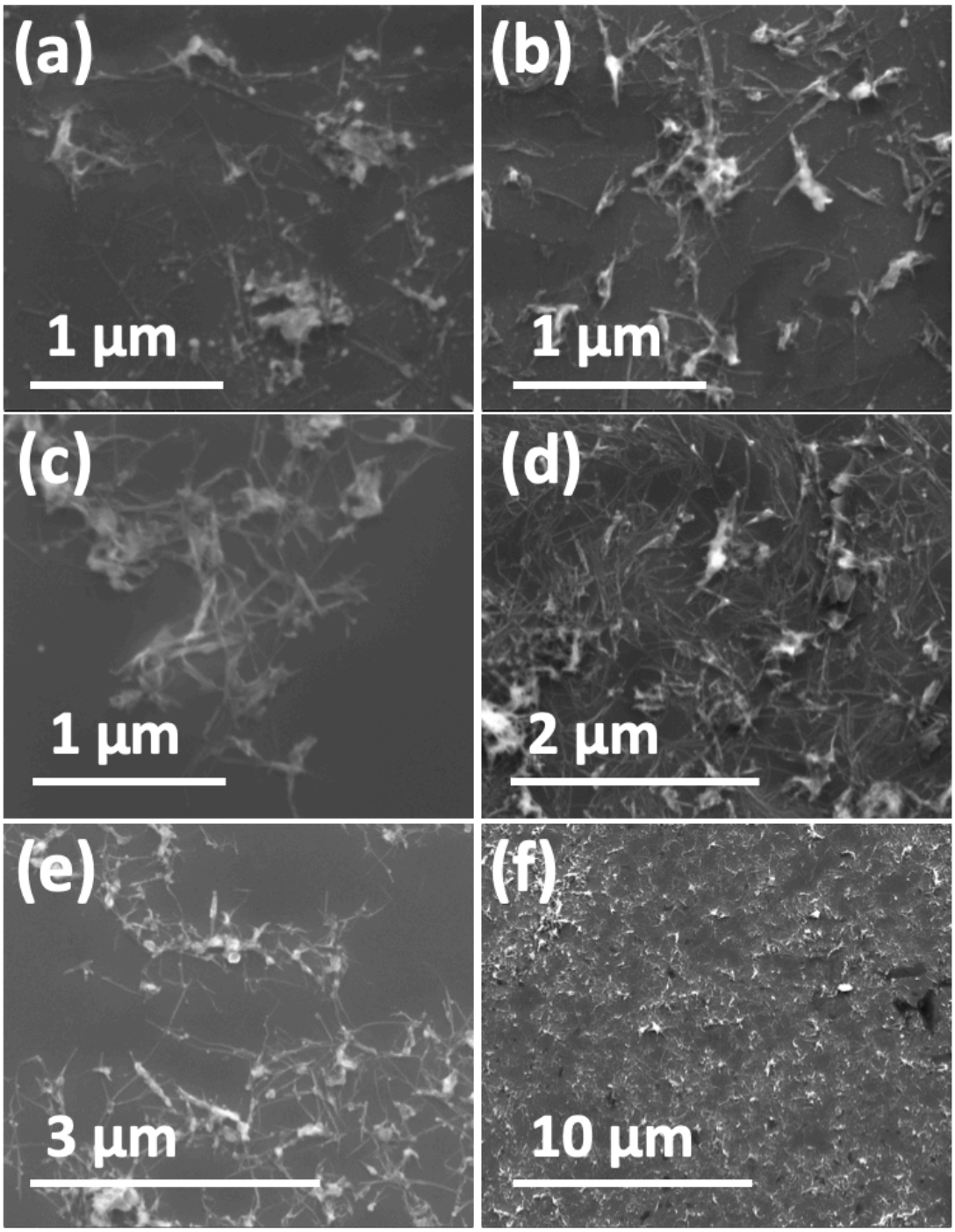

Figure S6.10. SEM images of drop cast sliced BNNTs in IPA and water (1:1) after processing in the VFD with a pulsed laser operating at 1064 nm and 250 mJ, concentration 0.1 mg/mL, flow rate 0.45 mL/min, rotational speed 8.5k rpm and 45^{o} tilt angle.

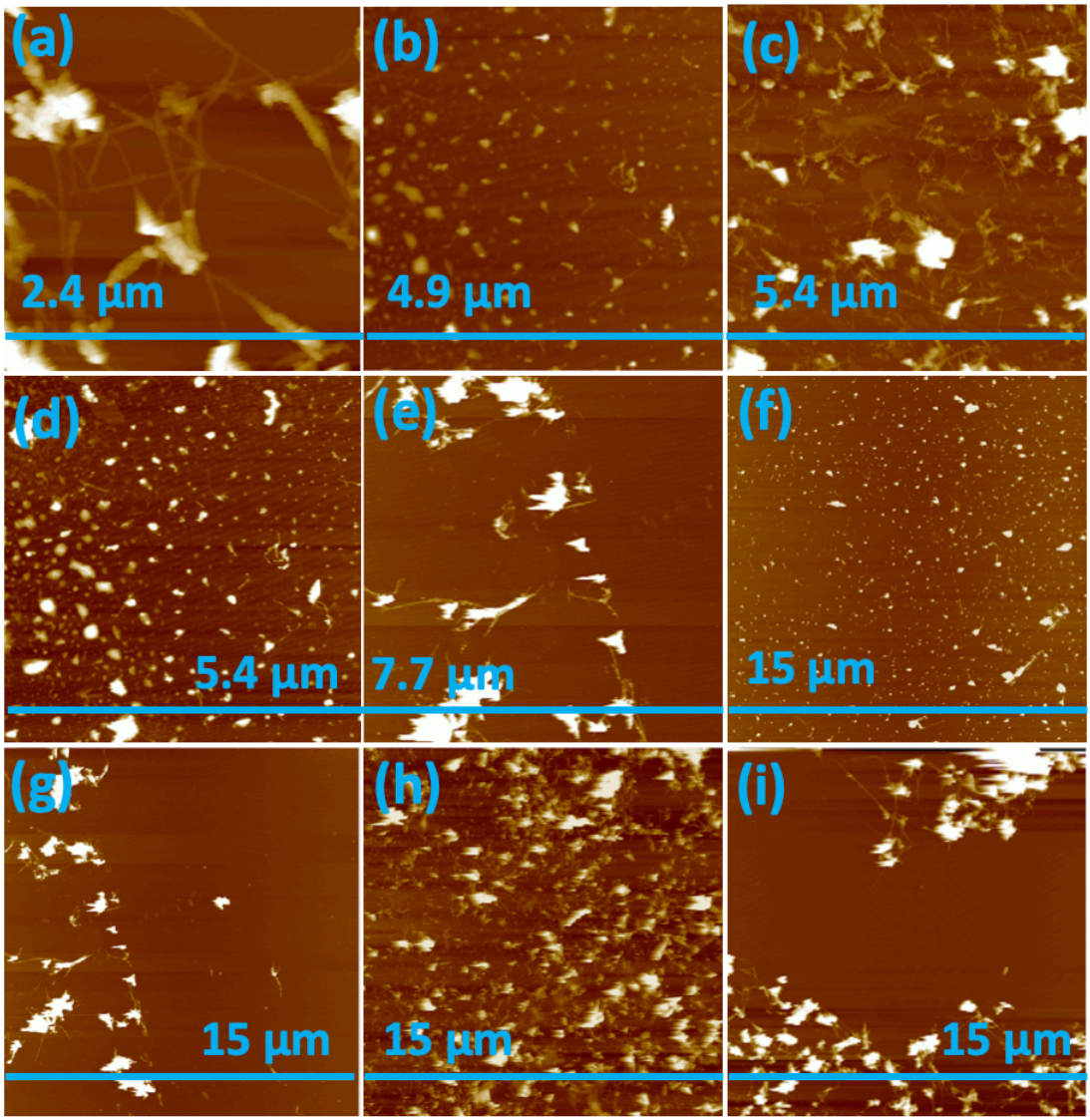

Figure S6.11. AFM images for drop cast sliced BNNTs prepared in IPA and water (1:1) after processing in the VFD with a pulsed laser operating at 1064 nm and 250 mJ, concentration 0.1 mg/mL, flow rate 0.45 mL/min, rotational speed 8.5k rpm and 45^{o} tilt angle.

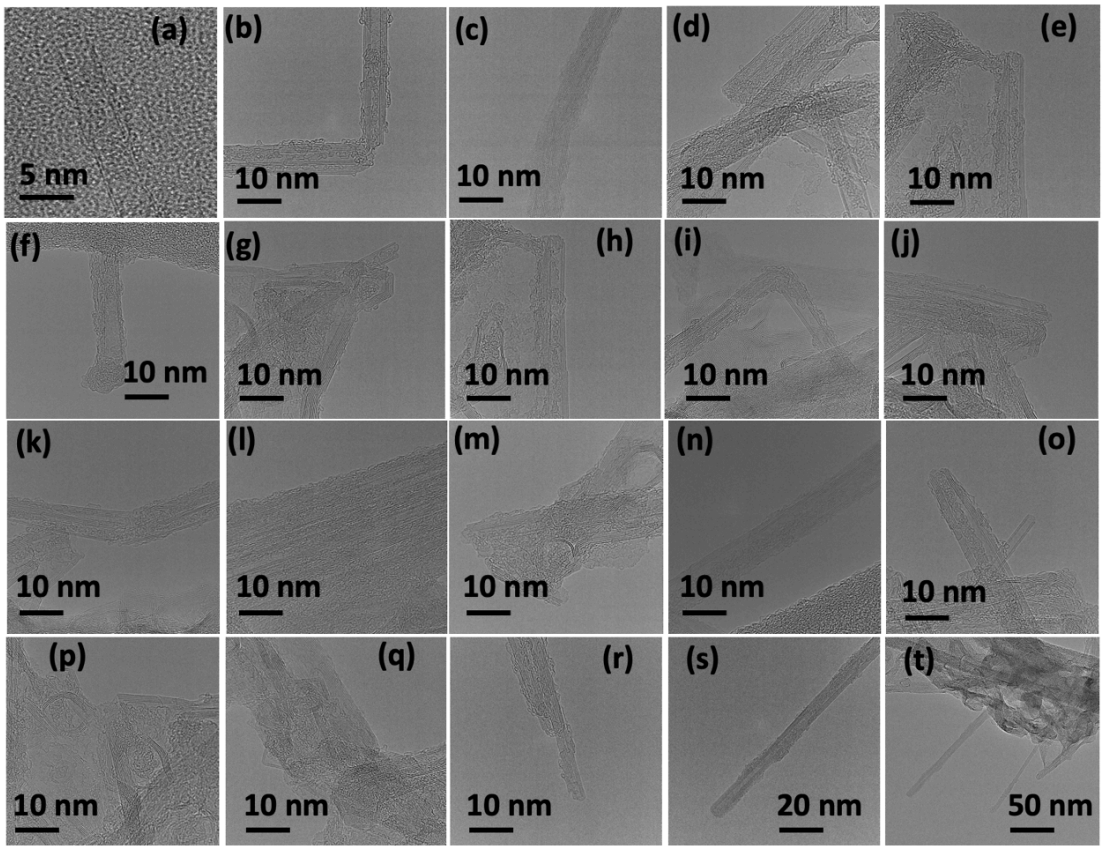

Figure S6.12. HRTEM images of drop cast sliced BNNTs in IPA and water (1:1) after processing in the VFD with a pulsed laser operating at 1064 nm and 250 mJ, concentration 0.1 mg/mL, flow rate 0.45 mL/min, rotational speed 8.5k rpm and 45^{o} tilt angle.

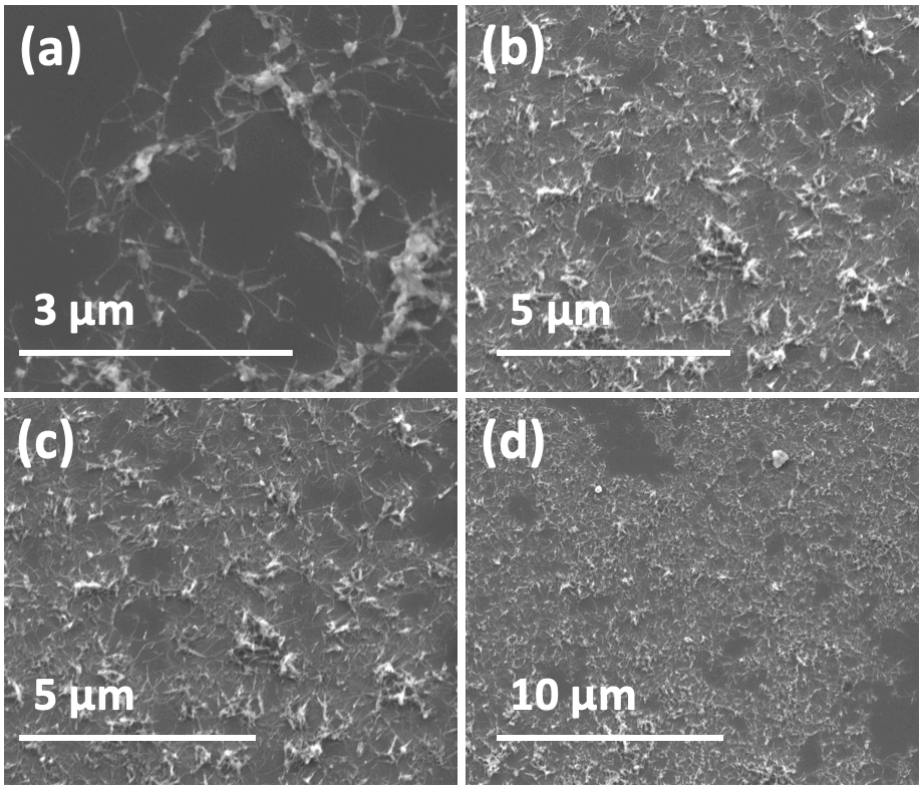

Figure S6.13. SEM images for drop cast of BNNTs in IPA and water (1:1) after processing in a VFD, concentration 0.1 mg/mL, flow rate 0.45 mL/min, rotational speed 8.5k rpm with 45^{o} tilt angle.

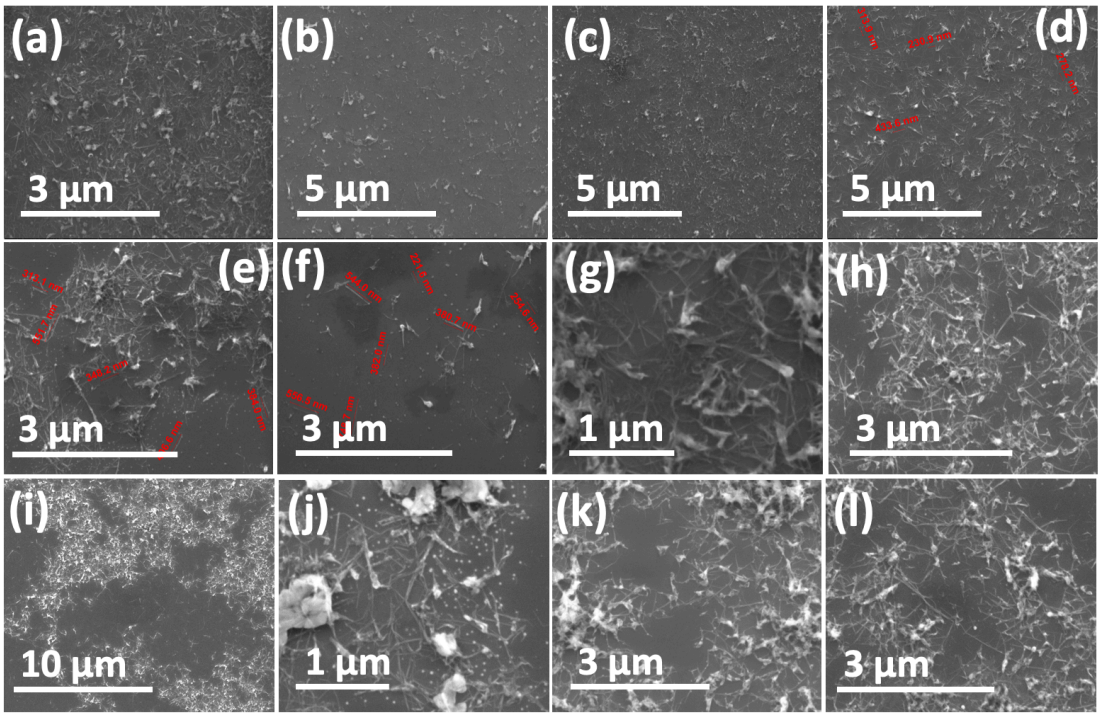

Figure S6.14. SEM images for drop cast of BNNTs (0.1 mg/mL) after processing in a VFD while irradiated with a 250 mJ NIR laser, flow rate 0.45 mL/min and 45° tilt angle. (a-c) DMF as the solvent, rotational speed 6k rpm. (d-f) DMF as the solvent, rotation speed 8.5k rpm. (g-i) DMF and water (1:1) as the solvent, rotational speed 8.5k rpm. (j-l) Water as the solvent, rotational speed 8.5k rpm.

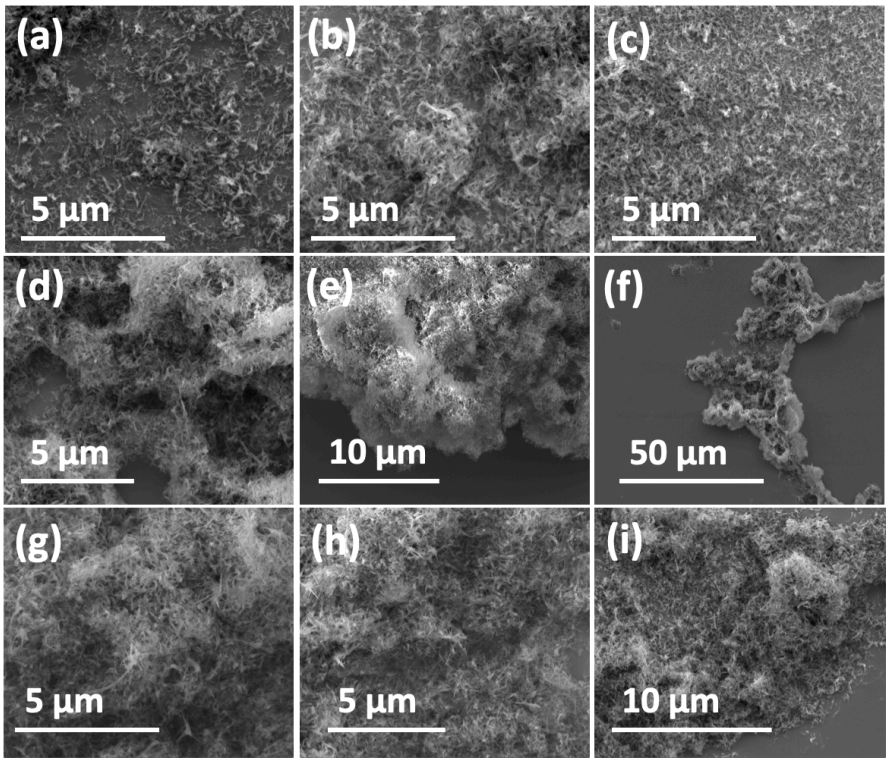

Figure S6.15. SEM images for drop cast of BNNT (0.2 mg/mL) in toluene and water (1:1) after sonication for 30 mins, with 1 mL of the milky suspension used in the confined mode of operation of the VFD for 15 mins, 45° tilt angle. (a-c) Rotational speed 4k rpm. (d-f) Rotational speed 6k rpm. (g-i) Rotational speed 8k rpm.

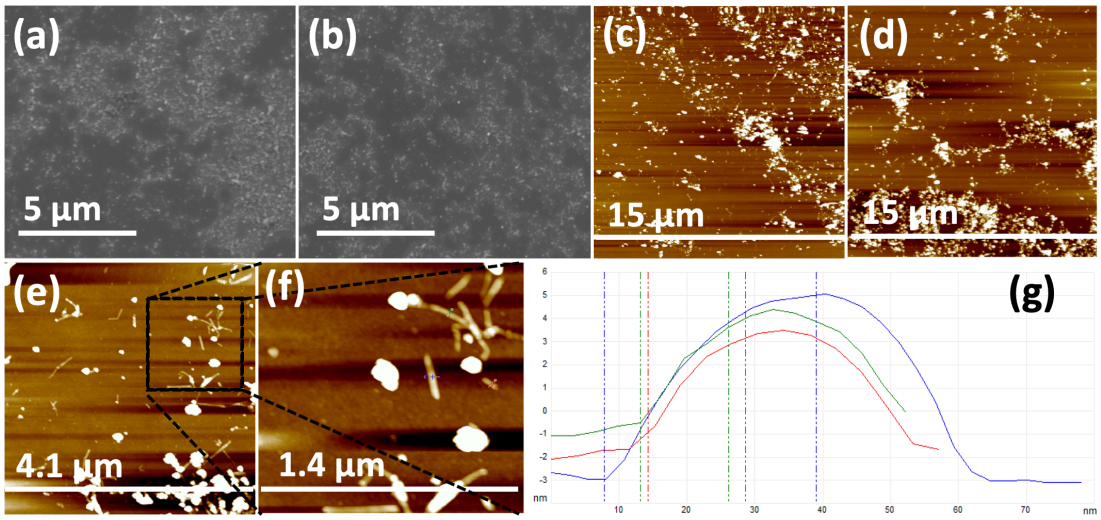

Figure S6.16. Drop cast of BNNTs in water (0.1 mg/mL) after VFD processing, flow rate 0.3 mL/min, rotational speed 7.5k rpm and 600 mJ NIR laser, with the tube at 45° tilt angle. (a, b) SEM images. (c-f) AFM images. (g) Height of three tubes measured from AFM images.

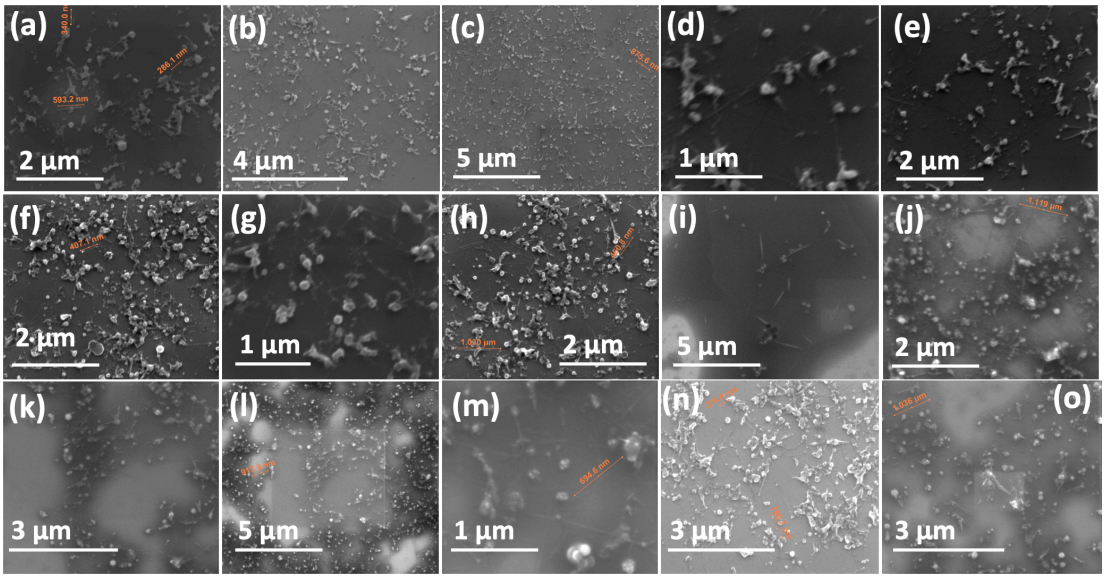

Figure S6.17. SEM images for drop cast BNNTs (0.1 mg/mL) in NMP, rotational speed 7.5k rpm, confined mode, 45° tilt angle. (a-c) 10 min, 280 mJ NIR laser irradiation. (d-f) 30 mins, 280 mJ NIR laser irradiation. (g-i) 1 h, 280 mJ NIR laser irradiation. (j-l) 30 mins, 400 mJ NIR laser irradiation. (m-o) 1 h, 400 mJ NIR laser irradiation.

Chapter 7: Continuous flow copper laser ablation synthesis of copper (I and II) oxide nanoparticles in water

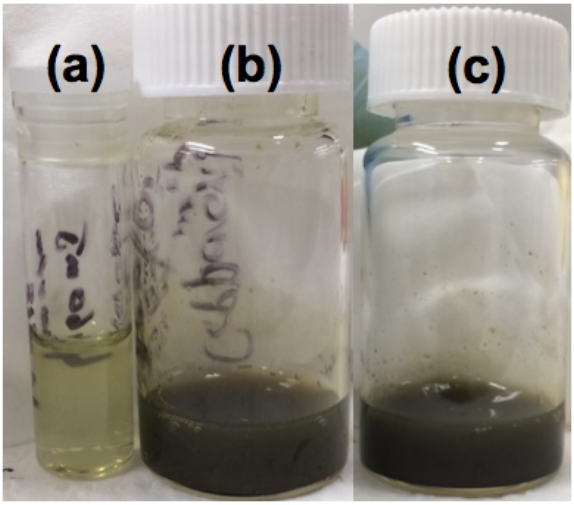

Figure S7.1. Confined mode synthesis in a VFD for 15 mins, for 1 mL of water, tilt angle 45º, and rotational speed 7.5k rpm, coupled with a 1064 nm pulse laser operating at (a) 450 mJ, (b) 550 mJ, and (c) 600 mJ.

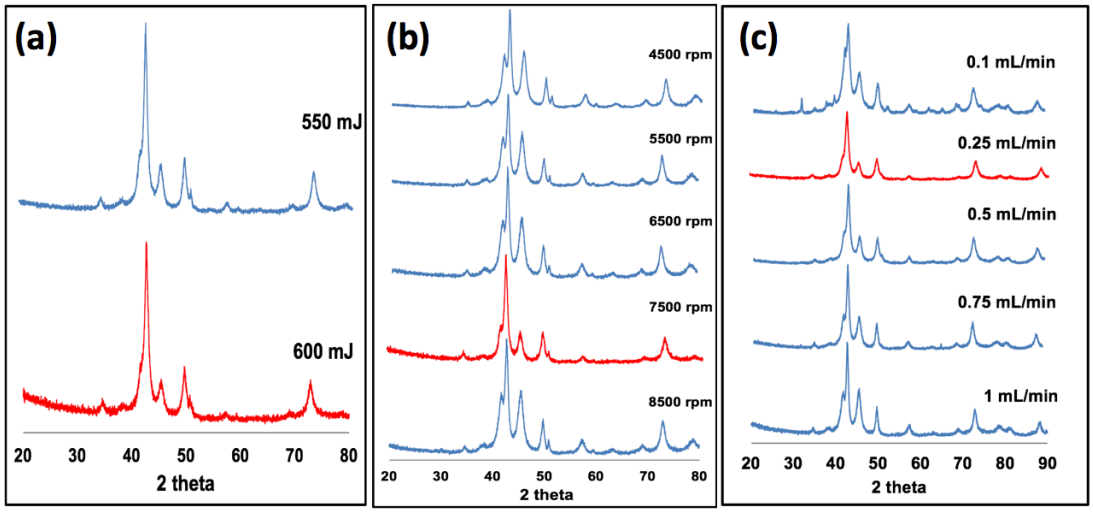

Figure S7.2. X-ray diffraction data (Co source, λ = 1.7889 Aº): (a) Different laser power (550 mJ, 600 mJ) for 15 mins of VFD processing in the confined mode, for 1 mL of water, and rotation speed 7.5k rpm. (b) Confined mode for 15 mins, 1 mL of water and laser power at 600 mJ with different rotation speeds of the glass tube in a VFD (4.5, 5.5, 6.5, 7.5 and 8.5k rpm). (c) Continuous flow processing at different flow rates (0.1, 0.25, 0.5, 0.75 and 1 mL/min), rotational speed 7.5k rpm, laser power 600 mJ, to collect 10 mL of the liquid. All experiments were at a tilt angle of 45º.

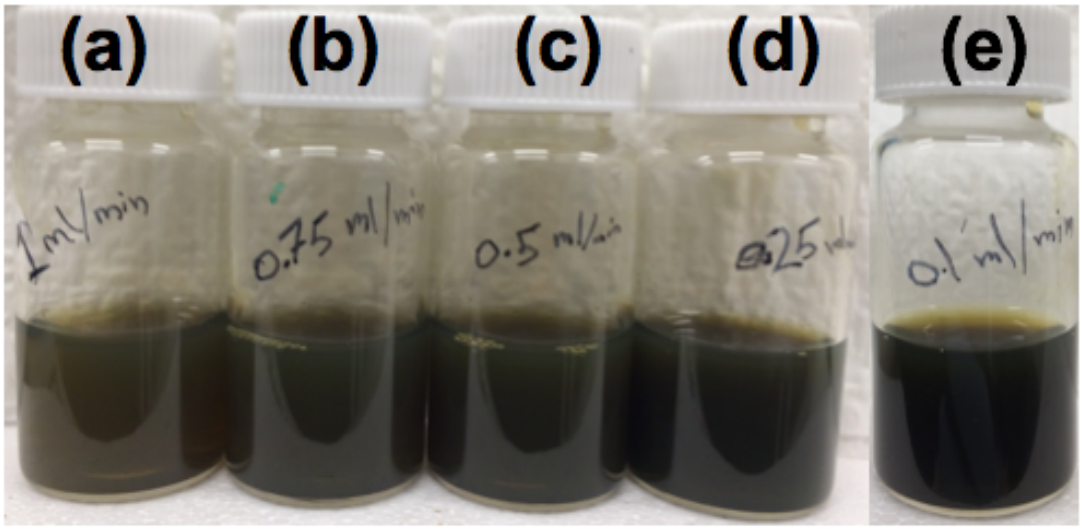

Figure S7.3. Photographs of solutions from 10 mL of processed liquid generated for the experiments in Fig.S2c at flow rates of (a) 1 mL/min, (b) 0.75 mL/min. (c) 0.5 mL/min, (d) 0.25 mL/min, (e) 0.1 mL/min.

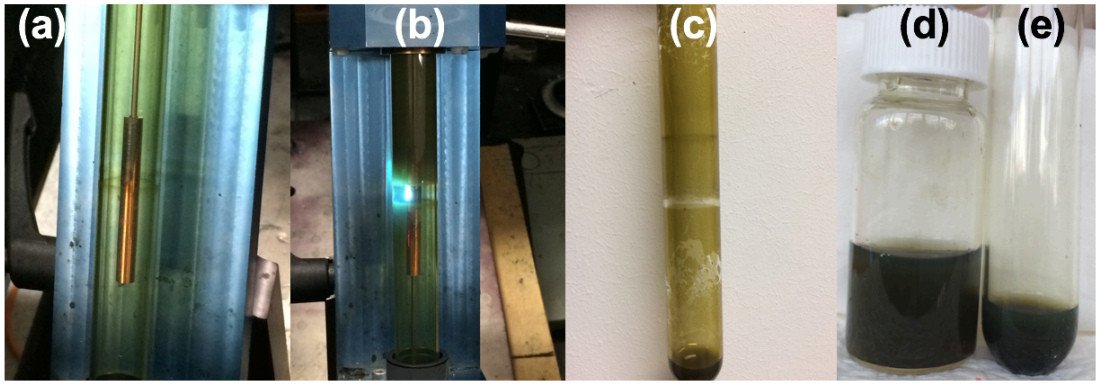

Figure S7.4. Photographs showing (a) the copper rod positioned inside the glass tube in a VFD rotating at 7.5k rpm, (b) 600 mJ pulsed laser irradiation (1064 nm wavelength) of the copper rod for (a) operating in the confined mode after 15 min, (c) the VFD tube after 2 h of continuous flow with the tube rotating at 7.5k rpm in the VFD housing the copper rod irradiated at 600 mJ, as for (a), (d) the solution exited from the VFD for experiments in (c), and (e) the solution left in the VFD tube after 2 h of the processing. All experiments were at a tilt angle of 45º.

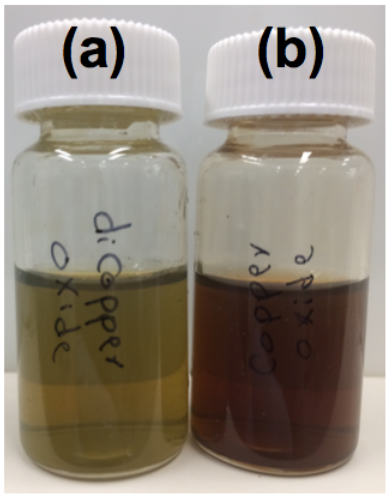

Figure S7.5. (a) Dispersion of Cu_2ONPs in water produced at 600 mJ pulsed laser power, 7.5k rpm rotational speed and at 0.25 mL/min, tilt angle 45º. (b) Dispersion of CuONPs after the solution from (a) was heated in oven at 50ºC for 10 h.

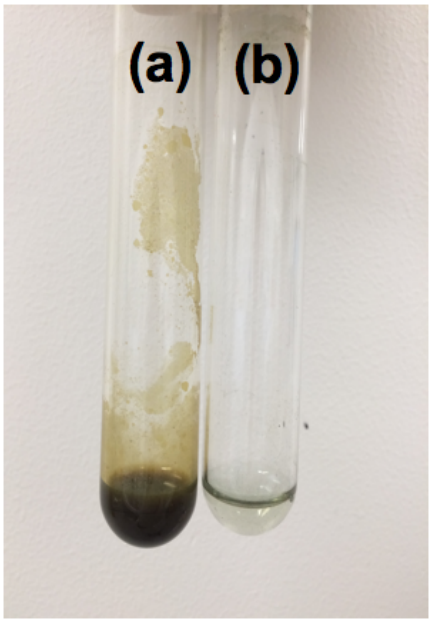

Figure S7.6. Solutions after 15 min confined mode experiments, rotational speed 7.5k rpm, pulsed laser 600 mJ and tilt angle 45º under different atmospheres: (a) air and (b) nitrogen gas.

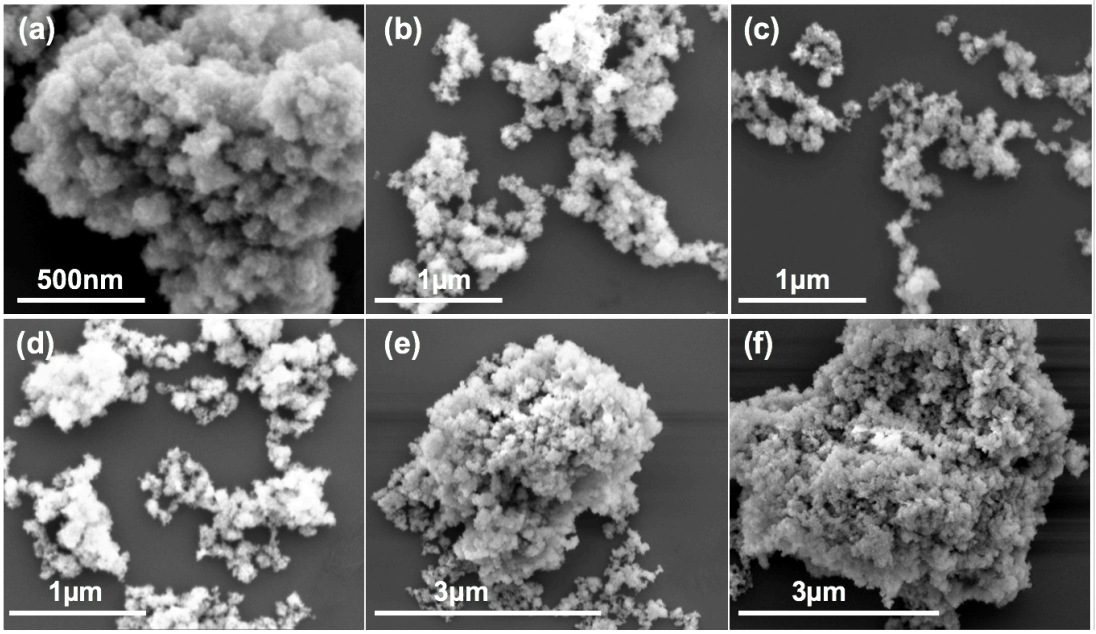

Figure S7.7. SEM images prepared via drop cast of material formed and spin coating, using a VFD under continuous flow of water at 0.25 mL/min, with the glass tube at 45º tilt angle and rotating at 7.5k rpm, using a 1064 nm pulsed laser operating at 600 mJ, irradiating a pure copper target, (a-c) as prepared Cu_2ONPs and (d-f) CuONPs after heating the as prepared solutions at 50ºC for 10 h.

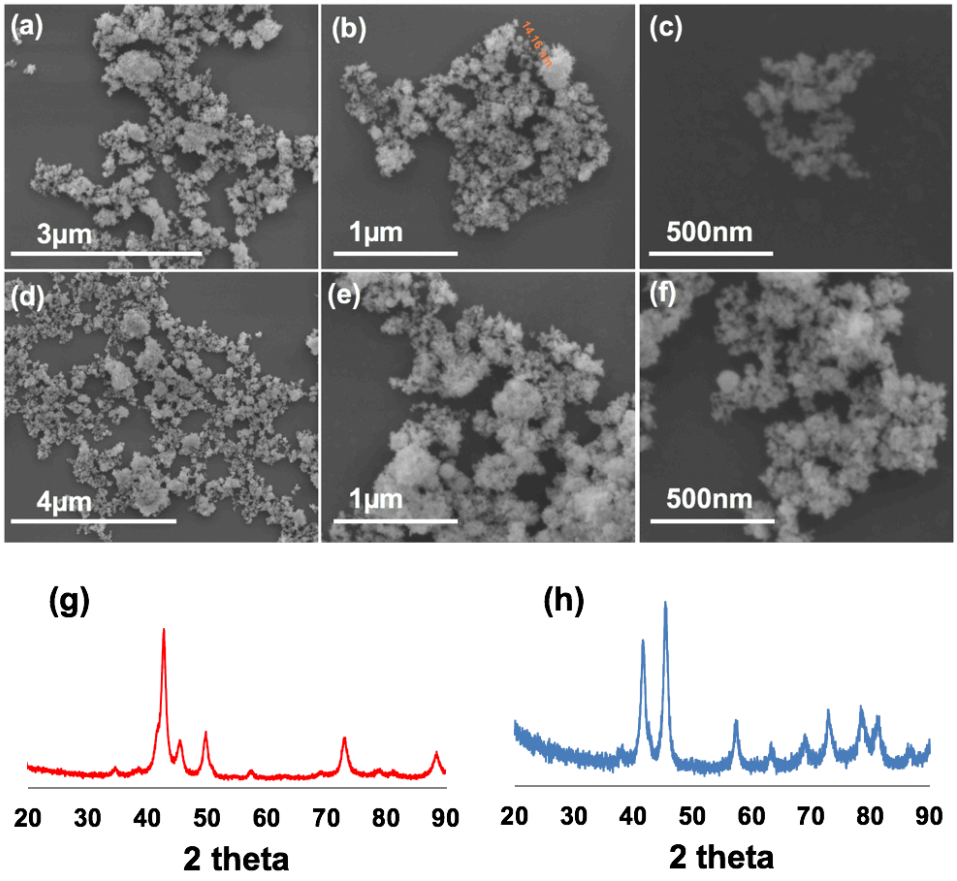

Figure S7.8. SEM images of material after drop casting solutions left in the tube following the experiments in Fig. S7: (a-c) Cu_2ONPs (d-f) CuONPs, (g) XRD for dicopper oxide in the tube, and (h) XRD for copper oxide after leaved Cu_2ONPs collected from the tube as solution in oven at 50ºC for 10 h.

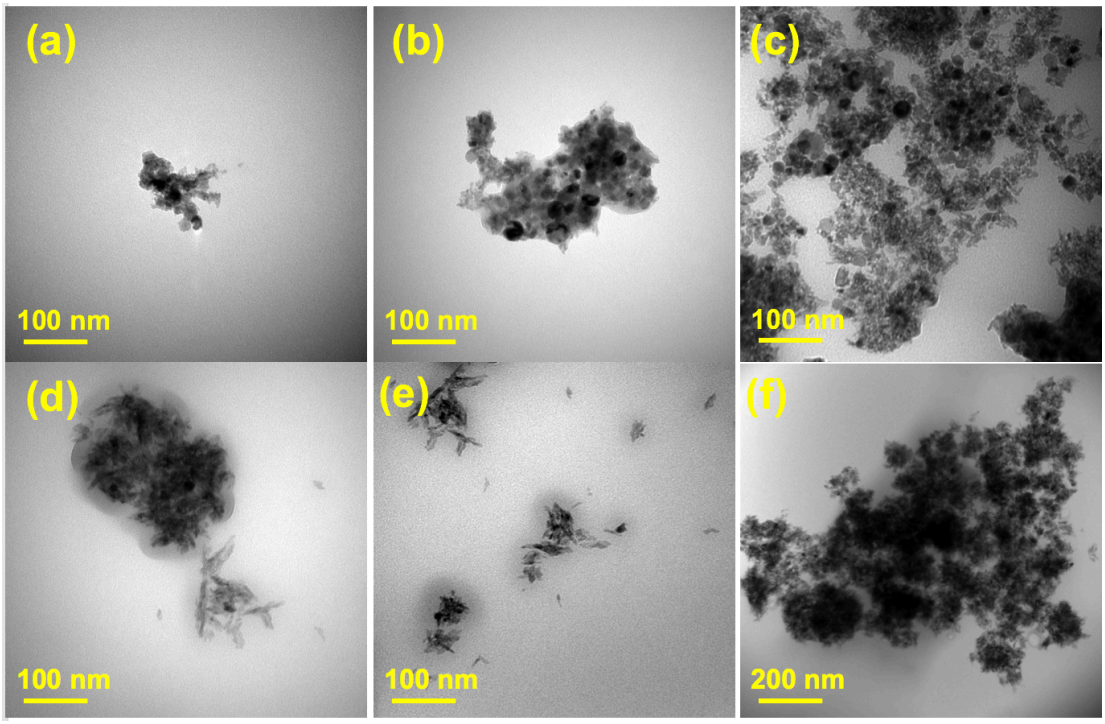

Figure S7.9. TEM images of material formed using a VFD under continuous flow of water at 0.25 mL/min, 45º tilt angle, using a 1064 nm pulsed laser operating at 600 mJ irradiating a copper target, (a-c) as prepared Cu_2ONPs and (d-f) CuONPs after heating as prepared solutions at 50ºC for 10 h.

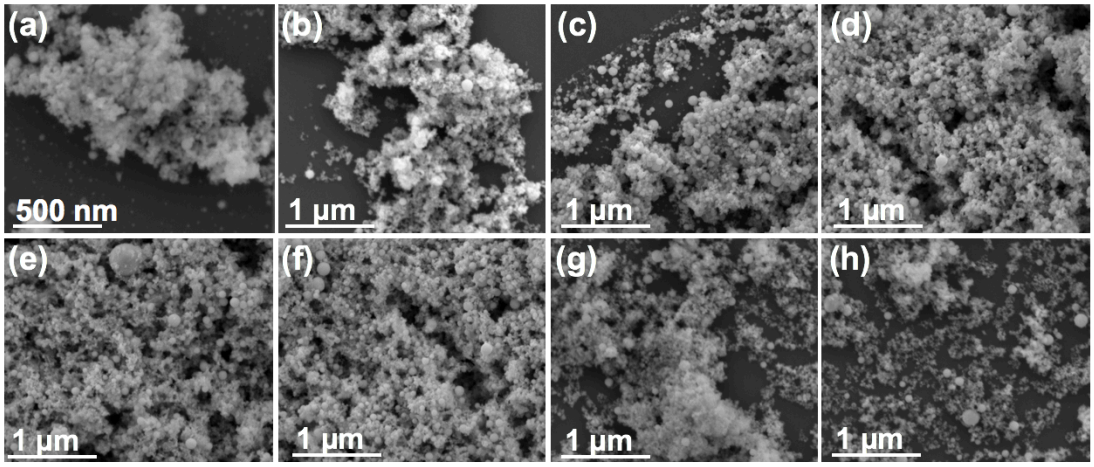

Figure S7.10. SEM images of material deposited by drop casting material formed using a VFD in the confined mode for 1 mL of water for 15 min, with the glass tube at 45º tilt angle and rotating at 4k rpm, using a 1064 nm pulsed laser operating at 600 mJ irradiating a copper target.